鉄基磁性微粒子を孤立分散した半導体酸化チタン膜の合成と磁気抵抗の光誘起効果の測定

（研究課題番号 １５３６０３３１）

平成１５年度～平成１７年度
科学研究費補助金（ 基盤研究(B)）研究成果報告書

平成１８年３月

研究代表者　　入戸野　修
福島大学　共生システム理工学類教授

本書は科学研究費補助金「基盤研究(B)」（鉄基磁性微粒子を孤立分散した半導体酸化チタン膜の合成と磁気抵抗の光誘起効果の測定）を得て行われた研究成果をまとめたものである。

本研究の目的は，異種物質を複合した膜中の隣接した異種物質（金属・半導体）の界面で起こる電子状態を光（含紫外線）照射により刺激して，電子授受の確率を増大させ伝導電子を過剰供給し孤立磁性微粒子間のトンネル電流の増大を図り，その結果として磁気抵抗効果を増大させること（光誘起磁気抵抗効果）を目指すものである．本研究では，対象とする透明材料として，光誘起による電子授受能の大きい透明半導体二酸化チタンを，また，磁性微粉体として純鉄を選出した．非磁性膜中に分散した磁性微粒子における磁気抵抗効果はグラニュラーＧＭＲとして知られる．一方，二酸化チタン（半導体）は光触媒として知られ，光学的にも安定性が高く，表面での光励起によりｄ電子の授受を利用して酸化分解による抗菌効果，セルフクリーニング効果が発現し，それらの機能は紫外線ＵＶ照射で活性化することが知られている．

本研究は，二酸化チタン中に鉄基磁性微粉体（径＜20nm）をトンネル電流が流れる程度に孤立分散させた膜を合成し，①膜の微細構造を解析し，②光吸収の測定，③外部からの光照射による膜の導電率変化を計測するとともに，④光と磁場の重畳した条件下での磁気抵抗を測定することで光誘起磁気抵抗効果を検証することを目指す基礎的研究である。

本研究の遂行中，各年度に想定外のターゲット配置設計上の不備，薄膜堆積時のガス流安定制御性や真空排気系の故障（ターボポンプの交換等のトラブル）などが発生し，さらに，研究代表者が不測の交通事故で約３ヶ月間試料膜の合成ができなかったこともあり，当初予定した研究計画の約５０％程度しか達成できなかった。しかしながら，本研究は基盤研究（基礎的研究）である性格上，同時に実施していた類似の機能性を有する薄膜作成の研究にも資する新しい発見や研究テーマの発掘などがあり，今後この種の機能性ナノコンポジット膜を合成するために有益な資料を多数集積することができた。

研究組織

研究代表者　：入戸野　修　（福島大学・共生システム理工学類教授）
研究分担者　：山 口　克彦　（福島大学・共生システム理工学類助教授）
研究分担者　：史　　蹟　（東京工業大学大学院理工学研究科助教授）

交付決定額（配分額）

（金額単位：円）

	直接経費	間接経費	合　計
平成１５年度	7,600,000	0	7,600,000
平成１６年度	5,000,000	0	5,000,000
平成１７年度	2,300,000	0	2,300,000
総　計	14,900,000	0	14,900,000

研 究 発 表（研究関連論文を含む）

（1）学会誌等：

1) Katsuhiko Yamaguchi, Shinya Tanaka, Osamu Nittono, Koji Yamada and Toshiyuki Takagi : Monte Carlo simulation for magnetic dynamic processes of micromagnetic clusters with local disorder, Physica B, 372, 251-255, (2006).

2) Katsuhiko Yamaguchi, Shinya Tanaka, Osamu Nittono, Koji Yamada and Toshiyuki Takagi : Monte Carlo Simulation for Magnetic Dynamic Process of Deformed Micro Magnetic Clusters, IEEE Trans. Magn., 42(4), 927-930, (2006).

3) Wanti Ekawati, Ji Shi, Yoshio Nakamura and Osamu Nittono : Co-ITO granular magnetoresistance films fabricated by precipitation of magnetic nanoparticles from amorphous oxide, J. Vac. Sci. TechnolA, 24(2), Mar/Apr 2006, (to be appeared).

4) Wanti Ekawati, Ji Shi, Yoshio Nakamura and Osamu Nittono : Effects of Pt addition on the formation of Co-ITO granular magnetoresistance films by a two-step method, J. Vac. Sci. TechnolA, 24(3), May/Jun 2006, (to be appeared).

5) Wanti Ekawati, Ji Shi, Yoshio Nakamura and Osamu Nittono : The influence of oxygen partial pressure during deposition on megnetoresistance of Co-Pt-ITO and Co(Pt)-ITO thin films, Applied Physics A, (to be submitted).

6) 山口 克彦, 入戸野 修 : 鉄鋼材の劣化診断システムの開発, 検査技術, 2005.11, 26-33, (2005).

7) Md. Abu Taher and Osamu Nittono : Doping Effect on Electrical and Galvanomagnetic Properties of Flash-Evaporated Thin InSb Films, Pro. Interl. Conf. on Bio-inspired computing (BIC'05), Malaysia, September 5-7, 2005.

8) Wnati Ekawati, Ji Shi, Yoshio Nakamura and Osamu Nittono : The effect of oxygen partial pressure on the magnetoresistance of Co(-Pt)-ITO thin films, Transactions of the Materials Research Society of Japan, 30(4), 1027-1030, (2005).

9) Yuuki Yamamoto, Ji Shi and Yoshio Nakamura : Perpendicular magnetic anisotropy of Co-Ti-N films, Transactions of the Materials Research Society of Japan, 30(4), 1109-1111, (2005).

10) Y. Hodumi, M. Uyama, J. Shi and Y. Nakamura : Perpendicular magnetic anisotropy of CoPt / AlN multilayer, Transactions of the Materials Research Society of Japan, 30(4), 1203-1205, (2005).

11) R. Zhou, C. C. Chen, M. Hashimoto, J. Shi and Y. Nakamura : Characterization of the interfacial reaction between sputter-deposited Ni film and Si substrate, Applied Physics A, 80, 179-182, (2005).

12) Kenji Makihara, Arpad Barna, Mitsuru Hashimoto, Ji Shi and Susumu Maruyama : Epitaxial growth of Ni films by radio frequency sputtering on GaAs(001) with a TiN buffer, Thin Solid Films, 485, 235-240, (2005).

13) K. Maruyama, E. Arakawa, K. Hirai, H. Yamaguchi, H. Numata, A. Matsushita, T. Yokoyama, T. Koide, K. Namikawa and O. Nittono : MAGNETIC PROPERTIES of NICKLE LAYERS ELECTRODEPOSITED on AMORPHOUS CARBON, Electrochemical society 206th meeting, 2004.

14) K. Yamaguchi, S. Tanaka, H. Watanabe, O. Nittono, T. Takagi and K. Yamada : Monte Carlo

Simulation for Barkhausen Noise, IEEE Trans. Magn., 40(2), 884-887, (2004).
15) Katsuhiko Yamaguchi, Shinya Tanaka, Osamu Nittono, Toshiyuki Takagi and Koji Yamada : Monte Carlo simulation of dynamic magnetic processes for spin system with local defects, Physica B, 343, 298-302, (2004).
16) Takumi Sannomiya, Yumiko Haga, Yoshio Nakamura, Osamu Nittono and Yoshio Takahashi : Observation of magnetic structures in Fe granular films by differential phase contrast scanning transmission electron microscopy, J. Appl. Phys., 95(1), 214-218, (2004).
17) Takumi Sannomiya, Ji shi, Yoshio Nakamura and Osamu Nittono : Correlation between magnetization performance and magnetic microstructure of patterned permalloy films fabricated by microcontact printing, J. Appl. Phys., 96(9), 5050-5055, (2004).
18) Takumi Sannomiya, Ji Shi and Yoshio Nakamura : Controllability of rotation of magnetization vortex in Fe particles, Transaction of the Materials Research Society of Japan, 29(4), 1505-1507, (2004).
19) Yuuki Yamamoto, Ji Shi, Yoshio Nakamura and Mitsuru Hashimoto : Perpendicular magnetic anisotropy of CoPt-TiN nanocomposite magnetic films, Transaction of the Materials Research Society of Japan, 29(4), 1569-1571, (2004).
20) Wnati Ekawati, Ji Shi, Yoshio Nakamura and Osamu Nittono : Magnetoresistance of Co-Pt-ITO composites film, Transactions of the Materials Research Society of Japan, 29(4), 1603-1606, (2004).
21) Hiroyuki Nakajima, Tetsuhiro Tanaka, Mitsuru Hasimoto, Ji Shi and Yoshio Nakamura : Growth structure and magnetic property of CoPt films on GaAs(001) by d.c.-sputter deposition, Thin Solid Films, 459, 156-159, (2004).
22) Kenrou Yamaguchi, Zhongyu Zhao, Changchuan Chen, Mitsuru Hashimoto, Ji Shi and Yoshio Nakamura : Structure and magnetic behavior of CoPt films prepared on MgO(001) substrates by dc plasma biased sputtering, Thin Solid Films, 459, 165-168, (2004).
23) Changchuan Chen, Ryo Sakurai, Mitsuru Hashimoto, Ji Shi and Yoshio Nakamura : Perpendicular magnetic anisotropy of CoPt-TiO_2 composite film with nano-fiber structure, Thin Solid Films, 459, 200-202, (2004).
24) Ryo Sakurai, Yuki Yamamoto, Changchuan Chen, Mitsuru Hashimoto, Ji Shi, Yoshio Nakamura and Osamu Nittono : Structure and magnetic behavior of reactive sputter deposited nanocomposite FePt-TiN films, Thin Solid Films, 459, 208-211, (2004).
25) C. C. Chen, M. Hashimoto, J. shi, Y. Nakamura, O. Nittono and P. B. Barna : Perpendicular magnetic anisotropy of Co-TiN composite film with nano-fiber structure, J. Appl. Phys., 93(10), 6273-6278, (2003).
26) A. G. Roy, *Member, IEEE* and O. Nittono : Annealing-Induced Properties of Al-N-M (M:Co, Fe) Thin Films, IEEE Trans. Mag., 39, 3025-3027, (2003).
27) J.Shi, Y. Hashiba and O. Nittono : Preparation and characterization of Ni-C composite films, J. Mater. Sci., 36, 343-349, (2001).
28) Md Abu Taher, Yumiko Haga, Yoshio Nakamura and Osamu Nittono : Quality Improvement by Annealing for Flash-evaporated Thin InSb Films, Materials Transactions, 42(12), 2584-2589, (2001).
29) Yumiko Haga, Noriyuki Nakaya, Eishi Takeda, Yoshio Nakamura and Osamu Nittono : Preparation and Magnetooptical Properties of AlN-Fe Granular Film, Jpn. J. Appl. Phys., 40,

6561-6565, (2001).
30) J. Shi, M.Azumi and O. Nittono : Structural and magnetic properties of Co-C composite films and Co/C multilayer films, Applied physics A, 73, 215-218, (2001).
31) Kohichi Maruyama, Hiroo Numata, Takashi Sato and Osamu Nittono : Electrochemical Characterization of the Electrical Deposition of Co and Properties of Deposited Films Using Amorphous Ribbons as Substrate, Electrical Engineering in Japan, 130(4), 17-25, (2000).
32) Osamu Nittono, Minako Azumi, Yuji Hashiba and Miku Wakamori : Common Features of Phase Changes in Metastable Transition Metal Carbides such as Fe-C, Ni-C and Co-C prepared by Reactive Sputtering, Pro. Interl. Conf. on Solid-Solid Phase Transformations'99 (JIMIC-3), The Japan Institute of Metals, 1309-1312, (1999).
33) 入戸野 修 : X線回折と材料科学の研究, 理学電機ジャーナル, 29(2), 8-21, (1998).

（2）口頭発表

1) 丸山耕一, 荒川悦雄, 開康一, 渡邊廣憲, 山口仁志, 沼田博雄, 松下明行, 横山利彦, 小出常晴, 並河一道, 入戸野修 : 電析ニッケル薄膜の磁気的特性, 日本物理学会 2004 年次大会, 2004.10.
2) 丸山耕一, 荒川悦雄, 古川貢, 開康一, 山口仁志, 酒井雅弘, 沼田博雄, 中村敏和, 森浩一, 横山利彦, 松下明行, 加藤立久, 小出常晴, 並河一道, 入戸野修 : 電析ニッケル薄膜の磁気的特性 II, 日本物理学会 2005 年次大会, 2005.3.
3) K. Maruyama, E. Arakawa, K. Hiraki, H. Yamaguchi, H. Numata, A. Matsushita, T. Yokoyama, T. Koide, K. Namikawa and O. Nittono : Magnetic Properties of Nickel Layers Electrodeposited on Amorphous Carbon, ECS, Hawaii, October3-8, 2004.
4) Wanti Ekawati, 史蹟, 中村吉男, 入戸野修 : The Effect of Pt Content on Magnetoresistance in Co-ITO Films, 日本金属学会, 2004.9.
5) Wanti Ekawati, 史蹟, 中村吉男, 入戸野修 : The effect of oxygen partial pressure on the magnetoresistance of Co(-Pt)-ITO thin films, Proc. Japanese Materials Research Society of Japan, 2005.
6) 入戸野修 : ナノ環境調和材料の研究 ; 福島市産学支援事業「材料評価研究会」2005.
7) Md. Abu Taher and Osamu Nittono : Doping Effect on Electrical and Galvanomagnetic Properties of Flash-Evaporated Thin InSb Films, Pro. Interl. Conf. on Bio-inspired computing (BIC'05), Malaysia, 2005.

（3）出版物

なし

研究成果による工業所有権の出願・取得状況

今後の研究結果の蓄積後, 光誘起効果が明確に検証できた時点で検討する,

研　究　成　果

［研　究　概　要］

［Ｉ］研究題目

鉄基磁性微粒子を孤立分散した半導体酸化チタン膜の合成と磁気抵抗の光誘起効果の測定

研究代表者　：入戸野　修　（福島大学・共生システム理工学類教授）
研究分担者　：山 口　克彦　（福島大学・共生システム理工学類助教授）
研究分担者　：史　　蹟　（東京工業大学・大学院理工学研究科助教授）

１）研究のねらいと独創的な点

物質の性質は，構成する原子や分子の固有の電子の状態に左右される．電気電導性，磁性，誘電性は物質中の電子による最も基本的な機能であり，社会や産業を根底から支える物性になっている．最近では異なる相（金属，無機，有機）をナノレベルで混合することで，電子状態が混成したハイブリッドナノ結晶が出現するとの報告があり，1988年に巨大磁気抵抗効果(GMR)，1995年にトンネル磁気抵抗(TMR)が発現している．

本研究の目的は，異種物質を複合した膜中の隣接した異種物質（金属と半導体）の界面で起こる電子状態を光（含紫外線）照射により刺激して電子授受の確率を増大させ伝導電子を過剰供給し孤立分散した磁性微粒子間のトンネル電流の増大を図り，その結果として磁気抵抗効果を増大させること（光誘起磁気抵抗効果）を目指すものである．そのため，光誘起による電子授受能の大きい透明半導体二酸化チタンを，また，磁性微粉体として鉄を選択した．非磁性膜中に分散した磁性微粒子における磁気抵抗効果はグラニュラーGMRとして知られる．一方，二酸化チタン（半導体）は光触媒として知られ，光学的にも安定性が高く，表面での光励起によりｄ電子の授受を利用して酸化分解による抗菌効果，セルフクリーニング効果が発現し，それらの機能は紫外線ＵＶ照射で活性化することが知られている．

本研究では，(1) 二酸化チタンの光触媒能は光照射により表面での電荷分布と電子状態が関与しているので，光照射で誘起されて電子授受の効果が，接触する磁性微粒子／二酸化チタンの界面状態に作用し電気的障壁を変化することが期待されるので，粒子間の電流が励起されてトンネルGMRが光照射で制御できる，(2) この現象は光触媒能を電気的信号に変換できる，(3) 光と磁場あるいは電場を外部から印加することで，膜の導電率を変化することが期待できるので，これらは環境調和材料としてセンサー機能を発揮できる，(4) 混合した異なる物質固有の特性を，互いに電子の授受の形で捉えることは，相乗効果を活用するもので発現する機能を増大あるいは消滅させると言う概念を提示するものである，(5) 異なる物質を混合することで新しく出現する異相界面での電子状態や電子の電荷自由度に加えてスピン自由度の変化も期待できるので，導電性と磁気抵抗特性の特定なサイズあるいは分布状態での特異性や極大化を示すことが期待できる．本研究は，二酸化チタン中に純鉄（および鉄基合金）磁性微粉体（径＜20nm）をトンネル電流が流れる程度に孤立分散させた膜を合成し，①膜の微細構造を解析し，②

光吸収の測定，③外部からの光照射による膜の導電率変化を計測するとともに，④光と磁場の重畳した条件下での磁気抵抗の増大を検出することを目指した．

この研究の学術的な特色・独創的な点及び予想される結果と意義は以下にまとめられる：(1) 異なる物質を複合化することでそれぞれが接合する界面において物質固有の電子状態を現出することで，一方をドナー，他方をアクセプターとして役割分担させ，結果的に電子の授受に起因する磁気抵抗効果の増大を目指している．(2) これらの効果を増大するために，製膜時に基板に一軸性の磁場を印加することで生成膜に磁気異方性を優先的に出現させることが期待される．(3) 光誘起GMRは基本的には光誘起導電率の変化に関連して検出されるので，光と磁場に対する複合膜のセンサー特性への応用が期待される．(4) 半導体と金属（金属酸化物）の界面における電子状態のハイブリッド化あるいは電子の電荷自由度を変化させ，スピン自由度を利用して，発現する機能性の増大を狙っている．(5) 島状微細磁性粒子と酸化チタンを交互に堆積した合成法で，磁性微粒子のサイズ・粒径および分散状態を調整することができ，発現機能を制御可能である．(6) 製膜条件や後熱処理で二酸化チタンの界面状態を変化することができ．光誘起効果と関連づけて解析できる．(7) 半導体二酸化チタンの光触媒脳と導電率の関係から，触媒能を定量的に評価できる．

・研究者の研究分担：

・入戸野　修　：　試料薄膜の合成，薄膜の結晶構造の解析，電磁気特性の測定および研究の総括

・山 口　克彦：　合成薄膜の光物性・光磁気物性測定とシミュレーション

・史　　蹟　：　合成薄膜試料の微細構造解析と磁気分析

・研究計画と研究分担は以下の通りであった：

（1）スパッタ装置の設計・配置等の改良：アルゴンおよび窒素ガスを含むスパッタガス中での膜製造の実施，２源スパッタ膜の堆積条件を制御して膜を構成する結晶構造の存在比を変化させた鉄微粒子孤立分散膜の製造．（入戸野）

（2）孤立分散膜の構造評価：アルゴンガスと窒素ガスを混合した雰囲気中でスパッタ源の距離・電力を変化させて鉄微粒子の不連続膜を製造する条件の設定と合成膜の構造との相関関係の確認．（入戸野，史）

（3）焼鈍膜の構造評価と光吸収特性の相関関係の調査：ルチル型よりアナターゼ型が安定な堆積膜の焼鈍温度および時間と膜の透明度の相関関係調査．（入戸野）

（4）磁気抵抗測定とその光誘起効果の測定：直流型電気抵抗測定はオーミック接続の課題を克服し，磁気抵抗効果とその光（可視光およびＵＶ）による誘起効果の検出を試みる．（入戸野，山口）

（5）合成膜の高分解能電子顕微鏡による微細構造の観察：この観察には試料片の作製が難しいので，いくつかの試料片に限定せざるを得ないが，良い試料片にて微細構造を直接観察することを試みる．（史，入戸野）

（6）上述の磁気特性測定結果と膜の微細構造の観察結果とを合わせて合成膜における巨大磁気抵抗の光誘起効果の機構モデルを構築する．（入戸野，山口，史）

最後に全体を総括し，今後の研究展開と応用展開等についての指針を示す．

2）これまでの研究例

透明磁性半導体を合成する試みはあった．二酸化チタンは，これまで光触媒材料として，応用面ばかりでなく，基盤的な立場から主に化学者が対象として来た材料である［A.Fujishima and K.Honda: Nature 238, 37(1972)］．　しかし，電子・磁気材料としての研究はなく，材料としては，ZnO や CuAlO などの透明酸化物電子材料の研究が活発化していた．　2001 年に松本ら[Y.Matsumaoto et al.: Science 291, 854(2991)]がコンビナトリアル材料開発技術を活用して二酸化チタン（半導体）と磁性金属Ｃｏの複合膜を分子線エピタキシーで合成し，酸化物で初めての希薄透明磁性半導体として報告して注目され，その後その延長線上で現在も酸化物エレクトロニクスの研究が進行中である．

本研究はこれらの研究とは全く異なる視点で開始されたものである．本研究開始後，二酸化チタンに関する文献検索の結果，透明磁性半導体としての研究との接点を持つことが分かった．　本研究は，研究代表者がこれまで実施してきた２つの素材をナノコンポジットの形態で合成する方法を発展させて，複合機能性（電子授受機能の関係する光触媒能とトンネル電流の磁場効果による巨大磁気抵抗効果を光誘起で増大させる）の発現を図るものである．これまでの複合材料の研究は巨視的な材料特性の加算化を図る方向と，微視的な加算化を図る方向とに大別される．本研究は後者に属する．最近，ナノ構造を対象とした研究では電子状態の混成化を意識した研究が成功しつつあり，最近では異なる相（金属，無機，有機）をナノレベルで混合することで，電子状態が混成したハイブリッドナノ結晶が出現するとの報告がある．特に，1988 年に巨大磁気抵抗効果(GMR)，1995 年にトンネル磁気抵抗(TMR)が発現している．したがって，異相界面の多い多結晶材料での電子状態に着目して物性発現をもたらすとの観点での機能性材料の創製の研究は始まったばかりである．本研究もそれらの一部であるが，複合膜の構成相をドナー／アクセプターとして捉えて電子授受に注目した研究例は少ない．

3）本研究対応の装置の設計と製作

合成膜の製造装置としては，低価格でしかも簡便な堆積様式であるスパッタリング装置を活用することにした．　松本らの分子線エピタキシー法は多数の堆積源を同時搭載し，効率的に薄膜あるいは多層膜を合成するには適しているが，装置本体と堆積制御機構が複雑で，かつ高価なものである．本研究では，ターゲット材が半導体であること，また，堆積時のスパッタリングの安定性のため高周波 RF スパッタ方式を採用した．

本研究で設計作製するスパッタ装置の設計指針を以下のように決定した．本研究の目的は，光誘起による電子授受能の大きい透明半導体として二酸化チタンを，磁性微粉体として鉄基材料を選択し，これらを複合した膜中の隣接した異種物質（金属・半導体）の界面で起こる電子状態を光（含紫外線）照射により刺激して電子授受の確率を増大させ伝導電子を過剰供給し孤立磁性微粒子間のトンネル電流の増大を図り，その結果として磁気抵抗効果を増大させること（光誘起磁気抵抗効果）を目指すものである．　したがって，複合薄膜中の異物質界面での電子状態変化を利用し，そこでの電子授受を相乗的に活用することで導電率の光誘起変化を発現する薄膜を創製することを実験的に検証する基礎研究である．透明半導体二酸化チタン膜中にトンネル電流が励起される試料膜を合成するには，二酸化チタン膜中に鉄基磁性微粉体（径＜20nm）をトンネル電流が流れる程度に比較的均一に孤立分散させた膜を合成する必要がある．また，膜の微細構造を解析し，光吸収の測定，外部からの光照射による膜の導電率変化，光と磁場の重畳した

条件下での磁気抵抗を測定することが可能な試料膜であることが重要である．そのためには，電気伝導性の低い二酸化チタンをスパッタリングさせる必要があり，高周波源を有するマグネとロンｒｆスパッタ膜堆積装置を使用する．この装置では，鉄基磁性微粒子の分散状態およびサイズは電圧・電流のスパッタ条件で堆積速度を変化させて制御し最適条件を決定することができるからである．

・目的を満足するための必要条件として，スパッタ装置として以下の仕様を有する．
（1）薄膜の堆積速度が出力で制御でき，膜厚制御が比較的容易にできること．
（2）異なる種類の複合膜をターゲット交換等の装置対応で容易に作製できること．
（3）合成する試料膜サイズ（25 mm x 25 mm）全体で均一組成ができること．
（4）不純物ガスの混入が最小限に抑制できる高真空対応型の装置であること．
（5）ターゲット材としては電気伝導性の良いものと低いものが使用できること．
（6）各種の高純度金属磁性材料をターゲット材として使用できること．

・これらの条件を必要とする理由として以下のように考えた：
（1）試料膜の特性は堆積速度や成膜の膜厚によって影響されるので，両者の制御は，膜特性の膜厚依存性を明確にするためにも不可欠である．
＊堆積膜量のその場計測・解析とスパッタ条件が制御できること（今回はガス流量とＲＦ電力をフィードバック制御することは整備する部品のコストの関係でできなかった．）
（2）試料複合膜は鉄およびコバルトの磁性微粒子の分散した薄膜であり，測定精度を高めるには多数の試料膜を測定する必要があり，迅速に多種類の複合膜が作製できることが重要で，それには簡単な操作でターゲット交換でき，試料作製時間を計り実験の効率化が図れることが不可欠である．
（3）試料膜の構成相の組成のバラツキは物性値のバラツキに関係するので，試料サイズ全体が均質組成の膜が作製できることが不可欠である．
＊スパッタ時の真空度をガスフローメータを使用してアルゴンガス流量を調節できるのが望ましいが，今回は整備のコストの関係でできなかった．
（4）不純物，特に残留酸素ガスは試料薄膜の特性に著しく影響するので，装置は可能な限り高真空対応型である必要がある．
（5）ターゲット材の電気伝導度はスパッタ速度の制御と関係しているので，電気の良導体ならびに低伝導体にも可能なＲＦ機能を有するものである必要がある．
（6）ターゲットサイズは可能な限り小さくできること．高純度金属ターゲットは高価格であり，価格の点から必要最小限のターゲットサイズを考慮する必要がある．

［参考資料］　設計製作した装置の仕様
（1）薄膜堆積源部分
①スパッタ装置（㈱アール・エス・ティー製MAK200-V を部分改良：図1，図2）
・ マグネトロンＲＦ型：高真空 0.5mTorr～低真空 500mTorr 対応である．
・ 収束型プラズマ方式：真空度によらずビーム収束度低下せず安定．
・ スパッタガス：低イオン化エネルギー不活性アルゴンガスて対応．
ターゲット表面の化合物の生成を抑制する．

・ スパッタリング安定稼働継続方式：ターゲット表面近傍で高磁場が存在し
プラズマ密度を高め，かつ閉じ込め効果を増大している．
・ターゲット／基板間距離可変型：均一堆積速度の範囲が制御可能である．
・装置の部品仕様：ターゲット材厚範囲　1.00～4.70 mm　　（図３）
（最大径 50.8mm 径）　ターゲット表面積20.27 cm^2．（均一領域：30mmX30mm）
・マグネット冷却方式：冷却水が直接ターゲット材に接触せず耐腐食性に優れる．
②スパッタリング用専用ＲＦ電源（自動整合機能付き）
・最大高周波電力ＲＦ：３００ W,　　（耐圧電圧：　２００～１０００Ｖ）

（2）真空容器部分　（図１，図２）
・チャンバー SSR-CH-1：高真空型対応，初期真空度　10^{-6}Torr 以下
（試料交換用蓋，架台，ガス導入・圧力調整系，追加部品取付設計機構，ターゲットおよび基板ホルダー・シャッターの増設可能型）
・ 装置全体のサイズ：約９００mm x ６００mm x １２００mm
・真空排気・計測計部：ピラニー・ペニング真空計
（作動開始時から製膜時まで使用可能：10^{-7} ～10^{-1}Torr，Pa 変換可）

図　１：　設計製作した装置全体図

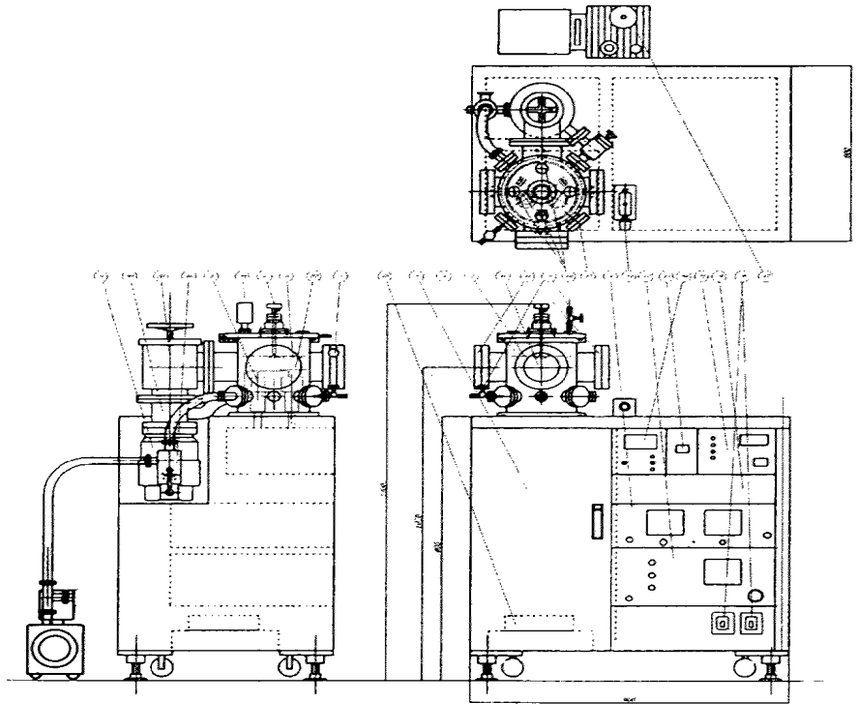

4）製膜条件等
（1）薄膜堆積条件：　室温　堆積速度　など
A）スパッタリング条件：
・初期真空度：4.5 x 10^{-7}Torr 以下，稼働時真空度：～6 x 10^{-2}Torr
・RF 出力電力:60～100 W　（合成膜圧に依存；手動制御）

・堆積速度： TiO_2：1.8 nm/min (RF 出力 80W)，　Fe：4.8 nm/min (RF80W)
(堆積時の RF 導入出力をガス圧を見て手動制御して製膜し，堆積後に膜厚を計測し，堆積時間で除して平均堆積速度を算出した)

本研究では図４のマスク(SUS304, 0.2mm 厚) を使用して製膜し，電気抵抗等の測定に使用した．また，同時に 10 mm x 10 mm の石英基板上に堆積した膜について，４端子接触法による電気抵抗測定，振動試料磁力計 (VSM) 測定法で磁気特性を測定した．

図２　ＲＦスパッタ装置全体

図３　ターゲット部分

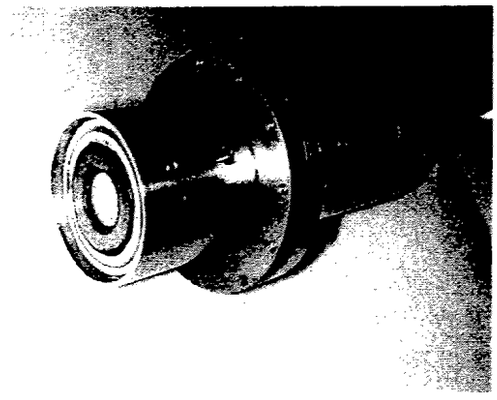

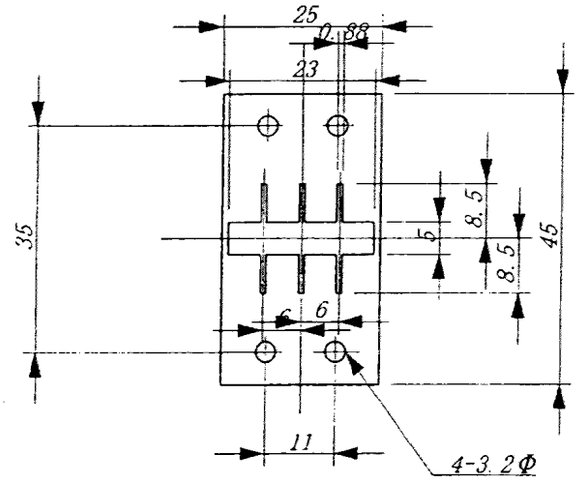

図 ４ 使用マスク

（２）合成膜の特徴：
本研究で合成した代表的に複合膜の金属光沢，透明度，電気抵抗測定可能，ＶＳＭ

測定可能な特徴を大雑把にまとめると表１のようになる.

表１　合成した複合膜（構成素，膜厚／堆積層数）の特徴

TiO2(Fe / TiO2)nTiO2	金属色	透明度	電気抵抗測定	ＶＳＭ	GMR
18 (14~5 / 18~9)$_4$ 4	○	X	◎	○	○
18 (5/9)$_4$ 4	◎	△	◎	△	△
18(2.5/9~5)$_4$ 4	△	△	△	○/△	—
18(1.6/18~9)$_4$ 4	△	△	X	—	—
18 (1.6/9)$_5$ 4	X	◎	X	—	—
18 (1.6/9)$_6$ 4	X	◎	X	—	—

＊膜表示：TiO_2膜厚(ｎｍ)（ Fe 膜厚 /TiO_2膜厚 ）$_{堆積数}$ TiO_2膜厚(nm)

５）実験結果の概要

主な実験結果の概要を以下に述べる.

（１）合成複合膜の結晶構造

X線回折法で調べると，合成複合膜は堆積したままでは，膜全体が非晶質構造であり，それを空気中 400℃で加熱処理した後では，膜の結晶構造は主に二酸化チタンの Rutile 型（図５(a)）とは異なる結晶構造を呈し，anatase 型に近い結晶構造をとっていることが分かった（図５(b)）．膜に透明度があり，電磁気特性の測定ができる複合膜の膜厚比（Fe 膜厚/ TiO_2膜厚）の最適範囲は掴めたが，手動制御で常に最適な測定膜厚の複合膜を製造するのは難しかった．（自動制御機構の必要性）

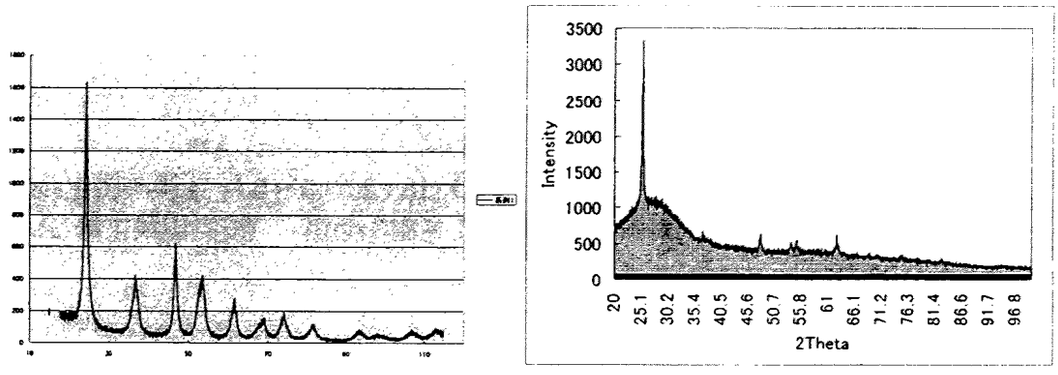

（a）　　（b）

図　５　合成膜の結晶構造　（ａ）二酸化チタン粉体　（ｂ）加熱後の合成膜

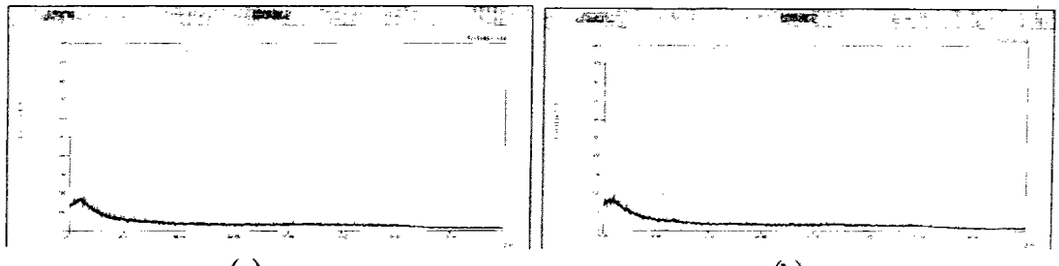

(a)　　(b)

図　６　膜厚が薄い場合 (a) 加熱処理前の合成膜　(b) 加熱処理後の膜
空気中の加熱処理により(b)膜は黄色を呈するが鉄酸化物は不検出

（2）磁気特性の測定結果

複合膜の膜厚が薄い場合は，可視光に対して透明あるいは半透明であり，金属光沢を示さず，それに関連して電気抵抗測定および磁気特性（H-B 曲線）の測定並びに巨大磁気抵抗効果（GMR:Giant Magnetic Resistance）の測定はできなかった．厚い膜では孤立分散した鉄微粒子の割合が多いので磁気特性の測定と一部 GMR 測定が可能であった（図7(b),図 8）．　鉄微粒子の量が電磁気特性の測定限度に関係しており，測定可能な複合膜を合成するには，堆積量の自動計測と堆積量制御が不可欠であることが判明した．　本研究では，装置設計時に膜圧測定系を配備できるようなチャンバー部の設計になっていたが，全体の研究経費の関係で実現できなかった．今後の研究では，スパッタ粒子の堆積量を膜厚計で計測し，同時にシャッター開閉駆動機構で基板に堆積する量を制御できる製膜方式に改良する方向で研究継続することを計画している．　図８に示すように僅かながら室温で GMR が観測される複合膜もいくつか合成できた．　低温での測定では GMR の増大は期待されたが（図９），今回は測定装置の使用調達の関係でできなかった．また，孤立分散鉄微粒子量を低下すると透明度は増すが，極端に電磁気特性の計測ができなくなり，GMR の測定はできなかった．　交互堆積量を精密に制御しないと適度に透明で GMR を示す複合膜は生成されない．今後最優先で改善すべき課題である．

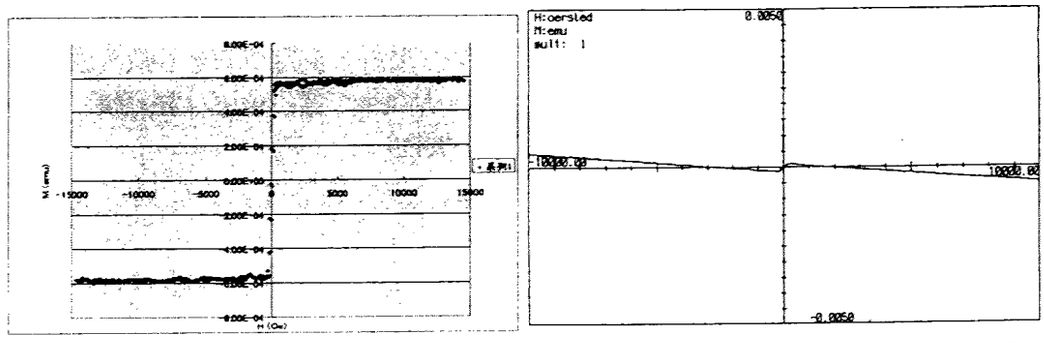

（a）純鉄膜の磁化極性　　（b）18(2.5/9~5)$_4$ 4膜の磁化曲線

図　7　振動試料型磁力計（ＶＳＭ）による磁化曲線　（反磁場補正無し）

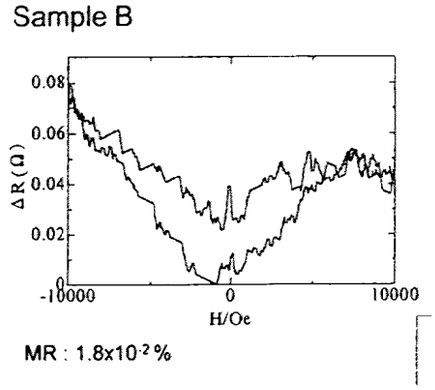

図　8　測定された巨大磁気抵抗効果の例
（測定温度：室温）18(15/10)$_4$4　膜

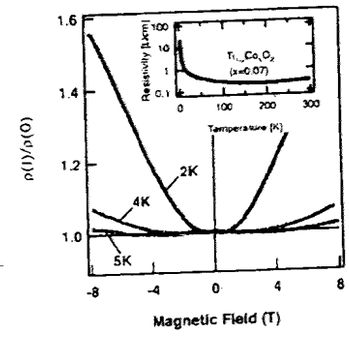

図９ 類似の報告例/TiOCo 膜
YMatsumoto et al.:Science, 291,854(2001)

6）まとめと今後の課題

本研究は当初研究計画したものに対して，設計製作した装置の設備の不完全な点もあり，さらに想定外の事故（薄膜堆積時のスパッタ粒子の混合，ガス流安定制御の問題や真空排気系の故障（ターボポンプの交換等のトラブル）の発生，研究代表者の交通事故遭遇など）が重なり，当初の研究計画の達成度は５０%程度であった．しかし，基盤研究と言うことで今後の研究継続のために解決すべき貴重な課題を抽出することができた．

本年度の研究の主な実験結果と今後の課題は以下の通りである：（1）鉄微粒子と酸化チタンが交互堆積した複合構造膜は，堆積時の酸化チタンはアモルファス状態であり低温加熱(200℃)で二酸化チタン膜となった．　合成した金属光沢を示す試料膜では微量ながら(MR=ΔR/R<0.02%)も磁気抵抗効果(GMR)を示した．しかし，鉄微粒子の堆積量が増大すると膜の透明度は著しく低下し，電気伝導性を示さず，従って室温での光照射による磁気抵抗効果の測定はノイズが大きくなり明確な検証はできなかった．このことは，堆積量を制御して製膜する機構が不可欠であることを示唆した．（2）窒素および酸素ガス中の加熱処理(400℃)後，膜の透明度は著しく増大することが分かった．しかし，鉄微粒子の堆積量が比較的多い交互堆積膜では，熱処理後に鉄の酸化によるものと思われる黄色を呈し，磁気測定の結果は，焼鈍前に比べて著しく磁化が低下した．これは，加熱温度域が合成酸化チタン膜の結晶構造がルチル型よりアナターゼ型が安定な温度域のためと鉄の酸化によるものと推測されたが，X線回折では鉄酸化物の存在は明確には検知されなかった．（3）複合膜の電気抵抗は合成直後で光学透明度と相関があり，透明度の高い膜は測定ができず，磁気抵抗効果の測定の難しさを示唆した．実際に合成時には微少な巨大磁気抵抗効果が認められたが，透明度を増した複合膜では測定ができなかった．

今後の研究で解決すべき装置改善の課題（ガス流量計，膜厚計測計などをチャンバーに装備しての製膜機構など）を研究費の確保を得て解決し，その上で当初計画していた半導体二酸化チタンのバンド幅を変化できると言われている窒素ガスを含むスパッタガス中で複合膜製造を行い，磁気抵抗効果の測定ならびに可視光とＵＶ照射効果によるトンネル電流によるTGRの光誘起効果の検証を明確に示す実験データを集積する方向で研究継続に努めたい．

［Ⅱ］研究題目

ゾル・ゲル法による金属イオンを内包した二酸化チタン膜の合成

1）研究のねらい

本研究では，ゾル・ゲル法は高価な設備を必要とせず、一度に大量かつ大面積にも膜を付着させることが出来るので，二酸化チタン膜の合成と磁性被粒子を複合生成する方法についても調べた．　金属アルコキシドからなるゾルを加水分解・重縮合反応により流動性を失ったゲルとし、このゲルを加熱し酸化物を得る方式であるゾル・ゲル法を用いて薄膜を形成している．この方法は高価な設備を必要とせず、大量作製可能なので、低コストに貢献できると考えられる．この方法でより効能の良い薄膜を作製することを試みた．特に，作製方法の改良に的を絞り，ゾルの作製条件，薄膜の焼結条件（焼結温度と焼結時間など）と光触媒能の関係について調べた．

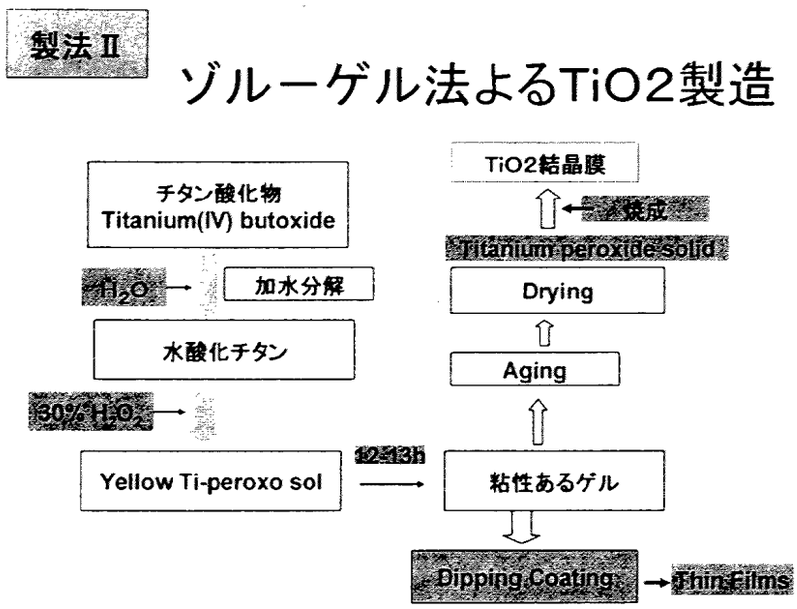

図1合成法

2）実験手法

（1）ゲルコーティング溶液の調製

二酸化チタン薄膜の作製のための溶液（二酸化チタン合成の前駆体）の合成手順:.

① Titanium Butoxide Ti[O(CH2)3CH3]4 4.8 g を電子はかりにて量る.

② 加水分解には, 35℃程度の H_2O で希釈された濃度 30%の H_2O_2 75ml を加える.

③ Yellow Ti Peroxosol（オレンジ色のゾル）ができる.

④ その後しばらく放置. 気泡を発しながら反応が進行.

《注意点》ゾルからゲルに反応するためには温度が関係している. 夏の暑い日であれば 48 時間程、常温で放置しておくことで充分な粘性が現れる. しかし、冬期のように気温が低い場合、48 時間以上放置しても変化が見られない. そのため、30℃程度に調節したホットプレート上で 20 時間保温を採用.

⑥Viscous Ti peroxo complex gel（黄色のゲル）ができる. このゾルは時間が経過していくにつれて、粒ができてしまうので注意.

（2）薄膜形成

基板スライドガラス（1.0～1.2mm x 76mm x 26mm）上にディップコーティング法で塗布した粘性の高い溶液（二酸化チタン合成の前駆体）を加熱して焼固め, 焼結中に反応が進行し, 前駆体から二酸化チタンが合成される.

（3）X線による膜の評価

焼結した薄膜が実際に二酸化チタン膜であるかをX線回折で調べた.

一般 に顔料つまり化粧品として利用される二酸化チタンはルチル型、光触媒として使われているのはアナターゼ型である.

（4）光触媒能の評価

光触媒機能の評価には、液層フィルム密着法やガスバック法などもある. 本実験ではメチレンブルーにより消色効果, 吸光度の減少により光触媒の機能を評価した. 塗布膜厚が一定でないためそれぞれの変化を相対的に評価する方法を採用した。

3）実験結果

（1）薄膜の結晶構造

測定したX線回折曲線から　400℃以上で加熱処理した膜の結晶構造はほとんどがアナターゼ型となっており，一部ルチル型構造になっていることが分かった.

（2）光触媒能と焼鈍条件の関係

空気中加熱温度と加熱時間の関係による光触媒能の変化を調べた. 700℃で加熱したものでは光触媒能の低下する膜になっていた.　図1に加熱温度は360～400℃で1～3時間処理した膜におけるUV照射中の吸光度の変化（光触媒能の強さに関係：ランバート･ベールの法則を用いて吸光度とメチレンブルーの濃度との関係を活用／ 参考資料／ ）の結果を示す.　360～380℃の加熱処理をした膜が比較的高い光触媒能を示すことが分かる.　図2は 380℃で加熱処理した加熱時間と光触媒能の関係を示す. いずれの合成膜でも1～3時間のUV照射で吸光度は低下し, 加熱時間の膜が5～6時間で比較的短時間に光触媒能が飽和している. さらに長時間の処理は実施していない。

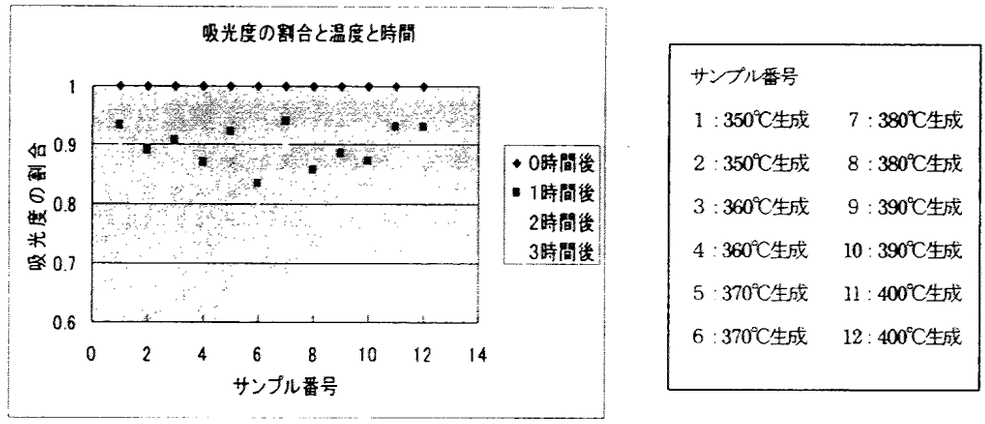

図　1　加熱処理した合成膜の光触媒能の違い
(ランバート・ベールの法則よる吸光度とメチレンブルーの濃度との関係)

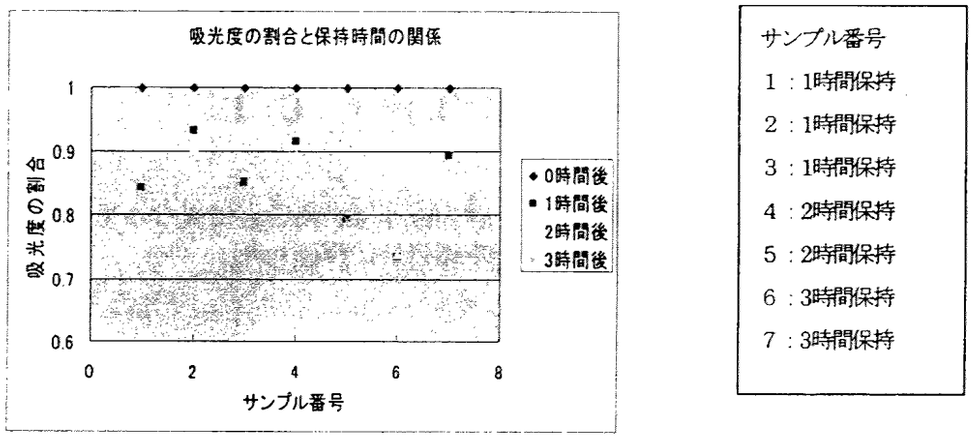

図　2　380℃での加熱処理時間と光触媒能の関係

4）まとめ

Titanium Butoxide Ti[O(CH2)3CH3]4 を用い，金属アルコキシドからなるゾルを加水分解・重縮合反応により流動性を失ったゲルとし，このゲルを基板に塗布し，加熱処理して二酸化チタン膜を生成した．ゾルの作製条件，薄膜の焼結条件（焼結温度と焼結時間）と光触媒能（メチレンブルーによる色素分解評価，吸光度）の関係について調べた．

その結果，焼結時間を1時間から3時間まで変化させたが、その範囲内では顕著な変化が見られなかった． 焼結温度に関しては370℃～380℃の薄膜作製条件が最適であることが分かった．光触媒能を紫外線ばかりでなく可視光線でも効果的に増加することを意図して行われた金属イオンの添加実験では，各種の条件で作製した前駆体に，今回は硝酸銀(AgNO3)の形で金属 Ag イオンを添加したが沈殿物が生成し，その後への膜ではＵＶ照射による吸光度の変化は全く観察されなかった．さらに，加熱処理して生成した二酸化チタン膜に希薄な硝酸銀(AgNO3)溶液を塗布して再度加熱処理して生成した膜について吸光度を測定したが，20時間後に僅かな変化が見られるだけであった． このゾル・ゲル法では化学変化を伴う金属塩の添加による金属イオンの添加については，金属塩の種類と添加時の溶液の塩基度等との関係でさらに詳しく検討する必要がある．一方，金属微粒子そのものをゾルの状態で添加する場合については，今後の研究計画として取り入れた．

この予備実験では，福島大学教育学部生涯学習課程環境科学教育コースの中村由香利氏の卒業研究によるところが多い．ここに記して謝意を表します．

［参考資料］

◎ Lambert－Beer（ランバート・ベール）の法則：

溶質（呈色物質）の吸光度（Abs）は，溶液（本研究ではメチレンブルー）の濃度（C）と液層の厚さ（L）に比例すると考える．入射光度（I_0），透過光度（I）の比を透過度（T）とすると，吸光度（Abs）は以下のように表される．

$$T = (I / I_0) = 10^{-\varepsilon CL}$$

$$\%T = T \times 100$$

$$Abs = \mathrm{Log}\,(1/T) = \mathrm{Log}(I/I_0) = \varepsilon \quad C \quad L$$

＊本研究では，基板上の二酸化チタン膜の膜厚は試料ごとに異なっていたので，それぞれの試料の吸光度の時間変化を相対的に評価した，

Available online at www.sciencedirect.com
SCIENCE DIRECT®
Physica B 372 (2006) 251–255
PHYSICA B
www.elsevier.com/locate/physb

Monte Carlo simulation for magnetic dynamic processes of micromagnetic clusters with local disorder

Katsuhiko Yamaguchi[a,*], Shinya Tanaka[a], Osamu Nittono[a], Koji Yamada[b], Toshiyuki Takagi[c]

[a]*Faculty of Symbiotic Systems Science, Fukushima University, 1 Kanayagawa, Fukushima City 960-1296, Fukushima, Japan*
[b]*Department of Material Sciences, Saitama University, Saitama 338-8570, Japan*
[c]*Institute of Fluid Science, Tohoku University, Sendai 980-8577, Japan*

Abstract

Magnetic dynamic processes for micromagnetic clusters with local disorder of crystal structure were simulated by pseudo-non-equilibrial Monte Carlo method. The magnetic field dependence of magnetization showed a little dip at zero magnetic fields. The dip becomes larger as the number of dislocations increase. Simulated Barkhausen noise at the dip was stronger than ordinal-simulated Barkhausen noise around coercivity. The snapshot of spins shows a magnetic fluctuation around dislocations. The result suggests a possibility of a new measurement with high sensitivity, to detect the deformation of micromagnetic clusters.

Keywords: Magnetic hysteresis; Barkhausen noise; Magnetic fluctuation; Micromagnetic clusters

1. Introduction

Recently a number of experimental studies have been made on magnetic dynamic processes for micromagnetic clusters such as magnetic nanowire or quantum dots [1–4]. For thin film type magnetic cluster, real-time measurements of magnetic domain wall movements have been tried mainly using magneto-optical Kerr effect [5,6]. On the other hand, other simulations for magnetic clusters like nanowires are dealing with magnetic dynamic process, especially hysteresis loops [7–10]. The information is becoming useful for developing high-density magnetic memories or micromagnetic devices. The influence of local disorder of crystal structure on dynamic magnetic properties, however, has not been considered sufficiently. The local disorder of crystals such as impurity, defects or dislocations is possible to exist even for a well-controlled grown cluster. The rate of disorder will increase as the size of the cluster decreases, and then it will be important to estimate its effect on the magnetic processes.

We have simulated the magnetic dynamic process using pseudo-non-equilibrial Monte Carlo (MC) method [11–14]. In this paper we will present the properties of the magnetic dynamic process for magnetic clusters with local disorder in the crystal structure.

2. Numerical method

It is not usual to simulate dynamic magnetic process, because the behavior of a spin system under continuously changing magnetic field has not yet been established. We have been trying to apply MC simulation for the dynamic magnetic process, especially like a Barkhausen noise (BN). The results showed good correspondence with experimental results, especially temperature dependences of BN. Moreover, the results suggested the possibility that closer observation of a magnetic dynamic process, such as BN, provide the information for the state of magnetic materials. The same method is applied in the following for plane type magnetic clusters which include dislocation loops.

In general, MC method deals with the thermal equilibrium state. The conventional process is as below, i.e. (i) at first an initial spin arrangement is set; (ii) then a spin is

*Corresponding author. Fax: +81 24 548 8189.
E-mail address: yama@sss.fukushima-u.ac.jp (K. Yamaguchi).

0921-4526/$ - see front matter © 2005 Elsevier B.V. All rights reserved.
doi:10.1016/j.physb.2005.10.060

focused in the spin cluster; (iii) next a trial spin-flip is executed for the focused spin; (iv) the local Hamiltonian of the focused spin is calculated for the state before and after spin-flip; (v) each spin state for the focused spin is decided by making a comparison between their energies, including thermal fluctuation effects. One MC step (1 MCS) means scanning up to the total cell a number of times for the process from (ii) to (v). Usually MC steps are repeated until one gets a stable state [15–21].

Now we stopped the repeat before getting a stable state, because of dealing with the magnetic dynamic processes for BN. Under the condition of constant magnetic field, the total spin is in a non-equilibrium state and going to an equilibrium state with progressing MC steps. The magnetic field slightly increases before it comes to the equilibrium state, then the total spin is kept under another non-equilibrium state again, while proceeding to a new equilibrium state. The operation is repeated until the final magnetic field is achieved. Because the change of the magnetic field is minute, it is regarded that a series of steps is an approximately continuous process through a pseudo-non-equilibrium state. Here we introduce an assumption that magnetization intensity (M), namely the summation of total spins ($M = \sum_i s_i$; s_i denotes the ith spin state), of each MC step can reflect the magnetic dynamic process on the magnetic hysteresis. Therefore, in this study, we differentiate the magnetic process for applied magnetic field ($dM/d(MCS)$) and deal with the discrete components of $dM/d(MCS)$ as simulated BN. Note that MCS on our simulation varies with time (t) on the real system.

Here, a spin system composed of $31^2 = 961$ cells ($0 \leqslant x \leqslant 30$, $0 \leqslant y \leqslant 30$) standing for a single square lattice was prepared as a normal spin system. The lattice constant is 1, and this is regarded as a criterion of length. Deformed spin systems were made by introducing one or two dislocation loops on the normal spin system, as shown in Fig. 1.

A simple Hamiltonian (H) was used for the simulation as shown below:

$$H = -\sum_{i,j} J_{ij} S_i S_j + B \sum_i S_i. \tag{1}$$

Here S_i denotes the spin state of ith cell, and J_{ij} stands for the effective exchange energy for ith and jth spins. B represents applied magnetic field. For simplicity, magnetic anisotropy and magnetic dipole interaction were neglected. This is justified because the cluster size was set small, and the number of magnetic particles is small. Here, we adopt the physical model of J_{ij} as a step function θ, viz.

$$J_{ij} = \theta(1 - r_{ij}) = \begin{cases} 1 & (r_{ij} \leqslant 1), \\ 0 & (r_{ij} > 1). \end{cases} \tag{2}$$

r_{ij} denotes the distance between ith and jth spins. Although the exchange energy of this model is supposed to be overestimated compared to real magnetic materials, it will be allowed for the purpose to derive intrinsic effect of local

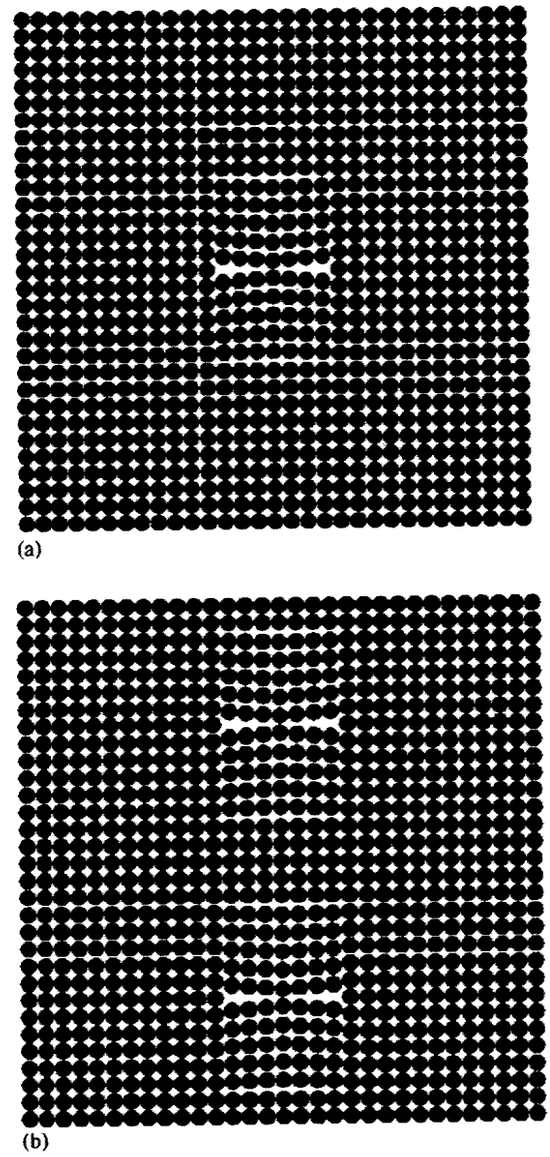

Fig. 1. Model of micromagnetic cluster with residual strain including (a) one dislocation loop and (b) two dislocation loops.

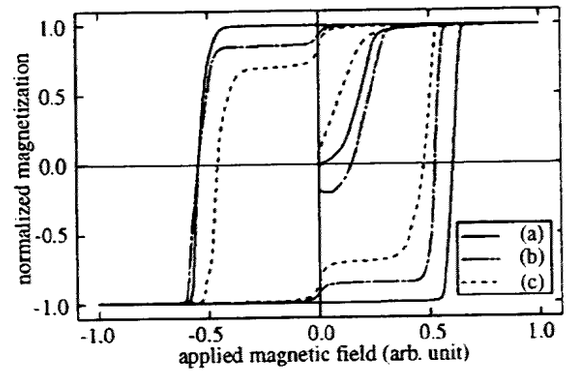

Fig. 2. Magnetic hysteresis curves for magnetic clusters including (a) no dislocation loop, (b) one dislocation loop and (c) two dislocation loops.

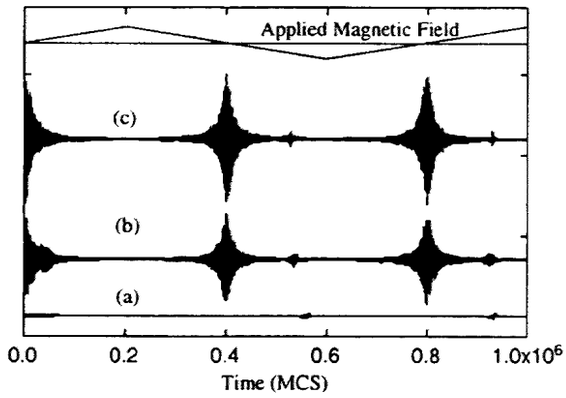

Fig. 3. Simulated Barkhausen noise (BN) for magnetic clusters including (a) no dislocation loop, (b) one dislocation loop and (c) two dislocation loops.

disorder in the crystal structure for dynamic magnetic process. For example, europium oxide (EuO), which is well known as a typical magnetic semiconductor, has a dominant exchange energy J_1 represented as an exponential function of the distance between individual states due to RKKY interaction. That is, the exchange interaction decreases rapidly as the distance increases. When the lattice deformation becomes large, the distribution of J_1 could be regarded as a function similar to Eq. (2).

The simulation was carried out by the use of the supercomputer, ORIGIN 2000 in the Institute of Fluid Science, Tohoku University.

3. Results and discussion

Fig. 2 shows the calculation results for magnetic field dependence of magnetization (magnetic hysteresis curve) for the magnetic clusters including (a) no dislocation loop, (b) one dislocation loop and (c) two dislocation loops when applied magnetic field (B) changes along $B = 0 \rightarrow +1 \rightarrow 0 \rightarrow -1 \rightarrow 0 \rightarrow +1$. Magnetization is normalized by the number of sites in the cluster. All hysteresis curves show the saturation magnetic field B_S around 0.5. The curves for the spin systems with dislocation loops have dips around zero magnetic field, but the dip cannot be seen for the normal spin system. Moreover, the dip depth increases as the number of dislocation loops increases.

Fig. 3 shows simulated BNs under an applied magnetic field of a triangular wave form for (a) no dislocation loop, (b) one dislocation loop, and (c) two dislocation loops. Large BNs are clearly seen in the magnetic field across the zero field when including (b) one dislocation loop and (c) two dislocation loops. The change of magnetization around the zero field is less than the one around coercivity. Small BNs exist around coercivity for all cases. These are supposed to be ordinal BNs which are produced by discontinuous magnetic domain walls movements [22,23].

For investigating the origin of BN around the zero magnetic field, let us follow the change of spins with

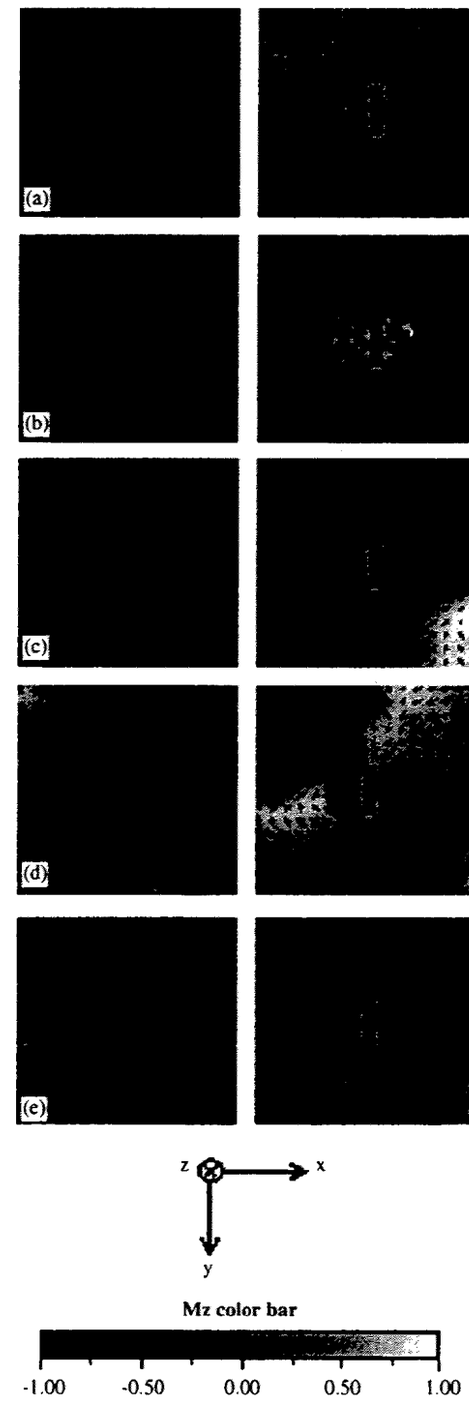

Fig. 4. Snapshots for micromagnetic clusters including no dislocation loop (left side) and one dislocation loop (right side) in a magnetic field changing along (a)$B = +1 \rightarrow$, (b)$B = 0 \rightarrow$, (c)$B = -0.3 \rightarrow$, (d)$B = -0.4 \rightarrow$, (e)$B = -0.6$ in Fig. 2.

triangular waveform magnetic field as time flows. Fig. 4 shows a series of snapshots for micromagnetic clusters including one dislocation loop in magnetic field change along $(a)B = +1 \rightarrow, (b)B = 0 \rightarrow, (c)B = -0.3 \rightarrow, (d)B = -0.4 \rightarrow, (e)B = -0.6$ in Fig. 2. We clearly see the furious spin disorders around the dislocation loop when the magnetic field is about zero. Hence, the origin of large

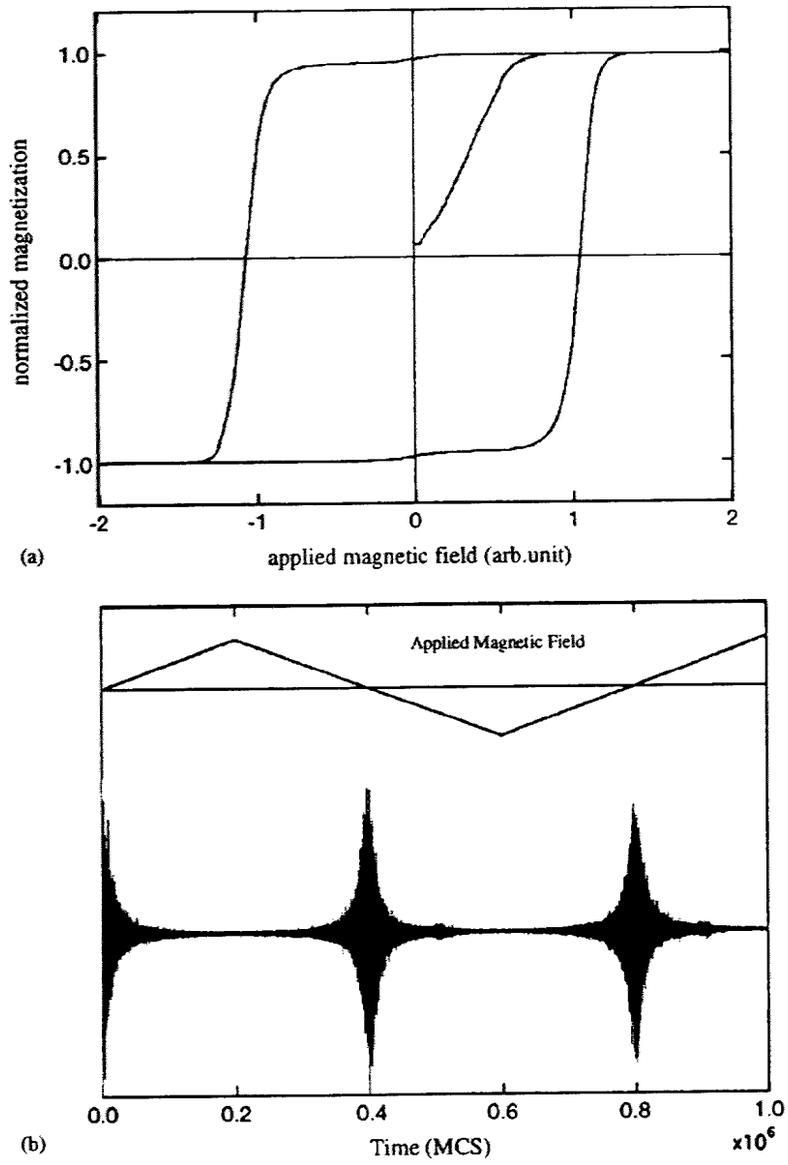

Fig. 5. (a) Magnetic hysteresis curve and (b) simulated BN for a three layer magnetic cluster including one dislocation loop on the intercalation middle layer.

BNs in Fig. 3 will be mainly due to the existence of dislocation. For ordinal magnetic materials, the rate of the area of local disorders in the crystallized magnetic clusters is very small and its effect could not be easily detected. In fact, as shown in Fig. 5(a), the dips around zero magnetic field on the hysteresis curves decrease rapidly when the micromagnetic cluster, including one dislocation loop, viz. a plane represented as Fig. 1(a), is intercalated between double perfect-crystallized planes composed of $31^2 = 961$ cells ($0 \leqslant x \leqslant 30$, $0 \leqslant y \leqslant 30$) without any dislocation loops. But the anomalous BN corresponding to the dip does not decrease, as shown in Fig. 5(b), although indicating that the anomalous BN is highly sensitive to such local disorders.

Fig. 6 shows the calculation of the magnetic after-effect under applied magnetic fields changing from $B = 1$ to $B = -1$ as a step function of time, as shown below:

$$B(t) = -2\theta(t) - 1 = \begin{cases} 1 & (t \leqslant 0), \\ -1 & (t > 0). \end{cases} \tag{3}$$

After changing the magnetic field to $B = -1$, the magnetization for the cluster without any dislocation loops gradually decreases and finally gets to the opposite saturated magnetization. On the other hand, the magnetization for the magnetic cluster including one dislocation loop has a tiny dip right after the magnetic field was switched. In this case it is also assumed that spin fluctuation exists around the local disorder.

The above results suggest the high fluctuating and stressful state of the spin system including local disorders. Our model for the simulation may include some extreme

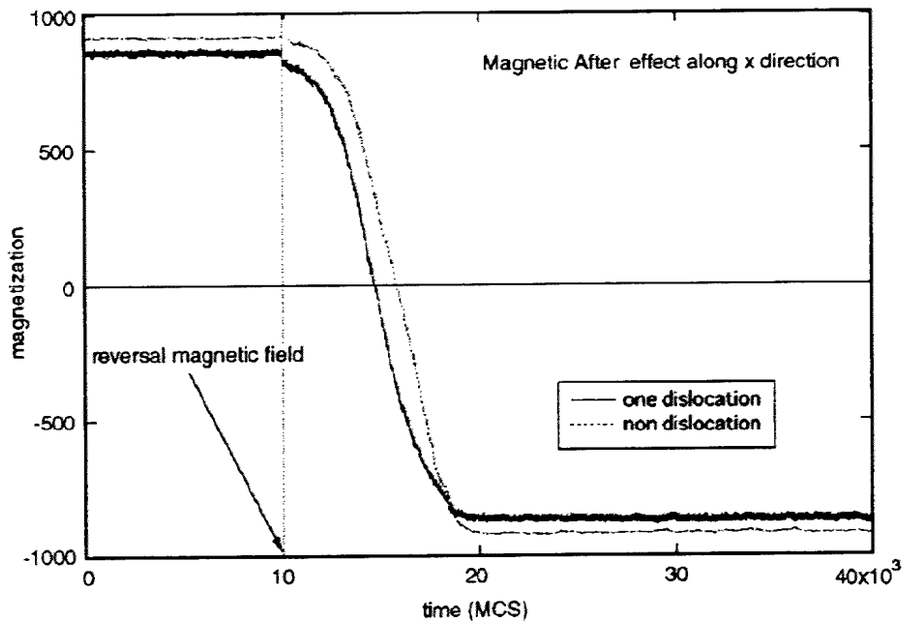

Fig. 6. Calculation of the magnetic after-effect under an applied magnetic field changing from $B = 1$ to $B = -1$ as a step function of time for the clusters without any dislocation loops and with one dislocation.

overestimation, especially about the exchange interaction which has a sharp cut-off length. But the tendency will still remain in some degree for the real system. Then we may have a new measurement tool using BN which can detect the local deformation in micromagnetic clusters.

Acknowledgement

We would like to express our thanks to T. Kinoshita in the Institute of Fluid Science, Tohoku University for helping with the parallel coding programs with Monte Carlo simulation.

References

[1] S. Zapperi, G. Durin, Comput. Mater. Sci. 20 (2001) 436.
[2] R. Varga, K.L. Garcia, A.P. Zhukov, M. Vazzquez, Physica B 343 (2004) 403.
[3] Z. Hao, Y. Shaoguang, N. Gang, Y. Dongliang, D. Youwei, J. Magn. Magn. Mater. 234 (2001) 454.
[4] K. Xue, G. Pan, M. Pan, M. Lu, G. Wang, Superlattice. Microstruct. 33 (2003) 119.
[5] D. Kim, S. Choe, S. Shin, J. Magn. Magn. Mater. 272–276 (2004) 720–721.
[6] T.A. Moore, S.M. Gardiner, C.M. Guertler, J.A.C. Bland, Physica B 343 (2004) 337.
[7] D. Hinzke, U. Nowak, J. Magn. Magn. Mater. 221 (2000) 365.
[8] M. Vazquez, K. Nielsch, P. Vargas, J. Velazquez, D. Navas, K. Pirota, M. Hernandez-Velez, E. Vogel, J. Cartes, R.B. Wegrspohn, U. Gosele, Physica B 343 (2004) 395.
[9] R. Hertel, J. Magn. Magn. Mater. 249 (2002) 251–256.
[10] J. Fuzi, G. Kadar, Physica B 343 (2004) 293.
[11] K. Yamaguchi, K. Yamada, S. Shoji, Y. Uno, H. Takeda, S. Toyooka, H. Tsuboi, IEEE Trans. 36 (2000) 1710.
[12] K. Yamaguchi, K. Yamada, T. Takagi, IEEE Trans. Magn. 38 (2002) 865.
[13] K. Yamaguchi, S. Tanaka, O. Nittono, T. Takagi, K. Yamada, Physica B 343 (2004) 298.
[14] K. Yamaguchi, S. Tanaka, H. Watanabe, O. Nittono, T. Takagi, K. Yamada, IEEE Trans. Magn. 40 (2004) 884.
[15] N. Metropolis, A. Rosenbluth, M. Rosenbluth, A. Teller, J. Chem. Phys. 21 (1953) 1087.
[16] D.W. Heermann, Computer Simulation Methods in Theoretical Physics, Springer, Berlin, 1990.
[17] K. Binder, in: C. Domb, M.S. Green 5B (Eds.), Phase Transitions and Critical Phenomena, Academic Press, London, 1976.
[18] G. Parisi, Statistical Field Theory, Addison-Wesley, Redwood, 1988.
[19] C. Ebner, Phys. Rev. B 28 (1983) 2890.
[20] C. Ebner, Phys. Rev. A 22 (1980) 2776.
[21] J. Marro, R. Dickman, Nonequilibrium Phase Transitions in Lattice Models, Cambridge University Press, Cambridge, 1999.
[22] H. Kronmuller, in: J. Evetts (Ed.), Coercivity and Domain Wall Pinning in Magnetic and Superconducting Materials, Pergamon Press, Oxford, 1992.
[23] H. Kronmuller, J. Magn. Magn. Mater. 24 (1981) 159.

Monte Carlo Simulation for Magnetic Dynamic Process of Deformed Micro Magnetic Clusters

Katsuhiko Yamaguchi[1], Shinya Tanaka[1], Osamu Nittono[1], Koji Yamada[2], and Toshiyuki Takagi[3]

[1]Faculty of Symbiotic Systems Science, Fukushima University, Fukushima 960-1296, Japan
[2]Faculty of Engineering, Saitama University, Saitama 338-8570, Japan
[3]Institute of Fluid Science, Tohoku University, Sendai 980-8577, Japan

Magnetic hysteresis and Barkhausen noise for deformed micro magnetic clusters were simulated by pseudo-nonequilibrial Monte Carlo method. The magnetic hysteresis curve showed a little dip around zero magnetic fields. Barkhausen noise on the dip was stronger than ordinal Barkhausen noise around coercive force. The result suggests a new measurement to reveal deformation of micro magnetic clusters.

Index Terms—**Magnetic hysteresis modeling, magnetization processes, Monte Carlo method.**

I. Introduction

RECENTLY there have been many experimental reports for magnetic dynamic process and micro magnetic clusters such as quantum dots or nano-wires [1]–[9]. These studies will be available to realize high density magnetic memories or micro magnetic device. The deformation of these clusters, however, has not been considered sufficiently, although it affects the magnetic properties. In the near future, control of the deformation of micro magnetic clusters would be taken up as an important product process for keeping up the high magnetic properties.

We have studied magnetic dynamic process, such as hysteresis and Barkhausen noise using pseudo-nonequilibrial Monte Carlo (MC) method [10]–[15]. In this paper we will present the relation between deformation of magnetic cluster and magnetic properties.

II. Numerical Method

At first, a spin system composed of $31^2 = 961$ cells ($0 \leq x \leq 30, 0 \leq y \leq 30, Z = 0$) standing for a single square lattice was prepared as normal spin system. The lattice constant is 1 and this is regard as criterion of length. Next a deformed spin system was modeled on the normal spin system introducing loop dislocation as shown in Fig. 1. A simple Hamiltonian was used for the simulation as follows:

$$H = -\sum_{i,j} J_{ij} S_i S_j + B \sum_i S_i. \tag{1}$$

Here S_i denotes the spin state of ith cell, and J_{ij} stand for the effective exchange energy for ith and jth spins. B represents applied magnetic field. Here, we adopt the physical model of J_{ij} as a step function, namely

$$J_{ij} = \theta(1 - r_{ij}) = \begin{cases} 1 (r_{ij} \leq 1) \\ 0 (r_{ij} > 1) \end{cases} \tag{2}$$

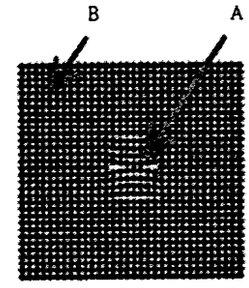

Fig. 1. Deformed spin system introducing loop dislocation [17]–[21].

where r_{ij} denotes the distance between ith and jth spins. Although the exchange energy of this model is supposed to be overestimated comparing with real magnetic materials, it will be allowed for the purpose to derive intrinsic effect of local deformation of crystal structure for dynamic magnetic process. For example, Europium Oxide (EuO), which is well known as typical magnetic semiconductor, has dominant exchange energy J_1 represented as exponential function of the distance between each site due to RKKY interaction, that is, the exchange interaction decreases rapidly as the distance increases. In the case that the lattice deformation becomes large, the distribution of J_1 could be regarded as a function similar to (2).

In general, MC method deals with thermal equilibrium state. Therefore usually MC steps are repeated until getting a stable state [16]-[22]. Here 1 MC step (MCS) means scanning up to the total cell number of times for the spin-flip process. But now we stopped the repeating before getting a stable state because of dealing with magnetic dynamic processes for BN. Under the constant magnetic field condition, the total spin is in an nonequlibrium state and going to an equilibrium state with progressing MC steps. The magnetic field slightly increases before achievement of the equilibrium state, then the total spin is kept under another nonequlibrium state again and proceeding to a new equilibrium state. The operation is renewed until achievement of final magnetic field. Because the change of the magnetic field is minute, it will be able to regard approximately that a series of steps is continuous process through an pseudo-nonequilibrium state. Here we introduce an assumption that magnetiza-

Digital Object Identifier 10.1109/TMAG.2006.872514

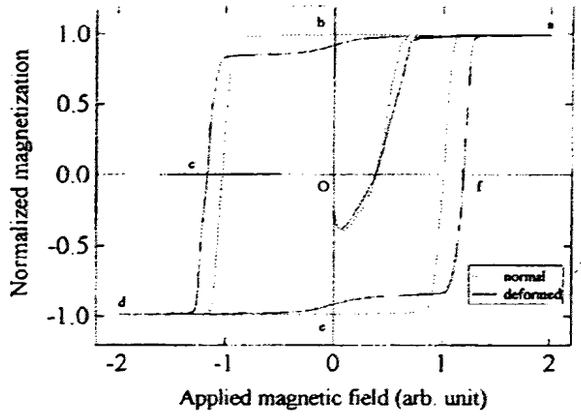

Fig. 2. M–H curve for the normal and deformed spin systems.

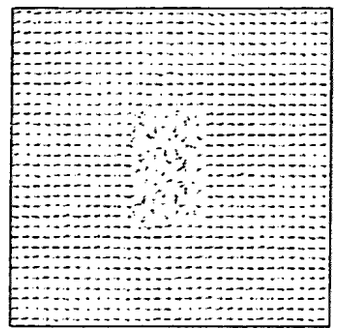

Fig. 3. Snapshot at "b" for deformed spin system.

tion intensity (M), namely the summation of total spin, of each Monte Carlo step can reflect the magnetic dynamic process on magnetic hysteresis. In this study, therefore we perform differential calculus dM/d(MCS) of the magnetic process for applied magnetic field and deal with the discrete components of dM/d(MCS) as simulated BN. Note that MCS on our simulation alternates time (t) on real system. For more details, see [12].

III. Results and Discussion

Fig. 2 shows the magnetic field dependence of magnetization (M–H curve) for the normal and deformed spin systems under applied magnetic field formed as triangle wave along the magnetic processes of O → a → b → c → d → e → f → a. The M–H curve for the deformed spin system has dull shrinks around "b" and "e" which can not be seen for the normal spin system. Snapshot of spin configurations at "b," for the deformed spin system is shown in Fig. 3. It is clearly seen that many spins fluctuate around a loop dislocation. The exchange interaction J_{ij} as a step function would cause anisotropy of Hamiltonian for each spin differently in the area around the loop dislocation. The state may be regard as magnetic crystal introducing partially spin glass.

Simulated BN of the magnetic process of O → a → b → c → d → e → f → a are shown in Fig. 4 for the normal and deformed spin systems. The great discrepancy between the two spin systems is the existence of large BN around "b" for

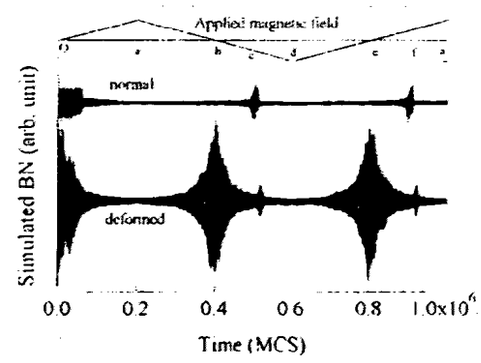

Fig. 4. Simulated BN for the normal and deformed spin systems. Time is represented using Monte Carlo step (MCS).

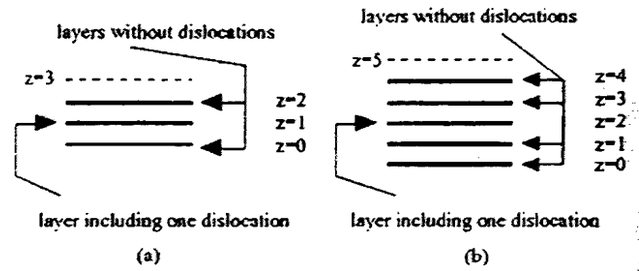

Fig. 5. Multilayer spin system intercalated layer including one dislocation. (a) 3 layers. (b) 5 layers.

the deformed spin system. The lowering of the absolute value of the magnetization is not so much around "b" for even the deformed spin system, however, the peak of the BN at "b" for the deformed spin system is dominant over all.

For the real materials, such a deformed area is submerged in the system including plenty normal spin area. Then multilayer spin systems are also prepared as shown in Fig. 5. Fig. 5(a) shows 3 layers spin system which includes two normal layers ($z = 0, 2$) without any dislocation loops to be piled on the both sides of the layer ($z = 1$) including dislocation loops. Fig. 5(b) also shows 5 layers spin system composed of $z = 0, 1, 3, 4$ layers without dislocations and $z = 2$ layer with one dislocation. Notice that both multilayer spin systems have only one loop dislocation. The dips around zero magnetic fields on M–H curves decrease rapidly as increasing normal layers as shown in Fig. 6. For that reason the magnetization itself is not so sensitive for the local deformation in a magnetic cluster.

On the other hand there is a possibility that BN for the multilayer spin system is still sensitive for the existence of local disorder. Fig. 7 shows simulated BN for 3 layers and 5 layers spin systems in Fig. 5. The peak intensities of the anomalous BN corresponding to the dip is not so decrease for both multilayers.

Above discussion, simulated BN is dealt as the derivative of magnetization which is summation of each spin, in other words, the measurement of such a BN is performed as detecting the whole sample simultaneously using larger pick up coil than the sample. Considering the scale of the sample as a micro magnetic cluster, it seems reasonable. But now let's suppose to measure using a less detector than the sample or distribution of magnetic

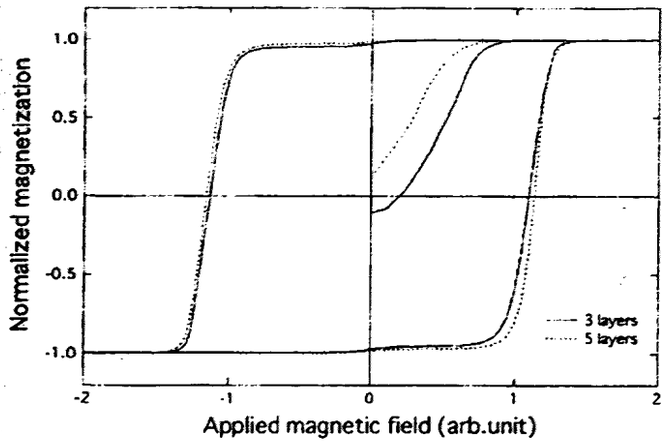

Fig. 6. M–H curve for 3 layers and 5 layers spin system in Fig. 5.

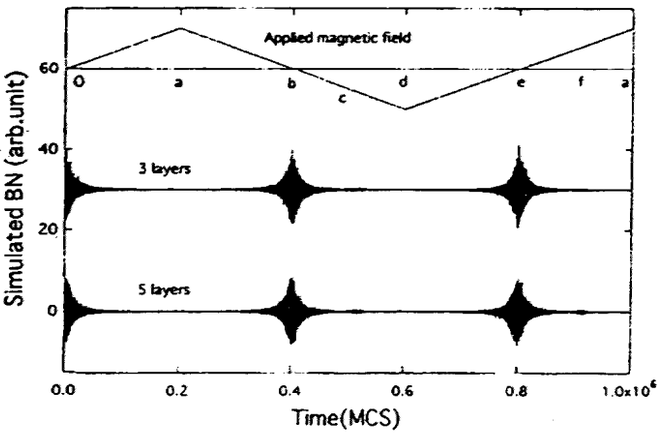

Fig. 7. Simulated BN for 3 layers and 5 layers spin system in Fig. 5.

field near the surface of the sample, which originated from magnetic moments of all spins. In general, a magnetic moment M produces a magnetic field H as the following equations:

$$H_r = \frac{M}{4\pi\mu_0}\frac{2\cos\theta}{r^3} \tag{3}$$

$$H_\theta = \frac{M}{4\pi\mu_0}\frac{\sin\theta}{r^3} \tag{4}$$

here r represents a distance between a magnetic dipole and a location for observation of magnetic field. The direction of r is at an angle of θ to the direction of magnetic dipole moment. M represents strength of magnetic dipole moment and μ_0 is permeability of vacuum, but now for simplicity $M/4\pi\mu_0$ is set as 1. At a location for observation, the magnetic field H is composed as summation over the contribution from all magnetic dipoles, namely spins in our model. Of course such a magnetic field H depends upon the location for observation. Here 2 locations is chosen as A point and B point in Fig. 1, that is, the center of the layer plane ($x = 15, y = 15$) and the location near a corner of the plane ($x = 5, y = 5$) respectively. There are lift off distances of 1 from the surface plane in both cases. Then the location of height is set as $z = 1$ for 1 layer spin system as shown in Fig. 1, $z = 3$, and $z = 5$ for 3 layers and 5 layers as shown in Fig. 5, respectively. When external magnetic field formed as triangle wave is applied for the spin systems, the discrete change

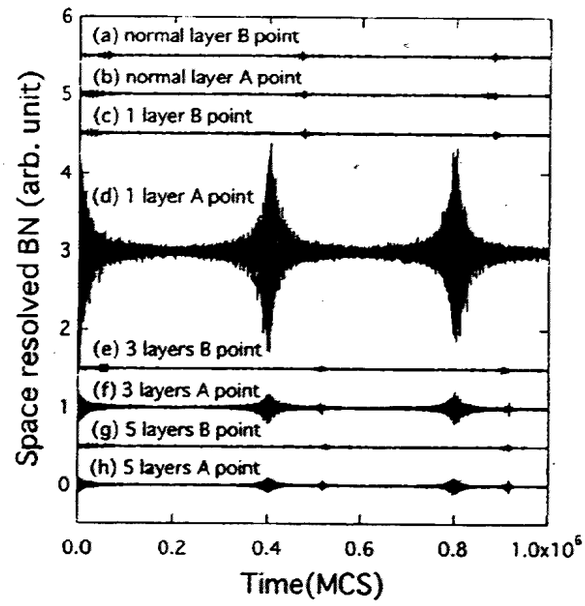

Fig. 8. Simulated space resolved BN for (a), (b) 1 layer normal spin system, (c), (d) 1 layer spin systems including one loop dislocation, (e), (f) 3 layers systems in Fig. 5 and (g), (h) 5 layer spin systems. A and B points show the area on surface in Fig. 1.

of H for time (or MCS) will give a kind of Barkhausen noise depending on the location. Then we call the Barkhausen noise simulated space resolved BN.

Fig. 8 shows the results of simulated space resolved BN for (a), (b) 1 layer without any dislocation and (c), (d) including one dislocation, (e), (f) 3 layers in Fig. 5(a) and (g), (h) 5 layers in Fig. 5(b). For a normal layer there is not much of difference of the space resolved BN between A point and B point as shown in Fig. 8(a) and (b). The result suggests the edge effect of the spin system can be neglect even B point because now the lift off distance is very small and the effect to H from farther spins is weak. On the other hand, for the 1 layer including one dislocation, there is a obvious difference between A point and B point. At A point, large anomalous BN is clearly seen in the magnetic field across the zero field as shown in Fig. 8(d). Notice that A point is just above the dislocation. But at B point of same spin system, there is no anomalous BN as same as a normal layer. The tendency remains for multilayers for Fig. 8(e) and (f), Fig. 8(g) and (h), although the peak intensity of anomalous BN becomes weakening as more layers due to increasing the distance of height between the dislocation and the observed location. The intensities of normal BNs around coercivity almost equal except for Fig. 8(d), probably owing that there are normal layers just below the location for observation.

IV. Conclusion

The above calculation results suggest high fluctuated and stressful state of spin system including local deformation. Our model for the simulation may include extreme over estimation, especially about the exchange interaction has sharp cut-off length. But the tendency will still remain in some degree for the real system. Then we may have a new measurement tool using BN for micro magnetic clusters to detect the deformation.

ACKNOWLEDGMENT

This work was supported in part by the Fukushima University Research Fund. The authors would like to express their thanks to T. Kinoshita in the Institute of Fluid Science, Tohoku University for helping in parallel coding program with MC simulations.

REFERENCES

[1] S. Zapperi and G. Durin, "New perspectives for the Barkhausen effect," *Comput. Mater. Sci.*, vol. 20, pp. 436–442, 2001.

[2] R. Varga, K. L. Garcia, A. P. Zhukov, and M. Vazzquez, "Switching field fluctuations in bitable microwires," *Physica B*, vol. 343, pp. 403–409, 2004.

[3] Z. Hao, Y. Shaoguang, N. Gang, Y. Dongliang, and D. Youwei, "Study on magnetic proprety of $Fe_{14}Ni_{86}$ alloy nanowire array," *J. Magn. Magn. Mater.*, vol. 234, pp. 454–458, 2001.

[4] K. Xue, G. Pan, M. Pan, M. Lu, and G. Wang, "Magnetic behavior of arrays of nickel nanowires with small diameter," *Superlattices Microstructures*, vol. 33, pp. 119–129, 2003.

[5] D. Kim, S. Choe, and S. Shin, "Statistical analysis of fluctuating domain wall during Barkhausen avalanche in Co nanofilms," *J. Magn. Magn. Mater.*, to be published.

[6] T. A. Moore, S. M. Gardiner, C. M. Guertler, and J. A. C. Bland, "Real time magnetization reversal dynamics in epitaxial Fe/GaAs(001)," *Physica B*, vol. 343, pp. 337–342, 2004.

[7] D. Hinzke and U. Nowak, "Magnetization switching in nanowires: Monte Carlo study with fast Fourier transformation for dipolar fields," *J. Magn. Magn. Mater.*, vol. 221, pp. 365–372, 2000.

[8] M. Vazquez, K. Nielsch, P. Vargas, J. Velazquez, D. Navas, K. Pirota, M. Hernandez-Velez, E. Vogel, J. Cartes, R. B. Wegrspohn, and U. Gosele, "Modeling hysteresis of interacting nanowires arrays," *Physica B*, vol. 343, pp. 395–402, 2004.

[9] R. Hertel, "Computational micromagnetism of magnetization processes in nickel nanowires," *J. Magn. Magn. Mater.*, vol. 249, pp. 251–256, 2002.

[10] K. Yamaguchi, K. Yamada, S. Shoji, Y. Uno, H. Takeda, S. Toyooka, and H. Tsuboi, "Simulation for nondestructive evaluations by magnetic sensors," *IEEE Trans. Magn.*, vol. 36, no. 4, pp. 1710–1713, Jul. 2000.

[11] K. Yamaguchi, K. Yamada, and T. Takagi, "Monte Carlo simulation for magnetic materials including dislocations," *IEEE Trans. Magn.*, vol. 38, no. 2, pp. 865–868, Mar. 2002.

[12] K. Yamaguchi, S. Tanaka, O. Nittono, T. Takagi, and K. Yamada, "Monte Carlo simulation of dynamic magnetic processes for spin system with local defects," *Physica B*, vol. 343, pp. 298–302, 2004.

[13] K. Yamaguchi, S. Tanaka, H. Watanabe, O. Nittono, T. Takagi, and K. Yamada, "Monte Carlo simulation for Barkhausen noise," *IEEE Trans. Magn.*, vol. 40, no. 2, pp. 884–887, Mar. 2004.

[14] K. Yamaguchi, S. Tanaka, O. Nittono, K. Yamada, and T. Takagi, "Monte Carlo simulation of Barkhausen noise for micromagnetic clusters," *IEEE Trans. Magn.*, vol. 41, no. 5, pp. 1536–1539, Sep. 2005.

[15] K. Yamaguchi, S. Tanaka, H. Watanabe, O. Nittono, K. Yamada, and T. Takagi, "Analysis of Barkhausen noise using Monte Carlo simulation for nondestructive evaluation," *J. Mater. Process. Technol.*, vol. 161, pp. 338–342, 2005.

[16] N. Metropolis, A. Rosenbluth, M. Rosenbluth, and A. Teller, "Equation of state calculations by fast computing machines," *J. Chem. Phys.*, vol. 21, pp. 1087–1092, 1953.

[17] D. W. Heermann, *Computer Simulation Methods in Theoretical Physics*. Berlin, Germany: Springer-Verlag, 1990.

[18] K. Binder, *Phase Transitions and Critical Phenomena*, C. Domb and M. S. Green, Eds. London, U.K.: Academic, 1976, vol. 5B, pp. 2–100.

[19] G. Parisi, *Statistical Field Theory*. Redwood, CA: Addison-Wesley, 1988.

[20] C. Ebner, "Phase diagrams of multilayer films and the Potts lattice-gas model of adsorption," *Phys. Rev. B*, vol. 28, pp. 2890–2892, 1983.

[21] ——, "Film formation on a weakly attractive substrate within the lattice-gas model," *Phys. Rev. A*, vol. 22, pp. 2776–2781, 1980.

[22] J. Marro and R. Dickman, *Nonequilibrium Phase Transitions in Lattice Models*. Cambridge, U.K.: Cambridge Univ. Press, 1999, pp. 12–60.

Manuscript received June 20, 2005 (e-mail: yama@sss.fukushima-u.ac.jp).

Co-ITO granular magnetoresistance films fabricated by precipitation of magnetic nanoparticles from amorphous oxide

Wanti Ekawati, Ji Shi,[a] and Yoshio Nakamura
Department of Metallurgy and Ceramics Science, Tokyo Institute of Technology, 2-12-1 O-okayama, Meguro-ku, Tokyo 152-8552, Japan

Osamu Nittono
Faculty of Symbiotic System Science, Fukushima University, 1 Kanayagawa, Fukushima 960-1296, Japan

(Received 25 August 2005; accepted 12 December 2005; published 27 February 2006)

 [DOI: 10.1116/1.2165662]

Tunneling magnetoresistance has been found in the metal-insulator Co–Al–O granular films.[1] The characteristic of such films is that the magnetic Co particles uniformly distribute in the insulating aluminum oxide matrix. Since the difference in oxygen affinity between Co and Al is large, Co and aluminum oxide separate from each other during deposition; thus a granular structure is formed and the films show relatively high magnetoresistance (MR).[2–4] However, it is reported that the MR ratio of the films decrease upon thermal annealing.[5,6] The authors attribute the decrease of magnetoresistance to the formation of larger magnetic particles.[5] These results show that the structure of the films changes unfavorably during thermal annealing. It is known that, in practice, the fabrication of MR head requires heat treatment at around 270 °C.[7] Therefore MR films with thermal stability up to 300 °C are desirable.

In this work, we use a two-step method to fabricate the granular films in order to ensure the film is stable at about 300 °C. The first step is to form an amorphous phase containing magnetic atoms, and the second to make the magnetic particles precipitate from the amorphous phase through thermal annealing at 300 °C or above. For this purpose, Co and ITO (indium tin oxide) are selected because the difference in oxygen affinity between Co and In is small compared to Co and Al. In this way, we expect that the separation of Co and ITO during deposition can be prevented, and a complex amorphous phase can be formed. Then, we can expect the precipitation of Co particles to take place and form nanosize Co particle in the amorphous ITO through thermal annealing at appropriate temperature. Besides the consideration of the oxygen affinity, ITO is chosen as a matrix also due to the fact that it easily forms an amorphous phase and the amorphous ITO is of high resistivity.[8,9]

A two-facing target dc magnetron sputtering system is used to prepare the Co-ITO films. Two ITO targets were used in this work, and the Co chips were placed on the surface of one of ITO targets. The composition of Co is changed by changing the number of Co chips.

The resistivity and magnetoresistance of Co-ITO films annealed at various temperatures is shown in Fig. 1. At low Co volume fraction (10%), the film shows relatively high resistivity in the order of 10^5 $\mu\Omega$ cm. However, the resistivity decreases as the annealing temperature increases [Fig. 1(a)]. The increase of annealing temperature increases the MR ratio of this film up to 250 °C. Annealing the films at above 250 °C causes a drop of magnetoresistance (MR) ratio. The change of resistivity (ΔR) with applied field of this film is plotted in Fig. 2(a). The maximum ΔR of the film annealed at 250 °C is about 1.2 Ω. The above results show that small

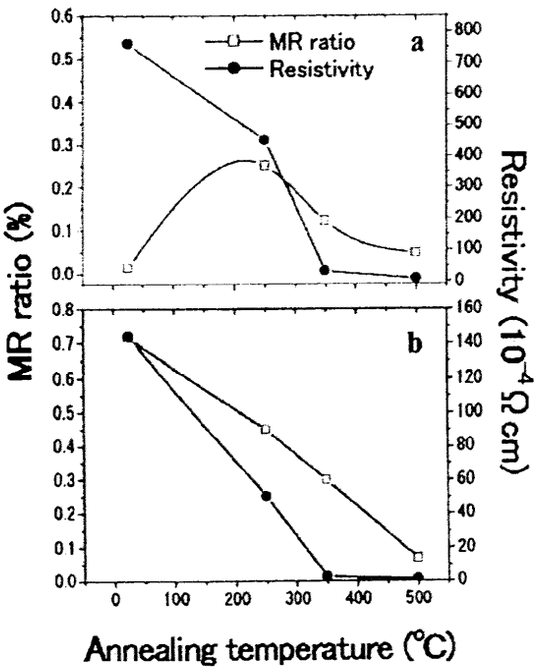

FIG. 1. Resistivity and MR ratio of Co-ITO films with different Co volume fractions annealed at various temperatures. (a) Co volume fraction: 10%. (b) Co volume fraction: 33%.

[a]Electronic mail: shi@mtl.titech.ac.jp

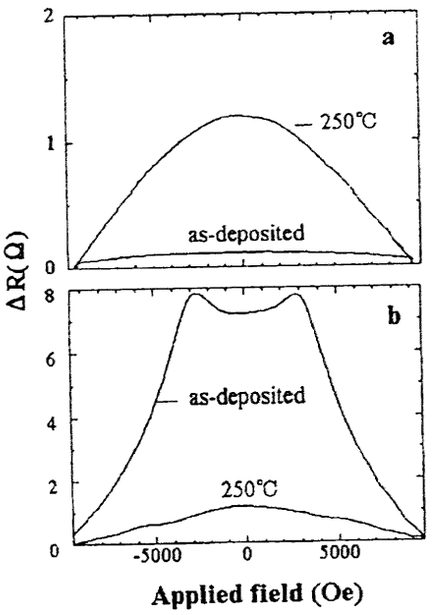

FIG. 2. ΔR curves of as-deposited Co-ITO films and the films annealed at 250 °C. (a) Co vol. fraction: 10%. (b) Co vol. fraction: 33%.

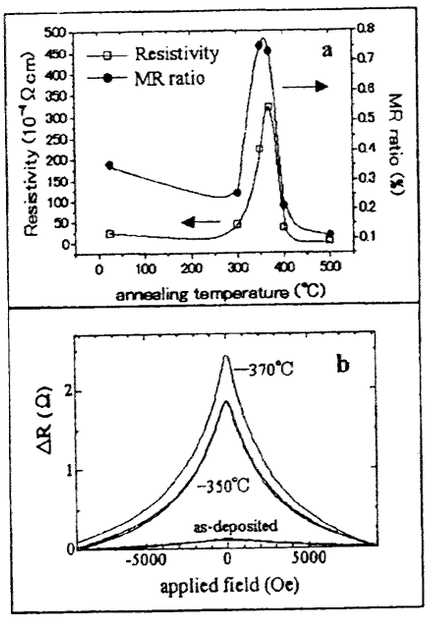

FIG. 3. Resistivity, MR ratio, and ΔR curves of Co–Pt-ITO films annealed at various temperatures. (a) Resistivity and MR ratio. (b) ΔR curves.

amount of Co can be incorporated into the amorphous ITO in the as-deposited state and through thermal annealing Co particles are formed in the film, as a result, the magnetoresistance appears. However, since the film contains low concentration of Co, the magnetoresistance is small.

At higher Co volume fraction (33%), as-deposited film shows high resistivity and magnetoresistance. However, both resistivity and magnetoresistance rapidly decrease with increasing annealing temperature [Fig. 1(b)]. It can be seen from the ΔR curve that a ΔR value as high as 8 Ω is observed for as-deposited film [Fig. 2(b)]. The ΔR curve of this film shows a saddle shape which implies that the magnetic coupling between Co particles exist in this film.[10] The above result suggests that at high Co volume fraction, some amount of Co has been segregated during deposition. In this case, thermal annealing cannot improve the distribution of Co particles in the amorphous matrix. It seems that the oxygen affinity factor alone cannot assure the sufficient solubility of Co in amorphous ITO. In order to improve this solubility, we tried adding an additional element to the Co-ITO films. We believe that many aspects of the films will be affected by adding an additional element into the film, such as the surface diffusivity during deposition and the oxidation state of Co. The properties of the additional element itself, its atomic or ionic radius, its oxygen affinity, will also affect the formation and structure of the Co-ITO film. Therefore we think that the solubility of Co in amorphous ITO can be improved by adding an appropriate element into the film. Pt was tentatively chosen for this purpose in the present work because of the fact that its atomic (ionic) radius is between that of Co and In,[11] and that it does not impair the magnetic moment of Co when forming a Co(Pt) solid solution.[12] In addition, the formation of Co(Pt) solid solution, instead of Co, during precipitation and crystallization is also expected to affect the thermodynamics and kinetics of such processes favorably. The atomic ratio of Co to Pt is fixed to about 5:1 in the present work.

The resistivity and MR ratio of Co–Pt-ITO films are shown in Fig. 3. Figure 3(a) shows that the as-deposited film has a resistivity of 2.5×10^{-3} Ω cm. The films annealed at 300 °C shows almost no change of resistivity, indicating the amorphous phase is stable up to 300 °C. However, above 300 °C, the resistivity increases drastically and reaches the maximum value at 370 °C. This suggests that Co atoms begin to precipitate at a temperature above 300 °C. Further

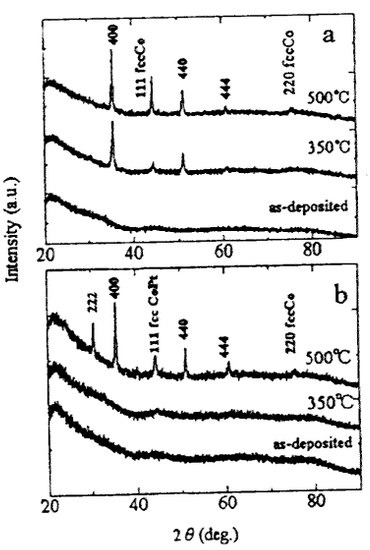

FIG. 4. XRD profiles of Co-ITO films (a) and Co-Pt-ITO films (b) annealed at various temperatures.

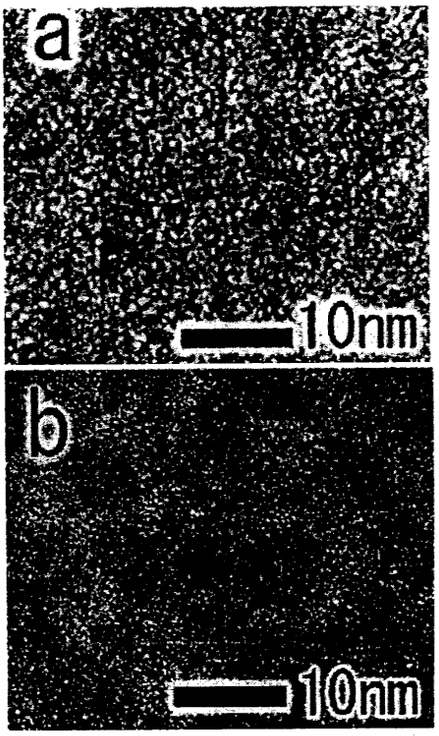

FIG. 5. HRTEM images of as-deposited Co–Pt-ITO films (a), and the films annealed at 350 °C (b).

increasing the annealing temperature to 400 °C causes an abrupt drop of resistivity. The MR ratio shows a similar tendency to resistivity. Maximum MR ratio is observed when the film in annealed at 350 °C. The ΔR curves of Co–Pt-ITO films are shown in Fig. 3(b). The shape of ΔR curve is greatly improved compared to those of the Co-ITO films, indicating the improvement of magnetic particles distribution in the granular films.

To understand the electrical and magnetic behaviors of the films, the structural properties were characterized by x-ray diffraction (XRD) and the result is shown in Fig. 4. The volume fractions of Co in the Co-ITO film and Co(Pt) in the Co–Pt-ITO film are both 33%. Although the resistivity and magnetoresistance measurements have suggested the existence of Co particles in the as-deposited state of Co-ITO films, there is no obvious peak on the XRD profiles. We consider that this is due to the small size of Co particles. The structure of the as-deposited films of Co-ITO films were further studied by transmission electron microscopy, and the results will be presented elsewhere. When the film is annealed at 350 °C, the diffraction peaks from both ITO and Co are observed, which indicates that the film has crystallized at this temperature. The change in resistivity and magnetoresistance can be explained from the structural change. With increasing annealing temperature, the part of Co originally dissolved in the amorphous ITO precipitates, and then the crystallization of amorphous ITO occurs. Crystalline ITO and Co separate from each other during the crystallization process. These changes in film structure lower the resistivity and thus the magnetoresistance of the film. On the other hand, it seems that Co–Pt-ITO film annealed at 350 °C shows no obvious changes in crystal structure compared with the as-deposited film as shown in Fig. 4(b). However, a weak peak corresponding to Co(Pt) (111) is detectable. When it is annealed at 500 °C the film fully crystallize. Comparing the result of Co-ITO films, we can say that the crystallization of the amorphous matrix is postponed to higher temperature by adding Pt in the film. Figure 5(a) shows the HRTEM images of the as-deposited Co–Pt-ITO film and the film annealed at 350 °C. It reveals that as-deposited film is basically amorphous as expected, in accordance with the XRD result. For the film annealed at 350 °C, Co(Pt) particles of 5–10 nm in diameter are seen distributed uniformly in the amorphous matrix, indicating that the Co–Pt-ITO granular film has been formed [Fig. 5(b)]. In view of the structure and the high resistivity of the Co–Pt-ITO film, it can be concluded that the magnetoresistance is originated from spin-dependent tunneling process.[13,14] This also implies that the conduction in the Co–Pt-ITO film is tunneling dominant, i.e., the volume fraction of Co(Pt) is below the percolation limit, which may be as high as 47% for a metal-nonmetal granular film.[15]

Based on the above results, we could confirm that Co atoms could be dissolved in amorphous ITO. However, the solubility of Co in amorphous ITO matrix is not sufficient for the purpose to fabricate magnetoresistance Co-ITO granular films by the two-step method. Our results have also shown that the addition of Pt into Co-ITO film increases the solubility of Co and increases the crystallization temperatures of the complex amorphous ITO, making it possible to fabricate Co–Pt-ITO granular films with magnetic particles distributed in an amorphous ITO matrix through thermal annealing. Such films show relative high resistivity and magnetoresistance.

[1]H. Fujimori, S. Mitani, and M. Ohnuma, Mater. Sci. Eng., B **31**, 219 (1995).
[2]K. Kamei, M. Yonemura, and K. Hanafusa, J. Mater. Sci. **12**, 569 (2001).
[3]S. Mitani, H. Fujimori, and M. Ohnuma, J. Magn. Magn. Mater. **165**, 141 (1997).
[4]M. Ohnuma, K. Hono, E. Abe, H. Onodera, S. Mitani, and H. Fujimori, J. Appl. Phys. **82**, 5647 (1997).
[5]J. G. Ha, S. Mitani, K. Takanashi, M. Ohnuma, K. Hono, and H. Fujimori, J. Magn. Magn. Mater. **198**, 21 (1999).
[6]M. Ohnuma, K. Hono, H. Onodera, S. Mitani, J. G. Ha, and H. Fujimori, Nanostruct. Mater. **12**, 573 (1999).
[7]H. Yamamoto and K. Yamada, Mater. Sci. Eng., B **31**, 207 (1995).
[8]D. C. Paine, T. Whitson, D. Janiac, R. Beres Ford, and C. Ow-Yang, J. Appl. Phys. **85**, 8445 (1995).
[9]F. O. Aduroja, H. Izumi, T. Ishihara, H. Yoshioka, and M. Motoyama, Sol. Energy Mater. Sol. Cells **71**, 1 (2002).
[10]T. Sannomiya, Y. Haga, Y. Nakamura, and O. Nittono, J. Appl. Phys. **95**, 214 (2004).
[11]C. Kittel, *Introduction to Solid State Physics*, 7th ed. (Wiley, New York, 1996), p. 24–28.
[12]S. Chikazumi, *Physics of Ferromagnetism*, 2nd ed. (Oxford, New York, 1997), p. 173–174.
[13]H. Fujimori, S. Mitani, and K. Takanashi, Mater. Sci. Eng. **165**, 141 (1997).
[14]P. M. Levy, Sol. State Phys. **47**, 367 (1994).
[15]B. Abeles, H. L. Pinch, and J. I. Gittleman, Phys. Rev. Lett. **35**, 247 (1975).

Effects of Pt addition on the formation of Co–ITO granular magnetoresistance films by a two-step method

Wanti Ekawati, Ji Shi,[a] and Yoshio Nakamura
Department of Metallurgy and Ceramics Science, Tokyo Institute of Technology, 2-12-1 O-okayama, Meguro-ku, Tokyo 152-8552, Japan

Osamu Nittono
Faculty of Symbiotic System Science, Fukushima University, 1 Kanayagawa, Fukushima 960-1296, Japan

(Received 30 September 2005; accepted 13 February 2006)

Platinum (Pt) has been added to Co–ITO (ITO: indium tin oxide) films to promote the formation of Co(Pt)–ITO granular structure by a two-step method which includes sputtering deposition at room temperature and postdeposition thermal annealing in a vacuum. Such films consist of magnetic Co(Pt) nanoparticles distributed uniformly in an amorphous ITO matrix. The Co(Pt) particles are formed during the thermal annealing by precipitation, and the matrix also contains certain amount of Co and Pt that suppress the crystallization temperature of the amorphous ITO. Pt plays an important role in controlling the precipitation of Co(Pt) particles and the microstructure formation. First, by adding Pt into the films, more Co can be incorporated into the amorphous phase in the as-deposited state, which ensures sufficient Co to form magnetic particles through precipitation. Second, by incorporating Co and Pt into the film, the crystallization temperature of amorphous ITO is also increased to a temperature as high as 400 °C. These two effects make it possible to fabricate the Co(Pt)–ITO granular magnetoresistance films by the two-step method. © *2006 American Vacuum Society.* [DOI: 10.1116/1.2186652]

I. INTRODUCTION

Metal-insulator granular films have been intensively investigated recently in order to obtain films showing both high resistivity and magnetoresistance.[1–5] A typical and intensively investigated system among the granular films is Co–Al–O system.[3,4,6,7] One of the important features of this system is the relatively large difference in oxygen affinity between Co and Al. This causes the separation between Co and aluminum oxide during deposition, thus the granular structure with nanosized magnetic Co particles distributed in the insulating aluminum oxide matrix is formed. It has been reported that as-deposited Co–Al–O films with proper composition exhibit tunnel-type magnetoresistance (MR) as high as 8% and a resistivity of about 10^4 $\mu\Omega$ cm.[8] However, upon thermal annealing, the MR ratio of the film decreases.[9,10] The decrease of MR ratio is attributed to the formation of larger magnetic particles during annealing.[9]

It is also known that for practical applications such as magnetic head, the MR film should be thermally stable up to 300 °C.[11] For this purpose, we have proposed a two-step method to fabricate the metal-oxide MR films[12] which consists of the formation of amorphous phase during deposition and the precipitation of magnetic particles from the amorphous phase during thermal annealing. Co and indium tin oxide (ITO) are chosen for the magnetic particles and the matrix, respectively, because of the small difference in oxygen affinity between Co and In. In this way, we expect that an amorphous Co–ITO film will be formed in as-deposited films without phase separation. Moreover, by controlling the precipitation of Co through thermal annealing at an appropriate temperature, the Co–ITO granular structure with nanosized magnetic particles distributed in the amorphous ITO is expected. However, it is found that only 10% (volume) of Co can be incorporated into the amorphous phase. In other words, the apparent solubility of Co in amorphous ITO is low. Above this limit, Co atoms segregate out of the amorphous phase in the as-deposited state. In order to improve this solubility, we tried to add other elements into the Co–ITO films. Pt is found to be very effective,[12] and Co(Pt)–ITO granular films with relatively high resistivity and MR are formed by the two-step method with an annealing temperature of 350 °C. Nevertheless, the role played by Pt in this film is still not clear. Therefore, our objective for the present work is to clarify in what way Pt has affected the microstructure formation of Co(Pt)–ITO films during deposition and thermal annealing.

II. EXPERIMENT

Co(Pt)–ITO films were prepared at room temperature by using two-facing-target dc magnetron sputtering system. ITO compound, Co and Pt chips were used as targets in this work. The composition of Pt is changed by adjusting the number and size of Pt chips placed on the surface of Co target. For most films, the volume fraction of Co(Pt) is fixed, and only the Co to Pt ratio is changed. Silica glass and Si wafer with a thickness of 0.5 mm were used as substrates for various characterizations. The sputtering chamber was evacuated to a pressure of around 8×10^{-5} Pa before deposition. Only Ar was introduced into the sputtering chamber and the Ar pressure was kept at 0.2 Pa during deposition. The deposition

[a]Electronic mail: shi@mtl.titech.ac.jp

rate is around 0.37 Å/s, and the average film thickness is controlled to about 2000 Å. After deposition, the films were annealed in a vacuum of about 1×10^{-5} Pa for an hour at various temperatures. Structural properties of the films were characterized by x-ray diffraction using Cu $K\alpha$ radiation. X-ray photoelectron spectroscopy (XPS) was used to identify the atomic composition ratio of each film. Film resistivity and magnetoresistance was measured using a four-point probe magnetoresistance measurement unit. The magnetic properties were examined using a vibrating sample magnetometer (VSM). A transmission electron microscope (TEM) was used to examine the microstructure of these films.

III. RESULTS

A. Resistivity and MR ratio of Co(Pt)–ITO films

The resistivity and MR ratio of Co(Pt)–ITO films with different Pt contents are shown in Fig. 1. The volume fraction of magnetic metal [Co(Pt)] to ITO matrix is fixed at around 1:2 as confirmed by XPS analysis. The MR ratio is measured at room temperature under an applied field of 10 kOe. The as-deposited Co–ITO film, i.e., the film without Pt addition, exhibits relatively high resistivity and magnetoresistance. However, both resistivity and MR decrease monotonically with increasing annealing temperature, as shown in Fig. 1(a). Figure 1(b) represents the resistivity and MR ratio of $Co_{95}Pt_5$–ITO film. This film shows almost the same behavior as the Co–ITO film. The $Co_{83}Pt_{17}$–ITO film shows clearly a different behavior, as seen in Fig. 1(c). The as-deposited $Co_{83}Pt_{17}$–ITO film has low resistivity and MR ratio. Both resistivity and MR exhibit a maximum at an annealing temperature of 350 °C. This indicates that a Co(Pt)–ITO granular MR film is formed after annealing at this temperature. Thereafter, the resistivity and MR ratio decrease abruptly with annealing temperature. The increase in resistivity is due to the precipitation of Co(Pt) from the amorphous ITO matrix which decreases the carrier density in the amorphous oxide. On the other hand, the abrupt decrease of resistivity at an annealing temperature of 400 °C is due to the crystallization of the amorphous ITO matrix. The change of film structure will be further discussed in the next section. At higher Pt content ($Co_{75}Pt_{25}$–ITO), the film shows a similar tendency as the $Co_{83}Pt_{17}$–ITO film. However, excess Pt seems to lower the maximum value of both resistivity and MR ratio indicating that there is an optimum Pt content for the resistivity and MR ratio in this film [Fig. 1(d)].

Because the as-deposited Co–ITO film shows relative high resistivity and MR ratio, it is conceivable that Co separated with the amorphous ITO in the as-deposited state. On the other hand, the as-deposited $Co_{83}Pt_{17}$–ITO film shows relatively low resistivity and MR ratio, and maximum resistivity and MR ratio are obtained after thermal annealing at 350 °C. This result implies that most Co(Pt) atoms are incorporated into the amorphous phase, and precipitate as magnetic particles during thermal annealing. These speculations are also confirmed by ΔR curves, as shown in Fig. 2. Figure 2(a) shows the ΔR curves of the Co–ITO films without Pt addition. It shows a saddle shape that is a feature for the granular films where the magnetic particles have strong interaction with each other.[13] For films with strong interaction between magnetic particles, magnetization loops are formed[14] that involve several magnetic particles. Moreover,

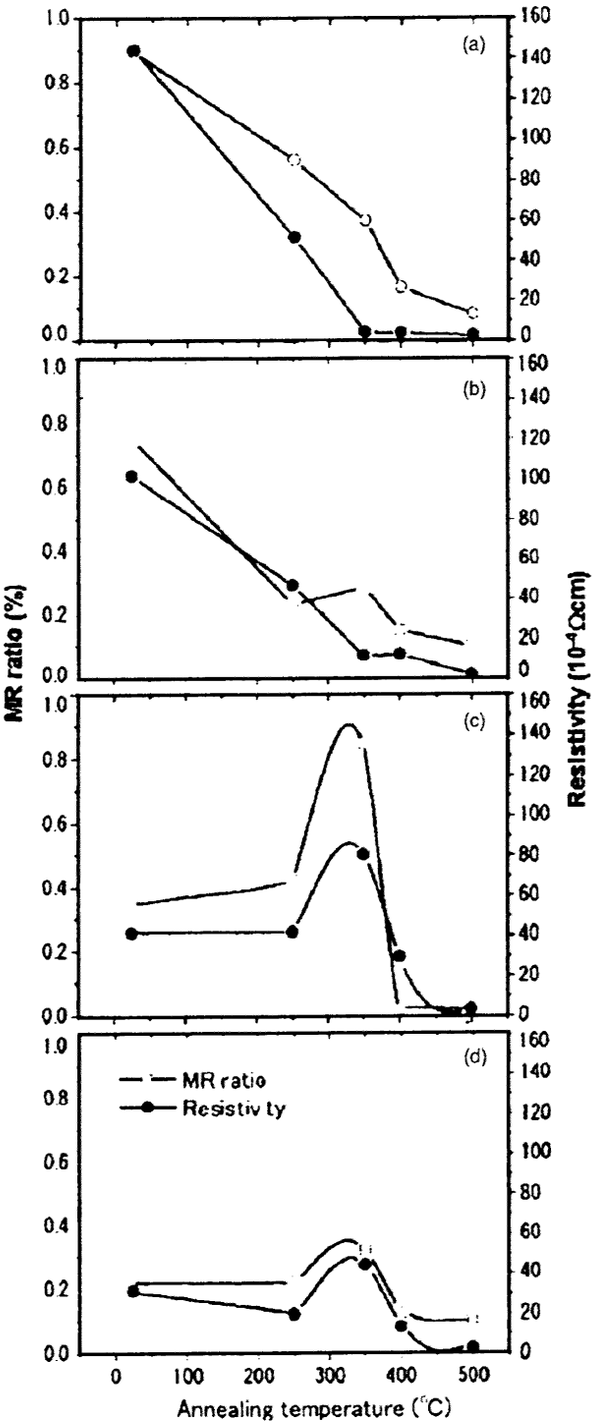

FIG. 1. Change of resistivity and MR ratio of Co(Pt)–ITO films with annealing temperatures. (a) Co–ITO, (b) $Co_{95}Pt_5$–ITO, (c) $Co_{83}Pt_{17}$–ITO, (d) $Co_{75}Pt_{25}$–ITO.

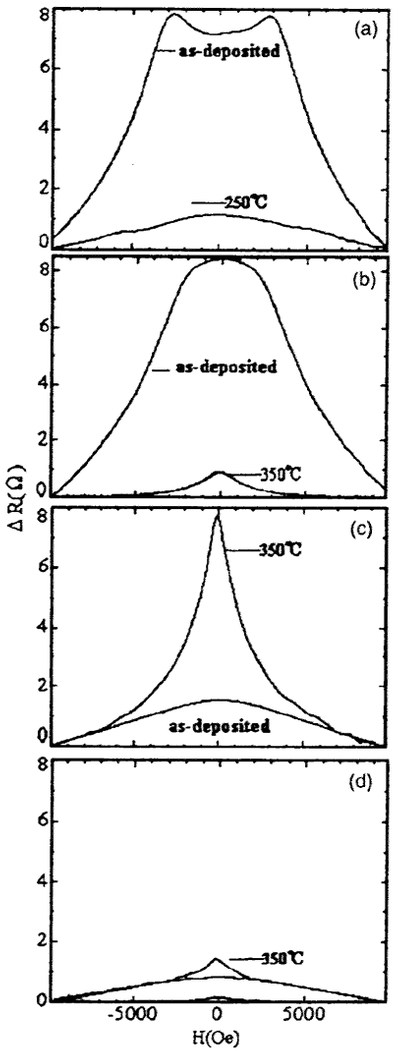

FIG. 2. ΔR curves of as-deposited and annealed Co(Pt)–ITO films. (a) Co–ITO, (b) $Co_{95}Pt_5$–ITO, (c) $Co_{83}Pt_{17}$–ITO, and (d) $Co_{75}Pt_{25}$–ITO.

when two elongated loops with opposite rotation sense are aligned side by side, the magnetizations of neighboring straight parts are parallel to each other. We consider that there are many such regions inside the film in the demagnetized state, which would explain the relative low resistance at zero fields. With the increase of the applied field, the above-mentioned parallel regions are destroyed gradually, and therefore the resistance increases with the applied field. With further increases of the applied field, the magnetization of the particles tends to align with the field, and the resistance decreases. The ΔR curve of the as-deposited $Co_{95}Pt_5$–ITO film [Fig. 2(b)] shows different shapes from the film without Pt addition. The resistance decreases monotonically with the applied field. This result suggests that the interaction between magnetic particles become weaker; the film becomes less populated with the magnetic particles. Therefore, we consider that by adding Pt into the film, more Co is incorporated into the amorphous phase. The as-deposited

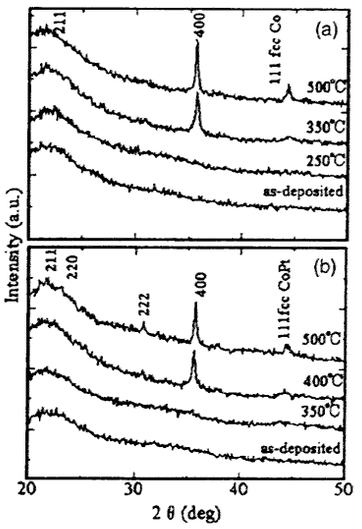

FIG. 3. X-ray diffraction profiles of (a) Co–ITO films and (b) $Co_{83}Pt_{17}$–ITO films.

$Co_{83}Pt_{17}$–ITO film shows much smaller ΔR value, implying that almost no Co(Pt) particles in the film. This result indicates that most of the Co and Pt atoms are incorporated into the amorphous phase. By thermal annealing at 350 °C, Co(Pt) precipitate from the amorphous phase as magnetic particles, the ΔR value increases greatly, and the ΔR curve becomes much sharper, as shown in Fig. 2(c). With further increasing Pt content ($Co_{75}Pt_{25}$–ITO), the ΔR values of both the as-deposited and the annealed films decrease, indicating that the precipitation of magnetic Co is suppressed [Fig. 2(d)]. The above results have shown that the Co(Pt)–ITO film formed by the two-step method, i.e., the magnetic particles, is formed by precipitation during thermal annealing; the ΔR curve is much sharper compared with films in which the magnetic particles are formed during deposition.

B. Structure of Co(Pt)–ITO films

In order to understand the electrical and magnetic behaviors of the Co(Pt)–ITO films in view of the film microstructure, the films were characterized by x-ray diffraction and cross-section transmission electron microscopy. Figure 3(a) shows the x-ray diffraction profiles of Co–ITO films, i.e., the films without Pt addition. There is no obvious peak for the as-deposited films, indicating that the film is amorphouslike. Even after thermal annealing at 250 °C, it seems that there is no obvious change in the film structure. Increasing the annealing temperature to 350 °C causes the crystallization of ITO and the separation between Co and ITO, since diffraction peaks from both ITO and Co can be seen on the diffraction profile. For the film with Pt addition, the as-deposited film is also amorphouslike, as can be seen from Fig. 3(b). However, the film remains uncrystallized even after annealing at 350 °C; the crystallization of ITO takes place at about 400 °C. These results show that adding Pt to the Co–ITO film increases the crystallization temperature of ITO.

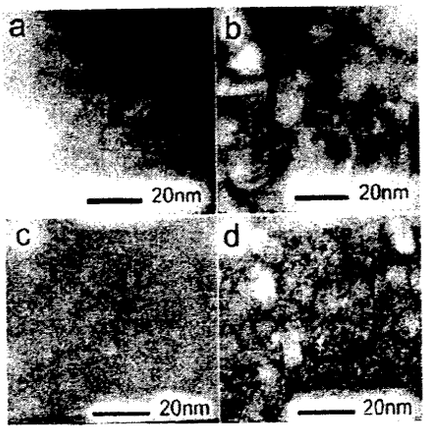

FIG. 4. High resolution cross-section TEM images of Co(Pt)–ITO films. (a) As-deposited Co–ITO film, (b) Co–ITO film annealed at 250 °C, (c) as-deposited $Co_{83}Pt_{17}$–ITO film, and (d) $Co_{83}Pt_{17}$–ITO film annealed at 350 °C.

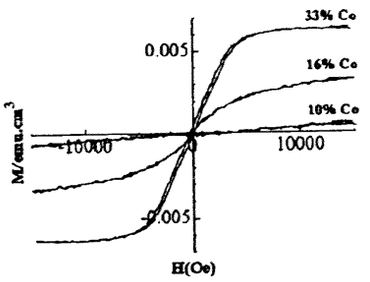

FIG. 5. *M-H* curves of as-deposited Co–ITO films of different Co volume fractions.

The cross-section TEM images of Co–ITO and $Co_{83}Pt_{17}$–ITO films are shown in Fig. 4. From Fig. 4(a) it is clearly seen that the Co particles exist in the amorphous ITO matrix in the as-deposited Co–ITO film. The Co particles are of an average size of less than 10 nm, and some of them are of irregular shape. The microstructure feature together with the fact that amorphous ITO is almost insulating[15,16] explain the appearance of magnetoresistance in the as-deposited state. According to the microstructure, we consider that the magnetoresistance is tunnel type, which is the same type as found in other metal-oxide granular system.[2,3] Upon thermal annealing at 250 °C, some areas of the amorphous ITO crystallize [Fig. 4(b)]. Round shape crystallites of both Co and ITO can be seen in the image, and the average size of the crystallites is less than 20 nm in diameter. The crystallization of amorphous ITO explains the decreases in resistivity and MR after thermal annealing at 250 °C, because the tunnel process is no longer dominating the electron conduction in the film. It seems that the x-ray diffraction results are not consistent with TEM observation results for the as-deposited film and the film annealed at 250 °C, which is due to the small size of the crystal phases in the films.

$Co_{83}Pt_{17}$–ITO films show quite different features. Although some small contrast is visible in the cross-section TEM image, the as-deposited film is basically amorphous, as can be seen in Fig. 4(c). After thermal annealing at 350 °C, fine Co(Pt) particles with an average size of about 10 nm are formed in the film [Fig. 4(d)]. On the other hand, the ITO remains amorphous, thus a granular structure of Co(Pt)–ITO is formed with Co(Pt) particles distributed uniformly in the amorphous ITO matrix. The relative high resistivity and MR are attributed to the formation of Co(Pt)–ITO granular structure.

IV. DISCUSSION

Figure 5 shows the *M-H* curves of Co–ITO films with different Co volume fractions. When the volume fraction of Co is 10%, the film is paramagnetic, indicating that Co atoms are dissolved into the amorphous phase. However, with increasing the Co volume fraction to 16% and 33%, the films show superparamagnetic and ferromagnetic behaviors, respectively, indicating the existence of Co particles in the as-deposited films, and that the magnetic coupling between the Co particles become stronger with higher Co content. These results suggest that there is an apparent solubility of Co in the amorphous ITO.[11] By saying apparent solubility, we mean that it is not like the equilibrium solubility of an element in a solid solution, but the amount that can be incorporated into the amorphous oxide during deposition. In order to fabricate Co–ITO granular MR film, it is necessary to increase the apparent solubility.

The solubility of Co in amorphous ITO is increased substantially by adding proper amounts of Pt into the Co–ITO films, as can be seen from the structural characterization of the films. With proper amounts of Pt, the film remains amorphous for a Co(Pt):ITO volume ratio of 1:2, namely, without apparent separation between Co(Pt) and ITO. We have also prepared Pt–ITO films and $Co_{83}Pd_{17}$–ITO film. In both cases, amorphous phase is obtained when the *M*(Co,Pd,Pt):ITO volume ratio is 1:2. Because the atom sizes of Pt and Pd are larger than that of Co, we consider that the atom size is an important factor that affects the solubility of *M*(Co,Pd,Pt) in amorphous ITO.

Another requirement for fabricating Co–ITO granular films by precipitation of magnetic particles (Co) is that the ITO does not crystallize during thermal annealing at elevated temperatures (300–400 °C). The crystallization temperature for ITO films prepared by the same method as used here is between 150 and 200 °C, which is in accordance with the results of ITO films fabricated by other methods.[17,18] Although the mechanism is still unclear, the results of the present work have shown that incorporating metal element such as Co into the films suppresses the crystallization temperature of the amorphous ITO. In the case of Co, the crystallization temperature of the amorphous phase is about 250 °C, i.e., over 50 °C higher than that of pure ITO. However, 250 °C is still not high enough from the viewpoint of practical applications. In the case of Co(Pt)–ITO films with proper amounts of Pt, the crystallization temperature of amorphous ITO is also increased to about 400 °C. It has been reported that the crystallization temperature of amorphous ITO can be increased to higher temperatures, such as

in the case of adding H_2O vapor to the sputtering gas during deposition.[19–21] The increase of crystallization temperature is attributed to several reasons. A convincing explanation is that bonding between oxygen and element other than In in the amorphous ITO suppresses the crystal growth by hampering reconstruction of the In–O networks.[18,19] This explanation is believed to be applicable to our Co(Pt)–ITO films, because the Co–O bonding is formed in the amorphous phase.

Based on the above considerations, the microstructure evolution and the changes in properties with thermal annealing can be well explained. For the film with proper amount of Pt addition, the as-deposited film is amorphous and has lower resistivity compared with the film without Pt addition [comparing Figs. 1(a) and 1(c)]. This is because the Co and Pt atoms incorporated into the amorphous phase supply free electrons as carriers to the amorphous ITO. When the film is annealed at 350 °C, Co(Pt) precipitate out to form nanosized particles that distributed uniformly in the remaining amorphous phase. Thus the carrier density in the amorphous phase becomes smaller, and the resistivity increases. There are still small amounts of Co and Pt remaining in the amorphous phase, which suppress crystallization of the amorphous ITO. MR is also obtained at this annealing temperature, which is tunnel-type MR, and is attributed to the formation of the granular structure and the high resistivity of the matrix. When the film is annealed at 400 °C, Co and Pt atoms contained in the amorphous phase precipitate out and the amorphous ITO becomes unstable and then finally crystallizes, and thus both resistivity and MR decrease abruptly, as shown in Fig. 1(c). Although the MR ratio of $Co_{83}Pt_{17}$–ITO film is not as high as that reported in other systems, the film is still believed to be of great importance in view of practical applications. Because the base resistivity (10^4 $\mu\Omega$ cm) and ΔR are relatively high, the ΔR curve is sharp which render the film good sensitivity to magnetic field.

V. CONCLUSIONS

Co(Pt)–ITO granular films with relative high resistivity and MR are fabricated by the two-step method. Pt plays an important role in controlling the precipitation of magnetic Co(Pt) particles in the amorphous ITO during the fabrication process. First, by adding Pt in the film, the apparent solubility of Co in the amorphous ITO is increased to a volume fraction of 33% (including Pt). Second, as a result of the large amount of Co and Pt incorporated into the amorphous ITO, the crystallization temperature of the amorphous phase is increased to as high as 400 °C. These two effects of Pt addition are essential for fabricating precipitation-controlled Co(Pt)–ITO granular MR films.

[1]M. Ohnuma, K. Hono, and H. Onodera, J. Appl. Phys. **87**, 817 (1999).
[2]K. Zhu and Y. J. Wang, Phys. Rev. B **60**, 11918 (1999).
[3]S. Ohnuma, H. Fujimori, S. Mitani, and T. Matsumoto, J. Appl. Phys. **79**, 5130 (1996).
[4]M. Ohnuma, K. Hono, E. Abe, H. Onodera, S. Mitani, and H. Fujimori, J. Appl. Phys. **82**, 5646 (1997).
[5]S. Sankar, D. Dender, J. Borchers, D. J. Smith, R. W. Erwin, S. R. Kline, and A. E. Berkowitz, J. Magn. Magn. Mater. **221**, 1 (2000).
[6]H. Fujimori, S. Mitani, and S. Ohnuma, Mater. Sci. Eng., B **31**, 219 (1995).
[7]K. Kamei, M. Yonemura, and K. Hanafusa, J. Mater. Sci.: Mater. Electron. **12**, 569 (2000).
[8]S. Mitani, H. Fujimori, and S. Ohnuma, J. Magn. Magn. Mater. **165**, 141 (1997).
[9]J. G. Ha, S. Mitani, K. Takanashi, M. Ohnuma, K. Hono, and H. Fujimori, J. Magn. Magn. Mater. **198**, 21 (1999).
[10]M. Ohnuma, K. Hono, H. Onodera, S. Mitani, J. G. Ha, and H. Fujimori, Nanostruct. Mater. **12**, 573 (1999).
[11]H. Yamamoto and K. Yamada, Mater. Sci. Eng., B **31**, 207 (1995).
[12]E. Wanti, J. Shi, Y. Nakamura, and O. Nittono (unpublished).
[13]A. E. Berkowitz *et al.*, Phys. Rev. Lett. **68**, 3745 (1992).
[14]T. Sannomiya, Y. Haga, Y. Nakamura, and O. Nittono, J. Appl. Phys. **95**, 214 (2004).
[15]D. C. Paine, T. Whitson, D. Janiac, R. Beresford, and C. Ow-Yang, J. Appl. Phys. **85**, 8445 (1995).
[16]F. O. Aduroja, H. Izumi, T. Ishihara, H. Yoshioka, and M. Motoyama, Sol. Energy Mater. Sol. Cells **71**, 1 (2002).
[17]S. Muranaka, Jpn. J. Appl. Phys., Part 2 **30**, L2062 (1991).
[18]S. Muranaka, Y. Bando, and T. Takada, Thin Solid Films **25**, 355 (1987).
[19]M. Ando, E. Nishimura, K. Onisawa, and T. Minemura, J. Appl. Phys. **93**, 1032 (2003).
[20]E. Nishimura, H. Ohkawa, P. K. Song, and Y. Shigesato, Thin Solid Films **445**, 235 (2003).
[21]S. Ishibashi, Y. Higuchi, Y. Ota, and K. Nakamura, J. Vac. Sci. Technol. A **8**, 1399 (1990).

The influence of oxygen partial pressure during deposition on magnetoresistance of Co-Pt-ITO and Co(Pt)-ITO thin films

Wanti Ekawati, Ji Shi[a], Yoshio Nakamura

[a]Department of Metallurgy and Ceramics Science, Tokyo Institute of Technology

2-12-1 O-okayama, Meguro-ku, Tokyo 152-8552, JAPAN

Osamu Nittono

Faculty of symbiotic science, Fukushima University

1 Kanayagawa, Fukushima 960-1296, JAPAN

The granular Co(Pt)-ITO films have been fabricated by a two-step method. The film shows the magnetoresistance phenomena after annealing at appropriate temperature, where fine Co(Pt) particles distribute in the amorphous ITO matrix during thermal annealing. Such film shows high magnetoresistance at high resistivity. This suggests that by increasing the resistivity, the magnetoresistance of Co(Pt)-ITO film may also increase. Since it is known that the resistivity of ITO films is very sensitive to the partial pressure of oxygen during deposition, we investigate the oxygen partial pressure dependence of magnetoresistance in Co(Pt)-ITO thin films. It is found that the magnetoresistance increases with the increasing of oxygen partial pressure. However, there is an optimum partial pressure where the magnetoresistance decreases. On the other hand, the resistivity continuously increases with increasing of oxygen partial pressure due to the existence of CoO. Co(Pt)-ITO film has higher MR value compare to Co-ITO film as the matrix still in amorphous phase after annealing at 350°C, while the matrix of Co-ITO film has crystallized. The existence of Pt is proved to increase the solubility of Co in the amorphous phase and increase the film crystallization to higher temperature.

I. INTRODUCTION

Metal-oxide nano-granular structures have attracted a great deal of research interest due to their unique properties and great application potentials. Tunneling magnetoresistance have been found in nano-structured magnetic granular materials such as Co-Al-O[1,2] and Fe-Al_2O_3.[3] On the other hand, some metal-oxide granular films also show excellent soft magnetic behavior at high frequency region.[4] In both cases, high resistivity of the films is required, because for the magnetoresistance films, high resistivity is essential to the formation of tunneling junctions inside the films[4-6], and for the soft magnetic films, high resistivity helps suppress the eddy current loss and thus maintain high permeability at high frequency.

In our previous work, we have reported precipitation-controlled magnetoresistance of Co(Pt)-ITO films.[] Although crystalline ITO (indium tin oxide) is highly conductive, amorphous ITO films has extremely high resistivity. Therefore, granular films composed of Co granules and amorphous ITO matrix are expected to show tunneling-type magnetoresistance. We have found that by adding proper amount of Pt in the Co-ITO films, granular films with Co(Pt) granules distributed in an amorphous ITO matrix can be formed by thermally annealing the sputter-deposited amorphous Co-Pt-ITO films at about 350 °C. Compared with the Co-ITO granular films fabricated directly by sputter deposition, i.e. Co and amorphous ITO separated with each other during sputtering deposition, Co(Pt)-ITO granular films fabricated through precipitation of Co(Pt) show much high sensitivity to the applied field. However, the MR value of such a film is still low, only about 0.7%, much lower than the reported value of other granular structure such as Co-Al-O. And it is also found that higher MR values are obtained from the films with higher resistivity. This result suggests that by increasing the resistivity of the Co(Pt)-ITO films, the magnetoresistance may also be increased. It is reported that the resistivity of metal-oxide granular films can be improved by adding O_2 to the sputtering gas, Ar.[] Moreover, it is known that the resistivity of ITO films is very sensitive to the presence of oxygen during deposition.[11-14] Therefore, in the

present work, we investigate the effect of oxygen addition during deposition on the resistivity and magnetoresistance of Co(Pt)-ITO films.

II. EXPERIMENTAL

A two-facing-target dc magnetron (TFTM) sputtering apparatus was used to prepare the Co-ITO and Co(Pt)-ITO films. Silica glass and Si wafer with the thickness of 0.5 mm were used as substrates for various characterizations. The sputtering chamber had been evacuated to a pressure around $8x10^{-5}$Pa before deposition. Argon and oxygen gasses were introduced into the sputtering chamber through mass flow controller. The mixed of Ar + O_2 pressures was kept constant at 0.2 Pa during deposition. The oxygen partial pressure was controlled by changing the flow rate ratio of oxygen to argon gas. The volume fraction of Co to ITO matrix is fixed at around 1:3, only Co to Pt ratio is changed. The Co to Pt ratio in this film is about 7:1. The film thickness was controlled to about 2000Å with the deposition rate of 0.37 Å/sec. After the deposition, films were then annealed in a vacuum of $1x10^{-5}$Pa for an hour at various temperatures. Structural properties of films were characterized by X-ray diffraction analysis (XRD). X-ray Photoemission Spectrometry measurement (XPS) was employed to identify the atomic composition ratio of each film. Film resistivity and magnetoresistance were measured using four-point probe MRHC-500 magnetoresistance measurement unit. The magnetic properties were examined using vibrating sample magnetometer. A transmission electron microscope (TEM) was employed to observe the microstructure of this film.

III. RESULTS

III. a. Resistivity and magnetoresistance dependence on oxygen partial pressure

Figure 1 shows the change of resistivity of Co-ITO films with oxygen partial pressure during deposition. One can see that, for the as-deposited film, the resistivity increases monotonically with increasing

3

oxygen partial pressure. After thermal annealing, the resistivity of the films decreases rapidly, especially for the films deposited with higher oxygen partial pressure. We also note that the resistivity of Co-ITO films decreases abruptly with increasing annealing temperature when films were annealed at temperatures below 350°C. There is no obvious change in resistivity between the films annealed at 350°C and 500°C.

The relationship between the ΔR and the applied magnetic field for the films deposited with different oxygen partial pressures are shown in Fig.3. The film deposited without oxygen addition shows a ΔR of 0.75Ω at 10kOe [Fig. 2(a)]. However, upon thermal annealing ΔR decrease rapidly with increasing annealing temperature. On the other hand, the films deposited in mixed $Ar+O_2$ atmosphere behave differently [Fig. 2(b) and Fig. 2(c)]. At first, the Co-ITO film deposited with oxygen partial pressure of 0.2% shows a ΔR of 1.6Ω and increases to 5Ω, which is about 5 times larger than as-deposited film, and 7 times larger than the maximum value shown by films deposited without oxygen. The increase of annealing temperature to 350°C causes an abrupt drop of ΔR. The film deposited with oxygen partial pressure of 0.6 % shows similar behavior. Therefore, we consider that the optimum annealing temperature to achieve large ΔR thus large magnetoresistance ratio is at about 250°C.

The magnetoresistance ratio (MR) and resistivity of Co-ITO films are plotted in Fig. 3 as a function of oxygen partial pressure. The MR ratio is calculated by equation of $MR = \Delta\rho/\rho_0 \times 100\%$, where ρ_0 is the zero field resistivity and $\Delta\rho$ is define as $\rho_{0kOe}-\rho_{10kOe}$. All the films were annealed at 250°C. We can see from the figure that below the oxygen partial pressure of 0.2%, MR ratio increased with increasing oxygen. After reaches its maximum at 0.2% of oxygen partial pressure, thereafter the MR ratio decreases with increasing the oxygen partial pressure, and the maximum value of MR is about 1%. In addition, all the film exhibit super-paramagnetic behavior as seen in Fig. 4, implying the small size of Co particles in this film. Furthermore, the hysterisis curves also show that the saturation magnetization of Co-ITO film decreases with increasing oxygen partial pressure during deposition.

III. b. Microstructure of Co-ITO films

In order to understand the electrical and magnetic performances of the Co-ITO films, the microstructure of the films was studied by transmission electron microscopy. Figure 5 shows the cross-section TEM image and selected area diffraction (SAD) pattern of the Co-ITO film, which was deposited at room temperature without oxygen partial pressure. Two broad rings are seen in the diffraction pattern, the outside one is overlapped by another spotty ring. The spotty ring is the 111 reflection from fcc-Co according to the d-spacing calculated from it. The broad rings indicate the existence of an amorphous phase in the film. The microstructure of the film is featured with Co particles in amorphous matrix as can be seen from the image. The average size of Co particles is about 5 nm. Since the amorphous ITO has relatively high resistivity[15,16], we consider that the Co particles in the film form the path for electrical conduction. According to the microstructure of this film, we attribute the magnetoresistance phenomena observed in Co-ITO film to tunnel-type magnetoresistance. Figure 6 shows the cross section images and SAD patterns of Co-ITO films annealed at 250°C. Compared with the as-deposited films (Fig. 5), the most important feature of the annealed films is that the ITO in the films is almost full crystallized, as the diffraction spots from ITO can be seen clearly from the SAD patterns. The size of Co particles decreases with increasing oxygen partial pressure from 15 nm to 5 nm. The above results have shown that the microstructure configurations are different before and after annealing. Before annealing the Co particles distributed in amorphous ITO matrix, and it becomes Co particles mixed with crystalline ITO grains. With the increasing of oxygen partial pressure the Co particles decrease into fine particles. However, the proper Co particle size is observed at 0.2% oxygen, where optimum MR is obtained.

III. c. Effect of oxygen addition on Co(Pt)-ITO films

Considering the relationship between resistivity and the oxygen partial pressure during deposition, Co(Pt)-ITO film shows similar tendency with Co-ITO films, the resistivity increases with increasing oxygen

partial pressure as shown in Fig. 7. On the other hand, the dependence of resistivity on the annealing temperature shows quiet different feature. In the case of Co-ITO film, the resistivity decreases rapidly when the film was annealed at 250°C and 350°C as shown in Fig. 1. However, in Co(Pt)-ITO case, especially film deposited with oxygen partial pressure, the resistivity first increases with increasing the annealing temperature, reaching its maximum at 350°C, and then decreases abruptly when film was annealed at 500°C. This suggest that the microstructure evolution during thermal annealing for Co(Pt)-ITO film is different from Co-ITO films. Furthermore, the optimum annealing temperature in view of MR is found at 350°C, about 100°C higher than Co-ITO films. This indicate that the crystallization temperature of the film increase to higher temperature with the addition of Pt. The ΔR curve of this film shows the same tendency to the resistivity as shown in Fig. 8. The as-deposited film has small ΔR, which indicate that most of Co(Pt) metallic are incorporate into the amorphous ITO. At 350°C annealing temperature, ΔR value increases rapidly and a sharp ΔR curve is obtained. This may explains the precipitation of magnetic particle from the amorphous phase by thermal annealing at 350°C. The addition of oxygen cause increasing of ΔR value of the film as shown in Fig. 8(b). However, the excess of oxygen in this system causes a drop of ΔR. Figure 9 shows the change of MR ratio with oxygen partial pressure during deposition for Co(Pt)-ITO films. All the films were annealed at 350°C. It is seen from this figure that Co(Pt)-ITO films show similar tendency with Co-ITO films (Fig. 3), except that the maximum MR ratio is slightly higher. The cross-section TEM image and SAD pattern of Co(Pt)-ITO film annealed at 350°C at different oxygen partial pressure are shown in Fig. 10. We can see from the diffraction pattern that the ITO still remains to be amorphous, because there are only broad rings seen in the SAD pattern. With the oxygen addition at 0.2%, the surrounding nano-particles Co(Pt) of 5-10 nm in diameter are isolated by oxide channel thus increase the interference between magnetic particle, as a result the tunneling mechanism could dominate the electron conduction in this film [Fig. 10(b)]. At higher oxygen partial pressure, the oxide channel thickness increase

greatly and completely separate the Co(Pt) particles, reduces the tunneling conduction in this system. These results indicate that Pt plays a role in increasing the solubility of Co into the amorphous phase and increases the crystallization to higher temperature. This effect will be reported elsewhere.

IV. Discussion

As describe above, the microstructure of the as-deposited Co-ITO films is a granular network of two phases, one is metallic and magnetic Co and the other is the insulating ITO matrix. The size of Co particles is in the order of nanometer distributed in ITO matrix, which is proved by cross-section TEM images and emphasized by the VSM curves showing the typical of superparamagnetic behavior. This film has very high resistivity in the order of 10^{-2}-$10^{-1}\Omega$cm. The resistivity itself continuously increases as increasing oxygen partial pressure during deposition. This could be reasonably explained from the XPS spectra of Co as shown in Fig.11. Specimen deposited without oxygen partial pressure has high intensity of Co2p electron states [Fig. 11(a)]. Meanwhile, the film deposited with oxygen shows a shoulder next to $Co2p_{3/2}$ spectrum which is found at 780,2eV. Since normally CoO is observed at 780-780.2eV, we could confirm the presence of CoO in this system[16]. VSM curves also emphasize the decreasing of magnetic Co particles as shown in Fig. 4. The optimum oxygen partial pressure is found at 0.2%, which enhance the MR ratio. The annealing optimum temperature is observed at 250°C. At this temperature, the ITO matrix has crystallized, scattering conduction electron between Co grains which has reach its proper size and distribution, thus enhance the MR ratio. In the case of Co(Pt)-ITO film, the maximum resistivity and MR ratio is observed with the optimum annealing temperature which is observed at around 350°C. At this temperature the matrix is in amorphous, from the x-ray result the crystallization of ITO in this film is found at 400°C. The nano-sized Co(Pt) particles are immersed in the proper size and distribution thus enhance the MR by tunneling mechanism which is occurred between Co(Pt) particles in insulating amorphous ITO. Since the matrix is still in amorphous, Co(Pt)-ITO film exhibits higher magnetoresistance than Co-ITO film.

IV. CONCLUSIONS

The presence of oxygen partial pressure during deposition increases the resistivity of both Co-ITO and Co(Pt)-ITO film and decreases the size of metallic particles in ITO matrix. Proper amount of oxygen partial pressure during deposition optimize the size of magnetic particles, and enhance the magnetoresistance in this system.

REFERENCES

[1]M. Ohnuma, K. Hono, H. Onodera, J. Appl. Phys., **87**(2), 817 (1999)

[2]K. Kamei, M.Yonemura, K. Hanafusa, J. Mater. Sci. Material in electronic **12**, 569 (2000)

[3]T. Zhu, Y. Wang, Phys. Rev. B, **60**, 17, 11 918 (1999)

[4]H. Fujimori, S. Mitani, S. Ohnuma, Mat. Sci. Eng. B **31**, 219 (1995)

[5]S. Ohnuma, H. Fujimori, S. Mitani and T. Matsumoto, J. Appl. Phys., **79**, 5130 (1996)

[6]M. Ohnuma, K. Hono, E. Abe, H. Onodera, S. Mitani and H. Fujimori, J. Appl. Phys., **82** (11), 5646 (1997)

[7]S. Mitani, H. Fujimori and S. Ohnuma, J. Magn. Magn. Mater., **165**, 141 (1997)

[8] J. G. Ha, S. Mitani, K. Takanashi, M. Ohnuma, K. Hono, H. Fujimori, J. Mag. Mag. Mater., **198**, 21 (1999)

[9] M. Ohnuma, K. Hono, H. Onodera, S. Mitani, J. G. Ha, H. Fujimori, Nanostructure Mat., **12**, 573 (1999)

[10]Wanti E., J. Shi, Y. Nakamura, O. Nittono (submitted)

[11]M.Higuchi, S.Uekusa, R.Nakano and K.Yokogawa, J.Appl.Phys.,**74**(11), 6710 (1993)

[12]John.C.C.Fan, Frank J.Bachner and Goerge H.Foley, Appl.Phys.Lett.,**31**, 773 (1977)

[13]M.Higuchi, M.Sawada and Y.Kuronuma, J.Electrochem.Soc.,**140**, 1773 (1993)

[14]R.Mientus, K.Ellmer, Surf.Coat.Tech.**142**, 748 (2001)

[15]M.Bender, W.Seelig, C.Daube, H.Frankenberger, B.Ocker, J.Stollenwerk, Thin Solid Films **326**, 72 (1998)

[16]D.C.Paine, T. Whitson, D. Janiac, R.Beresford, and Cleva Ow Yang, J.Appl.Phys. 85(12), 8445 (1999)

[17]F. O. Aduroja, H. Izumi, T. Ishihara, H.Yoshioka, M. Motoyama, Solar Energy Mat.Solar Cell **71**, 1 (2002)

Figure captions

FIG.1

The resistivity of Co-ITO film as a function of oxygen partial pressure

FIG.2

ΔR curves of Co-ITO films deposited at different oxygen partial pressure and annealed at various temperatures.

a. Without oxygen addition, b. 0.2% oxygen partial pressure c. 0.6% oxygen partial pressure.

FIG.3

The resistivity and magnetoresistance of Co-ITO film annealed deposited at various oxygen partial pressure.

FIG.4

The M-H curves of Co-ITO films deposited at various oxygen partial pressures and then annealed at 250°C.

FIG.5

Cross section TEM image and SAD patterns of Co-ITO films deposited at room temperature

FIG.6

Cross section TEM image and SAD patterns of Co-ITO films deposited at different oxygen partial pressure (Ta : 250°C). a. no oxygen, b. 0.2% oxygen partial pressure, c. excess of oxygen.

FIG.7

The resistivity of Co(Pt)-ITO films as a function of oxygen partial pressure.

FIG.8

ΔR curves of Co(Pt)-ITO films deposited at different oxygen partial pressure and annealed at various temperatures. a. Without oxygen addition, b. 0.2% oxygen partial pressure c. 0.6% oxygen partial pressure.

FIG.9

Resistivity and MR ratio of Co(Pt)-ITO film as a function of oxygen partial pressure.

FIG.10

Cross section TEM images and SAD pattern of Co(Pt)-ITO film at 0.2% oxygen partial pressure, Ta : 350°C.

FIG.11

XPS profiles of $Co2p_{1/2}$ and $Co2p_{3/2}$ spectra of Co-ITO films a. 0.6% oxygen partial pressure, b. without oxygen.

10

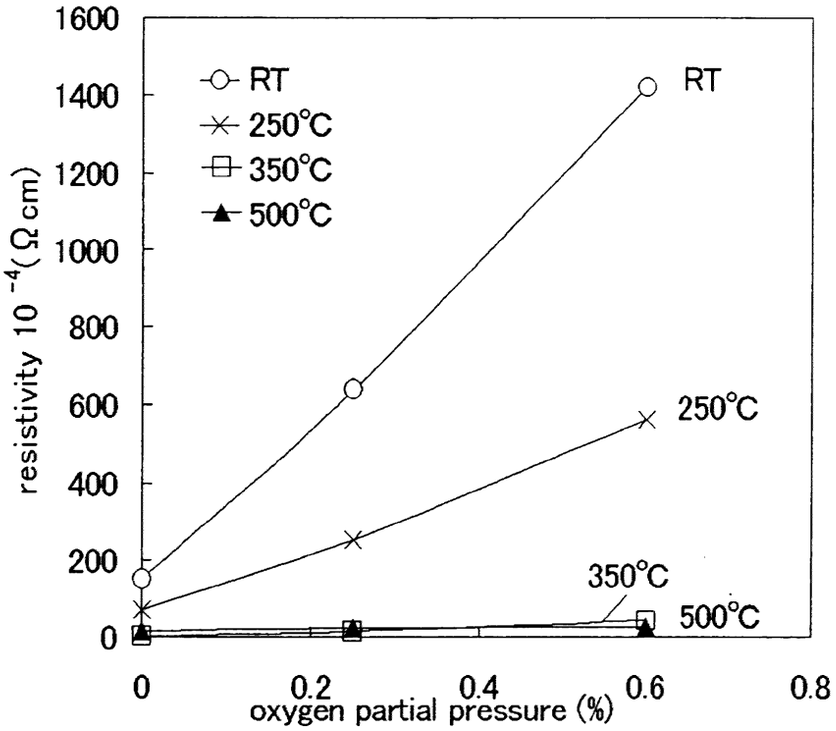
1600
1400
1200
1000
800
600
400
200
0
resistivity 10 -4(Ω cm)
RT
250°C
350°C
500°C
RT
250°C
350°C
500°C
0
0.2
0.4
0.6
0.8
oxygen partial pressure (%)

FIG. 1

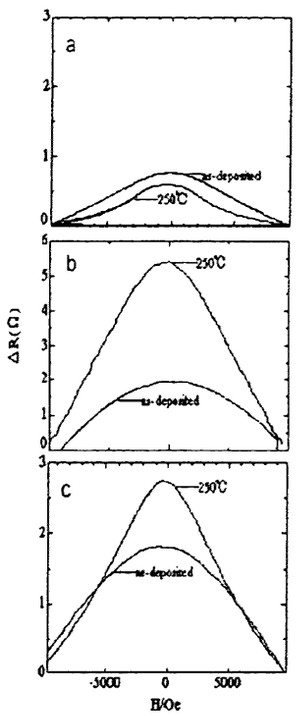
a
b
c
ΔR(Ω)
250℃
as-deposited
-5000
0
5000
H/Oe

Fig. 2

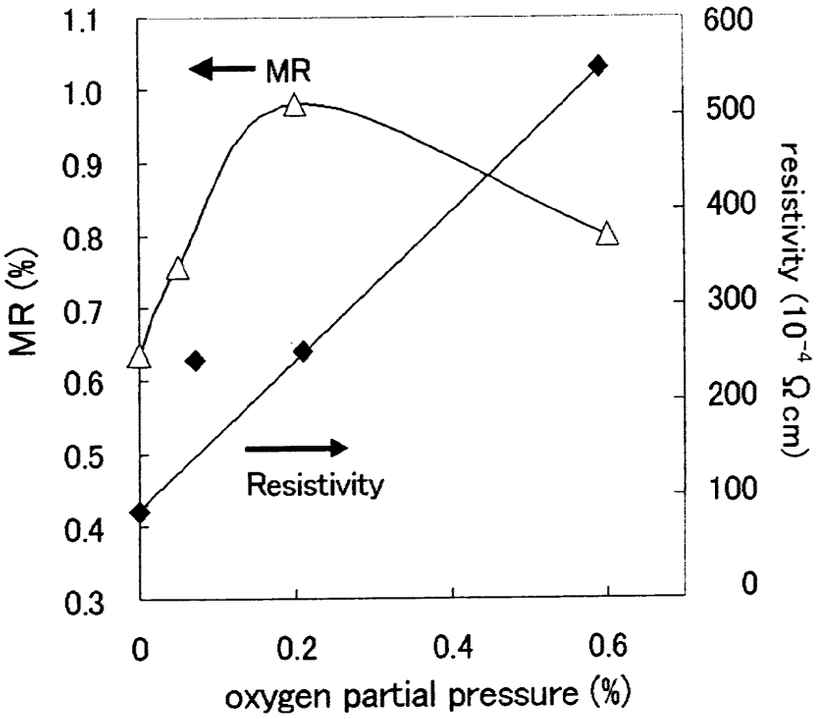
MR
Resistivity
MR (%)
resistivity (10^{-4} Ω cm)
oxygen partial pressure (%)
1.1
1.0
0.9
0.8
0.7
0.6
0.5
0.4
0.3
600
500
400
300
200
100
0
0
0.2
0.4
0.6

FIG. 3

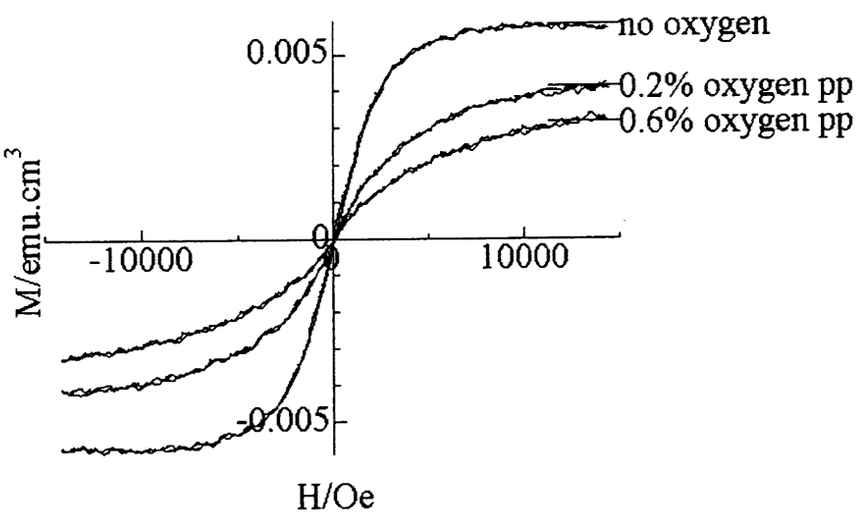
no oxygen
0.2% oxygen pp
0.6% oxygen pp
0.005
-0.005
0
-10000
10000
M/emu.cm^3
H/Oe

F I G. 4

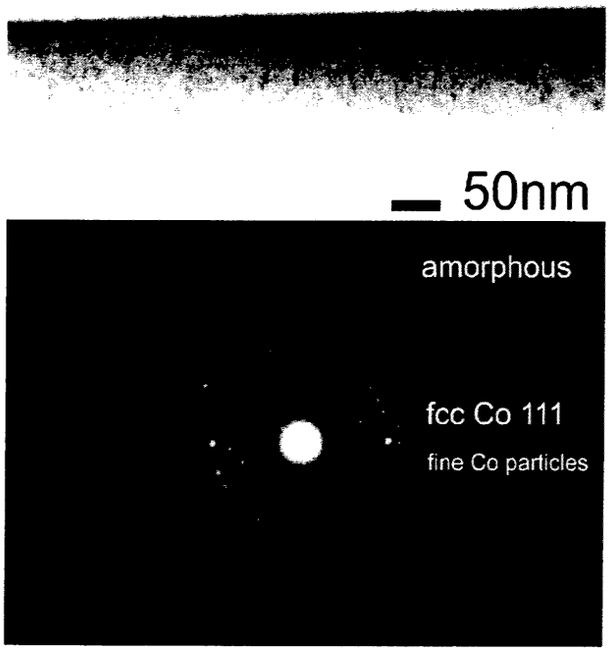
50nm
amorphous
fcc Co 111
fine Co particles

FIG. 5

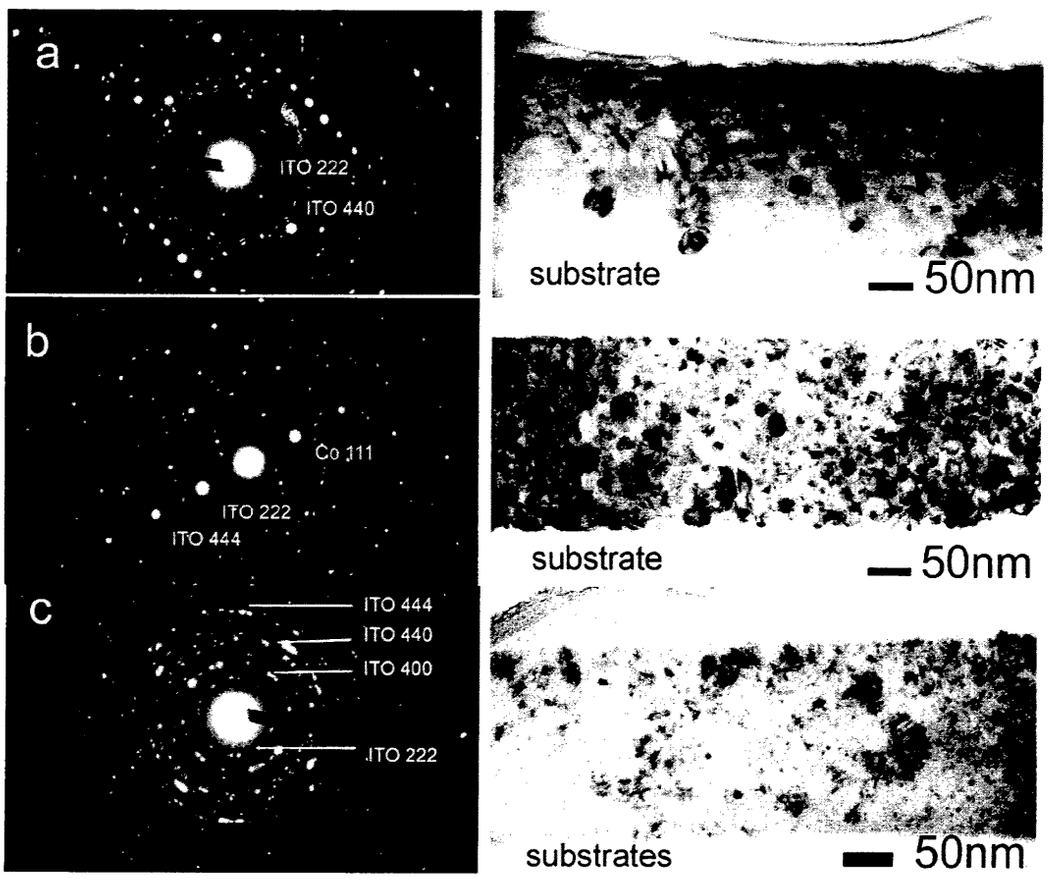
a
ITO 222
ITO 440
substrate
50nm
b
Co 111
ITO 222
ITO 444
substrate
50nm
c
ITO 444
ITO 440
ITO 400
ITO 222
substrates
50nm

FIG. 6

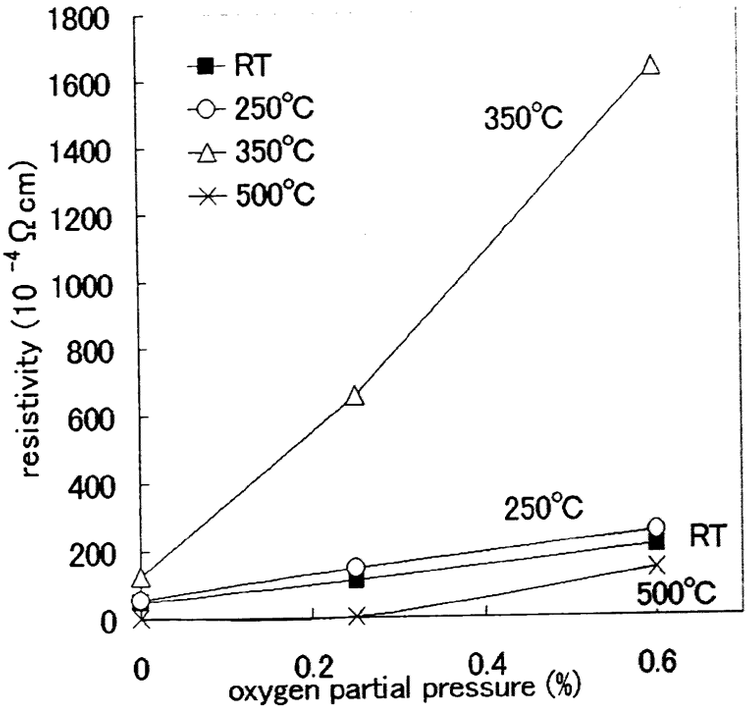
1800
1600
1400
1200
1000
800
600
400
200
0
resistivity (10^{-4} Ω cm)
RT
250°C
350°C
500°C
350°C
250°C
RT
500°C
0
0.2
0.4
0.6
oxygen partial pressure (%)

FIG. 7

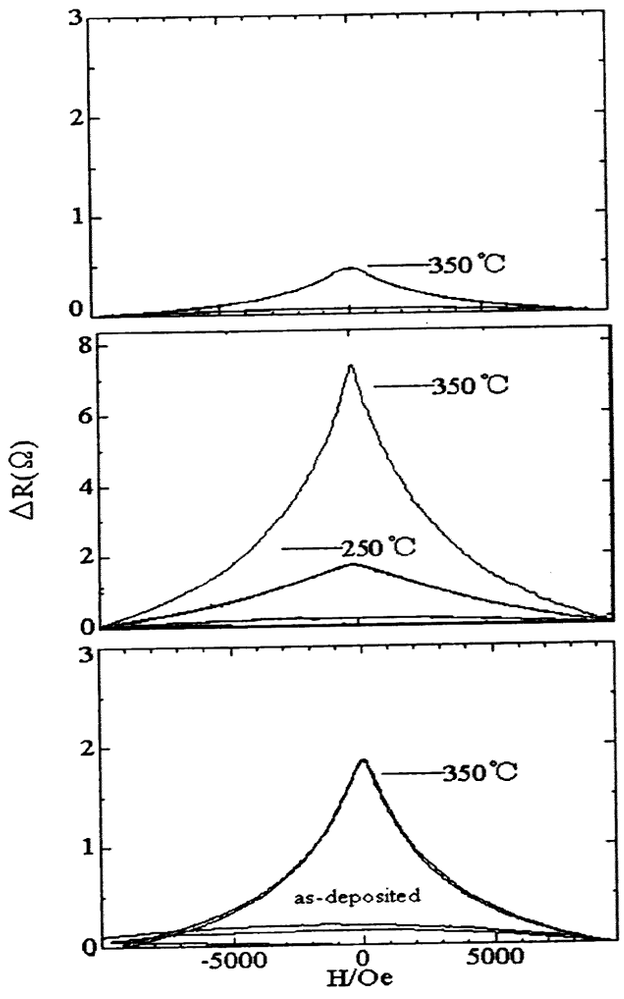
3
2
1
0
350℃
8
6
4
2
0
ΔR(Ω)
350℃
250℃
3
2
1
0
350℃
as-deposited
-5000
0
5000
H/Oe

FIG. 8

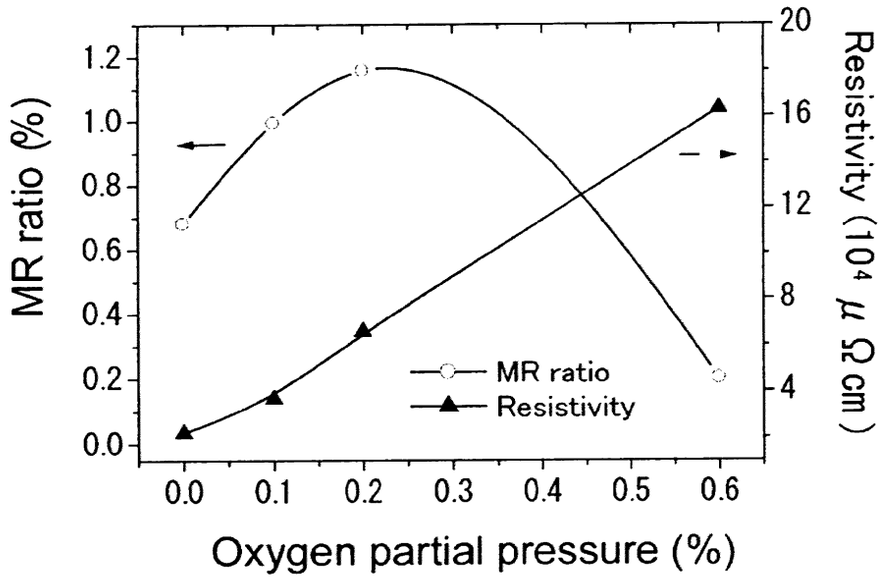
MR ratio (%)
Resistivity (10^4 μ Ω cm)
Oxygen partial pressure (%)
MR ratio
Resistivity
1.2
1.0
0.8
0.6
0.4
0.2
0.0
20
16
12
8
4
0.0
0.1
0.2
0.3
0.4
0.5
0.6

FIG. 9

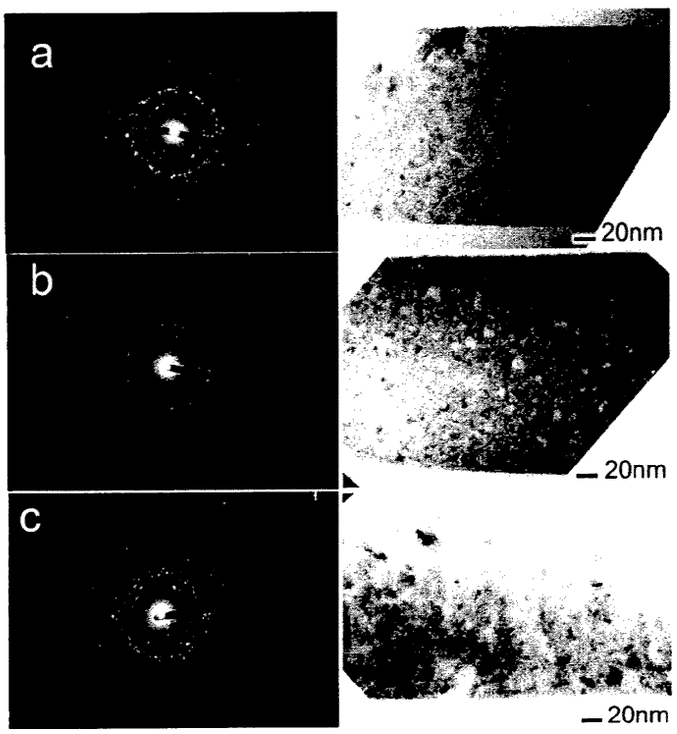
a
b
c
20nm
20nm
20nm

FIG. 10

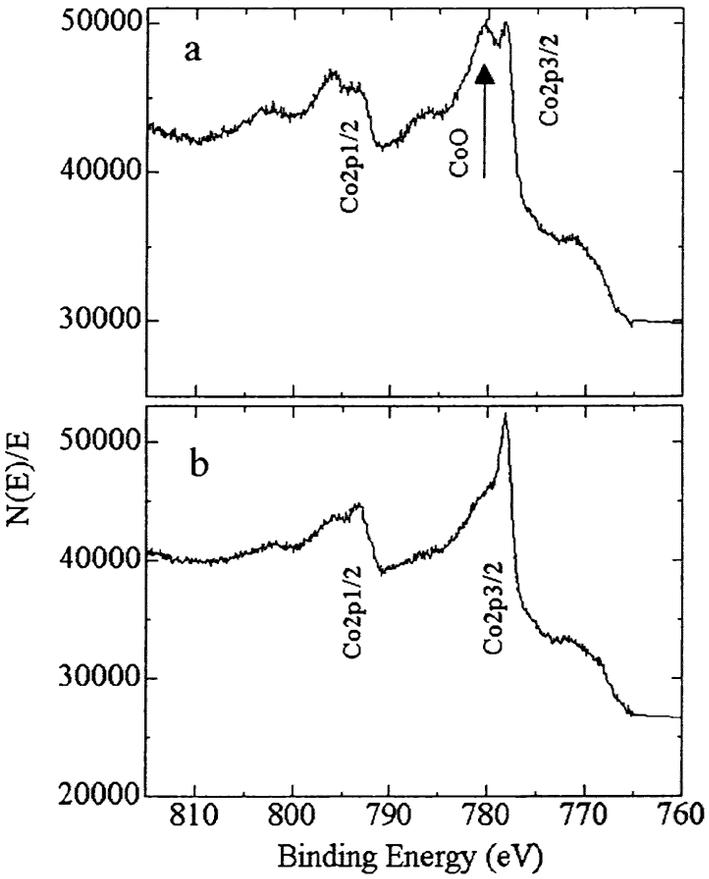
a
b
Co2p1/2
CoO
Co2p3/2
Co2p1/2
Co2p3/2
N(E)/E
50000
40000
30000
50000
40000
30000
20000
810
800
790
780
770
760
Binding Energy (eV)

FIG. 11

1342-9825/05/¥500/論文/JCLS

P 0505-06

技術トピックス／土木

鉄鋼材の劣化診断システムの開発

福島大学　山口　克彦・入戸野　修

はじめに

橋脚や原子炉など各方面において、構造材料として用いられている鉄鋼材の劣化を早期に検出することは、我々の社会基盤を維持し、安全に生活していくために非常に重要である。そのため超音波や渦電流などを利用した非破壊検査手法の開発が活発に行われてきた。特に超音波による非破壊検査手法は対象を鉄鋼材に限らずひび割れ検出などのために広くいきわたっている。そして通常の使用においては重大な破損が起こる以前に、維持基準を充分満足させながら、劣化部位を発見することが可能と考えられている。

しかし近い将来、より初期の劣化部位を検出することが求められる場合も増えてくることが考えられる。特に劣化部位の進み具合が加速度的に早くなると予想されるケースではいかに早い段階で劣化を検出できるかが問題とされるだろう。例えば高速流体の触れる壁面で生じる小さなささくれは、管全体の対称性を崩し、その結果乱流の発生と、引き続く非線形的な相乗効果による急速な破壊を引き起こす可能性がある。このような場合、通常の超音波検査が劣化を検出するような実際のひび割れや乖離・剥離が起こってからでは遅すぎる恐れがある。そのためひびや剥離といった幾何的損傷にはまだ至っていないものの、局所的に応力が集中しはじめ、歪みを起こしている段階で検出できる技術が求められるようになるだろう。これはいわば原子レベルの差異から引き起こされる物性的変化を検出するようなものである。

いくつかある非破壊検査手法のうち、磁気的非破壊検査は古くから試みられているもののひとつである。特に磁性体でもある鉄鋼材に対して、印加磁場を変化させた場合に測定されるバルクハウゼンノイズ（BN）は磁気的非破壊検査の代表例といえるだろう。しかしそのデータの分析手法が確立されていないことや定量化が困難なことから、超音波診断などに比べると実用レベルにはまだ達していないといえる。だが物質のもつ磁性というものは、その物性が原子サイズレベルで引き起こされる極めてミクロ的なものであり、今後の微細診断技術を担う可能性がある。本記事では歪みをもった鉄鋼材のバルクハウゼンノイズが角度依存性をもち、そこから歪み検出が可能であることを紹介したあとで、バルクハウゼンノイズのような動的磁化過程によりどのような情報が取得可能であるのかをモンテカルロシミュレーションの結果を用いて示すこととする。

バルクハウゼンノイズの測定

まず実例として、バルクハウゼンノイズの測定システムと引っ張り試験機によって限界域まで引き伸ばした鉄鋼材（SS400）のリューダス帯での測定結果を示そう。第１図は標準的なバルクハウゼンノイズ測定システムである。周波数発生器から得られる15Hz程度の三角波を増幅して磁気コイルに電流を流し磁場を発生させ、その磁場によりサンプルを磁化していく。このような動的磁化過程のもとで検出コイルはコイル中を貫く磁場の変化に生じた電圧をアンプにより増幅させた上でADコンバータを介してＰＣに取り込む。検出コイル直後のハイパスフィルターは印加磁場と同期する出力信号を抑えるために100Hz程度のカットオフを持たしてある。

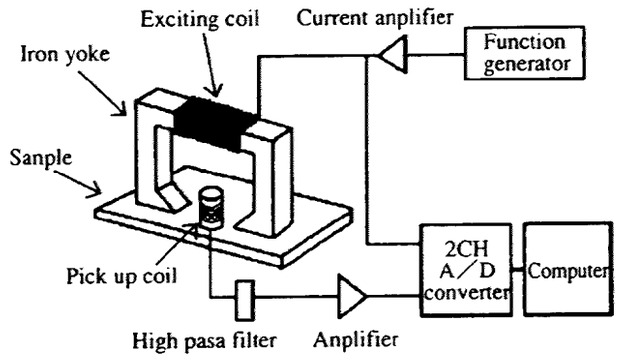

第１図　バルクハウゼンノイズ測定システムの例

参考として、このシステムを用いてSS400の板状サンプルのバルクハウゼンノイズを測定した結果を第２図に示す。図中の破線は磁気コイルに流した電流の変化を表し、BNと指し示されたグラフが測定されたバルクハウゼンノイズである。ノイズは磁気コイルに流れる電流がゼロを横切るあたりで急速に大きくなり、図中aやbの位置でピークを持つ。図中cやdで切り落とされたようにノイズが減っているが、これは飽和磁化に達する前に磁場が弱くなってしまったからだと考えられる。これまで多くのバルクハウゼンノイズについての研究報告が、このような生のノイズではなく、二乗平均などの値を用いて議論されているが、後で述べるようにノイズの分布自体が多様な情報を含んでいる可能性があり、安易に縮約した値を用いるべきではないと考えている。

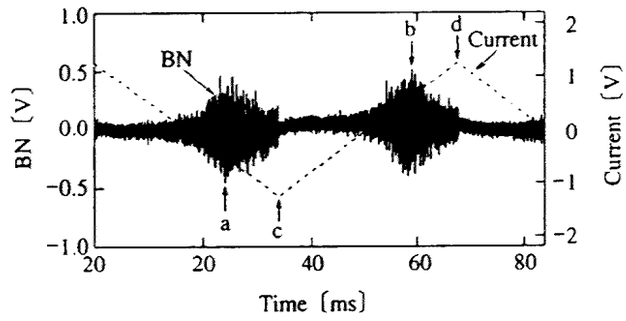

第２図　バルクハウゼンノイズ測定例

次に角度分解バルクハウゼンノイズ測定について説明しよう。これは第１図の磁気ヨークを検出コイルを中心として数度ごとに回転させていき、それぞれの印加磁場方向においてバルクハウゼンノイズを検出し、その異方性を解析するものである。原子力プラントなどに用いられるA533B鉄鋼に540MPaの引っ張り応力を加えた際に生じるリューダス帯(残留応力集中箇所)において山田らは角度分解バルクハウゼンノイズを測定し、平均不連続磁化磁界の差としてその異方性を示している[1][2]。ここで平均不連続磁化磁界〈H〉は、周期Tをもつ三角波形の印加磁場をB(t)とし、その際に検出コイルに現れる誘導電圧をE(t)とすると次の式、

$$\langle H\rangle=\int_0^{T/4}|E\cdot B|dt\Big/\int_0^{T/4}|E|dt$$

で表される量で、おおよそバルクハウゼンノイズのピーク値における磁場となる。我々はこれを発展させ、４極ヨークを用いて印加磁場を発生させ、スピーディかつ安定して測定が行えるようなシステムを構築した。第３図は４極ヨークによる印加磁場システムの概略図である。

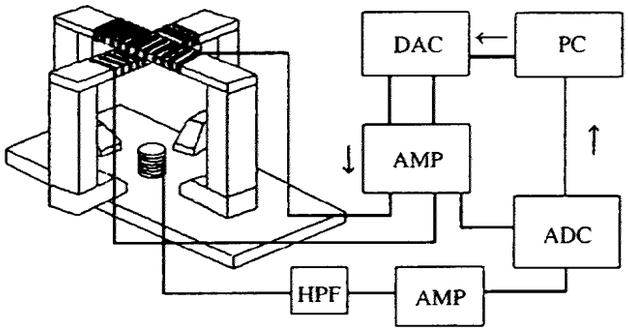

第3図　4極ヨークを用いた角度分解バルクハウゼンノイズ測定システム

計測制御用コンピュータから2チャンネルのDAコンバータとアンプを介して、2つのヨークそれぞれに異なる振幅値の三角波電流を流し、任意の角度に合成磁場を発生できるようにしている。

鉄鋼材としてよく使用されるSS400を第4図のように加工し、アニール処理をして残留応力を軽減させたサンプルを用いて応力印加前後の角度分解バルクハウゼンノイズを測定した。応力は第5図のように引っ張り試験機で破断直前まで与えた。

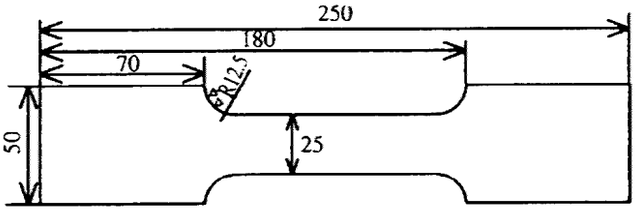

第4図　切り出されたSS400サンプルの一例

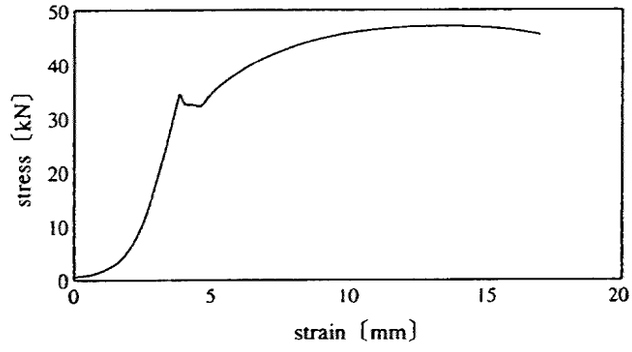

第5図　引っ張り試験機による応力印加時の応力－歪み曲線

第6図、第7図はそれぞれ応力印加の前と後で測定した角度分解バルクハウゼンノイズから解析した平均不連続磁化磁界〈H〉を示す。前述の4極ヨークを用いて、10度ごとにバルクハウゼンノイズを測定したデータから算出した平均不連続磁化磁界を極座標として表している。点が各角度における〈H〉である。実線は参照のための単位円である。応力印加前ではほぼ等方的であるのに対して、印加後では45度方向に大きく〈H〉が伸びており顕著な異方性が現れている。これはリューダス帯が45度方向に引き伸ばされ

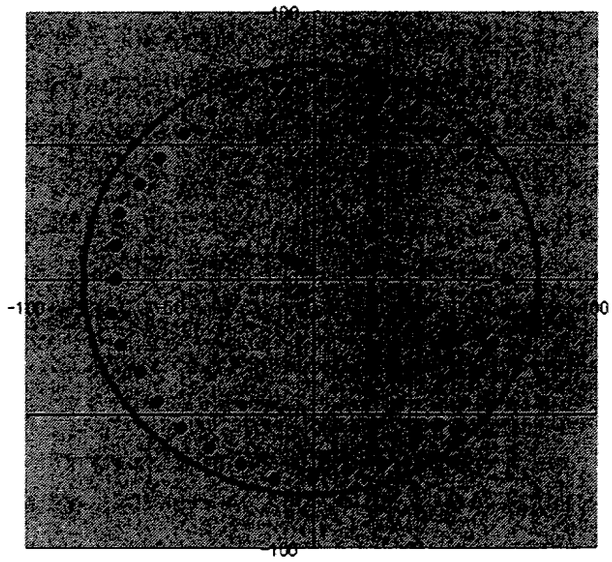

第6図　応力印加前の試料に対する〈H〉の角度依存性

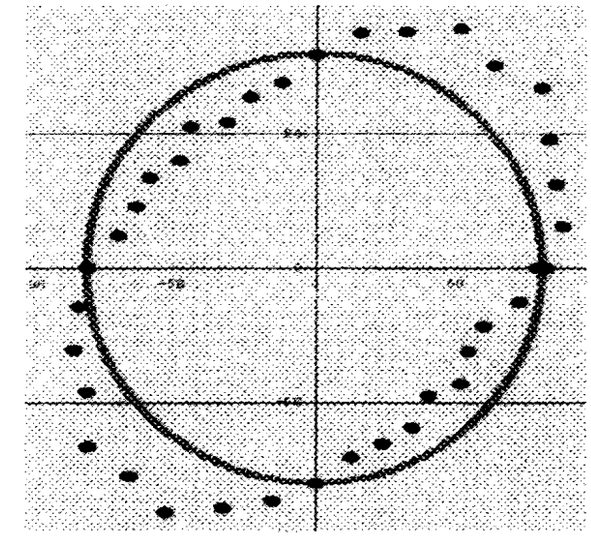

第7図　応力印加後の試料に対する〈H〉の角度依存性

ていることに対応していると考えられる。このように特定方向のバルクハウゼンノイズの絶対値を単に比較するのではなく、角度分布がどう変わるかを評価することで、残留応力の有無およびその方向性までも検出できるようになる。

モンテカルロシミュレーションによるバルクハウゼンノイズの解析

上述のようにバルクハウゼンノイズは鉄鋼材の残留応力などの劣化特性を検出するための有用な情報を与える可能性が大きいが、まだ適切な解析手法が確立されていない。その主な理由はバルクハウゼンノイズが印加磁場を変化させていく際に現れる動的磁化過程であることと、磁気特性を左右する残留応力の起源が刃状転位などの原子スケールの現象であるからだと考えられる。そこで我々はモンテカルロ法を擬似動的に扱い、バルクハウゼンノイズをシミュレートする技法を開発した[3]。以下にこの方法とそこから引き出せる解析手法について述べる。なお以下の計算は東北大学流体研究所のスーパーコンピュータOrigin2000を用いて行った。

はじめに通常のモンテカルロ法による磁場中の磁性体の磁化シミュレーションについて簡単に触れよう。まず磁性体をミクロな磁気モーメントを担ったn個のスピンの集まりとしてモデル化する。このときスピン間には交換相互作用、磁気双極子相互作用、磁気異方性が働くとする。ただしミクロな集まりとしては交換相互作用が他の二つの作用に比べて非常に大きいので、ここでは簡単のために交換相互作用のみを考える。また外的要因として印加磁場および系の温度を与える。そこでこの系の持つエネルギー(ハミルトニアンH)を

$$H=-\sum_{ij}J_{ij}S_iS_j+B\sum_i S_i \qquad \cdots(1)$$

とする。ここで第1項はi番目のスピンS_iとj番目のスピンS_j間の交換相互作用でJ_{ij}は交換相互作用定数を表わす。また第2項は外部磁場Bによるゼーマンエネルギーを示す。

このような各スピンをまずランダムな方向に設定する。これは系全体を高温にしたことと等価である。そしてこの初期状態のスピン配置(状態1)から得られる系全体のエネルギーH_1を(1)式から算出する。次に系から任意のスピンをひとつ選び、その方向を乱数的にかく乱させ状態1とわずか異なる状態2を作り再び全エネルギーH_2計算する。H_1とH_2の値と温度T(K)とから状態1と状態2それぞれの実現確率をボルツマン分布的に想定し、更に乱数を用いてその確率の下でどちらかの状態を選び取り新たにこれを初期状態とする。この後、再び任意のスピンを選び出し、上記のプロセスを繰り返す。このプロセスを系に含まれるスピンの数nまで繰り返した場合を1モンテカルロステップ(1MCS)と呼ぶ。通常nMCS計算を繰り返すと定常状態に達する。

今、各辺それぞれ31個のスピンが単純立方格子状に配置されたスピン系を考えよう。どの最隣接スピン間の距離も等しく、これを1とする。このスピン系に対して無磁場中で高温から低温へと変化させた場合に、そのスピンの総和(磁化)を各温度ごとにシミュレートした結果が第8図に示されている。縦軸は磁化で、最大磁化(すなわち31×31×31=29,791)を1に規格化してある。温度をT=3から下げていくと初めはほ

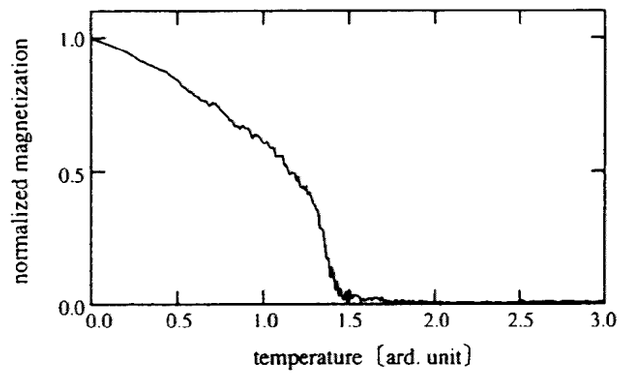

第8図　磁化の温度依存性シミュレーション

ほぜロのまま、すなわち各スピンがランダムな方向を向いており互いにキャンセルしているが、T=1.5付近から磁化を持ち始め、低温になるにつれて磁化が大きくなっていく。これはキュリー・ワイス則に従う典型的な強磁性体の温度－磁化曲線を表わし、T=1.5はこの系の磁気相転移温度（キュリー点T_C）を示している。すなわち実際の温度とTとの関係は $T=T_C/1.5$ のように換算して考えればよい。なお鉄鋼材ではキュリー点は約1000K程度である。

次にキュリー点より十分低温で磁場を与えていった場合をシミュレートしてみる。第９図はT=0.1で磁場を変化させた場合の磁化の様子（ヒステリシス曲線）を表わしている。ほぼ磁場がB=0.1では磁化が飽和していることがわかる。通常このような磁化の印加磁場依存性をシミュレートする際には、磁場を一定にして前述したようにnMCS程度の十分な回数繰り返し計算をさせ、定常状態になった値を結果として用いる。実験と比較するとこれは十分な時間、磁場を一定にして測定することに相当する。磁化測定によく用いられる試料振動型磁気測定器（VSM）や超伝導干渉磁束計（SQUID）では、定常磁場での磁化を測定するので実際のデータ点はそれぞれの定常磁場に対応してとびとびとなっていることと同様である。これに対して、バルクハウゼンノイズなどは磁場が変化している最中に起こる現象であり、それゆえ定常磁場下での静的過程とは違った動的磁化過程をシミュレートしなければならない。

そのため第９図の磁化曲線を得るために印加した磁場は第10図(a)のような局所的に見れば一定磁場であるがそのステップを非常に細かくしてあるので全体としてみると三角波形を成すように設定してある。図中のO→a→b→c→d→e→fは第９図の各過程と対応させてある。また第10図(b)はこの三角波形の印加磁場に対応した磁化を示しているが、これは第９図を時間軸にそって記述したものと対応している。ただし時間はMCS単位で計られる。この第10図(b)は全体的には滑らかな曲線に見えるが、細かく見るとノイズを伴っていることがわかる。特にこれは磁化の変化が大きい部分で顕著となる。この磁化曲線を時間で微分dM／dt（実際には隣り合うMCSごとの差分）したものを第10図(c)に表わす。実験で測定されるバルクハウゼンノイズは検出コイルの誘起電圧であり、これは磁化の変化分であることから磁化の微分と同様であり、第10図(c)と比較しうる量である。

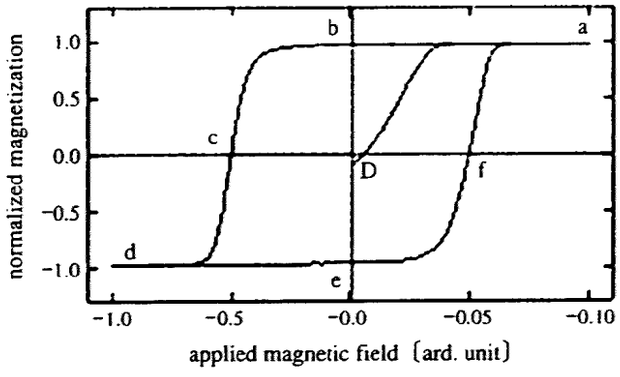

第９図　磁化の印加磁場依存性シミュレーション

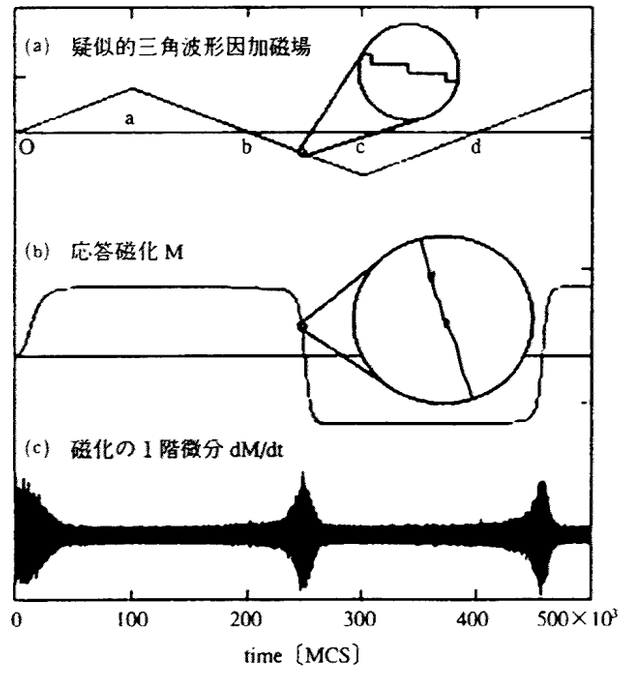

第10図　MCS単位で表わした時間変化

実際にこのdM／dtがバルクハウゼンノイズと対応しうる量なのかを検討するために、温度変化を実験と比較してみよう。第11図はSS400のバルクハウゼンノイズを室温（RT：300K）と液体窒素温度（LNT：77K）で測定したものである。LNTではRTに比べてノイズ全体の大きさが小さく、またそのピークが遅れていることがわかる。これは低温では熱雑音が弱くなり、かつヒステリシスカーブにおける保持力が大きくなったことに対応していると考えられる。このようなバルクハウゼンノイズの温度依存性は近年マイクロワイヤーでも測定されており、同様の傾向が報告されている[5]。一方第12図はシミュレーションのdM／dtの温度依存性を示している。第８図に従い、T=1.5をキュリー点T_Cとして温度を表わしている。第12図(a)ではキュリー点より高温側では熱雑音によってノイズのピークが見られないのに対して、低温になるにつれてピークがはっきりとわかるようになる。キュリー点近傍ではピークはほぼ印加磁場がゼロでその向きが反転するときに現れているが、より低温になるとピーク位置の遅れが生じる。この傾向をより詳しく示したものが第12図(b)である。この図ではピークの位置を明らかにするためにピークの大きさで規格化している。(1／3) T_Cから (1／5) T_Cまではノイズのピークはほぼ印加磁場がゼロを横切る付近にあるが、

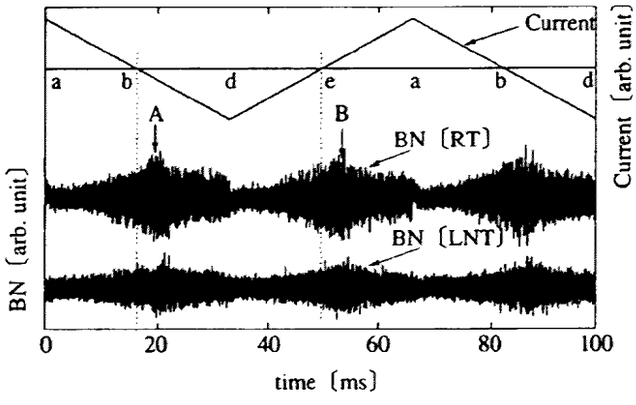

第11図　室温(RT)と液体窒素温度(LNT)で測定されたSS400のバルクハウゼンノイズセス図

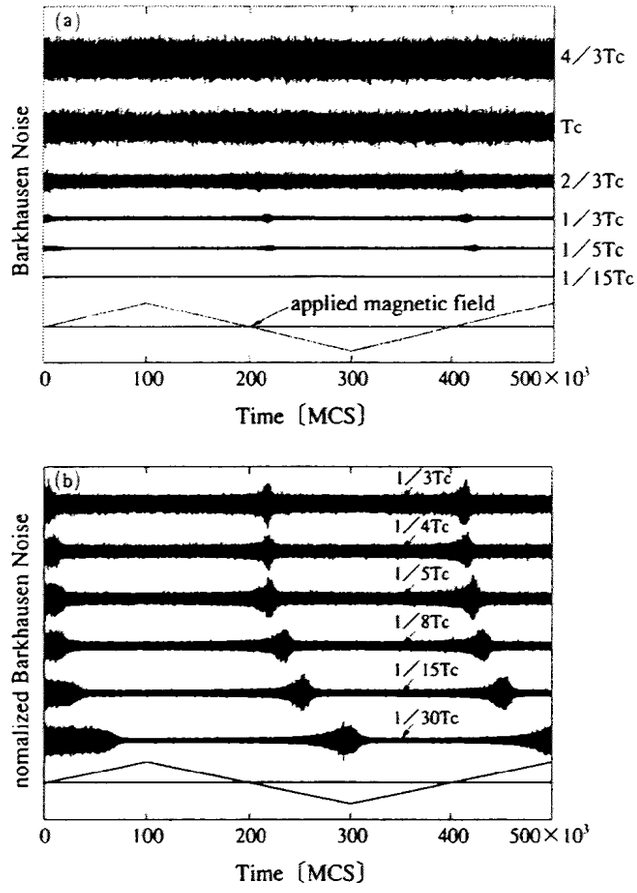

第12図　(a)バルクハウゼンノイズの温度依存性のシミュレーション結果と(b)TC以下のバルクハウゼンノイズをピーク値で規格化したシミュレーション結果

(1／8) T_Cでは遅れが生じはじめ、(1／15) T_C、(1／30) T_Cとなるに連れて急速に遅れが大きくなっていく。このシミュレーション結果は実験で得られたバルクハウゼンノイズの温度依存性とよい対応を示している。このことから我々は以上のような手法で得られたdM／dtをバルクハウゼンノイズのシミュレーションとして扱うこととする。

モンテカルロ法を用いたこのようなシミュレーションの利点は、原子レベルでの転位や空孔、歪みなどを自由に想定して計算できることである。ただ現在取り扱える粒子数は最大でも100万個程度（100×100×100の立方体）であり、磁気双極子相互作用なども含めた計算をする場合にはより少数の粒子数からなるクラスターについての計算に甘んじなければ

ならない。そのため現実の鉄鋼材のようにマクロな系では、有限のクラスターで計算された特性がマクロ的にも反映されているはずだ、という仮定を置いていることになる。

上記のことに気をつけた上で、いくつかのシミュレーションを行ってみよう。一つ目は鉄鋼材のグレインサイズが違う場合にバルクハウゼンノイズがどう変わるかを見てみよう。第13図は一辺の長さLが30（一方向に並んだスピン数は31個）と60（同61個）の立方体に対してのシミュレーション結果である。ノイズ強度はスピン数で規格化してある。これより同一のスピン数が含まれる試料であっても、大きな塊が少数あるよりも小さな塊が多数ある方がバルクハウゼンノイズの強度は強くまたそのピーク幅はシャープになる。第14図は、このノイズの形状をガウス関数でフィッティングして、そのピーク強度と半値幅が一辺の長さとどう対応するかを示している。これは実験による結果ともよい一致を示している[6]。第13図ではノイズの形状が必ずしもガウス関数的であるわけでなく、この形状にもいろいろな情報が含まれていると考えられる。そのため従来のバルクハウゼンノイズ測定のようにピーク強度の平均値を取るだけでなく、より詳細な形状データを活用していくことが今後有効となるであろう。

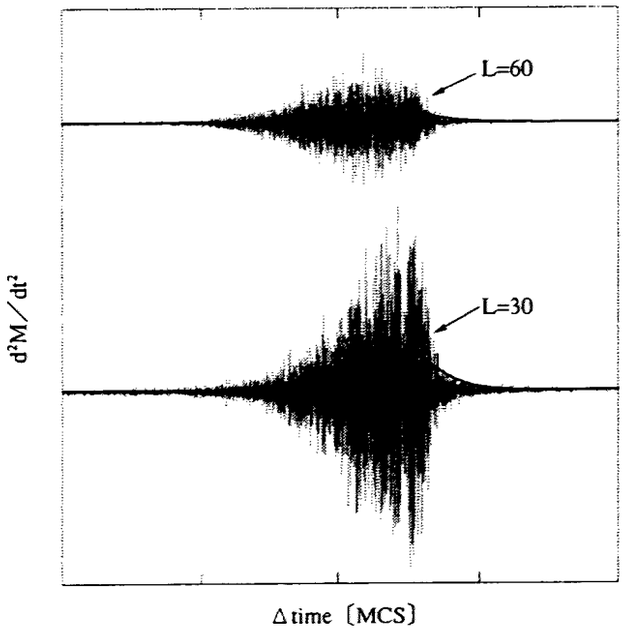

第13図　バルクハウゼンノイズのグレインサイズ依存性のシミュレーション結果

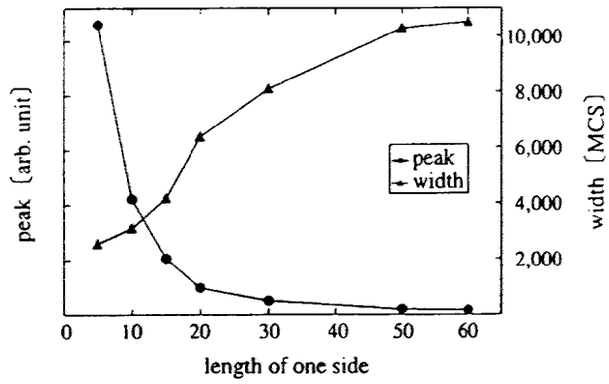

第14図　シミュレーションされたノイズのピーク値と半値幅のクラスターサイズ依存性

最後に一辺の長さLが30（一方向に並んだスピン数は31個）の立方体の中央部に線状の空孔を配置して刃状転位をモデル化したスピン系についての動的磁化過程を述べる。第15図は空孔を入れていないものと入れたものとにそれぞれ磁場を加えていった場合のスピンの変化をスナップショットとして示したものである。空孔が入っていない左列のスピン変化ではx方向への磁場が強まるにつれて磁壁移動がおき、徐々にスピンがx方向を向いていく様子が伺える。一方y方向に空孔を並んで入れたものに対してx方向の磁場をかけていくと（中列）比較的容易にスピンがx方向を向くのに対して、y方向への磁場を印加すると（右列）なかなかスピンが揃っていかないことがわかる。このスピンの総和が磁化であり、その微分がシミュレーションされたバルクハウゼンノイズと考えているので、このx方向、y方向に対するスピンの揃い方のずれがすなわちバルクハウゼンノイズの角度依存性を与えていると考えられる。またこのようにモンテカルロ法でのシミュレーションではスナップショットとして変化を描写できるので、不純物や転位などの混入とバルクハウゼンノイズの

関連を調べる上でも重要な知見を与えてくれる。

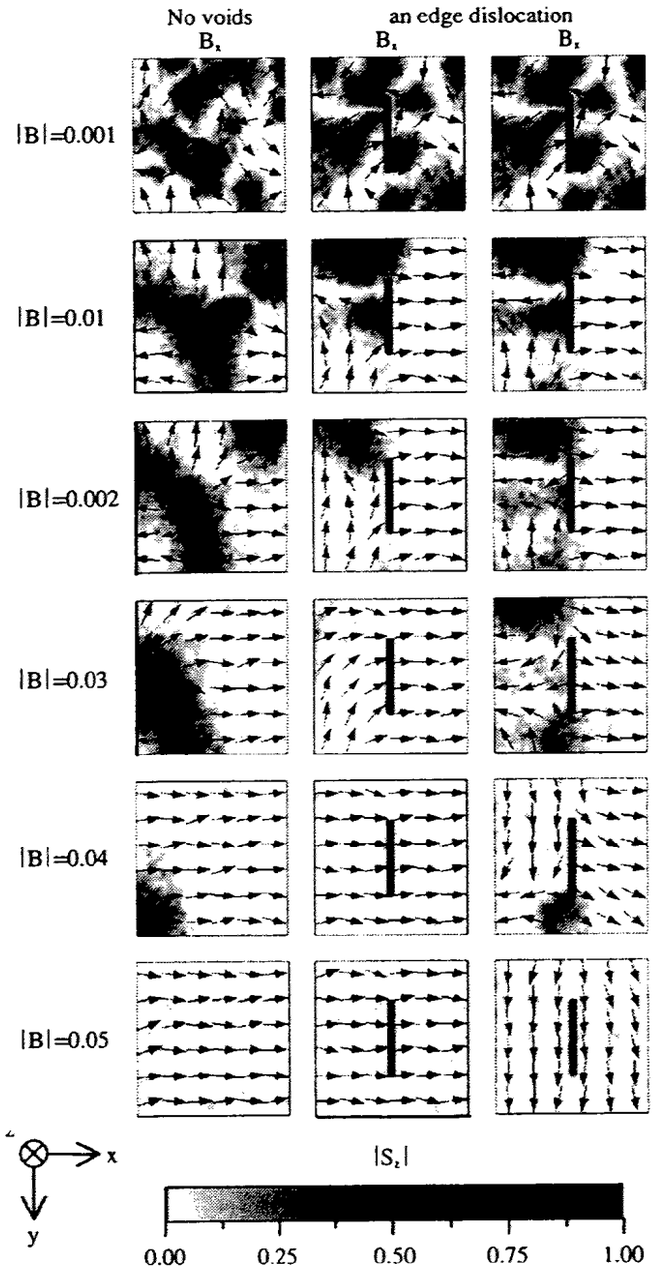

第15図　刃状転位を導入した系の印加磁場に対するスピンスナップショット
左列：参照のために転位を導入していない系にx方向に磁場を印加した場合、
中列：y方向に刃状転位を導入しx方向に磁場をかけた場合、
右列：中列とどうようの系にy方向の磁場を印加した場合

おわりに

以上述べたように鉄鋼材の変質をバルクハウゼンノイズなどの動的磁化過程によって測定することはこれまで見落としがちであった初期劣化の検出に有効だと考えられる。またモンテカルロ法を用いた動的磁化過程の解析シミュレーションは、より微細な構造変化を定量的に調査していく際の大事な手段として、今後価値が高まると思われる。

【謝辞】

本研究は福島大学大学院の田中信也氏（現富士通サポート&サービス株式会社）および福島大学教育学部今江一仁氏（現有限会社ハヤマ）との共同研究として行われました。また研究の遂行にあたって埼玉大学工学部・山田興治教授、東北大学流体科学研究所・高木敏行教授に大変お世話になりました。各氏に深く感謝いたします。

＜参考文献＞

(1) K.Yaamada, Y.Tanaka, Y.Uno, H.Takeda, S.Toyooka and Y. Isobe：J. Magn. Soc. Japan 23,（1999）pp.718-720.

(2) K.Yamaguchi, K.Yamada S.Shoji, Y.Uno, H.Takeda, S. Toyooka and H. suboi："Simulation for nondestructive evaluations by magnetic sensors", IEEE Transactions, Vol.36 pp.1710-1713, 2000.

(3) K.Yamaguchi, S.Tanaka, O.Nittono, T.Takagi, K.Yamada："Monte Carlo simulation of dynamic magnetic processes for spin system with local defects," Physica B, Vol.343, pp.298-302, 2004.

(4) K.Yamaguchi, S.Tanaka, H.Watanabe, O.Nittono, T.Takagi, K.Yamada："Monte Carlo Simulation for Barkhausen Noise," IEEE Transactions on magnetics, Vol. 40, pp.884-887, 2004.

(5) R.Varga, K.L.Garcia, A.P.Zhukov, M.Vazzquez："Switching field fluctuations in bitable microwires," Physica B, Vol. 343, pp.403-409, 2004.

(6) R.Hill, A.Cowking, J.Mackersie：NDT & E Int., 24（1991）p.179.

（筆者紹介はp.77参照）

筆者紹介

山口克彦
福島大学
共生システム理工学類　人間支援システム専攻
助教授
〒960-1296　福島市金谷川1
TEL：024-548-8189　FAX：024-548-8189
E-mail：yama@sss.fukushima-u.ac.jp

入戸野修
福島大学
共生システム理工学類　産業システム工学専攻
教授
〒960-1296　福島市金谷川1
TEL：024-548-8191　FAX：024-548-3181
E-mail：onittono@sss.fukushima-u.ac.jp

山田　吉郎
㈱テクノス　代表取締役社長
〒108-0014　東京都港区芝4-2-3
TEL：03-3453-9111　FAX：03-5484-6785

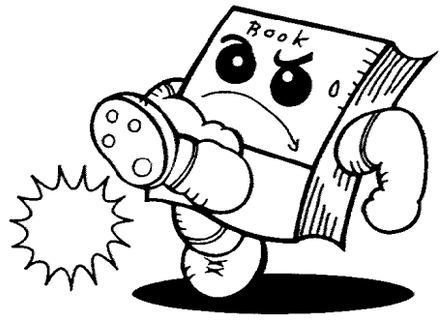

深澤亮一
㈲スペクトルデザイン
取締役
㈱栃木ニコン　テラヘルツ事業企画リーダー兼技術アドバイザー兼任
〒324-0403　栃木県那須郡湯津上村湯津上285-1
TEL：0287-98-3066　FAX：0287-98-3066
E-mail：r.fukasawa@spectra-dsn.co.jp

＜主なる業務歴及び資格＞

テラヘルツテクノロジーフォーラム、テラヘルツテクノロジー動向調査委員会、㈳電子情報通信学会「テラヘルツ応用時限研究専門委員会」専門委員

＜過去の執筆実績＞

"テラヘルツイメージングシステムの開発"光アライアンスVol.14、No.11、2003.11、p30

有限会社スペクトルデザイン
＜代表者名＞　深澤朗美
＜本社住所＞
〒324-0403　栃木県那須郡湯津上村湯津上285-1
TEL：0287-98-3066　FAX：0287-98-3066
URL：http://www.spectra-dsn.co.jp
E-mail：r.fuksawa@spectra-dsn.co.jp
＜資本金＞ 3百万円
＜従業員数＞ 3名
＜主要取引先＞ ㈱栃木ニコン、他数社
＜事業内容及び会社近況＞

㈲スペクトルデザインは、電磁波を用いた計測装置の製品企画、開発、市場調査、情報サービスを中核業務とし、新しい電磁波技術の産業化を推進する役割を担いたいという目的から2004年10月に設立され、幅広い活動を開始しています。

Proceedings of the of the International Conference on Bio-inspired computing (BIC'05), Malaysia, September 5-7, 2005.

Doping Effect on Electrical and Galvanomagnetic Properties of Flash-Evaporated Thin InSb Films

Md. Abu Taher[1], Osamu Nittono[2]
[1]*Dept. of CSE & CIS, Daffodil International University, 102 Sukrabad, Dhaka-1207, Bangladesh.*
[2]*Faculty of Symbiotic Systems Science, Fukushima University, 1 kanayagawa, Fukushima, Japan.*
E-mail: taher2000bd@yahoo.com, onittono@sss.fukushima-u.ac.jp

Abstract

Sn-doped InSb films were prepared by evaporating extremely pure (99.999%) InSb compound with a very small amount of SnSb alloy in a high vacuum system less than 10^{-5} Pa. The microstructure and galvanomagnetic properties of the films were investigated in terms of heat treatment procedure including capped-annealing. Both as-deposited and annealed films were found to have polycrystalline structure and their characteristics were strongly influenced by doping ratio and successive annealing. The Hall mobility as well as the magnetoreistance decreased with increasing doping ratio. The temperature co-efficient of resistivity (TCR) reduced drastically by doping Sn in the film. This small temperature dependence was expected to be advantageous for producing MR devices that can be used for applications in a wide driving temperature range.

1. Introduction

Indium antimonide (InSb) has a phonon-limited electron mobility of 7.8×10^4 $cm^2V^{-1}s^{-1}$ at room temperature, resulting in a large Hall voltage, which makes it applicable for magnetic field sensing devices such as Hall effect sensors and magnetoresistors [1, 2]. The InSb magnetoresistors are reported to have extremely high sensitivity [3]. A great interest has been growing in magnetic sensors using the magnetoresistance (MR) effect of the InSb thin films as well as the Hall effect because such sensors would broaden the application of magnetic sensing. In general, most of the device applications of semiconductors require the doping process with donor or acceptor impurities to stabilize the electron density against temperature changes. This process has recently been widely studied for InSb and the related compound films, especially obtained by metalorganic chemical vapor deposition (MOCVD) and molecular beam epitaxy (MBE) methods [4, 5]. Few investigations have so far been carried out on non-epitaxial III-V compound films.

However, in comparison with the wider gap III-V compounds, such as GaAs, the literature dealing with the behavior of group IV elements in InSb is rather scarce [6]. Among group IV elements, Sn is of particular interest because tin (Sn), indium (In) and antimony (Sb) all have almost the same tetrahedral covalent radii [10]. Hence, it may be anticipated that Sn can be substituted for both In and Sb elements, acting respectively as donor and acceptor on those sites. Such expected amphoteric behavior was experimentally confirmed by Edmond [7]. In general, Sn in InSb is thought to be an effective donor dopant for obtaining a high electron concentration.

The band gap energy of InSb is 0.17 eV, however, so above room temperature the electron concentration increases rapidly with temperature. This large temperature dependence of resistivity (-2%/K) limits the driving temperature and this is the biggest problem in the practical application of InSb MR devices [8]. On the other hand, Sn element as a donor dopant is expected to stabilize the electron density against temperature changes. Partin et. al. [9] demonstrated that Sn is incorporated well as an n-type dopant and, that it does not self-compensate or suffers from a serious memory problem.

In this study, we tried to incorporate Sn into InSb thin films by using SnSb, and Sn-doped InSb films were produced on glass substrates by using vacuum flash evaporation method [10]. The characteristics of thus prepared films have been investigated in terms of successive procedures including annealing capped with SiO_2 layer.

2. Experimental Procedure

Sn-doped InSb films were prepared by mixing a small amount of SnSb alloy into InSb compound as a source material. First of all, SnSb alloy was produced by using equivalent weight of antimony (Sb: 0.50 gm) and tin (Sn: 0.50 gm): Sb and Sn shots were first inserted into a glass tube. Then the glass tube was evacuated under the vacuum of 10^{-3} Torr by a rotary pump, and heated by using gas flame. The melted SnSb was shacked several times for uniform and homogeneous mixing, and thus an

SnSb alloy ingot was formed. This melting procedure was repeated three times so that SnSb alloy might be formed homogeneously in concentration. The resultant InSb alloy ingot was cut into small pieces by using a pre-cleaned punch. Sn-doped InSb films were then prepared by evaporating a mixture of InSb compound and small pieces of SnSb alloy with different weight ratios, SnSb/InSb (hereafter referred to as doping ratio).

Pre-annealed Corning 7059 glass (size: 21×26×1.1 mm) was used as a substrate with a mask for electrical measurements (size: 3×19 mm with six terminals). It is reported that higher substrate temperatures above 473K lead to the deviation from stoichiometry of the InSb film [8]. Thus, the substrate was not heated intentionally, but only irradiated from the tungsten crucible (< 323K). The distance between source material and substrate was about 10 cm. The source temperature and thus the deposition rate (0.5- 20 nm/s) were adjusted by changing the electric current flow through the crucible and flow time. In this study, the deposition rate was evaluated directly by a thickness monitor using a quartz crystal sensor (CRTM-5000), set-up near the substrate.

The deposited films were annealed in a vacuum of around $1x10^{-4}$ Pa at elevated temperatures between 623K and 773K by using an image furnace (MILA-3000, ULVAC SHINKU-RIK0). Before each annealing process, the furnace used was pre-heated up to 873K for cleaning.

X-ray diffraction analysis (XRD) was performed for both as-deposited and annealed films to evaluate the crystallinity. The surface morphology of the films was observed by a field emission scanning electron microscope (FE-SEM). The chemical composition of the films was examined by X-ray Fluorescence (XRF) (RIX 2000, Rigaku). A standard four-probe method was used to measure the resistivity and temperature co-efficient of resistivity of films. Van der Pauw Hall measurement was carried out at room temperature in a magnetic field (H) up to 1T to investigate the electrical properties together with galvanomagnetic properties including magnetoresistance (MR), defined as $\frac{\Delta R}{R_O} = \frac{R_H - R_O}{R_O}$, where R_H and R_O are the resistance at H = 0 and H = 1T, respectively.

3. Experimental Results and Discussion

3.1 Characteristics of as-deposited films

3.1.1. Structural Evaluation. The structural properties of as-deposited films with different doping ratios (SnSb/InSb) are analyzed by X-ray diffraction and the results are summarized in Fig. 1. Our previous report [10] showed that an optimum deposition rate is 10 nm /s. Therefore, all the films were deposited at this deposition rate. The result of un-doped InSb film is also shown here (Fig. 1a) as a comparison. The result proves that un-doped InSb film has only one phase, consisting of four peaks of 111, 220, 311 and 422 for InSb. When a small amount of SnSb (SnSb/InSb = 0.002) is added to the mother InSb compound, the deposited film (Fig. 1b) shows almost the same profiles as that of undoped film, indicating that the deposited film possesses nearly the same constitution. Appreciable profile changes took place as the doping ratio increased. Figure 1(c) shows the doped film with a doping ratio of 0.005, where a small peak of 202 for Sb (Sb 202) was observed.

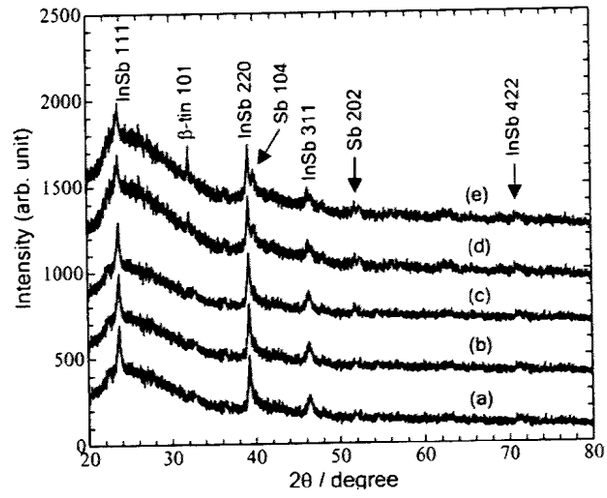

Figure 1. X-ray diffraction results of films at different doping ratio (SnSb/InSb): (a) un-doped InSb; (b) SnSb/InSb = 0.002; (c) SnSb/InSb = 0.005; (d) SnSb/InSb = 0.01; (e) SnSb/InSb = 0.012. Film thickness: 3000Å.

Heavily doped InSb films showed remarkable changes in profile together with the appearance of β-tin 101 phase and another additional peak (104) for Sb: β-tin 101 peak increases with increasing doping ratio, and InSb 111 peak seems to decrease slightly for heavily doped films as shown in Figs. 1(d) and (e). These results indicate that the addition of impurity elements can be used effectively to change the film constitution that may affect on the electrical and galvanomagnetic properties of the InSb films. It is noted here that un-doped and doped films, deposited at N_2 atmosphere, showed a similar profile (or constitution) as shown in Fig. 1, although they are not given here.

3.1.2. Electrical and Galvanomagnetic Properties. The deposition ratio dependence of Hall mobility and carrier density was investigated and shown in Fig. 2 for the films

deposited with and without nitrogen atmosphere. Solid and dashed curves represent the results of Hall mobility and carrier density respectively. The carrier density increases with increasing doping ratio. The carrier density for the films deposited at N_2 atmosphere is slightly higher than that of films deposited without nitrogen atmosphere.

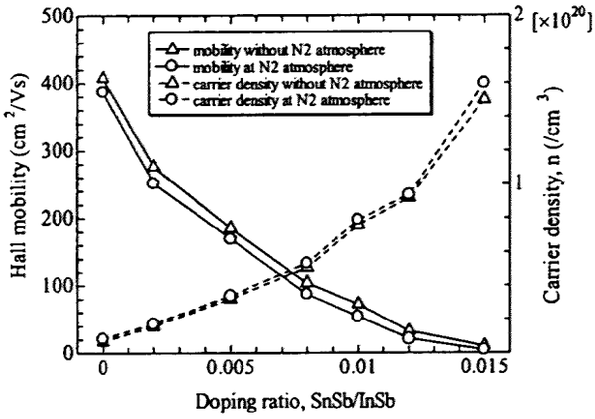

Figure 2. Dependence of Hall mobility and carrier density on doping ratio, SnSb/InSb.

On the other hand, the Hall mobility decreases with increasing doping ratio. The Hall mobility for the films deposited with N_2 atmosphere is slightly lower than that of films deposited without N_2 atmosphere. This is thought to be associated with the impurity scattering. The increment of carrier density with the addition of impurity may be ascribed to the increment of donor concentration. Both the results are consistent with each other, because two properties are inversely related to each other [Hall mobility, $\mu_H = |R_H|\sigma = |1/ne|\sigma$, where R_H = Hall co-efficient, σ = conductivity, n = carrier concentration and e = charge of electron].

The dependence of resistivity and magnetoresistance on impurity addition is shown in Fig. 3. The resistivity of the deposited film decreases gradually with increasing doping ratio. In general, doped films have polycrystalline, thus containing lots of lattice defects including impurities, resulting in the increment of resistivity. However, the present results are contradictory. This may be mainly ascribed to the inherent resistivity of SnSb alloy: the resistivity of SnSb film was found to be slightly lower than that of InSb film with the same thickness. Thus, the resistivity can decreases with increasing doping ratio. Surface morphology also revealed that the grain size of doped films was slightly larger than that of un-doped films. This grain size may be related to lower resistivity for doped films. However, the films deposited at N_2 atmosphere possesses slightly lower resistivity than that of films deposited without N_2 atmosphere. This may be also ascribed to the increment of carrier density as shown in Fig. 2.

Figure 3 also showed that the magnetoresistance (MR) decreases drastically with increasing impurity content. Ohshita et. al. [2] investigated that the magnetoresistance of thin films is dependent strongly on the homogeneity in concentration of the film, resulting in a fluctuation or gradient of carrier concentration under magnetic field.

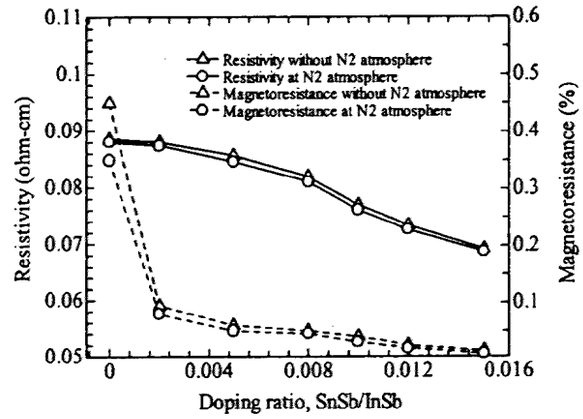

Figure 3. Dependence of resistivity and magnetoresistance on doping ratio, SnSb/InSb.

In this study, the inhomogeneity is thought to be induced by rapid or flash evaporation of multi-elements. This point must be improved experimentally.

3.2. Characteristics of Annealed Films

3.2.1. Annealing without capping layer. The electrical and crystalline properties of the InSb films are dependent strongly on annealing temperature and time [11].The heat treatment of the films was performed by using an image furnace under a vacuum of 10^{-4} Pa. The annealing temperature varied from 623K to 773K, in this study, because the melting point of InSb is 798K and the solid phase recrystalization takes place appreciably under these annealing conditions.

Figure 4 shows the relationships between Hall mobility and annealing temperature for InSb films without capping SiO_2 layer when annealed for 900s. All the films have the same thickness of 300 nm. All the curves in figure show a similar tendency that the Hall mobility first increases with annealing temperature, and then decreases at higher annealing temperatures. The decrement of Hall mobility is due to the re-evaporation of Sb because of its high vapor pressure, as already explained in our previous studies [10, 12].The highest Hall mobility of 6.4×10^3 cm^2/Vs was obtained for undoped InSb films annealed at 743K. The Hall mobility of InSb films deposited at N_2 atmosphere showed the

maximum value of 4.9×10^3 cm^2/Vs when annealed at 733K. It is also shown that, for doped films, Hall mobility increases up to 733K, and then decreases, whereas, for undoped films the Hall mobility increases up to 743K.

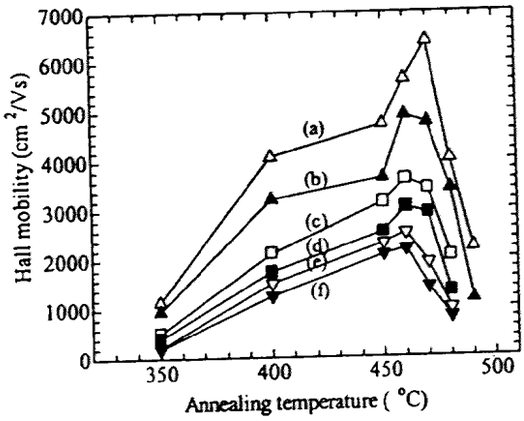

Figure 4. The relationships between Hall mobility and annealing temperature for without capping undoped and doped films: (a) undoped InSb films; (b) InSb films deposited at N_2 atmosphere; (c) Sn-doped InSb films (SnSb/InSb=0.005); (d) Sn-doped InSb films (SnSb/InSb=0.005) at N_2 atmosphere; (e) Sn-doped InSb films (SnSb/InSb=0.012); (f) Sn-doped InSb films (SnSb/InSb=0.012) at N_2 atmosphere.

Therefore, this reason may be ascribed to the melting point and hardness of the deposited films. The differential thermal analysis (DSC) suggested that the melting point of doped films was slightly lower than that of undoped films, and in this connection, hardness measurements revealed that doped films were slightly softer than undoped films. Thus it is thought that the doped films are thermally unstable and re-evaporation might be occurred even at 733K, resulting in lower mobility above 733K. It is also shown that for the annealed films Hall mobility gradually decreases as the doping ratio increases. This is consistent with the results shown in Fig. 3. This is also related with the results of annealing temperatures, as shown later.

3.2.2. Annealing with capping SiO_2 layer. For the quality improvement of the films by annealing, a procedure needs to prevent Sb from self-evaporating during annealing. Therefore, an attempt was carried out to cap the InSb films with SiO_2 layer (capped films) before annealing. For the capping process, an Sn-doped InSb film was first deposited on a glass substrate, and then SiO_2 layer of about 250 nm thick was deposited on the doped InSb film in the same vacuum chamber, and thus prepared InSb films were subjected to vacuum annealing. After the annealing process, the SiO_2 layer was removed by wet etching (HF: 20% solution), and gold contacts were then deposited on such InSb films for electrical measurements. By introducing this capped-annealing, the Sn-doped InSb films were found to be annealed up to 773K without any change in Hall mobility in the higher temperature region, as will be shown later.

The relationship between the Hall mobility and the annealing temperature for capped films annealed for 3.6×10^3 s (60 min) is shown in Fig. 5. All the curves show a similar tendency that the Hall mobility increases with increasing annealing temperature and does not decrease further even when annealed at 773K. The results indicate that the capping with SiO_2 layer can protect effectively InSb films from re-evaporating, resulting in superior electrical characteristics.

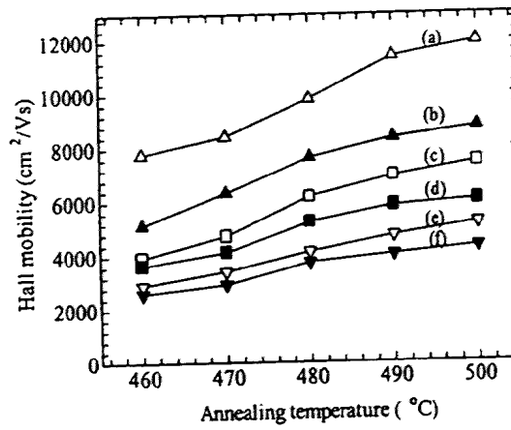

Figure 5. Relationships between Hall mobility and annealing temperature for films capping with SiO_2 layer before annealing. In figure, (a) undoped InSb films; (b) InSb films deposited at N_2 atmosphere; (c) Sn-doped InSb films (SnSb/InSb=0.005); (d) Sn-doped InSb films (SnSb/InSb=0.005) at N_2 atmosphere; (e) Sn-doped InSb films (SnSb/InSb=0.012); (f) Sn-doped InSb films (SnSb/InSb=0.012) at N_2 atmosphere.

The maximum Hall mobility of 1.23×10^4 cm^2/Vs was obtained for the undoped InSb films annealed at 773K for 3.6×10^3 s (60 min) with the thickness of 300 nm. A comparatively lower mobility was obtained for doped films and the mobility gradually decreases with increasing doping ratio. Annealing process is reported to improve the film quality. Therefore, long annealing is expected to further improvement of the film quality such as Hall mobility.

The Hall mobility is also reported to depend on film thickness [11, 13]. Therefore, the Hall mobility of

undoped and doped films was investigated with reference to film thickness. Figure 6 shows the dependence of Hall mobility on film thickness of undoped and Sn-doped InSb films annealed with capping SiO_2 layer at 773K for 3.6×10^3 s. The Hall mobility increases with increasing film thickness.

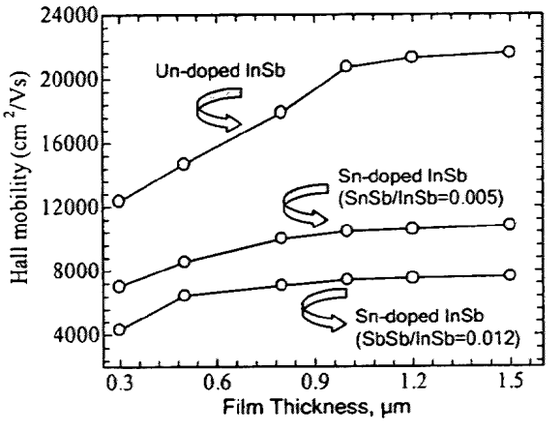

Figure 6. Thickness dependence of Hall mobility for capping films annealed at 500°C for 60 min.

The undoped InSb films of 1.0 μm thick, annealed at 773K, showed the Hall mobility of 2.1×10^4 cm^2/Vs and electron concentration of 9.6×10^{16} $/cm^3$ with a good reproducibility. The Hall mobility decreased as a result of Sn doping. The Hall mobility of lightly doped (SnSb/InSb = 0.005) films and heavily doped (SnSb/InSb = 0.012) films of 1.0 μm thick was 1.05×10^4 cm^2/Vs and $7.5 \times 10^3 cm^2/V$, respectively, with the carrier concentration of 7.6×10^{18} $/cm^3$ and $9.5 \times 10^{19}/cm^3$. The mobility for both undoped and Sn-doped films increased as the film thickness increased up to 1.0 μm. But above 1.0 μm, the Hall mobility was approximately constant regardless of the film thickness. The study of N. F. Teede [13] showed a similar breakpoint on the mobility-thickness curve at about 1.0 to 4.0 μm thick films prepared by the flash evaporation method. The present results of mobility-thickness curve show a similar tendency to the results of M. Tomisu et. al. [11] and N. F. Teede [13]. This trend is thought to be common with the films prepared by vacuum evaporation.

The present films were also processed to test the shape effect of the magnetoresistance (MR) devices. The amount of the MR is reported to strongly depend on a geometrical factor L/W, [14] where L is the length of the rectangular devices and W is the width of the current path. This geometrical effect is important for practical applications [2]. The MR geometrical effect was observed for various films and the results are plotted in Fig. 7 as a function of applied magnetic field, B (T).

The magnetoresistance is reported to depend on Hall mobility and magnetic field [5, 8, 14]. According to their theoretical results, the MR is proportional to the square of the magnetic field and to the square of the Hall mobility of the film. Figure 7 shows the MR effect on with-capping InSb films measured when L/W = 4mm/3mm = 1.33. The MR increases with increasing applied magnetic field. The MR is observed to be much larger for undoped InSb films than for doped InSb films, mainly because the electron mobility of the undoped InSb films is much higher than that of the doped films. The maximum MR value of 80% was obtained for undoped InSb films with the magnetic field of 1 T.

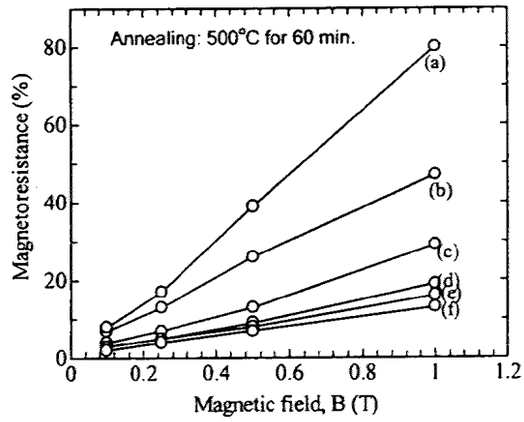

Figure 7. Magnetoresistance effect of 1.0 μm thick InSb films capping with SiO_2 layer before annealing. In figure, (a) undoped InSb films; (b) InSb films deposited at N_2 atmosphere; (c) Sn-doped InSb films (SnSb/InSb=0.005); (d) Sn-doped InSb films (SnSb/InSb=0.005) at N_2 atmosphere; (e) Sn-doped InSb films (SnSb/InSb=0.012); (f) Sn-doped InSb films (SnSb/InSb=0.012) at N_2 atmosphere.

The temperature dependence of resistivity (temperature co-efficient of resistivity, TCR) is also an important factor for producing magnetoresistance devices [5]. The temperature dependence of resistivity could be reduced by increasing the electron concentration (by adding impurity), that would be a promising material for practical magnetic sensors. Figure 8 shows the temperature dependence of resistivity (TCR) for capping undoped and Sn-doped InSb 1.0 μm thick films with capping layer, annealed at 773K for 3.6×10^3 s (60 min). The undoped film having electron concentration of 9.6×10^{16} $/cm^3$ showed a very large temperature dependence of resistivity (-0.06/K around room temperature). This may be associated with the fact that the thermally activated concentration became dominant for undoped InSb films.

The resistivity for the InSb films deposited at N_2 atmosphere (electron concentration, n = 6.4×10^{17} /cm^3) shows less temperature dependence than undoped InSb films.

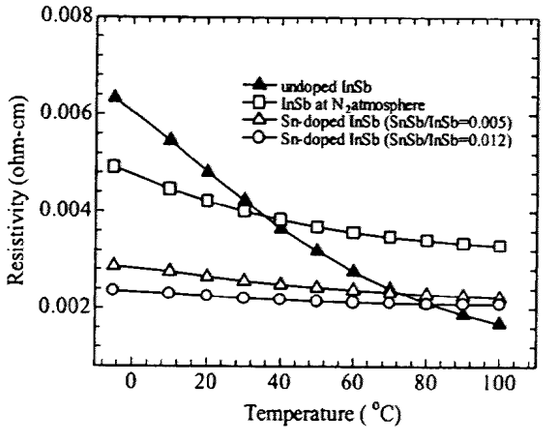

Figure 8. Temperature dependence of resistivity for capping films annealed at 500°C for 60 min.

On the other hand, the resistivity for Sn-doped films remains almost constant as the temperature changed, although they show a slight decreasing in resistivity. This may be ascribed to the fact that the impurity concentration becomes more dominant than the thermally activated concentration. These results indicate that the temperature dependence of resistivity can be reduced effectively by Sn doping. The film with the lower doping concentration (7.6×10^{18} /cm^3, SnSb/InSb=0.005) TCR showed a temperature co-efficient of resistivity of -0.01/K at around room temperature. The film with the higher-level doping concentration (9.5×10^{19} /cm^3, SnSb/InSb=0.012) TCR showed slightly smaller temperature dependence (–0.005/K) than the film with the lower doping concentration. This very small temperature dependence is advantageous for producing MR devices that can be used as a magnetoresistance sensor device to detect the abnormality of human blood flow.

4. Conclusion

Sn-doped InSb films were prepared on glass substrates by flash vacuum evaporation (including low cost production process). The effects of donor doping on electrical and galvanomagnetic properties were investigated with reference to annealing temperature. Several samples were also produced in N_2 atmosphere to examine the effect of N_2 as a donor dopant on InSb films. Undoped InSb films with an electron mobility of 2.1×10^4 cm^2/Vs annealed at 773K were reproducibly achieved. There appeared a strong correlation between the electron mobility and the Sn concentration. The Hall mobility as well as the magnetoresistance decreased with increasing doping ratio, mainly ascribed to the impurity scattering of conduction electrons. The Sn-doped InSb films showed very small temperature dependence in their resistivity (small TCR) over a wide temperature range. The present study suggests that InSb thin films prepared by the flash vacuum evaporation can be effectively used as a highly sensitive MR device that would be open up new areas for the magnetic field sensor applications that would be used as a detector to detect the abnormality of a human blood flow.

5. References

[1] J. Heremans, "Solid state magnetic field sensors and application", *J. Phys. D*; Appl. Phys., 26 (1993), pp. 1149-1153.

[2] M. Ohshita, "InSb films for magnetic sensors", *Sensors and Actuators A*, 40 (1994) pp. 131-134.

[3] D. L. Partin, J. Heremans and C. M. Trush, "Dopping profiles for indium antimonide magnetoresistors", *Sensors and Actuators A*, 69 (1998), pp. 39-45.

[4] Seong-Il Kim, Chang-Sik Son, Sang Wook Chung, Young K. Park, Eun Kyu Kim and Suk-Ki Min, "Temperature-dependant Hall analysis of carbon-doped GaAs", *Thin Solid Films*, 310 (1997), pp. 63-66.

[5] Atsushi Okamoto, Takashi Yoshida, Shogo Muramatsu and Ichiro Shibasaki, "Magneto-resistance effect in InSb thin film grown using molecular beam epitaxy", *Journal of Crystal Growth*, 201/202 (1999), pp. 765-768.

[6] O. Madelung, *Physics of III-V compounds*, Wiley, New York, 1964.

[7] J. Edmond, "Proc. Phys. Soc. 73 (1959) pp. 622.

[8] Atsushi Okamoto, Arata Ashihara and Ichiro Shibasaki, "Magnetoresistance effect in Si-doped InSb thin films grown on GaAs substrate",*Trasducers'* 99, June 7-10, 1999 Sendai, Japan, pp. 514-517.

[9] D. L. Partin, L. Green, J. Heremans and C. M. Thrush, "Growth of Tin-Doped Indium Antimonide for Magnetoresistors", *J. Elect. Mater.*, 26 (1997), 1237-1243.

[10] M. A. Taher, Y. Haga, Y. Nakamura and O. Nittono, "Quality Improvement by Annealing for Flash-evaporated Thin InSb Films" *Materials Transactions*, Vol. 42, No. 12 (2001), pp. 2584-2589.

[11] M. Tomisu, N. Inoue and Y. Yasuoka, "Annealing effect of vacuum evaporated InSb thin films", *Vacuum*, 47 (1996) 239-242.

[12] M. A. Taher, D. Fukushima and O. Nittono, "Phase Changes in Compound Films Prepared by Alternate Stacking of In and Sb Layers", *Proceedings of the International Conference on Solid-Solid Phase Transformations '99*, Japan Institute of Metals, (JIMIC-3), Kyoto, Japan, May 24-28, 1999, pp. 1317-1320.

[13] N. F. Teede, "Single Crystal InSb Thin Films by Electron Beam Re-Crystallization", *Solid-State Electronics*, 10 (1967) 1069-1076.

[14] H. Weiss: *Structure and Application of Galvanomagnetic Devices*, Pergamon Press, 1969.

Transactions of the Materials Research Society of Japan 30[4] 1027-1030 (2005)

The effect of oxygen partial pressure on the magnetoresistance of Co(-Pt)-ITO thin films

Wanti Ekawati[1], Ji Shi, Yoshio Nakamura, Osamu Nittono[2]
[1]Department of Metallurgy and Ceramics Science, Tokyo Institute of Technology
Fax: 81-3-5734-3145, e-mail: wanti@mtl.titech.ac.jp
[2]Department of education, Material Science laboratory, Fukushima University
Fax: 81-24-548-3181, e-mail: onittono@educ.fukushima-u.ac.jp

We have proved that the microstructure and magnetoresistance of granular Co-ITO thin films can be controlled by thermal annealing. As it is known that the resistivity of ITO films is very sensitive to the partial pressure of oxygen during deposition, in this experiment we investigate the oxygen partial pressure dependence of magnetoresistance in Co(-Pt)-ITO thin films. The results show that the magnetoresistance increases with the increasing of oxygen partial pressure. However, excess oxygen partial pressure decreases the magnetoresistance of this film. On the other hand, the resistivity continuously increases with increasing of oxygen partial pressure, which is due to the oxidation of Co as shown by XPS analysis. The magnetoresistance of Co-Pt-ITO films show the similar tendency as Co-ITO film, but higher magnetoresistance value at optimum oxygen partial pressure. For Co-ITO, the magnetoresistance appears when the film consists of Co particles in crystalline ITO matrix. Film shows high resistivity due to the oxygen addition which strongly influence the resistivity of crystalline ITO. Meanwhile in the Co-Pt-ITO film, the magnetoresistance arises with amorphous ITO matrix. The existence of Pt is believed to stabilize the amorphous phase. Both Co-ITO and Co-Pt-ITO films show higher magnetoresistance at higher resistivity. The oxygen addition is proved to influence the film resistivity, structure and magnetoresistance of this film.

Key words: magnetoresistance, resistivity, oxygen, Co-ITO

1. INTRODUCTION

Recently, tunneling type magnetoresistance in granular material has been intensively reported in metal-insulator granular films. Several works on Co-Al-O[1], Co-Si-O[2], Fe-Al-O[3] show similar configuration where magnetic particles distributed in the insulating matrix. The resistivity of these films are relatively high in the order of 10^4-10^9 $\mu\Omega$cm[4]. In the previous work, we had observed the magnetoresistance in Co(-Pt)-ITO film where the resistivity and magnetoresistance could be controlled through thermal annealing[5]. As it is known that the resistivity of indium tin oxide (ITO) matrix is very sensitive to the oxygen addition during deposition, we investigate the oxygen partial pressure dependence on the magnetoresistance of Co-ITO and Co-Pt-ITO in this experiment. The oxygen influence on the resistivity, structure and magnetoresistance of Co(-Pt)-ITO films are explained at the present work.

2. EXPERIMENTAL PROCEDURE

Co-ITO and Co-Pt-ITO films are prepared using two-facing-target DC magnetron (TFTM) sputtering apparatus. The schematic diagram of two-facing-target magnetron sputtering apparatus is shown in Fig.1. Silica glass and Silicon wafer with the thickness of 0.5 mm were used as substrates for various characterizations. The sputtering chamber had been evacuated to a pressure around 8×10^{-5}Pa before deposition. Argon and oxygen gasses were introduced into the sputtering chamber through mass flow controller. The mixed Ar + O_2 pressure was kept at 0.2 Pa during deposition. The oxygen partial pressure was controlled by changing the flow rate ratio of oxygen to argon gas. The film thicknesses were fixed around 2000 Å and the deposition rate was about 0.37 Å/sec. After the deposition, films were annealed in a vacuum for an hour at various temperatures. Structural properties of the films were characterized by X-ray diffraction. XPS measurement was used to identify the atomic composition ratio of each film. Film resistivity and magnetoresistance were measured using four-point probe MRHC-500 magnetoresistance measurement unit.

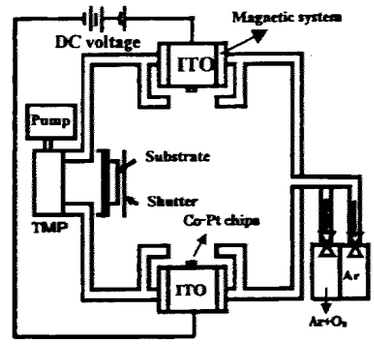

Fig.1. Schematic diagram of two facing target DC magnetron system.

The magnetic properties were examined using BHV-50H vibrating sample magnetometer (VSM). JEM3010 transmission electron microscope was used to observe the microstructure of the films.

3. RESULTS AND DISCUSSION

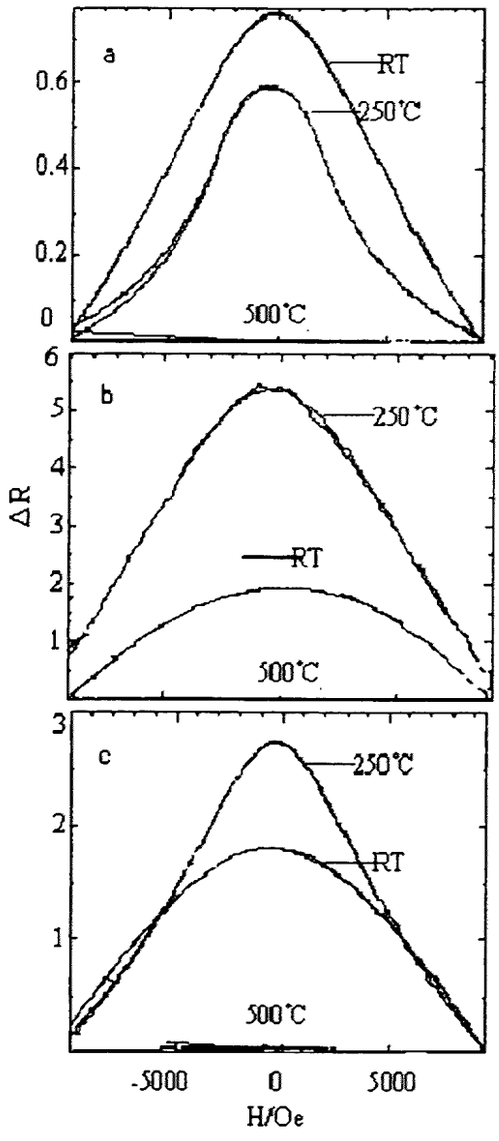

Fig.2. The ΔR(Ω) of Co-ITO films deposited at different oxygen pp and then annealed at various temperatures. a. without oxygen addition, b. 0.2% oxygen pp, c. 1% oxygen pp.

To understand the effect of oxygen partial pressure (pp) on magnetoresistance and their relation with thermal annealing, we observed the ΔR of Co-ITO films deposited at different oxygen pp and then annealed at various temperatures as shown in Fig.2. The volume fraction of Co to ITO is 1:2 in this experiment. Figure 2a shows the Co-ITO specimen annealed at different temperature without oxygen addition. In this figure, as-deposited film shows highest ΔR, and as increasing the annealing temperature ΔR continuously decreases. This is consistent with our previous research[5], considering the magnetic particle has already precipitated in the as-deposited film and through thermal annealing the magnetic particle size continuously increases, decreases the ΔR. However when oxygen is added in during deposition, film shows rapid increasing of ΔR values at 250℃ annealing temperature, ten times higher compared to specimen deposited without oxygen addition (Fig.2b). At higher oxygen partial pressure, the specimen show similar ΔR-T relation (Fig.3c).

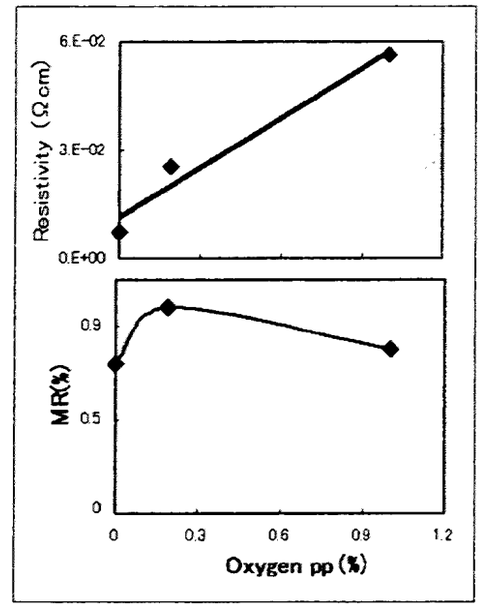

Fig.3. The magnetoresistance and resistivity of Co-ITO films as increasing of oxygen pp (T_a=250℃).

The resistivity and MR ratio of Co-ITO films as increasing of oxygen partial pressure are shown in Fig. 3. The MR ratio was measured at room temperature under the applied field of 10kOe. The specimen are annealed at 250 ℃ after deposition. Without oxygen addition introduced during deposition, specimen shows low magnetoresistance. As increasing the oxygen pp the magnetoresistance increases, however further increasing the oxygen pp the magnetoresistance decreases. On the other hand, the electrical resistivity continuously increases as increasing of oxygen partial pressure in this experiment.

As it is necessary to understand the magnetic properties of this film, we investigate the corresponding M-H curves of specimen deposited at different oxygen pp and then annealed at various temperatures. Figure 4a shows the M-H curves of specimen deposited without any oxygen, at room temperature film exhibits superparamagnetic behavior. Increasing of annealing temperature gradually increases the magnetization of this film and shows clear remanence at 350 ℃ annealing temperature. Further annealing at 500℃, the film shows clear hysterisis loop. When oxygen is added during deposition, specimen shows higher saturation magnetization as increasing the annealing temperature.

Further annealing at 500 ℃, film shows higher magnetization saturation and clear remanence appears.

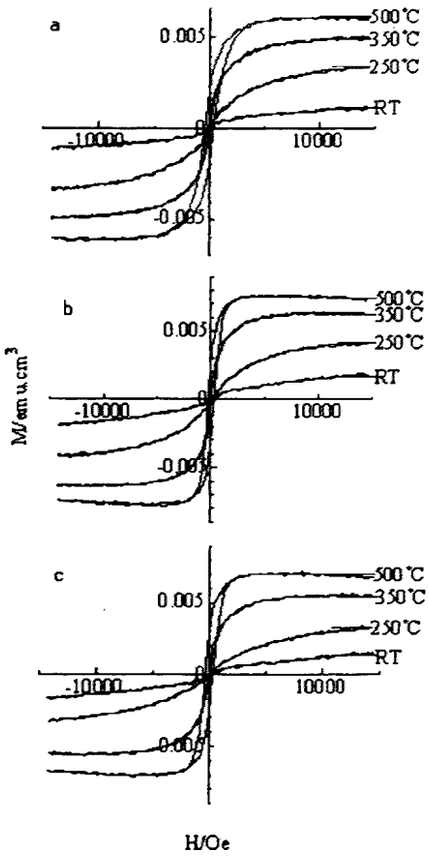

Fig.4. The corresponding M-H curves of Co-ITO films deposited at different oxygen pp then annealed at various temperatures. a. No oxygen, b. 0.19% oxygen pp, c.1% oxygen pp.

Figure 4c shows the M-H curves of specimen deposited at 1% oxygen pp. This figure shows increasing of magnetization as increasing the annealing temperature. However at room temperature films has low magnetization, even thought after annealing at 250℃ film shows only small increases of magnetization. From M-H curves, we could notice that the further increasing of oxygen pp decrease the magnetic particles in as-deposited film. It is considered that the decreasing of magnetization is relevant to the increasing of resistivity due to oxidation of Co as shown in XPS analysis results (Fig.5).

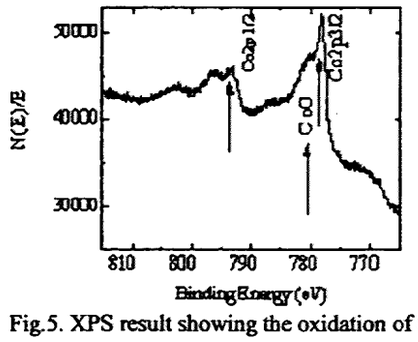

Fig.5. XPS result showing the oxidation of Co.

Clear information about the effect of oxygen on size distribution of magnetic particles and the structural properties of this film, however could not be seen clearly. For this reason, we investigate the microstructure of this film using transmission electron microscope (TEM) as shown in Fig.6.

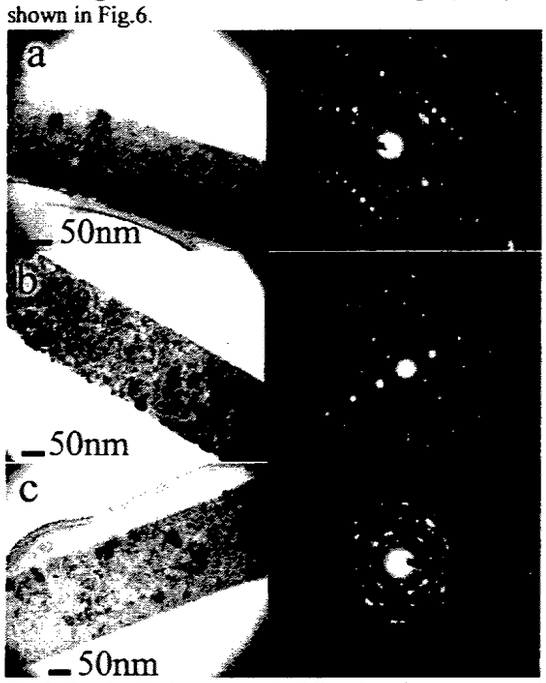

Fig.6. Bright field image and diffraction ring patterns of Co-ITO films deposited at different oxygen pp. a. no oxygen pp, b. 0.19% oxygen pp, c. excess of oxygen pp.

Figure 6a shows the bright-field images and diffraction pattern of Co-ITO films deposited without oxygen. This figure shows both the Co and ITO are in crystalline state. This film consists of large metallic Co grains in the size of 20nm. The distance between grains are narrow without almost no physical spacing. This explains the relative low resistivity and small MR found in this film. However, as increasing the oxygen pp film shows fine Co grains disperses in crystalline ITO matrix in the size of 5 to 15nm, which give rise to the magnetoresistance in this film. From the diffraction pattern as shown in Fig.6b, we could see that both of Co and ITO are in crystalline phases. The increasing resistivity in this film is due to the influence of oxygen pp on the ITO resistivity at crystalline phase. The increasing of oxygen is known to continuously increases the crystalline ITO resistivity. Figure 6c represents the microstructure of Co-ITO film when the excess of oxygen is found in this film. Both ITO and Co are in crystalline phases, however the ITO structure seems to growth in to bigger grain shape as shown in black grain of about 50nm in size .This film has very high resistivity in the order of $10^4 \mu\Omega$cm. The oxidation of Co particles is also considered to enhance the resistivity in this film.

The magnetoresistance that is found in Co-Pt-ITO films has similar tendency to Co-ITO films, only in higher MR ratio value which is observed at optimum oxygen partial pressure at 350℃ annealing temperature. Figure 7 represents the resistivity and MR ratio of Co-Pt-ITO

films as increasing of oxygen pp during deposition. This films are annealed at 350℃ after deposition, where the optimum MR is observed in this film. The electrical resistivity of this film is continuously increases as increasing of oxygen pp. Without oxygen addition the specimen has low MR ratio. The increasing oxygen pp up to 0.19% pp increases the MR ratio, however further increasing oxygen decreases the MR ratio.

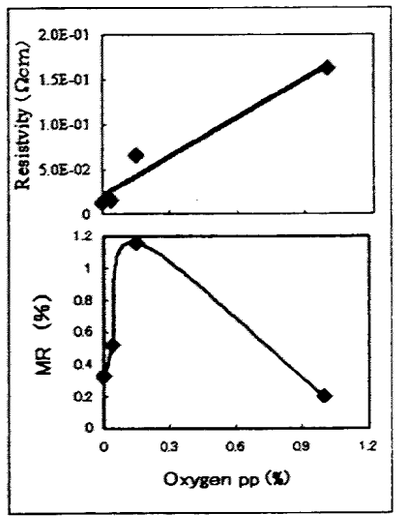

Fig.7.The MR ratio and resistivity of Co-Pt-ITO films as increasing the oxygen pp

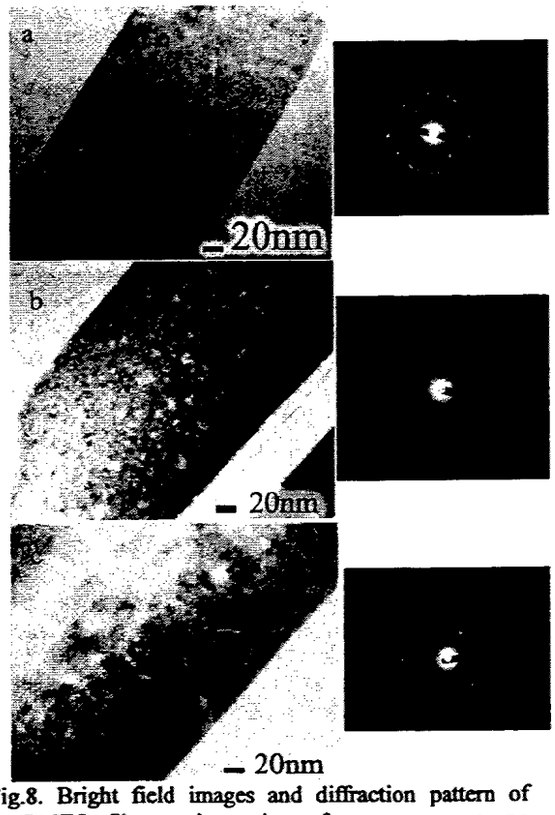

Fig.8. Bright field images and diffraction pattern of Co-Pt-ITO film as increasing of oxygen pp. a. no oxygen, b. 0.19% oxygen, c. excess of oxygen pp.

Figure 8 shows the microstructure of Co-Pt-ITO film as increasing of oxygen partial pressure. The phenomena of MR in this film is simply different compare to the magnetoresistance which is observed in Co-ITO films. Without addition of oxygen, we found fine Co are dispersed in amorphous ITO matrix but the some Co are growth in bigger shape, this probably could explain the relatively small MR in this film. However when oxygen is introduced during deposition, film consists uniform distribution of fine particle metallic Co dispersed homogeneously in amorphous ITO matrix with high resistivity. The average size of fine Co particles are around 5 to 10 nm. The certain additional of oxygen during deposition is found effective to enhance the MR ratio in this film. At higher addition of oxygen, specimen shows white long shape image which separate the magnetic particles. The addition of oxygen is considered to enhance the Indium oxide channel, which separate the grains, decreases the MR in this film. The addition of Pt is believed to stabilize the amorphous state in this film, keeping the ITO structure in amorphous phase.

4. CONCLUSION

The resistivity of ITO films is proved to be very sensitive to the partial pressure of oxygen during deposition. The magnetoresistance increases with the increasing of oxygen partial pressure. However, excess of oxygen decreases the magnetoresistance of such film. On the other hand, the resistivity continuously increases with increasing of oxygen partial pressure, due to the oxidation of Co as shown by XPS analysis. In Co-ITO case, the magnetoresistance appears when both Co and ITO are crystalline. Film shows high resistivity in this film due to the oxygen addition that strongly influence the resistivity in crystalline ITO. In Co-Pt-ITO film, the high magnetoresistance exists in amorphous ITO matrix. The resistivity of this film is relatively high in the order of 10^3-10^4μΩcm, compared to the other metal oxide. The existence of Pt is believed to stabilize the amorphous phase.

5. REFERENCES

[1]M.Ohnuma,K.Hono,H.Onodera,J.Appl.Phys.87,(2) 817 (1999)
[2]A.Milner. A.Gerber, B. Groisman, M.Karpovsky, A.Gladkikh, Physics. Rev. Letter 76,475 (1996)
[3]K.Kamei,M.Yonemura,K.Hanafusa, Journal of Mat. Science: Materials in electronic 12, 569-574 (2000)
[4]M.Ohnuma, K.Hono, E.Abe and H.Onodera, S.Mitani, H.Fujimori, J.Appl.Phys.82,(11)5646 (1997)
[5]Wanti Ekawati, Ji Shi, Yoshio Nakamura, Osamu Nittono, Trans. Magn. Research Soc.Japan 29[4] 1603(2004)

(Received December 24, 2004; Accepted February 28, 2005)

Transactions of the Materials Research Society of Japan 30[4] 1109-1111 (2005)

Perpendicular magnetic anisotropy of Co-Ti-N films

Yuuki Yamamoto, Ji Shi, Yoshio Nakamura
Dept. of Metallurgy and Ceramics Science, Tokyo Inst. Tech., Japan
(Fax: 81-3-5734-3145, e-mail: lestat@mtl.titech.ac.jp)

In recent years, the magnetic nano-granular film is considered promising to be applied as next generation magnetic recording media. In this work, we have investigated the magnetic property and microstructure of Co-Ti-N nano-granular films using VSM, XRD and TEM. The precursor films have been deposited on fused quartz substrates at room temperature by DC reactive sputtering with N_2 as reactant gas.
The as-deposited films are amorphous-like state by XRD results, and the formation of (FCC) Co and TiN crystallites have been confirmed by electron diffraction when the films were thermally annealed at temperatures above 600°C.
It have been confirmed by VSM measurement that the films annealed at appropriate temperatures have perpendicular magnetic anisotropy, which is due to the unique microstructure of the films. TEM observation of the films reveals that such films are featured with columnar structure with the nano-sized fibers which are perpendicular direction to the substrate surface. The fibers are composed of Co and TiN crystallites, and Co nano-fibers are separated by TiN.
Therefore we have concluded that Co crystallites are magnetically coupled more closely in a perpendicular direction than in a in-plane direction and thus perpendicular anisotropy is developed.

Key words: perpendicular anisotropy, shape anisotropy, columnar structure, granular film

1. INTRODUCTION

Magnetic films for perpendicular magnetic recording media has been studied extensively in recent years. Generally, perpendicular magnetic anisotropy of thin film is obtained through utilizing the magnetocrystalline anisotropy of magnetic materials, such as employing magnetic materials with $L1_0$ magnetic particles dispersed in nonmagnetic matrices(e.g. CoPt/Ag, CoPt/C, CoPt/SiO_2, CoPt/Al_2O_3)[1-5]. However in such a case, control of preferred orientation or even epitaxial growth of the film is necessary. This increases the complexity of the film growth process. For the arising problem mentioned above, instead of a method utilizing $L1_0$, we suggest a simple method to obtain films with perpendicular magnetic anisotropy, which utilizes the columnar structure of a magnetic - nonmagnetic granular film. The role of non-magnetic is to decouple magnetic interaction in an in-plane direction.

Our recent investigations demonstrated that magnetic - nonmagnetic granular films of (FCC) CoPt-TiN reveal perpendicular magnetic anisotropy due to shape anisotropy of columnar structure. This columnar structure of the films is formed by shadowing effect during sputtering at comparatively high working pressure[6,7]. The relative proportion of Co, Pt and Ti was 3:1:1 at that experiment. Namely, the relative proportion of magnetic and nonmagnetic was 4:1.

It is thought that this content of Ti as nonmagnetic matter is not enough to decouple magnetic interaction of FCC-CoPt in an in-plane direction.

In order to enhance perpendicular magnetic anisotropy of FCC-Co based magnetic-nonmagnetic granular films, we have decided optimal content of Ti as nonmagnetic matter to decouple magnetic interaction in an in-plane direction and optimal film thickness to exert its magnetic performance. VSM measurement, ICP-OES analysis and TEM observation have been conducted and the results have clarified the relation between Ti content of the films and perpendicular magnetic anisotropy.

2. EXEPERIMENTAL

Co-Ti-N films were deposited onto fused quartz substrates by non-magnetron DC reactive sputtering with pure Ar as sputtering gas and N_2 as reactant gas. The sputter-target consists of a pure Co disc at the back, Ti sheets and a donut-shape Ti disc at the front. The control of Ti composition was done with changing the number of Ti sheets.

The composition of the film could were controlled by changing the number and size of Ti sheets at the front. The vacuum chamber was evacuated under 2.0×10^{-5} Pa before depositions. Then Co-Ti-N films were prepared in Ar + N_2 atmosphere, where partial pressure of N_2 gas was set to 2.4×10^{-3} Pa, and total pressure of Ar + N_2 gas was set to 7.5×10^{-2} Pa. The working (sputtering) gas pressure was about 10 Pa. All the depositions were conducted at the room temperature. The cathode voltage and discharge current were 2.5kV and 12mA respectively. After deposition without breaking vacuum, thermal annealing of the films were conducted in a same chamber at 800°C for 180 min.

The composition of the films was analyzed by inductively coupled plasma optical emission spectroscopy(ICP-OES). The magnetic properties, including in-plane and perpendicular saturation magnetization(4πMs), coercivity(Hc) and squareness ratio(Rs=Mr/Ms) were measured by vibrating sample

magnetometer(VSM). X-ray diffractometer(XRD) was used to evaluate the crystal state. And the nano-structure of the films was characterized by transmission electron microscopy(TEM).

3. RESULTS AND DISCUSSION

3.1 magnetic properties measured by VSM

The dependence of in-plane and perpendicular magnetic properties on Ti content has been studied. Fig. 1 shows transition of M-H loop of Co-TiN film annealed at 800°C in a vacuum for 180min after deposition with increasing Ti content. In fig.2-a, the values of Hc are sorted out in order to make a clear understanding of the dependence of magnetic properties on Ti content. As increasing Ti content, the values of Hc of the films rise up, and the values are larger in a perpendicular direction than in an in-plane direction until relative atomic ratio of Ti and Co becomes 2.3:1. Further increasing Ti content over the ratio of 3:1, the values of Hc in a perpendicular direction are almost same with the values in an in-plane direction. The values of Rs are also sorted out in fig.2-b. The values of Rs of the films rise up as well, and the values are larger in a perpendicular direction than in an in-plane direction until relative atomic ratio of Ti and Co becomes 3:1. Further increasing Ti content, the values of Rs in a perpendicular are almost same with the values of in an in-plane direction. By the way, we regard the differences of the value of Hc and Rs between in-plane direction and perpendicular direction as an empirical indicator of magnetic anisotropy, and the difference of the value between in-plane and perpendicular becomes maximum at the ratio of 3:1. From this viewpoint, the films in this system have the best perpendicular magnetic anisotropy at the atomic ratio of Ti:Co=3:1

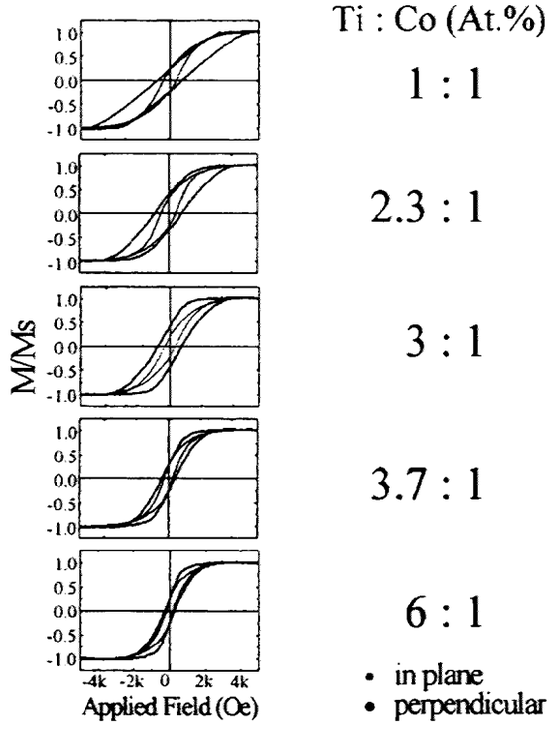

Fig. 1. Transition of M-H loop of Co-TiN film with increasing Ti content.

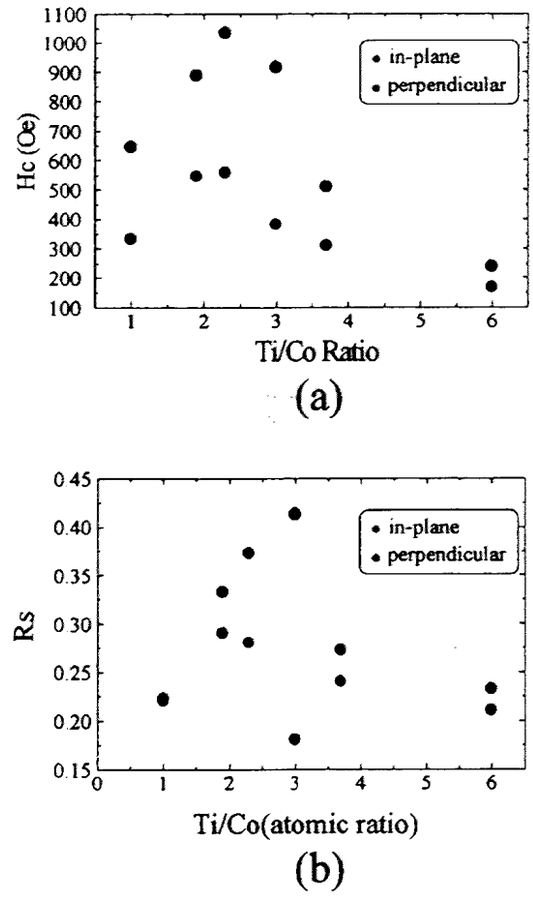

Fig. 2. Dependence of magnetic property on Ti content. **a.** Relation between Ti content and Hc, **b.** Relation between Ti content and Rs.

The dependence of magnetic properties in terms of a film thickness has also been investigated. Fig.3 shows dependence of magnetic properties on film thickness. Film thickness was controlled by deposition time, which is about 2nm/min.

Fig.3-a indicates that both direction(in-plane and perpendicular) of Hc become large with deposition time until 80min. We can see that the film deposited for 80min has a peak value of Hc. Deposition time being longer than 80min, the values of Hc become lower gradually. Tendency of in-plane and perpendicular Hc resembles each other.

The relation between deposition time and Rs appears in fig.3-b. The value of Rs in a perpendicular direction increases with deposition time and have its peak at deposition time 70min and then Rs value decreases by degrees. On the other hand, Rs value in an in-plane direction decreases modestly. As well as the case of fig.2, we have estimated the differences of the values between in-plane direction and perpendicular direction as an empirical degree of magnetic anisotropy. Accordingly, the film which was deposited for 70min has best perpendicular anisotropy in this system.

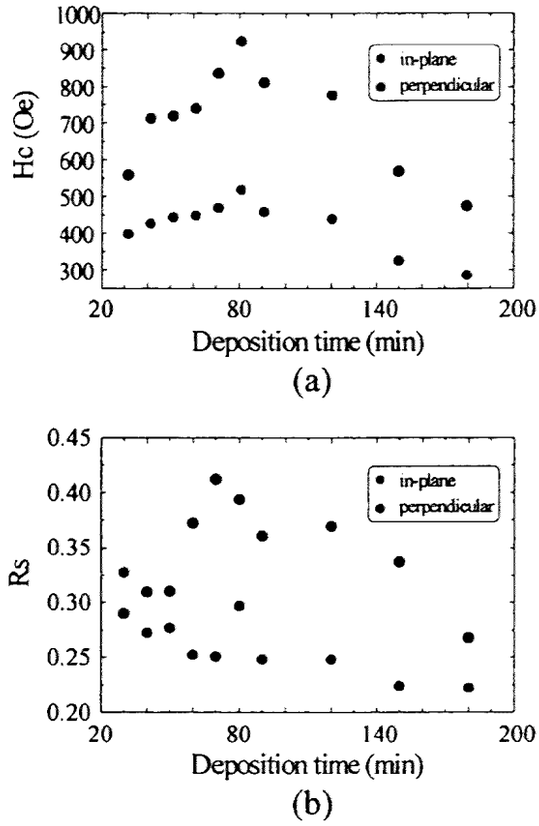

Fig. 3. Dependence of magnetic property on film deposition time(film thickness). **a.** Relation between deposition time and Hc, **b.** Relation between deposition time and Rs.

3.2 Nano-structure by TEM image

To clarify magnetic performance of the films stated above in terms of nano-structure, we carried out XRD analysis and TEM observation.

Crystal structure of films couldn't be evaluated by XRD, for the reason of its smallness of particles which constitute the film.

Cross-sectional HREM image of Co-based magnetic–nonmagnetic granular film appears in fig.4. In the first place, we can interpret perpendicular anisotropy of the film derives from fibrous Co particles(high contrast parts) which induce shape anisotropy as shown in fig.4.

By the optimization of Ti content(Ti:Co=3:1) in the film, in-plane interaction of Co fibers reduces. With excess of Ti content, magnetic interaction is decoupled not only in an in-plane direction, but in a perpendicular direction.

With increasing film thickness, aspect ratio which decides shape anisotropy of Co fibers also increases and then perpendicular anisotropy is enhanced until about 140nm in film thickness. As film thickness becomes over 140nm, Co fibers can't extend in perpendicular direction any more so that aspect ratio of the fibers can't become high.

Thus magnetic performance of films in this experiment has been correlated with film nano-structure.

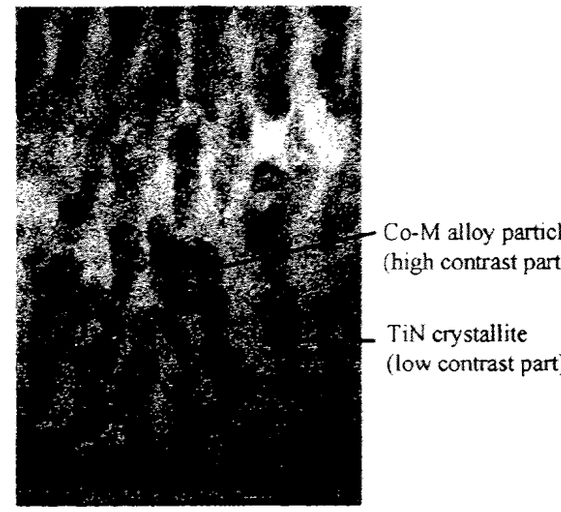

Fig. 4. Cross-sectional HREM image of Co-based magnetic-nonmagnetic granular film

4. CONCLUSIONS

Successfully, Co-TiN granular films which indicate stronger magnetic anisotropy in perpendicular direction than in an in-plane direction have been prepared. It has been figured out that the optimum atomic ratio of Ti and Co is 3:1 and optimal film thickness for this system is about 140nm. The films with such composition and thickness show the best perpendicular magnetic anisotropy.

5. REFERENCES

[1] S. Stavroyiannis, I. Panagiotopoulos, D. Niarchos, J. A. Chistodoulides, Y. Zhang, and G. C.Hadjipanayis, *J. Appl. Phys. Lett.*, **73**, 3453 (1998).
[2] S. Stavroyiannis, I. Panagiotopoulos, D. Niarchos, J. A. Chistodoulides, and G. C.Hadjipanayis, *J. Magn. Magn. Mater.*, **93**, 18 (1999).
[3] M. Yu, Y. Liu, A. Moser, D. Weller, and D. J. Sellmyer, *J. Appl. Phys. Lett.*,**73**, 3592 (1999).
[4] C. Chen, O. Kitakami, S. Okamoto, Y. Shimada, K. Shibata, and M. Tanaka, *IEEE Trans. Magn.*, **35**, 3466 (1999).
[5] K Ichihara, A. Kikitsu, K. Yusu, F. Nakamura, and H. Ogiwara, *IEEE Trans. Magn.*,**34**, 1603 (1998).
[6] J. A. Thornton, *J. Vac. Sci. T.*, **11**, 666 (1974).
[7] J. A. Thornton, *J. Vac. Sci. T.*, **A4** (6), 3059 (1986).

(Received December 24, 2004; Accepted August 19, 2005)

Transactions of the Materials Research Society of Japan 30[4] 1203-1205 (2005)

Perpendicular magnetic anisotropy of CoPt/AlN multilayer

Y. Hodumi, M. Uyama, J. Shi and Y. Nakamura
Department of Metallurgy and Ceramics Science, Tokyo Institute of Technology. Meguro-ku Oookayama 2-12-1
E-mail: hodumi@mtl.titech.ac.jp

CoPt/AlN multilayer films have been prepared by a two-facing-target magnetron sputtering apparatus at room temperature. The thickness of AlN layer was fixed to 20nm, and the thickness of CoPt layer was varied from 1 to 8 nm. It is found that all as-deposited film show in-plane magnetic anisotropy. After vacuum annealing at 400 °C for 3h, CoPt/AlN films with CoPt thickness below 4nm show perpendicular magnetic anisotropy. Among these annealed films, the one with CoPt thickness of 2nm exhibits clearly uniaxial magnetic anisotropy. Cross-section TEM observation has proved that the CoPt layers have {111} preferred orientation, while the AlN layers have (001) preferred orientation. We believe that for the CoPt/AlN multilayer film to show perpendicular magnetic anisotropy, it is important that the CoPt layers are coherent with the neighboring AlN layers.
Key words: perpendicular magnetic anisotropy, inverse magnetostriction, TEM

1. INTRODUCTION

In order to increase the areal density of recording media to the order of 100 Gbit/in^2, the size of recording bit must be smaller than 10 nm[1]. However, such a small dimension of magnetically decoupled ferromagnetic particles would make the media thermally unstable. In order to overcome this problem, it is necessary to use a ferromagnetic phase with a large perpendicular magnetic anisotropy. Therefore, perpendicular magnetic anisotropy make use of magnetocrystalline anisotropy and interface magnetic anisotropy was studied[2-4].

CoPt/AlN multilayer films have been grown by a sputter-deposition method in order to study the CoPt order transition in such layered-structure. However, it is interesting to find that CoPt/AlN multilayer films deposited at room temperature show strong preferred orientation with CoPt(111) // AlN(001). And the magnetic properties of this structure changed significantly after annealing. Before the annealing, the easy axis of magnetization of this structure is in the film plane. However, the easy axis takes the normal direction after the annealing, indicating perpendicular magnetic anisotropy was developed[5-6].

In the past, the effect of magnetic layer thickness on the magnetic properties has not been reported. Additionally, it is important to find out the most suitable thickness of both AlN and CoPt. In this paper, We examine how magnetic properties are affected by CoPt layer thickness, and explain the mechanism which induces perpendicular magnetic anisotropy.

2. EXPERIMENTAL

CoPt/AlN multilayer films were prepared on fused quartz glass at room temperature by two-facing-target DC magnetron sputtering. The base pressure of chamber was less than 10^{-4} Pa. The chamber pressure was 0.2 Pa during sputtering. The gas was a mixture of Ar and N_2. The ratio of Ar to N_2 was 7:3, which was controlled by mass flow controller. The sputtering apparatus has two sets of targets in the same chamber. One set of the targets consists of Co and Pt disks to produce the Co-Pt layer. And the other one set consists of two Al disks to produce AlN layers by reactive sputtering with N_2 gas. A discharge current of 80 mA and a voltage of 900 V yield a coating rate of 0.085nm/sec for CoPt,and a discharge current of 200 mA and a voltage of 400 V yield a coating rate of 0.098nm/sec for AlN. Substrate holder was placed on the center of a vacuum chamber, and the rotation of a holder was controlled by a preset computer program (hyper terminal) to produce different layer thickness which is a parameter of this experiment. The thickness of AlN layers was kept at 20nm. The rotation was repeated five times. Finally, AlN layer (20 nm) was deposited as a capping layer. After deposition, the samples were annealed in a vacuum. Annealing temperature and duration are 400 °C and 3 hours, respectively. Then the sample was cooled in the vacuum to room temperature. The structure of the films was examined by the X-ray diffraction (XRD) and transmission electron microscope (TEM) observation. The magnetic properties of the films were examined by a vibrating sample magnetometer (VSM).

3. RESULT AND DISCUSSION

1. *Structure of the film*

Fig. 1 shows X-ray diffraction profiles of CoPt/AlN multilayer films with different CoPt layer thickness. Fig. 1 (a) shows the results of as-deposited film, and Fig. 1 (b) shows those of annealed film. All CoPt/AlN multilayer show that AlN layers have (001) preferred orientation and CoPt layer have (111) preferred orientation. CoPt layer is fcc structure and AlN layer is hcp structure. In addition, the intensity of AlN (001) and CoPt (111) peaks becomes stronger with

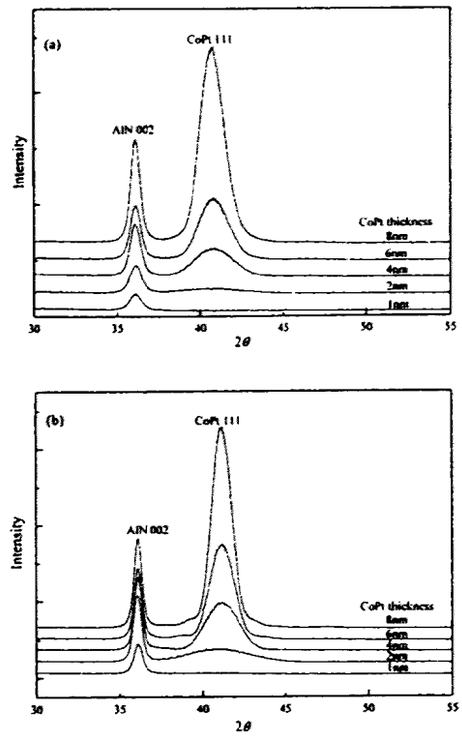

Fig.1. X-ray diffraction profiles of CoPt/AlN films with different CoPt layer thickness; es, (a) as-deposited and (b) annealed at 400℃ for 3 hours

increasing thickness of CoPt. On the other hand, the peak positions of AlN (001) and CoPt (111) reflections do not depend on CoPt thickness. Furthermore, the peak position of AlN $(001)_{hcp}$ reflection was not affected by annealing. However, the CoPt (111) reflection shifts toward higher angle after annealing. This fact indicates that gas atoms incorporated into multilayer film during deposition have been released from the film, which caused the CoPt lattice to shrink. It is considered that the shrinkage of CoPt lattice is mainly in the perpendicular direction, because the shrinkage in the in-plane directions was hindered by interface restriction. Therefore, a tensile stress was introduced into the CoPt layers. As a result, perpendicular magnetic anisotropy was caused by inverse magnetostriction.

Fig. 2 shows bight filed images from Cross-section transmission electron microscope observation. Fig. 2 (a), (b) and (c) correspond CoPt thickness of 1 nm, 2 nm and 8 nm respectively. When thickness of CoPt is 1 nm, interfaces between CoPt and AlN layers are rough. However, when the thickness of CoPt is 2 nm and the 8 nm, interfaces are flat. From this result and the result of X-ray diffraction, it is seen that the AlN layer surface becomes slightly rough at the thickness of 20 nm. The growth of subsequent CoPt layer may regain the flatness of the growing surface. For this purpose, the minimum thickness of CoPt layer required to 2nm. Also the preferred orientation of both AlN and CoPt layers are enhanced by alternate growth.

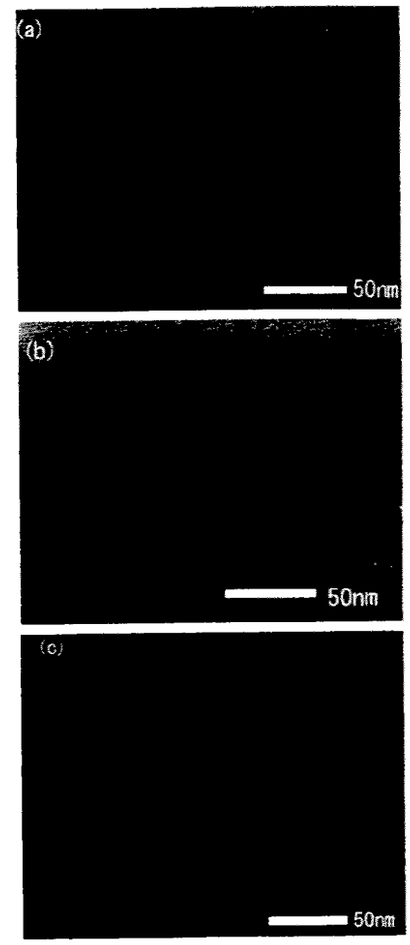

Fig.2. Cross-section TEM bright field image from annealed CoPt/AlN multilayer; thickness of CoPt layer is (a) 1 nm, (b) 2nm, (c) 8nm.

II .*Magnetic properties*

All as-deposited CoPt/AlN multilayer films exhibit in-plane easy magnetization axises. Fig. 3 shows M-H loops of annealed CoPt/AlN multilayer films with CoPt layer thickness varied between 1 nm and 8 nm. Axis of easy magnetization takes vertical direction as thickness of CoPt layer becomes thin. It is argued that the reason of this perpendicular anisotropy is the elastic stress brought into the CoPt layers by interface restriction. For this reason, too thick CoPt layers spoil perpendicular magnetic anisotropy, because relaxation occurred. However, the CoPt/AlN film with a CoPt layer thickness of 1 nm shows poor perpendicular anisotropy as shown in Fig. 3 (a). This is originated from the relative rough interfaces between AlN and CoPt layers as described above, because the rough interfaces result in poor preferred orientation of both AlN and CoPt layers and poor coherent at AlN-CoPt interfaces.

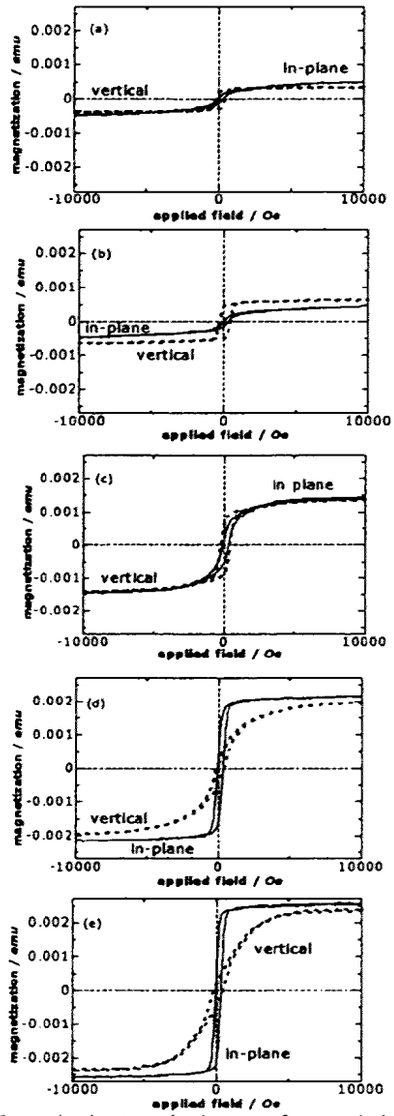

Fig.3. Magnetic hysteresis loops of annealed CoPt/AlN multilayer films; thickness of CoPt layer is (a) 1 nm, (b) 2 nm, (c) 4 nm, (d) 6 nm and (e) 8 nm.

4. CONCLUSION

We investigated the perpendicular magnetic anisotropy in annealed CoPt/AlN multilayer films and found the followings. The surface of AlN layer become rough at a thickness of 20 nm. While the subsequent CoPt layer can restore a flat surface provided the thickness of CoPt layer is 2 nm and above. The CoPt/AlN multilayer films grown in this manner are highly orientated. The preferred orientation of CoPt layer is (111) and that of AlN layer is (001). The CoPt/AlN multilayer films with suitable CoPt layer thickness exhibit, strong perpendicular magnetic anisotropy which is caused by tensile stress in the CoPt layers.

5. REFEENCES

[1] Y. K. Takahashi M. Ohnuma and K. Hono, J. J. Appl. Phys., 40, 1367-1369 (2001)

[2] V. Georgescu V. Mazur and B. Pushcashu, Mat. Sci. Eng. B68, 131-137 (2000).

[3] S.Hasimoto Y.ochiai and,K.Aso, J. Appl. Phys., 66, 4909-4916 (1989)

[4] Jun Wu Yunkun Pan Liangwei Chen Yongli Zhang Run Wu Changsheng Xie and Aihua Wang., Surface and Coatings Thechnology. 176, 357-364 (2004)

[5] Y. Kato *Dept. Metallurgy, Tokyo Institute of Technology*: Master's Thesis (2003)

[6] M. Uyama *Dept. Metallurgy, Tokyo Institute of Technology*: Bachelor's Thesis (2003)

(Received December 24, 2004; Accepted June 30, 2005)

Appl. Phys. A 80, 179–182 (2005)
DOI: 10.1007/s00339-003-2448-2

Applied Physics A
Materials Science & Processing

R. ZHOU[1]
C.C. CHEN[1]
M. HASHIMOTO[1,✉]
J. SHI[2]
Y. NAKAMURA[2]

Characterization of the interfacial reaction between sputter-deposited Ni film and Si substrate

[1] Department of Applied Physics and Chemistry, University of Electro-Communications, Chofu, Chofugaoka 1-5-1, Tokyo 182-8585, Japan
[2] Department of Metallurgy and Ceramics Science, Tokyo Institute of Technology, Meguro-ku 2-12-1, Tokyo 152-8552, Japan

Received: 20 October 2003/Accepted: 27 October 2003
Published online: 21 January 2004 • © Springer-Verlag 2004

ABSTRACT In the present work, we report the interfacial reaction characteristics between sputter-deposited Ni film and a single crystalline Si substrate. The effect of substrate bias during the deposition process on the interfacial reaction is also discussed. It was found that sputter deposition with a substrate bias can promote the interfacial reaction between Ni film and Si substrate. Under our experimental conditions, Ni_2Si (orthorhombic) with good crystallinity formed in the film when it was deposited at 200 °C and with a −80 V substrate bias. Such films had relatively low resistivity. Upon thermal annealing at 500 °C, NiSi formed through further reaction, however there is almost no change in resistivity.

PACS 67.57.Np; 68.55.-a; 68.35.Fx

1 Introduction

Metal silicides grown on a Si substrate are used as low-resistivity interconnects and contact materials in microelectronic applications [1–3]. This has expedited the investigation of interface reaction between metal films and Si substrate, and of the formation process of silicides. Among those metals, Ni and Co have been mostly studied because of the fact that Ni di-silicide ($NiSi_2$) and Co di-silicide ($CoSi_2$) have a similar crystal structure with Si (CaF_2 type), and the lattice mismatches of such silicides with Si are very small, 0.46% and 1.2% respectively at room temperature, and that therefore such silicides can be grown epitaxially on Si substrates [4–10]. Up to now, most of the metal films, such as Ni films, have been prepared by an evaporation method. In our previous work, we have found that sputter deposition with a substrate bias can tailor the films crystallinity quite well [11–13]. In the present work, we investigate the characteristics of interfacial reaction between sputter-deposited Ni film and a single crystalline Si substrate, and the results are discussed in comparison with those for evaporated Ni films.

2 Experimental procedure

Ni films were deposited onto Si(100) substrate by dc sputtering method. Pure Ni (99.99%) plate was used as the target and Ar gas was used as the sputtering gas. Prior to depositions, Si substrates were etched in hydrofluoric acid in order to remove the natural surface oxide. Then, after being dried, they were loaded into the vacuum chamber immediately. A turbo-molecular pump backed up with a mechanical rotary pump evacuated the vacuum chamber. In addition, a cylindrical liquid nitrogen trap is set around the target and substrate holder, and was filled with liquid nitrogen during deposition processes. Base pressures of less than 1×10^{-4} Pa were obtained before depositions, and the Ar pressure was 5 Pa during deposition. The substrate bias was either 0 V or −80 V during deposition. The substrate temperatures were either room temperature or 200 °C. Thermal anneals were conducted in a vacuum, and at 500 °C for 30 min. The electrical properties were measured by four-probe method. The as-deposited and annealed films were characterized by X-ray diffraction (XRD), cross-sectional transmission electron microscopy (XTEM), and X-ray photoelectron spectroscopy (XPS).

3 Results and discussions

Figure 1 shows the XRD results of Ni films on Si(100) substrate deposited at room temperature. Peaks from metallic Ni can be observed on the profiles of both the unbiased and biased films. It should be noted that the intensity of the Ni111 peak for the biased film is much stronger than that for the unbiased film. In addition, a Ni200 peak is observed for the biased film but not for the unbiased film. These results suggest that biased film is of much better crystallinity compared with the unbiased film, indicating that the crystallinity of Ni films on Si substrate can be greatly improved by applying a substrate bias during sputter deposition. It is known that by applying a small negative bias voltage to the substrate during sputter deposition, low energy ions and neutrals bombard the surface of the growing film. This phenomenon will not only enhance the surface diffusivity of adatoms, but also remove impurity atoms from the growing surface, and thus improving the crystallinity of the growing film [14, 15]. The XRD results of the films deposited at 200 °C are shown in Fig. 2. The intensity of Ni peaks decreases significantly for both unbiased and biased films compared with that of Ni films deposited at room temperature. Furthermore, some small peaks are observed for both unbiased and biased films,

✉ Fax: +81-424/43-5461, E-mail: mituru@pc.uec.ac.jp

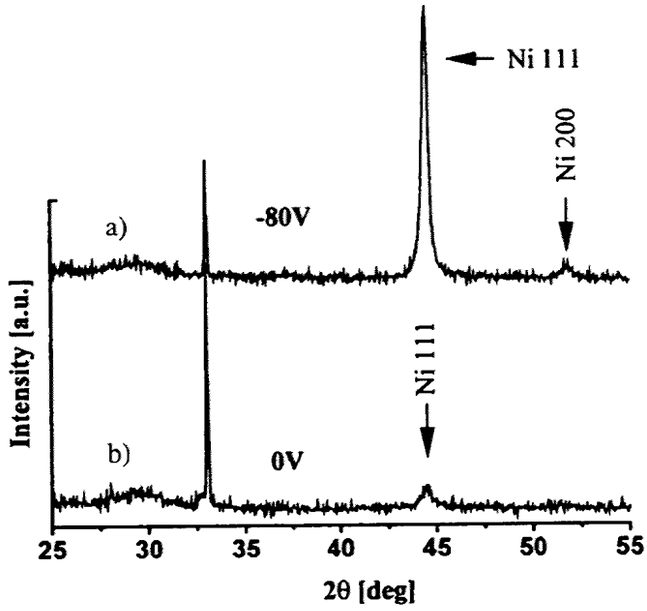

FIGURE 1 The XRD profiles of the Ni films on Si(100) substrate deposited at room temperature. (a) unbiased, (b) biased with $Vs = -80$ V. The peak at 33° is due to Si substrate, the same situation can also be seen for Figs. 2 and 4

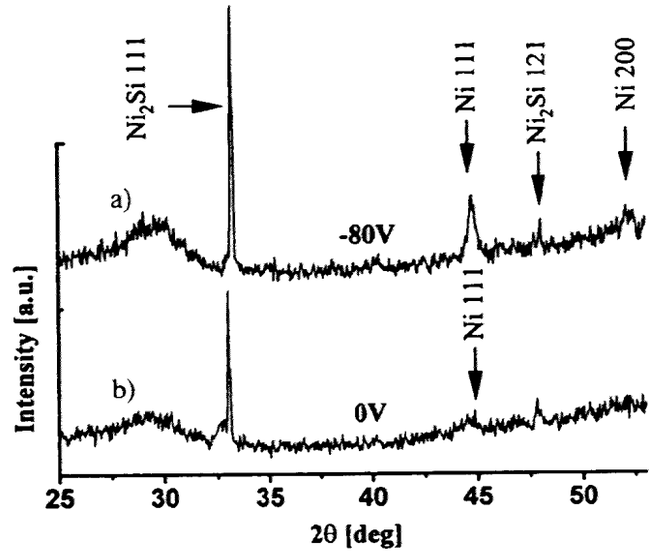

FIGURE 2 The XRD profiles of the Ni films on Si(100) substrate deposited at 200 °C. (a) unbiased, (b) biased with $Vs = -80$ V

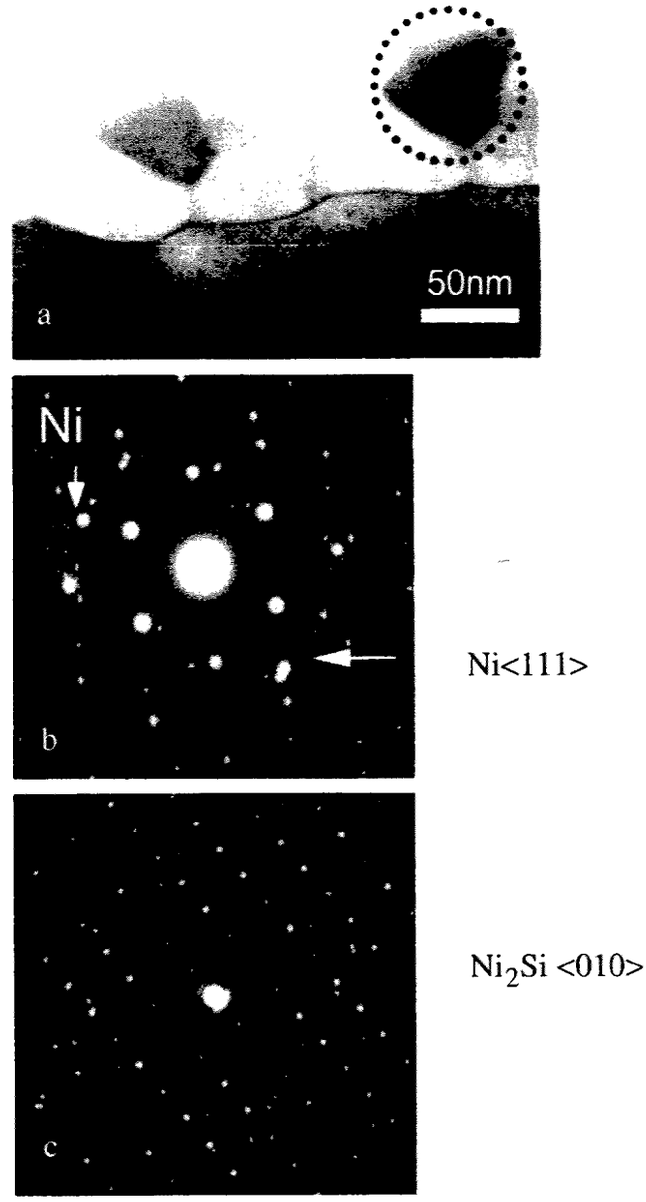

FIGURE 3 XTEM image and selected area diffraction patterns of a Ni film on Si(100) substrate deposited at 200 °C with $Vs = -80$ V

which can be indexed as the reflections from Ni_2Si with orthorhombic structure. Therefore, we consider that the Ni partially reacted with Si substrates during the deposition processes. In order to confirm the formation of the Ni silicide in the films, XTEM observation of the samples deposited at 200 °C was conducted. Figure 3 shows the electron micrograph and electron diffraction patterns of the biased film deposited at 200 °C. It can be seen from the bright field image (Fig. 3a) that the film is composed of randomly orientated large grains. In addition, the interface between the film and Si substrate is curved, implying a reaction between the film and the substrate. Figure 3b shows the selected area diffraction pattern taken from a large area that includes both films and substrate with the beam incident along the ⟨110⟩ direction of the Si substrate. A weak ring can be seen on the diffraction pattern which is the 111 reflection of Ni, and in addition, some strong spots due to Ni (indicated by an arrow) are also seen on the ring. This indicates that some large Ni grains exist in the film, and it seems that such Ni grains do not have a specific crystallographic relationship with the Si substrate. On the other hand, some of the spots in the diffraction pattern could not be indexed as the diffraction spots from Ni. Figure 3c shows a diffraction pattern taken from a single grain that is indicated by a circle in the figure. This diffraction pattern can be indexed as one from Ni_2Si with incident beam along the ⟨010⟩ direction. This result indicates that large grains of Ni_2Si are formed in the film, and is in accordance with that of XRD.

As previously reported, Ni silicides were generally formed by the evaporation of Ni onto a clean Si substrate, followed by thermal annealing. In such a process, the reaction prod-

uct between Ni film and Si substrate is Ni_2Si at temperatures lower than 250 °C, and Ni is the dominant diffusing species during the reaction [16, 17]. It is known that the energy required to break a Si covalent bond at a low-index surface is of the order of 3 eV. Therefore it is energetically unfavorable for Si atoms to initiate compound formation at 200 °C [18]. In the case of evaporation deposition, low-temperature silicide formation is initiated by Ni atoms diffusion into the Si lattice as interstitial defects, and thus to weaken the bond of Si [18, 19]. In this sense, sputter-deposition is favorable to the formation of silicide because metal atoms reach the substrate surface with higher kinetic energy than those in the case of evaporation deposition. This is especially true when a negative bias is applied to the substrate, because in this situation not only constituent metal atoms but also some Ar ions will bombard the substrate surface with relatively high kinetic energy. Such processes will help metal atoms diffuse into the lattice of Si and break the bond of Si atoms. The detailed reaction mechanism under such conditions is still under investigation.

Figure 4 shows the XRD results of both unbiased and biased films deposited at 200 °C and followed by thermal annealing at 500 °C for 30 min. After the thermal annealing, strong peaks which are indexed as the 011 reflection from NiSi are observed on the XRD profiles, meanwhile the peaks due to metallic Ni disappeared, indicating that both the Ni and Ni_2Si transformed into NiSi. The crystal structure of the NiSi is also orthorhombic. In addition, the NiSi shows a strong (011) preferred orientation on Si(100) surface. Here the reaction product is different from that of the evaporation and thermal annealing process; for such a process, the reaction product is $NiSi_2$ at temperatures around 500 °C [20, 21]. The formation of NiSi is further confirmed by TEM observation. Figure 5 shows the electron micrograph and electron diffraction pattern of the biased film annealed at 500 °C. The diffraction

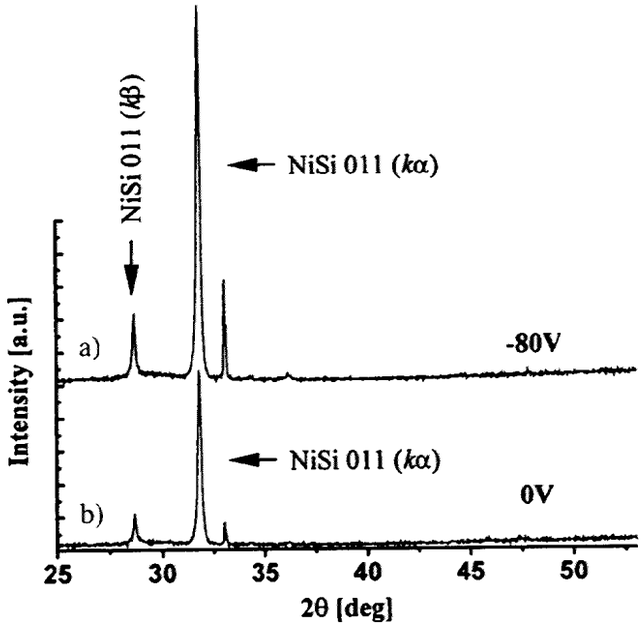

FIGURE 4 The XRD profiles of the annealed Ni films on Si(100) substrate. The films were originally deposited at 200 °C with $Vs = 0$ V (a), -80 V (b). Annealing temperature was 500 °C

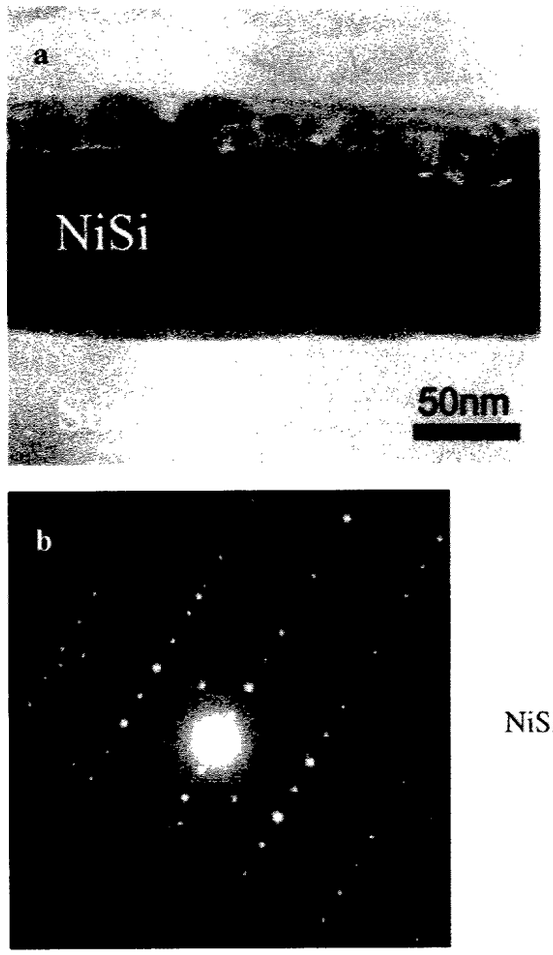

FIGURE 5 XTEM image and selected area diffraction patterns of a biased film annealed at 500 °C

pattern can be indexed as one from NiSi with incident beam along the ⟨120⟩ direction. Furthermore the NiSi is of good crystallinity as can be seen from the bright field image.

Figure 6 shows the electrical measurement results of the as-deposited (at 200 °C), and the films annealed at 500 °C. According to this figure, all the films show metallic behavior, i.e. the resistivity of the films increases with increasing temperature. For the unbiased film (Fig. 6a), the resistivity decreases substantially after thermal annealing. This can be ascribed to the formation of NiSi and to the improvement of the crystallinity of the film. Furthermore, comparing the unbiased films with the biased ones, one can see that in the as-deposited state, the biased film has lower resistivity, the same level as that of the annealed unbiased film. This result indicates that substrate bias can effectively improve the resistivity of the film through the promotion of silicide formation with good crystallinity. However, there is no further obvious change in the resistivity after annealing for the biased film (Fig. 6b).

4 Conclusions

Our results indicate that sputtering deposition of Ni film onto the Si substrate, especially with a negative substrate bias effectively promotes the interfacial reaction. Large grains of Ni_2Si are readily formed when Ni was deposited onto Si

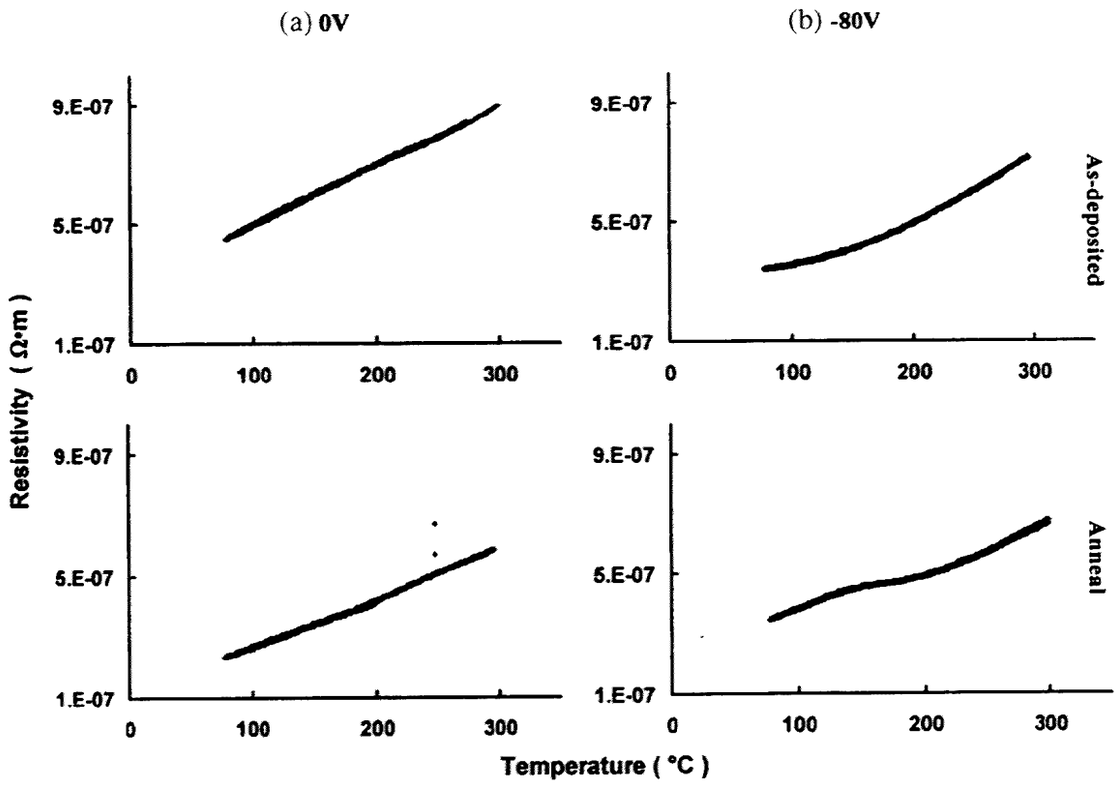

FIGURE 6 Electrical measurement results for both the unbiased and biased films

substrate at 200 °C. Such films feature relative low resistivity, and there is no further increase in the resistivity after annealing at 500 °C.

ACKNOWLEDGEMENTS The authors thank Prof. Q. Hong and Dr. G.H. Zhang of the University of Science and Technology Beijing for their technical support on the measurement of electrical properties. This work was partly supported by the Hungarian National Science Foundation under Contract No. JAP-26/00.

REFERENCES

1 S. Furukawa, H. Ishiwara: Jpn. J. Appl. Phys. **22** 21, Suppl. 1 (1983)
2 S.P. Murark: J. Vacuum Sci. Technol. B **4**, 1325 (1986)
3 H. von Kaneal: Mater. Sci. Rep. **8**, 193 (1992)
4 F.M. D'Heurle: J. Mater. Res. **3**, 167 (1988)
5 F.M. D'Heurle, C.S. Petersson: Thin Solid Films **128**, 283 (1985)
6 L. Van den hove, R. Wolters, K. Maex, R. De Keersmaeker, G. Declerck: J. Vacuum Sci. Technol. B **4**, 1358 (1986)
7 R.T. Tung: Appl. Phys. Lett. **68**, 3461 (1996)
8 H.S. Rhee, B.T. Ahn: Appl. Phys. Lett. **74**, 3176 (1999)
9 C. Detavernier, R.L. Van Meirhaeghe, F. Cardon, K. Maex, H. Bender, B. Brijs, W. Vandervorst: J. Appl. Phys. **89**, 2146 (2001)
10 J. Shi, T. Irie, F. Takahashi, M. Hashimoto: Thin Solid Films **375**, 37 (2000)
11 T. Shinmitsu, J. Shi, M. Hashimoto: Surf. Coat. Technol. **151/152**, 55 (2002)
12 J. Shi, D. Kojima, M. Hashimoto: J Appl. Phys. **88**, 1679 (2000)
13 J. Shi, R. Zhou, M. Hashimoto: J. Vacuum Sci. Technol. **A19**, 2979 (2001)
14 M. Ohring: *The Materials Science of Thin Films* (Academic Press, San Diego, 1991) pp.129–131
15 Chapman: *Glow Discharge Processes* (Wiley, New York 1980) pp. 215–237
16 H. Foll, P.S. Ho, K.N. Tu, Phil. Mag. A **45**, 31 (1982)
17 F. d'Heurle, C.S. Petersson, J.E.E. Baglin, S.J. La Placa, C.Y. Wong: J. Appl. Phys. **55**, 4208 (1984)
18 Y-J Chang, J.L. Eriskine: Phys. Rev. B **26**, 4766 (1982)
19 A. Hiraki: Surf. Sci. **168**, 74 (1986)
20 L.R. Zhengm L.S. Hung, J.W. Mayer: Mater. Res. Soc. Symp. Proc. **54**, 45 (1986)
21 F. d'Heurle, C.S. Petersson, L. Stolt, B. Stritzker: J. Appl. Phys. **53**, 5678 (1982)

Available online at www.sciencedirect.com

SCIENCE DIRECT

Thin Solid Films 485 (2005) 235 – 240

www.elsevier.com/locate/tsf

Epitaxial growth of Ni films by radio frequency sputtering on GaAs(001) with a TiN buffer

Kenji Makihara[a,*], Arpad Barna[b], Mituru Hashimoto[c], Ji Shi[d], Susumu Maruyama[a]

[a]*Department of Electronics, Tokyo University of Technology, 1404-1 Katakura, Hachioji, Tokyo 192-0982, Japan*
[b]*Research Institute for Technical Physics and Materials Science of Hungarian Academy of Sciences, P.O.B.49, H-1525 Budapest, Hungary*
[c]*Department of Applied Physics and Chemistry, University of Eelectro-Communications, 1-5-1 Chofugaoka, Chofu, Tokyo 182-8585, Japan*
[d]*Faculty of Engineering, Tokyo Institute of Technology, 2-12-1 Ookayama, Meguro, Tokyo 226-8552, Japan*

Received 22 January 2004; received in revised form 3 March 2005; accepted 3 March 2005
Available online 23 May 2005

Available online at www.sciencedirect.com

SCIENCE DIRECT

Thin Solid Films 485 (2005) 235 – 240

www.elsevier.com/locate/tsf

Epitaxial growth of Ni films by radio frequency sputtering on GaAs(001) with a TiN buffer

Kenji Makihara[a,*], Arpad Barna[b], Mituru Hashimoto[c], Ji Shi[d], Susumu Maruyama[a]

[a]Department of Electronics, Tokyo University of Technology, 1404-1 Katakura, Hachioji, Tokyo 192-0982, Japan
[b]Research Institute for Technical Physics and Materials Science of Hungarian Academy of Sciences, P.O.B.49, H-1525 Budapest, Hungary
[c]Department of Applied Physics and Chemistry, University of Eelectro-Communications, 1-5-1 Chofugaoka, Chofu, Tokyo 182-8585, Japan
[d]Faculty of Engineering, Tokyo Institute of Technology, 2-12-1 Ookayama, Meguro, Tokyo 226-8552, Japan

Received 22 January 2004; received in revised form 3 March 2005; accepted 3 March 2005
Available online 23 May 2005

Abstract

A study is made of the epitaxial growth structure of a Ni film 123 nm thick on the GaAs(001) pre-covered with a TiN film of 3 to 118 nm in thickness. First, the TiN buffer layer is prepared on the GaAs at a temperature from 100 to 700 °C by reactively rf sputtering Ti in N_2 gas flowing at a rate from 1 to 10 sccm. Then the Ni film is deposited on the fresh TiN film at a temperature between 200 and 500 °C by rf sputtering Ni in pure Ar gas. X-ray diffraction and transmission electron microscopy are used to analyze the crystal and compositional structure of the samples.

In our experiments, the highly ordered epitaxial growth was obtained with the crystallographic relationship of Ni(001)[001]// TiN(001)[001]//GaAs(001)[001] by the TiN deposition at 500 °C in N_2 gas flowing at 1.0 sccm, followed by the Ni deposition at 300 °C, where the degree of the Ni film epitaxy depends on the TiN thickness. In conclusion, the highest ordered epitaxial Ni film is grown on the 13 nm thick TiN buffer.

Keywords: Epitaxial growth; Ni film; TiN buffer; GaAs substrate; Reactive sputtering; X-ray diffraction; Transmission electron microscopy

1. Introduction

Thin film growth of magnetic materials on the semiconductor substrate has been investigated from both scientific and practical interests concerning devices such as non-volatile magnetic memories, microwave devices, spin injection devices [1]. Homogeneously grown epitaxial films with well controlled interface structure should be important for practical applications. In fact, much work with typical magnetic metals (such as Fe and Co) has been carried out on their thin film growth structure on GaAs(100) or GaAs(110) substrate by MBE deposition [2–5]. As far as the authors know, however, there have been few reports on Ni which is one of typical magnetic metals. According to recent reports, Ni films deposited directly on GaAs(001) substrate by dc-biased plasma-sputter-deposition retain a [001] textured polycrystalline structure forming the $NiAs_2$ compound at the interface [6], and Ni films deposited on the 10 nm thick Ti overlaid GaAs(001) by rf sputtering retain a [111] textured structure with a relation of Ni(111)//Ti(00·1)//GaAs(001) and Ti(11·0)//GaAs(110) where Ni(001) is nearly parallel to GaAs(111), without compound formation at the interfaces [7]. In both cases, however, the perfectly epitaxial Ni film did not grow. For the present work, in order to prepare the epitaxial film system of Ni/Buffer Film/GaAs on the basis of the previous results [7], the Ni film is deposited on the GaAs(001) substrate pre-covered with the TiN film by reactively rf-sputtering Ti, in addition, the TiN is practically useful as a semiconductor and, in addition, is believed to be useful as a buffer for epitaxial growth of the Ni film on the GaAs(001) substrate because TiN has the same

* Corresponding author. Tel.: +81 426 37 2111x2396; fax: +81 426 37 2112.
E-mail address: makihara@so.teu.ac.jp (K. Makihara).

0040-6090/$ - see front matter © 2005 Elsevier B.V. All rights reserved.
doi:10.1016/j.tsf.2005.03.028

cubic crystalline symmetry as Ni and GaAs with the lattice constant of $a_{TiN}=0.4242$ nm which is more or less comparable to $a_{Ni}=0.3524$ nm and $a_{GaAs}=0.5654$ nm. Thus, a study is made of the epitaxial growth condition as well as the growth structure of the Ni/TiN/GaAs system as a function of film preparation conditions such as the substrate temperature during the film growth, the nitrogen gas flow rate during the TiN film growth, and the TiN thickness.

2. Experimental procedure

The rf magnetron sputtering system to which targets of Ni and Ti (both 4 N in purity) were attached was used to deposit the films of TiN or Ni. The GaAs(001) substrates were pre-cleaned with $H_2SO_4+H_2O_2+H_2O$ solution. After being evacuated to 10^{-5} Pa, at first, the reactive sputtering of Ti started to deposit the TiN film as a buffer on the GaAs substrate in a mixed gas of Ar and N_2 of 0.5 Pa in total pressure and then the sputtering of Ni was followed on the fresh TiN film in a pure Ar gas of 0.5 Pa to complete the Ni/TiN/GaAs sample. The flow rate of N_2 gas was adjusted at 1.0, 6.0 or 10.0 sccm during the TiN deposition while that of Ar was adjusted at a constant value of 2.5 sccm during both TiN and Ni depositions. Substrates were heated to a temperature ranged from 100 to 700 °C during the TiN deposition and 200 to 500 °C during the Ni deposition. Film thickness was controlled by adjusting the deposition time and evaluated by the stylus method or directly by cross-section transmission electron microscopy (TEM) observation. The structure and composition of the films were investigated by X-ray diffraction (XRD) with the use of the X-ray diffractometer of a Cu-K_α beam (Rigaku Denki), and by cross section TEM with the use of the electron microscope of 200 kV in accelerated voltage (JEOL). The lattice images of some typical films were investigated by cross section high resolution TEM (cross section HRTEM) with the use of the electron microscope of 300 kV in accelerated voltage (Philips). Samples for TEM as well as HRTEM investigation were prepared by mechanical grinding followed by ion milling with a glancing angle ion thinning unit (Linda and Japan Physitech) [8,9]. The presence of compounds formed within the regions thinner than 100 nm at the interfaces was examined by grazing incident XRD [10] with the use of the grazing angle X-ray diffractometer of the Cu-K_α beam incident at 1–3° (Rigaku Denki).

3. Results and discussion

3.1. Preparation condition of TiN film on GaAs(001)

At first, the preparation condition of the epitaxial TiN buffer film on the GaAs(001) substrate was investigated with a constant TiN thickness at 118±5 nm.

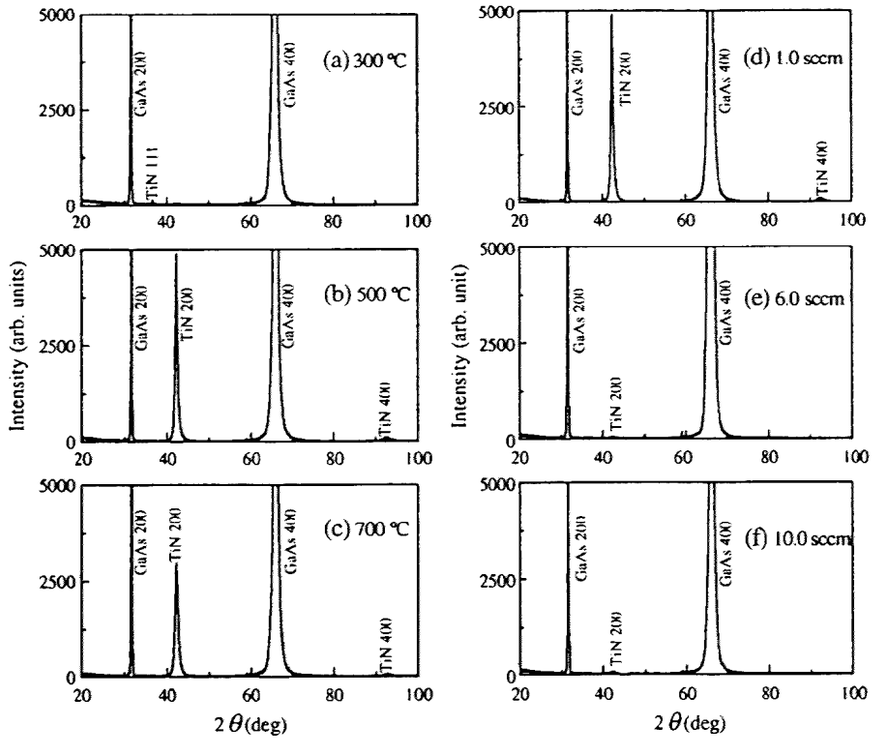

Fig. 1. XRD spectra of the TiN films deposited on GaAs(001) at various substrate temperatures of (a) 300 °C, (b) 500 °C, (c) 700 °C with N_2 flow rate of 1.0 sccm, and at 500 °C with various N_2 flow rates of (d) 1.0 sccm, (e) 6.0 sccm, (f) 10.0 sccm, respectively.

3.1.1. Results of XRD observation

Fig. 1(a) to (c) show the XRD spectra of the TiN films deposited onGaAs(001) at verious temperatures with a constant N2 flow rate of 1.0 sccm, and Fig. 1(d) to (f) show the XRD spectra of the TiN films deposited on GaAs(001) at a constant substrate temperature of 500 °C with verious N2 flow rates. As clearly shown in Fig. 1(a) to (c), the 200 textured growth of the TiN film is detected with increasing the substrate temperature from 300 °C to 500 °C or above; the strength ratio of the TiN-200 peak to the GaAs-400 one is 0% (undetected) at 300 °C, 0.9% at 500 °C and 0.5% at 700 °C and the FWHM (full width of half maximum intensity) of the TiN 200 peak is undetected at 300 °C, 0.54°at 500 °C and 0.66°at 700 °C, respectively. In Fig. 1(d) to (f), it is evident at a glance that the TiN-200 textured growth is enhanced at the N_2 flow rate of 1.0 sccm as compared to the cases of higher N_2 flow rate. From these XRD results, the conditions for the substrate temperature and the N_2 flow rate for the TiN-200 textured growth are determined to be 500 °C and 1.0 sccm, respectively.

3.1.2. Results of cross-section TEM and cross-section TED observations

Fig. 2 shows the cross-section TEM microphotograph (a), its diffraction (cross-section TED) pattern (b) taken with the electron beam along the GaAs[110] direction and the reconstructed cross-section TED pattern (c) of the TiN film prepared on GaAs(001) under the above determined conditions. As seen in Fig. 2(a), its surfaces to be smoothly parallel to each other with the sharp interface between TiN and GaAs(001), where a thin layer observed on the TiN film is a carbon film as a glue used during ion milling. As illustrated in Fig. 2(b) and (c), the TiN film grows on GaAs(001) with the highly ordered epitaxial mode of TiN(001)[001]//GaAs(001)[001]. There is no indication for the compound formation at the TiN/GaAs interface.

3.2. Preparation and structure of the Ni/TiN/GaAs sample

The epitaxial growth condition of the Ni film deposited on the fresh TiN film prepared on GaAs(001) at the above determined conditions (the Section 3.1) was investigated as a function of the TiN/GaAs-substrate temperature as well as of TiN thickness, where the Ni thickness was constantly adjusted at 123±9 nm thick.

3.2.1. Results of XRD and grazing incident XRD observation

Fig. 3(a) to (c) shows the XRD spectra of the Ni films deposited on the 118 nm±5 nm thick TiN film at 200, 300 and 400 °C. As seen in Fig. 3(a) to (c), the Ni-100 textured growth is clearly detected. The strength ratio of the Ni-200 peak to the GaAs-400 one is evaluated to be 4.4% at 200 °C, 6.9% at 300 °C, 5.4% at 400 °C respectively. So, the optimum substrate temperature for the Ni-100 textured growth is determined to be approximately 300 °C. Fig. 3(d)

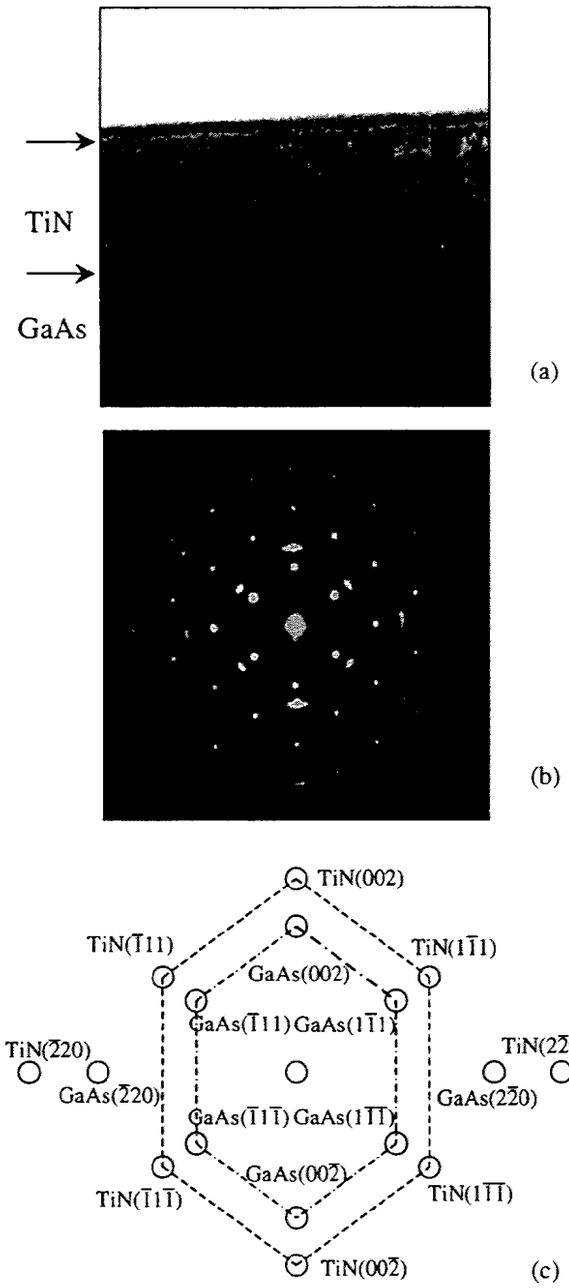

Fig. 2. (a) The cross-section TEM microphotograph of the TiN 118 nm thick/GaAs(001) sample with a N_2 flow rate of 1.0 sccm at 500 °C, (b) its cross-section TED pattern taken with the electron beam directed to GaAs[110] and (c) the reconstructed cross-section TED pattern.

to (g) shows the XRD spectra of the Ni films deposited on the TiN films of 118 nm, 55 nm, 13 nm, 3 nm in thickness at 300 °C. As one can clearly see in Fig. 3(d) to (g), within this range of the TiN thickness, the Ni-100 textured growth is particularly enhanced on the 13 nm thick TiN, suggesting that there exists the optimum TiN thickness for the Ni textured growth. In fact, the intensity ratio of the Ni-200 peak to the GaAs-400 one changes with the TiN thickness as follows; 6.9% at 118 nm, 22.8% at 55 nm, 30.6% at 13 nm and 19.6% at 3 nm and besides the FWHM of the Ni-200

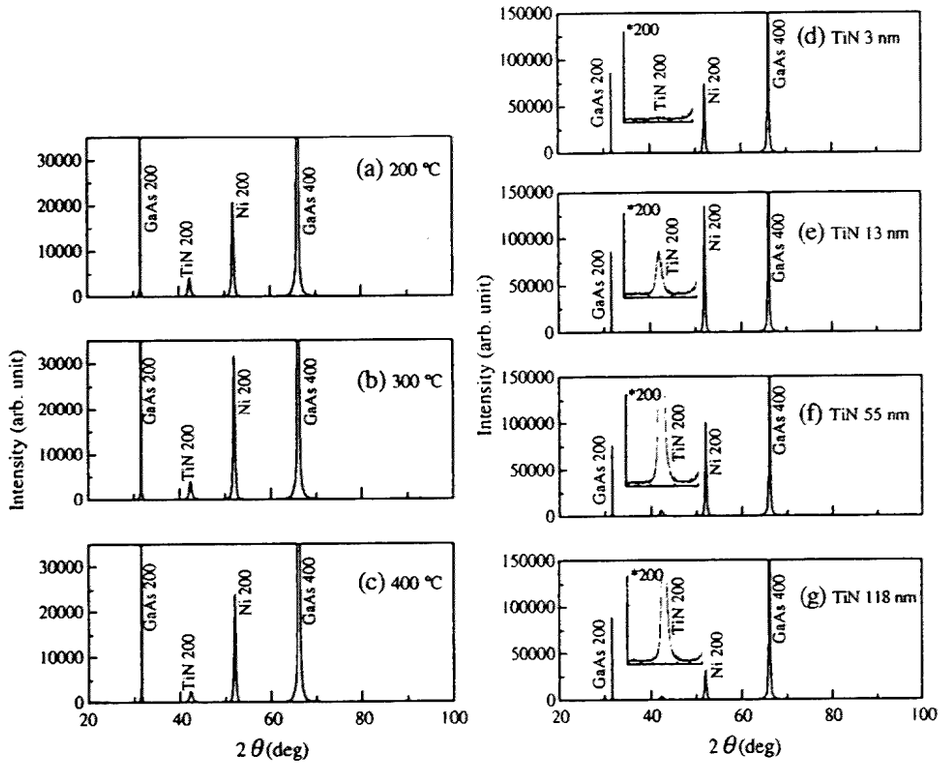

Fig. 3. XRD spectra of the Ni films 123 nm thick deposited on the TiN film 118 nm thick at various temperatures of (a) 200 °C, (b) 300 °C, (c) 400 °C, and on the TiN films of various thicknesses of (d) 3 nm, (e) 13 nm, (f) 55 nm, (g) 118 nm at 300 °C, respectively.

peak changes as follows; 0.38° at 118 nm, 0.30° at 55 nm, 0.28° at 13 nm and 0.41° at 3 nm, respectively. Thus it is suggested that the 13 nm TiN film on GaAs(001) retains particularly a surface condition to promote the 100 textured or epitaxial growth of the Ni film. Now, a possible change of the surface condition of the TiN film as a buffer could result from deformation due to a lattice misfit to the GaAs substrate crystal. The analysis of the XRD spectra (Fig. 3(d) to (g)) can give the averaged values of TiN(002) spacing vertical to the film surface as a function of the TiN thickness as shown in Fig. 4 where the range of error bars is estimated from the half value width of the XRD signals shown in Fig. 3(d) to (g). It is suggested in Fig. 4 that the averaged TiN(002) spacing tends to be enlarged with a decrease in the TiN thickness as compared to the value of the bulk crystal, 0.2121 nm though, in fact, the TiN(002) spacing values shown in Fig. 4 are to give the values averaged over the thickness range from the interface at the GaAs substrate to the interface at the Ni film. Thus, it can be said that, assuming the volume of the crystal is to remain constant in

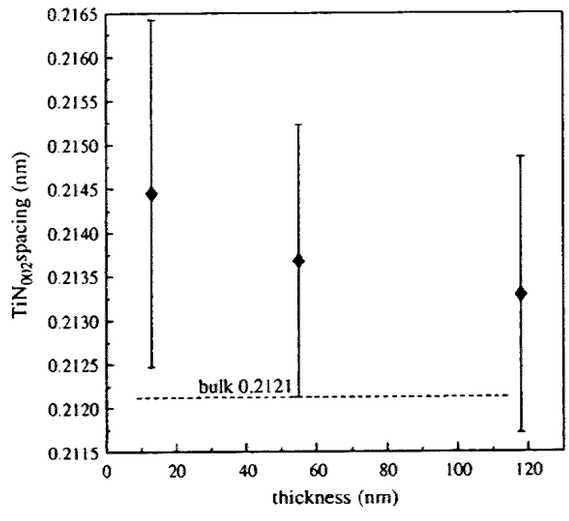

Fig. 4. The TiN(002) spacing of the TiN film as a function of TiN thickness.

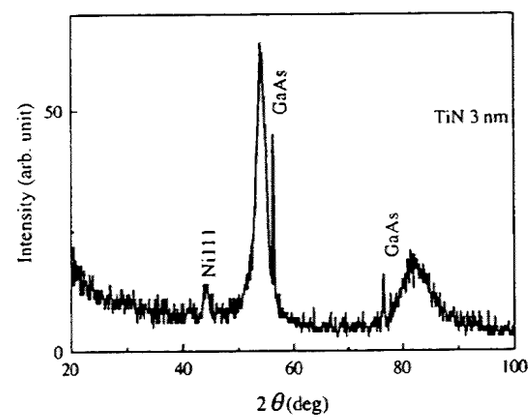

Fig. 5. The grazing incident XRD spectrum of the Ni 123 nm thick/TiN 3 nm thick/GaAs(001) sample.

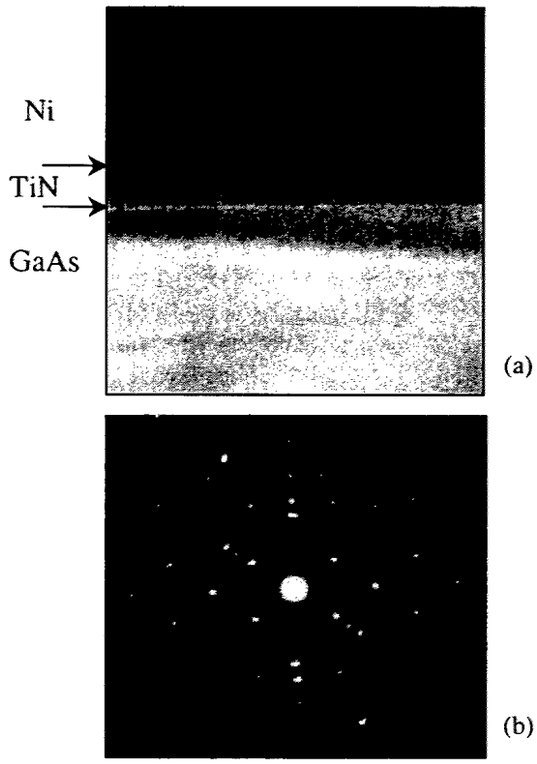

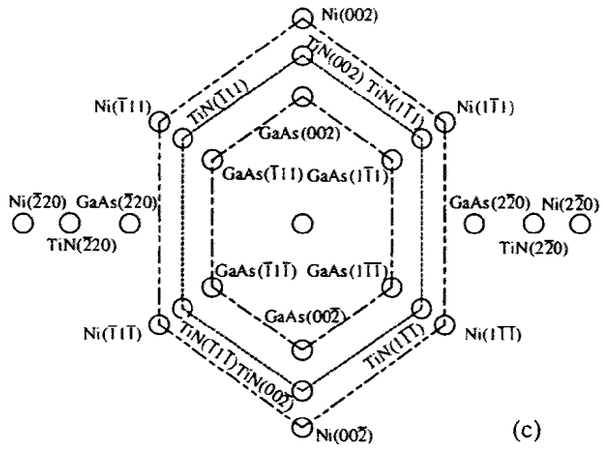

Fig. 6. (a) The cross-section TEM microphotograph of the Ni 123 nm thick/TiN 13 nm thick/GaAs(001) sample, (b) its cross-section TED pattern and (c) the reconstructed cross-section TED pattern.

the present specimen, the averaged lattice spacing along the film surface tends to contract resulting in reduction of the lattice misfit along the interface between TiN and Ni films as compared to the case of the bulk to bulk contact. A general tendency of the Ni/TiN lattice misfit reduction is qualitatively consistent with the result of cross section high resolution TEM (HRTEM) observation shown below (Fig. 7). As a result, the epitaxial growth of the Ni film can be the more readily promoted on the thinner TiN film. On a 3 nm TiN film, however, the Ni-200 peak intensity is reduced because the TiN film 3 nm thick may have a granular uneven surface giving a suppressive effect on the Ni epitaxial growth, i.e., a few nm thick film should have a rough or granular surface with different crystal facets because it is considered to still stand near the coalescence growth stage from the island to continuous structure. Alternatively, the surface roughening of the very thin TiN film may be enhanced by residual species on the air-cleaved GaAs (001) surface. As a result, it can be said that the highest ordered epitaxial Ni film is grown on the 13 nm thick TiN buffer. Finally, Fig. 5 shows the grazing incident XRD spectrum with the incident angles of 3° for the 123 nm thick Ni/3 nm thick TiN/GaAs(001) sample. No compound formation could be detected at the interfaces between Ni, TiN and GaAs, as shown in Fig. 5. A narrow peak beside each main GaAs peak comes from crystal defects which remain inevitably in the GaAs crystal, as well known.

3.2.2. Results of cross-section TEM and cross-section TED and cross-section HRTEM observations

Fig. 6 shows the cross-section TEM microphotograph (a) and its cross-section TED pattern of the Ni 123 nm thick/TiN 13 nm thick/GaAs sample (b) with the reconstructed cross-section TED pattern for identification (c). They were taken by the GaAs[110]-incident electron beam. As seen in Fig. 6(a),

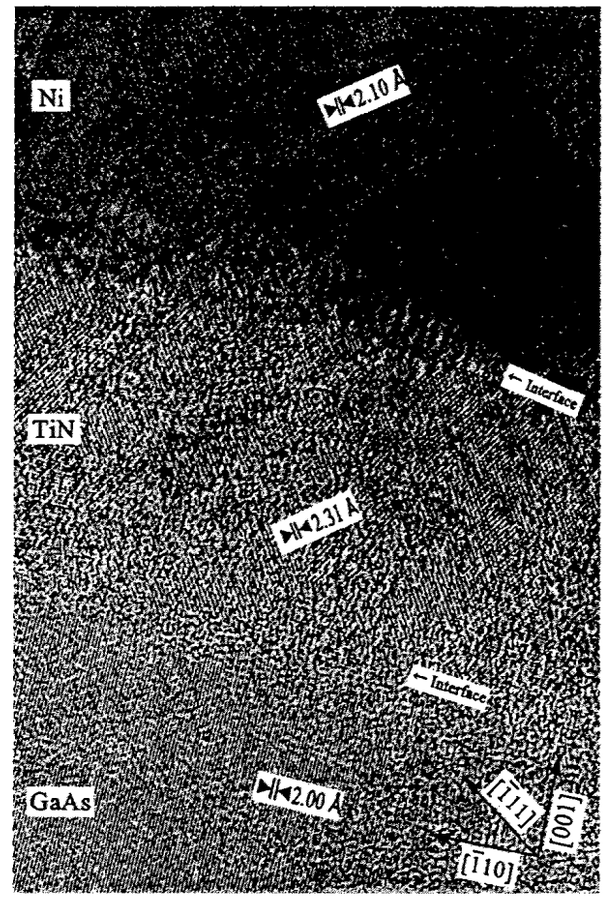

Fig. 7. The cross-section HRTEM microphotograph of the same sample as shown in Fig. 6. The lattice spacings of GaAs-220, TiN-111 and Ni-111 planes are inserted in the microphotograph.

the interfaces between Ni, TiN and GaAs are rather sharp and smooth, and as one can see in Fig. 6(b) and (c) the Ni film grows on the TiN film with the Ni(001)[001]//TiN(001)[001] mode, i.e., as a whole, the highly ordered epitaxial mode of Ni(001)[001]//TiN(001)[001]//GaAs(001)[001]. Now, Fig. 7 shows the cross-section HRTEM microphotograph of the same sample and taken by the same incident electron beam as previously shown (Fig. 6), where a columnar like pattern observed at the interface between Ni and TiN is considered to originate from the sample thickness variation induced during the ion thinning process. Each lattice spacing value of GaAs-220, TiN-111, and Ni-111 planes is inserted in the cross-section HRTEM microphotograph. The values for TiN-111 and Ni-111 were computed with an error of ± 4% averaging over the nearly whole area of each film, where the GaAs-220 spacing was assumed to equals to its bulk value, 0.200 nm. Thus, it is confirmed that the lattice spacing values for TiN-111 and Ni-111 in the film to film contact approach each other as compared to the case of the bulk to bulk contact, i.e., the lattice misfit between TiN-111 and Ni-111 defined by $f=(d_{\text{Ni-111}}-d_{\text{TiN-111}})d_{\text{TiN-111}}^{-1}$ decreases from $f_B=-0.171$ (or −17.1%) for the bulk case to $f_F=-0.091$ (or −9.1%) for the film case, where $d_{\text{Ni-111}}=0.203$ nm, $d_{\text{TiN-111}}=0.245$ nm for the bulk case and $d_{\text{Ni-111}}=0.210$ nm, $d_{\text{TiN-111}}=0.231$ nm for the film case as indicated in Fig. 7. Thus, $f_F^{-1}=1/0.091=10.98$ as compared to $f_B^{-1}=1/0.171=5.84$, where f^{-1} means the interval of the misfit dislocations in the unit of the lattice spacing at the interface. This result shows that the density of misfit dislocation induced at the real Ni/TiN interface is almost one half of that at the bulk contact. Such the situation results in the relaxation of the strain energy induced by the mismatched lattice contact to promote the epitaxial growth of the Ni film in the Ni/TiN/GaAs system studied.

4. Summary

The epitaxial growth condition of a Ni film 123 nm thick on the GaAs(001) pre-covered with a TiN film of 3 to 118 nm in thickness was investigated. The TiN film as a buffer was prepared on the GaAs by reactively rf sputtering Ti in a mixed gas of Ar and N_2, and then the Ni film was in situ deposited on the fresh TiN film by rf sputtering Ni in pure Ar gas. The highly ordered epitaxial growth with the crystallographic order of Ni(001)[001]//TiN(001)[001]//GaAs(001)[001] is achieved by TiN deposition on GaAs(001) at 500 °C in N_2 gas flowing at 1.0 sccm followed by Ni deposition at 300 °C. The strain energy induced by the mismatched lattice contact of TiN to Ni films is appreciably relaxed by the lattice deformation at the interface to promote the epitaxial growth of the Ni film in the Ni/TiN/GaAs system studied. A too thin TiN buffer, however, gives a suppressive effect on the Ni epitaxial growth because a few nm thick film should have a rough or granular surface with different crystal facets standing at or before the coalescence growth stage. Thus there exists the optimum TiN thickness for the Ni textured growth. In conclusion, the highest ordered epitaxial Ni film is grown on the 13 nm thick TiN buffer.

Acknowledgement

This work was partly supported by the Hungarian National Science Foundation under Contract No. JAP-26/00.

References

[1] G.A. Prinz, in: B. Heinrich, J.A.C. Bland (Eds.), Ultrathin Magnetic Structures, vol. II, Springer-Verlag, Berlin, 1994, p. 1.
[2] G.A. Prinz, Phys. Rev. Lett. 54 (10) (1985) 1051.
[3] C. Carbone, B.T. Jonker, K.-H. Walker, G.A. Prinz, E. Kisker, Solid State Commun. 61 (5) (1987) 297.
[4] J.J. Kreb, B.T. Jonker, G.A. Prinz, J. Appl. Phys. 61 (7) (1987) 2596.
[5] Y.U. Iderda, B.T. Jonker, W.T. Elam, G.A. Prinz, J. Vac. Sci. Technol., A, Vac. Surf. Films 8 (3) (1990) 1572.
[6] J. Yang, K. Makihara, H. Nakai, M. Hashimoto, A. Barna, P.B. Barna, Thin Solid Films 319 (1998) 115.
[7] K. Makihara, J. Shi, M. Hashimoto, S. Maruyama, A. Barna, J. Vac. Sci. Technol., A, Vac. Surf. Films 19 (5) (2001) 2494.
[8] A. Barna, Mater. Res. Soc. Symp. 254 (1991) 3.
[9] A. Barna, B. Pecz, M. Menyhard, Micron 30 (1999) 267.
[10] X. Jiang, X.Z. Jiang, W. Jiang, Q. Jia, W. Zheng, D. Xian, X. Wang, Nucl. Instrum. Methods A467/468 (2001) 362.

MAGNETIC PROPERTIES of NICKEL LAYERS ELECTRODEPOSITED on AMORPHOUS CARBON

K. Maruyama[1], E. Arakawa[2], K. Hiraki[3], H. Yamaguchi[4], H. Numata[5], A. Matsushita[4], T. Yokoyama[1], T. Koide[6], K. Namikawa[2], and O. Nittono[7]
[1]Institute of Molecular Science, [2]Tokyo-Gakugei Univ., [3]Gakushuin Univ., [4]National Institute for Material Science, [5]Tokyo Institute of Technology, [6]Photon Factory of KEK, [7]Fukushima Univ. [1]Myodaiji, Okazaki, Aichi, 444-8585, Japan, [2]4-1-1, Nukuikita-machi, Koganei, Tokyo, 184-8501, Japan, [3]1-5-1, Mejiro, Toshima, Tokyo, 171-8588, Japan, [4]1-2-1, Sengen, Tukuba, Ibaraki, 305-0047, Japan, [5]2-12-1, Ookayama, Meguro, Tokyo, 152-8552, Japan, [6]1-1, oho, Ibaraki, 305-0801, Japan, [7]1, Kanayagawa, Fukushima, Fukushima, 960-1296, Japan

ABSTRACT

The Nickel layer is electrodeposited on amorphous carbon. Electrochemical behavior and morphology obtained are dependent on the deposits thickness at the initial stage influenced by "electrode catalysis". Nanostructure and unknown chemical phases peculiarly were obtained for deposits thinner than a few monolayer, and such the deposits exhibited an abnormal large magnetization. The relationship between nanostructure and magnetic properties of deposits was experimentally referred, and was bound to the electrochemical behavior.

INTRODUCTION

Magnetic thin films and multilayers are prepared not only by the dry processes but also by the wet processes.(1) Electrodeposition is one of the simple techniques for preparations of advanced magnetic devices, such as amorphous films(2), magnetic recording medias(3), magnetic resistance multilayers(4), MEMS(5), and so on. Nanostructure and their magnetic properties of these materials must be strictly governed in the future nanotechnology.(6) There still exists a problem of the "electrode catalysis", which is effective to the initial stage of the electrode reaction.(7) The electrochemists have not been focused on the electrodeposition of 3d transition metal elements such as iron, nickel, and cobalt. This may be because the electrodeposition behavior of their metals is more complicated than that of noble metals. The atomistic view for such the electrodeposition of gold, platinum, and palladium has been made clear by many electrochemists.(8)

On the other hands, if anything, the non-electrochemists such as us are interested in the properties of magnetic electrodeposits, themselves, and the comparison of them to that of the films prepared by the other techniques.(9) This might be because the advanced function of the electrodeposits is scientifically anticipated in terms of the "electrode catalysis" of the electrochemical reaction.

Our previous investigation was to confirm the relationship between the structural and morphological properties of cobalt electrodeposited on copper substrate, and their electrochemical behavior at the initial stage.(7) The electrode potential was successively detected on the pulse-off time during the pulsed current electrodeposition. The magnitude of electrode potential of deposit surface shifts at the initial stage of electrodeposition less than about 50 monolayer (ML) toward the steady state. It is difficult to interpret this

behavior influenced by the exposure of underlayer surface, and, there is a possibility of the mixing between cobalt and copper elements. Another problem is that the deposited cobalt begins to dissolve into the solution immediately over the electrodeposition process. This made the properties estimation of the thinner film strictly difficult.

Our comprehensive view is to clarify the properties of any electrodeposit continuously bound by the surface nature of deposits subsequently to that of substrates. As a first step of this view, we adopted nickel and carbon as a deposit and a substrate species, respectively. It is easily supposed to resolve the above problems simultaneously, and it is possible to observe the magnetic properties of thinner nickel films. In this study, our interest is focused on nanostructure and magnetization of the nickel deposits thinner than 50 ML, and particularly on the abnormal increase in magnetization at room temperature dependent on the deposit thickness. Some these properties may be determined by the electrodeposition behavior at the initial stage.

EXPERIMENTAL

Electrodeposition was occurred on amorphous carbon (AC-20S, plate of 7×7×1 mm, Nisshinbo Co. Ltd.) immersed into a solution prepared by ourselves. Chemicals and their concentrations are listed in Table 1. A usual three electrodes cell was constructed of a working electrode of carbon substrate, a counter electrode of platinum wire, and a reference electrode of SCE (or nickel electrodeposit on copper). The pulsed current or the steady one is controlled, and the corresponding potential signal is handled, by a potentiostat/galvanostat (HA-501G, HOKUTO DENCO Co. Ltd.) and a function generator (HB-501, HOKUTO DENCO Co. Ltd.). The transit of potential signals corresponding to the pulsed current was acquired for the output signal of this equipment through a PCMCIA card of AD-converter (REX-5025, RATOC Co. Ltd.). Mass analysis was occurred by means of ICP-AES (inductively coupled plasma atomic emission spectrometer, Optima 3300DV, Perkin-Elmer) and EC-QCM (electrochemical – quartz crystal microbalance, HQ-101B, HOKUTO DENKO Co. Ltd.)

Table 1 Chemicals and their concentration, and condition of electrodeposition.

Chemicals	concentration
$NiSO_4 \cdot 6H_2O$	0.05 mol/L
$(NH_4)_2SO_4$	0.1 mol/L
conditions	
pH adjustment	5.0 with NH_3 solution
Bath temperature	313 K
Stirring	500 r.p.m.

An area of substrate plates acts as a plating surface, with the other part of an insulated coating. Surface morphology of deposits was observed by the tapping mode of ex-situ AFM (atomic force microscopy, Dimension 3000, DIGITAL INST. Co. LTD or JSTM-4200D, JEOL Ltd.) Chemical states of them were analyzed by XPS (x-ray photoelectron spectroscopy, ESCALAB 220i-XL, FISION INST. Co. Ltd.) using a Mg-kα x-ray source.

XAS (x-ray absorption spectroscopy) and MCXD (magnetic circular soft x-ray dichroism) were measured at PF-AR NE1B helical-undulator soft x-ray grating monochromator station of Photon Factory, KEK. The magnetic field of 1.1T is in the direction of the out-of sample plane. The signal detection was due to the total yield of sample current. Magnetic hysteresis behavior or magnetization was measured by SQUID (superconductive quantum interference device, MPMS-7, QUANTUM DESIGN Co. Ltd.), and then the magnetic field was applied into the sample plane in the maximum magnitude of 7T. The sample for SQUID magnetometry was prepared using the substrate

covered not by the insulated coating but by a holder of the fluoride resin (PCTFE). This plating holder was made by us in order to remove any magnetic impurity of the coating matter, from the samples. And also the gold-coated sample was used for preventing the surface oxidation of deposits. For this coating, the samples were immersed into a commercial solution (LECTROLESS D-1, TANAKA KIKINZOKU Group) kept at 60 °C, immediately over the electrodeposition of nickel.

RESULTS and DISCUSSION

Electrochemical behavior of nickel

Pulsed current electrodeposition(10) was adopted mainly in this investigation, and it was due to two reasons. At first, the homogeneous film can be deposited due to the competition of charge of ions into the electric double layers during pulse-off time. Secondly, the electrode potential of deposit surface may be acquired on pulse-off time, if the solution phase reaches to the steady state at that time.(7) Figure 1(1) is the potential-time curve during the electrodeposition of nickel on a carbon substrate. The current i is 25 mA cm^{-2}, and T_{on}=100 ms, and T_{off}=1000 ms, where the deposit of 1 monolayer (ML) approximately is obtained for the unit number of pulsed current, on the assumption of the Faraday law and the current efficiency of 50%. In this article, the magnitude of ML is described on this assumption. There is a pair of 100 numbers of pulse-on and pulse-off in this electrodeposition. The immersion potential (E_{imm}) of carbon substrate is 0.27 (V vs. SCE), and E_{on} or E_{off} reach to the steady value, -0.36 V or -1.2 V, which is the electrode potential of pulse-on or pulse-off, respectively. As mentioned above, the steady value of E_{off} seems to be E_{imm} of the thick nickel deposit immersed into this solution. It is noted that, at the initial stage of this electrodeposition, E_{on} and E_{off} shifts in less and more noble potential, dependent on the deposit thickness, respectively. This behavior of E_{on} and E_{off} is predominated in the region less than about 50 ML.

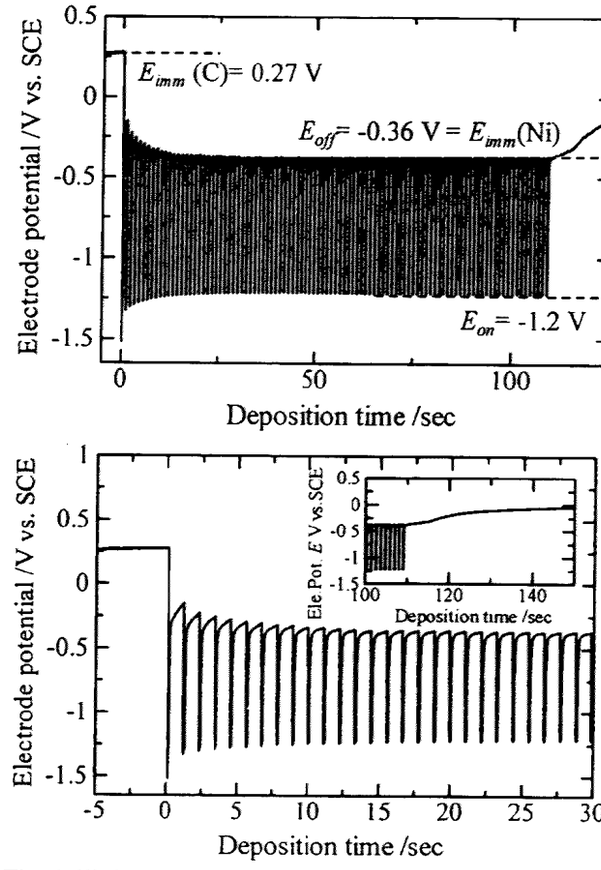

Fig. 1 (1) (*upper side*) Transit (electrode potential - time curve) of nickel electrodeposition on amorphous carbon. Pulsed current (I=25mA cm^{-2}) is controlled by 100 numbers of T_{on}=100 ms, T_{off}=1000ms. (2) (*lower side*) Transit expands in the initial stage, and the inset is after finishing the electrodeposition.

In Fig. 1(2), it is easy to look into the potential behavior at the initial stage. Every E_{off} reach to the steady state for each pulse-off time, except for the first several pulse-off one. Therefore, the surface nature of deposits changes and will be different from that of

3

the thicker deposits, which corresponds to the E_{off} shift. And also the potential difference between E_{on} and E_{off} in every pair of pulse-on and -off times changes is obtained pulse by pulse in the same region, which means that the chemical potential or the overpotential of the electrodeposition must successively change at the initial stage. The inset of Fig. 1(2) denotes a part of the curve after finishing the electrodeposition. The gradual shift of the potential may be due to a little dissolution or passivity of the deposit surface, hence the sample obtained need to be whipped out of the solution immediately over the deposition process. ICP-AES analysis results in nickel mass almost proportional to the pulse number of electrodeposition, in this manner.

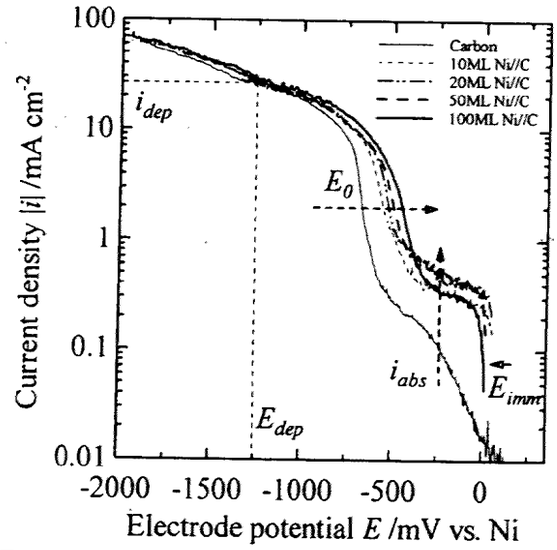

Fig. 2 Cathodic polarization curves of a carbon substrate and several nickel deposits on it. The deposition potential (E_{dep}) is prospected by the deposition current (i_{dep}). E_0 is defined in the text. The immersion potential (E_{imm}) and E_0 are dependent on the deposit thickness.

The supposition of the electrochemical behavior at the initial stage would be confirmed by a polarization measurement. Figure 2 shows the cathodic polarization curves for a carbon substrate and several deposits (10-100 ML) on it used as the working electrodes. As defined in our previous report(7), E_0 is the potential value for the sudden increase in current value when the potential sweeps in less noble direction, at which the cathodic deposition happens to begin. It was confirmed by EC-QCM that the deposition did not occurred in the more noble direction of E_0. Hence, the current around more noble region of E_0 is consumed for any adsorption of some ions on the electrode surface, irrespective of the cathodic deposition, where we call it the "absorption current", i_{abs}. The E_0 for bare carbon substrate significantly shifts to the less noble direction, which is a kind of the well-known "overpotential deposition"(11). That for the other deposits on the substrate shifts to the more noble direction with an increase in deposits thickness. And also the Eimm shift shown in Fig.2 is qualitatively consistent with the shift of Eoff denoted by Fig.1. Moreover, the magnitude of i_{abs} for the carbon substrate is much smaller than that for the deposits, and that is also dependent on the thickness of them. This behavior of i_{abs} must be due to the surface nature of each electrode, which might result in the behavior of E_{imm} and E_0.

We previously proposed(7) that this E_0 shift at the initial stage affect the overpotential for the electrodeposition of cobalt on copper substrate, and is involved in the surface nature of deposits or E_{imm} just before the pulse-on time. This proposition might be realized by using carbon substrates in this study. However, the origin of E_0 and E_{imm} shifts and the relationship between these two potentials still remain as a problem of the "electrode catalysis" dependent on the species of substrates.

Nanostructure of nickel deposits

In the previous chapter, the electrochemical behavior proves to vary in the region less than about 50 ML. The observation has been focused on morphology and chemical states of the thinner nanostructured deposits, in our continuous investigation.

4

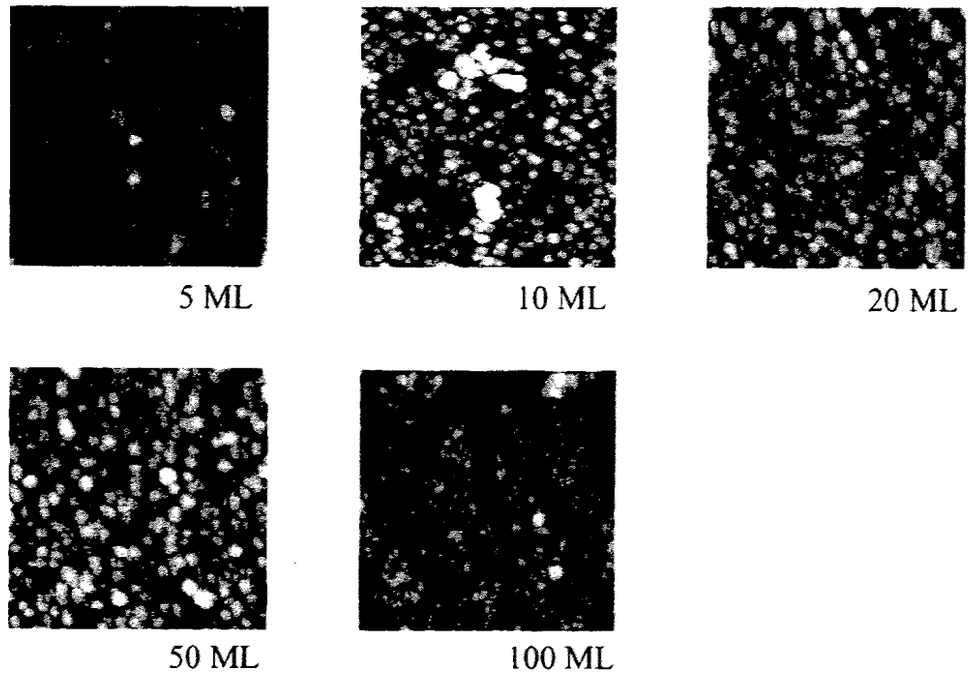

Fig. 3 Ex-situ AFM surface images of nickel deposits (5 ML to 100 ML) in air, for pulsed current electrodeposition. The image size is 2 μm×2 μm.

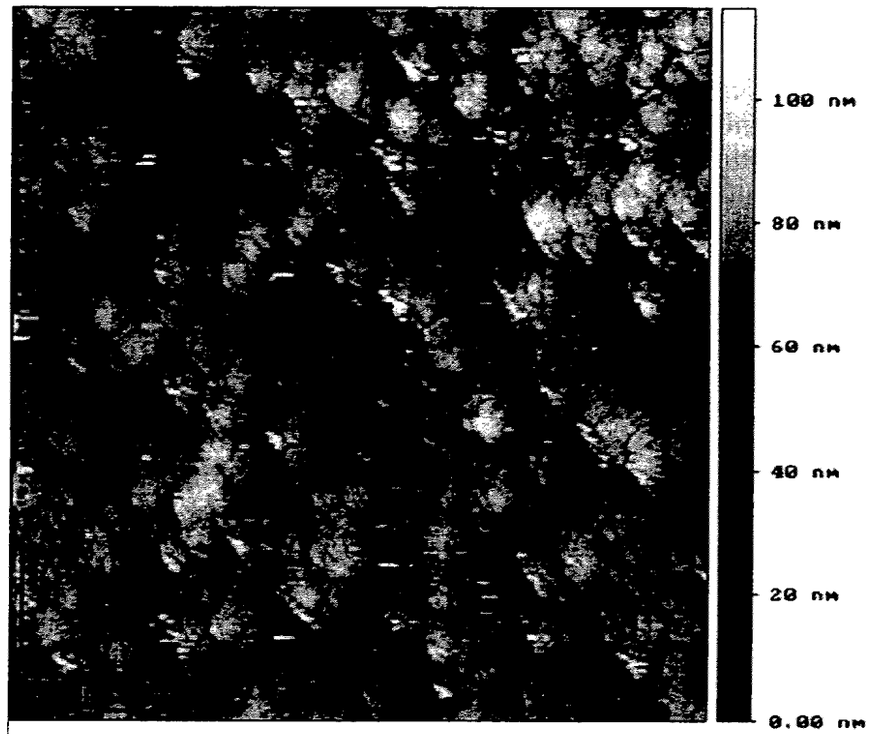

Fig. 4 (1) Ex-situ high resolution AFM image of nickel deposit (20 ML), for galvanostatic electrodeposition. The image size is 2 μm×2 μm.

5

The surface of electrodeposits usually is obtained not as the strict layer structure but as the cluster or nanostructure of grains.(12) Figure 3 shows the ex-situ AFM images in air for the picked-up several thickness of deposits. Morphology, and crystal shape and size drastically vary in the region of about 50 ML, which is resulted from nucleation and crystal growth of electrodepositions. A lot of rock-shaped clusters are obtained in these images grow homogeneously in sizes slightly dependent on the deposition time in almost region less than about 50 ML. The cluster's size for a few ML deposits is much smaller than that for the other deposits. The homogeneous clusters, afterwards, change little in their sizes with an increase in the deposition time, which is confirmed for deposits less than 200 ML. However, it is observed that each cluster might be constructed with several sub-structures. Unfortunately we can not analyze this behavior in more detail probably because of a lack of the image resolution.

We have proceeded to examine the deposits of the similar conditions to make clear their nanostructure. Figure 4 is the AFM images of nickel electrodeposited on carbon substrate with the non-pulsed current of 5 mA cm^{-2}. The clusters and some sub-structures in each them is observed clearly, which behavior is the similar to that reported in a manuscript.(13) They call the clusters and the sub-structures, the "mounds" and "grains", respectively, and compare the deposits between the pulsed and non-pulsed current electrodepositions. On the other hands, our interests will be focused on the nanostructure of deposits at the initial stage of such the electrodepositions. The dependency of sizes on deposits thickness is separately displayed for the mounds and the grains in Fig. 4(2). The mounds' size significantly changes with increasing the deposit less than 100 ML, and saturate afterwards. And also, the change in grains' size corresponding to the thickness is small but is prominent in the region less than 50 ML. R.M.S. (root-mean-square) of deposits surface is shown in Fig. 4(3). It is interesting that the dependency of R.M.S. on deposits thickness is qualitatively similar not to that of cluster sizes but that of grain sizes.

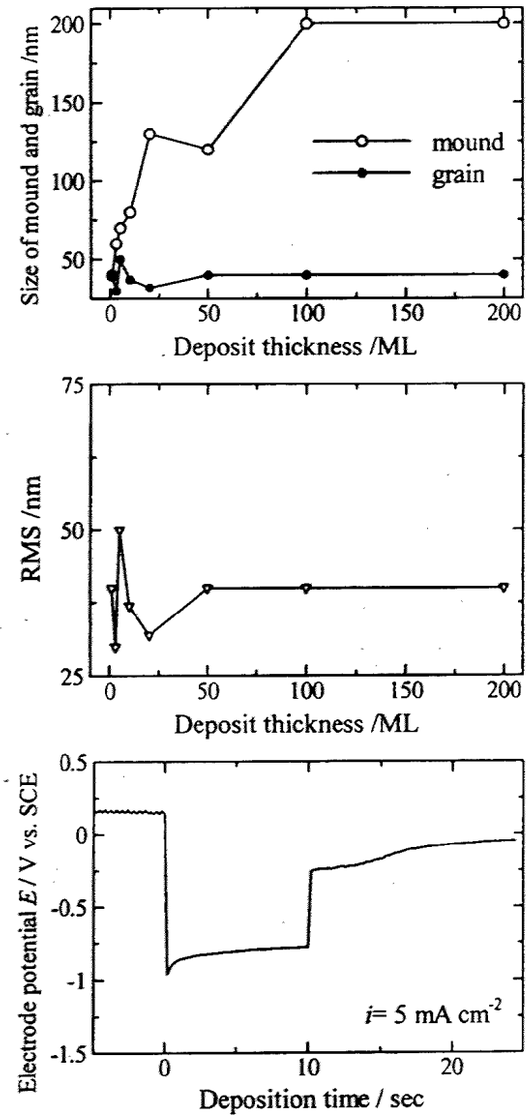

Fig. 4 (2) (*upper side*) Size analysis of "mound" and "grain". The "mound" means the rock-shaped cluster, and the "grain" is sub-structure in the "mound". (3) (*middle side*) RMS (root-mean-square) of deposits surface. (4) (*lower side*)Transit of galvanostatic mode.

The behavior of nucleation and crystal growth at the initial stage might be visualized even from such the rough estimation of AFM images. This observation must

6

be extended to more precise and strict in-situ one in the future study. Furthermore, the behavior of pulsed current electrodepositions is substantially different from that of non-pulsed current one. This might appear, for instance, in the dependency of "mounds" size on deposits thickness described in Fig. 3 that is not strictly consistent with the behavior of shown in Fig. 4(2). In spites, there exist some similarities in both modes. Figure 4(4) is the potential curve for this galvanostatic mode. The behavior of deposition potential for the galvanostatic mode, which corresponds to E_{on}, is similar to that for the pulsed current mode. And also, the dependency of R.M.S. for the non-pulsed current mode, shown in Fig. 4(3) is similar to that for the pulsed current one as shown in Fig. 3.

Here, this separable analysis of the "mounds" and the "grains" will teach us some important suggestions to our object. The change in mounds' size dependent on the deposit thickness less than 100 ML is consistent with that of the electrochemical behavior, E_{imm}, E_0, and E_{dep}. This must be simply explained from the change in the "overpotential" at the initial stage of electrodepositions, if it is possible to apply the conventional "Pangaro'v theory"(14) to the behavior or E_{dep} - E_0 at that stage. Furthermore, the change in grains' size is remarkable in more initial region at that stage as shown Fig. 4(2). If they would permit an analogy of the behavior between the galvanostatic and pulsed current modes, we will argue that a varies of grains size within 50 nm is effective to the magnetic properties of themselves and mounds aggregated with them, in terms of the single domain or superparramagnetic behavior and so on.(15)

The electrodeposits are generally obtained not for the objective pure metals but for their impurities and their oxide phase together with them.(16) The chemical analysis of deposits for 0.5 to 50 ML was occurred by XPS as shown in Fig. 5. The XPS profiles of 50 ML and 10 ML deposits exhibited the peaks of Ni_{2p} (at 873 and 869 eV) for pure nickel, and Ni_{2p} (at 856, 861, and 873 eV) for NiO, which was that of nickel sheet etched in a dilute HNO_3 solution and the commercial NiO powder, respectively. The oxide phase may exist mainly at the surface region of such the deposits. For deposits thinner than 5ML, peaks of Ni_{2p} appear unclearly and those of NiO shift to the lower energy points dependent on the deposit thickness. Such the unknown phases may be not due to the surface layer oxidation in air but due to a kind of oxide or hydroxide phase formed during the electrodeposition process.(17)

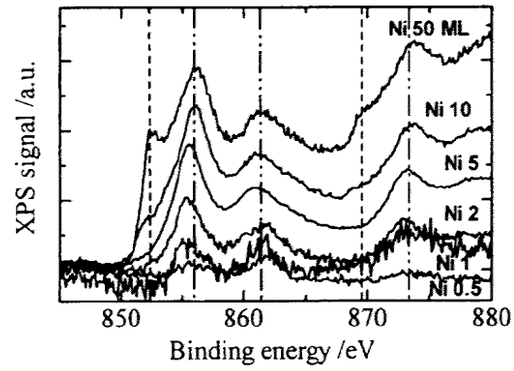

Fig. 5 XPS of nickel deposits for pulsed current mode. Lines denote the peak position of Ni_{2p} for pure nickel and nickel oxide (NiO).

We conclude that nanostructure or mounds' structure of nickel deposited on amorphous carbon is mutually affected by the electrochemical behavior, in terms of the "overpotential" of electrodepositions in the region less than about 50 ML, and more significant variety of morphology and chemical state of grains is obtained for narrower region or several ML deposits. We will anticipate some functional magnetic properties to such the nanostructural aggregation of grains.

Magnetic properties of deposits and their prospective origin

It is generally difficult to detect magnetization of only the thin film layer deposited on any substrate. This is not only because the thin film layer exhibits very small amount of the total magnetization, but also because the substrate does

7

non-ferromagnetic (diamagnetic or paramagnetic) components and very weak ferromagnetic ones of some impurities. The use of MCXD however solves such the problems, because MCXD detects the magnitude of magnetic moment separable to the magnetic element. Our investigation was naturally focused on magnetic moment of nickel element, and the signals were presented at Ni L absorption edge directly reflecting 3d electron polarization.

Figures 6 (1) and 6(2) show XAS and MCXD of various electrodeposits of 3 to 100 ML, and the vapor-evaporated gold (2nm) / nickel (15nm) // carbon sample used as a reference. XAS is normalized for zero and unit at pre-edge of L_3 and much higher energy point or about 900 eV above L_2 edge, respectively, in a conventional manner. And then, MCXD is usually defined as the difference between a pair of XAS in applications of plus and minus magnetic fields. XAS for deposits thicker than 50 ML exhibits the similar to that for the reference sample. For these samples, satellite peaks at energy points a little higher than L_3 (and L_2) peaks exist like that for bulk nickel sample. There were no or unclear satellite peaks for deposits thicker than 10 ML. An increase in intensity of L_3 peak is characteristic of the deposits with a decrease in their thickness, such as shown in the inset of Fig. 6(1). And also, the intensity of the energy region between L_3 and L_2 peaks, and that higher than L_3 peak up to unity obviously decreases with a decrease of deposits thickness. On the other hand, MCXD for deposits thicker than 50 ML shows the similar to that for the reference sample. Peak intensity at L_3 and L_2 edges of the deposits thinner than 50 ML decreases with a decrease in their thickness, and reach to almost zero for the deposits thinner than 3 ML. This behavior around L_3 edge is shown in the inset of Fig. 6(2).

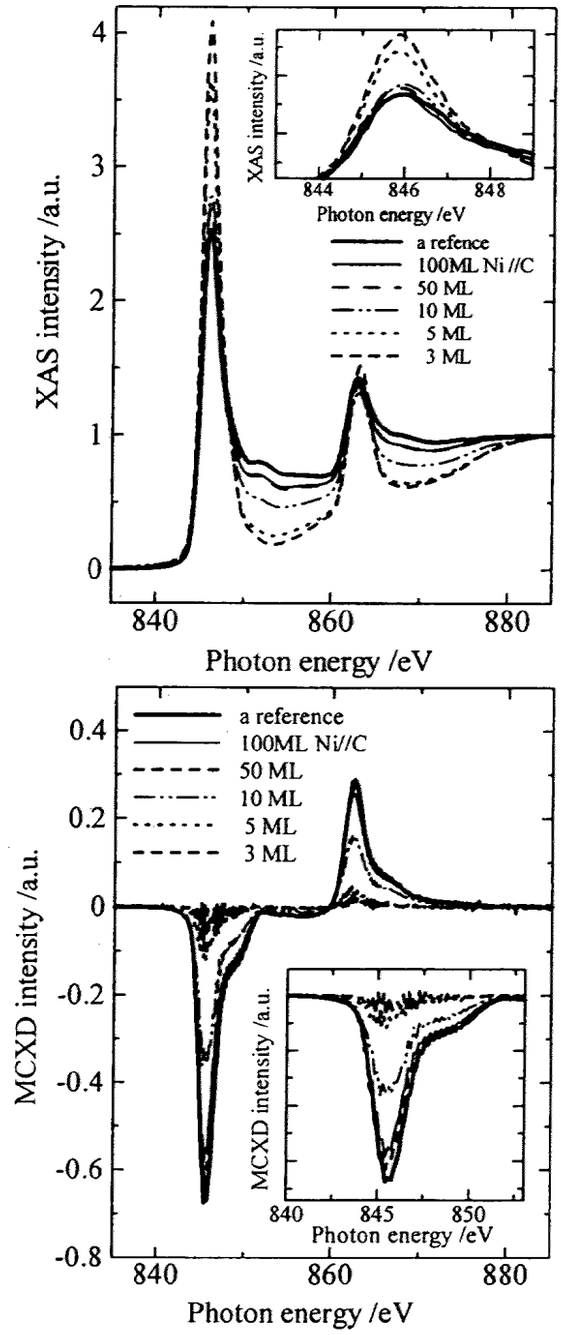

Fig. 6 (1) (*upper side*) XAS of nickel deposits for pulsed current mode. The reference sample is the vapor-evaporated gold/nickel//carbon. Inset is expanded around L_3 peak. (2) (*lower side*) MCXD of these deposits, normalized in a conventional manner.

8

We presume that each XAS mainly contains nickel metallic phase and nickel oxide phase, and then MCXD is not correctly analyzed in the conventional manner, because of non-ferromagnetization of the oxide phase. Hence we try to separate each XAS into the two phases from both XAS of the reference sample and 3ML deposit, which are assumably only the nickel metallic phase and only the nickel oxide phase, respectively. A measured XAS should be fitted using these two XAS. For the 25 ML deposit, a few kinds of XAS calculated by a given "Ni ratio" is shown in Fig. 7(1), where the "Ni ratio" is a mass ratio of Ni phase to both phases, and be unit for the reference sample and be zero for 3ML deposit. The optimum value of the "Ni ratio" is determined by the minimum of the mean squared error between the observed spectra and the calculated one, as shown in the inset of Fig. 7(1). The measured XAS of this deposit is fitted for the "Ni ratio" of 0.73.

We can obtain the MCXD modified in such the rough calculation of XAS, and some of them are denoted in Fig. 7(2). The modified MCXD intensity of electrodeposits is almost similar to that of the reference sample. This means that nickel electrodeposits exhibit the same spin- and orbital-magnetic moments per unit of nickel element as those of bulk nickel, by removing the contribution of the non-magnetic nickel oxide phase of surface layer to them. The inset of Fig. 7(2) is "Ni ratio" used in this calculation. It gradually decreases with a decrease of deposits thickness down to 10 ML, and rapidly reduces for the thinner deposits. It is unfortunately difficult to do this analysis of deposits thinner than 3 ML because of noisy unclear XAS, which might be resulted from the unknown phase as shown in Fig 5. We are now doing the MCXD experiment for gold-covered electrodeposits in order to

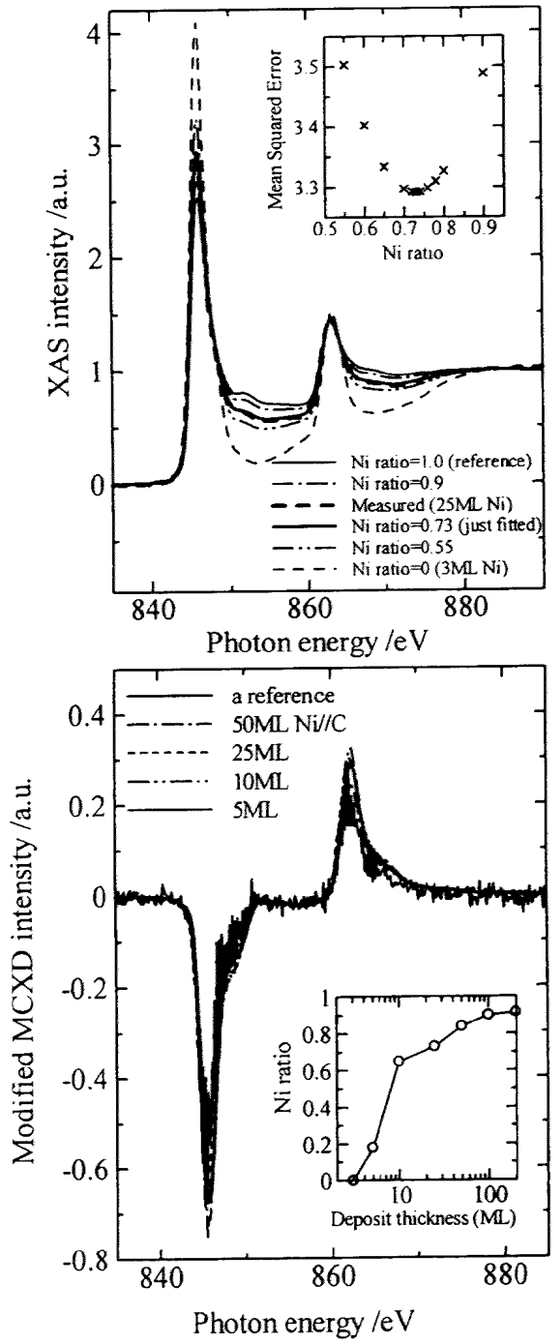

Fig. 7 (1) (*upper side*) Fitting of XAS measured, by using XAS assumed for nickel phase (the reference sample) and nickel oxide phase (3 ML deposit). Inset is MSE (mean squared error) between measured and calculated XAS. (2) (lower side) MCXD modified by the separation of ferromagnetic (nickel) phase and non-ferromagnetic (nickel oxide) phase. Inset is "Ni ratio" used in this modification of MCXD or determined by XAS fitting, and it is defined in the text.

9

remove a contribution of surface oxide layer from XAS, and will anticipate that clearer XAS of the thinner deposits is obtained and is suitable for more precise analysis of XAS and MCXD.

SQUID is well known as the magnetometry with great sensitivity. However it may be afraid that it is difficult to separate only the deposit signal from the sample one. In fact, magnetization is the same order of 10^{-5} emu, for both the thinner deposit and the carbon substrate. So we need the careful sample preparation and interpretation of signals measured. The substrates should not be adhered to other matter containing any ferromagnetic element, during the consecutive process of SQUID measurements subsequently to electrodepositions. The measurement must be occurred immediately after the sample preparation.

Figure 8(1) is magnetization loops for a carbon substrate and a 50ML nickel deposited on it, at room temperature. The inset of Fig. 8(1) is the enlarged loops around zero magnetic field. For the other thicker and thinner deposits, magnetization fully saturates in application of 1T. It is obviously difficult to refer to the fine structure of these loops obtained. Therefore we try to calculate slopes and intercepts of straight lines drawn between points of 1T and a given magnetic field (H_{gn}) up to 7T. Figure 8(2) plots such the slopes and intercepts versus H_{gn}, for a 2 ML deposit. Each value of slope or intercept is the averaged absolute value for pairs of four lines into a loop. Two kinds of slopes were clearly obtained in both the slope- H_{gn} and intercept- H_{gn} curves. For any other samples, boundary points of such slopes exist in the region between 3T and 4T. Such the behavior is not clearly obtained for only the substrate. This means that the region of 1 up to 3T corresponds to the ferromagnetic saturation, and that of 4 to 7T, the saturation of superparamagnetic phase in addition to ferromagnetic one (total magnetic saturation). In this manner, the magnitudes of magnetization saturation can be separable to two components. Each magnitude for only the deposit must be subtracted by that for a substrate from that for the entire sample, by using a pair of their intercept values.

In such the careful analysis, magnetizations were detected for deposits thicker than 0.5 ML. Figure 9(1) shows the total magnetization saturation of ferromagnetic and superparramagnetic phases versus deposit thickness, for gold-coated deposits and bare deposits. The "magnetization ratio" means a ratio

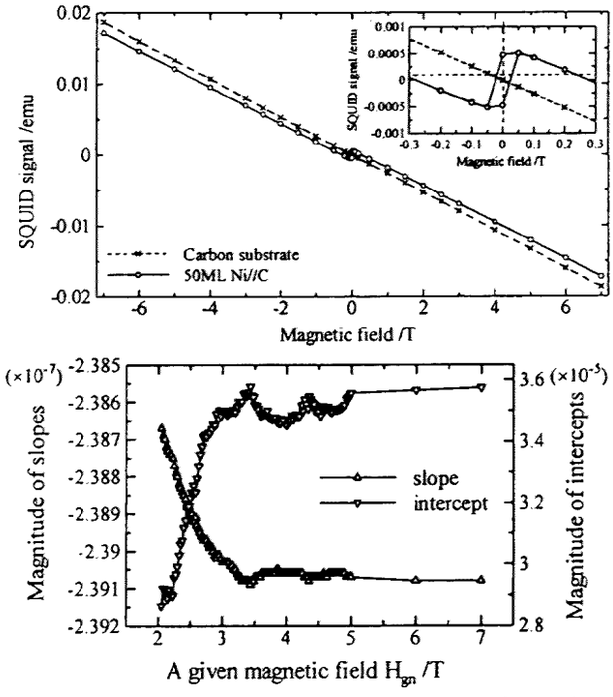

Fig. 8 (1) (*upper side*) Magnetization curves of a carbon substrate and 50 ML deposit by mean of SQUID. Inset is the curves expanded around zero magnetic field. (2) (*lower side*) Slope analysis of magnetization curve. Slope and intercept is calculated for the straight line from 1 T of magnetic field to a given field (H_{gn}). Each profile exhibits two kinds of slopes, the boundary of which exists around 3 to 4T. This behavior means that the ferromagnetic saturation is less than 3 or 4T and superparramagnetic saturation, in addition, is within 7T.

10

of a magnitude of magnetization for a given deposit to that for 100ML deposit. The surface oxidation of this deposit does not contribute much little to the reduction of magnetization than that estimated by MCXD, because of the difference of surface sensitivity between SQUID and MCXD. Error bars of data points represent the region of magnitudes calculated by using possible minimum and maximum values of the individual magnetization of carbon substrates. The magnetization ratio for gold-coated and bare deposits gradually decreases with a decrease of deposit thickness down to a few ML. This must be mainly due to the surface oxidation. It is noted that the surface oxidation was not completely stopped even for gold-coated deposits, which was confirmed by XPS. And also such the oxidation behavior is consistent with XAS and MCXD results of bare deposits as shown in Figs. 6 and 7. Taking account of this behavior, magnetization of deposits rapidly increased with an increase of deposit thickness less than a few ML. The reduction of magnetization of bare 0.5 ML deposit might be again due to the oxidation of surface, comparing with the corresponding gold-coated deposit.

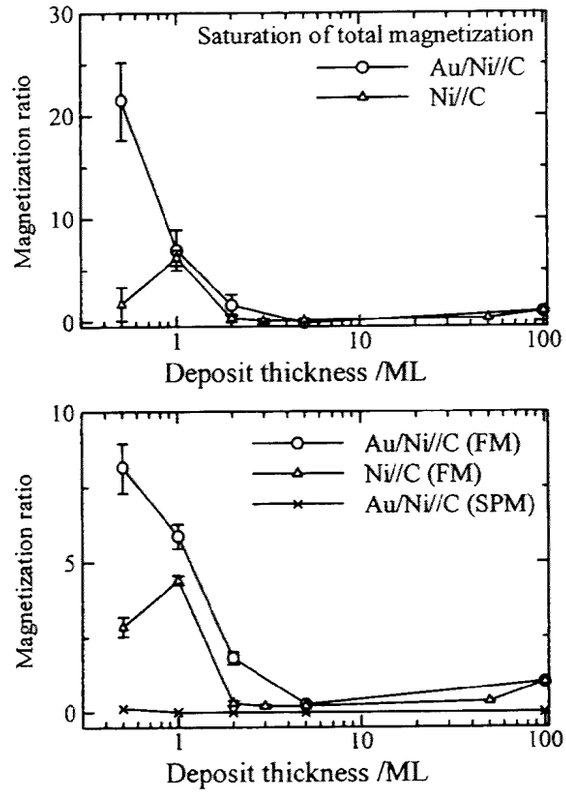

Fig. 9 (1) (*upper side*) Total magnetization saturation of both ferromagnetic and superparamagnetic phases, for gold-coated and bare nickel deposits. "Magnetization ratio" is defined as a ratio of magnetization for a deposit to that for 100 ML deposit. (2) (*lower side*) Separation of ferromagnetic and superparamagnetic saturation of deposits. "Magnetization ratio" is a ratio of the magnitude for ferromagnetic (FM) and superparramagnetic (SPM) saturation to that for 100 ML FM saturation.

Magnetization of ferromagnetic and superparamagnetic phases is separately described in Fig. 9(2). The "magnetization ratio" not only for ferromagnetic component but also for superparamagnetic one means a ratio to ferromagnetic magnetization for 100 ML deposit. The dependency of ferromagnetic saturation on deposits thickness is the similar to that of total magnetization for each gold-coated or bare deposit. A little more amount of superparramagnetic component slightly increases, the thinner the deposits are, and reach to a small amount in 10 %. This behavior is well consistent with MCXD which results in the spin- and orbital- magnetic moments independently of deposits thickness. Here the absolute value of magnetization is about 53 emu/g for 100ML deposits used as standard samples, which is calculated using the mass analysis of ICP-AES.

Therefore, an abnormal increase of magnetization will be ascribed to that of any ferromagnetic phase. This behavior is doubtful because it must not be explained even by the theory for the ultra-thin film or nanostructural particle of pure nickel.(18) Hence, we imagine that this magnetic behavior might be familiar with peculiar nanostructure of electrodeposits, and chemical states containing nickel, nickel oxide, and any unknown phase. However the reduction of magnetization for 0.5 ML bare deposit might mean that

11

nickel oxide phase does not contribute to ferromagnetization at all. We believe that advanced examination of MCXD and ESR (electron spin resonance) of such the deposits will exhibit more detail magnetic phases dependent on temperature for non-oxide surface. Furthermore, this abnormal increase in magnetization proves to be obtained for the deposits on the restricted species of substrates in addition to carbon. We have great expectation of such the magnetic properties dependent on the initial stage of the electrochemical behavior, in terms of the "electrode catalysis" influence by the substrate species.

SUMMARY

We prepared the thin nickel films electrodeposited on amorphous carbon substrates with pulsed current controlled. During this electrodeposition, the electrode potentials of Eimm and Edep shift to the steady state within the region less than about 50 ML. And also, E0 on beginning the reduction of nickel ion shifts up to about 100 ML deposit surface. The "mounds" size of deposit surface may be influenced by the overpotential at the initial stage in such the region less than 50 or 100ML deposits. There is a number of "grains" in the "mounds". The grains size and surface roughness (RMS) drastically change in the narrower region less than a few ML deposit. The variety of grains seem to exhibit for a few nm to 50 nm in size. Such the nanostructure contains not only pure nickel phase but also nickel oxide or unknown oxide phase. The ratio between the pure nickel phase and the oxide phase is analyzed by XAS even on a rough assumption of these two phases. This also results in the similar spin- and orbital-magnetic moments independently of the deposit thicker than 5ML. It is unfortunately difficult to analyze the MCXD for the thinner deposits, because of their complicated phases and the detective sensitivity of MCXD. By careful analysis of SQUID magnetometry, an abnormal increase of magnetization for the deposits thinner than a few ML obtains dependent on deposits thickness. There exist most of ferromagnetic phases and small amount of superparamagnetic one for all the deposits. A gold-coated 0.5 ML deposit exhibits magnetization larger by eighth than that of bulky nickel. This magnetic properties of deposits might be familiar with their peculiar nanostructure resulted from the electrochemical behavior, in terms of the "electrode catalysis" at the initial stage.

ACKNOWKEDGMENTS

MCXD and XAS experiments were performed at the Photon Factory, KEK, under the proposal number of 2000P016 and 2002G006.Thanks are due to Prof. H. Kawata (Photon Factory, KEK) and Prof. K. Mori (Ibaraki Prefectural Univ. of Health Sciences) for the useful discussions of MCXD experiment at the initial stage of this study. We thank many persons for the help of the experimental and technical supports. Dr. S. Abe (the then Myojyo Univ.), Dr. Mamiya (Kagoshima Univ.), Mr. Nakasumi (the then TIT), and Mr. H. Watanabe (IMS) cooperated with MCXD experiment, and Prof. T. Mizoguchi (Gakushuin Univ.) and his laboratory's students, for the AFM observation and the preparation of vapor-evaporated film samples. Dr. T. Nakagawa (IMS) helped us for the experiment of XPS. The production of some sample holders was supported by IMS's technicians, Mr. M. Sakai, Mr. N. Mizutani, and Mr. K. Suzui.

REFERENCE

(1) D. C. Jiles, *Acta Materialia,* **51**, 5907 (2003)

(2) Peng Liu, Qiqin Yang, Yexiang Tong and Yansheng Yang, *Electrochimica Acta,* **45**, 2147, (2000)
(3) A. A. Zhukov, M. A. Ghanem, A. V. Goncharov, P. N. Bartlett and P. A. J. de Groot, *J. Mag. Mag. Mater.*, **272-276**, E1369, (2004)
(4) W. Schwarzacher, D.S. Lashmore, *IEEE Trans. Magn.*, **32**, 3133, (1996)
(5) Nosang V. Myung, D. -Y. Park, B. -Y. Yoo and Paulo T. A. Sumodjo, *J. Mag. Mag. Mater.*, **265**, 189, (2003)
(6) M. Datta and D. Landolt, *Electrochimica Acta,* **45**, 2535, (2000)
(7) K. Maruyama, A. Matsushita, M. Imai, H. Numata, O. Nittono, in Magnetic Materials, Processes and Devices 2000, S. Krongelb, L.T. Romankiw, J.-W. Chang, W. Schwarzacher, C.H. Ahn, Ediotrs, PV2000-29, p. 197, The Electrochemical Society Proceedings Series, Arizona, USA, (2000)
(8) D. M. Kolb, *Surface Science,* **500**, 722, (2002)
(9) K. R. Pirota, D. Navas, M. Hernández-Vélez, K. Nielsch and M. Vázquez, *J. Alloys and Compounds,* **369**, 18, (2004)
(10) D. Landolt and A. Marlot, *Surface and Coatings Technology,* **169-170**, 8, (2003)
(11) Geoffroy R.P. Malpass, Maher Kalaji, Everaldo C. Venancio and Artur J. Motheo, *Electrochimica Acta,* **49**, 4933, (2004)
(12) A. Vicenzo and P. L. Cavallotti, *Electrochimica Acta,* **49**, 4079, (2004)
(13) M. Saitou, W. Oshikawa, M. Mori, and A. Makabe, *J. Electrochem. Soc.* **148**, C780, (2001)
(14) N.A. Pangarov, *Electrochim. Acta*, **7**, 139, (1962), N.A. Pangarov, *J. Electroanal. Chem.*, **9**, 70, (1965)
(15) A. H. MacDonald and C. M. Canali, *Solid State Communications,* **119**, 253, (2001)
(16) K. C. Chan, W. K. Chan and N. S. Qu, *J. Mat. Proc. Tech.*, **89-90**, 447, (1999)
(17) E. Gómez, R. Pollina and E. Vallés, *J. Electroana. Chem.*, **386**, 45, (1995)
(18) (for example) F. Mittendorfer, A. Eichler, and J. Hafner, *Surface Science*, **423**, 1, (1999), M. Alden, S. Mirbt, H. L. Skriver, N. M. Rosengaard, and B. Johansson, *Phys. Rev.*, **B46**, 6303, (1992)

Monte Carlo Simulation for Barkhausen Noise

K. Yamaguchi, S. Tanaka, H. Watanabe, O. Nittono, T. Takagi, and K. Yamada

***Abstract*—In this paper, a new method is proposed for analysis of Barkhausen noise, which is expected to be useful for nondestructive evaluations for iron-based materials, using Monte Carlo simulation. The results show typical properties of Barkhausen noise such as temperature dependence and grain size dependence are well reproduced by this method.**

***Index Terms*—Fatigue, magnetization processes, Monte Carlo method, nondestructive testing.**

I. Introduction

BARKHAUSEN NOISE (BN) is well known to be sensitive for states such as grain size or residual stress in magnetic materials [1]. Therefore, BN is expected as a useful way of nondestructive evaluations (NDE) and many researchers have studied BN for iron-based materials [1]–[9]. The mechanism of BN, however, has not been clearly understood, especially for the relations between BN and micromagnetic states such as grain size, residual stress, dislocations, voids, and so on. But the microscopic study for them is important for making NDE using BN fit for practical use because of quantitative analysis for fatigue.

The difficulty of analysis for BN seems to be in dealing with the dynamic magnetic processes including discontinuous hysteresis curve. For example, the Preisach model, which is well used for magnetic hysteresis analysis, consists of continuous hysteresis curves, hence it is not suitable for BN originally. Therefore, we attempted a new analytical method for BN using Monte Carlo (MC) simulation. We will show this method can reproduce several typical properties of experimental results for BN in this paper.

Fig. 1 shows an experimental setup that we use for measurement of BN. BN is detected by a pickup coil for applied magnetic field formed into a triangle wave (frequency = 15 Hz) between -1 and $+1$ A which are current flowing through an electromagnet. Fig. 2 shows a typical result of BN at room temperature (RT; 300 K) for SS400, which is a steel with a soft magnetic property. BN appears as an induced voltage (V_{BN}) of a pickup coil as shown in Fig. 2(b) with the current for each applied magnetic field in Fig. 2(a). In Fig. 2(b), V_{BN} contains a fluctuation with a triangle wave frequency (15 Hz) depending on a relative position of pickup coil from the magnetic yoke to apply magnetic field, although a high pass filter with a threshold

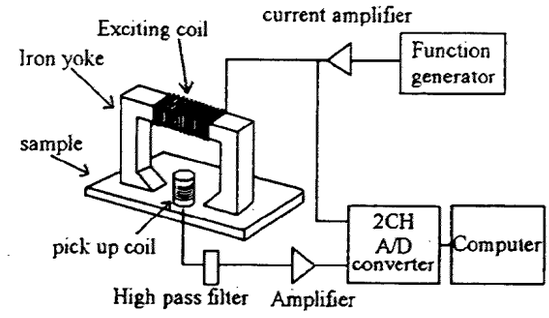

Fig. 1. Schematic view of experimental setup for measuring BN.

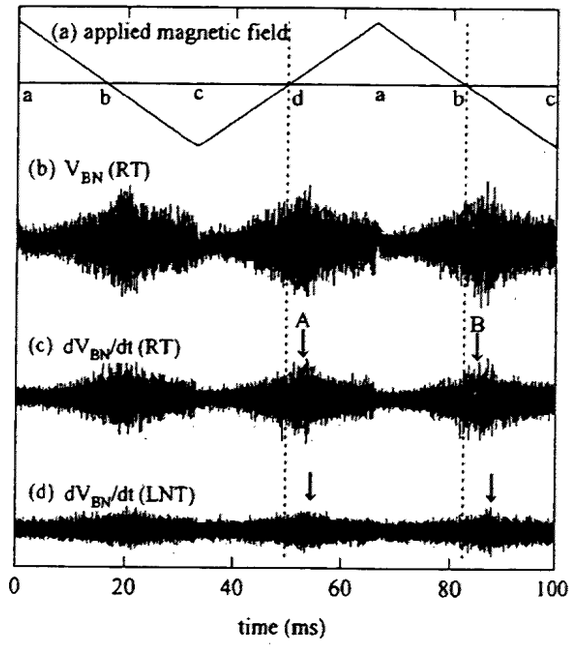

Fig. 2. Experimental results of BN for SS400 at room temperature (RT) and liquid nitrogen temperature (LNT). The intensities of V_{BN} and dV_{BN}/dt are given relatively. In this study, relative comparison between experiments and calculations is meaningful.

frequency of 100 Hz is inserted in the electrical circuit. Therefore, we deal with a first differentiation of V_{BN}; dV_{BN}/dt for analysis as shown in Fig. 2(c), because BN is discrete and it can be approximately regarded as δ function, then the first differentiation remains the information of the original function. On the other hand, the differentiation of the fluctuation is suppressed because of the gradual changes. The result of dV_{BN}/dt at liquid nitrogen temperature (LNT; 77 K) is also shown in Fig. 2(d). We can see some typical properties of BN as follows. The noise intensities show the maximum around at both "A" and "B" (pointed by the arrows in this figure) which locate at the currents just after zero fields ("b" and "d"), and BN decreases

Manuscript received July 1, 2003. This work was supported in part by the Fukushima University Research Promotion Fund.

K. Yamaguchi, S. Tanaka, H. Watanabe, and O. Nittono are with Fukushima University, Fukushima 960-1296 Japan (e-mail: yama@educ.fukushima-u.ac.jp).

T. Takagi is with the Institute of Fluid Science, Tohoku University, Sendai 980-8577, Japan (e-mail: t.takagi@ieee.org).

K. Yamada is with the Faculty of Engineering, Saitama University, Saitama 338-8570, Japan (e-mail: yamasan@fms.saitama-u.ac.jp).

Digital Object Identifier 10.1109/TMAG.2004.824589

around at the turning current points of "c" and "a." It is apparent that the average BN intensity decreases with the lowering temperatures. Furthermore, "A" and "B" field points are influenced by the ambient temperatures. Namely, these fields at LNT are delayed more than those at RT. It may be attributed to the change in the pinning forces for magnetic domain shifts accompanied with thermal spin fluctuations.

The above properties are reproduced by MC simulation as shown in the following sections.

II. Numerical Method

We use a simple spin Hamiltonian of a spin system describing magnetism for simplicity as follows:

$$H = -\sum_{i,j} J_{ij} S_i S_j + B \sum_i S_i. \tag{1}$$

Here S_i denotes the spin state of ith cell, and J_{ij} stands for the effective exchange energy between ith and jth spins. B represents an applied magnetic field. Now the first summation of (1) runs over the nearest neighbor cells with a constant exchange energy J. In the conventional Monte Carlo method, after an initial spin arrangement is first set, the local Hamiltonian of a focused spin is calculated including thermal fluctuation effects. Then a new arrangement is decided by comparison with the energy of other states of this spin. This cycle is ordinarily repeated until getting a stable state [10]–[16]. But now we stopped the repeating before getting a stable state because of dealing with pseudodynamic processes for BN. One MC step (1 MCS) means scanning up to the total cell number of times and 1000 MCS was carried out for one applied magnetic field. Under the constant field condition, the total spin is in an unequilibrium state and going to an equilibrium state with progressing MC steps. The applied magnetic field is given as a step function of MC steps. The step width is taken to be 0.001 and the field changes as a triangle wave between -0.1 and $+0.1$, overall.

As for a typical spin system, a single cubic lattice system composed of $31^3 = 29791$ spin cells ($0 \le x \le 30, 0 \le y \le 30, 0 \le z \le 30$), was prepared for simplicity, although the real α-iron takes the b.c.c. lattice. The single cubic lattice has each side length (L) of 30, given by using one lattice constant as the unit.

Fig. 3 shows an example of a calculation result for magnetization M in (b) and the second differentiation of the magnetization d^2M/dt^2 in (c) under applied magnetic field formed as a pseudotriangle wave in (a). As shown in the upper circle, the triangle wave is constructed from numerous tiny steps. One step is held for 1000 MCS. In a few steps as shown in the lower circle, magnetization has discrete changes, although it has a tendency to decrease in this region on the whole. Here, it is worthwhile to note that the data obtained in the regions less than 1000 MCS are usually renounced because of the data in the meaningless nonequilibrium state. On the contrary, the data elucidate the nonequilibrium state in the steps less than 1000 MCS especially in the transient applied fields. The second derivative of the magnetization including the discrete change with respect to time; d^2M/dt^2

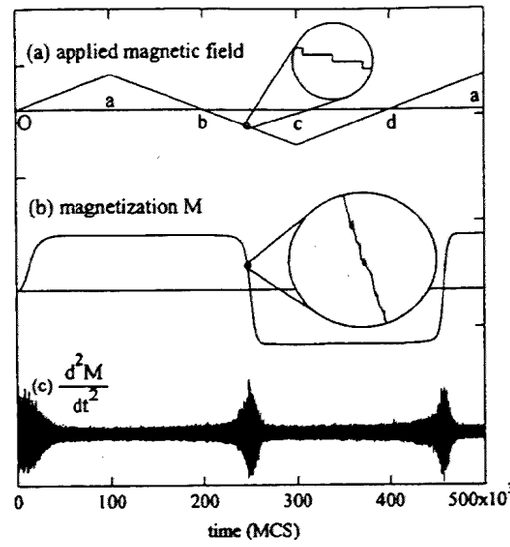

Fig. 3. Example of a calculation result for (b) magnetization M and (c) the second differentiation of the magnetization d^2M/dt^2 under (a) applied magnetic field formed as a pseudotriangle wave.

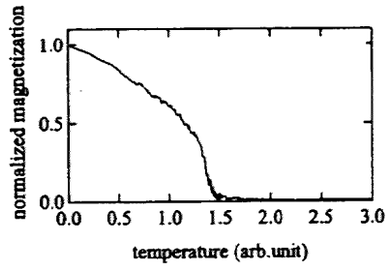

Fig. 4. Temperature dependence of magnetization for a single lattice cubic system composed of 31^3 spin cells.

was calculated to compare with experimental data of dV_{BN}/dt.

The simulations were carried out by using the super-computer, ORIGIN 2000 in the Institute of Fluid Science, Tohoku University. 1 MCS took about 0.3 s and the total CPU time was 99 900 s for a typical calculation.

III. Results and Discussion

Fig. 4 shows the temperature dependence of magnetization in zero external magnetic field under the initial condition of the random spin arrangements corresponding to the paramagnetic state at high temperatures. The calculated result was found to obey well the Curie–Weiss law; therefore, the Curie temperature was estimated at about $T_C = 1.5$. Hereafter, we use this value as the criterion for the temperature.

Fig. 5(a) shows the temperature dependence of the second derivative of the magnetization (d^2M/dt^2) accompanied with applied magnetic field formed as a pseudotriangle wave for the temperature from $T = 0.05$ ($(1/30)T_C$) to $T = 2.0$ ($(4/3)\ T_C$). In the region of higher temperatures than T_C ($T = 1.5, 2.0$), each d^2M/dt^2 shows only a large constant noise and it does not show any particular peak. In the lower temperatures than T_C, the constant noise decreases as temperature goes down. And then noise peaks are revealed in

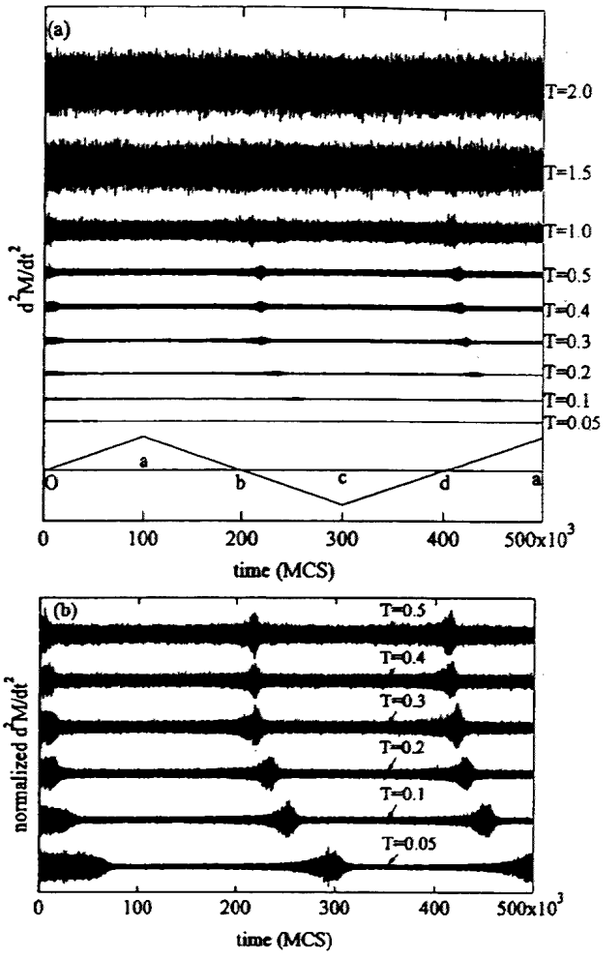

Fig. 5. (a) Temperature dependence of d^2M/dt^2 accompanied with applied magnetic field formed as a pseudotriangle wave for the temperature from $T = 0.05$ ($(1/30)\,T_C$) to $T = 2.0$ ($(4/3)\,T_C$). (b) Normalized d^2M/dt^2 for the temperature from $T = 0.05$ to $T = 0.5$.

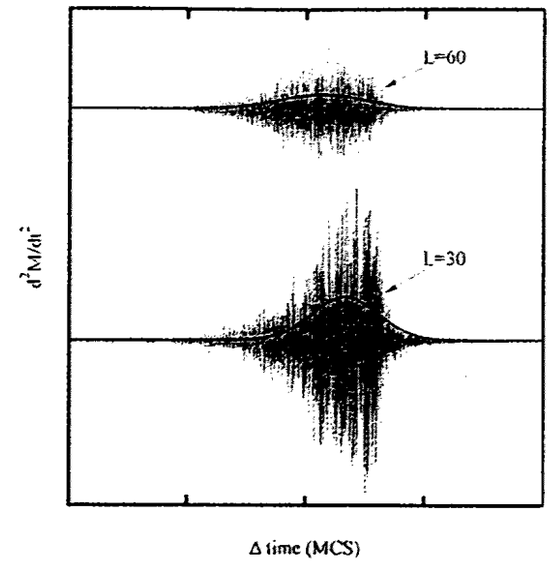

Fig. 6. Normalized d^2M/dt^2s by the number of spin cells at $T = 0.1$ for the spin system with $L = 30$ and 60. Black lines show the Gaussian fitting curve.

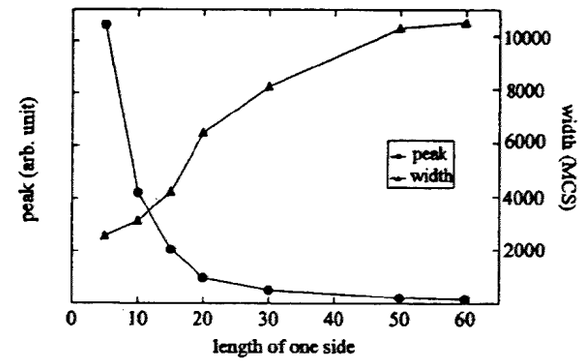

Fig. 7. Grain size dependence of peak intensity and peak width of d^2M/dt^2.

the region of magnetic field between "b" and "c", or "d" and "a." The peak intensity decreases with the temperature.

For more exact analysis, d^2M/dt^2 results normalized by the maximum intensity of themselves are also shown in the region of temperatures under T_C in Fig. 5(b). The amplitude peak of d^2M/dt^2 at $T = 0.5$ appears just after the zero magnetic fields ("b" and "d") and those peaks delay gradually in the lower temperatures. Moreover the deviation of the peak increases as the temperature decreases.

These properties of d^2M/dt^2s well reproduce experimental results of dV_{BN}/dt, namely (i) the average noise intensity decrease with temperature; (ii) the peak of the noise at lower temperatures than T_C appears just after the zero magnetic fields; (iii) the peak at lower temperatures delays; and (iv) the peak intensity decreases with temperature. Therefore, we regard d^2M/dt^2 are a simulated dV_{BN}/dt, namely calculated BN.

The method was applied to the study of the relation between the grain size (i.e., size of spin system) and the behavior of BN. We prepared various sizes of spin systems arrayed as the single cubic lattice with each side length (L) of 5, 10, 15, 20, 30, 50, and 60. Fig. 6 shows the normalized d^2M/dt^2s by the number of spin cells at $T = 0.1$ for the spin system with $L = 30, 60$ on magnetic processes between "b" and "c" of applied magnetic field in Fig. 5(a). The peak intensity of d^2M/dt^2 per a spin cell for $L = 30$ is larger than one for $L = 60$, namely the assembly of the smaller grain induces the greater BN. The Gaussian fitting curves of the absolute normalized d^2M/dt^2s are also displayed as the black line in Fig. 6. We can see the grain size dependences of the peak intensity and the peak width. Fig. 7 shows the dependence for the spin system with $L = 5, 10, 15, 20, 30, 50, 60$. It is clearly seen that the peak intensity decreases and the peak width increases as one side length of spin system becomes larger. Usually BN is measured as the average intensity of induced voltage of pick up coil [17]. But the calculated result suggests that it is very important to measure raw BN data including the peak intensity and the peak width for evaluation of dynamic magnetic processes.

IV. Conclusion

A new analysis method for BN using Monte Carlo simulation reproduced the properties of experimental typical results of BN. The results of temperature dependence for calculated BN

would also be available to recent studies of BN for micromagnetic wires. The grain size dependence of calculated BN suggests that it is very important to measure raw peak features for the detailed analysis of the magnetic state. Moreover, for more exact analysis the peak shape of BN such as asymmetry may be useful. Finally, we can say that the present method has a great potential for analysis tool of BN including other microscopic information such as dislocations and voids.

ACKNOWLEDGMENT

The authors would like thank T. Kinoshita from the Institute of Fluid Science, Tohoku University, for helping in parallel coding programs with Monte Carlo simulation.

REFERENCES

[1] K. Yamada, Y. Tanaka, Y. Uno, H. Takeda, S. Toyooka, and Y. Isobe, "Nondestructive cross evaluations of iron-based material by magnetic sensors and by laser speckle interferometry," *J. Magn. Soc. Jpn.*, vol. 23, pp. 718–720, 1999.

[2] K. Yamaguchi, K. Yamada, S. Shoji, Y. Uno, H. Takeda, S. Toyooka, and H. Tsuboi, "Simulation for nondestructive evaluations by magnetic sensors," *IEEE Trans. Magn.*, vol. 36, pp. 1710–1713, July 2000.

[3] K. Yamaguchi, K. Yamada, and T. Takagi, "Monte Carlo simulation for magnetic materials including dislocation," *IEEE Trans. Magn.*, vol. 38, pp. 865–868, Mar. 2002.

[4] R. L. Pasley, "Barkhausen effect—An indication of stress," *Mater. Eval.*, vol. 28, p. 157, 1970.

[5] H. Kronmuller, "On the mechanism of work hardening in f.c.c. metals," *Can. J. Phys.*, vol. 45, pp. 631–661, 1967.

[6] R. Ranjan, O. Buck, and R. H. Thompson, "A study on the effect of dislocation on the magnetic properties of nickel using magnetic NDE methods," *J. Appl. Phys.*, vol. 61, pp. 3196–3198, 1987.

[7] D. C. Jiles, "Review of magnetic methods for nondestructive evaluation," *NDT Int.*, vol. 21, pp. 311–319, 1988.

[8] A. J. Birkett, W. D. Corner, B. K. Tanner, and S. M. Thompson, "Influence of plastic deformation on Barkhausen power spectra in steels," *J. Phys. D, Appl. Phys.*, vol. 22, pp. 1240–1242, 1989.

[9] H. Kronmuller, *Coercivity and Domain Wall Pinning in Magnetic and Superconducting Materials*, J. Evetts, Ed. New York: Pergamon, 1992.

[10] N. Metropolis, A. Rosenbluth, M. Rosenbluth, and A. Teller, "Equation of state calculations by fast computing machines," *J. Chem. Phys.*, vol. 21, pp. 1087–1092, 1953.

[11] D. W. Heermann, *Computer Simulation Methods in Theoretical Physics*. Berlin, Germany: Springer-Verlag, 1990.

[12] K. Binder, *Phase Transitions and Critical Phenomena*, C. Domb and M. S. Green, Eds. London, U.K.: Academic, 1976, vol. 5B, pp. 2–100.

[13] G. Parisi, *Statistical Field Theory*. Reading, MA: Addison-Wesley, 1988.

[14] C. Ebner, "Phase diagrams of multilayer films and the Potts lattice-gas model of adsorption," *Phys. Rev. B*, vol. 28, pp. 2890–2892, 1983.

[15] ——, "Film formation on a weakly attractive substrate within the lattice-gas model," *Phys. Rev. A*, vol. 22, pp. 2776–2781, 1980.

[16] J. Marro and R. Dickman, *Nonequilibrium Phase Transitions in Lattice Models*. Cambridge, U.K.: Cambridge Univ. Press, 1999, pp. 12–60.

[17] R. Hill, A. Cowking, and J. Mackersie, "The effect of nickel hardness and grain size on acoustic and electromagnetic Barkhausen emission," *Nondestruct. Test Eval. Int.*, vol. 24, p. 179, 1991.

Available online at www.sciencedirect.com
SCIENCE DIRECT®
Physica B 343 (2004) 298–302
PHYSICA B
www.elsevier.com/locate/physb

Monte Carlo simulation of dynamic magnetic processes for spin system with local defects

Katsuhiko Yamaguchi[a,*], Shinya Tanaka[a], Osamu Nittono[a], Toshiyuki Takagi[b], Koji Yamada[c]

[a] *Faculty of Education, Fukushima University, 1 Kanayagawa, Fukushima 960-1296, Japan*
[b] *Institute of Fluid Science, Tohoku University, Sendai 980-8577, Japan*
[c] *Department of Materials Science, Saitama University, Saitama 338-8570, Japan*

Abstract

Monte Carlo simulations of the dynamic magnetic processes were performed for spin systems with various lattice imperfections. From a physical point of view, the presented method might be the more useful tool for the analysis of the magnetic processes rather than those by Preisachs model.

PACS: 02.70.Uu; 75.60.Ej

Keywords: Monte Carlo method; Magnetization process; Barkhausen noise

1. Introduction

Localized potentials in magnetic materials generated by e.g. impurities, dislocations, voids, residual stress, play important roles for these magnetic properties. Especially, Barkhausen noise (BN) is sensitively generated by these localized potentials. Therefore, BN is expected as a measurement tool for nondestructive evaluation and many researchers have studied BN for iron-based materials [1–9]. The microscopic processes and the method of the analyses for BN, however, have not been sufficiently studied. The difficulty of BN analysis seems to be caused by the dynamic process including localized potentials intrinsically. The approach by the itinerant spin models for the iron-based materials such as the Storner model, seems attractive, because it can take in the microscopic interactions among the various magnetic states. However, it is evident that these are not suitable for the magnetic system with localized potentials because these models are developed under the homogeneous or periodic conditions. Preisach model has been frequently adopted for the simulations to derive the magnetic hysteresis. BN, however, are caused by the discontinuous magnetic dynamic processes. Therefore, Preisach model for the compositions of the complete continuous hysteresis loops could not be suitable for BN analyses. On this physical concept, we tried to adopt the Monte Carlo (MC) simulations of the magnetic dynamic processes for the spin systems

*Corresponding author. Fax: +81-24-548-8189.
E-mail address: yama@educ.fukushima-u.ac.jp (K. Yamaguchi).

0921-4526/$ - see front matter © 2003 Elsevier B.V. All rights reserved.
doi:10.1016/j.physb.2003.08.059

with various localized potentials. The method dealing with a discrete lattice system is known available to analyze the continuous material structures in vicinity of criticality [10–16]. Therefore, the method dealing with the local spin system has an advantage to derive the specific magnetic property caused by the various localized potentials, e.g. arbitrary local defects or dislocations. In this paper we discuss on the validity of the MC simulations for BN. A proposal of an alternative analysis is given for spin systems with localized potentials, rather than that by the Preisach model.

2. Numerical method

A simulation was performed for a typical spin system composed of $31^3 = 29791$ cells ($0 \leqslant x \leqslant 30$, $0 \leqslant y \leqslant 30$, $0 \leqslant z \leqslant 30$) standing for the single-cubic lattice instead of the α-iron (BCC), for simplicity. Here, we adopted a simple spin Hamiltonian describing the magnetism as below

$$H = -J \sum_{i,j} S_i S_j + B \sum_i S_i. \quad (1)$$

Here S_i denotes the spin state of ith cell (Heisenberg spin), and J stands for the effective exchange energy. B represents applied magnetic field. In general Hamiltonian should include other interactions, such as magnetic anisotropy or magnetic dipole interaction between spins which play important roles for formation of magnetic domains. Here, we neglect these interactions for simplicity. This assumption might be justified, because the BN is given rise to by the discrete movements of magnetic domain walls, and not by the domains themselves. Now the first summation of Eq. (1) runs over the nearest neighbor cells with a constant exchange energy $J = 1$. That is, the exchange interaction cannot reach between spins separated by the void planes directly. In general, the MC method is performed with an initial spin arrangement and the local Hamiltonian of a focussed spin is calculated under the thermal equilibrium. And then, a new spin arrangement is decided in comparison with the energy of another arrangement of the spins. Hitherto, this cycle is repeated until the stable state is obtained.

In the present trial, we stopped repeating the cycle before getting a stable state because we deal with pseudo-dynamic process for BN. Under the temporally increasing field condition, the total spin system is in a non-equilibrium state and shifts to another non-equilibrium state with progresses of the MC steps. So in this study, the magnetic fields were treated as quasi-static process. The applied fields were fixed for an extent of a time. Here, the "one MC step" (1MCS) means to scan up to the total cell number (31^3) and 1000 MCS was carried out for one applied magnetic field. The applied magnetic field is given as a step function of MC steps. The typical step width was taken to be $\Delta B = 0.01$ and the field changes as a pseudo-triangle wave between −1 and +1 overall. Fig. 1(a) shows an example for an applied magnetic field and the change of magnetization in a series of 5000 MCS, which are a part of the numerous MC steps. In a few steps, the magnetization shows discrete changes, although it reveals a tendency to decrease as shown in the circles in the whole range of this figure. Namely, the magnetization includes continuous component (M_C) and discontinuous component (M_D). Here it is worthwhile to note that the

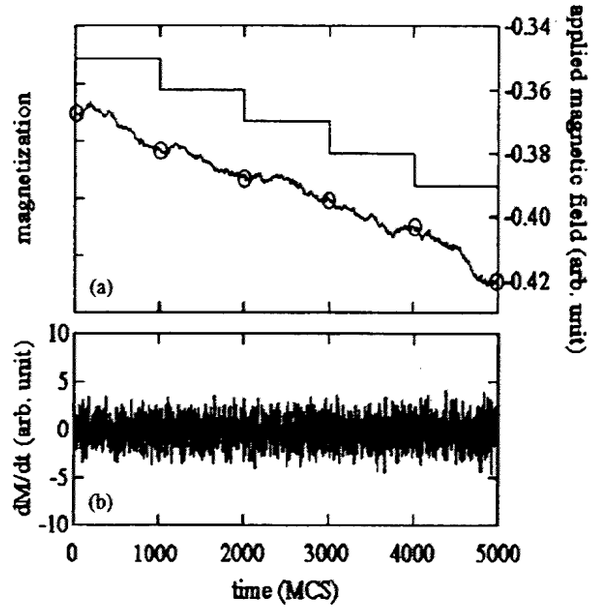

Fig. 1. An example of MC step dependence on (a) applied magnetic field and magnetization, (b) dM/dt.

data obtained in those less than 1000 MCS are usually renounced due to that in the meaningless non-equilibrium. On the contrary, the data elucidate the non-equilibrium state in the steps less than 1000 MCS especially in the transient applied fields. Fig. 1(b) shows the first derivatives of magnetization with respect to time: dM/dt using the method as explained above. Here $dM/dt = d(M_C + M_D)/dt \sim dM_D/dt$ (because of $dM_D/dt \gg dM_C/dt$).

The simulations were carried out by using the super-computer, ORIGIN 2000 in the Institute of Fluid Science, Tohoku University. 1MCS took about 0.3 s and the total CPU time was 99900 s for a typical calculation.

3. Results and discussion

Fig. 2 shows the temperature dependence of magnetization for the spin systems with three different sizes (total cell numbers $n = 16^3, 31^3, 51^3$) in zero external magnetic field under the initial condition of the random spin arrangements corresponding to the paramagnetic state at high temperatures. Each calculated result well obeys the Curie–Weiss law and the Curie temperature was estimated at about $T_C = 1.5$. In the lowest temperature the magnetization for $n = 51^3$ is not saturated yet, and it seems to attribute to an insufficiency of MCS for the larger spin systems than $n = 31^3$. We deal with a spin system composed of 31^3 cells in the discussions below.

The results for magnetic field dependence of magnetization (M–H curve) are shown in Fig. 3 at two temperatures; $T = T_C/2$ and T_C. Magnetization is saturated in the magnetic field of 0.7 at $T_C/2$. Here, we must discuss on the fact that the saturation fields in this calculation depend not only on the ambient temperatures, but also on the field increments, ΔB. These might be caused by the non-equilibrium state. Therefore, we should also regard ΔB as a parameter in our model and should take a suitable value of ΔB corresponding to a real spin system in comparison with the experimental values for the physically realistic analysis. Now for explaining our model accurately, we discuss on a fixed ΔB. Along the magnetic processes of O→a→b→c→d→e→f→a in Fig. 3, dM/dt were calculated at the temperatures of $T = T_C/2$, $3T_C/4$ and T_C as shown in Fig. 4. Fig. 5 shows the experimental results of BN for SS400, which is a steel with a soft magnetic property, at room temperature (RT:300 K) and liquid N_2 temperature (LNT:77 K), respectively. BN was detected by a pick-up-coil in the applied magnetic fields with a triangle waveform (frequency = 15 Hz, $I = \pm 1$ A in a solenoid coil). The noise intensities show the maximum about at both "A" and "B" (pointed by arrows in this figure) which locate at currents just after zero fields, and BN decreases around at the turning current points of "d" and "a". It is apparent that the average BN intensity decreases

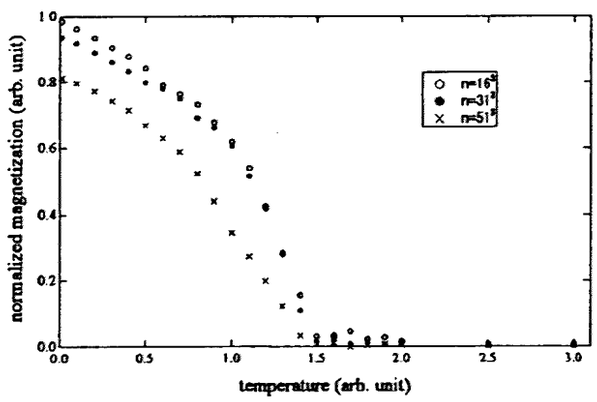

Fig. 2. Calculated result for temperature dependence of magnetization for the spin systems with three different sizes.

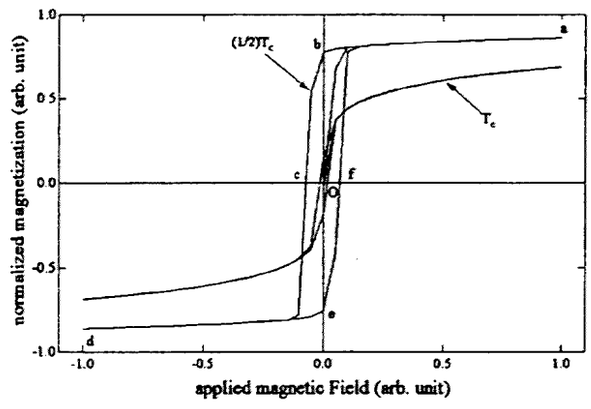

Fig. 3. Calculated result for magnetic field dependence of magnetization (M–H curve) at T_C ($T = 1.5$) and $T_C/2$ ($T = 0.7$).

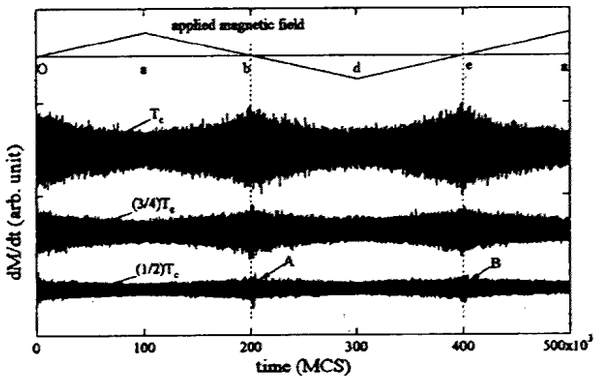

Fig. 4. Differential calculus dM/dt of the magnetic process under applied magnetic field formed into a pseudo-triangle wave.

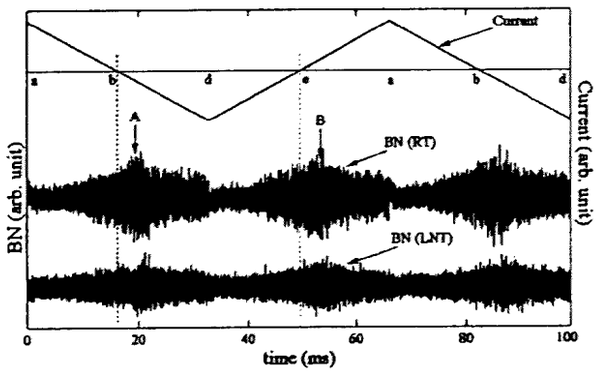

Fig. 5. Experimental result of Barkhausen noise for a steel (SS400) under applied magnetic field formed into a triangle wave at room temperature (RT:300 K) and liquid N_2 temperature (LNT:77 K).

with the lower temperatures. Further, "A" and "B" field points are influenced by the ambient temperatures. Namely, these fields at LNT are delayed more than those at RT. It will be attributed to the change in the pinning forces for magnetic domain shifts accompanied with thermal spin fluctuations. Simulated behaviors of dM/dt show a good accordance with experimental results of BN in some respects. The most important feature in this simulation is the elucidation of the temperature dependence of average BN intensity. Namely, the simulation successfully shows the decreasing tendency of the intensity with temperatures. The amplitude peak of dM/dt at T_C occurs close in the zero magnetic fields ("b" and "e" in Fig. 4) and those peaks at $3T_C/4$ and $T_C/2$ delay slightly in the lower temperatures. Taking account of Curie temperature of SS400 ($T_C \approx 1000$ K), the delay times from the cross point of zero magnetic fields to the ranges with the peak intensity of BN show a good coincidence between experimental BN and simulated dM/dt. Furthermore, in the field range between the peaks, a gradual and monotonic noise changes are realized in the present simulation. Therefore, we consider that BN is well simulated by the dM/dt in this model. One of discrepancies between experimental BN and simulated dM/dt is a tail shape over their peak intensities. It may be caused by the difference between the manner of the various imperfections and the simulations.

Further, the grain size dependence of dM/dt was calculated at temperature of $T_C/2$ as shown in Fig. 6. An original 31^3 spin cells-cluster was divided into 2, 4, 8, 27 and 64 clusters and inserted void planes at these planes to isolate both sides from the exchange interactions. The relationship between the cluster numbers and BN ($=dM/dt$) amplitudes shows monotonous decrease with increasing the spin numbers, similar to experimental results [17]. Finally, the influences of local defects were studied on the localized potential and these densities. One void plane for a role of the local defect accumulations was introduced into original 31^3 spin cells for modeling of the edge dislocation at $x = 15$, $8 \leqslant y \leqslant 22$, $8 \leqslant z \leqslant 22$. Periodic boundary condition was applied to the spin cell cluster surfaces in order to investigate on the influence only by the local defects to avoid the surface effects. To avoid thermal effects, temperature was set at $T = 0.1$. Fig. 7 shows an angle dependence of simulated BNs as a function of different applied magnetic fields between e→a in

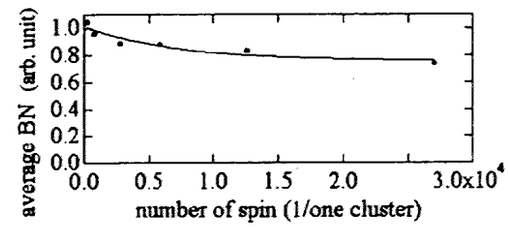

Fig. 6. Relation between average of Barkhausen noise and spin cluster size.

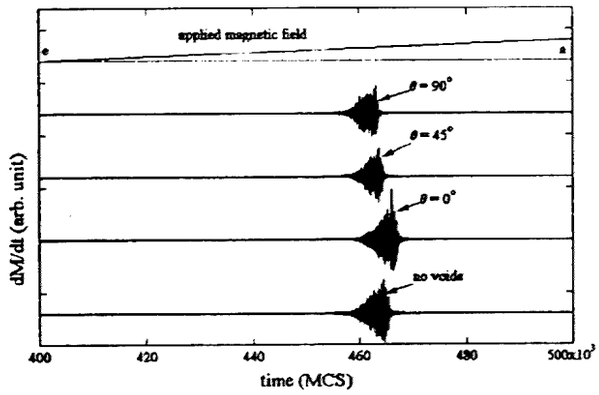

Fig. 7. Angle dependence of Barkhausen noise for the system with plane typed voids modeling of an edge dislocation at $\tilde{}=0.1$.

Fig. 3 with the field condition along the x-axis ($\theta=0$), inclined at 45° from x- to y-axis ($\theta=45$) and y-axis ($\theta=90$) for the presented spin system. It is apparently seen, the anti-symmetry behaviors between $\theta=0$ and 90. The tendency of angle dependence of simulated BN is correspondent to experimental data [2].

As mentioned above, a simulated BN by MC method well reproduced an experimental BN, and the method shows the possibility of a useful tool for the analysis of dynamic magnetic processes.

Acknowledgements

We would like to express our thanks to T. Kinoshita in the Institute of Fluid Science, Tohoku University for helping in parallel coding programs with MC simulation.

References

[1] K. Yamada, Y. Tanaka, Y. Uno, H. Takeda, S. Toyooka, Y. Isobe, J. Magn. Soc. Japan 23 (1999) 718.
[2] K. Yamaguchi, K. Yamada, S. Shoji, Y. Uno, H. Takeda, S. Toyooka, H. Tsuboi, IEEE Trans. 36 (2000) 1710.
[3] K. Yamaguchi, K. Yamada, T. Takagi, IEEE Trans. Magn. 38 (2002) 865.
[4] R.L. Pasley, Mater. Eval. 28 (1970) 157.
[5] H. Kronmuller, Can. J. Phys. 45 (1967) 631.
[6] R. Ranjan, O. Buck, R.H. Thompson, J. Appl. Phys. 61 (1987) 3196.
[7] D.C. Jiles, NDT Int. 21 (1988) 311.
[8] A.J. Birkett, W.D. Corner, B.K. Tanner, S.M. Thompson, J. Phys. D: Appl. Phys. 22 (1989) 1240.
[9] H. Kronmuller, in: J. Evetts (Ed.), Coercivity and Domain Wall Pinning in Magnetic and Superconducting Materials, Pergamon Press, Oxford, 1992.
[10] N. Metropolis, A. Rosenbluth, M. Rosenbluth, A. Teller, J. Chem. Phys. 21 (1953) 1087.
[11] D.W. Heermann, Computer Simulation Methods in Theoretical Physics, Springer, Berlin, 1990.
[12] K. Binder, in: C. Domb, M.S. Green (Ed.), Phase Transitions and Critical Phenomena, Vol. 5B, Academic Press, London, 1976, pp. 2–100.
[13] G. Parisi, Statistical Field Theory, Addison-Wesley, Redwood, 1988.
[14] C. Ebner, Phys. Rev. B 28 (1983) 2890.
[15] C. Ebner, Phys. Rev. A 22 (1980) 2776.
[16] J. Marro, R. Dickman, Nonequilibrium Phase Transitions in Lattice Models, Cambridge University Press, Cambridge, 1999, pp. 12–60.
[17] R. Hill, A. Cowking, J. Mackersie, NDT E Int. 24 (1991) 179.

Observation of magnetic structures in Fe granular films by differential phase contrast scanning transmission electron microscopy

Takumi Sannomiya, Yumiko Haga, Yoshio Nakamura,[a] and Osamu Nittono[b]
Department of Metallurgy and Ceramics Science, Tokyo Institute of Technology, 2-12-1 Ookayama, Meguro-ku, Tokyo, 152-8550, Japan

Yoshio Takahashi
Research and Development Group, Hitachi, Ltd., 1-280 Higashi-Koigakubo, Kokubunji, Tokyo 185-8601, Japan

(Received 27 June 2003; accepted 7 October 2003)

Differential phase contrast (DPC) scanning transmission electron microscopy was applied to investigate the magnetic structures of Fe granular films. The DPC images showed a cluster-like contrast of 200 nm in the lateral size, which could not be observed by Lorentz transmission electron microscopy in the Fresnel mode. The magnetization vector map reproduced from the DPC images indicated that a magnetization loop generally intersects several isolated particles of 20–40 nm in diameter. The films composed of densely dispersed magnetic particles showed larger magnetization loops, while more separately dispersed films tended to have smaller loops, or magnetization closures in one particle. The loop size is associated with the strength of magnetic interaction between magnetic particles. © *2004 American Institute of Physics.* [DOI: 10.1063/1.1630356]

I. INTRODUCTION

Magnetic granular films have been investigated extensively because of the unique properties of the granular system, such as tunneling magnetoresistance[1] and soft magnetic behavior.[2] The magnetic properties have been reported to be sensitive not only to the geometry of individual particles, such as size, shape, and crystal orientation, but also to the distribution of particles. The magnetic interaction between the particles has been one of the main topics of discussion for a wide variety of technological applications.[3–7] Magnetic granular systems have also been adopted in recording media where one recording bit consists of a number of magnetic particles. Magnetization fluctuation is a problem at the interface of neighboring recording bits as it is one of the main causes for recording noise. Such magnetization fluctuation can be reduced by isolating the magnetic particles to reduce the exchange interaction. In the next-generation recording method, called the "dot-bit method," one recording bit would be a single isolated magnetic particle. In either case, magnetic dipole interactions exist among the particles. Therefore, a better understanding of the magnetic interactions in granular systems is needed. As the magnetic structure can reflect the magnetic interaction, microscopic observations of both the magnetic structure and the corresponding film microstructure are effective approaches to evaluate local magnetic interactions.

Magnetic force microscopy (MFM) is widely used for micromagnetic observation because of both its relatively high resolution and convenience.[3–6] However, the contrast of the images produced by this method is rather difficult to interpret. MFM detects only the leakage of magnetic flux from the specimen, and the surface roughness disturbs the magnetic information, which is a common problem in other types of scanning probe microscopy. The defocused Fresnel mode of Lorentz transmission electron microscopy (LTEM) is also a popular method for analysis of thin films although the resolution of this method is not sufficient to allow acquisition of fine magnetic structures.

In this study, we adopted differential phase contrast scanning transmission electron microscopy (DPC–STEM), which is a method for the direct observation of internal magnetization of specimens with both high spatial and magnetic resolution.[8–11] This method allows simultaneous acquisition of both magnetic and microstructural images in the same area.

Ohnuma *et al.* proposed that the soft magnetic granular system has a larger magnetic structure than particle size.[12] Zhu *et al.* demonstrated by simulation that magnetic particles interact with each other to form magnetization loops.[13] The aim of the present study was to experimentally confirm the magnetic interaction of the particles with direct comparison of the distributions of particles.

In this article, we first describe the effectiveness of DPC–STEM observation on the magnetic granular system in comparison with the Fresnel mode of LTEM, and then discuss the magnetic structures of two specimens with different film microstructures. We also discuss the experimental results in terms of magnetic interactions.

II. EXPERIMENT

Specimens were prepared by ion beam sputtering using Xe gas. The base pressure was less than 3×10^{-6} Pa. A SiO_2 amorphous film deposited on a cleaved NaCl plate was used as a substrate. After the deposition of a very thin Fe granular

[a]Electronic mail: yoshio@mtl.titech.ac.jp
[b]Present address: Faculty of Education, Fukushima University, 1 Kanayagawa, Fukushima 960-1296, Japan.

layer, the surface was covered again with a SiO_2 layer to avoid oxidation. SiO_2 and Fe targets can be changed in the same vacuum chamber so that all the layers can be deposited without exposure to air. The SiO_2/Fe/SiO_2 sandwich film was then floated on pure water, where the NaCl plate was dissolved, and was skimmed with a Cu No. 400 grid. Two types of Fe granular films, samples I and II, with different particle sizes and distributions were prepared by controlling the substrate temperature (up to 400 °C) and the sputtering rate. Before transmission electron microscopy (TEM) and DPC–STEM observations, all the specimens were ac-demagnetized at room temperature.

A conventional transmission electron microscope (CTEM) (JEM3010) was used to determine the dispersion as well as the microstructure of the film. For DPC–STEM observation, we used a modified STEM based on HF-2000, which has a new specimen position, a magnetic shield that protects the specimen from the magnetic field due to lenses, and a four-segmented detector. The focused electron beam traveling through the specimen is deflected by magnetization of the specimen. The angle and amplitude of the Lorentz deflection are calculated by differentiation of the detected signal along x and y axes of the segmented direction of the detector.[9] As the Lorentz deflection is proportional to the magnetization of the film, quantitative analysis is potentially possible, although such analyses were not performed in this study. The DPC signal was divided by the total signal so that absorption contrast and crystalline contrast were cancelled out, hence, allowing extraction of the magnetic contrast. The spatial resolution was estimated to be about 5 nm, and the residual magnetic field in the specimen position was less than 1 Oe.[14] We confirmed that the magnetic field from the objective or condenser lenses did not influence the initial magnetic state of the films during observation by rotating the specimen horizontally in the specimen holder or by setting the specimen twice.

It is generally difficult to determine the absolute value of the Lorentz deflection angle, or color of zero value with no reference. We set the average value of the contrast as zero, because the film has no magnetization on average in the ac-demagnetized state. As the Lorentz deflection is perpendicular to the magnetization, the DPC-x image shows the y component of magnetization in the film, while the DPC-y image shows the x component. Combination of the images of the x and y components enables us to reproduce the magnetization mapping of the film.[8–11]

III. RESULTS

A. Sample I

The particles in the film were mostly rotational ellipsoid in shape with a height of less than 10 nm, as determined by field emission scanning electron microscopy of the films without a covering SiO_2 layer. The easiest axis of magnetization of particles of this shape is along the film plane due to the strong shape anisotropy. Therefore, it can be assumed that magnetization inside the particle aligns along the film plane. Figure 1 shows a CTEM micrograph of a film consisting of particles of 30–40 nm in diameter (sample I). In

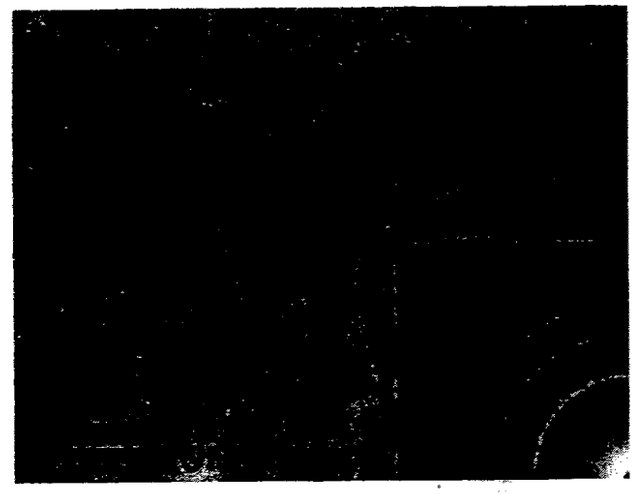

FIG. 1. CTEM bright-field image of sample I. The particle size and the gap were estimated to be 30–40 and 2–5 nm, respectively. The inset shows the electron diffraction pattern.

places, groups of two or three particles are connected to form islands 80–100 nm in length. The number of connected particles, however, did not exceed five. The average distance among the constituent particles was estimated to be 2–5 nm. Although some tiny particles were found among the main particles, they were considered to be superparamagnetic at room temperature and not to influence the ferromagnetic behavior of the film. The electron diffraction pattern of the film is also shown in the inset. Only α-Fe (bcc) Debye rings were found with no preferential orientation. Thus, the magnetic easy axis of the particles had a random orientation.

To understand the relationship between TEM images (or microstructure) and magnetization, we first used the Fresnel mode of LTEM. A Fresnel image of the film subjected to ac-demagnetization is shown in Fig. 2. Although the contrast due to magnetization in the film (or magnetic contrast) was not obvious, the hazy appearance of magnetic contrast changed appreciably after different magnetic treatments (data not shown). Therefore, the magnetic information was thought to be included in the image. However, it was very difficult to interpret, because the contrast derived from scat-

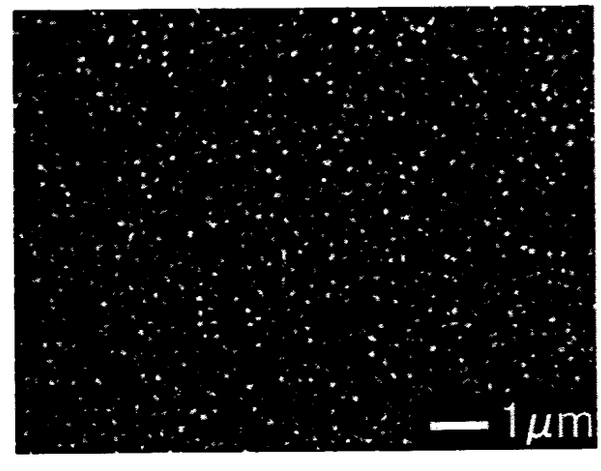

FIG. 2. Fresnel image of sample I after ac-demagnetization.

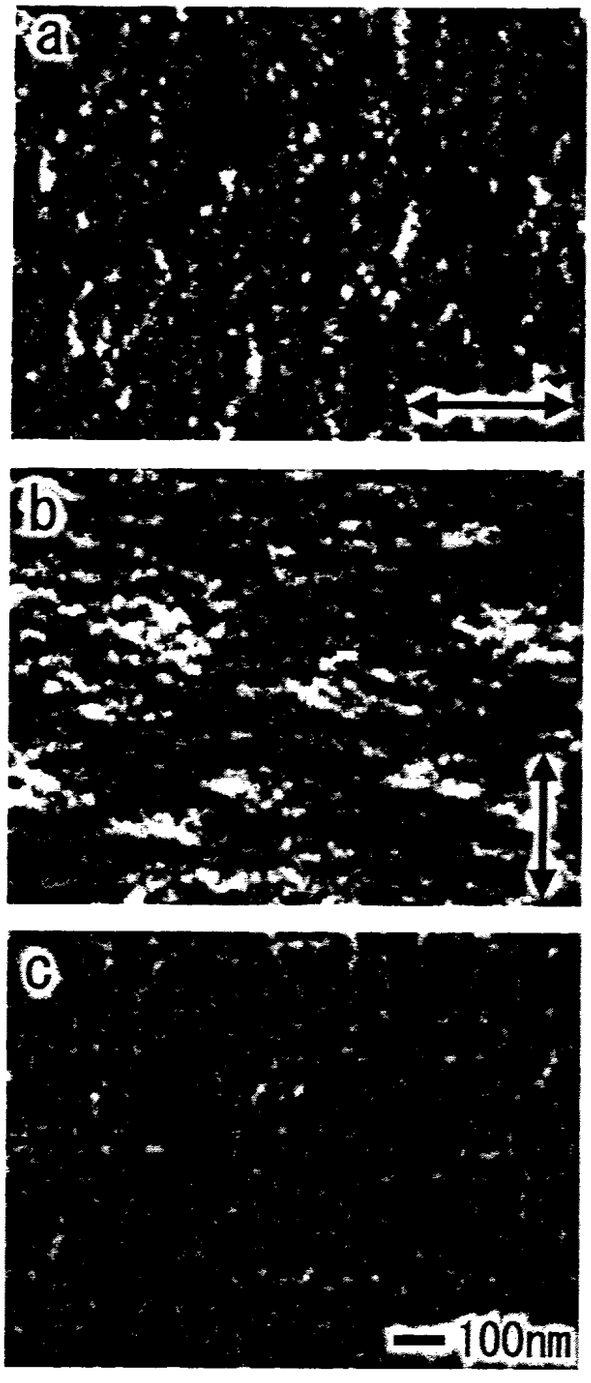

FIG. 3. DPC images of sample I. The arrows indicate the direction of differentiation. (a) Differentiated along the x axis, corresponding to the y component of magnetic flux. (b) Differentiated along the y axis. (c) STEM bright-field image. Three images were acquired simultaneously.

tering due to the inner potential of the particles disturbs the magnetic contrast under conditions of large defocus, which is inevitable in the Fresnel mode.

For further or qualitative interpretation of magnetization in the film, we employed DPC–STEM observation. The DPC images shown in Figs. 3(a) and 3(b) display clear black and white regions of 200–300 nm in diameter, which appear to be elongated in the y direction for Fig. 3(a), and in the x direction for Fig. 3(b). They were much larger than the particle size observed in the corresponding STEM bright-field

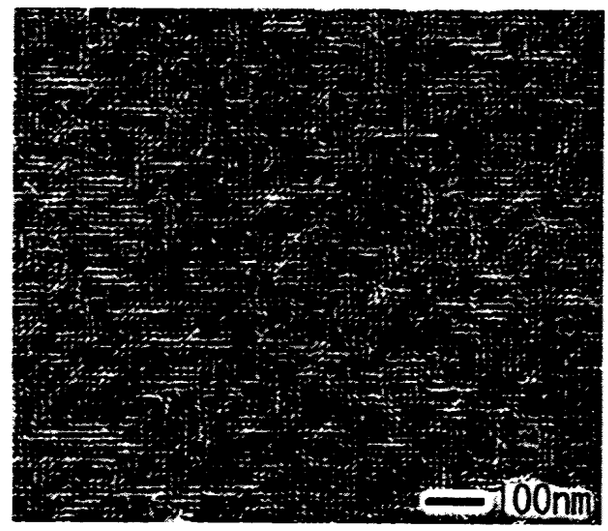

FIG. 4. Vector map of magnetization of sample I. The STEM bright-field image is superimposed on the vector map.

(BF) image [Fig. 3(c)]. A magnetization vector map was produced from the results of analysis of two DPC images as shown in Fig. 4, where the corresponding STEM BF image is superimposed on the vector map to allow for comparison with the microstructure of the film. The arrows indicate the average magnetization vectors corresponding to areas of about 10×10 nm. The length of the arrow is equivalent to the magnitude of the magnetization vector.

The magnetization state in the film was fairly continuous throughout several physically isolated particles. This observation indicated that the ferromagnetic interaction between neighboring Fe particles aligns the internal magnetization of each particle and thus the magnetic flux bridges the nonmagnetic gaps between neighboring particles. The magnetic flux tends to be straight when the gap distance is short, or turns toward other closer particles where the magnetic interaction is stronger. In this manner, the magnetic flux results in formation of magnetization loops and thus reduces magnetostatic energy by averting free magnetic poles in the film. The elongated black/white region in the DPC images, as shown in Figs. 3(a) and 3(b), was due to the morphology of the loop. These results indicate that the interaction between neighboring particles can be analyzed by a combination of a vector map and the corresponding BF image.

B. Sample II

For comparison, we observed another film with larger gap distances than sample I. Figure 5 shows a CTEM BF image of such a film consisting of particles of 25–40 nm in diameter with gap distances of 4–6 nm (sample II). Individual Fe particles, equivalent in size and shape to those of sample I, had few connections with neighboring particles. The Fresnel image was similar to that of sample I except that sample II showed a slightly weaker contrast than sample I under the same defocus conditions.

Figure 6 shows a magnetization vector map reproduced from the DPC images taken from sample II. The STEM BF image was again superimposed on the vector map, which

FIG. 5. CTEM bright-field image of sample II. The particle size and the gap were 25–40 and 4–6 nm, respectively. The inset shows the electron diffraction pattern.

differed in appearance from that of sample I. Comparison of the two maps indicates that the continuous regions of magnetization were very sparse in sample II, and even in such continuous regions the magnetic flux indicated by the arrows showed small closed loops including fewer particles.

IV. DISCUSSION

A. Evaluation of magnetization using vector maps

The magnitudes of the magnetic flux, or the length of the arrow on each point in the film, were not always constant. Possible reasons for this include: (1) local fluctuations in magnetic flux may have reduced the average vector slightly; (2) there may have been overlapping of the nonmagnetic contrast from the edge of the particle;[15] (3) leakage flux running in the opposite directions above and below the film may have canceled out the Lorentz deflection from the film; or (4) there may be a perpendicular component of magnetization.

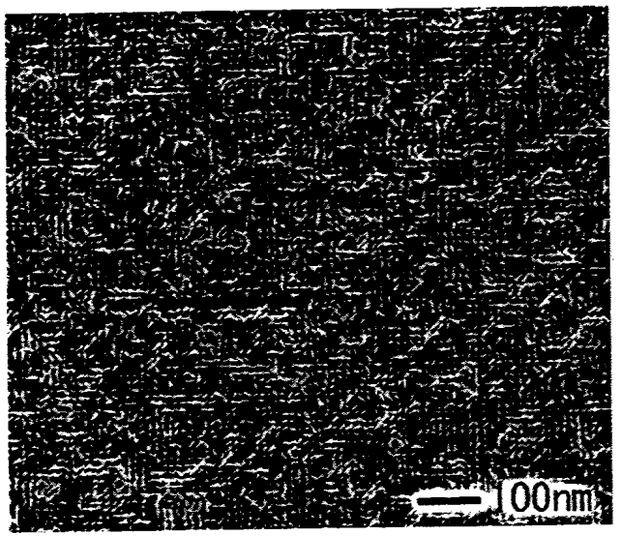

FIG. 6. Vector map of magnetization of sample II. STEM bright-field image is superimposed on the vector map.

With the exception of the second possibility, other factors do not alter the direction of the vector significantly. The nonmagnetic contrast is, however, negligible under appropriate observation conditions, such as with optimal defocus.[15] Although we chose focusing conditions in which the nonmagnetic contrast from the particles was minimized, such a contrast is visible around the particles, where aberrations in the focus can occur, or when small signals due to Bragg reflection enhance the nonmagnetic edge contrast. However, the magnetic contrast was confirmed by under- and overfocusing in the present study.

B. Comparison of the two samples

Comparison of the two samples with different particle distributions confirmed that a slight difference in the gap between the particles can affect the granular interaction to form magnetic clusters consisting of several particles that result in large magnetization loops. In the case of iron particles of about 30 nm in diameter observed in this study, the critical distance is around 2–3 nm. With gaps smaller than this value, the particles tend to form magnetic clusters, or closed magnetization loops in a large region, as shown in Fig. 4. On the other hand, when the gap is larger, the magnetic flux tends to be closed inside the particle or to form smaller magnetization loops, as shown in Fig. 6. We conclude that the granular interaction and the resulting magnetization loops reflect the macroscopic magnetic properties of these heterogeneous films.

C. Magnetic interaction

After ac-demagnetization, in the case of completely isolated single domain particles, the magnetization of each particle should be randomly distributed along the easy axis of Fe particles, because no preferential orientation was found in the electron diffraction patterns. When the magnetostatic energy is dominant compared to magnetocrystalline anisotropy energy or exchange energy, the magnetization inside the particle is known to be closed axial-symmetrically, as single-domain particles have more magnetostatic energy without any magnetic interaction.[16] That is, the magnetic flux makes a vortex inside the particle. In fact, we confirmed such a magnetization vortex in perfectly isolated particles in other films. Sample II resembles this case.

Zhu *et al.* conducted a simulation of magnetization for a magnetic granular system, and demonstrated that when the interaction becomes weaker, the loop of the magnetic flux becomes smaller.[13] Their results were qualitatively consistent with our experimental results. It has also been reported that the formation of such closed loops always showed demagnetizing interaction, or negative deviation in the remanence plot.[17] The elongated magnetization loops consist of magnetization of one direction and its counterpart, where neighboring particles have opposite magnetization. Such magnetic structures may exhibit negative deviation in the remanence plot.

The following macroscopic magnetic behaviors can be presumed in our samples. Sample I would have larger susceptibility and show a squarer $M-H$ curve, as the particles

behave in a group and flip the direction together as an "avalanche" in magnetization reversal.[18] Meanwhile, the particles of sample II behave individually with less interaction, and the resultant macroscopic magnetic behavior would be a simple sum of those of single particles.

When the particles interact strongly with each other as observed in sample I, the film is expected to show soft ferromagnetic properties. Ohnuma *et al.* reported that Co granular film exhibited soft magnetic properties when the particles were magnetically connected with a cylinder-like morphology with no preferential crystalline orientation, while it exhibited TMR when the particles were isolated by a sufficient distance.[12] Their cylinder interpretation of the small angle x-ray scattering spectrum profile probably corresponds to the straight parts of the elongated magnetization loops observed in the Fe granular system in the present study.

In a granular recording medium, the magnetic interaction betweens the magnetic particles should be reduced to realize more stable bits throughout the film. For the dot-bit recording method, individual particles must be perfectly magnetically isolated, whereas to increase the recording density the particles must be located as closely as possible to each other.

V. CONCLUSIONS

Using the DPC–STEM, we examined the fine magnetic structure of granular films consisting of physically isolated ferromagnetic particles dispersed two-dimensionally without overlapping particles. Simultaneous observation of both the magnetic and geometrical structure indicated that the local interparticle distance determines the alignment of magnetization of the particles. After ac-demagnetization, the magnetic flux in the local regions linked throughout several particles in the closely dispersed film, and as a result, loops were formed including several particles. On the other hand, a more dispersed film showed smaller loops of magnetic flux. We confirmed experimentally that magnetic interactions between the particles resulted in magnetization loops the size of which was associated with the strength of the magnetic interaction.

ACKNOWLEDGMENTS

This work was supported by Special Coordination Funds for Promoting Science and Technology on "Nanohetero Metallic Materials" and a Grant-in-Aid for Scientific Research (No. 15360331) from the Japanese Ministry of Education, Culture, Sport, Science, and Technology.

[1] J. Q. Xiao, J. S. Jiang, and C. L. Chien, Phys. Rev. Lett. **68**, 3749 (1992).
[2] S. Ohnuma, S. Furukawa, H. Fujimori, S. Mitani, and T. Masumoto, J. Alloys Compd. **222**, 167 (1995).
[3] H. Takahoshi, S. Ishio, H. Saito, and K. Kobayashi, J. Magn. Magn. Mater. **237**, 231 (2001).
[4] V. Franco, X. Battle, and A. Labarta, J. Magn. Magn. Mater. **221**, 45 (2000).
[5] Q. Y. Xu, H. Chen, H. Sang, X. B. Yin, G. Ni, J. Lu, M. Wang, and Y. W. Du, J. Magn. Magn. Mater. **204**, 73 (1999).
[6] V. Franco, X. Battle, A. Valencia, A. Labarta, K. O'Grady, and M. L. Watson, IEEE Trans. Magn. **34**, 912 (1998).
[7] H. Weinforth, Ch. Somsen, B. Rellonghaus, A. Carl, and E. F. Wassermann, IEEE Trans. Magn. **34**, 1132 (1998).
[8] J. N. Chapman, P. E. Batson, E. M. Waddell, and R. P. Ferrier, Ultramicroscopy **3**, 203 (1978).
[9] J. N. Chapman, I. R. McFadyen, and S. McVitie, IEEE Trans. Magn. **26**, 1506 (1990).
[10] J. N. Chapman, Mater. Sci. Eng., B **3**, 355 (1989).
[11] Y. Yajima, Y. Takahashi, M. Takeshita, T. Kobayashi, M. Ichikawa, Y. Hosoe, Y. Shiroishi, and Y. Sugita, J. Appl. Phys. **73**, 5811 (1993).
[12] M. Ohnuma, K. Hono, H. Onodera, S. Ohnuma, and J. S. Pedersen, J. Appl. Phys. **87**, 817 (2000).
[13] J. G. Zhu and H. N. Bertman, IEEE Trans. Magn. **27**, 3553 (1991).
[14] Y. Yajima and Y. Takahashi, Hitachi Instrument News **25**, 3 (1993).
[15] Y. Takahashi and Y. Yajima, J. Appl. Phys. **76**, 7677 (1994).
[16] M. L. Néel, Comtes rendus des séances de l'Academie des Sciences **224**, 1488 (1947).
[17] V. Patel, M. El-Hilo, K. O'Grady, and R. Wchantrell, IEEE Trans. Magn. **29**, 3622 (1993).
[18] G. F. Hughes, J. Appl. Phys. **54**, 5306 (1983).

Correlation between magnetization performance and magnetic microstructure of patterned permalloy films fabricated by microcontact printing

Takumi Sannomiya, Ji Shi,[a] and Yoshio Nakamura
Department of Metallurgy and Ceramics Science, Tokyo Institute of Technology, 2-12-1 Ookayama, Meguro-ku, Tokyo 152-8550, Japan

Osamu Nittono
Faculty of Education, Fukushima University, 1 Kanayagawa, Fukushima 960-1296, Japan

(Received 29 March 2004; accepted 2 August 2004)

Permalloy films were patterned by two simple methods, direct etching and lift-off, which are based on the microcontact printing method. Several kinds of patterns, including chessboard, stripe, grid, and rectangular dot patterns, have been produced. These patterned permalloy films reveal varied magnetization behavior that originate from the differences in the shape of the pattern-consisting elements. The magnetic structure of the chessboard pattern film was investigated by Fresnel and Foucault modes of Lorentz transmission electron microscopy. It is found that the square elements of the patterned film exhibit vortexlike magnetization closures, although some connections between the elements remained due to insufficient etching. The macroscopic magnetization process of the chessboard-patterned film was explained in reference to the *in situ* magnetization-distribution observation of the specimen along a minor magnetization loop. We also tried to control the rotational sense of the "vortices" in the square elements by using a gradient field. © *2004 American Institute of Physics*. [DOI: 10.1063/1.1796512]

I. INTRODUCTION

Fabrication methods of patterned magnetic thin films have been extensively investigated due to the great potential of such patterned magnetic films as high-density magnetic recording media for the next generation. As patterning by self-assembled methods introduces inevitably defects such as "vacancies" or "dislocations" into the patterned films, artificial lithography is considered to be the most reliable and direct approach.[1] Several different lithographic methods have been applied to the patterning of magnetic films so far, e.g., electron beam lithography, photo lithography using UV light or x rays, and soft lithography.[2–5] Among them, microcontact printing (μCP), one of the techniques of soft lithography, has attracted great attention because of its high resolution, easiness for handling, low cost, and versatile applications.[6,7] Owing to these advantages, the μCP-assisted lithography is considered suitable for contrastive studies between macroscopic and microscopic magnetization behaviors as well as mass production.[8] Meanwhile, in order to understand the magnetic performance of a patterned magnetic film, and to determine the dimension of the elements consisting of the pattern for practical application, it is necessary to know the magnetic structure of the film, especially the magnetic structure inside an element. Lorentz transmission electron microscopy (LTEM) has been proved to be a powerful means to observe the magnetization distribution in magnetic films because of its relative high resolution and straightforward magnetic contrast compared with other methods such as magnetic force microscopy.[9]

In the present study, we propose a simple method for patterning permalloy films, which utilizes the μCP technique to form alkanethiol self-assembled monolayer mask on the surface of a gold/permalloy film. The patterned permalloy films were evaluated through macroscopic magnetization measurements and LTEM observations of magnetization distribution. We have previously reported that the magnetization distribution of a sample could be controlled by use of the objective lens field of a TEM,[10] we also conducted such controlling operations for the patterned films in this work.

II. EXPERIMENTS

A. Preparation of patterned films

Poly-dimethylsiloxane (PDMS) stamps used in this work were molded from the ultrasharp silicon gratings (Mikro Masch) with Sylgard 184 silicone elastomer (Dow Corning). Ethanol solution of 1 mM dodecanethiol was used as the ink for the μCP. Two patterning methods, direct etching and lift-off, were employed for the patterning of 78-permalloy films, which are schematized in Fig. 1.

For the direct-etching method, a permalloy film of 50 nm in thickness was first magnetron-sputtering deposited onto the surface of a silicon wafer with natural oxide layer. Then a gold layer of 50 nm was deposited onto the surface of the permalloy film by evaporation [Fig. 1(a)]. After the gold/permalloy film was deposited, the dodecanethiol ink was printed onto the surface of the gold layer with a stamp to form a pattern which functions as a mask for the following wet etching. The masked film was then dipped into the etching solution, a mild ferri/ferrocyanide solution, until nonmasked areas of the gold layer were etched completely. The

[a]Electronic mail: shi@mtl.titech.ac.jp

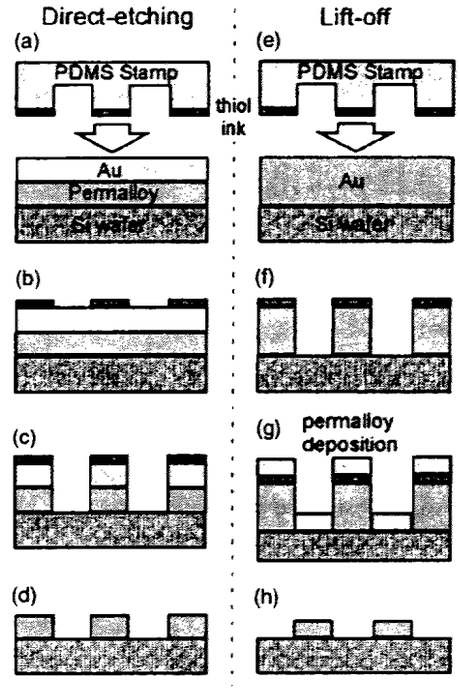

FIG. 1. Schematized processes for patterning permalloy film by direct-etching (a)–(d) and lift-off (e)–(h) methods.

pattern was transferred to the permalloy film by further selective wet etching with 5% nitric acid solution, and in this circumstance, the patterned gold layer worked as a mask [Fig. 1(c)]. For the preparation of TEM specimens, the gold mask layer was removed by excessive etching with ferri/ferrocyanide solution in order to reduce the thickness of the specimens [Fig. 1(d)].

For the lift-off method, a gold layer of 100 nm was deposited on a silicon substrate by evaporation and was then patterned by the μCP with dodecanethiol [Fig. 1(f)]. In this case, a titanium layer less than 3 nm thick was introduced between silicon and gold to improve the adhesion. The patterned gold layer worked as a resist for the following hard lift-off process. Following the patterning of the gold-layer, a 40 nm permalloy layer was deposited onto the sample surface by magnetron sputtering and then the gold resist was removed by ferri/ferrocyanide solution [Figs. 1(g) and 1(h)]. As seen in Fig. 1(f), the permalloy pattern fabricated by lift-off method is just the negative of the initial gold resist pattern.

B. Characterization

A scanning laser microscope (SLM, Olympus, OLS 1200) capable of imaging the specimen surface with submicron spatial resolution for a large area was used for the characterization of the patterned films. Since the contrast of SLM depends mainly on the reflectivity of the film surface, the surface morphology was further confirmed by atomic force microscopy (AFM, Seiko Instruments, Nanopics 1000) that gives surface roughness information. Magnetization curves of the patterned films were measured by vibrating sample magnetometer (VSM, Riken Denshi, BHV-50H). A transmission electron microscope (TEM, JEOL, JEM 2010, 200 kV)

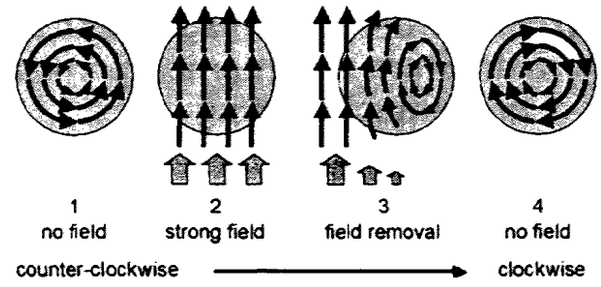

FIG. 2. Schematic illustration of rotational control method by use of gradient magnetic field. The black and the gray arrows indicate the magnetic flux and the applied magnetic field, respectively.

was used to observe the microstructure and the magnetic structure in the patterned permalloy films, and the TEM specimen was thinned by ultra low angle ion milling. Fresnel and Foucault modes of LTEM were employed to observe the magnetic structures in a complementary manner. For these modes, a lens located 10 cm below the specimen was used as an objective lens instead of the conventional objective lens whose location is near the specimen position, so that the specimen would not be magnetized by the lens field. On the other hand, for the observation of the *in situ* magnetization process, the magnetic field was applied to the specimen by the conventional objective lens. In this case, the specimen was tilted from the horizontal position, so that the in-plane component of the magnetic field was utilized. We considered that the field was effective only along the specimen plane because of the strong demagnetizing field in the perpendicular direction caused by the shape anisotropy.[11] The applied field was reversed before saturation. The control of the rotational senses of the magnetization vortices was also tried by means of applying gradient field as shown in Fig. 2. It is known that the objective lens of a TEM produces a strong local magnetic field around the specimen position. Therefore, by drawing out the specimen from the specimen position gradually, the specimen is subject to a field gradient.[10] Furthermore the specimen was tilted 70° from the horizontal position in order for the specimen to be magnetized in the in-plane direction, and the specimen was kept tilted while being drawn out.

III. RESULTS AND DISCUSSION

A. Pattern morphology

SLM images of the patterned films fabricated by the direct-etching method are shown in Fig. 3. As the subsequent etching of the gold capping layer [as illustrated in Fig. 1(f)] was not conducted for this observation, the bright contrast corresponds to the remaining gold/permalloy layers; this was also confirmed by AFM. Three different patterns of chessboard, stripe, and grid were fabricated with good uniformity for a large area (1.8×1.8 mm^2 for the chessboard, 3×3 mm^2 for the stripe and grid). The grid pattern was produced by stamping the stripe stamp twice at the right angle. The chessboard pattern consists of arrays of 1.2×1.2 μm^2 squares that are partly connected to each other at the corners.

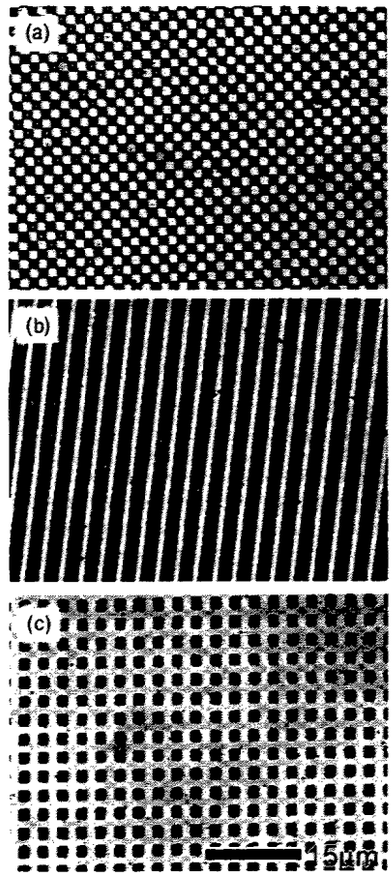

FIG. 3. SLM images of gold/permalloy films patterned by direct-etching method. (a) chessboard, (b) stripe and (c) grid patterns.

The stripe in the stripe-patterned permalloy film in Fig. 3(b) has a dimension of 3 mm $\times$ 2 μm $\times$ 50 nm with a spacing of 1 μm.

Using the lift-off method, a pattern of isolated rectangular dot arrays was fabricated with permalloy film (Fig. 4), which corresponds to the negative of the grid pattern shown in Fig. 3(c). Each dot has a dimension of 1 μm $\times$ 0.5 μm $\times$ 40 mm and was arrayed with a pitch of 3 μm. However, the pattern was not uniformly generated over the whole stamped area (3 $\times$ 3 mm^2), which is probably because that the edges of the film was covered by permalloy layer, and the

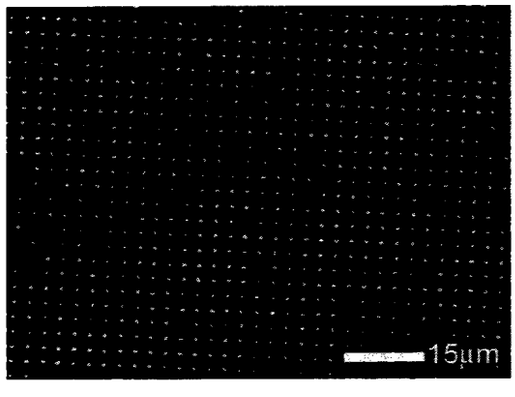

FIG. 4. SLM image of permalloy rectangular dot arrays patterned by lift-off method.

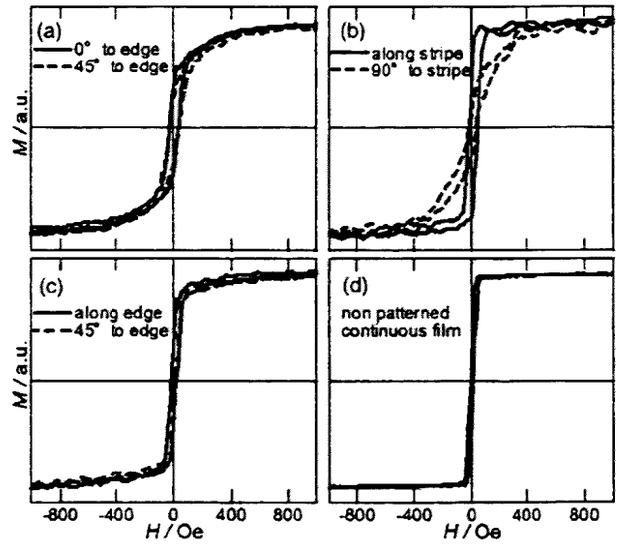

FIG. 5. Magnetization curves of permalloy films patterned by direct-etching method. The measuring angles are different for different patterns: (a) chessboard pattern measured at 0° (solid) and 45° (dashed) to the edge line, (b) stripe pattern measured at 0° (solid) and 90° (dashed) to the stripe line, (c) grid pattern measured at 0° (solid) and 45° (dashed) to the edge, and (d) nonpatterned continuous film.

subsequent gold etching in the lift-off process [Figs. 1(g) and 1(h)] did not work perfectly. Eventually, the uniformly patterned area was about 1 $\times$ 3 mm^2.

To summarize the above results, we consider that the μCP-assisted lithography, such as the direct etching and the lift-off methods as we proposed in this paper, is an easy and inexpensive large area patterning technique for magnetic films. Moreover, it is also applicable to mass production since it is possible to produce a pattern of large area by using the rolling stamp method.[12]

B. Magnetization curves

Macroscopic magnetization curves of uniformly patterned films by direct-etching method were measured by VSM. Figure 5 shows the magnetization curves of the patterned films of (a) chessboard, (b) stripe, and (c) grid features. The measurements were conducted along different directions depending on the feature of the patterns, because the magnetization behaviors of the pattern-consisting magnetic elements depend on the measuring direction in which the magnetic field is applied owing to the shape anisotropy.[5,13] In the present work, all the measurements were conducted along the film plane, and the measuring angle was rotated laterally. The measuring angles were 0° and 45° to the edge of a square element for the chessboard pattern, 0° and 90° to the stripe for the stripe pattern, and 0° and 45° to the lattice line for the grid pattern, respectively. The magnetization curve of a nonpatterned permalloy film is also shown in Fig. 5(d) for comparison. It is seen from the figures that the patterned film with chessboard feature was not easily saturated along both directions and has a rather high coercivity compared to the other patterned films. The magnetic performance of the chessboard pattern will be discussed in more detail in a later section with reference to the observation of the mag-

netic structure. For the stripe-patterned films, the demagnetizing field due to the shape anisotropy is explicit when the measurement is conducted along the direction perpendicular to the stripes. Since the effective field can be calculated for a cuboidal object, the magnetization curve measured along the perpendicular direction was corrected and the result is consistent with that measured along the stripes, whose demagnetizing field is negligible. The grid pattern film shows small deviation from the nonpatterned film as the grid pattern is basically continuous and the square holes do not function as effective pinning sites. Therefore the domain wall propagation can occur easily, resulting in a large permeability. However, the grid pattern film needs stronger field for complete saturation than the nonpatterned film does, which is probably due to the fact that the magnetization lies along the edges of the square holes. It has been reported that the remanent ratio of such a grid pattern film exhibited periodic measuring-angle-dependence, and the measurements at angles of 0° and 45° to the lattice line show the lowest and the highest remanent ratio respectively.[5] Figure 5(c), however, shows weak angle dependence probably due to the large size of the features. The edge effect would be stronger with a smaller feature size of the pattern.

C. TEM observation of chessboard patterns

The microstructure of the patterned films, including grain size and crystalline orientation, is one of the crucial factors to determine the magnetic properties as well as shape anisotropy. The bright field image and selected area diffraction patterns proved that the permalloy film had grains of around 10 nm in diameter without any preferential crystalline orientation. As the grain size was far smaller than the element size, the crystalline effect was considered to be negligible.

Magnetization distribution of the chessboard pattern, whose magnetic behaviors could not be easily explained, was observed by Fresnel and Foucault modes of LTEM. The specimen was first magnetized perpendicular to the film plane and was then demagnetized to ensure a demagnetized state at the beginning, and we observed the same area by different modes of LTEM to avoid misinterpretation of the magnetic contrasts. Overfocused and underfocused Fresnel images and Foucalt images with different aperture placements are shown in Fig. 6. The contrasts of some areas are not very clear owing to the thickness of the remaining silicon substrate. This can be overcome by comparing the images of different modes. It is noted that some corners of the square elements are connected to the neighboring elements, although not all the corners are connected. In addition, some small-scale contrasts can be observed along the edges of the square elements, which may be originated from the defects or contaminations introduced to the elements during the preparation the TEM specimen by ion milling.

In the case of Fresnel mode observation, the magnetic domain walls are imaged as dark or bright lines, and the contrasts of the magnetic domain walls are reversed by underfocusing and overfocusing. While magnetic domains are imaged as dark or white regions in the case of Foucault mode

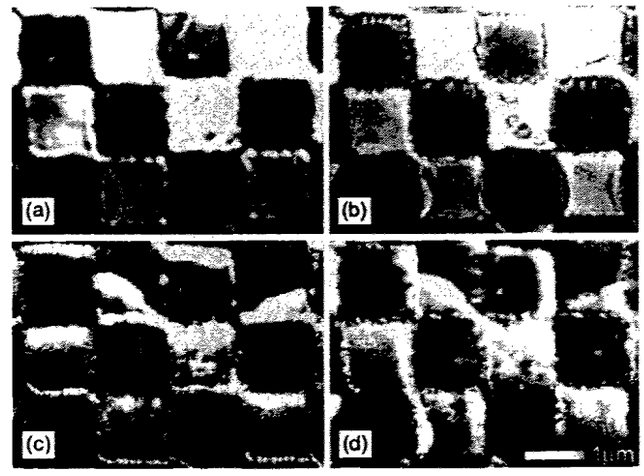

FIG. 6. LTEM images of the chessboard pattern, (a) Fresnel mode, underfocused, (b) Fresnel mode overfocused; (c) and (d) Foucalt modes. The defocus length is about 3 mm for (a) and 1 mm for (b); and in (c) and (d) vertically and horizontally deflected electron beams were used.

observation, and domains with different magnetic moment orientations can be observed by choosing the deflected electron beams with an aperture. In this manner, it is possible to reproduce the magnetization distribution from the four images of Fig. 6, and the result is shown in Fig. 7. It is seen that the magnetization forms a closure in each square element to avoid the formation of magnetic poles at the edges, and magnetic domain walls extended from the center to the corners. It is also found that the rotation of the magnetization closure has only one "vortex" center and two opposite senses of rotation, clockwise and counter clockwise. The rotational senses of the neighboring elements tend to be opposite when they are connected to each other to have parallel magnetization at the adjoining parts. This magnetic structure of the magnetization closure is similar to the magnetization vortex in a circular-shaped magnetic dot.[11]

The magnetization process was examined *in situ* by the underfocused Fresnel mode (Fig. 8). In this mode, the center of the clockwise magnetization vortex exhibits a bright spot. The external magnetic field was applied along the diagonal direction of the square and was then reversed before saturation. The magnetizing process therefore corresponds to a minor loop. Because the field was applied by tilting the sample, the square elements appear deformed in the images. Without the field, the vortex center is located at the center of the square elements, indicating that the total magnetization is

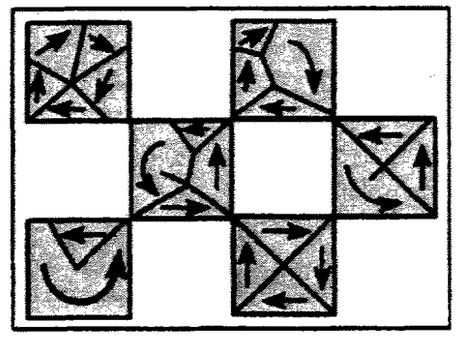

FIG. 7. Reproduced magnetization distribution from the images of Fig. 6.

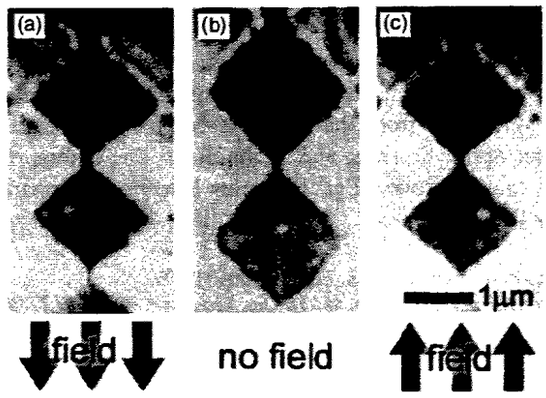

FIG. 8. Underfocused Fresnel images of the square elements with clockwise closures along a minor loop.

zero. On the other hand, the vortex center shifts in a direction perpendicular to the field when the element is magnetized, which is consistent with the magnetizing process of a circular shaped magnetic dot.[11] Therefore it is expected for a square element to have discontinuous changes in the magnetization curve at the field of the vortex annihilation and nucleation similar to a circular dot.[10,14] We have confirmed the existence of jumps at the nucleation/annihilation field of the vortex through computer simulation of the magnetization process of a square element by micromagnetic calculation. The simulation result is shown in Fig. 9. The calculation was conducted for a square element consisting of 169 magnetic clusters with ferromagnetic interaction, and the demagnetizing field calculated from the potential distribution were taken into account. Furthermore, the calculated minor loop (solid line with circular dots in Fig. 9) is well consistent with the experimental results.

The annihilation and nucleation field of the vortex would be probably influenced by the connection of the elements at the corners. Also the size of the connection parts may play an important role in controlling the vortex formation and rotation sense in the elements, because it determines the interaction between the elements, and thus the vortex nucleation

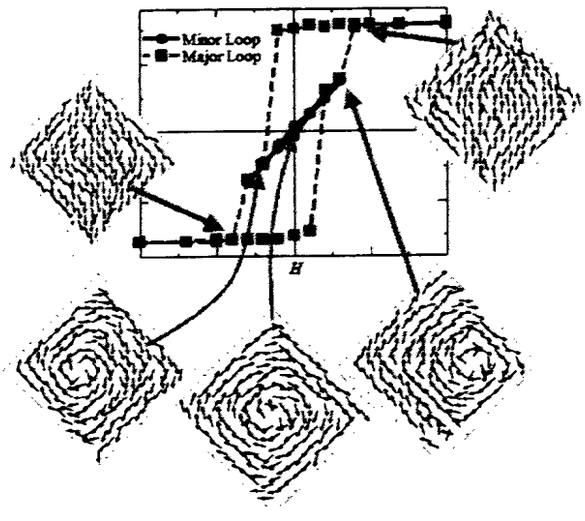

FIG. 9. Simulated magnetization curves and the magnetization distributions at the points indicated by the arrows.

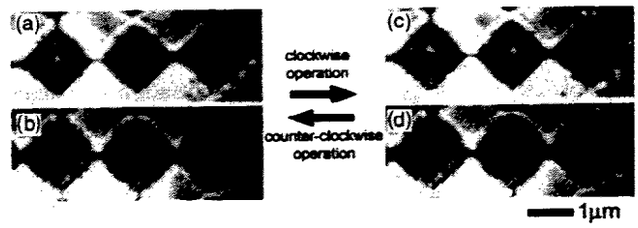

FIG. 10. Underfocused Fresnel images of the square elements after the rotational control operation.

and annihilation field. During the magnetization process, a vortex would not easily annihilate when it shifts and meets a neighboring vortex with the opposite rotational sense at the corners, and vortex centers with a same rotational sense would not interact with each other because the centers shift in the same direction. During the demagnetization process from saturation, an antidomain and a vortex center would nucleate at the corner; in such a circumstance, different sizes of the connected parts would result in a different nucleation field. Further experiments are needed to clarify the role of the contact point size quantitatively. Even without direct connection, magnetic interaction could be induced when the elements are very close to each other.[15] At the corner of the square element, the interaction between the elements would become stronger since it is the place where magnetic poles inevitably exist. This strong interaction could facilitate or prevent the vortex annihilation and nucleation. Accordingly, the magnetization shown in Fig. 5(a) is considered to be the total magnetization of the square elements with different annihilation and nucleation fields of magnetization vortices. Therefore, for the magnetization saturation, rather strong field was required compared to the nonpatterned continuous film because some elements may have large annihilation fields. The coercivity also appeared slightly larger because some elements may have large nucleation fields.

D. Vortex control of the square elements in the chessboard pattern

As the magnetic structure of the square element is similar to that of the magnetic vortex particle, we conducted the rotational control operation on the patterned permalloy film with chessboard. Figure 10 shows the underfocused and overfocused Fresnel images after the clockwise and the counter-clockwise operations. The external field was applied along the diagonal direction of the squares. However, the operation did not work as expected, there were some "stable" vortices whose rotational sense did not change after the operation. In addition, there were also "opposite" ones that behaved oppositely to the supposed manner, as well as "obedient" ones that followed the operation. Size diversity of the magnetic element is considered one of the possible reasons that cause the disturbance to the vortex control operation. Since the element size is quite uniform in this work, this reason can be ruled out. On the other hand, since the size of the contact point may affect the vortex nucleation and annihilation field of the neighboring elements as above mentioned, it is probable that the nonuniformity of the contact point caused the divergent responses of the elements to the

vortex control operation. That is to say the applied field gradient was not large enough to control the rotation of all the elements because of the differences in nucleation and annihilation field among the elements, and the insufficient field gradient may result in the opposite behavior as described in a previous study.[10]

IV. CONCLUSIONS

Patterning of permalloy films over a large area of several square millimeters has been accomplished by two methods based on the μCP technique, namely direct etching and lift-off. Chessboard, stripe, and grid patterns were homogeneously produced by the direct-etching method, while isolated rectangular dot array patterns were fabricated by the lift-off method. Macroscopic magnetization measurements of the patterned permalloy films have revealed a strong dependence of magnetization behavior on the shape of the pattern element.

For the patterned film with chessboard feature, we have observed the magnetic structure by Fresnel and Foucault modes of LTEM, and confirmed the formation of magnetization closure inside the square element. The magnetization process by use of the objective lens of a TEM was observed *in situ* by the Fresnel mode of LTEM. The macroscopic magnetic property was correlated with the micromagnetic structure.

ACKNOWLEDGMENTS

This work was supported by Special Coordination Funds for Promoting Science and Technology on "Nano-hetero Metallic Materials" from the Japanese Ministry of Education, Culture, Sport, Science, and Technology. The author would like to thank Hironori Eguchi for his help in the preparation of the TEM specimen.

[1]A. Hawryliw, Microelectron. Eng. **35**, 501 (1997).
[2]Z. Zhong, B. Gates, Y. Xia, and D. Qin, Langmuir **16**, 10369 (2000).
[3]J. Q. Wang, L. M. Malkinsiki, Y. Hao, C. A. Ross, J. A. Wiemann, and C. J. O'Connor, Mater. Sci. Eng., B **76**, 1 (2000).
[4]V. Novosad, K. Y. Guslienko, H. Shima, Y. Otani, K. Fukamichi, N. Kikuchi, O. Kitakami, and Y. Shimada, IEEE Trans. Magn. **37**, 2088 (2001).
[5]S. P. Li, A. Lebib, D. Peyrade, M. Natali, Y. Chen, W. S. Lew, and J. A. C. Bland, J. Appl. Phys. **90**, 521 (2001).
[6]Y. Xia and G. M. Whitesides, Annu. Rev. Mater. Sci. **28**, 153 (1998).
[7]M. D. Porter, T. B. Bright, D. L. Allara, and C. E. D. Chidsey, J. Am. Chem. Soc. **109**, 3559 (1987).
[8]S. P. Li, M. Natali, A. Lebib, A. Pépin, Y. Chen, and Y. B. Xu, J. Magn. Magn. Mater. **241**, 447 (2002).
[9]J. N. Chapman, J. Phys. D **17**, 623 (1984).
[10]T. Sannomiya, J. Shi, and Y. Nakamura, Trans. Mater. Res. Soc. Jpn. (in press).
[11]M. Schneider, H. Hoffman, and J. Zweck, J. Magn. Magn. Mater. **257**, 1 (2003).
[12]Y. Xia, D. Qin, and G. M. Whitesides, Adv. Mater. (Weinheim, Ger.) **8**, 1015 (1996).
[13]P. Candeloro *et al.*, Jpn. J. Appl. Phys., Part 1 **41**, 5149 (2002).
[14]R. P. Cowburn, D. K. Koltsov, A. O. Adeyeye, M. E. Welland, and D. M. Tricker, Phys. Rev. Lett. **83**, 1042 (1999).
[15]T. Sannomiya, Y. Haga, Y. Nakamura, O. Nittono, and Y. Takahashi, J. Appl. Phys. **95**, 214 (2004).

Transactions of the Materials Research Society of Japan 29[4] 1505-1507 (2004)

Controllability of rotation of magnetization vortex in Fe particles

Takumi Sannomiya, Ji Shi and Yoshio Nakamura
Department of Metallurgy and Ceramics Science, Tokyo Institute of Technology, Tokyo, Japan
Fax: 81-3-5734-3144, e-mail: yoshio@mtl.titech.ac.jp

The controllability of rotational sense of the magnetization vortex was studied by Fresnel mode of Lorentz transmission electron microscopy. In iron particles of around 100 nm in diameter, magnetization vortex was found to be stable, and two different rotational senses, clockwise and counter-clockwise, of magnetization vortex were observed. In order to control the rotational sense of the vortex, gradient magnetic field was applied to the specimen by making use of the objective lens field of a TEM. The results have shown that for the examined 120 particles, one rotational sense increased 20% than the other after application of gradient field, although some particles behaved oppositely or remained unchanged.
Key words: Lorentz electron microscopy, magnetization vortex, rotational sense, gradient field

1. INTRODUCTION

The dot-bit magnetic recording, in which one bit-cell consists of an isolated magnetic particle, has been considered as promising next-generation high density recording method. In an isolated circular-shaped magnetic particle the competition among magneto-static energy, quantum exchange interaction and crystalline anisotropy determines the magnetization distribution. A number of studies have dealt with the dependence of the magnetization feature on particle size [1-3]. One unique characteristic of such magnetic particles is the formation of magnetization vortex, i.e. the magnetic flux is closed inside the particle to avoid free magnetic poles. For the evaluation of a characteristic of submicron magnetic particles, Lorentz transmission electron microscopy(LTEM) is a powerful means[4]. We have experimentally confirmed that magnetically isolated disc-like iron particles of certain sizes have magnetization vortices using several modes of LTEM, such as Fresnel, Foucault, and differential phase contrast modes. Two rotational senses of vortices (clockwise or counter-clockwise) were found equally in number. In this study we focus on the controllability of the rotational sense of the magnetic vortices and investigate the possibility of its application in developing a new recording method. We propose to control the rotational sense by applying a strong lateral field and then removing it in a direction vertical to the field as shown in Fig.1.

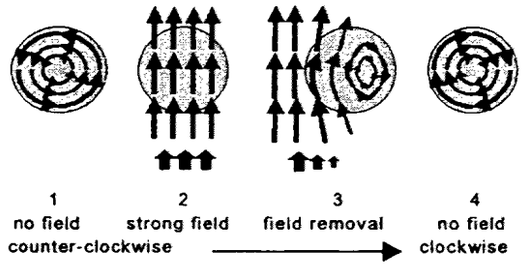

Fig.1 Schematic illustration of rotational control operation

2. EXPERIMENTAL

Iron particles were prepared by ion beam sputtering. Amorphous carbon films were used as support and protective top layer. Both materials were deposited in the same vacuum chamber without exposure to air. The (100) cleaved surface of NaCl single crystal was used as the substrate, which was removed by floating and skimming the film on water after deposition. The film was annealed at about 600°C to promote the grain growth up to a proper size.

The lateral gradient field was applied by making use of the objective lens field of a TEM(JEM2010). It is known that the objective lens produces strong magnetic field vertical to the observation plane. In our experiment, the specimen was tilted by an angle of 70°, namely the angle between the specimen and the magnetic field was 20°. We consider that the magnetic field was strong enough to make the specimen magnetically saturated in this direction. Then gradient field was exerted to the specimen by pulling out the specimen gradually from the field while keeping the specimen tilted. Tilting the specimen to opposite direction (ex. from 70° to -70°) and pulling it out in the same direction reverse the field direction in Fig.1, that is, the rotational sense of the magnetization vortex would be controlled by changing the tilt direction. With the specimen tilt of 70°, 94% of the field was effectively applied to the specimen in the lateral direction. In this manner, the rotational sense and its controllability of 120 particles of 100-200nm in diameter were investigated by Fresnel mode of LTEM.

We also conducted a simulative computation of magnetization distribution with the aid of MATLAB (copyright Mathworks Inc.).

3. RESULTS AND DISCUSSION

The shapes of the particles were characterized by scanning transmission electron microscope as ellipsoid, or spheroid, and there was a relatively wide particle size distribution.

Under-focused Fresnel images of the Fe particles after applying the two different gradient fields are shown in Fig.2. The bright spot at the center of the particle corresponds to the center of the magnetic vortex, which is equivalent to the domain wall in a magnetic domain structure. The clockwise vortex exhibits a bright spot

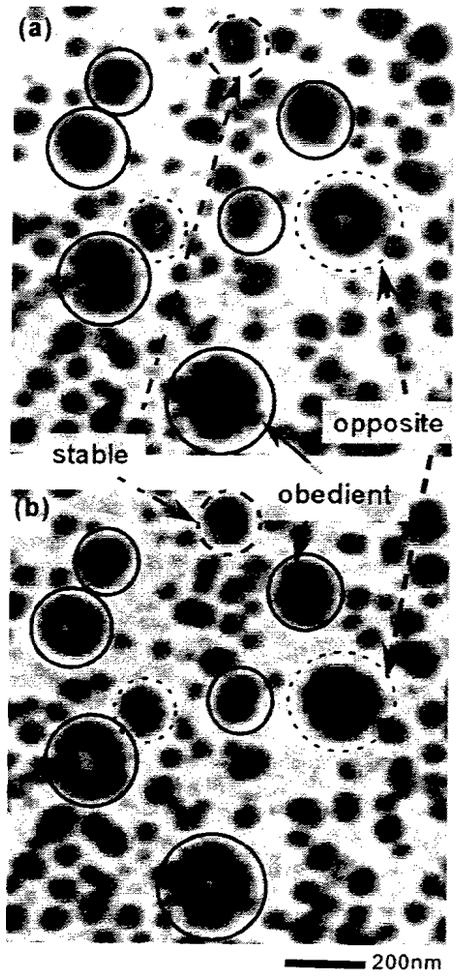

Fig.2 The Fresnel images of iron particles after application of gradient field for counter-clockwise(a), and that for clockwise(b).

in under-focused images, on the other hand the counter-clockwise vortex exhibits a dark spot. We have confirmed that the particles with sizes of 100-200 nm tended to have stable magnetic vortex structure and the rotational sense of such a vortex was readily recognizable.

As shown in Fig.2 the rotational sense of some particles changed following the controlling operation (comparing the particles indicated by solid circles between Fig.2(a) and (b)), while others behaved oppositely or remained unchanged (indicated by dotted and chained circle respectively). The statistic examination results of 120 particles (100-200 nm) subjected to repeated reversal procedure have shown that the clockwise vortex increased by 20% after "clockwise operation". We also found that the reversal of the rotational sense was well reproducible. This is also true for the particles which opposed to the operation. That is some particles always behave in accordance with the applied gradient field (as shown in Fig.1), and some particles always behave oppositely.

A possible reason for the opposite behavior is the intrinsic magnetic anisotropy. Because of the deviation from the perfect circular shape of the particle, shape anisotropy could be induced. Besides, crystalline anisotropy may not be negligible although pure iron has a low anisotropy constant. The anisotropy could cause preferential magnetization orientation in certain part of a particle which would determine the whole magnetization distribution, or the rotational sense of the vortex. In our method of applying the gradient field, the direction of the field vector was changed by tilting the specimen to opposite direction while the direction of field removal was fixed. In the case that after saturation the magnetization at one side of the particle persisted, where the field is weaker than the other side (Fig.1-3), the vortex would evolve from the other side where the field is stronger. Thus the rotational sense could follow the direction of external field rather than that of field gradient.

We have studied another possibility by computing the magnetization distribution during the rotational control operation, and have conducted a simulation for an isotropic circular particle exerted in a gradient field. A vortex particle, which has a stable magnetic vortex at zero field, was prepared and was confirmed to exhibit a typical magnetization curve as shown in previous work[1-3]. The particle was assumed to have no crystalline anisotropy and consist of two-dimensionally distributed magnetic clusters. The computation showed that the magnetization rotation would be opposite to the

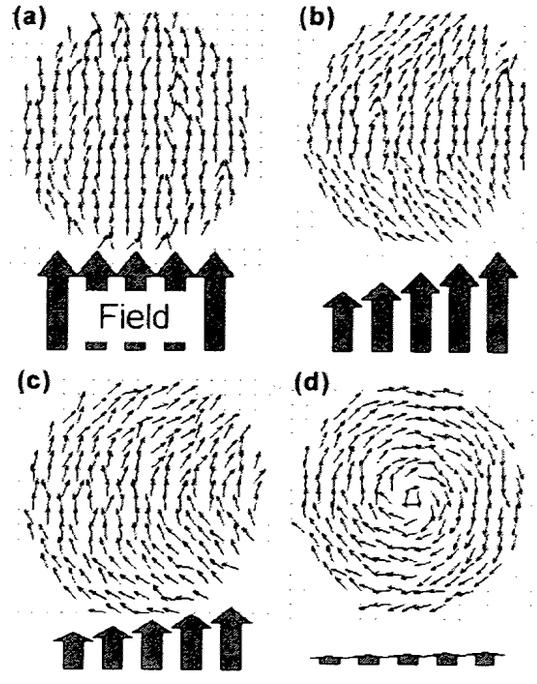

Fig.3 Simulated rotational operation on a circular particle. The thin arrows represent the magnetization inside the particle and the thick ones external field. After saturation(a), the field was removed with small gradient(b,c). The resulting rotation is opposite to the counter-clockwise intention(d).

intended sense when the field gradient is too small (Fig.3). After saturation, a gradient of the field was generated, and then the intensity of the field was decreased. The magnetization in the part of the particle where the field was stronger kept in the same direction with the external field while that of the other part curved in order to avoid formation of magnetic poles. Eventually, as shown in Fig.3, the magnetization tends to rotate clockwise although the applied lateral gradient field was intended to be the counter-clockwise operation. Note that the direction of the field gradient is opposite to that of Fig.1 while the resulting vortex exhibits the same rotational direction as Fig.1. In our experiment, the field gradient might not be large enough to realize the ideal operation (Fig.1) on all the particles.

It is known that the magnetization vortex state becomes less stable as the diameter of the particle becomes smaller and there is critical size where the magneto-static energy of the single domain state is equivalent to the spin exchange energy of the vortex. In case of a spherical iron particle, this critical diameter has been estimated to be around 32nm[5], although a particle of this size is difficult to be experimentally examined. With the magneto-crystalline anisotropy, a single domain state would be more stable for a single crystalline particle. In case of flat disc-shaped particles, it has been shown that the larger the thickness/diameter ratio becomes, the smaller the size limit becomes [1]. However, by applying homogeneous external field, such as in magnetization curve measurement, only the single domain state may appear [2] even when the vortex state is energetically the most stable magnetic structure. In order to experimentally investigate the stability of magnetic vortices, a strong gradient field should be applied to the specimen instead of using a uniform field.

Since one particle can have two different magnetic states, clockwise magnetic vortex or counter-clockwise, and the possibility to control the rotational sense has been proved, a vortex can be used as a recording bit. In this recording method arrays of very closely-packed dots would be allowed because there is no stray field from the neighboring particles. In addition the size of the particle with stable vortex structure can be reduced by use of isotropic material. The lateral field gradient could be easily produced by the small recording head with strong field. Thus we consider that the magnetic vortex has potential possibility to be applied in high density magnetic recording.

4. CONCLUSION

Magnetization vortices were confirmed on iron particles, and were basically able to be controlled by external lateral gradient field. Although the sense of the magnetic particles were likely to behave oppositely under improper conditions such as large magnetic anisotropy or small field gradient, the possibility of new recording method using the rotational sense of the magnetic vortex has been indicated.

5. ACKNOWLEDGEMENT

This work was supported by Special Coordination Funds for Promoting Science and Technology on "Nanohetero Metallic Materials" from the Japanese Ministry of Education, Culture, Sport, Science, and Technology.

6. REFERENCES

[1] M. Schneider, H. Hoffman and J. Zweck, *J. Magn. Magn. Mater.*, **257**, 1-10 (2003)
[2] R. P. Cowburn, D. K. Koltsov, A. O. Adeyeye, M. E. Welland and D. M. Tricker, *Phys. Rev. Lett.*, **85**, 1042-45 (1999)
[3] A. Fernandez, C. J. Cerjan, *J. Appl. Phys*, **87**, 1395-1401 (2000)
[4] J. N. Chapman, M. R. Scheinfein, , *J. Magn. Magn. Mater.*, **200**, 729-40 (1999)
[5] M. L. Néel, *Comptes rendus des séances de l'Academie des Sciences*, **224**, 1488-91(1947)

(Received October 8, 2003; Accepted January 26, 2004)

Transactions of the Materials Research Society of Japan 29[4] 1569-1571 (2004)

Perpendicular magnetic anisotropy of CoPt-TiN nanocomposite magnetic films

Yuuki Yamamoto, Ji Shi, Yoshio Nakamura, Mitsuru Hashimoto*
Dept. of Metallurgy and Ceramics Science, Tokyo Inst. Tech., Japan
(Fax: 81-3-5734-3145, e-mail: lestat@mtl.titech.ac.jp)
*Dept. of Applied Physics and Chemistry, The Univ. of Electro-Communications, Japan
(e-mail: mituru@ pc.uec.ac.jp)

Magnetic nanocomposite has been considered promising as next generation magnetic recording media. In this work, we investigate the magnetic property and microstructure of CoPt-TiN nanocomposite. The reason titanium nitride (TiN) was chosen as the matrix is that this material is wear resistive, thermally and chemically stable, such properties may contribute to the reliability and durability of magnetic recording media. The precursor films were DC-sputter deposited on fused quartz substrates at room temperature. The as-deposited films are amorphous-like, and the formation of CoPt (FCC) and TiN crystallites are confirmed by diffraction methods when the films were thermally annealed at temperatures above 600°C. One of the interesting properties of such films is that they show perpendicular magnetic anisotropy, which is considered due to the unique microstructure of the films. Cross-sectional TEM observation of the films reveals that such films are featured with fibrous microstructure with the nano-sized fibers perpendicular to the substrate surface. The fibers are composed of CoPt crystallites and separated by TiN. We consider that CoPt crystallites are magnetically coupled more closely in perpendicular direction than in the longitude direction and thus perpendicular anisotropy developed.

Key words: perpendicular anisotropy, shape anisotropy, annealing temperature, nano-fiber

1. INTRODUCTION

Magnetic films for perpendicular magnetic recording material were studied by many researchers in recent years. As methods of preparing films for perpendicular magnetic anisotropy material, for example, making films with $L1_0$ or applying CoCr systems are prevailing [1]. But we haven't chosen method getting films with $L1_0$ structure. We are aiming to obtain CoPt-TiN films with perpendicular anisotropy by applying shape anisotropy. Because TiN films have a property to deposit with a fibrous structure, TiN has been selected as matrix to gain films with shape anisotropy of the film. This research has been conducted to clarify how the columnar fiber structure of films is effective for the material of perpendicular magnetic recording. Especially in this paper, we report about how the thermal annealing temperatures take effects on perpendicular magnetic property.

2. EXEPERIMENT

Co-Pt-Ti-N films were deposited onto fused quartz substrates by the DC reactive sputtering, with pure Ar as the sputtering gas and N_2 as the reactant gas. A complex target set was used which consists of a pure Co disc at the back and Pt chips fixed with a center-holed Ti disc at the front.

The composition of the film can be controlled by changing the number of Pt chips at the front. The vacuum chamber was evacuated to 1.3×10^{-4} Pa before depositions. Then Co-Pt-Ti-N as precursor films were prepared at Ar + N_2 atmosphere, where N_2 gas pressure has been set to 6.7×10^{-4} Pa, and Ar gas pressure has been set to 1.6×10^{-1} Pa. The working gas pressure was about 5 Pa. All the depositions were conducted at the room temperature (especially not adjusted), at the power of 2.5kV, 12mA for 120 mins. Thermal annealing of the films was conducted in vacuum at the range from 600°C to 800°C for 180 mins.

The annealed films were evaluated by cross-sectional transmission electron microscopy (cross sectional TEM). The crystallinity of the films was evaluated by X-ray diffract meter (XRD). The in-plane and perpendicular saturation magnetization ($4\pi Ms$) and coercivity (Hc), hysteresis curve of the films were measured by vibrating sample magnetometer (VSM). The composition of the films was analyzed by X-ray photoelectron spectroscopy (XPS).

3. RESULT AND DISCUSSION

3.1 VSM measurement

The dependence of in-plane and perpendicular magnetic properties on the annealing temperature with range from 600°C to 800°C was studied. Here, Fig. 1 shows the hysteresis loops of $Co_{75}Pt_{25}$-TiN film annealed at 600°C, 700°C and 800°C respectively. Each value of perpendicular magnetic properties is greater than value of in-plane. The highest perpendicular Hc and Ms value was obtained at 700°C. The annealing temperature at under 500°C was not so effective for developing ferromagnetic coupling. In Fig.1, perpendicular hysteresis loops are corrected for the demagnetizing field by applying demagnetizing factor N according to the formula about demagnetizing field

$$\mathbf{H_{eff} = H_{appl} - NM.}$$

(H_{eff} : effective field, H_{appl} : applied field).

But this correction is provisional, not exactly essential.

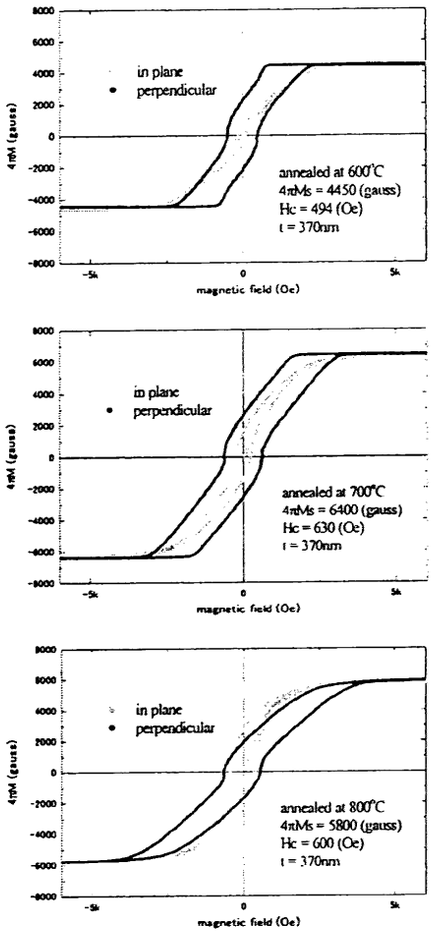

Fig. 1. Dependence of Transition of hysteresis loop on annealing temperatures.

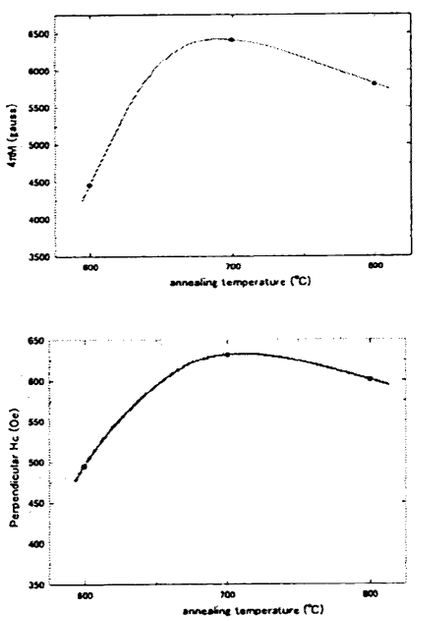

Fig. 2. Dependence of magnetic property on annealing temperature.

Because the loops showed in Fig.1 are distorted around the origin of graph. So these loops cannot be corrected simply by applying demagnetizing factor. This treatment will be challenge in future work.

Supposing it were corrected properly, except for distortion, each loop of 600°C and 700°C would be rectangle shape which is characteristic of perpendicular hysteresis. At 800°C, the shape of loop is collapsed. In this case, we can suppose that some change of structure has arisen in a film. To clarify the cause of transition depending on annealing temperature, we have carried out cross sectional TEM observations.

3.2 XRD and cross sectional TEM observation

XRD evaluations and cross sectional TEM observations were conducted about above three samples (three kinds of annealing temperature). Now we show three XRD profiles and TEM bright field images in Fig.3 and Fig.4. Images showed in Fig.3 and Fig.4 are 600°C, 700°C and 800°C annealing in order. In Fig.3, we can see that a film annealed at 600°C consists of fine fibrous structure. On XRD profile, a film annealed at 600°C has been amorphous-like. At 700°C, microcrystallite has begun to appear in fiber and fiber has become bold. At 800°C, microcrystallite has grown still larger and fiber has collapsed completely [2]. As in Fig.3, above 700°C, XRD profiles have revealed that the crystallinity of films has been developed. Obviously, these developments of crystallinity result from the growth of microcrystallites.

To refer past paper[3], the film which has been annealed at 600°C can be classified into zone 1, at 700°C can be classified into zone 2 and at 800°C can be classified into zone 3. At 600°C, thermal diffusion has not advanced so much. Thus its fibrous structure has remained without collapse. At 700°C, in comparison with 600°C, diffusion has taken advances, and then adjoining columns have united with each other into bold column. At 800°C, columns have diffused into like blocks, and microcrystallites have grown up. So, perpendicular magnetic anisotropy has decayed.

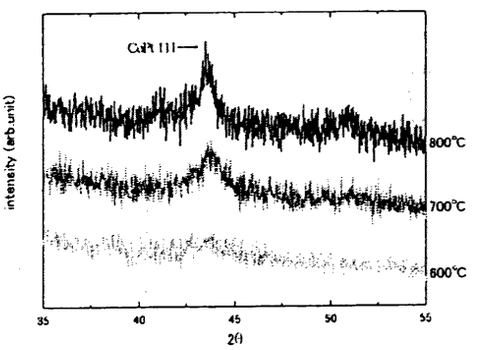

Fig. 3. XRD profiles at three kinds of annealing temperatures.

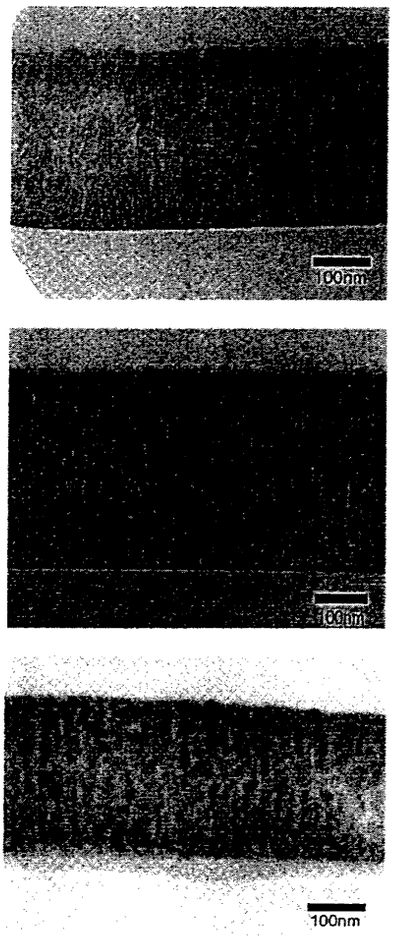

Fig. 4. Transition of cross sectional structure depending on annealing temperature. (from top 600°C, 700°C and 800°C annealing.)

4. CONCLUSION

The magnetic properties of $Co_{75}Pt_{25}$-TiN films for perpendicular magnetic recording media were studied in terms of the annealing temperature to confirm their potential. A film annealed at 700°C showed highest perpendicular coercivity(Hc) value greater than 600 Oe and saturation magnetization($4\pi Ms$) value greater than 6000 gauss. But in terms of perpendicular hysteresis shape, a film annealed at 600°C has more ideal perpendicular hysteresis loop (rectangle shape) than annealed at higher temperatures.

On TEM observation, it is turned out that the structure changes cause hysteresis transition. Fiber structure becomes collapsed as annealing temperature becomes higher [3]. And by the result of XRD profiling, the crystallinity and the quality of perpendicular magnetic properties are not so related. Perpendicular properties are more related to the structure rather than crystallinity.

All hysteresis loops have been distorted around the origin. Resolution of this issue needs to be more detailed investigations.

5. ACKNOWLEDGEMENT

We would like to express special thanks to all co-workers.

6. REFERENCES

[1] Toshiaki Keitoku et al. *J. Magn. Magn. Mater.*, **235** 34–39 (2001).
[2] J. A. Thornton, *J. Vac. Sci. T.*, **11**, 666-670 (1974).
[3] J. A. Thornton, *J. Vac. Sci. T.*, **A4** (6), 3059-3065 (1986).

(Received October 8, 2003; Accepted March 4, 2004)

Transactions of the Materials Research Society of Japan 29[4] 1603-1606 (2004)

Magnetoresistance of Co-Pt-ITO composites film

Wanti Ekawati[1], Ji Shi, Yoshio Nakamura, Osamu Nittono[2]
[1]Department of Metallurgy and Ceramics Science, Tokyo Institute of Technology
Fax: 81-3-5734-3145, e-mail: wanti@mtl.titech.ac.jp
[2]Department of education, Material Science laboratory, Fukushima University
Fax: 81-24-548-3181, e-mail: onittono@educ.fukushima-u.ac.jp

Co-Pt-ITO thin films are prepared by two-facing-target DC magnetron sputtering, and then annealed at various temperatures to control the magnetoresistance. As-deposited film shows an amorphous phase with low resistivity. When the films are annealed at around 350℃, precipitation of Co-Pt metallic particles takes place in amorphous matrix, and leads to the highest magnetoresistance obtained in our experiments. Meanwhile, concentration of metal in the amorphous matrix decreases and film shows highest resistivity. The corresponding M-H curve shows slightly increase of saturation magnetization than those films deposited at room temperature. The existence of remanence is not detected and the film is still superparamagnetic. XRD patterns of films annealed at temperature higher than 400℃ exhibit crystalline ITO as well as the fcc CoPt. Resistivity of film decreased suddenly and magnetoresistance disappeared. Microstructure of films together with relation between resistivity and magnetoresistance are discussed from the viewpoints of size and distribution of magnetic phases.

Key words: Co-Pt-ITO, magnetoresistance, TFTM sputtering, resistivity

1. INTRODUCTION

In recent years, granular magnetic systems have been intensively studied due to their numerous technological application potentials. A granular magnetic system basically consists of nanometer-sized magnetic particles dispersed in a non-magnetic matrix[1]. Recently, the configuration of granular material has been widely reported both in metal-metal granular films such as Co-Cu[2], and in metal-insulator granular material as reported in Co-Al-O[3,4,5] and Fe-Al_2O_3[6]. In such metal-insulator granular systems, several methods have been applied in order to control the distribution of metallic magnetic particle. These methods include the controlling of Ar/O_2 partial pressure during sputtering[7], the adjustment of rotation speed of substrate holder during deposition[8] and particularly through thermal annealing[9]. The research reported in Co-Al-O granular film generally shows higher magnetoresistance at room temperature and after thermal annealing the magnetoresistance decreases[10]. In other words, the distribution of magnetic metal particle seems difficult to be controlled by thermal annealing.

In this work, we try to adjust the distribution of magnetic particles by controlling the precipitation of metallic magnetic particles from the amorphous matrix during thermal annealing. In view of the encouraging results obtained with Indium Tin Oxide (ITO) films in our previous work, we fabricated various films using amorphous ITO as matrix and Co-Pt as metallic magnetic particles. ITO is chosen as a matrix since it easily forms an amorphous phase and has lower crystallization temperature. Such Co-ITO and Co-Pt-ITO composites films are investigated in order to understand the annealing temperature dependence of magnetoresistance of this material, which is discussed in the viewpoints of size and distribution of magnetic phase.

2. EXPERIMENTAL PROCEDURE

Two-facing-target DC magnetron (TFTM) sputtering system was used in this experiment. In this sputtering system, ITO and Co-Pt targets were set parallel to each other as shown in Fig.1. Corning 7059 glass and SiO_2 glass with the thickness of 0.5 mm were used as substrates for various characterizations. The sputtering chamber had been evacuated to a pressure around $8x10^{-5}$Pa before deposition. No oxygen was added, and Ar was the only gas that was introduced into the sputtering chamber. The Ar pressure was kept at 0.2 Pa during deposition. The sputtering voltage was kept at 500 volt and the sputtering current was fixed around 50 μA. Pre-sputtering was carried out for about 30 minutes with Ar gas before deposition to obtain an identical surface condition in each deposition. Film deposition itself was carried out for one and half hours. The film thicknesses were fixed around 2000 Å and the deposition rate was about 0.37 Å/sec. After the deposition, films were annealed in a vacuum for an hour at various temperatures. Structural properties of the films were characterized by X-ray diffraction using Cu Kα radiation. JEM3010 transmission electron microscope was used to take the high-resolution images. Film resistivity and magnetoresistance were measured using four-point probe MRHC-500 magnetoresistance measurement unit. The magnetic properties were examined using BHV-50H vibrating sample magnetometer (VSM).

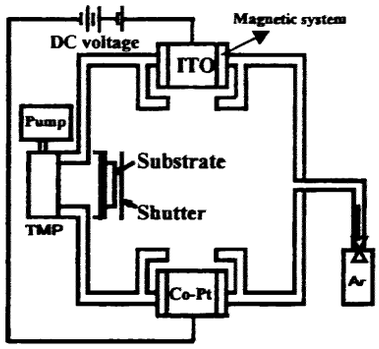

Fig.1. Schematic diagram of two facing target DC magnetron system.

3. RESULTS AND DISCUSSION

In this experiment, the result concerning Co-ITO film will be firstly described. Figure 2 represents the resistivity and magnetoresistance ratio of Co-ITO films annealed at various temperatures. As-deposited films have shown highest resistivity and MR ratio in this experiment, and with increasing the annealing temperature both resistivity and magnetoresistance gradually decreases. It is considered that metallic Co particles have already existed in the amorphous ITO matrix in as-deposited film. With increasing the temperature, the precipitations of metallic particles continue to occur, lowering the resistivity and MR ratio. Specimen annealed at 500°C exhibits the crystalline ITO and the magnetoresistance disappears. We are unable to control the distribution of metallic particles in this Co-ITO system, through thermal annealing.

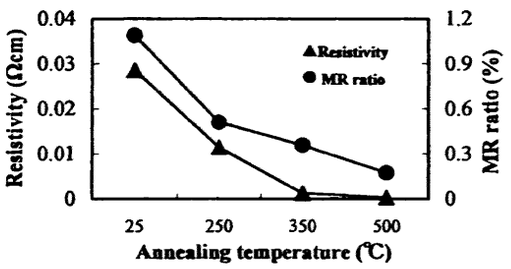

Fig.2. The resistivity and magnetoresistance ratio of Co-ITO films as a function of annealing temperature.

However, a drastic change of the thermal annealing effect is found in Co-ITO films with small addition of Pt as a second element. The atomic ratio of Co to Pt contained in Co-Pt-ITO film is around 5:1. The electrical properties of Co-Pt-ITO films annealed at various temperatures are shown in Fig.3. This figure reveals the relation between the resistivity and annealing temperature. As-deposited film has low resistivity compare to amorphous ITO. The specimen annealed below 300°C shows almost no change in resistivity. Upon further annealing up to 350°C, the resistivity increases rapidly and it reaches the maximum value at 370°C. Further annealing at above 400°C shows sudden decrease of resistivity.

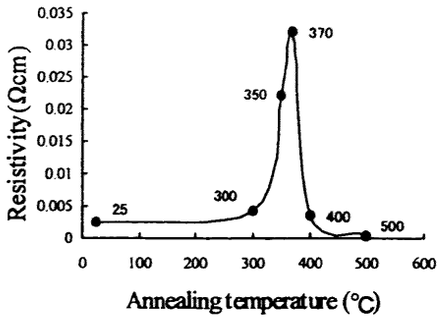

Fig.3. The resistivity of Co-Pt-ITO films as function of the increasing annealing temperature.

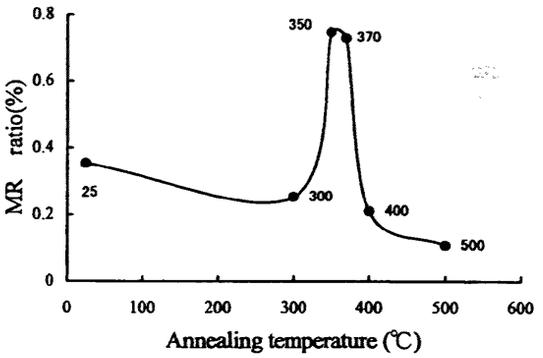

Fig.4. The MR ratio of Co-Pt-ITO films as function of annealing temperature.

The temperature dependence of magnetoresistance in Co-Pt-ITO film is also given in Fig.4. Magnetoresistance was measured under external magnetic field up to 10kOe, which was applied in plane of the films. All the measurements were carried out at room temperature. We define the magnetoresistance ratio as $\Delta\rho/\rho_{(0)}$x100%, where $\Delta\rho$ is equal to $\rho_{(0KOe)}$-$\rho_{(10KOe)}$. As-deposited film has small magnetoresistance ratio. With the increasing annealing temperature below 300°C, film shows slight decrease in magnetoresistance ratio. However, when the annealing temperature increases at above 300°C, film shows drastically increase of magnetoresistance and at 350°C film exhibits the maximum value. The specimen annealed at temperature above 400°C shows the decrease of magnetoresistance.

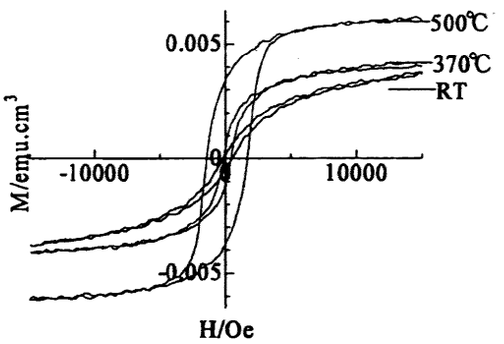

Fig.5. The M-H curves of Co-Pt-ITO films annealed at various temperature.

Figure 5 represents the M-H curves of Co-Pt-ITO films annealed at various temperatures. As-deposited film shows an amount of magnetization and superparamagnetic like behavior. The specimen annealed at 370°C shows slightly increase of the saturation magnetization with higher permeability but no existence of remanence is detected. The specimen annealed at 500°C has higher saturation magnetization and the remanence is observed.

To understand the structural properties of this film, we observed the X-ray diffraction pattern of specimen annealed at various temperatures, as shown in Fig. 6. As-deposited film shows an amorphous like pattern. The specimen annealed below 370°C has no crystalline peak, indicating the amorphous phase. Within further annealing at 500°C, film exhibits clear crystalline peaks of ITO and fcc Co-Pt. However, the XRD pattern of specimens annealed at 400°C presents the broaden peaks, which could not clearly identified. The occurrence of metallic particles could not be clearly detected in X-ray diffraction pattern of the specimen annealed below 370°C, therefore for more precise analysis the electron diffraction observation is needed.

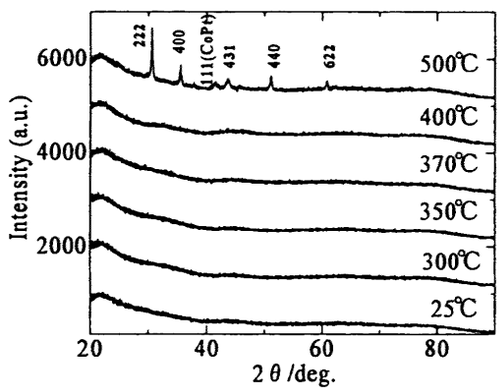

Fig.6. XRD pattern of Co-Pt-ITO films annealed at various temperature.

In order to get the information concerning the size and distribution of metal precipitation in matrix, the microstructures of specimen annealed at various temperatures are observed by TEM. The results are given in Fig.7. As-deposited films basically consist of amorphous phase as shown in Fig. 7a. This film has lower resistivity than pure amorphous ITO because the specimen contains large amount of metal elements in the matrix. The specimen annealed at 350°C has amorphous matrix and metallic particles with the size around 8 nm as seen in Fig. 7b. We could confirm that the metallic particles are in crystalline phases by HRTEM. The microstructure of Co-Pt-ITO film annealed at 500°C shows the metallic particle that has grown up to 20 nm in size. In this figure, the ITO matrix and fcc Co-Pt are both in crystalline phases. Corresponding to the TEM micrographs we also observed the diffraction patterns. The diffraction of as-deposited film shows a halo pattern, representing the amorphous phase. Specimen annealed at 350°C shows a halo pattern and weak metal rings of fcc Co-Pt particles, which are identified as 111 and 220. Upon further annealing at 500°C, specimen shows clear ring patterns of crystalline ITO.

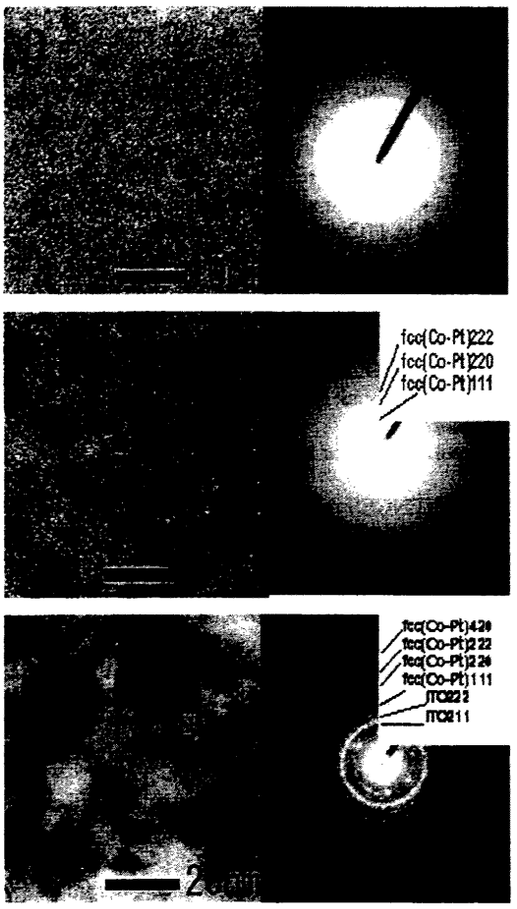

Fig.7. TEM micrograph and diffraction ring patterns of Co-Pt-ITO films. a. at RT, annealed at b. 350°C and c. 500°C.

Based on the above experimental results, we could summarize the structural, electrical and magnetic properties. As-deposited films are basically amorphous and the resistivity is lower than the pure amorphous ITO. This film show superparamagnetic behavior and magnetoresistance. Although the film is amorphous, it is considered that there exist magnetic clusters in the amorphous matrix that lead to small magnetoresistance. Film annealed at 350°C still has an amorphous matrix with crystalline Co-Pt magnetic particles. Resistivity of this film increases because concentration of the matrix decreases. Metallic particles with size of nanometer distribute in the matrix lead to the highest MR in our experiments. When films are annealed at 500°C, crystallization of ITO starts so that resistivity of the film suddenly decreases and magnetoresistance disappears. This film has the remanence with higher saturation magnetization. It is noted that the highest MR and highest resistivity are achieved at the same time. If the crystallization of ITO matrix with certain amount of metallic element does not start at around 400°C, we probably could get higher MR film. It means that the

control of the crystallization temperature of amorphous ITO is important to our study.

4. CONCLUSION

As-deposited film containing small amount of Pt in Co-ITO films is basically amorphous with low resistivity. At around 350°C to 370°C, the precipitation of crystalline Co-Pt particles occurs in the amorphous matrix, decreasing the metal concentration which leading to highest resistivity. In the meantime, the distribution of metallic particles with the size of nanometer in ITO matrix leads to maximum MR. Upon further annealing at above 400°C, the crystallization of ITO matrix started, as the result the film resistivity decreased and magnetoresistance disappeared. The structure of fine Co-Pt particles distributed in amorphous ITO matrix can be successfully controlled through thermal annealing and achieve the magnetoresistance, this film shows highest magnetoresistance at highest resistivity.

5. REFERENCES

[1]J.Q.Xiao,J.S.Jiang and C.L.Chien. Physics. Rev.Lett.68, 3749 (1992)
[2]A. E. Berkowitz, J. R. Mitchell,M.J. Carey, A.P. Young, S.Zhang,F.E. Spada, F.T. Parker, A.Hutten, and G.Thomas, Physics. Rev. Letter 68,3745 (1992)
[3]M.Ohnuma, K.Hono, E.Abe and H.Onodera, S.Mitani, H.Fujimori, J.Appl.Phys.82,(11)5646 (1997)
[4]K.Takahashi, S.Mitani, J.Chiba, H.Fujimori, J.Appl.Phys.82,(9)6331 (2000)
[5]H.Sato. Y.Kobayashi, K.Hashimoto, Y.Aoki, H.Sugawara, S.Ohnuma, S.Mitani, H.Fujimori, J.Magn.Soc.Japan 23, 73-75(1999)
[6]K.Kamei,M.Yonemura,K.Hanafusa, Journal of Mat. Science: Materials in electronic 12, 569-574 (2000)
[7]T.Zhu and Y.J.Wang, Physics.Rev.B.60(17)11 918 (1999)
[8]N.Koayashi, S.Ohnuma, T.Masumoto, H.Fujimori, J.Magn.Soc.Japan Vol.23 76-78 (1999)
[9]Jae-geun Ha, S.Mitani, K.Takahashi, H.Fujimori, J.Magn. Soc.Japan.Vol.23, 79-81(1999)
[10]M.Ohnuma, K.Hono, H.Onodera, S.Mitani,J.G.Ha H.Fujimori, Nanostructure materials Vol.12 573-576 (1999)

(Received October 8, 2003; Accepted March 1, 2004)

Available online at www.sciencedirect.com
SCIENCE DIRECT®
Thin Solid Films 459 (2004) 156–159
thin solid films
www.elsevier.com/locate/tsf

Growth structure and magnetic property of CoPt films on GaAs(001) by d.c.-sputter deposition

Hiroyuki Nakajima[a], Tetuhiro Tanaka[a], Mituru Hashimoto[a,*], Ji Shi[b], Yoshio Nakamura[b]

[a]*Department of Applied Physics and Chemistry, University of Electro-Communications, Chofu, Chofugaoka 1-5-1, Tokyo 182-8585, Japan*
[b]*Department of Metallurgy and Ceramics Sciences, Tokyo Institute of Technology, Meguro-ku 212-1, Tokyo 152-8552, Japan*

Available Online February 12 2004

Abstract

Co–Pt films were deposited on GaAs(001) substrates at room temperature or 200 °C by dc plasma sputtering with an application of a bias of 0 V or −150 V to the substrate. The Co–Pt films retain the face-centered cubic (fcc) structure grown with the 111-texture but the atomic composition in the films depends on both the substrate bias and the substrate temperature. The crystalline quality of the film is improved mainly by application of the substrate bias. However, the atomic composition of the film is affected by both the substrate bias and the substrate temperature, by applying the substrate bias, the averaged atomic ratio ⟨Co/Pt⟩ decreases drastically on the unheated substrate but only a little on the heated substrate. These phenomena are explained in terms of two factors, first, preferential re-sputtering of Co by the incident particles generated under the bias voltage and, second, preferential atomic diffusion of Co into the substrate enhanced by elevating the substrate temperature.

PACS: 68.55-a; 75.20En; 75.30Gw; 75.50Kj; 75.50Vv; 7570Ak; 81.10-h; 81.15Cd

Keywords: Co–Pt film; Substrate bias; Preferential resputtering; Atomic diffusion

1. Introduction

Ferromagnetic Co–Pt alloy films have been investigated because of their scientific and technical importance. They retain face-centered cubic (fcc) structure, hexagonal closed packed (hcp) structure, or ordered phases with $L1_0$ structure (CoPt) and $L1_2$ structure (Co_3Pt) depending on preparation conditions [1–4]. Also Co–Pt alloys with $L1_0$ structure have high crystalline magnetic anisotropy, which promises high-density magnetic recording media [5–8]. Co–Pt films have been frequently prepared by sputter-deposition. It has been shown [9–13] that the structure and thus the physical properties of the sputter-deposited films can be modified. The present work, as the subsequent work to the recent report on Co–Pt/Si(001) [14], aims to investigate the effects of both the substrate bias and substrate temperature on the growth structure and properties of Co–Pt films sputter-deposited on GaAs(001) substrates.

*Corresponding author. Tel./fax: +81-424-43-5461.
E-mail address: mituru@pc.uec.ac.jp (M. Hashimoto).

2. Experimental procedure

The films were deposited on GaAs(001) substrates by d.c. sputtering in pure Ar gas. The GaAs substrates were pre-cleaned with $H_2SO_4 + H_2O_2 + H_2O$ solution just prior to be loaded into a vacuum chamber. The target used includes a Pt plate (52 mm in diameter) at the back and a Co plate (52 mm in diameter, 2-mm thick) with a hole of 30 mm in diameter at the front. The chamber was evacuated using a turbo-molecular pump backed with a mechanical rotary pump. Besides, a cylindrical liquid nitrogen trap is placed around the target and the substrate holder, and the trap was filled with liquid nitrogen during depositions. A pressure generally reaches less than 1.3×10^{-4} Pa before sputtering and the Ar pressure was maintained at 4.0 Pa during sputtering. The films were deposited on the unbiased substrates or the biased substrates (with $V_s = -150$ V). And the depositions were conducted at room temperature or 200 °C for 30 min. Film thickness was estimated by the cross-sectional transmission electron microscopy (XTEM). The films were characterized by X-ray dif-

0040-6090/04/$ - see front matter © 2003 Elsevier B.V. All rights reserved.
doi:10.1016/j.tsf.2003.12.121

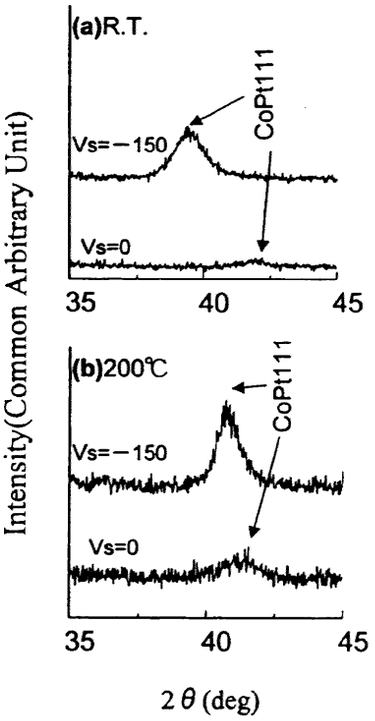

Fig. 1. The XRD profiles of the Co–Pt films on unbiased and biased substrates at room temperature (a) and at 200 °C (b).

fraction (XRD), X-ray photoelectron spectroscopy (XPS), i.e. the mean composition ratio Co/Pt of the film was determined with the use of the lattice spacing evaluated from XRD spectrum assuming that the Vegard's law holds for the Co–Pt system, and in order to determine the depth profile of the atomic composition in the film XPS signals was observed on the film surface after every 1 min-etching by 2 keV-Ar ion beam. The in-plane magnetization hysteresis curves of the films were observed to measure their magnetic properties using a vibration sample magnetometer (VSM).

3. Results and discussion

Fig. 1 shows the XRD profiles of the films on unbiased and biased substrates at room temperature (a) and at 200 °C (b). As shown in Fig. 1, generally the fcc–Co–Pt films grow in the 111-texture for the films investigated, and their crystalline quality is improved mainly by application of the substrate bias (V_s) but partly by elevation of the substrate temperature (T_s). In addition, the position of the Co–Pt 111-diffraction peak changes depending on both V_s and T_s, which suggest the atomic composition in the film, changes with these parameters. In fact, assuming that the Vegard's law holds for the Co–Pt system as above mentioned, it can be estimated that with application of the substrate bias the averaged atomic ratio ⟨Co/Pt⟩ of Co to Pt in the film decreases from 0.8 to 0.2 on the unheated substrate but remains nearly unchanged at approximately 0.4 on the heated substrate. That is, with elevation of the substrate temperature the ⟨Co/Pt⟩ decreases from 0.8 to 0.4 in the unbiased film but increases from 0.2 to 0.4 in the biased film. These results of XRD are further confirmed by XPS analysis results. The depth profiles of the atomic peak height ratio of the XPS spectra for the Co–Pt films on unbiased substrates and biased substrates at room temperature (a, b) and at 200 °C (c, d) are shown in Fig. 2. It can be seen that Co and Pt distribute more or less uniformly across the thickness for the unbiased films but the Co/Pt peak height ratio

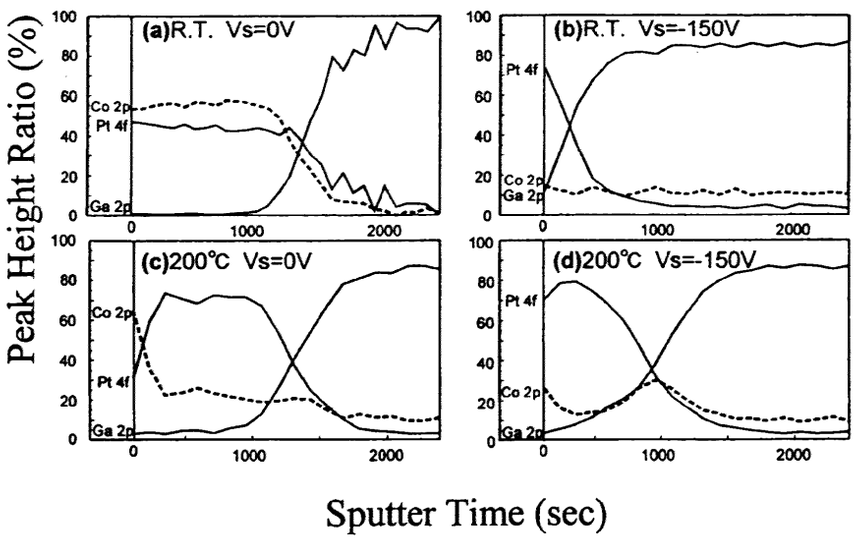

Fig. 2. The depth profiles of the atomic peak height ratio of the XPS spectra for Co films on unbiased substrates and biased substrates at room temperature (a, b) and at 200 °C (c, d).

becomes smaller for the films on the biased substrate or on the heated substrate, indicating the decrease of cobalt content in the films on the biased substrate or on the heated substrate and that the film thickness generally tends to be smaller for the biased films although the effects of V_s on the film thickness and cobalt content are rather weakened on the heated substrate.

It is known that by applying a small negative bias voltage (V_s) to the substrate during sputter-deposition, energetic particles (ions and neutrals) bombard the growing film with a broad energy distribution around an energy E_A less than eV_s [15]. This phenomenon will affect the growth behavior of the film and thus the structure of the film. First, the crystallinity of the film can be improved because of the enhanced surface diffusivity of adatoms [13]. This explains the improvement of crystallinity of the biased films on both unheated and heated substrates in the present work. Moreover, the present results indicate that the application of V_s rather than the elevation of T_s contribute to the improvement of the crystallinity of the film. Second, the surface or adatoms of the growing film may be re-sputtered by the incoming energetic particles [16]. In the present work, both Co and Pt may be re-sputtered because the estimated value of E_A at $V_s = -140$ V is 25.2 eV larger than the threshold values of E_A for Co and Pt, which are 25 eV for both metals [17]. However, the sputtering yields Y of them at low incident particle energy region, i.e. at E_A less than 100 eV are quite different such that $Y_{Co} > Y_{Pt}$, e.g. $Y_{Co}/Y_{Pt} = 0.048/0.033 = 1.5$ at $E_A = 60$ eV [18]. This difference in Y accounts, partially at least, for the preferential sputtering of Co observed in the present work. However, as clearly seen in the XPS analysis results (Fig. 2), the preferential atomic diffusion of Co into the GaAs(001) substrate is appreciably enhanced by elevating T_s, which also results in the decease of Co composition in the film. Such the preferential atomic diffusion of cobalt into the substrate was not observed in the Co–Pt film d.c.-sputter-deposited on Si(001) [14].

In-plane magnetization hysteresis curves for the Co–Pt films are shown in Fig. 3. The saturation magnetization ($4\pi M_s$) is the maximum for the film prepared on the unbiased and unheated substrate. With applying V_s, $4\pi M_s$ decreases on the unheated substrate but slightly increases on the heated substrate.

The change of $4\pi M_s$ may be explained in view of the changes of both the cobalt content and the crystallinity of the Co–Pt films with substrate bias as well as substrate temperature. As shown above, application of the substrate bias or elevating the substrate temperature more or less induces competitive effects on $4\pi M_s$, the decrease of $4\pi M_s$ due to the decreases cobalt content and the increase of $4\pi M_s$ due to the improvement of the crystallinity.

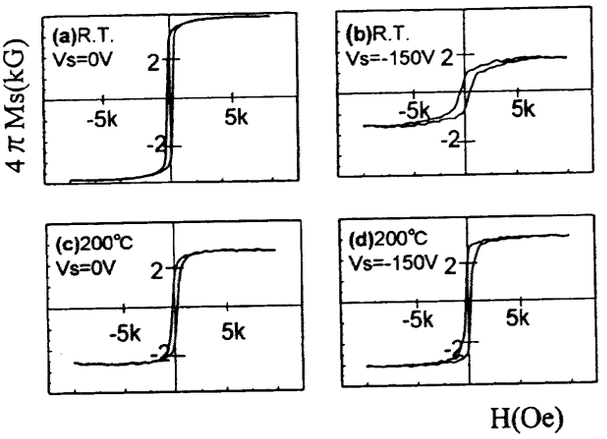

Fig. 3. In-plane magnetization hysteresis curves for the Co–Pt films unbiased and biased substrates at room temperature (a, b) and at 200 °C (c, d).

4. Conclusion

The effects of substrate bias and substrate temperature on the composition and the structure of d.c.-sputter-deposited Co–Pt films have been investigated. The results are summarized as following:

1. The Co–Pt films retain the face-centered cubic (fcc) structure grown with the 111-texture.
2. The atomic composition of the Co–Pt films is altered through the preferential resputtering of Co by applying the bias to the substrate as well as through the preferential atomic diffusion of Co into the substrate by elevating the substrate temperature.
3. The crystalline quality of the film is improved mainly by application of the substrate bias.
4. The saturation magnetization of the Co–Pt film is determined through the competitive factors: the change of Co content and the improvement of crystallinity.

Acknowledgments

This work was partly supported by the Hungarian National Science Foundation under Contract No. JAP-26/00.

References

[1] M. Hansen, Constitution of Binary Alloys, 2nd ed, McGraw-Hill, New York, 1958, p. 492.
[2] K. Barmak, R.A. Ristau, K.R. Coffey, M.A. Parker, J.K. Howard, J. Appl. Phys. 79 (1996) 5330.
[3] S. Jeong, Y.-F. Hsu, M.E. Michael, D.E. Laughlin, J. Appl. Phys. 87 (2000) 6950.
[4] M. Maret, C. Ulhaq-Bouillet, W. Staiger, M.C. Cadeville, S. Lefebvre, M. Bessiere, Thin Solid Films 319 (1998) 191.

[5] G. Choe, S. Funada, A. Tsoukatos, S. Gupta, J. Appl. Phys. 81 (1996) 4894.
[6] K. Xun, M. Li, J. Zhou, D. Shen, Thin Solid Films 347 (1999) 253.
[7] S.H. Liou, S. Huang, E. Klimek, R.D. Kirby, Y.D. Yao, J. Appl. Phys. 85 (1999) 4334.
[8] J.A. Christdoulides, Y. Huang, Y. Zhang, G.C. Hadjipanayis, I. Pnangiotopoulos, D. Niarchos, J. Appl. Phys. 87 (2000) 6938.
[9] B. Chapman, Glow Discharge Processes, John Wiley and Sons, New York, 1980, pp. 215–236.
[10] M. Ohring, Materials Science of Thin Films, Academic Press, San Diego, 2002, pp. 210–211.
[11] H. Qiu, H. Nakai, M. Hashimoto, G. Safran, M. Adamik, P.B. Barna, E. Yagi, J. Vac. Sci. Technol.A 12 (1994) 2855.
[12] M. Ishino, J. Yang, K. Makihara, J. Shi, M. Hashimoto, J. Vac. Sci. Technol.A 18 (2000) 2339.
[13] J. Shi, D. Kojima, M. Hashimoto, J. Appl. Phys. 88 (2000) 1679.
[14] T. Shinmitsu, J. Shi, M. Hashimoto, Surf. Coat. Technol. 151–152 (2002) 55–58.
[15] H. Qiu, The Ph.D. thesis of the University of Electro-Communications, 1994, 79.
[16] J. Shi, R. Zhou, M. Hashimoto, J. Vac. Sci. Technol. A 19 (2001) 2979.
[17] M. Ohring, Materials Science of Thin Films, Academic Press, San Diego, 2002, p. 113.
[18] B. Chapman, Glow Discharge Processes, John Wiley and Sons, New York, 1980, pp. 394–395.

Available online at www.sciencedirect.com
SCIENCE DIRECT®
Thin Solid Films 459 (2004) 165–168
thin solid films
www.elsevier.com/locate/tsf

Structure and magnetic behavior of CoPt films prepared on MgO(001) substrates by dc plasma biased sputtering

Kenrou Yamaguchi[a], Zhongyu Zhao[a], Changchuan Chen[a], Mituru Hashimoto[a,*], Ji Shi[b], Yoshio Nakamura[b]

[a]*Department of Applied Physics and Chemistry, University of Electro-Communications, Choufu, Chofugaoka 1-5-1, Tokyo 182-8585, Japan*
[b]*Department of Metallurgy and Ceramics Science, Tokyo Institute of Technology, Meguro-ku 212-1, Tokyo 152-8552, Japan*

Available Online February 12 2004

Abstract

CoPt films were prepared on MgO(001) substrates at 230 °C by d.c. sputtering. Both films on the unbiased and the biased (−150 V) substrates grow with the crystallographic orientation of CoPt(001)[100]//MgO(001)[100]. In fact, the unbiased film is deformed from the perfect face-centered cubic (fcc) structure towards the face-centered tetragonal (fct) structure with an incomplete ordered phase, while the biased film retains normally the fcc structure. Both films show the in-plane magnetic anisotropy with coercivity less than 1000 Oe. Upon the thermal anneal at 800 °C×30 min, the unbiased film is transformed completely into the L1o-fct structure while the biased film is transformed into the fct structure but not completely into the complete L1o structure. The unbiased film shows clearly the perpendicular magnetic anisotropy with the squareness equal to unity, while the biased film shows only the weaker perpendicular magnetic anisotropy with the squareness less than 0.7. The perpendicular coercivity is estimated at 3200 Oe for the unbiased film and 2200 Oe for the biased film.

PACS: 68.55-a; 75.20En; 75.30Gw; 75.50Kj; 75.50Vv; 75.70Ak; 81.10-h; 81.15Cd

Keywords: CoPt alloy; Sputtering; L1o structure; Perpendicular magnetic anisotropy; Coercivity

1. Introduction

CoPt alloy retains the face-centered cubic (fcc) structure with disordered state or the face-centered tetragonal (fct) structure with ordered state (L1o) depending on preparation conditions [1]. The latter induces a strong uniaxial crystalline magnetic anisotropy (anisotropy constant 7×10^7 erg/cm) along [001] direction [2] due to the contraction of c/a to 0.97 [3]. So the nanocomposite films of CoPt embedded in non-magnetic medium and in addition, grown with the 001-texture have been investigated as candidates for high-density recording materials [4–6]. This work aims to investigate the structure and magnetic behavior of the CoPt films deposited on MgO(001) substrates by d.c. sputtering, focusing on the effect of both the substrate bias and the thermal anneal.

*Corresponding author. Tel./fax: +81-424-43-5461.
E-mail address: mituru@pc.uec.ac.jp (M. Hashimoto).

2. Experimental procedure

CoPt films were deposited on MgO(001) substrates by d.c. sputtering. A complex target was used, which includes a Pt plate (52 mm in diameter) at the back and a Co plate (60 mm in diameter) with a concentric hole (30 mm in diameter) at the front, giving a Co/Pt area ratio of 1/1. The deposition chamber was evacuated to a base pressure of 1×10^{-4} Pa and was filled with Ar to a pressure of approximately 5.7 Pa during deposition. In addition, a cylindrical liquid nitrogen trap was placed around both the target and the substrate holder, and was filled with liquid nitrogen during deposition. Both unbiased and biased films ($V_s=-150$ V) were prepared. The depositions were conducted at a substrate temperature of 230 °C and for a duration of 30 min. And annealing of the films was conducted in a vacuum at 800 °C for 30 min. The films were characterized by cross sectional transmission microscopy (XTEM) and X-ray diffraction (XRD). The magnetic behaviors of the

0040-6090/04/$ - see front matter © 2003 Elsevier B.V. All rights reserved.
doi:10.1016/j.tsf.2003.12.124

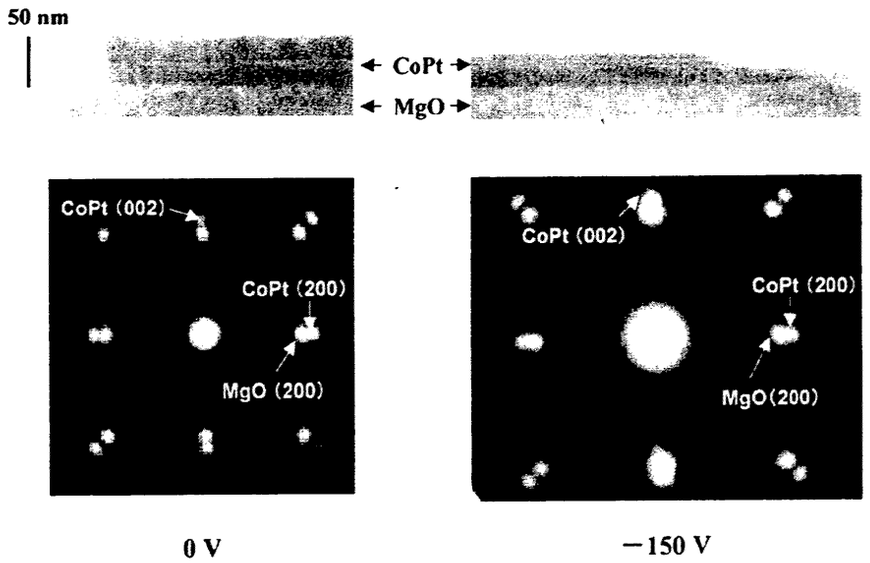

Fig. 1. The XTEM microphotographs (up side) and their XTED patterns (down side) of the as-deposited CoPt films on unbiased (left side) and biased (right side) MgO substrates. The XTED patterns were taken from the selected area at the CoPt/MgO interface with the 010-directed electron beam.

films were investigated by vibration sample magnetometer.

3. Results and discussion

Fig. 1 show the XTEM microphotographs (up side) and their diffraction (XTED) patterns (down side) of the as-deposited CoPt films on unbiased (left side) and biased (right side) substrates. The XTED patterns were taken from the selected area at the CoPt/MgO interface with the 010-electron beam. The XTED patterns show that the films grow mainly with CoPt(001)[100]// MgO(001)[100]. However, by analyzing the patterns in detail, it is found that the CoPt lattice in the unbiased film is deformed from the fcc structure towards the fct structure in contrast with the case in the biased film. That is, the ratio of the lattice spacing, d[CoPt-(002)] to d[CoPt-(200)] is measured to be 0.95 for the unbiased film and 0.99 for the biased film. Fig. 2a,b show the XRD profiles of the as-deposited films and the annealed films, respectively. As shown in Fig. 2a, on the profile of the unbiased film we can detect an additional weak peak at $2\theta=46.45°$ besides a strong main CoPt(002) peak at $2\theta=49.00°$. By the simple calculation, the lattice spacing ratio, $d(2\theta=49.00°)/d(2\theta=46.45°)$ is estimated to be 0.95, which is inconsistent with the ratio of d[CoPt-(002)]/d[CoPt-(200)] above estimated from the XTED patterns. Thus the weak peak at $2\theta=46.45°$ can be identified as the CoPt-(200) diffraction peak. For the biased film, such an additional peak could not detected because the small lattice deformation such as d[CoPt-(002)]/d[CoPt-(200)] = 0.99 may contribute only to the broadening of CoPt-(002) peak. Upon thermal anneal at 800 °C, as shown in Fig. 2b, the peak corresponding to the fct-(001) diffraction appears in both the unbiased and biased films. Besides, for the unbiased film the fct-(200) peak in addition to the fct-(002) peak are clearly detected, which indicates that the unbiased CoPt film is transformed completely into the ordered phase of fct structure, i.e. the L1o structure. For the biased film, the transformation into the L1o structure seems to be incomplete. It can be said that the lattice deformation induced in the unbiased CoPt film plays a role of the trigger to the transformation into the L1o structure by thermal anneal. With the application of the bias during deposition, Ar ions are accelerated towards the substrate and bombard the growing film. The energy E_A of the bombarding Ar ion at the bias of −140 V is calculated to be 25.2 eV [7]. So the film can epitaxially grow with the structure relatively free from the lattice deformation due to the energetic ion bombardment on the growing film [8]. And it is noted, as the other effect of the bias, that the atomic composition of the film may change due to the preferential re-sputtering during the film growth because of the difference in the sputtering yield among constituent elements [9]. With sputtering by Ar ions, the sputtering threshold energies for Co and Pt to be sputtered are 25 eV for both elements, but the ratio of the sputtering yield for Pt to Co is approximately 0.67 at $E_A=60$ eV or to be expected as lower than 0.67 at

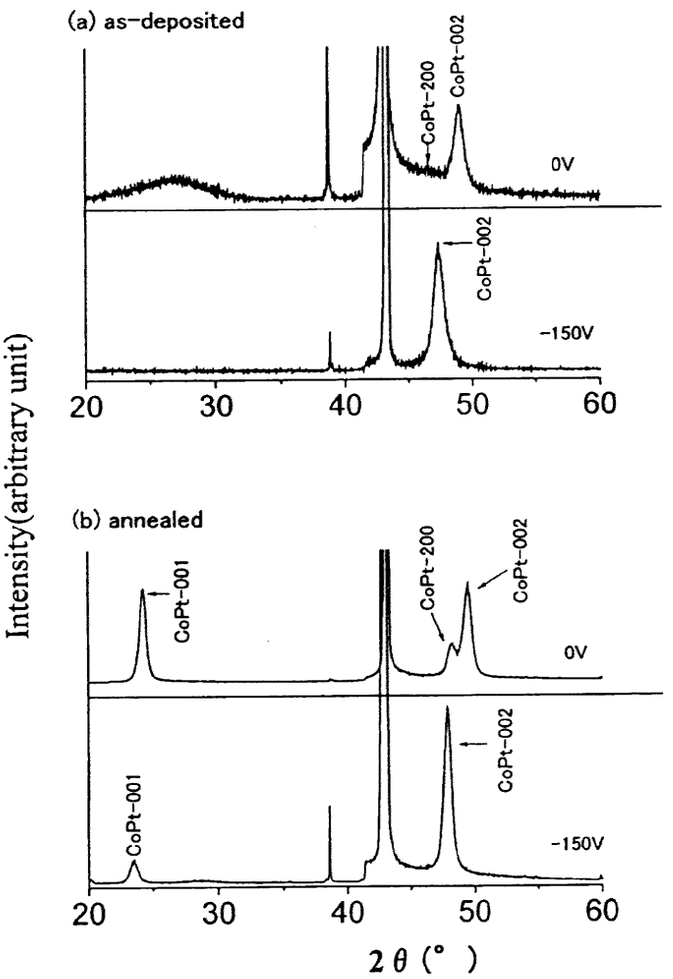

Fig. 2. The XRD profiles of the as-deposited films (a) and the annealed films (b).

$E_A = 25.2$ eV [10]. That is, as shown in Fig. 2, the CoPt-(002) and -(001) peaks of the biased film deviate towards the lower diffraction angle in comparison with the corresponding peaks of the unbiased film. Thus in addition, as a result, the biased film usually tends to be thinner than the unbiased film even for the same deposition time, as we can see in the XTEM microphotographs. In conclusion, upon the thermal anneal the unbiased film is completely transformed into the L1o structure with the 001-textured growth while the biased film is transformed into the fct structure but not completely into the L1o structure.

Fig. 3 shows the in-plane (left column) and the perpendicular (right column) magnetization hysteresis curves of the as-deposited films (a) and the annealed films (b), respectively. As shown in Fig. 3, the magnetization easy axes of the films on both the unbiased and the biased substrates change from the parallel (in-plane) direction to the perpendicular direction to the film surface with the thermal anneal. The unbiased film shows the perpendicular magnetic anisotropy with the squareness equal to unity and, while the biased film shows relatively the weaker perpendicular magnetic anisotropy with the squareness less than 0.7. The coercivities of the annealed films are two or three times higher than those of the as-deposited films. The perpendicular coercivity, for instance, increases from approximately 1000 Oe for both unbiased and biased films up to 3200 Oe for the unbiased film and up to 2200 Oe for the biased film, respectively, with the thermal anneal. The great increase of coercivity and the appearance of the perpendicular magnetic anisotropy suggest that the annealed films retain more or less the fct structure, which has a strong 001-uniaxial magnetic anisotropy in its ordered L1o structure, and simultaneously the 001-textured structure. Finally, as shown in Figure 3, the saturation magnetization is nearly unchanged with the thermal anneal, but decreases with the application of the

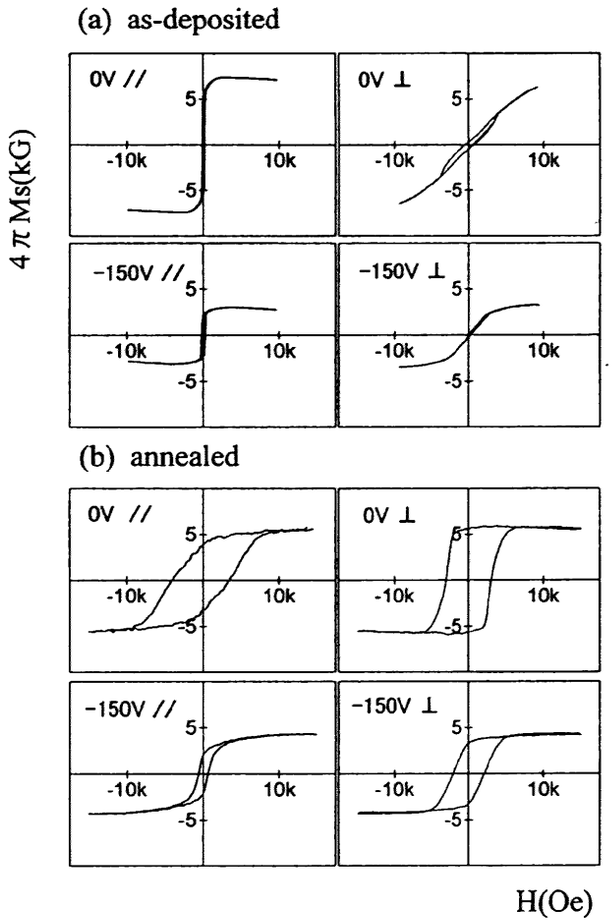

Fig. 3. The in-plane (left column) and the perpendicular (right column) magnetization hysteresis curves of the as-deposited films (a) and the annealed films (b).

substrate bias because of the preferential re-sputtering of Co.

4. Summary

CoPt films were prepared on MgO(001) substrates at 230 °C by d.c. sputtering. Both films on the unbiased and the biased (−150 V) substrates grow with the crystallographic orientation of CoPt(001)[100]// MgO(001)[100]. In fact, the unbiased film is deformed from the perfect fcc structure towards the fct structure with an incomplete ordered phase, while the biased film retains normally the fcc structure. Both films show the in-plane magnetic anisotropy with coercivity less than 1000 Oe. Upon the thermal anneal at 800 °C×30 min, the unbiased film is transformed completely into the L1o-fct structure, while the biased film is transformed into the fct structure but not completely into the L1o structure. Corresponding to their crystal structure, the unbiased film shows clearly the perpendicular magnetic anisotropy with the squareness equal to 0.98, while the biased film shows the weaker perpendicular magnetic anisotropy with the squareness less than 0.73. The perpendicular coercivity is estimated at 3200 Oe for the unbiased film and 2200 Oe for the biased film.

Acknowledgments

This work was partly supported by the Hungarian National Science Foundation under Contract No. JAP-26/00.

References

[1] M. Hansen, Constitution of Binary Alloys, 2nd ed, McGraw-Hill, New York, 1958, p. 492.
[2] G.H.O. Daalderop, P.J. Kelly, M.F.H. Schuurmans, Phys. Rev. B 44 (1991) 12 054.
[3] O.A. Ivanov, L.V. Solina, V.A. Demshira, L.M. Magat, Phys. Met. Metall. 35 (1973) 92.
[4] M. Yu, Y. Liu, A. Moser, D. Weller, D.J. Sellmyer, Appl. Phys. Lett. 75 (1999) 3992.
[5] H. Zeng, M.L. Yan, Y. Liu, D.J. Sellmyer, J. Appl. Phys. 89 (2001) 810.
[6] C.C. Chen, M. Hashimoto, J. Shi, Y. Nakamura, O. Nittono, P.B. Barna, J. Appl. Phys. 93 (2003) 6273.
[7] H. Qiu, Structural and Physical Properties of Nickel Films Biased-DC-Sputter-Deposited on Si(001), SiO_2 and MgO(001), The Ph.D. thesis of the University of Eelctro-Communications, 1994, p. 79.
[8] H. Nakai, H. Qiu, M. Adamik, G. Safran, P.B. Barna, M. Hashimoto, Thin Solid Films 263 (1995) 159.
[9] J. Shi, R. Zhou, M. Hashimoto, J. Vac. Sci. Technol. 19 (2001) 2979.
[10] B. Chapman, Grow Discharge Process, Wiley, New York, 1980, p. 374 and 394.

Available online at www.sciencedirect.com
SCIENCE DIRECT®
Thin Solid Films 459 (2004) 200–202
thin solid films
www.elsevier.com/locate/tsf

Perpendicular magnetic anisotropy of CoPt–TiO_2 composite film with nano-fiber structure

Changchuan Chen[a], Ryo Sakurai[a], Mituru Hashimoto[a,*], Ji Shi[b], Yoshio Nakamura[b]

[a]*Department of Applied Physics and Chemistry, University of Electro-Communications, Chofu, Chofugaoka 1-5-1, Tokyo 182-8585, Japan*
[b]*Department of Metallurgy and Ceramics Science, Tokyo Institute of Technology, Megro-ku 212-1, Tokyo 152-8552, Japan*

Available Online March 24 2004

Abstract

Co–Pt–Ti–O films were prepared by sputtering a Co–Pt–Ti composite target in $Ar+O_2$ atmosphere. Upon thermal anneal at elevated temperatures, fcc-CoPt and TiO_2 are formed in the film as a separated phase from one other. Both phases develop as the fiber-like columnar grains of less than 10 nm in their lateral size, and are distributed separately from each other. The film does not show perpendicular magnetic anisotropy unless it is thicker than approximately 50 nm, which is explained in terms of strong shape anisotropy of magnetic CoPt nano-fibers vertical to the substrate. The TiO_2 in the film plays a role to separate CoPt nano-fibers from one another and to reduce their mutual magnetic interaction. The nano-scale nature and perpendicular magnetic anisotropy of the CoPt–TiO_2 film make it a very promising candidate for future recording media with ultra-high area density.

PACS: 81.15.Cd; 75.30.Gw; 75.50.Kj; 75.70.Ak

Keywords: Sputtering; Perpendicular magnetic anisotropy; CoPt–TiO_2 film; Nano-fiber; Shape anisotropy

1. Introduction

Magnetic nanocomposite films have been investigated to realize the high-density magnetic recording devices with high-thermal stability [1–3]. The nanocomposite film is commonly composed of a magnetic phase such as Co or its alloy, and a non-magnetic phase such as SiO_2, Al_2O_3, and both phases are to be distributed with nano-scale sizes leading the high-area magnetic density. In addition, it is very promising for the ultra-high area recording to develop the nanocomposite film with the perpendicular magnetic anisotropy [4–6]. However, to increase the high-thermal stability, CoPt and FePt alloys have a great advantage because of their high crystalline magnetic anisotropy constants in the ordered L1o structure, i.e. 5×10^7 erg/cm^3 for CoPt, and 7×10^7 erg/cm^3 for FePt, respectively [7–10].

In the present work, subsequently to the recent work for Co–Ti–N ternary alloy [8], Co–Pt–Ti–O alloy is employed to form a CoPt-based nanocomposite. The Ti and O are designated to form TiO_2 as the non-magnetic phase in the nanocomposite, analogously to the TiN in the Co–Ti–N system. Both TiO_2 and TiN are known as the material with high hardness, thermal and chemical stability. In this article, we report the perpendicular anisotropy of the CoPt–TiO_2 nanocomposite films.

2. Experimental procedure

Co–Pt–Ti–O films were deposited onto SiO_2 glass substrates at room temperature by reactive sputtering with Ar as the sputtering gas, and O_2 as the reactant gas. A complex target set was used which includes a Pt plate at the back, a Co plate with a concentric hole (h_{Co} in diameter) in the medium, and a Ti plate with a concentric hole (h_{Ti} in diameter $> h_{Co}$) at the front. The composition of the film can be controlled by changing the inner diameter of the Ti plate and the number of the Pt tip. The vacuum chamber was evacuated to 1.3×10^{-4} Pa before sputtering and the working pressure was 4 Pa with 1/200 of the pressure ratio of O_2 to Ar. The films with different thickness were prepared by changing the deposition time. The films were annealed in vacuum at a temperature of 400, 500, 700 or 800 °C for 2 h. The composition of the film was analyzed by

*Corresponding author. Tel./fax: +81-424-43-5461.
E-mail address: mituru@pc.uec.ac.jp (M. Hashimoto).

0040-6090/04/$ - see front matter © 2004 Elsevier B.V. All rights reserved.
doi:10.1016/j.tsf.2003.12.083

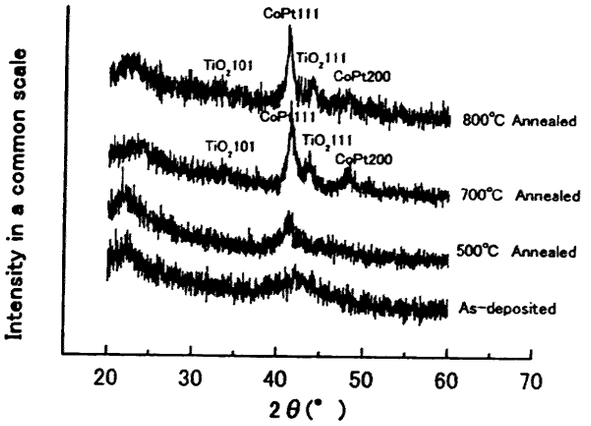

Fig. 1. The XRD profiles of the Co–Pt–Ti–O films, 450-nm thick, prepared by thermal anneal at different temperatures.

X-ray photoelectron spectroscopy (XPS), and the structures of the as-deposited and annealed films were characterized by X-ray diffraction (XRD), plan-view and cross-sectional transmission electron microscopy (TEM). The magnetic properties of the film were measured by vibration sample magnetometer at room temperature.

3. Results and discussion

The sputter-deposited Co–Pt–Ti–O films grow generally in the amorphous state. The averaged atomic composition ratio in the as-deposited films investigated is estimated to be Co/Pt/Ti/O=41/39/8/12. As confirmed by XRD profiles (Fig. 1), upon the thermal anneal at a temperature equal to or higher than 700 °C, the film is transformed into the CoPt–TiO_2 film where the face centered cubic (fcc) CoPt alloy and the rutile (TiO_2) coexisted separately from one another, and the TiO_2 phase is considered to be amorphous or composed of fine crystallites as expected from its XRD peaks. Fig. 2 shows the XTEM microphotograph (a) and its diffraction (TED) pattern (b) of the CoPt–TiO_2 film, 450-nm thick, prepared by thermal anneal at 700 °C. The film is composed of fiber-like columnar grains of 10 or less nanometers in the averaged lateral size as seen from the XTEM microphotograph, and the fcc-CoPt structure is formed as seen from the XTED pattern. The diffraction signals from the TiO_2 could not be detected on the XTED pattern, which suggests that its grains are too fine to be detected. Though one cannot distinguish between grains of CoPt and TiO_2 on the XTEM microphotograph, considering the result of the magnetic property dependence on the thickness described below (Fig. 3), it can be speculated that the CoPt grains are embedded in finer TiO_2 grains such that the CoPt grains may be mutually separated from one another to reduce the magnetic interaction among themselves.

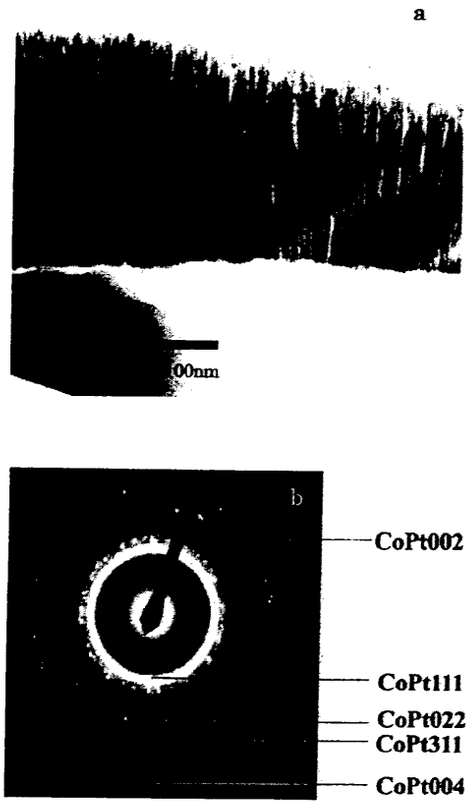

Fig. 2. The XTEM microphotograph (a) and its diffraction (TED) pattern (b) of the CoPt–TiO_2 film, 450-nm thick, prepared by thermal anneal at 700 °C.

It is found that the CoPt–TiO_2 film shows the perpendicular magnetic anisotropy only when its thickness is larger than 50 nm. Fig. 3 shows the typical magnetization hysteresis curves of the CoPt–TiO_2 films, 50-nm thick and 100-nm thick, prepared by thermal anneal at

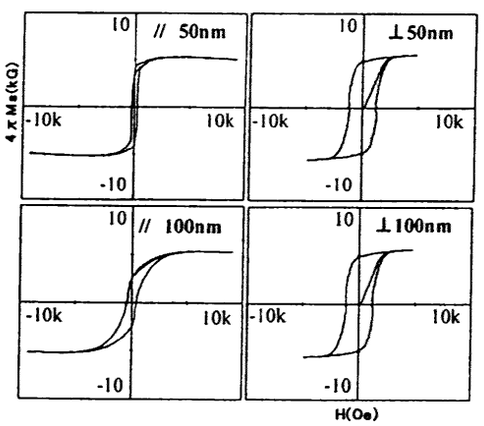

Fig. 3. The typical magnetization hysteresis curves of the CoPt–TiO_2 films, 50-nm thick and 100-nm thick, prepared by thermal anneal at 700 °C. The marks, // and ⊥ refer to the in-plane magnetization curve and the perpendicular magnetization curve, respectively.

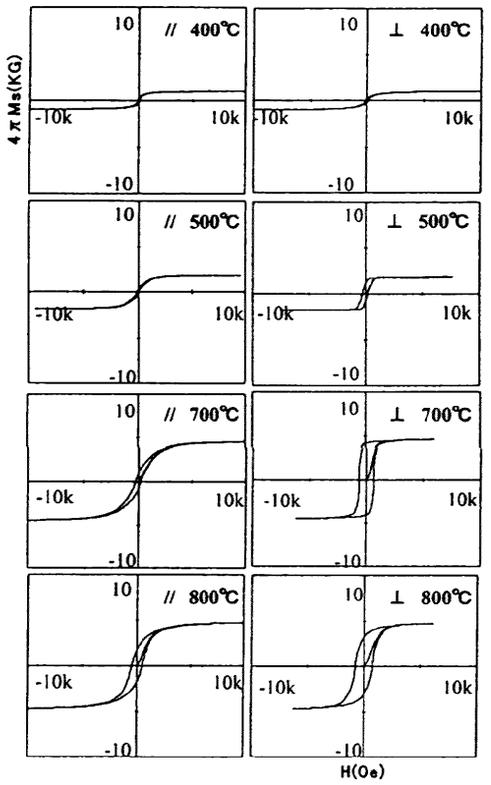

Fig. 4. The magnetization hysteresis curves of the CoPt–TiO_2 films, 450-nm thick, prepared by thermal anneal at 400, 500, 700 and 800 °C.

700 °C. Such a dependence of the magnetization easy axis on thickness suggests that the observed perpendicular magnetic anisotropy is induced by the magnetic anisotropy due to the strong shape anisotropy of the CoPt nano-fibers grown vertical to the substrate, which are mutually separated by the non-magnetic TiO_2 fiber grains. This mechanism for the perpendicular magnetic anisotropy to be induced has been suggested previously in the Co–TiN film where the Co phase retains the fcc structure [6]. The effect of the anneal temperature on the magnetization easy axis is typically shown in Fig. 4, where the magnetization hysteresis curves of the CoPt–TiO_2 films, 450-nm thick, prepared by the thermal anneal at 400, 500, 700 and 800 °C are shown. As estimated from Fig. 4, the squareness of the perpendicular magnetization curve reaches unity only when the CoPt–TiO_2 film is annealed at 700 °C. This result is well consistent with the result of the XTEM observation that the nano-fiber growth vertical to the substrate is mostly enhanced for the anneal at 700 °C without any unnecessary chemical reaction such as the oxidation. In conclusion, the perpendicular squareness, the perpendicular coercivity, and the saturation magnetization ($4\pi M_s$) of the CoPt–TiO_2 film prepared with the typical conditions such as 100 nm in thickness and 700 °C in annealing temperature are unity, 1200 Oe and 4.5 kG, respectively.

4. Summary

Co–Pt–Ti–O films were prepared by sputtering a Co–Pt–Ti in $Ar+O_2$ atmosphere. Upon thermal anneal at elevated temperatures, fcc-CoPt and TiO_2 are formed in the film as a separated phase from one another. Both phases develop as the fiber-like columnar grains of less than 10 nm in their lateral size, and are distributed separately from each other. The film does not show the perpendicular magnetic anisotropy unless it is thicker than approximately 50 nm, which is explained in terms of strong shape anisotropy of magnetic CoPt nano-fibers vertical to the substrate. The TiO_2 in the film plays a role to separate CoPt nano-fibers from one another, and to reduce the magnetic interaction among them. The CoPt–TiO_2 film, 100-nm thick, prepared with the typical conditions gives unity in perpendicular squareness, 1200 Oe in perpendicular coercivity, and 4.5 kG in saturation magnetization. Such perpendicular magnetic properties of the CoPt–TiO_2 nanocomposite film make it a very promising candidate for future recording media with ultra-high area density.

Acknowledgments

This work was partly supported by the Hungarian National Science Foundation under Contract No. JAP-26/00. The authors would like to thank M. Katsuki and his colleagues at Riken Denshi Co. for their assistance in magnetic measurements.

References

[1] T. Hayashi, S. Hirono, M. Tomita, S. Umemura, Nature (London) 381 (1996) 772.
[2] C.P. Luo, D.J. Sellmyer, Appl. Phys. Lett. 75 (1999) 3162.
[3] H. Wang, S.P. Wong, W.Y. Cheung, N. Ke, M.F. Chiah, H. Liu, X.X. Zhang, J. Appl. Phys. 88 (2000) 2063.
[4] G.T. Kraus, Y.-V. Lu, J.E. Trancik, D.M. Mitro, E.P. Giannelis, M.O. Thompson, S.L. Sass, J. Appl. Phys. 82 (1997) 1189.
[5] C.P. Luo, S.H. Liou, L. Gao, Y. Liu, D.J. Sellmyer, Appl. Phys. Lett. 77 (2000) 2225.
[6] C.C. Chen, M. Hashimoto, J. Shi, Y. Nakamura, O. Nittono, P.B. Barna, J. Appl. Phys. 93 (2003) 6273.
[7] M. Yu, Y. Liu, A. Monser, D. Weller, D.J. Sellmyer, Appl. Phys. Lett. 75 (1999) 3992.
[8] C.-M. Kuo, P.C. Kuo, J. Appl. Phys. 87 (2000) 419.
[9] H. Zeng, M.L. Yan, Y. Liu, D.J. Sellmyer, J. Appl. Phys. 89 (2000) 810.
[10] D.H. Ping, M. Ohnuma, K. Hono, J. Appl. Phys. 90 (2002) 4708.

Available online at www.sciencedirect.com
SCIENCE DIRECT®
Thin Solid Films 459 (2004) 208–211
thin solid films
www.elsevier.com/locate/tsf

Structure and magnetic behavior of reactive sputter deposited nanocomposite FePt–TiN$_x$ films

Ryou Sakurai[a], Yuki Yamamoto[a], Changchuan Chen[a], Mituru Hashimoto[a,*], Ji Shi[b], Yoshio Nakamura[b], Osamu Nittono[b]

[a]*Department of Applied Physics and Chemistry, University of Electro-Communications, 1-5-1 Chofugaoka, Chofu-shi, Tokyo 182-8585, Japan*
[b]*Department of Metallurgy and Ceramics Science, Tokyo Institute of Technology, 2-12-1 O-okayam, Meguro-ku, Tokyo 152-8552, Japan*

Available Online February 26 2004

Abstract

FePt–TiN nanocomposite films have been prepared on fused-quartz substrates by reactive sputtering and post-deposition thermal annealing. The effect of Fe/Pt ratio on the ordering transition behavior of FePt in such films was investigated. It was found that compared with the film with a nearly equiatomic Fe/Pt ratio, Pt-rich films tend to undergo ordering transition at lower temperature, and the ordered phase formed has a higher value of ordering parameter provided the films were annealed at the same temperature. In addition, for the Pt-rich films, with the formation of ordered FePt phase in the film, perpendicular anisotropy is developed even though there is no crystallographic preferred orientation for the FePt phase. We consider that fibrous grain structure may be formed in such FePt–TiN nanocomposite films, which contributes to the magnetization in the perpendicular direction.

PACS: 75.30.Gw; 75.50.Kj; 75.50.Vv; 75.70.Ak

Keywords: FePt–TiN; Nanocomposite; Ordering transformation; $L1_0$ structure; Magnetic property

1. Introduction

Nanocomposite films with FePt and CoPt magnetic particles have attracted much research interest during the past several years [1–8], because such films are considered promising as the next generation ultra-high density magnetic recording media. It is known that in order to improve the area density of the magnetic recording media, the bit cell or the magnetic particles must be as small as possible. However, the concern of thermal stability emerges when reducing the particle size to some extent (e.g. <10 nm). In such cases, high-anisotropy energy is needed for the magnetic particles to retain thermal stability. The ordered phase between Fe and Pt with a tetragonal $L1_0$ structure (FePt) is known to have magnetic anisotropy energy as high as 10^7 J/m^3 [9], therefore the material is considered very promising. In addition to the high anisotropy energy, another requirement for the ultra-high density recording media is that the magnetic particles have to be isolated with each other by the second non-magnetic phase, in order to reduce the interaction among the magnetic particles, and thus to lower media noise [10]. The choice of the non-magnetic phase is also important because a properly chosen non-magnetic phase will not only isolate the magnetic particles, but also provide chemical and mechanical protection for the media. In this work, a well known hard coating material, TiN was used as the non-magnetic phase, and the structure and magnetic properties of FePt–TiN nanocomposite films were studied.

2. Experimental procedure

FePt–TiN nanocomposite films were prepared on fused quartz glass by reactive sputtering at room temperature, followed by thermal annealing at elevated temperatures. A complex target set was used which includes a Pt plate at the back, Fe and Ti plate with concentric holes fixed at the front side. The Fe/Pt ratio can be controlled by changing the front Fe plate with

*Corresponding author. Tel./fax: +81-424-43-5461.
E-mail addresses: mituru@pc.uec.ac.jp (M. Hashimoto), shi@mtl.titech.ac.jp (J. Shi).

0040-6090/04/$ - see front matter © 2003 Elsevier B.V. All rights reserved.
doi:10.1016/j.tsf.2003.12.085

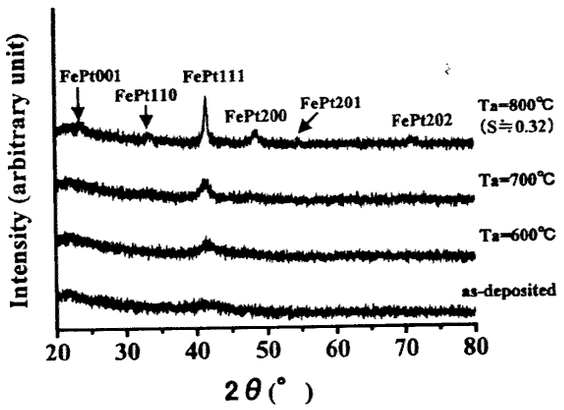

Fig. 1. X-Ray diffraction profiles of FePt–TiN nanocomposite films with a Fe/Pt ratio near to 1. (T_a is the annealing temperature).

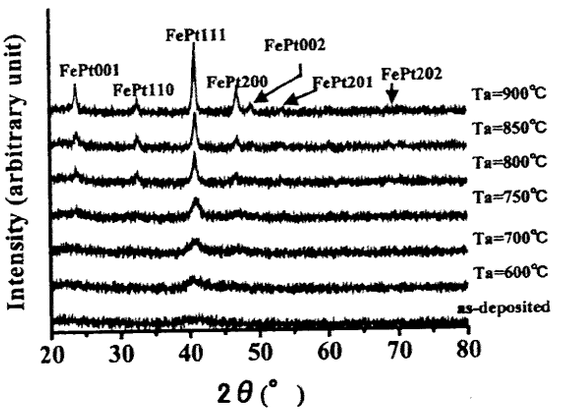

Fig. 2. X-Ray diffraction profiles of Pt-rich FePt–TiN nanocomposite films. (T_a is the annealing temperature).

holes of different sizes, and the Ti content was fixed for all samples in the present work. Ar gas was used as the sputtering gas and N_2 was used as the reactant gas. The vacuum chamber was evacuated to 1.3×10^{-4} Pa before depositions, and the working pressure was approximately 1.6×10^{-1} Pa. Sputter depositions were conducted at a N_2 partial pressure of 6.7×10^{-4} Pa. The deposition rate was approximately 4.5 nm/min. Post-deposition annealing of the films was conducted in a vacuum, at temperatures ranging from 400 to 900 °C, and for 120 min. The composition of the films was estimated by X-ray photoelectron spectroscopy (XPS). The structures of the as-deposited and annealed films were characterized by X-ray diffraction (XRD) and transmission electron microscopy (TEM). The magnetic properties of such films were measured by vibrating sample magnetometer (VSM) at room temperature.

3. Results and discussion

Fig. 1 shows the XRD results of the as-deposited and thermal annealed films. The Fe/Pt ratio of the films is to be nearly equiatomic as estimated by XPS. The results have shown that the as-deposited film is amorphous, since there is only a broad peak at about 41°. After the thermal anneal at 600 and 700 °C, the peak, which is identified to be 111 reflection of face-centered cubic (fcc) FePt according to its position, increased in intensity, indicating that FePt crystallites formed in the film. Further increase in annealing temperature resulted in the ordering transition of FePt, i.e. from fcc structure to face-centered tetragonal (fct) structure (namely the $L1_0$ structure), as the peaks due to the super lattice are seen on the XRD profiles. The ordering parameter S is 0.3 as estimated using the following equation [11],

$$S^2=\frac{1-(c/a)}{1-(c/a)_{S_F}},$$

where $(c/a)_{S_F}$ is the axial ratio for fully ordered phase, and (c/a) is for the partially ordered phase.

The XRD results of a Pt-rich film are shown in Fig. 2. One can see that although the Ft/Pt ratio deviated from the equiatomic one, FePt starts ordering transition at 750 °C. Also, as shown in Fig. 3, the S approaches quickly to unity when the films were annealed at temperatures above 750 °C. The S for the film annealed at 800 °C is 0.9, which is much greater than that of the film with a nearly equiatomic Fe/Pt ratio. These results indicate that it is easier for the Pt-rich FePt alloy to undergo the ordering transition. This was further confirmed by the magnetic measurements.

Fig. 4 shows the electron diffraction pattern and bright field image of the Pt-rich FePt–TiN film annealed at 750 °C. The diffraction result is in good agreement with XRD result, and the particle size of FePt was <10 nm as seen from the image. It is noted that there is no reflection from TiN either in the XRD profiles or the electron diffraction pattern, implying that the TiN remains amorphous-like even after thermal annealing. Another possible reason is that the amount of TiN in

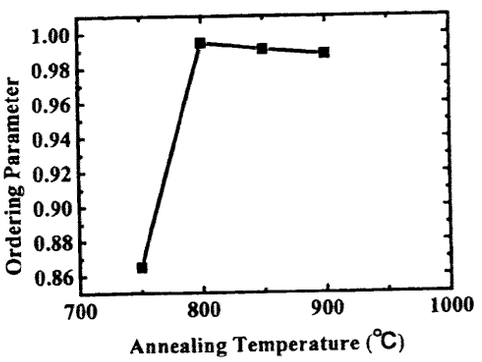

Fig. 3. Change of ordering parameter S with annealing temperature for the Pt-rich FePt–TiN films.

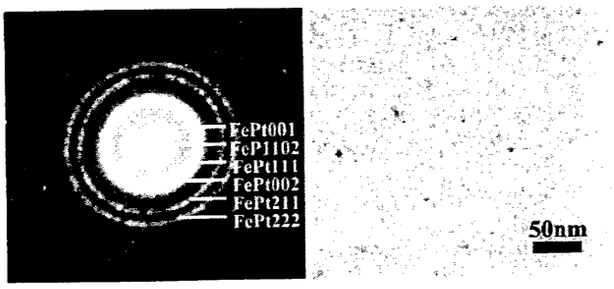

Fig. 4. Electron diffraction pattern and bright field image of a Pt-rich FePt–TiN nanocomposite film annealed at 750 °C.

the film is rather small, especially compared with the Co–TiN nanocomposite films we reported previously [12], for which the reflections from TiN are seen on the electron diffraction pattern.

The M–H curves of the Pt-rich FePt–TiN film annealed at various temperatures are shown in Fig. 5. The as deposited film show fairly soft magnetic performance as shown in Fig. 5a, with magnetic easy axis lying in the film plane. Annealing at 600 °C only caused an increase in saturation magnetization (Fig. 5b). However, the coercivity increases abruptly with increasing annealing temperature to 750 °C (Fig. 5c), moreover, the film annealed at 800 °C cannot be magnetically saturated by a magnetic field of 15 kOe (Fig. 5d). It should also be noted that for the film annealed at 750 °C, there is almost no difference between the magnetization along the in-plane and the perpendicular directions. This is possibly due to the formation of fibrous grain structure along the perpendicular direction, which favors the magnetization in the perpendicular direction [13]. The changes of coercivity with annealing temperature are shown in Fig. 6a. The abrupt increase in coercivity corresponds to the formation of $L1_0$ structure FePt in the film, in accordance with XRD results. However, the coercivity of the films with a nearly equiatomic Fe/Pt increases gradually with increasing temperature. This

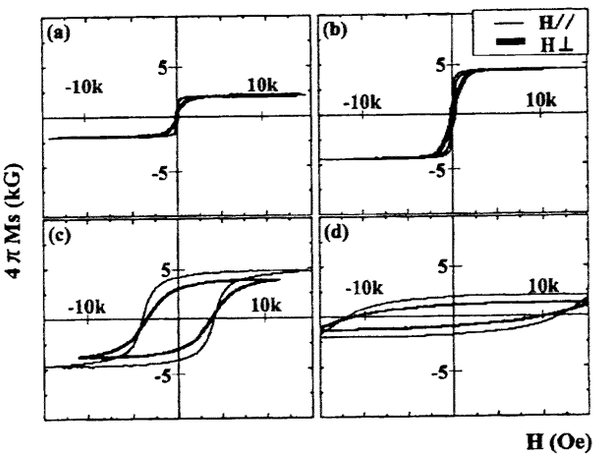

Fig. 5. M–H loops of the Pt-rich films measured at room temperature. (a) as-deposited, (b) 600 °C annealed, (c) 750 °C annealed, (d) 800 °C annealed.

again suggests that it is difficult for the film of this composition to undergo ordering transition, although the mechanism is not clear at present.

4. Conclusions

FePt–TiN nanocomposite films have been prepared by reactive sputtering, followed by thermal annealing at elevated temperatures. Structural characterization has shown that the as-deposited films are amorphous. For the Pt-rich films, ordering transition occurred upon thermal anneal at 750 °C, and FePt with the $L1_0$ structure formed in the film. The in-plane size of the FePt particles is < 10 nm in diameter for such films. However, the films with a nearly equiatomic Fe/Pt ration are found difficult to undergo ordering transformation. The as-deposited films show fairly soft magnetic performance with in-plane anisotropy due to its amorphous nature. The formation of ordered FePt phase results in

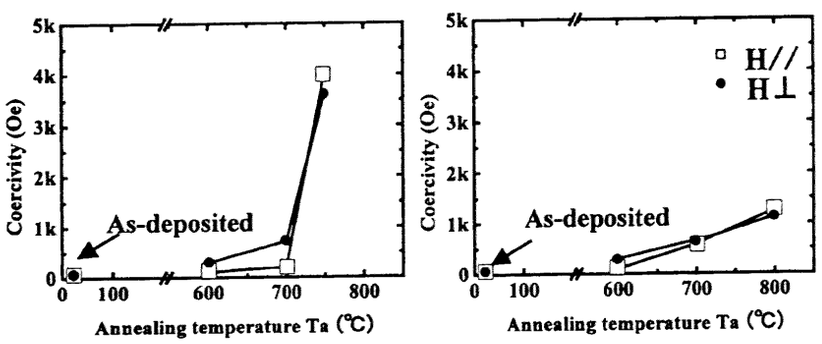

Fig. 6. Dependence of coercivity on the annealing temperature of (a) Pt-rich FePt–TiN nanocomposite films, and (b) the films with equiatomic Fe/Pt ratio.

an abrupt increase in coercivity for the Pt-rich films. Meanwhile, perpendicular anisotropy is also developed possibly because of the formation of fibrous grain structure along the perpendicular direction.

Acknowledgments

This work was partly supported by the Hungarian National Science Foundation under Contract No. JAP-26/00.

References

[1] C.P. Luo, D.J. Sellmyer, Appl. Phys. Lett. 75 (1999) 3162.
[2] C.P. Luo, S.H. Liou, L. Gao, Y. Liu, D.J. Sellmyer, Appl. Phys. Lett. 77 (2000) 2225.
[3] C.M. Kuo, P.C. Kuo, J. Appl. Phys. 87 (2000) 419.
[4] D.H. Ping, M. Ohnuma, K. Hono, M. Watanabe, T. Iwasa, T. Masumoto, J. Appl. Phys. 90 (2001) 4708.
[5] M. Yu, Y. Liu, A. Moser, D. Weller, D.J. Sellmyer, Appl. Phys. Lett. 75 (1999) 3992.
[6] C. Chen, O. Kitakami, S. Okamoto, Y. Shimada, Appl. Phys. Lett. 76 (2000) 3218.
[7] C. Chen, O. Kitakami, S. Okamoto, Y. Shimada, J. Appl. Phys. 87 (2000) 6947.
[8] H. Kanazawa, G. Lauhoff, T. Suzuki, J. Appl. Phys. 87 (2000) 6143.
[9] A. Ceollada, D. Weller, J. Sticht, R. Harp, R.F.C. Fallow, R.F. Marks, R. Savoy, J.C. Scott, Phys. Rev. B 50 (1994) 3419.
[10] M.R. Kim, S. Guruswamy, K.E. Johnson, IEEE Trans. Magn. 29 (1993) 2673.
[11] B.W. Robarts, Acta Metall. 2 (1954) 597.
[12] C.C. Chen, J. Shi, M. Hashimoto, Surf. Coat. Technol. 151–152 (2002) 59.
[13] C.C. Chen, M. Hashimoto, J. Shi, Y. Nakamura, O. Nittono, P.B. Barna, J. Appl. Phys. 93 (2003) 6273.

Perpendicular magnetic anisotropy of Co–TiN composite film with nano-fiber structure

C. C. Chen and M. Hashimoto
Department of Applied Physics and Chemistry, The University of Electro-Communications, 1-5-1 Chofugaoka, Chofu-shi, Tokyo 182-8585, Japan

J. Shi,[a] Y. Nakamura, and O. Nittono
Department of Metallurgy and Ceramics Science, Tokyo Institute of Technology, 2-12-1 Meguro-ku, Tokyo 152-8552, Japan

P. B. Barna
Hungarian Academy of Sciences, Research Institute for Technical Physics and Materials Science, 29-33 Konkoly Street, Budapest, Hungary

(Received 16 September 2002; accepted 22 February 2003)

Co–Ti–N films have been prepared by sputter deposition of Co and Ti in $Ar+N_2$ atmosphere. Upon thermal anneal at elevated temperatures, Co (face-centered cubic) and TiN were formed in the film and separated from each other. Fiber-like microstructure developed with Co nano-fibers vertical to the substrate surface, and with their lateral size being less than 10 nm. The magnetic anisotropy of such films depends strongly on the film thickness. The Co–TiN films with their thickness above 100 nm show perpendicular magnetic anisotropy, which is explained in terms of shape anisotropy. Considering their microstructure, it is concluded that the diameter to length ratio of Co nano-fibers is an important factor controlling the magnetic anisotropy. For the Co–TiN film to show perpendicular magnetic anisotropy, the diameter to length ratio has to be smaller than 0.07 according to the experimental results. TiN in the films plays an important role in separating Co nano-fibers and thus to reduce the lateral magnetic interaction among them. The nano-scale nature and perpendicular magnetic anisotropy of the Co–TiN nanocomposite film make it a very promising candidate for future ultrahigh magnetic recording media. © *2003 American Institute of Physics.*
[DOI: 10.1063/1.1567032]

I. INTRODUCTION

Due to their unique structure and exceptional properties, magnetic nanocomposites are considered promising materials for future high-density magnetic recording.[1–3] A magnetic nanocomposite film is generally composed of a magnetic phase such as Co and its alloys, and at least one nonmagnetic phase (SiO_2, Al_2O_3, Si_3N_4, etc.). Incorporation of such a nonmagnetic phase in the film plays an important role in tailoring the film for desired properties. First of all, the existence of such phase obstructs the growth of grains of magnetic phase during thermal processes; as a result nano-size grains of the magnetic phase can be obtained, which is of great advantage in achieving ultrahigh areal density when the films are used as recording media. Furthermore, the nonmagnetic phase inclusion will separate the grains of magnetic phase and thus reduce the magnetic exchange coupling among the magnetic grains, which is a source of media noise. An additional advantage of using a nanocomposite as recording media is that the incorporation of a properly chosen nonmagnetic phase can provide chemical and mechanical protection for the grains of the magnetic phase, which will certainly improve the reliability of devices in practical application.

Early work on magnetic nanocomposites has found that Co-based nanocomposite films show good soft magnetic properties, i.e., extremely low coercivity and high frequency response of permeability.[4] Furthermore, such films, depending on compositions, also show giant magnetoresistance due to the spin-dependent tunneling effect, which originates from the granular structure of the films.[5,6] Lately, magnetic nanocomposite films have been studied as recording media. It is known that for ultrahigh density recording, the media should have high-anisotropy energy to retain thermal stability. For this purpose, CoPt and FePt alloys have been extensively studied as the magnetic phase in nanocompsite films, because such alloys form an ordered phase with a $L1_0$ structure, which has a high-anisotropy constant, 5×10^7 erg/cm^3 for CoPt and 7×10^7 erg/cm^3 for FePt, respectively.[7–10] Nevertheless, little has been reported about the perpendicular anisotropy of nanocomposite films.[11,12]

In the present work, Co–Ti–N ternary alloy is employed to form a Co-based nanocomposite. The Ti and N are designated to form TiN as the nonmagnetic phase in the nanocomposite, which is a structural material known for its high hardness, thermal and chemical stability. In this article, we report

[a]Author to whom correspondence should be addressed, electronic mail: shi@mtl.titech.ac.jp

the perpendicular anisotropy of the Co–TiN nanocomposite films.

II. EXPERIMENT

Co–Ti–N films were deposited onto single crystalline MgO (001) substrates by reactive sputtering method, with pure Ar as the sputtering gas and N_2 as the reactant gas. A complex target set was used which includes a Co–Ti alloy plate at the back and a Ti plate with a concentric hole at the front. Changing the front Ti plate with different size of the hole can control the composition of the film. The vacuum chamber was evacuated to 1.3×10^{-4} Pa before depositions and the working pressure was 5–6 Pa. Co–Ti–N films were prepared at N_2 partial pressure range of $1.3\times10^{-4}-6.7\times10^{-3}$ Pa, and all the depositions were conducted at room temperature. The deposition time was varied from 15 to 120 min in order to prepare the films with different thicknesses. Postdeposition annealing of the films was conducted in a vacuum, at temperatures from 400 to 900 °C and for 180 min. The composition of the Co–Ti–N film was analyzed by x-ray photoelectron spectroscopy (XPS), and the structures of the as-deposited and annealed films were characterized by x-ray diffraction, plan-view and cross-sectional transmission electron microscopy (TEM). The magnetic properties of Co–Ti–N films were measured by vibrating sample magnetometer at room temperature.

III. RESULTS AND DISCUSSIONS

A. Perpendicular magnetic anisotropy of Co–Ti–N films

Figure 1 shows the magnetic hysteresis loops of Co–Ti–N films of different thicknesses. All the films were annealed at 700 °C for 3 h. The magnetic field was applied both parallel and perpendicular to film surface. One can see that for the films with thickness less than 100 nm, similar magnetization behavior has been shown in both parallel and perpendicular directions. However, when the film thickness was increased to 100 nm and above, perpendicular direction becomes the easy axis of magnetization as shown in Figs. 1(e)–1(h), indicating that perpendicular magnetic anisotropy is developed. These results indicate that the magnetic anisotropy depends strongly on the film thickness. It is also seen from Figs. 1(f) and 1(h) that the remanent magnetization (Mr) of the films is very close to their saturation magnetization (Ms), i.e., the squareness ratio (Mr/Ms) is close to unity. Furthermore, the anisotropy field (H_k) and anisotropy energy (K_u) are 4 kOe and 6×10^5 erg/cc, respectively, and the latter is determined by $K_u=M_sH_k/2$.

The change of saturation magnetization and coercivity (Hc) of the Co–Ti–N films measured in the perpendicular direction with film thickness is shown in Fig. 2. Both the Ms and Hc increase with increasing the film thickness. The Hc tends to saturate when the film thickness exceeds 100 nm, while the Ms keeps increasing with the film thickness.

In order to understand the origin of the magnetic anisotropy and the relation between film structure and magnetic properties, the films were characterized by transmission electron microscopy (TEM) and x-ray diffraction. Figure 3

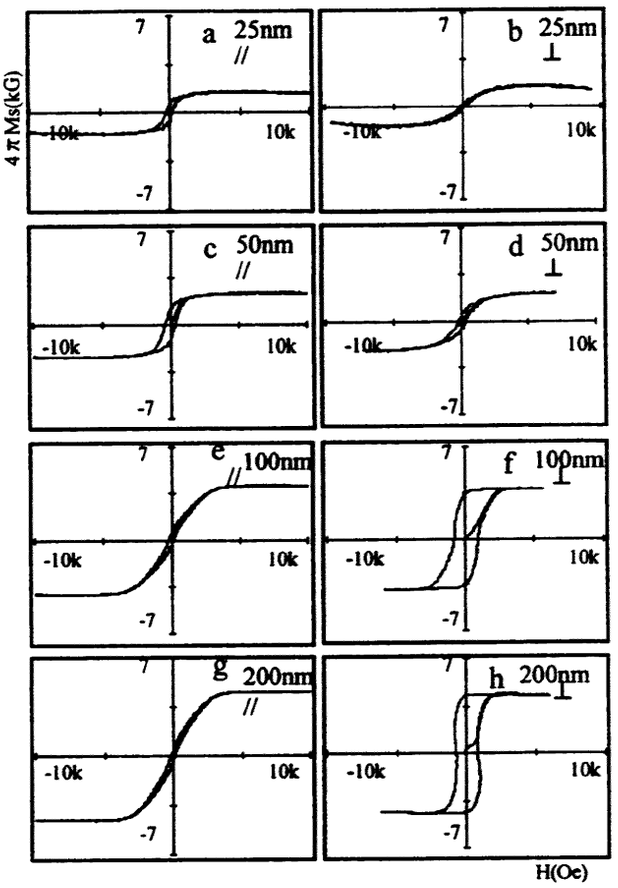

FIG. 1. Magnetic hysteresis loops of Co–TiN films of various thicknesses. The loops on left side were measured along the parallel direction, and the loops on right side were measured along a perpendicular direction.

shows the electron diffraction pattern and plan-view TEM image of the Co–TiN film of a thickness of 200 nm after thermal anneal at 700 °C. From the indexing results of electron diffraction [Fig. 3(a)], it is known that the film is composed of Co and TiN. And the crystal structure of the Co is face-centered cubic (fcc) rather than a hexagonal close-packed (hcp) structure. The bright field image of the film is shown in Fig. 3(b). From this micrograph one can see that the microstructure is featured with fine particles with their

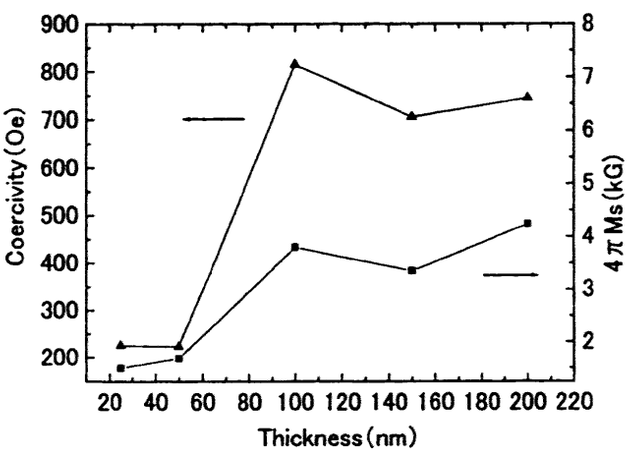

FIG. 2. The changes of saturation magnetization and coercivity of Co–TiN film measured in a perpendicular direction with film thickness.

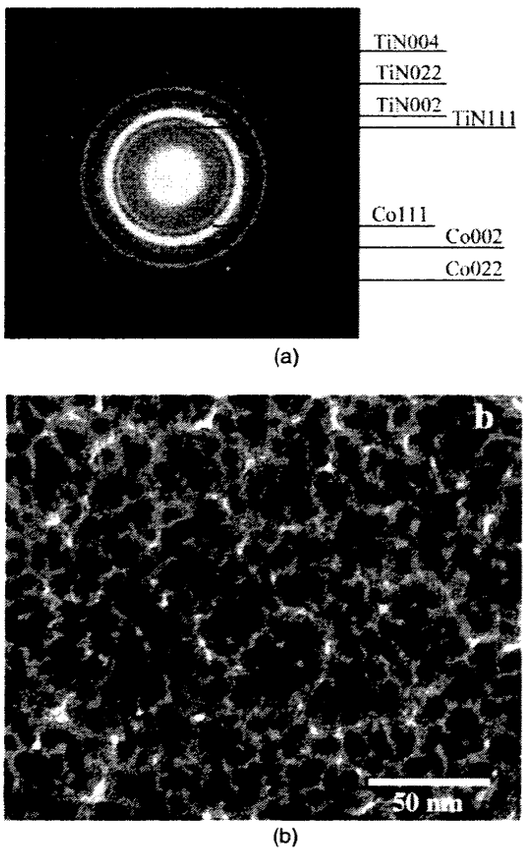

FIG. 3. Selected-area electron diffraction pattern with indexing result (a), and plan-view TEM bright-field image of Co–TiN film (b).

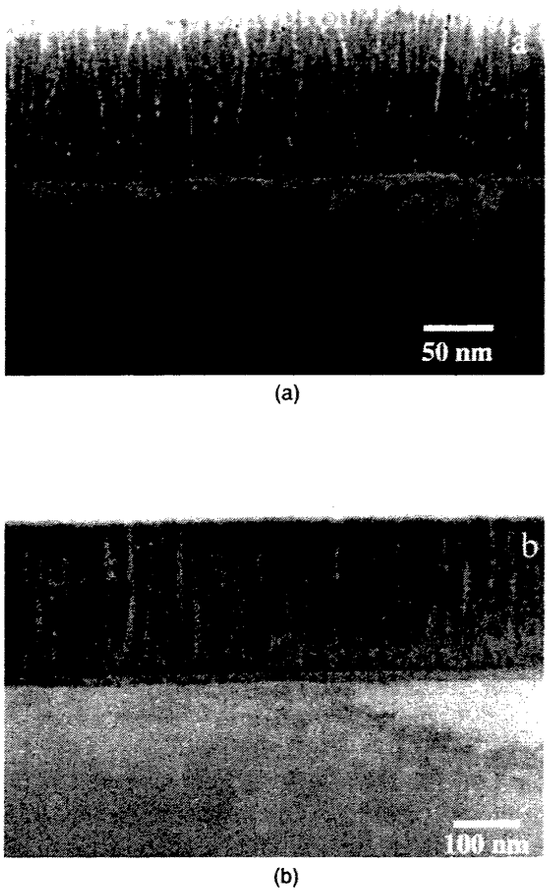

FIG. 4. Cross-sectional TEM bright-field image of the same Co–TiN film as shown in Fig. 3: (a) as-deposited film, and (b) the film annealed at 700 °C.

in-plane sizes ranging from 5 to 10 nm in diameter. Owing to the fact that the diffraction rings of Co are rather spotty campared with those from TiN as shown in Fig. 3(a), it is conceivable that the particles with diffraction contrast are Co, and the phase with brighter contrast around the particles is TiN. This result shows that the Co–TiN film has a granular structure, and we believe that the small in-plane size of Co particles and the way they are ditributed in the film are important factors that affect the magnetic performance of the films. However, considering the depth dependence of magnetic anisotropy, we thought that the microstructure feature in the depth direction may be more determinant for the magnetic anisotropy of the film. Therefore, cross-section microstructure observation was also conducted. Figure 4 shows the cross-sectional TEM images of the same film before and after thermal anneal (at 700 °C). Both micrographs show fiber-like structure along the depth direction. The as-deposited film hardly shows diffraction contrast, indicating the amorphous-like nature of the film. On the other hand, fine particles can be seen for the annealed film, again these particles are believed to be Co particles that are in good accordance with those observed in the in-plan view image both in size and distribution. The cross-section observations indicate that the fiber-like structure is formed during the deposition, and Co particles are formed within the fibers during the anneal process. This fiber-like feature of the Co–TiN film is considered to be responsible for the perpendicular magnetic anisotropy of the Co–TiN films.

Several reasons may cause pependicular magnetic anisotropy in magnetic films, although generally the easy axis lies in the film plane due to the magnetostatic energy condition. These reasons include preferred crystalline orientation (crystalline anisotropy),[12] special shape (shape anisotropy),[13] and stress in the film (stress anisotropy).[14] In the present work, the crystal structure of the magnetic phase Co is fcc, and neither the electron diffraction nor the x-ray diffraction result show obvious preferred orientation in the film. Therefore, we can omit the possiblity of crystalline anisotropy. As mentioned above, Co particles form fibers along the depth direction, therefore, these fibers may behave as nanowires, which have been reported to exhibit perpendicular magnetic anisotropy when their diameter to length ratios are small enough.[13,15] We attribute the perpendicular magnetic anisotropy of Co–TiN in the present work to a kind of shape effect; and by saying shape effect, we do not mean the shape of a single magnetic particle, but the shape of a collective of magnetic particles, i.e., the fiber. The thickness of the fiber cannot be determined exactly from Fig. 4 because of the superimposition of fibers in the direction of observation. Suppose the average diameter of the fibers is the same as the average diameter of Co particles observed in Fig. 3(b), about 7 nm, and the films begin to exhibit perpendicular anisotropy at a thickness around 100 nm, therefore the critical diameter to length ratio is estimated to be 0.07. It has been shown in the present work that all the Co–TiN films with diameter to

length ratios samller than 0.07 show perpendicular magnetic anisotropy.

It has been reported that Co nanowires, 40 nm in diameter and 1600 nm in length, show perpendicular magnetic anisotropy; this gives a diameter to length ratio of 0.025.[13] And the authors attribute the perpendicular magnetic anisotropy to the shape effect. Co and CoFe alloy nanowires with diameters of 18 nm and lengths of 1100 and 3200 nm, respectively, have also been reported to show perpendicular magnetic anisotropy, and in this case, the diameter to length ratios are approximately 0.016 and 0.006, respectively.[15] On the other hand, Co and CoFe alloy nanowires with diameters of 78 nm and lengths of 840 and 890 nm (diameter to length ratios are about 0.09) did not show perpendicular magnetic anisotropy at all. Summarizing the above results and discussion one can see that the geometrical arrangement of the magnetic phase (crystal) in a film plays an important role in determining the magnetic anisotropy of the film.

Another important condition for such nanowires or fibers to exhibit perpendicular magnetic anisotropy is that they are to be separated by nonmagnetic phases thus to decouple the lateral magnetic interaction between nanowires or fibers, or at least to weaken the interaction to a certain extent.[13,15] In the present work, the atomic ratio of Co to Ti is 1:1 as estimated by XPS analysis. Since both Co and TiN have a fcc structure, and the lattice constants of them are 3.545 and 4.242 Å, respectively,[16,17] the volume ratio of Co to TiN is approximately 1:1.7 in the Co–TiN films. It is believed that the TiN in the film effectively keeps the Co fibers from strong lateral magnetic interaction in the present work.

The reason that Ms increases with film thickness is not clear yet. Ms value of the Co–TiN film with a thickness of 200 nm is about 4.2 kG. Considering the volume fraction of Co in the film, the effective Ms of the Co is about 11 kG, which is only 62% of the bulk value of Co. This is probably due to the very fine size and distribution of the Co in the film, which leads to a situation that a rather large fraction of Co atoms is at the interface (grain boundaries). And such atoms might contribute smaller moments than those within the crystals do.[12]

B. Effect of N_2 partial pressure on the magnetic properties of Co–Ti–N films

Figure 5 shows the dependence of saturation magnetization of Co–Ti–N films on the N_2 partial pressure (P_{N_2}) during sputtering deposition. All the films were *ex situ* annealed at 700 °C for 3 h. It is found that the saturation magnetization of the Co–Ti–N films, both measured in longitude and perpendicular directions, depends strongly on P_{N_2}. At low P_{N_2}, the saturation magnetization is extremely low; with increasing P_{N_2} it increases abruptly to a maximum at P_{N_2} around 1.3×10^{-3} Pa. Thereafter, the saturation magnetization drops to a low level again with increasing P_{N_2}. It is also found that the films deposited at 1.3×10^{-3} Pa show poorer squareness than the films deposited at 6.7×10^{-4} Pa, as measured in the perpendicular direction. Therefore, we consider that 6.7×10^{-4} Pa is the optimal P_{N_2} for preparing Co–TiN films.

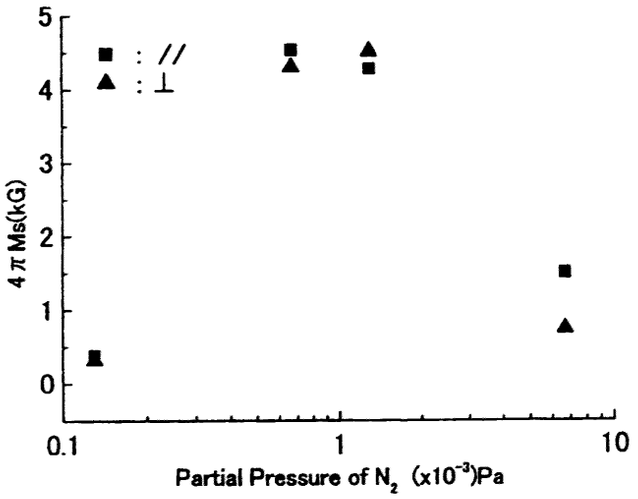

FIG. 5. The relationship between saturation magnetization and N_2 partial pressure during deposition of Co–Ti–N film. All the films were annealed at 700 °C after deposition.

The structure of the films was analyzed by x-ray diffraction in order to understand the dependence of saturation magnetization on P_{N_2}, in view of the film structure. However, the results have shown that all the measured films are x-ray amorphous, i.e., there is no observable peak on the x-ray diffraction profiles, possibly due to the ultrafine grain structure of the Co–Ti–N films, even though MgO single crystal substrates were used. Although we cannot determine the structure of the films definitely from the x-ray diffraction results, it is conceivable that a part of Co atoms may be bound to Ti atoms for the films deposited at low P_{N_2} and then annealed at 700 °C, since Co and Ti form several compounds under thermal equilibrium conditions,[18] and the amount of N incorporated into the films deposited at low P_{N_2} is not sufficient to grab most of the Ti atoms from the Co–Ti bonds during the thermal anneal processes. Furthermore, our previous work has shown that for the films deposited at appropriate P_{N_2}, Ti reacts with N during the thermal anneal and Co is separated out, thus to form Co–TiN structure. It is evident also in the present work, because the saturation magnetization of the film deposited at a P_{N_2} of 1.3×10^{-3} Pa is several times higher than that of the film deposited at low P_{N_2} (1.3×10^{-4} Pa). However, excess P_{N_2} will cause the nitridation of Co to form $(Ti_xCo_{1-x})N$ with NaCl-type structure during the thermal anneal, and thus to impair the magnetic properties.[19]

C. Dependence of magnetic properties on anneal temperature

Figure 6 shows the magnetic hysteresis loops of as-deposited Co–Ti–N films and those films annealed at different temperatures. All the films were prepared with a thickness of 200 nm. It is seen that the as-deposited film hardly shows ferromagnetic performance. For the films annealed at 500 and 700 °C, they show clearly ferromagnetic behavior and perpendicular magnetic anisotropy, because of the separation of Co and TiN during the annealing process. More-

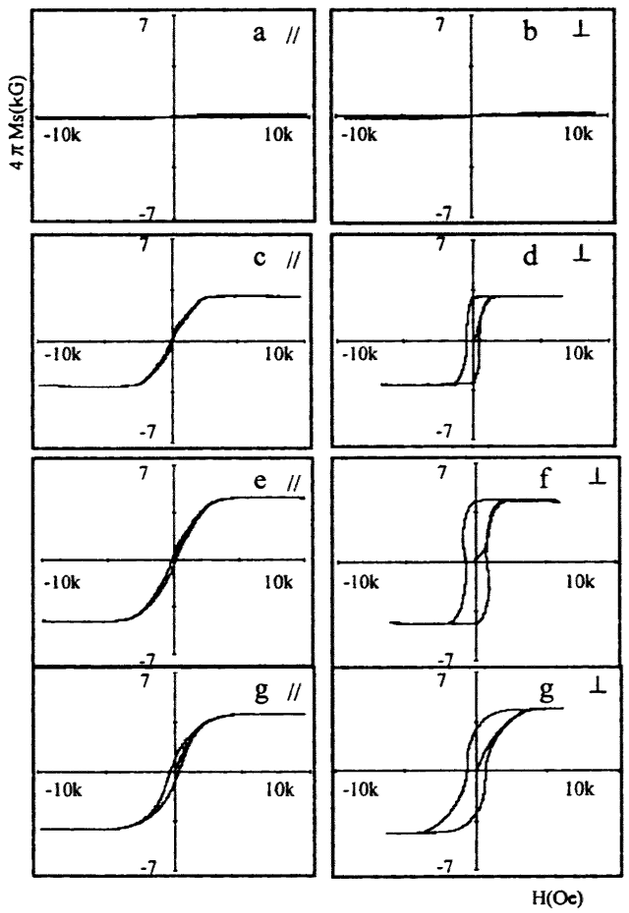

FIG. 6. Magnetic hysteresis loops of Co–TiN films annealed at various temperatures. The loops on the left side were measured along the parallel direction, and the loops on the right side were measured along a perpendicular direction.

over, both Ms and Hc are improved for the film annealed at 700 °C compared with the film annealed at 500 °C. However, further increasing the annealing temperature to 900 °C impairs the shape of the hysteresis loop, i.e., Mr decreases considerably and the squareness ratio drops from 1 to about 0.7. The changes of Ms and Hc in the perpendicular direction with annealing temperature are shown in Fig. 7. It is seen that below 700 °C, both Ms and Hc increase with increasing annealing temperature. The Ms tends to saturate at

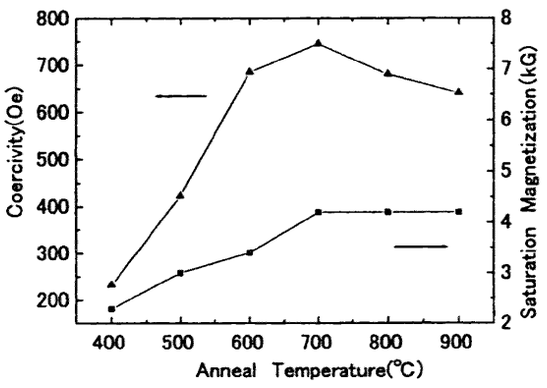

FIG. 7. The changes of saturation magnetization and coercivity of Co–TiN film measured in a perpendicular direction with anneal temperature.

700 °C; on the other hand, the Hc tends to decrease with increasing temperature above 700 °C, which is probably due to the lateral growth of Co. From the above results, it is seen that 700 °C is the optimal annealing temperature for the Co–Ti–N film to exhibit desired magnetic properties, which include perpendicular magnetic anisotropy, relatively large Ms, Hc, and Mr.

It is considered that the Co–TiN nanocomposite film with perpendicular anisotropy is a promising candidate for ultrahigh recording media. TiN in the film will add thermal stability and mechanical strength to the film, in addition to the role it plays in separating the magnetic phase (Co). Moreover, there is a good possibility of further improving the magnetic properties (such as Hc and Hk) to meet the requirement for recording media[20] by controlling the amount, distribution of Co in the film, and/or adding other elements to the film.

IV. CONCLUSIONS

Co–TiN nanocomposite films with perpendicular magnetic anisotropy have been successfully prepared by a simple method which includes sputter deposition of Co and Ti in the $Ar+N_2$ atmosphere and a postdeposition thermal annealing process. Such anisotropy is originated from the fiber-like microstructure of the film with Co developed into nano-size fibers vertical to the substrate surface. The diameter to length ratio of the Co fiber is an important parameter in controlling the magnetic anisotropy of the films, and the critical diameter to length ratio for the Co–TiN film is 0.07 as determined in the present work, i.e., only the films with the ratio smaller than 0.07 show perpendicular magnetic anisotropy.

It is found that there is optimal nitrogen content for the formation of Co–TiN film, and thus the magnetic properties of such film. Less nitrogen in the film leads to incomplete separation of Co and TiN, and excess nitrogen causes the nitridation of Co. In both cases the magnetic properties of the films are impaired.

The magnetic properties of the Co–TiN films, the value of Ms, Hc, and squareness ratio, depend strongly on annealing temperature. Optimal values are obtained at 700 °C.

ACKNOWLEDGMENTS

The authors are grateful to M. Katsuki and his colleagues at Riken Denshi Co. for their assistance with magnetic measurements.

[1] C. P. Luo and D. J. Sellmyer, Appl. Phys. Lett. **75**, 3162 (1999).
[2] T. Hayashi, S. Hirono, M. Tomita, and S. Umemura, Nature (London) **381**, 772 (1996).
[3] H. Wang, S. P. Wong, W. Y. Cheung, N. Ke, M. F. Chiah, H. Liu, and X. X. Zhang, J. Appl. Phys. **88**, 2063 (2000).
[4] S. Ohnuma, H. Fujimori, S. Furukawa, S. Mitani, and T. Matsumoto, J. Alloys Compd. **222**, 167 (1995).
[5] H. Fujimori, S. Mitani, and S. Ohnuma, Mater. Sci. Eng., B **31**, 219 (1995).
[6] Q. Y. Xu, G. Ni, H. Sang, and Y. W. Du, J. Appl. Phys. **87**, 3421 (2000).
[7] M. Yu, Y. Liu, A. Moser, D. Weller, and D. J. Sellmyer, Appl. Phys. Lett. **75**, 3992 (1999).
[8] C.-M. Kuo, and P. C. Kuo, J. Appl. Phys. **87**, 419 (2000).
[9] H. Zeng, M. L. Yan, Y. Liu, and D. J. Sellmyer, J. Appl. Phys. **89**, 810 (2001).

[10] D. H. Ping, M. Ohnuma, and K. Hono, J. Appl. Phys. **90**, 4708 (2002).
[11] G. T. Kraus, Y.-C. Lu, J. E. Trancik, D. M. Mitro, E. P. Giannelis, M. O. Thompson, and S. L. Sass, J. Appl. Phys. **82**, 1189 (1997).
[12] C. P. Luo, S. H. Liou, L. Gao, Y. Liu, and D. J. Sellmyer, Appl. Phys. Lett. **77**, 2225 (2000).
[13] D. H. Qin, M. Lu, and H. L. Li, Chem. Phys. Lett. **350**, 51 (2001).
[14] C. L. Platt, J. K. Howard, A. G. Roy, and D. E. Laughlin, J. Appl. Phys. **91**, 772 (2002).
[15] H. R. Khan and K. Petrikowski, Mater. Sci. Eng., **19**, 345 (2002).
[16] Joint Committee on Powder Diffraction Standards, JCPD card, No. 15-806.
[17] Joint Committee on Powder Diffraction Standards, JCPD card, No. 38-1420.
[18] J. L. Murray, in *Binary Alloy Phase Diagrams*, edited by T. B. Massalski, H. Okamoto, P. R. Subramanian, and L. Kacprzak (ASM International, Materials Park, OH, 1990), Vol. 1, p. 1250.
[19] C. C. Chen, J. Shi, and M. Hashimoto, Surf. Coat. Technol. **151/152**, 59 (2002).
[20] K. Ouchi and N. Honda, IEEE Trans. Magn. **36**, 16 (2000).

IEEE Trans. Mag. 39(2003) 3025-3027

Annealing-Induced Properties of Al-N-M (M: Co, Fe) Thin Films

A.G. Roy, *Member, IEEE* and O. Nittono

Abstract—**Al-N-M (Co, Fe) thin films were reactively deposited with two different combinations of targets, namely Al-Co50Fe50 and Al-Co20Fe80 targets, in a two-facing-target type dc sputtering (TFTS) system. Their structural changes were investigated together with the magnetic and electrical property changes accompanying annealing. The magnetization increases with annealing time and temperature for both types of film. All the films show semiconducting conduction except the annealed films prepared with the Al-Co50Fe50 target combination, which show ohmic conduction.**

Index Terms— **Al-N-M (M: Co, Fe) thin films, reactive sputtering, magnetization, resistivity, granular film, composite film.**

I. INTRODUCTION

Recently, very interesting results have been found on the design, synthesis, and properties of nanostructured composite materials. Among these materials, composite films, such as CoPtCr-SiO_2 [1] and FePt-Al_2O_3 [2], have been reported in respect to hard magnetic properties for recording media. On the other hand, Fe-M-O (M= Hf, Zr, rare earth metals [3], Fe-Hf-N [4] and Co- (Si, Al)-(N, O)[5], films have also been reported to have soft magnetic properties. These studies suggest that the soft and hard magnetic properties may be strongly related to the combination of the amount of metal and insulator matrix in the films.

In this study, we focus on nanocrystalline granular films in which small metal particles (Co, Fe) of nanometer size are embedded in an insulator (AlN) matrix. We investigate here annealing-induced magnetic and electric properties for the films with different compositions.

II. EXPERIMENTAL

In this work, an Al (99.95% pure) was used as an upper target while Co50Fe50 and Co20Fe80 alloy targets were used as lower targets. Corning glass (7059) was mostly used as a substrate. Deposition conditions were: target voltage -300V to -500V(DC), sputtering current 400mA, partial gas pressures PN_2/ Ptotal = 0.70 with Ptotal = 0.4Pa. The thickness of the films was about 500nm. The as-deposited films were annealed successively and isothermally in a vacuum of 2.6×10^{-4}Pa. The microstructure of these prepared films was examined by X-ray diffraction (XRD), and transmission electron microscopy (TEM). The composition of Al, Co and Fe elements in the films was evaluated by the inductively coupled plasma (ICP) analysis, and it was confirmed that the composition ratios of the deposited films are Al/Co//Fe = 1/0.14/0.14 for the films prepared with the Al-Co50Fe50 target combination (type-I), and Al/Co/Fe = 1/0.04/0.16 for the films prepared with the Al-Co20Fe80 target combination (type-II). Magnetic and electrical properties were measured by a vibrating sample magnetometer (VSM) and the four-probe method respectively.

Manuscript received January 6, 2002. A. G. Roy is with the Data Storage Systems Center, Carnegie Mellon University, Pittsburgh, PA 15213 USA (e-mail: agroy@ece.cmu.edu). O Nittono, was with Tokyo institute of technology, Japan. He is now with Fukushima University, 1 Kanayagawa, Fukushima, Japan 960-1296 (e-mail: onittono@educ.fukushima-u.ac.jp).

III. RESULTS AND DISCUSSION

The microstructures of as-deposited films were found to strongly depend on the alloy target composition. From XRD profiles shown in Fig.1, it is found that as-deposited type-I films are amorphous-like and no specific peak is observed while as-deposited type-II films show three broad peaks, which can be indexed as belonging to the AlN phase. In this connection, the results of ED patterns shown in Figs.2 (a) and (b) show that the type-I film is composed of very small particles of AlN phase and also a small amount of the Co_2Al_5 phase. The type-II film is composed of a large amount of AlN phase and small particles of Co_2Al_5 phase.

The microstructure of the films, including phase separation, depends strongly on the annealing conditions. Firstly, successively annealed films were examined by XRD, and it was revealed that the amorphous-like phase of as-deposited type-I film crystallizes into crystalline phases of AlN and FeCo/FexN around 723K, where FeCo/Fe_XN denotes that distinct identification was not carried out. A similar tendency of crystallization was also observed for type-II films. Secondly, we examined isothermally annealed films as shown in Figs.1 (a) and (b). For type-I films, phase separation of AlN and FeCo/Fe_XN takes place around 673K while type-II films give rise to phase separation appreciably around 773K. Figs.2 (c) and (d) show that the grain size increases and electron diffraction rings become much clearer because of phase separation after heat treatment. The rings present after annealing were identified as follows: Co_2Al_5 (hcp): 201 reflection; AlN (hcp): 100, 102, 110 reflections; and Fe_3N-Fe_2N (hcp): 002, 101, 102, 110, 200, 201, 202, 104 reflections, although they are not easily reproduced on the photos.

As-deposited films exhibit very small saturation magnetization (M_s). This probably suggests that the magnetic components in the as-deposited films are partly in a

nonmagnetic state at room temperature. From several measurements of magnetic properties, it was found that type-I and type-II films, when successively annealed at different temperatures showed monotonous increases in magnetization in a temperature range above 523K and 573K, respectively. The M_s was much higher for type-I films than for type-II films over measured temperature ranges. Figure 3 shows the variation of M_s as a function of annealing time for the films isothermally annealed at different temperatures. Figs.3 (a) and (b) show almost the same tendency of increment of magnetization with increasing annealing temperature (T_a). The changes in magnetization can be understood by the microstructural changes caused by heat treatment. A general increase of magnetization with increasing T_a is ascribed to crystallization and formation of magnetic phases induced by annealing. Crystallization and magnetic phase formation are dominant at higher temperatures, as already described, and thus the higher M_s is expected at higher T_a. However, it is noted that type-I film, when annealed at 773K in Fig.3 (a), shows a different tendency: the M_s rapidly increases at 10.8ks and then slightly decreases with increasing annealing time. The observed slight decrease of magnetization with annealing time may suggest the formation of lower magnetic moment phases, but the reason is not clear yet. It was also shown that the coercivity increased with increasing T_a and slightly increased with increasing annealing time. Magnetic properties obtained by heat treatments are summarized in Table I.

The resistivity of the films is also very sensitive to microstructural changes caused by successive and isothermal annealing. Fig.4 shows the results of resistivity for the films successively annealed at different temperatures. Type-II film has much higher resistivity at high T_a than type-I film, indicating that the amount of conducting (or magnetic) component of type-I film is much higher than that of type-II film. The resistivity for type-I films increases up to 723K and then decreases with increasing T_a. On the other hand, the curve for type-II films increases slowly with increasing T_a and then increases very rapidly above 773K. The results can be explained in terms of microstructural changes caused by annealing as follows: 723K and 773K are respective temperatures at which phase separation takes place for type-I and type-II films. Type-I films have much more conducting components than type-II films. Above the phase separation temperature, the formation of conducting phases can make some kind of conducting network for type-I films because of more conducting component, resulting in the decreases in resistivity. In contrast, for type-II films, newly formed conducting phases, which are isolated by insulating AlN matrix, are related to high resistivity, and also the dominant phase separation caused at higher temperatures may also contribute to the increment of resistivity. This speculation was confirmed by the variation of resistivity as a function of annealing time at different temperatures, as shown in Fig. 5. It is noted here that type-I film when annealed at 673K showed an increasing resistivity in the initial stage up to 10.8ks, which is consistent with the result in Fig. 4. This reason is not clear, but probably is related to the finding (Fig. 1(a)) that for type-I film amorphous AlN phase crystallizes around these temperatures.

The temperature dependence of resistivity of the films was also examined and is shown in Fig. 6. For as-deposited and annealed type-II films, there is no change in conduction mechanism: both films show semiconducting behavior. On the other hand, as-deposited type-I film shows semiconducting behavior, but annealed type-I film shows ohmic behavior. This is also explained by assuming that annealed type-I films make some kinds of conducting network after phase separation caused by annealing because of large amounts of conducting component. The resistivity of the films is shown in Table I.

IV. Conclusion

Magnetic and electric properties of reactively sputtered Al-N-M (M: Co, Fe) thin films containing different M components have been investigated. The effect of successive and isothermal annealing on magnetic and electric resistivity was explained in terms of microstructural changes caused by annealing. The M_s increases with increasing T_a because of the formation of magnetic phases during annealing. The films prepared with the Al-$Co_{50}Fe_{50}$ target combination show higher magnetization and smaller coercivity than the films prepared with the Al-$Co_{20}Fe_{80}$ target combination. The films also showed different conduction behavior, such as semiconducting and ohmic conductions, depending on the amount of the magnetic component.

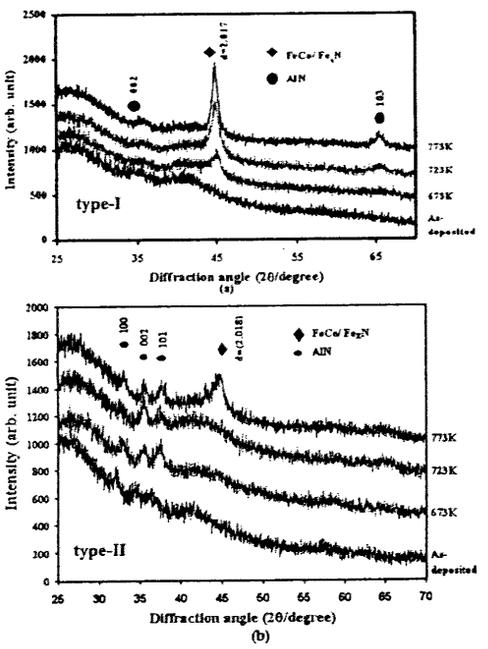

Fig. 1 XRD profiles of Al-N-Co-Fe films annealed at different temperatures for 118.8ks: (a) type-I, (b) type-II.

TABLE I PROPERTIES OF DIFFERENT TYPES OF FILMS ANNEALED UPTO 773K

Kind of film	Kind of target	Magnetization (emu/cm^3)	Coercivity (Oe)	Resistivity ($\mu\Omega$-cm)
Al-N-Co-Fe	Al-$Co_{50}Fe_{50}$	~638	30 ~ 80	~1700
Al-N-Co-Fe	Al-$Co_{20}Fe_{80}$	~450	50 ~ 90	~25×10^4

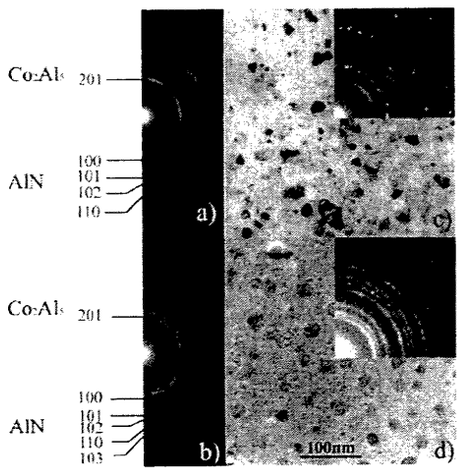

Fig. 2 ED and TEM images of Al-N-Co-Fe films prepared with type-I and type-II target combination: (a) as-deposited (type-I), (b) as-deposited (type-II), (c) and (d) annealed at 973K for 10.8ks for (type-I) and (type-II), respectively.

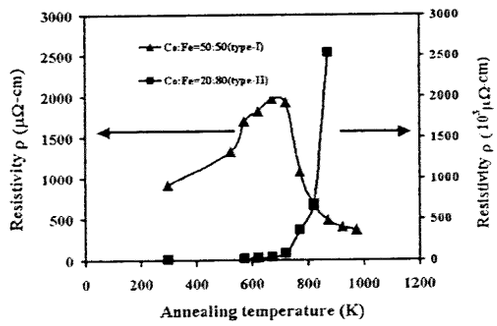

Fig. 4 Variation of resistivity as a function of annealing temperature for the films successively annealed at different temperatures for 10.8ks.

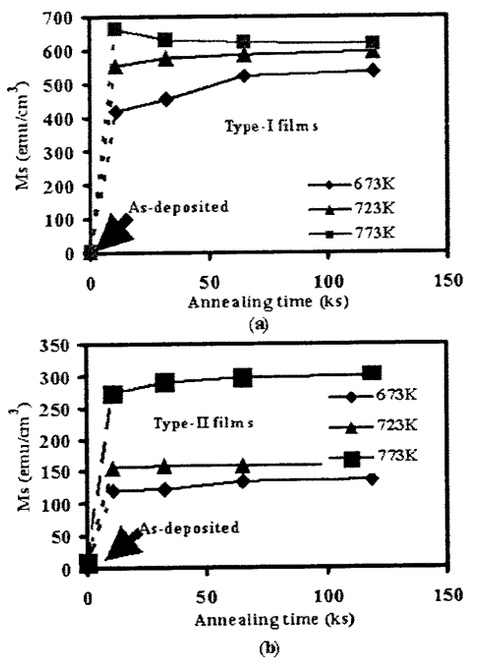

Fig. 3 Variation of saturation magnetization of Al-N-Co-Fe films with annealing time at different annealing temperatures: (a) type-I, (b) type-II.

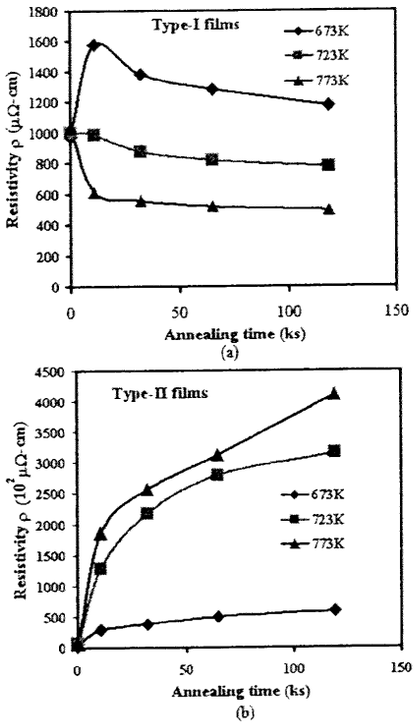

Fig. 5 Variation of resistivity as a function of annealing time at different annealing temperatures: (a) type-I, (b) type-II.

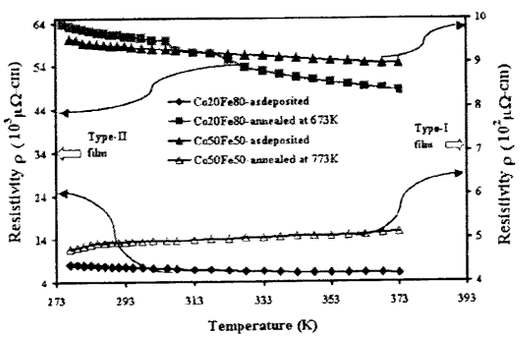

Fig. 6 Variation of resistivity as a function of temperature is shown for as-deposited and annealed type-I and type-II films.

REFERENCES

[1] T. Oikawa et al., "Microstructure and magnetic properties of CoCrPt-SiO_2 perpendicular recording media," IEEE Trans. Magn., vol.38, pp1976-1978, 2002

[2] N. Katayama, M. Matsumoto and A. Morisako, " Magnetic properties of FePt and FePt-Al_2O_3 granular films by post annealing" 47th MMM conference, Florida, 2002.

[3] Y. Hayakawa, A. Makino, H. Fujimori and A. Inoue, "High resistive nanocrystalline Fe-M-O (M=Hf, Zr, rare-earth metals) soft magnetic films for high frequency applications" J. Appl. Phys. 81, pp. 3747-3752, 1997.

[4] Makino and Y. Hayakawa, "Soft magnetic properties and microstructure of nanocrystalline Fe-Hf-N sputtered films," IEEE Trans. Mag. 31 (6), pp. 3874-3876, 1995.

[5] S. Ohnuma, H. Fujimori, S. Furukawa, S. Mitani and T. Masumoto, "Co-(N, O)-based granular thin films and their soft magnetic properties," J. Alloys and Compounds, 222, pp.167-172, 1995.

JOURNAL OF MATERIALS SCIENCE 36 (2001) 343–349

Preparation and characterization of Ni-C composite films

J. SHI*,‡, Y. HASHIBA, O. NITTONO
Department of Metallurgical Engineering, Tokyo Institute of Technology, 2-12-1, Oh-okayama, Meguro-ku, Tokyo 152-8552, Japan
E-mail: shi@pc.uec.ac.jp

Ni-C composite films were prepared using a codeposition method, their structure and electrical properties were investigated. Depending on experimental conditions, two typical structures are found for as-deposited Ni-C films: i) amorphous Ni-C alloy film; ii) granular film with Ni_3C granules and inter-granule amorphous carbon. The amorphous Ni-C films show ohmic conduction behaviour with very high resistivity. On the other hand, granular films with high carbon content show semiconductive characteristics. The electrical property and conduction behaviour are correlated with the film structure. Besides, the crystallization behaviour of the amorphous Ni-C film was also studied.

1. Introduction

Nanostructured composite films have attracted both scientific and technological interests in recent years because of their size-dependent novel properties, and the fact that their properties can be controlled by adjusting the deposition parameters [1]. Such films are generally prepared by sputtering, laser ablation of composite material targets, or by reactive sputtering of metal targets, with their structures covering the combinations of metal-insulator and metal-semiconductor [2, 3]. In our previous work [4], we have reported the formation of Ni_3C nanocrystallites in codeposited Ni-C films, in which amorphous carbon was also incorporated. Amorphous carbon films, due to their hardness and chemical inertness, are often used as protective coatings against friction and corrosion [5–7]. In addition, the conductivity of amorphous carbon films depends strongly on the bonding state of carbon, the films varied from insulators to semiconductors and even to conductors depending on the deposition method and conditions [8]. Therefore, nanostructure composite films combining metal and amorphous carbon may also yield novel mechanical and electrical properties. In the present work, the structure and electrical properties of Ni-C composite films were investigated.

2. Experimental

A dual-source deposition system was used to prepare the Ni-C composite films, which includes a Kaufman ion source [9] used for ion beam sputtering deposition of Ni, and a compact electron cyclotron resonance (ECR) plasma source for chemical vapor deposition (CVD) of carbon. Plasma CVD has been widely used for the deposition of carbon films such as diamond, diamond-like and a-C : H films [10–12]. During deposition, the Kaufman ion source was operated to produce an argon ion beam directing to a Ni target (99.99%) with an energy of 2 keV and a beam current of 20 mA. The reaction gases supplied to the ECR plasma source were premixed methane (CH_4) and hydrogen (H_2) gases with their flow rate controlled by mass flow controllers. The power supplied to the source was fixed to 245 W. The substrates used were freshly cleaved rock salt (NaCl) and glass slides respectively for structure analysis and property measurements. Nickel and carbon were codeposited onto these substrates by simultaneously operating the two sources. Before depositions, the system was evacuated to a base pressure of less than 6×10^{-5} Pa. The structure of the films were characterized by transmission electron microscopy (TEM), and the compositions of the films were determined by Auger electron spectroscopy (AES). The resistivity was measured by the four-probe method.

3. Results

3.1. Structure of Ni-C composite films

The color of the Ni-C films deposited at low CH_4 flow rates was the same as that of pure metal films, with the increase in CH_4 flow rate, the color of the films changed from silver to gray and dark gray but all with metallic luster. Fig. 1 shows the electron diffraction patterns and TEM bright field images of Ni-C composite films deposited at varied CH_4 flow rates, whereas the H_2 flow rate was fixed to 25 sccm. And all the

* Author to whom all correspondence should be addressed.
‡ *Present Address:* Department of Applied Physics and Chemistry, The University of Electro-Communications, 1-5-1, Chofugaoka, Chofu-shi, Tokyo 182-8585, Japan.

0022–2461

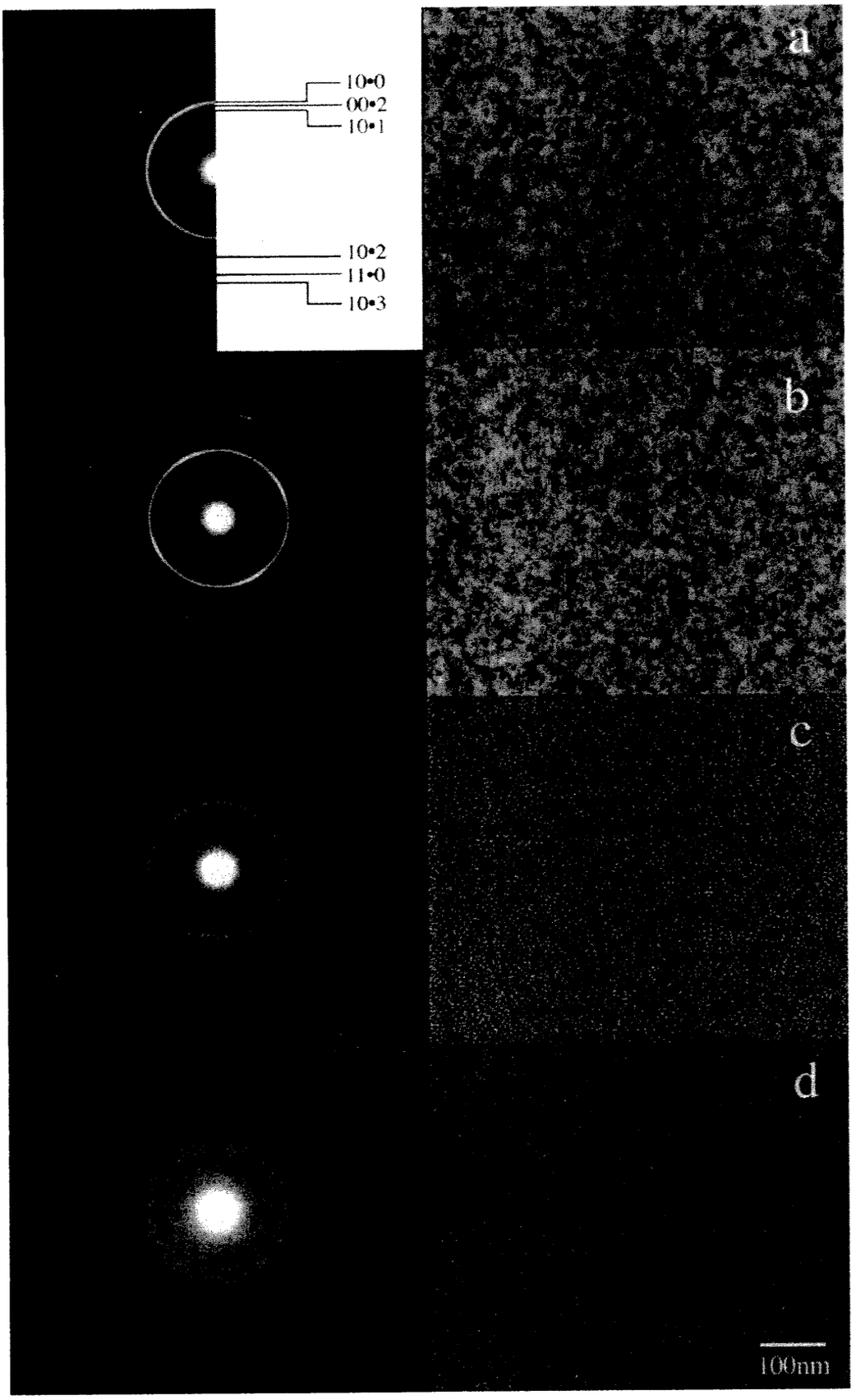

Figure 1 Electron diffraction patterns and TEM bright field images of Ni-C films deposited at ambient temperatures with CH_4 flow rate of (a) 0.1 sccm, (b) 0.2 sccm, (c) 0.35 sccm and (d) 0.5 sccm.

films were deposited at ambient temperatures which were about 50 °C, without intentionally heating the substrates. The indexing results of the diffraction pattern shown in Fig. 1a confirm the formation of Ni_3C carbide in the film, which is a phase with hexagonal close-packed (hcp) structure. No reflection from Ni can be observed in the diffraction pattern, indicating that the Ni in the film reacted with carbon completely. Increasing the CH_4 flow rate to 0.2 sccm did no change the crystal structure of the Ni-C film because the film deposited

at such condition exhibits similar diffraction pattern (Fig. 1b) with that shown in Fig. 1a. When the CH_4 flow rate was increased to 0.35 sccm and above, the electron diffraction patterns do not exhibit any sharp diffraction ring due to the Ni_3C carbide, broad halos take the place of the rings. The halos appear covering the positions of 0.1 reflection of the hexagonal close-packed (hcp) Ni_3C carbide and 111 reflection of the face centered cubic (fcc) Ni phase. These results indicate that the films deposited with a CH_4 flow rate of 0.35 sccm and above are amorphous.

For films deposited with the CH_4 flow rate below 0.35 sccm, the crystallites of Ni_3C carbide of less than 10 nm in diameter can be seen clearly in the TEM bright field images (Fig. 1a and b), and the size of these crystallites decrease slightly with increasing the CH_4 flow rate. With the change of film structure from nanocrystallites to amorphous, the microstructure of the films also changed abruptly. The amorphous Ni-C film reveals much finer and uniform microstructure compared with nickel carbide nanocrystallite films, and a comparison of Fig. 1d and e shows that the microstructure became even finer with increasing the CH_4 flow rate.

All the films deposited at 200°C are composed of Ni_3C carbide as can be seen from the diffraction patterns and indexing results. The TEM images in Fig. 2 also illustrate that these films reveal granular structures with Ni_3C granules, and the size of these granules decreases with increasing the CH_4 flow rate. Compared with those deposited at ambient temperatures, these films are characterized by some thin inter-granule regions with light contrast, which are possibly composed of amorphous carbon. The enlargement of the image shown in Fig. 2a is given in Fig. 3. This further confirms the existence of such inter-granule regions as indicated by arrows in the image.

Fig. 4 shows the change of relative nickel content in the film and deposition rate with CH_4 flow rate for

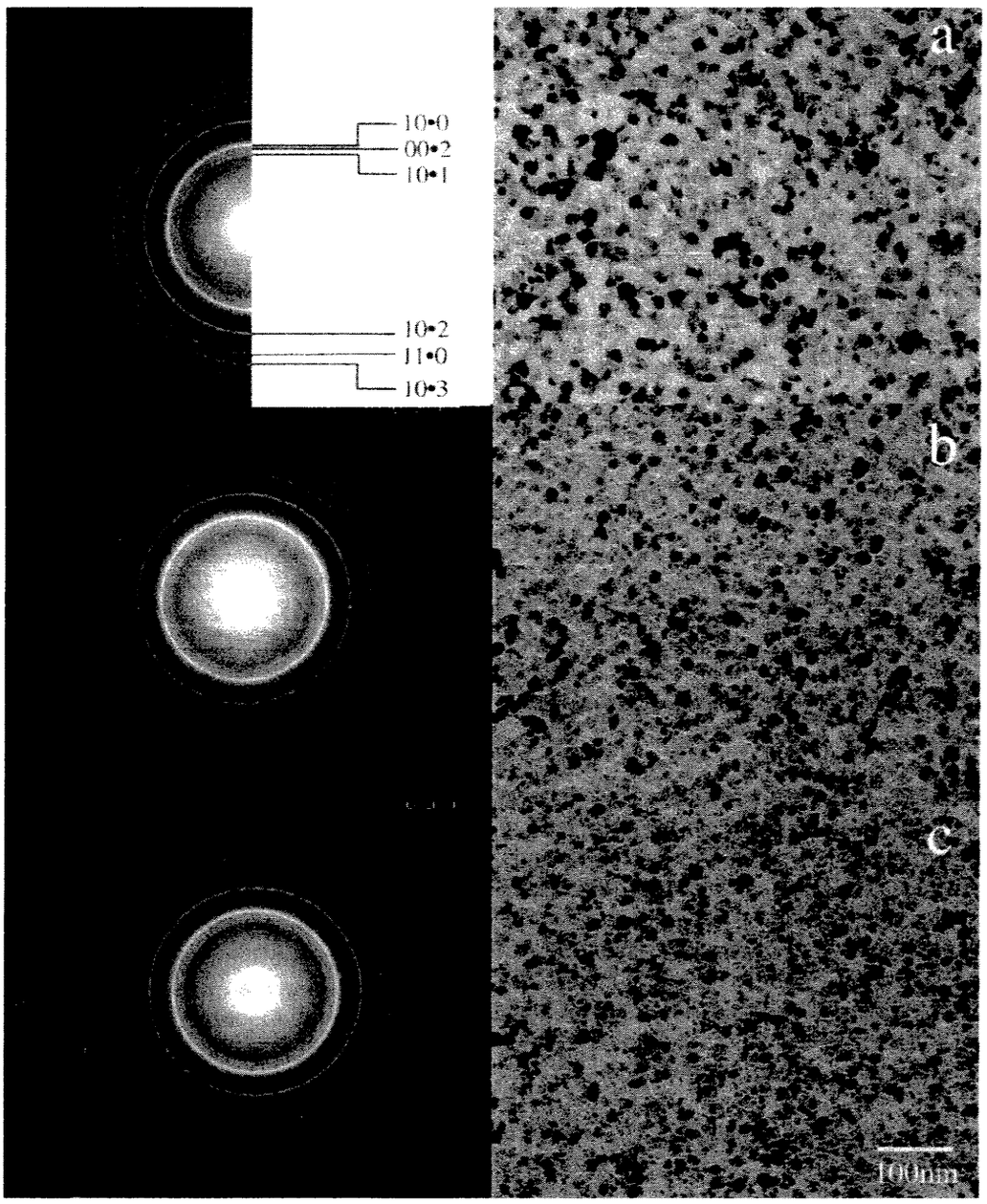

Figure 2 Electron diffraction patterns and TEM bright field images of Ni-C films deposited at ambient temperatures with CH_4 flow rate of (a) 0.02 sccm, (b) 0.2 sccm and (c) 0.35 sccm.

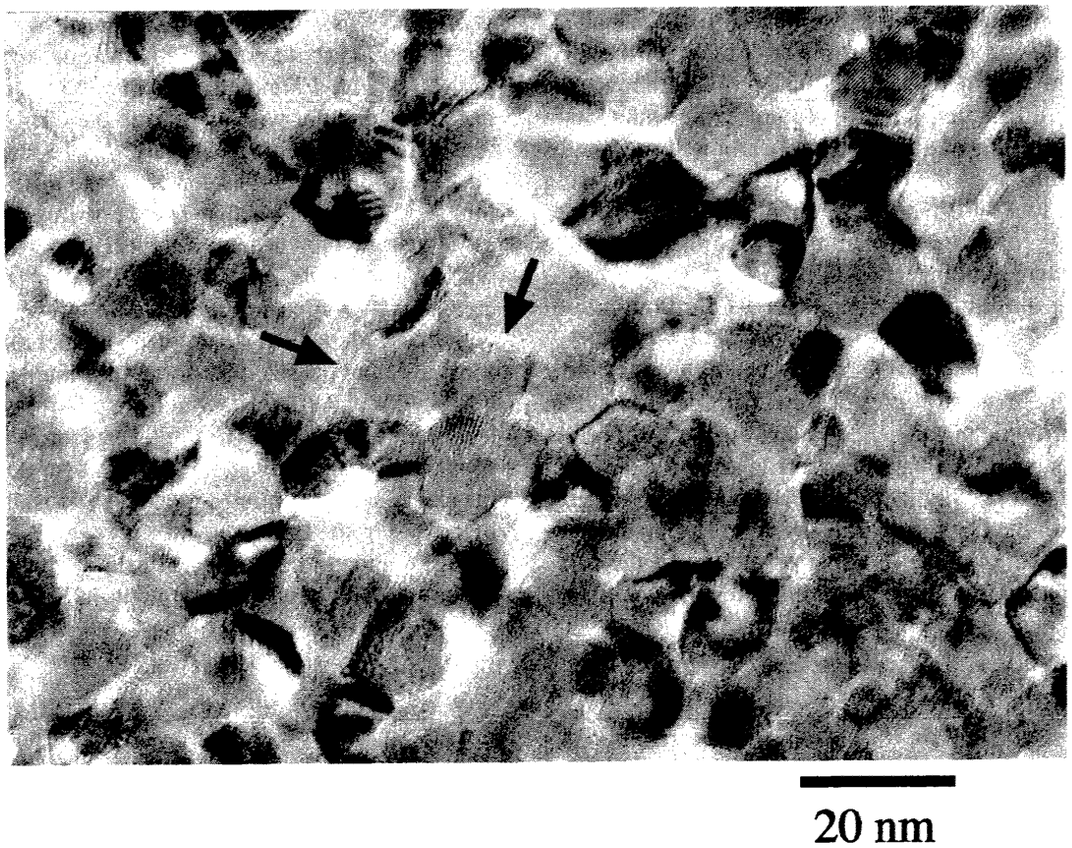

Figure 3 HRTEM image of Ni-C film deposited at 200 °C with a CH_4 flow rate of 0.02 sccm. The arrows indicate the inter-granule amorphous carbon.

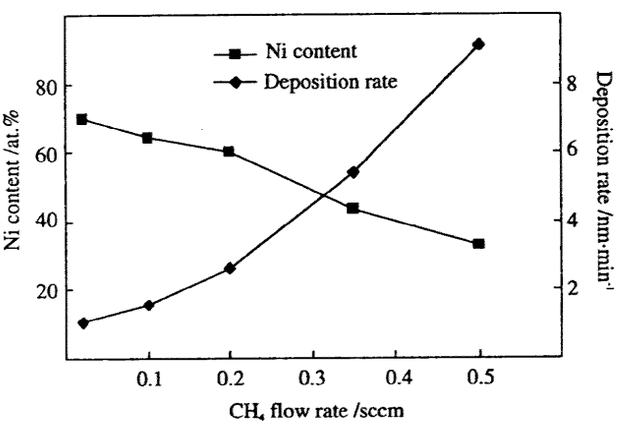

Figure 4 Dependence of Ni content, deposition rate for Ni-C films on the CH_4 flow rate.

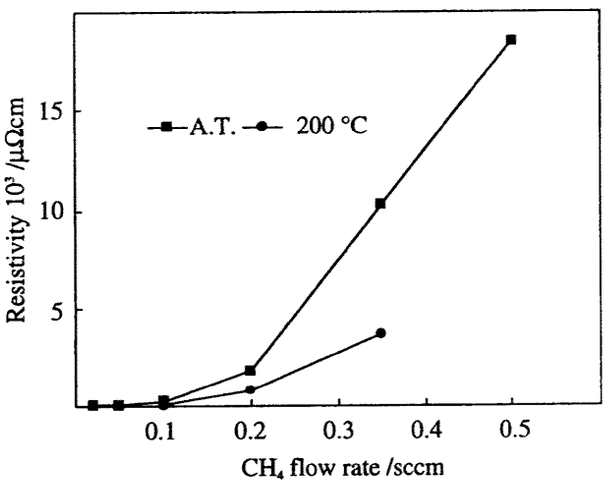

Figure 5 Dependence of resistivity of Ni-C films on the CH_4 flow rate. A.T. in the figure stands for ambient temperature.

films deposited at ambient temperatures. The relative nickel content decreases almost linearly with increasing CH_4 flow rate. It should be noted that the deposition rate and absolute load of Ni in the films were fixed for all the films, therefore this result indicates that the absolute content of carbon in the film increases with increasing CH_4 flow rate, and this leads to the increase of the deposition rate of Ni-C films. The deposition rate increases monotonically with a close to a parabolic law over the considered range of CH_4 flow rate.

3.2. Electrical properties of Ni-C composite films

Fig. 5 shows the change of resistivity of Ni-C films with CH_4 flow rate and deposition temperature. For films deposited at ambient temperatures, the resistivity increases gradually with the CH_4 flow rate below 0.2 sccm, and thereafter the resistivity goes up abruptly with increasing the CH_4 flow rate, which is the same tendency as deposition rate with CH_4 flow rate shown above. This increase of resistivity can be explained by the increase of carbon content in the films and the change of film structure from nanocrystallites of Ni_3C to amorphous. On the other hand, the granular Ni-C films deposited at 200°C reveal gradual increase in resistivity with increasing CH_4 flow rate. It should also be noted that the resistivity of Ni-C films deposited at 200°C is lower than that of films deposited at ambient temperature, because of the relatively large size of Ni_3C crystallites.

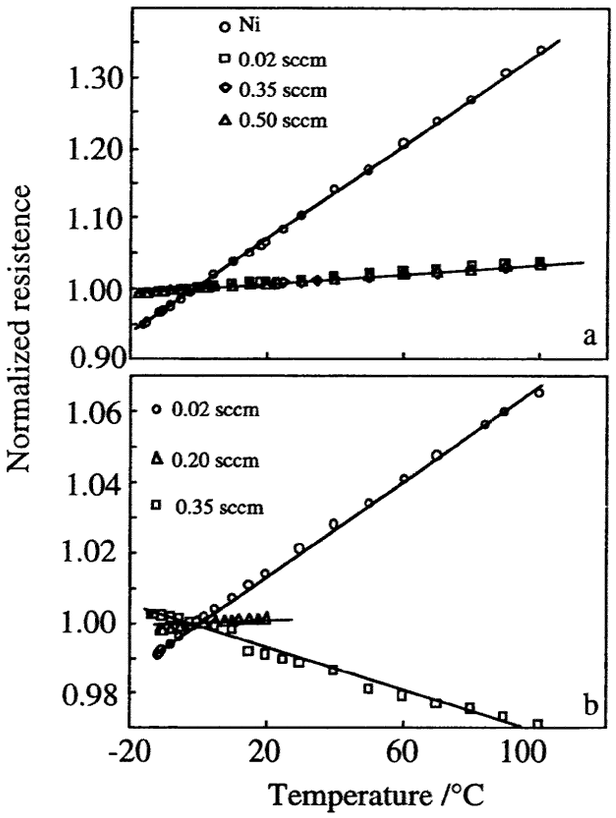

Figure 6 Temperature dependence of normalized resistence of Ni-C films deposited at (a) ambient temperature and (b) 200 °C.

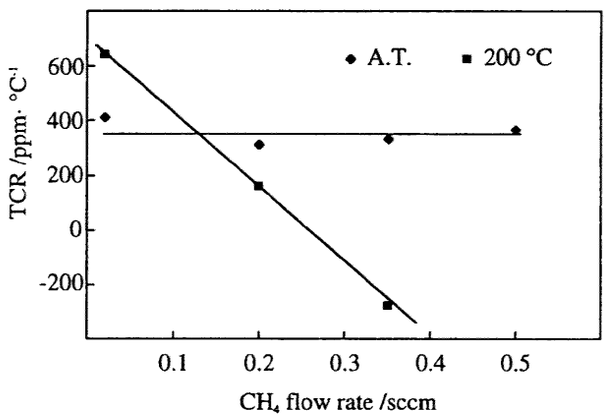

Figure 7 Relationship between TCR value and the CH_4 flow rate. A.T. in the figure stands for ambient temperature.

Fig. 6 shows the temperature dependence of normalized resistance of Ni-C films deposited at ambient temperatures and 200 °C. In Fig. 6a, the result for pure Ni film is also shown for reference. Values of temperature coefficients of resistance (TCR) for Ni-C films are shown in Fig. 7. It can be seen from Fig. 6a, Ni-C films deposited at ambient temperature show very low TCR values compared with that of metallic nickel film, nevertheless, all the films show ohmic characterization even for those in the amorphous state with very high resistivity. Besides, the TCR value does not change with increasing the CH_4 flow rate. While for films deposited at 200 °C, the TCR value decreases with increasing the CH_4 flow rate, especially, it changes the sign from positive to negative at a CH_4 flow rate of 0.35 sccm. This suggests that different processes are involved concerning the conduction mechanism.

3.3. Crystallization of amorphous Ni-C films

The crystallization behavior of amorphous Ni-C film was studied by annealing the films in a vacuum furnace ($<3 \times 10^{-4}$ Pa). Fig. 8 shows the electron diffraction patterns and TEM bright field images of the films annealed at various temperatures for 3 hours. For the films annealed below 300 °C, no perceivable change was observed either in the diffraction pattern or in the microstructure. When the film was annealed at 300 °C, the diffraction pattern shows several weak, broad, but recognizable diffraction rings, which can be identified to be the diffraction rings from the Ni_3C carbide and Ni (Fig. 8a). At this stage, the crystal sizes of Ni_3C and Ni are still not large enough to be visible in the bright field image. However, the film surface lost its original flatness because of the volume change caused by the transformation from amorphous to crystalline phases. For the film annealed at 400 °C, the diffraction rings from the Ni_3C carbide phase disappeared, and the diffraction rings from the fcc Ni phase became stronger, but still relative broad, indicating that the crystal size is still very small. In addition, the weak reflection from graphite begins to appear in the diffraction pattern, as a result of the decomposition of Ni_3C. Further increase in annealing temperature causes the increase of the Ni crystallites both in size and number. When the film was annealed at 600°C, a structure of Ni crystallites, several tens nanometers of size, uniformly dispersed in a amorphous carbon matrix, is seen from the bright field image.

According to these results, the crystallization process took place in the following sequence: in the temperature range from 300 to 400°C, very fine particles of Ni and Ni_3C precipitate from the amorphous phase and then at around 400°C, the Ni_3C carbide decomposes into Ni and graphite; thereafter, nickel precipitates gradually from the amorphous phase and the Ni particles keep growing, this can be seen from the light contrast around Ni particles. Therefore, from these results we conclude that the amorphous Ni-C phase is rather stable and does not show distinct crystallization temperature.

4. Discussion

According to the experimental results, we can see that deposition at lower CH_4 flow rate and higher temperature favors the formation of Ni_3C, which is a nonequilibium carbide phase [13–15]. While deposition at higher CH_4 flow rate and lower temperature favors the formation of Ni-C amorphous phase. Generally, it is extremely difficult to synthesize metal-carbon amorphous alloys by conventional methods such as splash-cooling, because of the high melting temperature of carbon. For example, a study has shown that even with the addition of another metalloid (eg. silicon), there was no amorphous phase formed in the Ni-C-Si system by conventional method [16]. The mechanism for the formation of Ni-C amorphous phase in the present work is considered to be associated with the high deposition rate of carbon when deposited at higher CH_4 flow rates. As stated above, the carbon content and deposition rate increases with increasing the CH_4 flow rate. Therefore

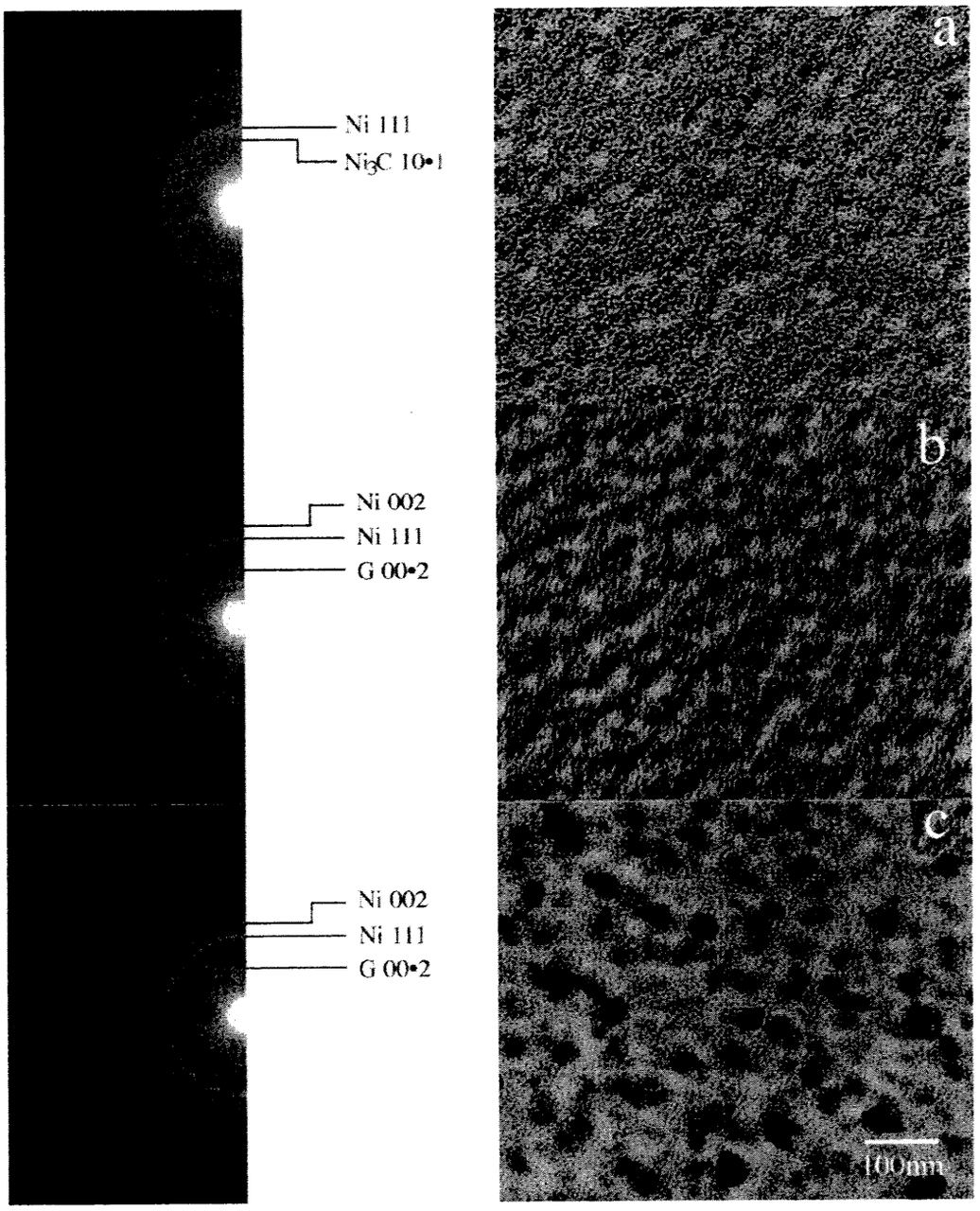

Figure 8 Electron diffraction patterns and TEM bright field images of amorphous Ni-C film after annealing at (a) 300 °C, (b) 400 °C and (c) 600 °C. The original film is shown in Fig. 1c.

we consider that the reaction between Ni and C is suppressed by the fast growth of carbon. Although short range arrangement may be formed in the film in the form of Ni and/or Ni_3C clusters during deposition process, the fast growth of carbon will prevent them from further growing, and thus the formation of amorphous Ni-C phase is promoted.

As shown in Figs 5 and 7, the Ni-C films deposited at ambient temperatures show high resistivity and low TCR values, especially for the amorphous Ni-C films. Both the high resistivity and the low TCR value can be explained by the small electron mean free path (MFP) within the film [17]. The strong scattering of conduction electrons in the present Ni-C films is considered to be caused by the large amount of disorder, very fine grain size, inclusion of amorphous carbon for the Ni-C films with Ni_3C crystallites and structural disorder for the amorphous Ni-C films. According to [18], the behavior of electrical conduction in a material with low TCR can be understood to a great deal if it is assumed that in these materials a lower limit of electron mean free path is reached. Such limit must exist because the MFP can not be smaller than the interatomic distance. If this limit is reached, further decrease in MFP due to phonon scattering is impossible. This may explain the low and almost constant TCR value for the films deposited at ambient temperatures.

On the other hand, Ni-C films deposited at 200 °C have relative low resistivity . However the TCR value of such films drops abruptly to a negative value with increasing CH_4 flow rate (Fig. 7), indicating the conduction behaviour changes to non-ohmic for the film deposited at high CH_4 flow rate. This can be explained in view of the change of films structure. As stated above, when deposited at 200 °C, the amorphus carbon are distribute at inter-granule region (Fig. 3). Therefore, with

increasing the CH_4 flow rate, more amorphous carbon will be incorporated into the film, and thus leading to the encapsulation of all the Ni_3C granules by amorphous carbon at certain CH_4 flow rate. The amorphous carbon incorporated into such films are found to be glassy carbon composed mainly of sp^2 hybridization in the form of disordered graphite [4]. Therefore in Ni-C films, when all the metallic granules are encapsulated by such amorphous carbon, the films show semiconductive characteristics.

5. Conclusions

Ni-C composite films have been prepared by a codepositiion method using ion beam sputtering and microwave plasma chemical vapor deposition. It has been found that the structure and electrical properties depend strongly on the flow rate of reaction gas (CH_4) for the deposition of carbon, and the substrate temperature. The structure of Ni-C film deposited at ambient temperatures changes from nanocrystallites of Ni_3C to amorphous Ni-C alloy with increasing the CH_4 flow rate. The resistivity of the Ni-C film also increases abruptly, but all the films show ohmic conduction behaviour with very low temperature coefficient of resistance.

The Ni-C amorphous phase remains stable below 300 °C. Annealing at 300 °C and above causes the crystallization of Ni, and a structure of nanocrystallites of Ni distributed in amorphous carbon matrix is formed finally.

Granular films with Ni_3C granules and inter-granule amorphous carbon are formed for Ni-C films deposited at 200 °C. The conduction behaviour of such films changes from ohmic for the films deposited with low CH_4 flow rate to semiconductive for the films deposited with high CH_4 flow rate, due to the encapsulation of metallic Ni_3C granules by amorphous carbon.

References

1. R. P. ANDRES, R. S. AVERBACK, W. L. BROWN, L. E. BROUS, W. A. GODDARD, III, A. KALDOR, S. G. LOUIE, M. MOSCOVITS, P. S. PEERCY, S. J. RILEY, R. W. SIEGEL, F. SPAEPEN and Y. WANG, *J. Mater. Res.* **4** (1989) 704.
2. B. ABELES, P. SHENG, M. D. COUTTS and Y. ARIE, *Adv. Phys.* **24** (1975) 407.
3. L. MAYA, W. R. ALLEN, A. L. GLOVER and J. C. MABON, *J. Vac. Sci. Technol.* **13B** (1995) 361.
4. J. SHI and O. NITTONO, *J. Mater. Sci. Lett.* **15** (1996) 928.
5. J. ROBERTSON, *Surf. Coatings Technol.* **50** (1992) 185.
6. A. BUBENZER, B. DISCHLER, G. BRANDT and P. KOIDL, *J. Appl. Phys.* **54** (1983) 4590.
7. H. C. TSAI and D. B. BOGY, *J. Vac. Sci. Technol.* **5A** (1987) 3287.
8. J. MORT and F. JANSEN, "Plasma Deposited Thin Films" (CRC Press, Florida, 1986) p. 2.
9. H. R. KAUFMAN, *J. Vac. Sci. Technol.* **15** (1978) 272.
10. C. R. EDDY, JR. B. D. SARTWELL and D. L. YOUCHISON, *Surf. Coatings Technol.* **48** (1991) 69.
11. W. VARHUE and P. PASTEL, *J. Mater. Res.* **5** (1990) 2441.
12. A. RAVEN, J. E. KLEMBERG-SAPIEHA, L. MARTINU and M. R. WERTHEIMER, *J. Vac. Sci. Technol.* **10A** (1992) 1723.
13. S. NAGAKURA, *J. Phys. Soc. Japan* **12** (1957) 482.
14. T. TANAKA, K. N. ISHIHARA and P. H. SHINGU, *Metall. Trans.* **23A** (1992) 2431.
15. J. WANG, X. F. WU, B. X. LIU and Z. Z. FANG, *Acta Metall. Mater.* **40** (1992) 1417.
16. A. INOUE, S. FURUKAWA and T. MATUMOTO, *J. Mater. Sci.* **22** (1987) 1670.
17. C. KITTEL, "Introduction to Solid State Physics" (John Wiley & Sons Inc, New York, 1996) p. 158.
18. J. H. MOOIJ, *Phys. Stat. Sol.* **17A** (1973) 521.

Received 28 December 1999
and accepted 26 June 2000

Materials Transactions, Vol. 42, No. 12 (2001) pp. 2584 to 2589

Quality Improvement by Annealing for Flash-evaporated Thin InSb Films

Md Abu Taher *, Yumiko Haga, Yoshio Nakamura and Osamu Nittono

Department of Metallurgy and Ceramics Science, Tokyo Institute of Technology, Tokyo 152-8552, Japan.

Thin InSb films were prepared at room temperature by a rapid vacuum evaporation (flash evaporation) method using indium antimonide compound as a source material. The characteristics of the films such as microstructure and electrical properties were investigated in terms of heat treatment procedure. The as-deposited InSb films were found to have polycrystalline structure, and their stoichiometry was much better at higher deposition rates. Their characteristics were strongly influenced by successive annealing. The evaporation of Sb from the film caused by annealing led to poor electrical properties of the films. In order to avoid the evaporation of Sb from the film, an attempt was made to cap an as-deposited film with SiO_2 layer before annealing. The microstructures as well as the galvanomagnetic properties were improved by introducing such capped-annealing. The highest Hall mobility of 2.1×10^4 cm^2/Vs was obtained in an InSb film of 1.0 μm thick, when it was prepared with a deposition rate of 10 nm/s and followed by capped-annealing at 773 K.

(Received August 30, 2001; Accepted October 15, 2001)

Keywords: *indium antimonide, flash evaporation, galvanomagnetic property, electrical resistivity, Hall mobility, Hall coefficient, magnetoresistance, capping effect*

1. Introduction

Fabrication of electronic devices such as infrared devices, Hall effect devices, and magnetoresistance devices[1,2] often requires semiconductor films with high carrier mobility, small band gap, and high magnetic sensitivity. Among the compound semiconductors, InSb has the highest electron mobility and small band gap (0.17 eV at 300 K). Therefore, InSb films appear to be one of the most promising candidates for these applications.

InSb thin films have been prepared by various methods such as vapor-phase-transport reaction,[3] rf sputtering,[4] vacuum evaporation (including flash evaporation and three-temperature evaporation),[5–12] zone-crystallization (melt-regrowth of polycrystalline film),[13] molecular beam epitaxy (MBE),[14–17] and metalorganic chemical vapor deposition (MOCVD).[18–20] InSb films with carrier mobility comparable to that of bulk single crystals are usually obtained by epitaxial growth using MBE or MOCVD on single crystal substrates. The single crystal substrate and the MBE or MOCVD apparatus, however, cost a lot. Therefore, it is especially interesting to develop and study low cost procedures of producing high quality thin InSb films on low cost substrates.

Conventional vacuum evaporation techniques have difficulties in maintaining the stoichiometry of deposited InSb compounds.[8,12,21] This is because In and Sb have very different vapor pressures (at 800 K, 7.51×10^{-6} Pa for In and 1.066 Pa for Sb), and a loss of volatile Sb takes place during vacuum evaporation. However, such kinds of difficulties could be overcome by employing a rapid vacuum evaporation (or a flash evaporation).[9] In this method, when the source materials are flashly evaporated, the average vapor composition can be almost stoichiometric, resulting in maintaining the stoichiometry of deposited films. It is also reported that the films are produced with a good quality when deposited at high deposition rates.[6,7,9] Recently, Tomisu *et al.*[12] also reported that the value of the ratio Sb/(In + Sb) is 50% for the InSb films prepared at the source temperature of 2030 K. This suggests that a high evaporation (or deposition) rate with a short deposition time can serve to reduce the deviation from stoichiometry.

In the present study, firstly we try to confirm the above speculation through a relationship between deposition rate and electrical property. Secondly, the characteristics of thus prepared films are investigated in terms of successive procedures including annealings without and with capping SiO_2 layer.

2. Experimental Procedure

Thin InSb films were prepared by evaporating high purity (99.999%) InSb compound in a high vacuum system less than 10^{-5} Pa. Pre-annealed Corning 7059 glass (size: 21 mm × 26 mm × 1.1 mm) was used as a substrate with a mask for electrical measurements (size: 3 mm × 19 mm with six terminals). The substrates were carefully cleaned before the deposition process: the glass substrates were first rinsed with water and dried, and then immersed into ethanol and rinsed ultrasonically for 600 s, and finally rinsed with acetone for 600 s and then dried. It is reported that higher substrate temperatures above 473 K lead to the deviation from stoichiometry of the InSb film.[12] In fact, we confirmed this in preliminary experiments. Thus, the substrate was not heated intentionally, but irradiated naturally from the crucible during deposition. The substrate temperature was estimated to be lower than 323 K from our previous experiments.[21] The present vacuum chamber has a heat-shielding wall having a small hole for evaporated vapor, which is set just above an alumina-coated tungsten basket (10 mm in diameter, 15 mm in depth). The distance between source material and substrate was about 10 cm. The source temperature and thus the deposition rate (0.5–20 nm/s) were adjusted by changing the electric current flow through the crucible and flow time. The source temperature was estimated to be higher than 2030 K by a pyrometer. In this study, the deposition rate was evaluated directly by a thickness monitor using a quartz crystal sensor

*Graduate Student, Tokyo Institute of Technology. Present address: Bangladesh University.

(CRTM-5000), set-up near the substrate. During deposition, the film thickness was always evaluated by a thickness monitor, and the films of 0.3 μm and 1.0 μm thick were prepared for measurements.

The deposited films were annealed at elevated temperatures between 623 and 773 K by using an image furnace (MILA-3000, ULVAC SHINKU-RIK0). Before annealing, the furnace was always pre-heated up to 873 K for cleaning the furnace, and the samples were annealed around 1×10^{-4} Pa.

The crystallinity was evaluated by X-ray diffraction analysis (XRD) using CuKα radiation for both as-deposited and annealed films. The surface morphology of the films was observed by a field emission scanning electron microscope (FE-SEM). The chemical composition of the films was examined by X-ray fluorescence (XRF) (RIX 2000, Rigaku) and electron probe microanalyzer (EPMA-8705, Shimadzu). A standard four-probe method was used to measure the electrical resistivity of the films. Van der Pauw Hall measurement was carried out for the films at room temperature in a magnetic field (H) of 1 T, and the electrical properties were evaluated together with galvanomagnetic properties including Hall mobility and magnetoresistance (MR), $\frac{\Delta R}{R_0} = \frac{R_H - R_0}{R_0}$, where R_0 and R_H are the resistances at a magnetic filed of $H = 0$ and $H = 1$ T, respectively.

3. Experimental Results and Discussion

3.1 Optimization of deposition condition

The deposition rate is an important factor when we produce thin InSb films by vacuum evaporation techniques. In general, deposited InSb films tend to deviate from stoichiometry because the vapor pressures of Sb and In differ remarkably from each other. In this study we investigated microstructure as well as electrical property of as-deposited InSb films with respect to the deposition rate, and determined optimum deposition rates.

Figure 1 shows the dependence of Hall mobility (μ) and electrical resistivity (ρ) on the deposition rate (d), for the as-deposited films at room temperature. The Hall mobility increases and the resistivity decreases gradually with increasing deposition rate up to 10 nm/s. Over 10 nm/s, the Hall mobility decreases gradually, while the resistivity increases slightly with increasing deposition rate. These results are consistent with each other, because the two properties are inversely related to each other. The maximum Hall mobility of 400 cm^2/Vs was obtained for a film deposited at 10 nm/s. The resistivity also showed the lowest value at the corresponding rate. The results indicate that 10 nm/s is one of the most suitable deposition rates for the present rapid vacuum evaporation system. In this connection, the deposition rate, 10 nm/s, is much higher than the previously reported value (210 nm/min or 3.5 nm/s) at the crucible temperature of 2030 K.[12]

In order to evaluate the crystallinity of the deposited films, several samples were examined by XRD. The results for three typical InSb samples deposited at 0.5, 5 and 10 nm/s are shown in Fig. 2. The film thickness was about 300 nm (or 0.3 μm). All the X-ray diffraction results prove that the films have polycrystalline structure. Figure 2(a) shows the result for a film deposited at 0.5 nm/s, which contains two

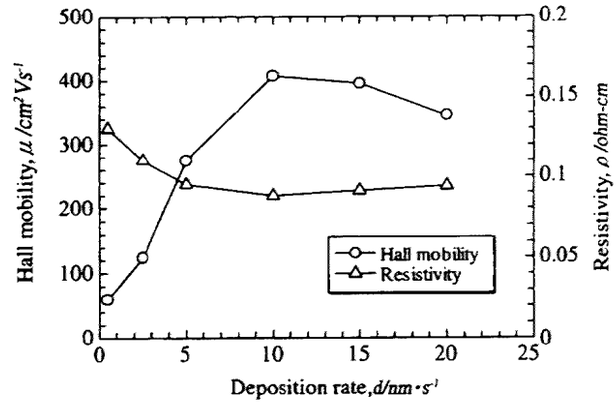

Fig. 1 Hall mobility and resistivity as a function of deposition rate for as-deposited films.

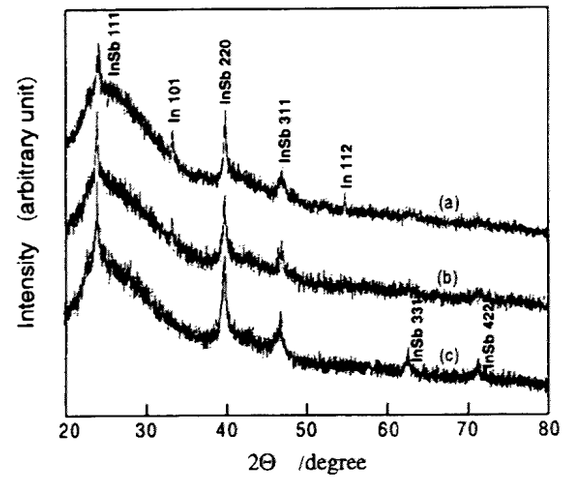

Fig. 2 X-ray diffraction results of InSb films prepared ar various deposition rates: (a) 0.5 nm/s, (b) 5 nm/s and (c) 10 nm/s. All the films have the same thickness of 300 nm.

phases: InSb phase with peaks 111, 220, 311 and In phase with two minor peaks 101, 112. The InSb peaks become much stronger, but In peak decreases gradually with increasing deposition rate. In the film deposited at 5 nm/s, In 112 peak disappeared but a weak In 101 peak still remains. All the In peaks disappeared completely for the films deposited at 10 nm/s. Moreover, two additional peaks (331 and 422) for the InSb are clearly seen in this film, and the other InSb peaks appeared with appreciable intensities. The films deposited at higher deposition rates than 10 nm/s, although they are not reproduced here, showed a similar to but less sharp X-ray profile than that of the films deposited at 10 nm/s. The results also support that the film deposited at 10 nm/s is highly stoichiometric, resulting in high electron mobility as shown in Fig. 1.

The composition ratio of these as-deposited films was analyzed by XRF. The composition ratio of Sb is defined as Sb/(In + Sb), supposing that the total atomic percent of (In + Sb) is 100%. The value of the ratio Sb/(In + Sb) was 50 ± 1% when the film deposited at 10 nm/s. On the contrary, the ratio was found as small as 35% when the film deposited at 0.5 nm/s. For more confirmation, some samples were analyzed by EPMA. The composition ratio obtained by EPMA was almost the same ($\cong$ 50%) as that of XRF analysis. The above results indicate that the stoichiometric film

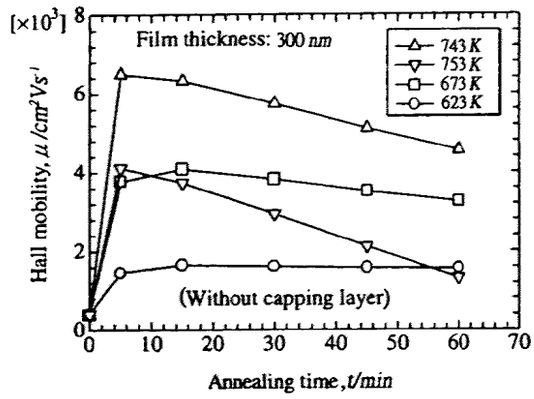

Fig. 3 Relationships between Hall mobility and annealing time for the films annealed at 623 m 673, 743 and 753 K. Deposition rate: 10 nm/s.

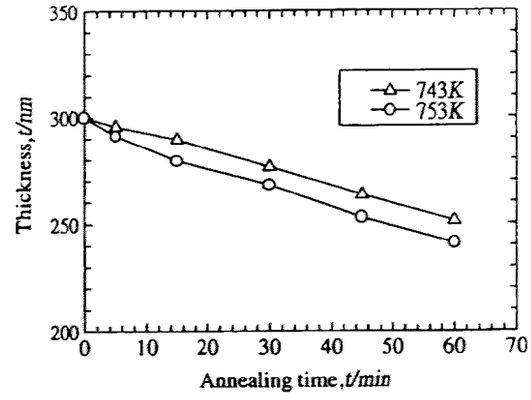

Fig. 4 Thickness changes with annealing time for the films annealed at 743 and 753 K.

can be obtained at 10 nm/s. Therefore, we determined that 10 nm/s is an optimum deposition rate in the present experiment. The reason why the nearly stoichiometric films were produced under these situations is not clear. It seems that a quasi-congruent evaporation took place under the present experimental conditions including room-temperature deposition and geometrical factors such as arrangements of crucible and substrate, source-substrate distance and a heat-shielding wall with a small hole (like a kind of quasi-Knudsen cell in MBE.) as well as the total deposition time of less than 30 s.

3.2 Improvement of film quality by annealing

3.2.1 Annealing without capping layer

The electrical and crystalline properties of the InSb films are strongly dependent on annealing temperature and time. In the present experiment, the annealing temperature varied from 623 to 773 K because the melting point of InSb is 798 K and thus solid-phase recrystalization can take place under these conditions.

Figure 3 shows the relationships between the annealing time and the Hall mobility for the films annealed at 623, 673, 743 and 753 K. The InSb films are not capped with SiO_2 layer before annealing. The Hall mobility increases after 300 s (5 min) annealing and then remains unchanged with annealing time for the films annealed at 623 K. However, in case of the films annealed at 673, 743 and 753 K the Hall mobility increases remarkably just after annealing and then decreases gradually with annealing time. This increase just after annealing may be due to structural relaxation caused by an initial annealing. A previous study[12] also showed a similar break point on the mobility vs annealing time curve for without-capping (hereafter referred to as uncapped) films prepared by using a rapid evaporation. We obtained the highest Hall mobility of 6.5×10^3 cm^2/Vs for the film annealed at 743 K for 300 s. In this connection, this result is about six times higher than that of Tomisu *et al.*[12] It is also shown that the Hall mobility of the film annealed at 753 K is inferior to that of the film annealed at 743 K. This is mainly due to the vaporization of Sb from the film at higher temperatures, as will be confirmed below.

The film thickness (or average thickness) was also measured after annealing by a surface profiler (Dektak^{3}ST). The change in film thickness is plotted as a function of annealing time for the films having initial thickness of 300 nm, as shown in Fig. 4. The film thicknesses were 255 and 240 nm after annealings at 743 and 753 K for 3.6×10^3 s (60 min), respectively. The XRF measurements also indicated that the composition ratios of Sb were 38 and 26% after annealings at 743 and 753 K for 3.6×10^3 s, respectively. Therefore, the decrease in film thickness is thought to be caused mainly by the vaporization of Sb from the film, though a small amount of In atoms is also ascribed to the decrease in film thickness.

Our previous study[21] showed a similar tendency that the Hall mobility decreased with increasing annealing temperature. The highest Hall mobility of 4.3×10^3 cm^2/Vs was found for a film annealed at 733 K with the initial thickness of 300 nm. All the films of our previous study were prepared under the average deposition rate of 0.5 nm/s. Therefore, the results are explained by the same reason described above, and are consistent with the present results.

3.2.2 Annealing with capping SiO_2 layer

In this study the annealed uncapped films showed sixteen times larger Hall mobility than the as-deposited films. However, they showed lower values for longer annealing periods and at higher annealing temperatures. For further quality improvement of the films, a procedure needs to prevent Sb from self-evaporating during annealing. Therefore, an attempt was carried out to cap the InSb films with SiO_2 layer before annealing. For capping process, an InSb film was first deposited on a glass substrate, and then SiO_2 layer of about 250 nm thick was deposited on the InSb film in the same vacuum chamber. Thus prepared InSb films were then annealed in a vacuum. After annealing, the SiO_2 layer was removed by wet etching (HF: 20% solution), and gold contacts were then deposited on the terminals of such InSb films for electrical measurements. In preliminary experiments, this capped-annealing was found to be very effective for InSb films to be annealed up to 773 K without any change in Hall mobility, as will be shown later.

The effect of annealing on surface morphology of InSb film was also examined and the results are shown in Fig. 5, which shows SEM micrographs of the films annealed without and with capping SiO_2 layer. An uncapped film, when annealed at 723 K for 3.6×10^3 s, is composed of small grains resulting in less smooth surfaces, and a lot of voids are seen throughout the film (Fig. 5(a)). These voids are thought to have been formed during annealing process, probably ascribed maily to

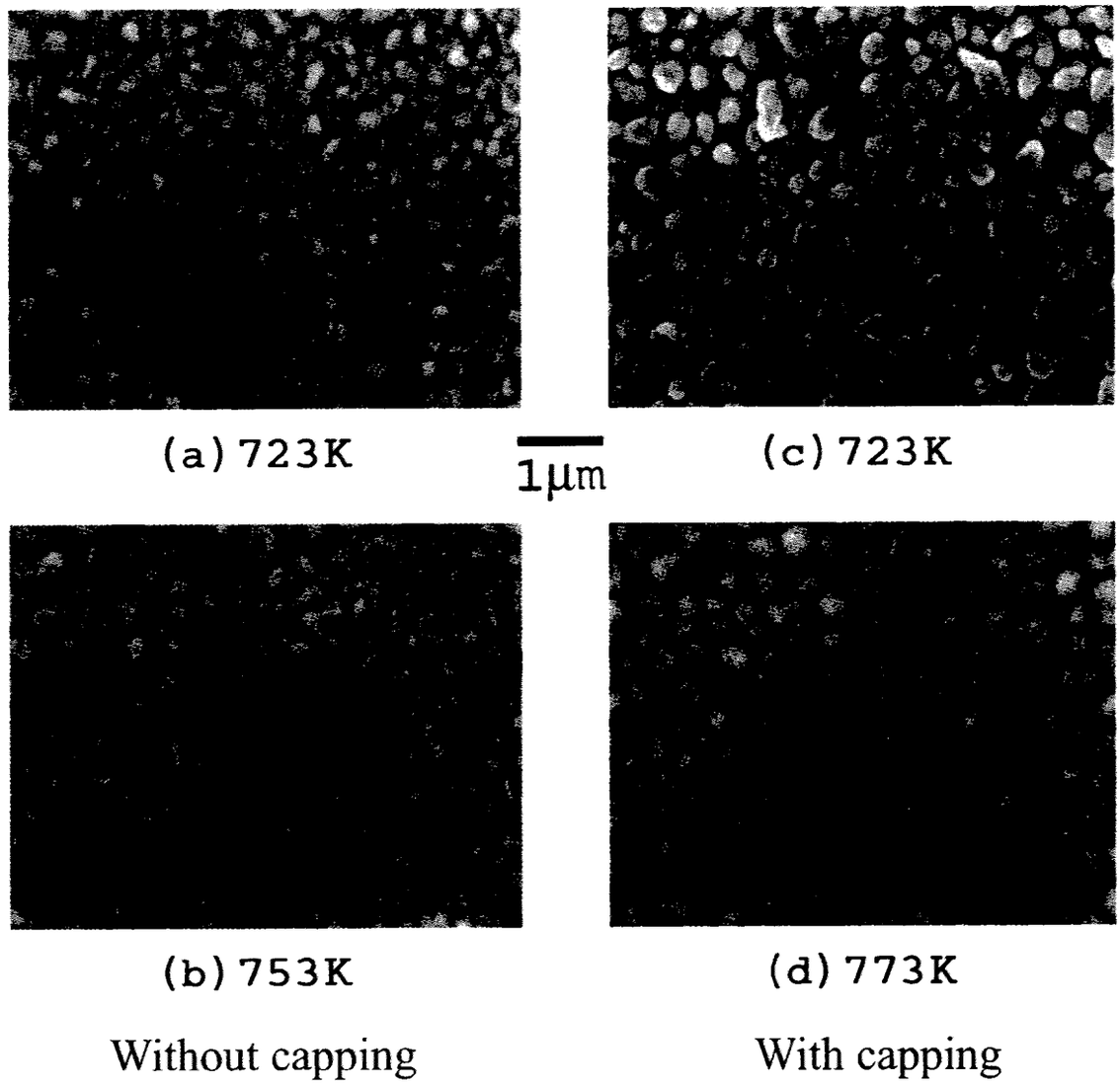

Fig. 5 SEM photographs showing surface morphology for the films without and with capping SiO_2 layer.

the evaporation of InSb, induced by initial vaporization of Sb atoms. The void size increases with increasing annealing temperature, as shown in Figs. 5(a) and (b), though the surface morphology appears to be suffered by the evaporation of InSb. The average size of the void is around 0.6 μm when the film was annealed at 753 K for 3.6×10^3 s. These voids may cause large electrical resistance or insulation for the films when annealed without capping SiO_2 layer. This can also explain why the Hall mobility decreases at longer annealing periods, as shown in Fig. 3. On the other hand, when annealed with capping SiO_2 layer, the films are composed of slightly rugged grains connecting with each other, as shown in Figs. 5(c) and (d). No voids are seen between adjacent grains in such capped films even when annealed at 723 K for 3.6×10^3 s. The XRF measurements also proved that the compositions of In and Sb in the capped films were nearly the same as those of as-deposited films. In this connection, neither appreciable decrease of the film thickness nor the ratio Sb/(In + Sb) was detected experimentally. The results indicate that the capping SiO_2 layer can prevent InSb from evaporating and hence the quality improvement of the films will be expected by a capped-annealing.

Figure 6 shows the relationships between the Hall mobility and the annealing time for such films annealed with and without capping SiO_2 layer. The Hall mobility of capped films increases instantly after short annealing time and then remains unchanged as the annealing time increases. This is quite different from the results of uncapped films. In the present study, the highest Hall mobility of 1.25×10^4 cm^2/Vs was obtained for a capped film of 300 nm thick, when annealed at 773 K.

The carrier concentrations of the InSb films together with the resistivity, Hall coefficient and Hall mobility are listed in Table 1. In this evaluation, the majority of carrier is assumed to be electron.[12] As the annealing temperature increases, the carrier concentration decreases up to 743 K for uncapped films. Above 743 K, the carrier concentration slightly increases. On the other hand, the carrier concentration for capped films decreases gradually with increasing annealing temperature. The lower the carrier concentration, the higher the Hall coefficient and the Hall mobility. This trend, however, must be examined in more detail.

The magnetoresistance (MR) effect was also investigated at room temperature in a magnetic field of 1 T. It is well known that the magnetoresistance is associated with the specimen

Table 1 Electrical properties of InSb films with respect to annealing temperature.

Film type	Annealing temperature* K(°C)	Carrier concentration n (cm^{-3})	Resistivity, ρ (Ω-cm)	Hall coefficient, R_H (cm^3/C)	Hall mobility, μ (cm^2/Vs)
Uncapped film	623 K(350)	2.34×10^{17}	2.31×10^{-2}	26.71	1.15×10^3
	673 K(400)	1.61×10^{17}	9.51×10^{-3}	38.84	4.08×10^3
	723 K(450)	1.44×10^{17}	9.12×10^{-3}	43.12	4.76×10^3
	733 K(460)	1.28×10^{17}	8.65×10^{-3}	48.71	5.62×10^3
	743 K(470)	1.17×10^{17}	8.34×10^{-3}	53.33	6.39×10^3
	753 K(480)	1.41×10^{17}	1.10×10^{-2}	44.20	3.91×10^3
Capped film	623 K(350)	2.18×10^{17}	2.12×10^{-2}	28.54	1.34×10^3
	673 K(400)	1.56×10^{17}	9.45×10^{-3}	39.86	4.21×10^3
	723 K(450)	1.51×10^{17}	8.28×10^{-3}	41.36	4.99×10^3
	733 K(460)	1.25×10^{17}	7.36×10^{-3}	49.91	6.77×10^3
	743 K(470)	1.16×10^{17}	6.69×10^{-3}	53.54	7.99×10^3
	763 K(490)	1.09×10^{17}	5.75×10^{-3}	56.93	9.89×10^3
	773 K(500)	9.99×10^{16}	4.99×10^{-3}	62.56	1.25×10^4

*Annealing time was 15 min. Film tickness: 300 nm.

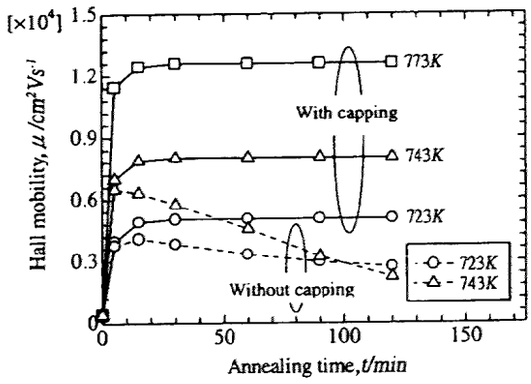

Fig. 6 Relationships between Hall mobility and annealing time annealed with and without capping SiO_2 layer. Deposition rate: 10 nm/s, film thickness: 300 nm.

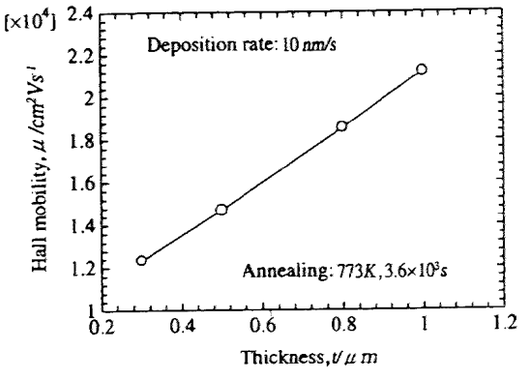

Fig. 7 Dependence of the Hall mobility on film thickness, when annealed at 773 K for 60 min (3.6×10^3 s).

factors such as thickness inhomogeneity, specimen shape and metallic inclusions.[2,22-24] In the present study, all the samples have the same thickness of 300 nm and the same shape (the length between adjacent electrodes; $l = 4$ mm and the width; $w = 3$ mm) with the length to width ratio of $(l/w) = 1.3$. The highest magnetoresistance of $\Delta R/R_0 = 60\%$ and 75% was obtained for uncapped films annealed at 743 K and capped films annealed at 773 K, respectively. As shown on SEM micrographs reproduced in Fig. 5, the uncapped films possess considerably rough surfaces with a lot of voids throughout the film, which may result in the inhomogeneity of carrier concentrations when subjected to a magnetic field. On the other hand, the capped films show considerably continuous surfaces without any voids, which result in homogeneity of carrier concentration throughout the films. Thus, a lower value of magnetoresistance for uncapped film may be due to such inhomogeneity. A room temperature MR value of 155% has been reported by Oshita *et al.*[2] for InSb films prepared by a source-temperature-programmed evaporation method. Therefore, further quality improvement will be expected by successive optimum procedures including longer annealings.

A significant increase in diffraction intensity of XRD was also seen for the annealed capped films, although the results were not reproduced here. This indicates that the crystallinity of the film including grain sizes can be improved remarkably after annealing at elevated temperatures. In fact, individual constituent grains become slightly large with less rugged shapes and are connecting densely with adjacent grains, as shown in Fig. 5(d). Thus, the film quality improvement can be mainly reflected on such morphological improvements caused by annealing with capping SiO_2 layer.

The Hall mobility is also reported to depend on the film thickness.[6,12] Therefore, in order to confirm this, we investigated the Hall mobility of the capped films as a function of film thickness. Figure 7 shows the variation of Hall mobility with film thickness for the films thinner than 1.0 μm thick. The Hall mobility increases with increasing film thickness, as theoretically expected.[13,25] The highest Hall mobility of 2.1×10^4 cm^2/Vs was achieved for InSb films with the thickness of 1.0 μm. In this connection, the single InSb crystal can show an electron mobility of 7.6×10^4 cm^2/Vs.[17] This result suggests us that thicker films can show a higher Hall mobility. Thus, we also measured the Hall mobility for several thicker films than 1.0 μm. As a result, no linear increase in Hall mobility was observed for thicker films with a slightly large fluctuation of data, probably due to the lack of homogeneity in thicker films. It is reported, however, that for thicker films

than 1.0 μm the Hall mobility increases gradually with increasing film thickness.[6,12,13,25] This point must be further examined in detail, because if the sample preparation conditions were guaranteed for the present films, a further high mobility will be expected by suitable procedures including annealing time and temperature.

4. Conclusions

InSb thin films were deposited on glass substrates by a rapid vacuum evaporation. The electrical and structural properties of the films were investigated in terms of heat treatment procedures. XRD, XRF and electrical measurements revealed that the film quality strongly depends on the deposition rate, and that the film deposited at 10 nm/s is highly stoichiometric. It was also found that the evaporation of Sb took place at higher annealing temperatures and for longer periods in a vacuum. Capped-annealing procedures can cause InSb films anneal up to 773 K in a vacuum. No further evaporation of Sb was observed for such capped films even for long annealing periods. The Hall mobility of 1.25×10^4 cm^2/Vs was obtained for a film annealed at 773 K with the thickness of 300 nm. It was also shown that, if the optimum preparation conditions are given, thicker InSb films can give a much higher mobility: in this study the highest electron mobility of 2.1×10^4 cm^2/Vs was successfully achieved for the films of 1.0 μm thick, when annealed at 773 K for 3.6×10^3 s. Further detailed experiments are now progress for thicker InSb films.

Acknowledgements

This study was partially supported by a Grant-in-Aid for Scientific Research (13875114) from the Ministry of Education, Sciencem Sports and Culture, Japan.

REFERENCES

1) Y. Yasuoka, T. Okuda and N. Inoue: Jpn. J. Appl. Phys. **27** (1988) L886–888.
2) M. Ohshita: Sens. Actuat A. **40** (1994) 131–134.
3) G. Ziegler: Solid-State Electron. **6** (1963) 680–681.
4) T. Miyazaki, M. Mori and S. Adachi: Appl. Phys. Lett. **58** (1991) 116–118.
5) Von K. G. Gunther and H. Freller: Z. Naturforsch **16a** (1961) 279–283.
6) J. A. Carrol and J. F. Spivak: Solid State Electron. **9** (1966) 383–387.
7) T. Berus, J. Goc, M. Nowak, M. Oszwaldowski and M. Zimpel: Thin Solid Films **111** (1984) 351–366.
8) H. Okimura, T. Matsumae and M. Ohshita: J. Appl. Phys. **66** (1989) 4252–4257.
9) M. Oszwaldowski and M. Slany: Vacuum **43** (1992) 617–618.
10) W. W. Lam and I. Shih: Mater. Lett. **16** (1993) 8–13.
11) H. Okimura, Y. Koizumi and S. Kaida: Thin Solid Films **254** (1995) 169–174.
12) M. Tomisu, N. Inoue and Y. Yasuoka: Vacuum **47** (1996) 239–242.
13) H. H. Wieder: J. Vac. Sci. Technol. **9** (1972) 1193–1196.
14) J. I. Chyi, D. Biswas, S. V. Lyer, N. S. Kumar, H. Morkoc, R. Bean, K. Zanio, H. Y. Lee and H. Chen: Appl. Phys. Lett. **54** (1989) 1016–1018.
15) P. E. Thompson, J. L. Davis, J. Waterman, R. J. Wagner, D. Gammon, D. K. Gaskill and R. Stahlbush: J. Appl. Phys. **69** (1991) 7166–7172.
16) W. K. Liu, W. T. Yuen and R. A. Stradling: J. Vac. Sci. Technol. B **13** (1995) 1539–1545.
17) A. Okamoto, T. Yoshida, S. Muramatsu and I. Shibasaki: J. Cryst. Growth **201/202** (1999) 765–768.
18) S. N. Song, J. B. Ketterson, Y. H. Choi, R. Sudharsanan and M. Razeghi: Appl. Phys. Lett. **63** (1993) 964–966.
19) D. L. Partin, L. Green and J. Heremans: J. Electron. Mater. **23** (1994) 75–79.
20) S. Li, Y. Ning, T. Zhou, Y. Jin and Y. Tian: Thin Solid Films **298** (1997) 245–248.
21) M. A. Taher, D. Fukushima and O. Nittono: *Proc. Int. Conf. on Solid-Solid Phase Transformations*, (The Japan Inst. Metals, 1999) p. 1317–1320.
22) H. Lippmann and Z. Kuhrt: Z. Naturforsch. **13a** (1958) 462–483.
23) S. Kataoka: Proc. I E E. **111** (1964) 1937–1947.
24) G. S. Nadkarni: Thin Solid Films **87** (1982) 17–21.
25) N. F. Teede: Solid State Electron. **10** (1967) 1069–1076.

Jpn. J. Appl. Phys. Vol. 40 (2001) pp. 6561–6565
Part 1, No. 11, November 2001

Preparation and Magnetooptical Properties of AlN–Fe Granular Film

Yumiko HAGA, Noriyuki NAKAYA, Eishi TAKEDA[1], Yoshio NAKAMURA and Osamu NITTONO

Department of Metallurgy and Ceramics Science, Tokyo Institute of Technology, 2-12-1 O-okayama, Meguro-ku, Tokyo 152-8552, Japan
[1]*Department of Physical Electronics, Tokyo Institute of Technology, 2-12-1 O-okayama, Meguro-ku, Tokyo 152-8552, Japan*

(Received June 29, 2001; accepted for publication July 26, 2001)

AlN films including Fe nanoparticles have been prepared from sputtered films with Al–N–Fe composition by annealing in a vacuum furnace. Faraday rotation angles and M–H loops of AlN–Fe granular films have been measured. The maximum value of Faraday rotation angle is estimated to be 1.1°/μm at a wavelength of about 500 nm. The microstructures of the films are characterized by transmission electron microscopy and X-ray diffractometry. The structural features are related to the magnetic properties.

KEYWORDS: Faraday rotation, AlN, sputtering, granular

1. Introduction

High density recording is a key issue for magnetooptical media. For this purpose, it is necessary to fabricate a small bit in the recording media. However, the low intensity of the read-out signal from a small bit is one of the problems. Various techniques to enhance the signal, such as the magnetic amplification magnetooptical system (MAMMOS),[1] have been investigated for storage devices. For these techniques, multilayered structures using functional or coating materials are available. The Faraday effect is useful for practical use of magnetooptical materials because it has the possibility of realizing large rotation angles by increasing film thickness. The Kerr rotation is also a useful magnetooptical effect but since it is inherent in materials the rotation angle remains constant. Typical important factors to be considered for application of Faraday effect are high transmittance of light at desired wavelength, large rotation angle and high respondency. AlN films have some useful properties for coating or substrate materials such as high hardness, high transmittance of visible light, high electrical insulation and high thermal stability. Ferromagnetic Fe has high saturation magnetization, moderate magnetic softness and is widely used. Therefore, a composite film of these two materials is expected to have suitable properties for use as functional coating films or substrates for magnetooptical storage media. Optimum film properties can be obtained by controlling the film thickness and the compositional ratio. In addtion, a large Faraday rotation angle is expected without loosing high transparency. The promising properties of composite and multilayer films of AlN and Fe or Fe nitride have been studied by Kikkawa *et al.*[2] Their study showed the structural variety of Al–N–Fe composite films. Film properties depend not only on the compositional ratio but also on structural features.

In this paper, the magnetic properties and structural features of AlN–Fe composite films prepared by dc sputtering and annealing are reported.

2. Experiment

The Al–N–Fe composite film was prepared by a facing target-type dc sputtering apparatus shown in Fig. 1. The optimum sputtering conditions in this experiment were as follows. The base pressure was lower than 2×10^{-4} Pa. Pure Ar (99.9999%) and N_2 (99.9999%) gases were used for sputtering. Flow rates of these gases were controlled independently using mass-flow controllers and the gases were mixed in the chamber. The total pressure $P_{total} = P_{Ar} + P_{N2}$ was maintained at 2×10^{-1} Pa during deposition. The gas pressure ratio given by P_{N2}/P_{total} was 0.4, which was an optimum value for forming AlN using our apparatus. AlN was formed under the condition of $P_{N2}/P_{total} > 0.2$. The preference of crystal orientation became more prominant with an increase of P_{N2}/P_{total}. On the other hand, plasma condition became unstable when P_{N2}/P_{total} was more than 0.4, because of the deposition of insulating AlN on the targets. Combined targets of Al and Fe were prepared as shown in Fig. 2(a). Pure Al disks (99.9%) with holes were placed on pure Fe disks (99.9%) with a diameter of 100 mm. The composition was controlled by changing the diameters and positions of these holes. The hole diameter was 22 mm to obtain the desired composition in this experiment. The number of holes was three to maintain homogeneity in the prepared film. The distance between the center of the hole and the center of the targets was 30 mm. The hole edges had a slight slant to stabilize the plasma condition. Fe was sputtered through these holes and Al–Fe–N mixture films were deposited on the substrate. The substrate was placed beside the targets in the distances of 140 mm from the center of one of the targets and was not directly exposed to plasma as shown in Fig. 2(b). The substrates were fused silica glasses with dimensions of 22 mm × 25 mm. The substrate

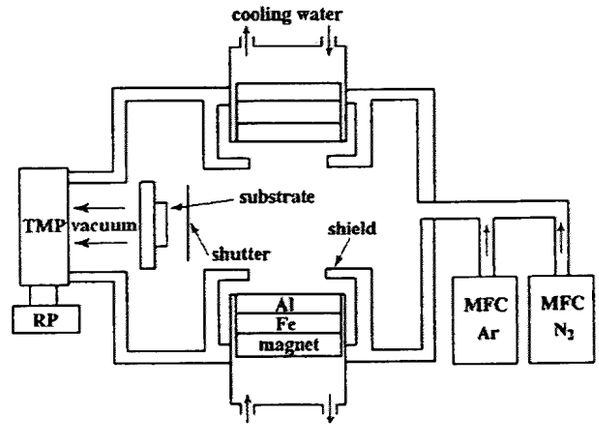

Fig. 1. Schematic diagram of our facing target-type dc sputtering apparatus.

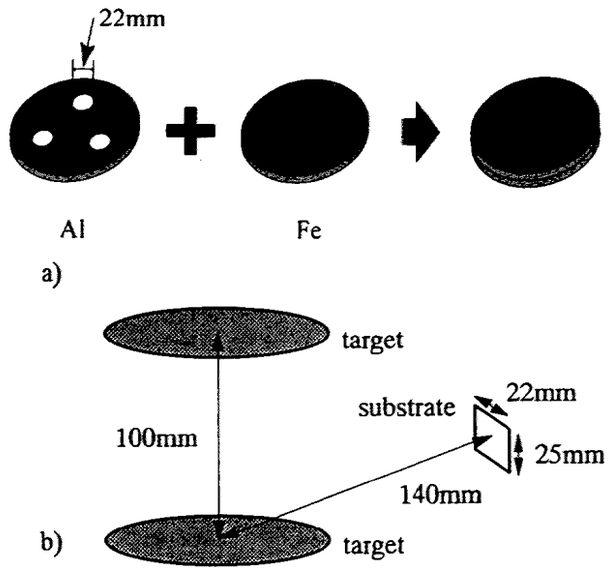

Fig. 2. Schematic diagrams of (a) handmade combined targets consisting of an Al plate with holes and an Fe plate, and relationship between targets and substrate position.

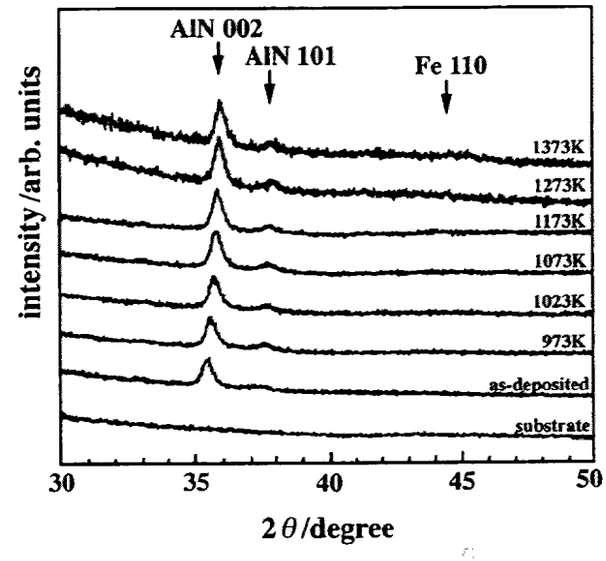

Fig. 3. XRD profiles of Al–N–Fe composite films after annealing at various temperatures. The structures were slightly changed by annealing.

was maintained at room temperature. Films were annealed in a vacuum furnace to precipitate Fe nanoclusters in the AlN matrix. The base pressure was lower than 5×10^{-4} Pa during annealing. The films were annealed in the furnace for 3 h. The annealing temperature range was from 473 K to 1373 K. After annealing, the specimens were cooled in the furnace. The film thickness was 300 nm as measured by a Taly-step profilometer.

The structure was characterized by X-ray diffractometry (XRD) and transmission electron microscopy (TEM, JEM-3010 and JEM-2010). XRD profiles were measured by a rotating anode type X-ray generator and a conventional diffractometer. X-ray power was 12 kW. Specimens for TEM observations were prepared using an ion-thinning system. The composition of films was determined by the Auger electron spectroscopy (AES) system calibrated using the standard of the sintered AlN bulk and energy-dispersed X-ray spectroscopy system (EDX) installed in TEM.

M–H loops were measured by a vibrating sample magnetometer (VSM). The maximum magnetic field was 1200 kA/m. The loops were measured along the directions of in-plane and perpendicular to the films. Magnetooptical properties were estimated using a handmade Faraday rotation system.

Generally, the Faraday rotation angle increases but the transmittance of light decreases with increasing Fe composition. Considering these two factors, Fe composition lower than 20 vol.% seems suitable for magnetooptical measurement. Along this guideline, we attempted to fabricate AlN–Fe films under various sputtering conditions. As a result, an optimum Fe composition was determined to be 10 at.% under stable plasma conditions during sputtering.

3. Results and Discussion

XRD profiles of the films are shown in Fig. 3. Broad reflections from AlN are observed. They show that the films consist of small crystallites or amorphous. The film structure does not undergo any significant chage by annealing. This indicates AlN is very stable against heating. A careful observation reveals that the peak intensity of AlN increases slightly with an increase of annealing temperature. This means that the crystallinity of AlN is slightly improved by annealing. No clear peak of bcc Fe was observed in these profiles. It is thought that Fe exists as nanocrystals or amorphous, otherwise as interstitial atoms in the AlN matrix. Any Al–Fe alloys or oxides are not observed.

The results of TEM observation are shown in Fig. 4. Diffraction patterns and bright field images are presented with annealing temperatures. The diffraction pattern of as-deposited film shows that small crystals of AlN form the matrix and Fe crystals do not appear. This result is consistent with the XRD result. The crystal size of AlN in the film plane do not show any drastic changes. Only AlN crystals grow slightly with increasing annealing temperature. The major diameter of AlN crystal is estimated to be about 30 nm in all the films investigated. The diffraction rings of bcc Fe are observed in Figs. 4(c-2)–(f-2). This indicates that crystallization of Fe starts at about 1073 K. Figures 5(a)–5(c) show dark field images of the AlN–Fe film annealed at 1373 K using diffraction rings indicated by the bold arrow in Fig. 5(d) under hollow-cone beam illumination. We cannot select the 110 diffraction rings of bcc Fe by the smallest objective aperture in our TEM. Then we take three dark field images; Fig. 5(a) is imaged using AlN 101 and Fe 110 reflections, Fig. 5(b) using the edge of AlN 101, Fe 110 and the edge of AlN 102 reflections and Fig. 5(c) using Fe 110 and AlN 102 reflections. The same bright particles as indicated by white arrows in the three images are found to be parts of Fe nanocrystals. The typical size of Fe crystal is estimated to be about 15 nm.

M–H loops measured by VSM are shown in Fig. 6. The loops in Fig. 6(a) are measured for in-plane and those in Fig. 6(b) are for perpendicular direction to the film plane. The shapes of loops chang by annealing. As-deposited films do not show magnetization. Magnetization is observed in the films annealed above 1073 K and increases with annealing temperature. The tendency of the annealing-induced mag-

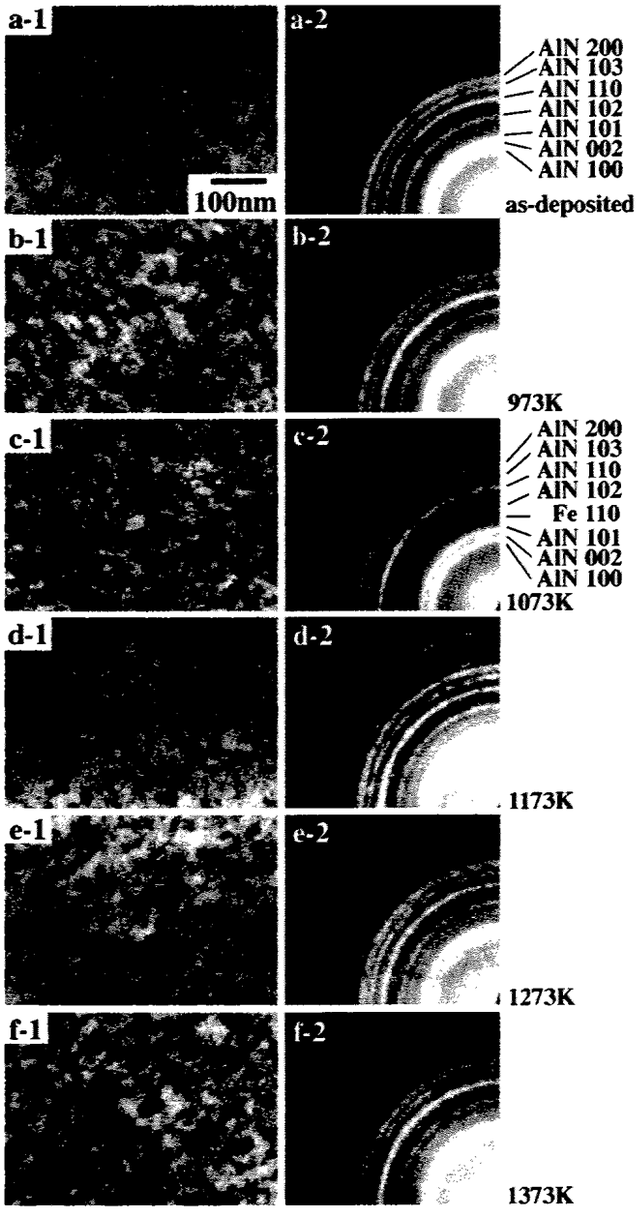

Fig. 4. Bright field images and diffraction patterns observed by TEM for films (a) as-deposited and annealed at (b) 973 K, (c) 1073 K, (d) 1173 K, (e) 1273 K and (f) 1373 K.

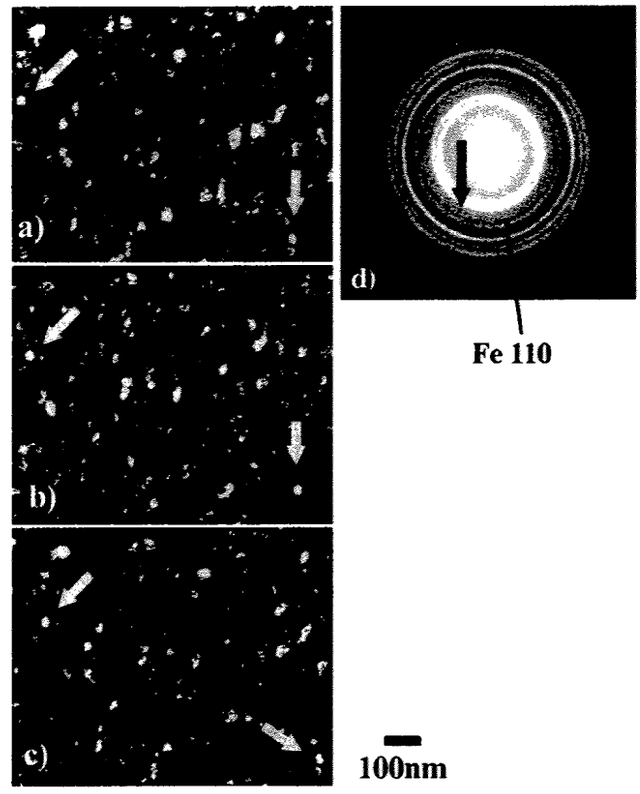

Fig. 5. Dark field images of the AlN–Fe film annealed at 1373 K under hollow-cone beam illumination. The images are obtained using (a) AlN 101 and Fe 110 reflections, (b) the edge of AlN 101, Fe 110 and the edge of AlN 102 reflections, and (c) Fe 110 and AlN 102 reflections. (d) is the corresponding diffraction pattern.

netization is not significantly different between in-plane and perpendicular directions. However, the loop shapes are different between the curves of the two directions. It is estimated that the shape or distribution condition of Fe particles is not homogeneous in the film. The saturation magnetizations are plotted in Fig. 7 as a function of annealing temperature. Fe is considered to exist in the film as nanoparticles having various diameters. When the annealing temperature is lower than 1073 K, Fe particles are considered to be in a superparamagnetic or nonmagnetic state in the composite film. Fe crystals grow by further annealing and show ferromagnetic properties. Even after annealing at 1273 K, precipitation of Fe has not been completeld. The effective amount of ferromagnetic region contributing to magnetization appears to be about 30% of the Fe content in the film. The result of transmissivity measurement is shown in Fig. 8. The spectra show a slight oscillation because of interferance effects in the film.

When the annealing temperature increases, the transmissivity decreases. This result can be explained by the precipitation of Fe particles. The dependence of the Faraday rotation angle on the annealing temperature is shown in Fig. 9. The rotation angles increase with the annealing temperature for all the wavelengths. The rotation angle depends on wavelength. It is difficult to explain this dependence because of the complex nature of the granular film. The rotation angles selected for three characteristic wavelengths are plotted as a function of saturation magnetizations in Fig. 10. The Faraday rotation angles linearly increase with an increase of magnetization for all wavelengths. The Faraday rotation angle is approximately explained by the equation given in ref. 3,

$$\begin{aligned}\theta_F &\approx -\{\pi l(N_+ - N_-)/\lambda\} \\ &\approx -(i\pi l/\lambda)(\varepsilon_{xy}/\varepsilon_{xx}^{1/2}) \\ &\approx -(i\pi l/\lambda)[\varepsilon_{xy}^{(1)}M/(\varepsilon_{xx}^{(0)} + 1/2\varepsilon_{xx}^{(2)}M^2)^{1/2}]. \end{aligned} \quad (1)$$

Here, θ_F is the Faraday rotation angle, N is the complex index of refraction, l is the unit vector of incident direction, λ is the wavelength of light, ε is the tensor component of dielectric constant and M is saturation magnetization. The $|\varepsilon_{xy}| \ll |\varepsilon_{xx}|$ is assumed and the equation is expanded in power series. The rotation angle is assumed to be proportional to magnetization when magnetization is sufficiently small. The maximum rotation angle is estimated to be $1.1°/\mu m$ at a wavelength of 500 nm. The value of θ_F/α which is defined as a figure of merit could not be calculated accurately from our experimental results because the absorption coefficients

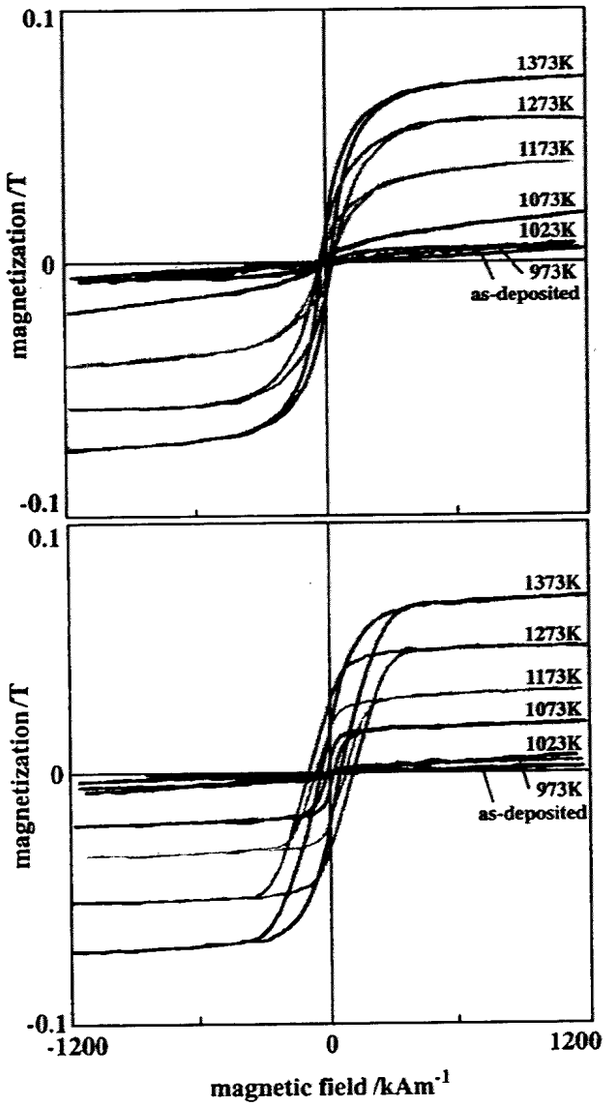

Fig. 6. *M–H* loops for AlN–Fe films annealed at various temperatures. They were measured for (a) in-plane and (b) perpendicular direction to the film plane.

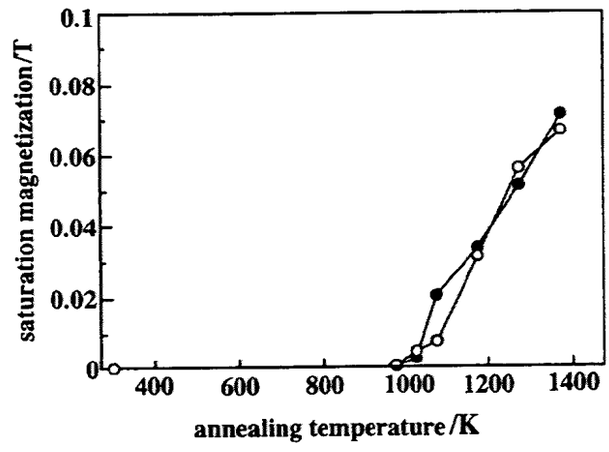

Fig. 7. The dependence of saturation magnetization on annealing temperature. The white circles indicate the data measured for in-plane and the black circles indicate those measured for the direction perpendicular to the film plane.

could not be measured correctly. Tentatively, we compared Faraday rotation angles and absorption coefficients measured from Fig. 8 where the absorption coefficients are normalized

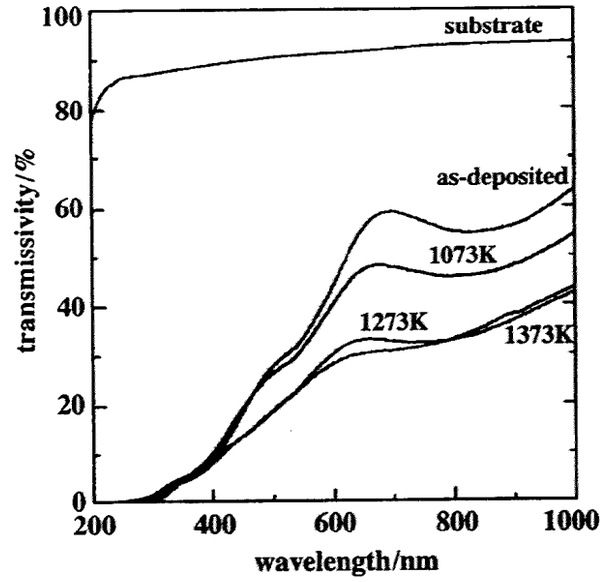

Fig. 8. Transmissivities of the films annealed at various temperatures.

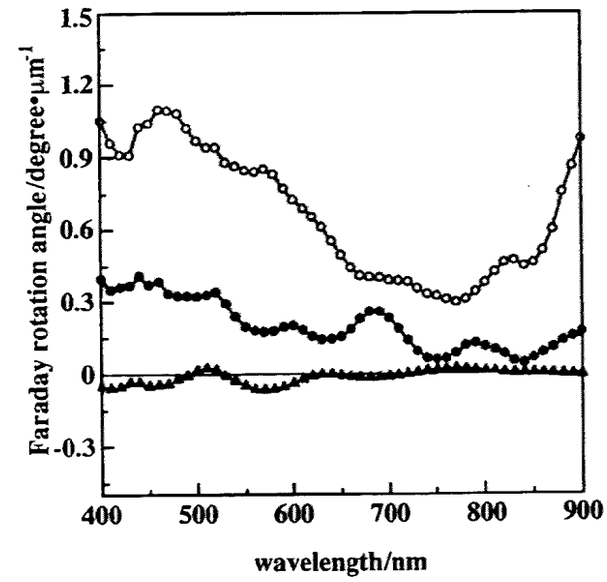

Fig. 9. Faraday rotation angle for films (a) as-deposited, (b) annealed at 1073 K and (c) annealed at 1273 K. Triangles indicate the results for as-deposited film, black circles indicate those for a film annealed at 1073 K and white circles indicate those for a film annealed at 1273 K.

by that of the substrate. The values ranged from about 0.02 to 0.08. Dispersion conditions of Fe particles and crystallinity of AlN matrix influence the transmissivity. Therefore, optimum properties could be obtained by controlling these factors.

4. Conclusions

AlN–Fe granular films are prepared by dc sputtering and annealing. Fe nanoparticles are dispersed in AlN polycrystalline matrix by annealing above 1023 K. Magnetooptical properties are measured for such AlN–Fe granular films. The maximum value of the Faraday rotation angle is measured to be 1.1°/μm at a wavelength of about 500 nm.

This work was partly supported by Special Coordination Funds for Promoting Science and Technology on

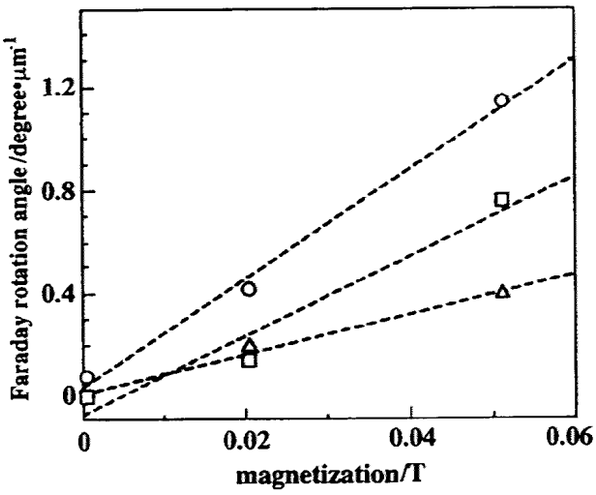

Fig. 10. The relationship between Faraday rotation angles for characteristic wavelengths and saturation magnetizations. The wavelength indicated by the circle is for 500 nm, that by the triangle is for 710 nm and that by the square is for 880 nm.

"Nanohetero Metallic Materials" from the Science and Technology Agency.

1) H. Awano, S. Ohnuki, H. Shirai and N. Ohta: Appl. Phys. Lett. **69** (1996) 4257.
2) S. Kikkawa, M. Fujiki, H. Sugiyama, S. Enomoto and M. Takahashi: Mater. Sci. Forum **308–311** (1999) 585.
3) Katsuaki Sato: *Hikari to Jiki* (Light and Magnetism) (Asakura Shoten, Tokyo, 1996) p. 28 [in Japanese].

Appl. Phys. A 73, 215–218 (2001) / Digital Object Identifier (DOI) 10.1007/s003390000682

Applied Physics A
Materials
Science & Processing

Structural and magnetic properties of Co-C composite films and Co/C multilayer films

J. Shi*,, M. Azumi, O. Nittono**

Department of Metallurgical Engineering, Tokyo Institute of Technology, 2-12-1 Oh-okayama, Meguro-ku, Tokyo, 152-8552, Japan

Received: 11 July 2000/Accepted: 13 July 2000/Published online: 30 November 2000 –

Abstract. Co-C composite films and Co/C multilayer films have been prepared by a method incorporating ion beam sputtering and plasma chemical vapor deposition. It has been found that the structure and magnetic properties of both the Co-C composite and the Co/C multilayer films depend strongly on the substrate temperature during deposition. The Co-C composite film deposited at room temperature is amorphous, with relatively low saturation magnetization and coercivity. On the other hand, the film deposited at 250 °C is composed of fine Co crystallites separated by amorphous C or Co-C phase. As a result, both the saturation magnetization and coercivity are increased compared with the film deposited at room temperature. When deposited at room temperature, the Co/C multilayer film exhibits good periodicity, with a period of 70 nm (Co: 40 nm, C: 30 nm) and sharp and flat Co-C interfaces. High magnetization (602 emu/cm^3) and low coercivity (1.6 Oe) are obtained for such a film. However, increasing the substrate temperature to 250 °C was found to be detrimental to the magnetic properties due to the formation of cobalt carbide at the Co-C interface.

PACS: 75.70.-i; 75.50.Kj; 68.55.Jk

Carbon-related materials show great application potential due to their unique structures and physical properties [1–7]. One of the important characteristics of such materials is that they can be incorporated with metals to form nanocomposite materials, of which novel properties are expected [8–11]. Carbon nanoparticles filled with pure iron, nickel, and cobalt have been synthesized [10]. Recently, copper nanowire encapsulated by carbon nanotubes has also been formed [11]. In the field of magnetic applications, cobalt nanocrystals encapsulated by graphite-like carbon have been prepared by ion beam sputtering for application as ultra-high density magnetic recording media [12]. In such a material, the incorporated carbon plays an important role in separating the cobalt crystallites and magnetically decoupling them, thus obtaining high coercivity. Besides application as magnetic recording media, magnetic films are also used in magnetic head and other high-frequency magnetic devices. For such applications, soft magnetic properties, i.e. low coercivity and good frequency response of the permeability are necessary. It is known that the frequency response of the permeability is limited mainly by eddy current loss and the resonance, therefore, high film resistivity is of benefit because of the reduction in eddy current loss. Recent approaches to reduce both coercivity and eddy current loss include incorporating insulating materials during the deposition of magnetic metal films and lamination of the magnetic thin film with insulating layers [13–16]. In the present work, amorphous carbon was used for this purpose. Co-C composite films and Co/C multilayer films were prepared, and their structure and magnetic properties were studied.

1 Experimental procedure

A dual-source deposition system was used to prepare the films, which included a Kaufman ion source for ion beam sputtering deposition of Co and a compact electron cyclotron resonance (ECR) plasma source for chemical vapor deposition (CVD) of C. During the deposition processes, the Kaufman ion source produced an Ar ion beam directed at a Co target (99.98%) with an energy of 2 keV. The reaction gas supplied to the ECR plasma source was a pre-mixed methane (CH_4) and hydrogen (H_2) gas mixture, and the power supplied to the source was fixed at 245 W. During deposition, the flow rate of CH_4 was controlled at 0.2 sccm by a mass-flow controller. For deposition of Co-C composite films, the sputtered cobalt flux and the ECR plasma were directed at the substrate simultaneously. For the deposition of Co/C multilayer films, the flux and plasma were directed at two different directions. In this case, cobalt and carbon layers were deposited sequentially at the two substrate pos-

*Corresponding author.
**_Present address:_ Department of Applied Physics and Chemistry, The University of Electro-Communications, 1-5-1, Chofugaoka, Chofu-shi, Tokyo 182-8585, Japan
(Fax: +81-424/435461, E-mail: shi@pc.uec.ac.jp)

itions by rotating the substrate holder periodically. Prior to the depositions, the system was evacuated to a base pressure of less than 3×10^{-5} Pa. The chamber pressures were around 1 Pa during depositions. Corning #7059 glass slides were used as substrates, and they were ultrasonically cleaned in acetone before mounting in the vacuum chamber. The structure of the films was characterized by X-ray diffraction (XRD) and transmission electron microscopy (TEM). For TEM plan-view observation, the samples were deposited on SiO supporting films directly. For the cross-section views, the samples were thinned by mechanical grinding and subsequent ion milling. The in-plane magnetic properties of the films were measured at room temperature by using a vibration sample magnetometer. The resistivity was measured by the four-probe method.

2 Results and discussion

2.1 Microstructure of Co-C composite films

Figure 1 shows the XRD profiles of Co-C films deposited at room temperature and at 250 °C. For the film deposited at room temperature, the profile shows only a broad peak covering a wide range of angular positions where several reflections from the ε-Co phase and the cobalt carbides are expected to appear, indicating the formation of a Co-C amorphous phase in the film. For the film deposited at 250 °C, the relatively sharp peak located at 44.5°, is identified as the $00 \cdot 2$ reflection from ε-Co (hexagonal close packed structure, hcp) phase, and the weak peak located at 51.5° is due to the α-Co (face-centered cubic structure, fcc) phase. This result indicates that the film is composed mainly of an ε-Co phase, with a strong $00 \cdot 1$ preferred orientation. In addition, small amount of α-Co phase is also formed in the film. No reflections from crystalline carbon phases were observed in the XRD profile, indicating the carbon incorporated in the film is still amorphous. Furthermore, according to our previous results, the amorphous carbon in the film is believed to be in a glassy carbon state, which is composed mainly of sp^2 hybridization in the form of disordered graphite [17].

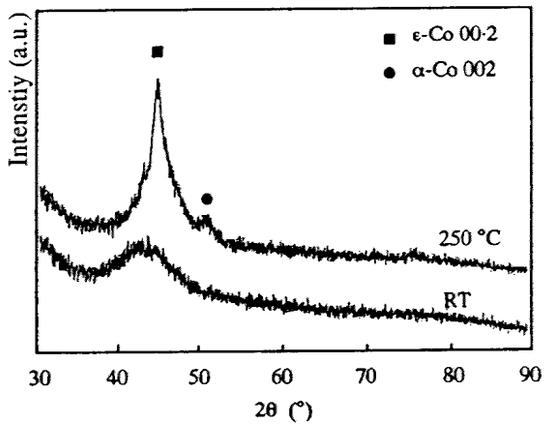

Fig. 1. X-ray diffraction profiles for the Co-C composite films deposited at room temperature and at 250 °C

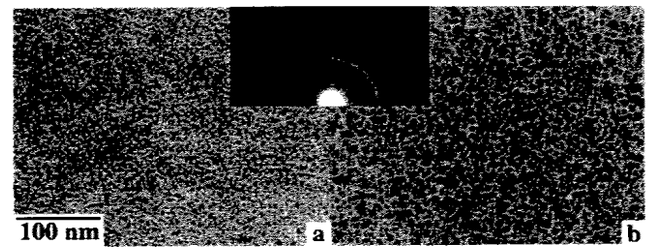

Fig. 2a,b. Electron micrographs for the Co-C composite films deposited at room temperature (**a**) and at 250 °C (**b**). *Insets* show the electron diffraction patterns of the films

Figures 2a and b show TEM bright field images of these two films respectively, and the insets show the electron diffraction patterns. For the film deposited at room temperature, although the TEM image reveals a grain-like structure, the halo diffraction pattern proves the amorphous nature of the film, consistent with the XRD result. The film deposited at 250 °C reveals a kind of granular structure [13], and the inset diffraction pattern confirms the formation of an ε-C (hcp) phase. The Co crystallites are round, and their average size is about 8 nm in diameter as estimated from the TEM observation. Since Co has almost no solid C solubility near room temperature [18], the probable location of most of the incorporated C is at the inter-grain regions. We noted that the inter-grain regions are about 1–2 nm in thickness and are characterized by light contrast, therefore we consider that such regions are composed of C or a Co-C amorphous phase. Similar structure has also been reported on Cu-C using a co-sputtering method [19], and the formation of such a structure is ascribed to the de-mixing of Cu and C during the deposition process. According to this formation mechanism, the de-mixing is caused by surface diffusion of the two species, which depends strongly on the energy of the incident species arriving at the surface of the substrate. This mechanism can be applied to explain our results. When the Co-C film was deposited at room temperature, Co and C species were trapped on the substrate surface due to their low energies and surface diffusivities, preventing the de-mixing process from occurring and leading to the formation of a Co-C amorphous phase. When the Co-C film was deposited at 250 °C de-mixing occurred due to the enhanced surface diffusivities, leading to the formation of Co crystallites and an amorphous C phase.

2.2 Structure of Co/C multilayer films

Figure 3 shows the XRD profiles of two Co/C multilayer films deposited at room temperature and at 250 °C respectively. For the film deposited at room temperature, the XRD profile shows a broad peak located around the angular position of 43°. The other broad peak at the left is due to the glass substrate. No perceivable reflection from crystalline carbon, such as graphite, can be observed on the profiles. These results indicate that both the cobalt and carbon layers are amorphous. For the film deposited at 250 °C, reflections from ε-Co and cobalt carbide (Co_3C, hcp) are observed in the profile, indicating that Co layers are composed of polycrystalline Co and the carbide was formed at the Co-C interfaces. In order to evaluate the period of the Co/C multilayer

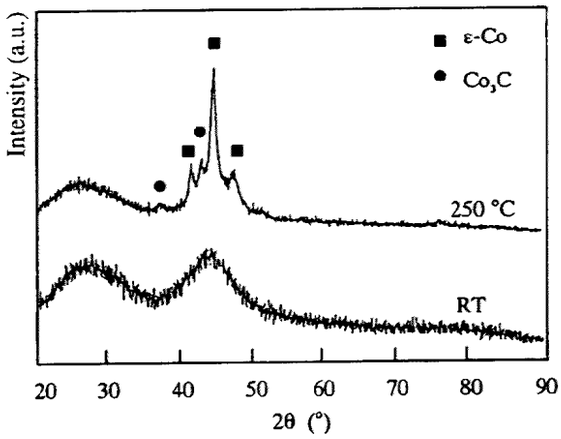

Fig. 3. X-ray diffraction profiles for the Co/C multilayer films deposited at room temperature and at 250 °C

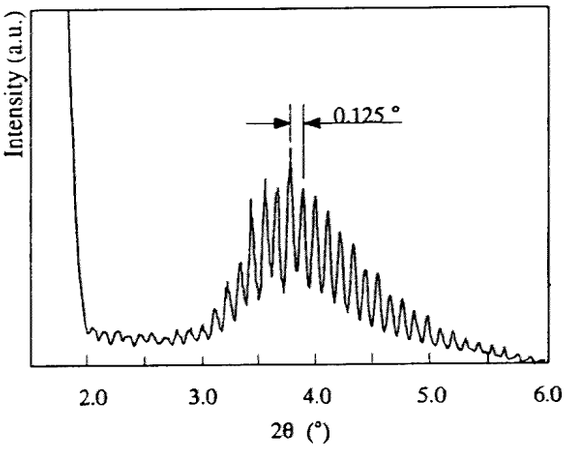

Fig. 4. Low-angle x-ray diffraction profile for the Co/C multilayer film deposited at room temperature

films, low-angle X-ray diffraction measurements and cross-sectional TEM observations were performed on the Co/C film deposited at room temperature. Figure 4 shows the low-angle X-ray diffraction profile. It contains a broad peak centered at 3.7°, which is superimposed by an oscillation. The broad peak represents a spacing of 2.4 nm, which corresponds to the cluster size in the amorphous film. The oscillation is caused by the interference of X-rays reflected by the Co-C interfaces. The period of the oscillation, 0.125°, represents a spacing of 70 nm, which is considered to be the period of the multilayer film. The good X-ray reflectivity also implies that the film has a smooth surface, and has flat and sharp interfaces within the film. Furthermore, the cross-sectional TEM image of the Co/C film is shown in Fig. 5. The dark layers are cobalt layers with a thickness of about 40 nm, and the bright layers are the carbon layers with a thickness of about 30 nm. The image also clearly shows the flat and sharp interfaces between cobalt and carbon layers. It is seen that these TEM results are in good agreement with the low-angle X-ray diffraction results. Moreover, the inset electron diffraction pattern shows a streak along the direction perpendicular to the film surface, which is composed of periodically arranged satellite reflections, indicating the good periodicity of the Co/C multilayer film.

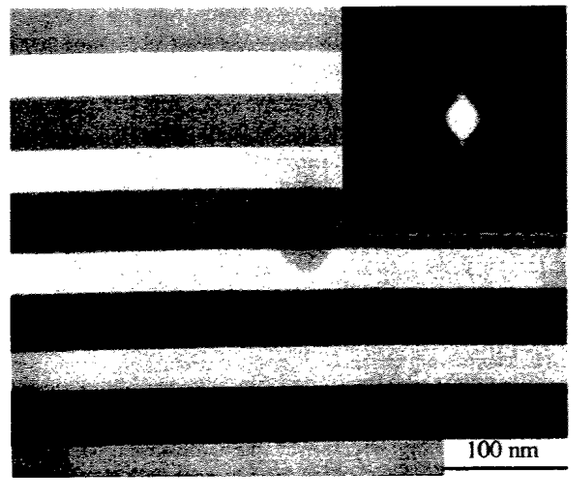

Fig. 5. Electron micrograph showing the cross-section of the Co/C multilayer film deposited at room temperature. *Inset* shows the electron diffraction pattern of the same film

2.3 Magnetic properties of Co-C composite and Co/C multilayer films

The saturation magnetization (Ms), coercivity (Hc) and resistivity (ϱ) of the Co-C composite films and Co/C multilayer films are listed in Table 1. It is seen that the Co-C composite film deposited at room temperature shows the lowest saturation magnetization, relatively low coercivity and the highest resistivity among the tested films. This is due to the amorphous nature of the film, and we consider that the cluster-scale mixing of Co and C also contributes to the low saturation magnetization and high resistivity. Increasing the substrate temperature to 250 °C resulted in significant changes in the magnetic and electrical properties. The saturation magnetization increased by more than a factor of two and the coercivity increased by more than five times the values for the film deposited at room temperature. Furthermore, the resistivity decreased to one percent of the value for the film deposited at room temperature. These changes are apparently due to the de-mixing of Co and carbon by surface diffusion and the formation of Co crystallites. According to Fig. 2b, the Co-C composite film deposited at 250 °C reveals small crystallites (sized about 8 nm) and small physical gaps (less than 2 nm) among the Co crystallites, which keep the Co crystallites magnetically interacted with each other [20]. Although magnetic films of such a structure are generally expected to yield good soft magnetic properties [13–21], in our experiment, the film reveals relatively large coercivity (63 Oe). A possible reason for this may be the growth of Co crystallites along the direction perpendicular to the film surface. This means

Table 1. The saturation magnetization (Ms), coercivity (Hc) and resistivity (ϱ) of Co-C composite films and Co/C multilayer films

	Ms (emu/cm^{-3})	Hc (Oe)	ϱ (Ωcm)
Co-C (R.T.)	293	12.0	5.4×10^{-1}
Co-C (250 °C)	611	63.5	5.0×10^{-3}
Co/C (R.T.)	602	1.6	2.1×10^{-6}
Co/C (250 °C)	579	349.2	–

that the crystallites are not spherical but columnar in shape. Such growth behavior has been observed for Cu-C films [19]. Therefore, different magnetic domains may exist in the crystallites in spite of their small in-plane size, and this prevents the film from exhibiting smaller coercivity [21].

The Co/C multilayer film deposited at room temperature shows relatively high saturation magnetization and low coercivity. Considering the volume fraction of Co in the film, the Co layers give an effective Ms of 1053 emu/cm^3, which is close to the bulk value of cobalt (1400 emu/cm^3). The coercivity of the film, 1.6 Oe, is comparable to that of Co-base granular soft magnetic films [13] and Fe-base multilayer films [14]. Moreover, there is a good possibility of further reducing the coercivity by optimizing the thickness of the cobalt and carbon layers. The film shows the lowest resistivity amongst the tested films because of the formation of continuous Co layers. For the Co/C film deposited at 250 °C, the saturation magnetization decreased and the coercivity increased remarkably. These changes are considered to be caused by the formation of cobalt carbide at the Co-C interface and the lateral growth of Co grains.

3 Conclusions

The experimental results have shown that:
(1) Co-C composite films can be fabricated by incorporating C during ion-beam sputtering deposition of Co. The Co-C film deposited at room temperature is amorphous, and the film deposited at 250 °C is composed of Co nanocrystallites which are separated by an amorphous C or Co-C phase at the inter-grain regions. The amorphous Co-C film deposited at room temperature shows relatively low saturation magnetization and coercivity. With the formation of Co crystallites in the film, the saturation magnetization is increased by a factor of two, and the coercivity is increased by a factor of five.
(2) Co/C multilayer films can be prepared by the sequential deposition of Co and C by ion beam sputtering and chemical vapor deposition respectively. Both the Co and carbon layers are amorphous in the Co/C film deposited at room temperature. The film shows good periodicity with a period of 70 nm (Co: 40 nm, C: 30 nm), the Co-C interfaces are sharp and flat. Such a film exhibits soft magnetic properties (Hc = 1.6 Oe) with relatively high saturation magnetization. For the Co/C film deposited at 250 °C, Co layers are crystalline. A cobalt carbide phase was formed in the film due to the interfacial reaction. As a result, the saturation magnetization was decreased, and the coercivity was increased significantly.

References

1. S. Iijima: Nature **354**, 56 (1991)
2. X.P. Xu, G.R. Brandes: Appl. Phys. Lett. **74**, 2549 (1999)
3. S. Iijima: J. Cryst. Growth **50**, 675 (1980)
4. D. Ugarte: Nature **359**, 707 (1992)
5. B.V. Spitsyn, L.L. Bouilov, B.V. Derjaguin: J. Cryst. Growth **52**, 219 (1981)
6. D.R. McKenzie, D. Muller, S.A. Pailthorpe: Phys. Rev. Lett. **67**, 773 (1991)
7. P.J. Fallon, V.S. Veerasamy, C.A. Davis, J. Robertson, G. Amaratunga, W.I. Milne, J. Koskinen: Phys. Rev. B **48**, 4777 (1993)
8. P.M. Ajayan, S. Iijima: Nature **361**, 333 (1993)
9. C. Guerret-Piecourt, Y.L. Bouar, A. Loiseau, H. Pascard: Nature **372**, 761 (1994)
10. V.P. Dravid, J.J. Host, M.H. Teng, B. Elliott, J.H. Hwang, D.L. Johnson, T.O. Mason, J.R. Weertman: Nature **374**, 602 (1995)
11. A.A. Setlur, J.M. Lauerhaas, J.Y. Dai, R.P.H. Chang: Appl. Phys. Lett. **69**, 345 (1996)
12. T. Hayashi, S. Hirono, M. Tomita, S. Umemura: Nature **381**, 772 (1996)
13. S. Ohnuma, H. Fujimori, S. Furukawa, S. Mitani, T. Matsumoto: J. Alloy. Compd. **222**, 167 (1996)
14. H. Ono, M. Fujinaga, T. Yonemoto, T. Miyagawa: Jpn. J. Appl Phys. **31**, 1045 (1992)
15. S. Ohnuma, H. Fujimori, N. Yano, S. Furukawa, S. Fujii, T. Matsumoto: J. Magn. Magn. Mater. **126**, 556 (1996)
16. K. Yamamoto, T. Kobayashi, M. Kitada, H. Matsuyama: J. Magn. Magn. Mater. **136**, 38 (1994)
17. J. Shi, O. Nittono: J. Mater. Sci. Lett. **15**, 928 (1996)
18. T.B. Massalski, J.L. Murray, L.H. Bennett, H. Baker: *Binary Alloy Phase Diagrams* (American Society for Metals, Materials Park, OH 1986)
19. T. Cabioc'h, A. Naudon, M. Jaouen, D. Thiaudière, D. Babonneau: Phil. Mag. B **79**, 501 (1999)
20. T. Yogi, T.A. Nguyen: IEEE Trans. Mag. **29**, 307 (1993)
21. G. Herzer: J. Mater. Eng. Perform. **2**, 193 (1993)

Electrical Engineering in Japan, Vol. 130, No. 4, 2000
Translated from Denki Gakkai Ronbunshi, Vol. 118-A, No. 6, June 1998, pp. 608–614

Electrochemical Characterization of the Electrical Deposition of Co and Properties of Deposited Films Using Amorphous Ribbons as Substrate

KOH-ICHI MARUYAMA,* HIROO NUMATA, TAKASHI SATO, and OSAMU NITTONO
Faculty of Engineering, Tokyo Institute of Technology, Japan

SUMMARY

Both nonelectrically deposited Co-P and Co-Fe-B and electrically deposited Co films were prepared on rapid-quenched amorphous alloy ribbons. These Co-based alloy deposits exhibited characteristic polycrystalline structures, surface morphology, and magnetic properties, which were dependent on the species of the amorphous substrates. The electrochemical polarization measurements of substrate electrodes revealed that the electrocatalysis of substrates (e.g., for the anodic oxidation of reducing agent) thoroughly interpreted the deposition potential and the rate of nonelectrical deposition, and the overpotential of electrical deposition were dependent on alloy element of substrate. These electrochemical parameters influence the initial step of deposition, and hence determine the structural and magnetic properties of the deposits obtained. Furthermore, a basic study of the electrical deposition processes on an amorphous ribbon substrate has been carried out in connection with the structural and magnetic properties of the deposits. © 2000 Scripta Technica, Electr Eng Jpn, 130(4): 17–25, 2000

Key words: Nonelectrical Co-based metal; electrically deposited Co metal; rapid-quenched amorphous alloy ribbon; electrochemical polarization property; electrocatalysis of electrode; overpotential of deposition.

1. Introduction

Both rapid-quenching amorphous ribbon and electrolytic-deposited film are well known as low-cost materials prepared from liquid phase. As far as we know, there has been little research on the bimetal material of electrolytic films deposited on ribbon. Our investigation of this bimetal material was mainly focused on how interface stress, which was induced by the crystallization of amorphous ribbon during annealing of the bimetal, affected the magnetic properties of the film layer [1]. On the other hand, a fundamental characterization of electrolytic deposition behavior [2] and the structural and magnetic properties [3, 4] of the film layer has been performed.

It is known that Co-Fe alloy exhibits increased saturation magnetization (M_s) and positive transition of the negative saturation magnetostriction (λ_s), with increasing Fe content. Therefore, the alloy enriched with Fe content is raising expectations as a soft magnetic material with a large M_s (larger than that of permalloy), and as a new material with M_s and large λ_s. However, there has been little work with respect to electrochemical deposition, because of the technical problems of Fe deposition from an aqueous solution.

Nonelectrical deposition proceeds by metal ion reduction accompanied by the anodic oxidation of the reducing agent in an electrolyte, while electrodeposition proceeds under an applied cathodic current. In the case of an electrolyte containing P (or B) and S as a complexing agent or a reductant, the metalloid element also deposits, forming an alloy-metalloid phase. Maruyama and colleagues showed that Co-Fe alloy deposits with a wide range of composition were obtainable on nickel-based amorphous alloy ribbons, by selecting the electrolytic conditions [4]. Furthermore, they found that the structural and magnetic properties of nonelectrically deposited Co-P alloys (a few micrometers in thickness) were dependent on the alloying element of the amorphous ribbons [2]. It is generally known that the properties of such thick deposits are obtained independently of the substrate species.

In this paper, the electrochemical behavior and the structural and magnetic properties of nonelectrically deposited Co-P and Co-Fe-B and electrodeposited Co were investigated in terms of the substrate species: Ni-, Co-, and Fe-based amorphous alloys and polycrystalline Cu.

*Presently with the National Research Institute for Metals.

2. Experimental

Nonelectric deposition and electrodeposition were carried out on an electrode (substrate) in an isothermal electrolytic cell (300 ml in volume). Table 1 shows the compositions of the electrolyte and the electrolytic conditions. Table 2 shows the compositions of the amorphous alloys (prepared by the single-roll method), which exhibited noncrystalline phase analyzed by X-ray diffractometry. Polycrystalline copper sheet (purity 99.9%, thickness 0.5 mm) was a commercial product. The substrate electrodes of 10 × 10 mm^2 in surface area for nonelectric deposition were used as a cathode after chemical polishing by rinsing in 10% HCl and 10% HF solutions for 30 min, in the case of Fe- and Co-based substrates, and Ni-based and copper ones, respectively, followed by the sensitizing and the catalyzing. The sensitizing and catalyzing solutions were 40 g/liter $SnCl_2 \cdot 2H_2O$ + 20 ml/liter HCl for 2 min, and 0.3 g/liter $PdCl_2 \cdot 2H_2O$ + 5 ml/liter HCl for 1 min. On the other hand, electrodeposition was carried out using a galvanostatic mode, after mechanical polishing with emery paper up to #1500 followed by ultrasonic rinsing.

The electrochemical polarization measurement was made in potential sweep mode (potential sweep rate 1 mV/s). The working electrode was a substrate treated under the same conditions as for deposition, the counterelectrode a spiral platinum wire, and the reference electrode a saturated silver electrode (SSE). For the nonelectrodeposition bath, which was designated as the *total bath*, an anodic and a cathodic polarization curve (*i–E* curve) were measured. The anodic and cathodic *i–E* curves were obtained for a solution without metal ions, the *anodic partial bath*, and one without a reducing agent, the *cathodic partial bath*. On the other hand, only the cathodic *i–E* curve was measured for the electrodeposition bath.

The film thickness was calculated from mass gain during the deposition using the density of Co and Co-Fe alloy. Composition of deposits was analyzed by atomic absorbance method. The current efficiency was estimated by the mass gain and the electric charge passed. Surface morphology of the deposit was observed by scanning electron microscopy (SEM), and the magnetic properties were estimated by vibrating magnetometry (VSM). The characterization of crystalline preferred orientation was obtained by X-ray diffractometry (XRD). The "degree of preferred orientation" was defined as the ratio of each peak intensity ratio obtained to that listed on the JCPDS card.

Table 1. Composition of nonelectrical CoP deposition bath (A), nonelectrical CoFe deposition bath (B), and electrodeposition bath of Co (C), and their deposition conditions

Chemicals/M	A : E.L. CoP	B : E.L. CoFeB	C : E. Co
Na-citrate	0.2	0.2	—
$CoSO_4 \cdot 7H_2O$	0.1	0.04	0.5
$(NH_4)_2Fe(SO_4)_2$	—	0.01	—
$NaH_2PO_2 \cdot H_2O$	0.2	—	—
DMAB	—	0.025	—
H_3BO_3	0.5	—	—
pH	8.2	10	5.0
pH of adjustment	NaOH solution	NH_4OH solution	H_2SO_4 solution
Bath temp.	85°C	85°C	30°C

Table 2. Composition of rapid-quenched amorphous alloy ribbons used as substrates

Species	Composition
15 BY	$Ni_{76}Si_4B_{20}$
S 265	$Fe_{84}Si_1B_{15}$
T 126	$Co_{66}Fe_4Si_{14}B_9Mo_2$

3. Results and Discussion

3.1 Nonelectrical Co and Co-Fe alloy deposition

The Co-P, Co-B, and Co-Fe-B were nonelectrically deposited on amorphous ribbons from an electrolyte containing sodium hypophosphite monohydrate ($NaH_2PO_3 \cdot H_2O$) or dimethylamineborane (DMAB) as a reducing agent. Since there have been reports on the electrochemical polarization behavior of Co-P deposition [2], and Co-B and Co-Fe-B deposition [3], and the structural and magnetic properties of Co-Fe-B deposits [4], we will discuss the influence of the alloying composition on the electrochemical parameters and the structural properties below.

3.1.1 Nonelectrical deposition from electrolyte containing $NaH_2PO_3 \cdot H_2O$

Figure 1 shows the XRD profiles of the nonelectrically deposited Co-P on the roll side surface of Fe- and Ni-based amorphous ribbons, and polycrystalline Cu sheet, where the deposits are (a) on noncatalyzed Fe-based alloy (S265), (b) on catalyzed Fe-based alloy (S265), (c) on catalyzed Cu, and (d) on catalyzed Ni-based alloy (15BY). The film thickness of deposits is shown on the right side of Fig. 1. Each thickness value was obtained after deposition for 1 h. The deposit was not obtained on the noncatalyzed Ni-based ribbon, Except for profile (d), the profiles contained the diffraction peaks of hcp Co, (1100), (002), and (101) in the deposits. Profile (d) exhibited only the (002) peak. Profiles (c) and (d) revealed diffraction from the substrate, two sharp peaks of fcc Cu and broad peak of

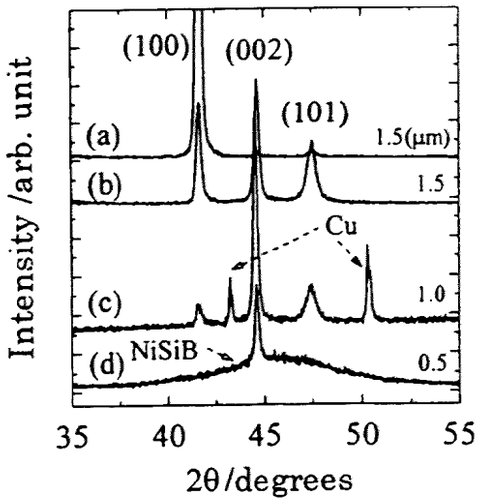

Fig. 1. XRD profiles of nonelectrically deposited CoP films on respective amorphous and Cu substrates. (a) Noncatalyzed FeSiB (S265) ribbon; (b) catalyzed FeSiB (S265) ribbon; (c) catalyzed polycrystalline Cu sheet; (d) catalyzed NiSiB (15BY) ribbon.

amorphous, respectively. It is clear that the crystalline preferred orientation of deposits were different from the alloying element of the substrate. A large intensity of (100) was obtained for the noncatalyzed iron-based amorphous ribbon substrate [profile (a)], and the broad Co peak for the other catalyzed substrates (the other profiles). Comparing among these profiles [(b) to (d)], the preferred orientation of deposits may be dependent even on the alloying element of the catalyzed substrate. Surface morphology of deposits was also dependent on the alloying elements of substrates [2].

In nonelectrical deposition, the cathodic reduction of metal ions to adsorbed atoms is the initial step, being followed by nucleation and crystal growth processes. Therefore, the difference of such deposit thickness as shown in Fig. 1 cannot be explained by the autocatalytic reaction of Co-P deposition on the Co-P electrode (deposit surface), which is characterized by the conventional polarization measurement. Our image is that the initial step of the deposition is familiar with the reaction on the substrate surface whose electrode potential is different from that of the deposit surface. We believe that this potential is determined by the electrocatalysis of substrate surface, which is designated as the *electrocatalysis of the substrate electrode*. In order to reveal this initial deposition, the electrochemical polarization (i–E) curves were measured using the substrate immersed as the working electrode. Then, the deposition potential and the rate of nonelectric deposition are evaluated from the anodic and cathodic polarization curves by the conventional method.

Figures 2(a) and 2(b) show the total (a) and the partial cathodic and anodic i–E curves (b) for nonelectric Co-P

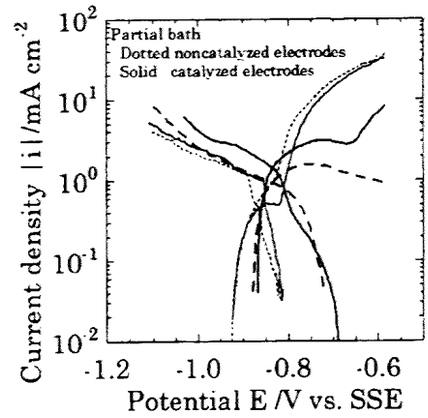

(a)

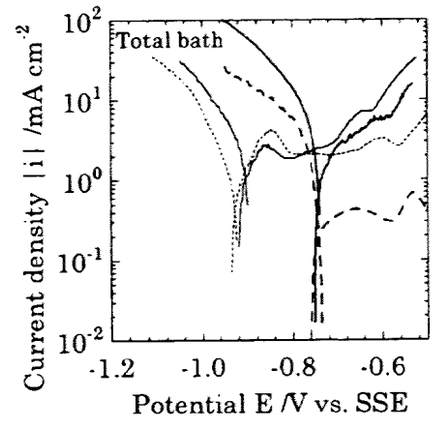

(b)

Fig. 2. Electrochemical polarization curves of amorphous FeSiB (S265) and NiSiB (15BY) ribbon electrodes. These curves are described as the thin and thick curves, respectively. (a) In the partial bath, E_{pl} = –0.87 (V versus SSE) and i_{pl} = 0.50 (mA/cm^2) for the noncatalyzed FeSiB electrode, and E_{pl} = –0.85 and i_{pl} = 0.51 for the catalyzed one. On the other hand, E_{pl} = –0.83 and i_{pl} = 0.94 for the noncatalyzed NiSiB electrode, and E_{pl} = –0.83 and i_{pl} = 1.4 for the catalyzed one. (b) In the total bath, E_{pl} = –0.93 and i_{pl} = 0.47 for the noncatalyzed FeSiB electrode, and E_{pl} = –0.90 and i_{pl} = 1.1 for the catalyzed one. On the other hand, E_{pl} = –0.74 and i_{pl} = 0.21 for the noncatalyzed NiSiB electrode, and E_{pl} = –0.74 and i_{pl} = 0.67 for the catalyzed one. Solid and dotted curves indicate those of catalyzed and noncatalyzed electrodes, respectively.

deposition on Fe- and Ni-based alloy ribbons, where the data for noncatalyzed and catalyzed amorphous alloys are shown as dotted and solid lines, respectively. In the partial bath, an intersection existed between the anodic and cathodic i–E curves. In the total bath, the deposition rate and the deposition potential were evaluated by extrapolating from two i–E curves, and the magnitude of the deposition rate above about 0.5 mA/cm^2 was obtained, except for the noncatalyzed Ni-based electrode. This means that whether nonelectric deposition has occurred is determined by the deposition rate on the substrate surface in the initial step [2]. In practice, the nonelectric Co-P deposit was not obtainable on noncatalyzed Ni-based amorphous ribbon and Cu sheet.

It is well known that the electrocatalysis for the anodic oxidation of reductant can be characterized by the potential of the anodic partial curve at a current density of 0.1 mA/cm^2 [5], which is designated as the anodic oxidation potential. Our idea is that the electrocatalysis of the amorphous ribbon is characterized from the polarization curves as shown in Fig. 2. At first, for the noncatalyzed electrodes, Fig. 2(a) shows that electrocatalysis of the Ni-based amorphous electrode is larger than that of the Fe-based amorphous one for the anodic oxidation of $NaH_2PO_3 \cdot H_2O$. The amount of the anodic current whose slope saturates (the limited current) for the Ni-based amorphous electrode is smaller than that for the Fe-based amorphous electrode. This is due to the difference of the Tafel slope of the anodic current, because of the potential of the Fe-based amorphous electrode at which the anodic current saturates similar to that of the Ni-based one. Such polarization behavior was consistent with the fact that Co-P was deposited on Ni-based amorphous electrode but on the Fe-based one. Second, we will discuss the effect the of the catalyzing treatment of these amorphous electrodes on the electrocatalysis. The anodic oxidation potential of each catalyzed electrode was smaller than that of each noncatalyzed one. This result was explained by the anodic oxidation potential of the Pd electrode being less noble than that of the Fe-based and Ni-based amorphous electrode, which was consistent with the investigation of the electrocatalysis for the electrodeposited Pd, Ni, etc. [5]. For the Ni-based amorphous electrode, the amount of the limited current was significantly increased by the catalyzing treatment. This means that the Tafel slope of the anodic current of the Ni-based amorphous electrode was larger than that of the Fe-based one. We believe that the electrocatalysis was determined not only by the anodic oxidation potential but also by the Tafel slope of the anodic current. Therefore, the deposit was obtained not on the noncatalyzed Ni-based amorphous electrode but on the catalyzed one. We experimentally revealed that the deposit thickness was related to the electrocatalysis of the substrate electrode, so that this electrocatalysis may be effective even with a thickness on the micrometer order.

3.1.2 Nonelectrical deposition from electrolyte containing DMAB

It is possible to nonelectrically deposit Co-B and Co-Fe-B on noncatalyzed Ni-based amorphous ribbon in an electrolyte, using DMAB as a reducing agent. We have elsewhere described the details of the deposition behavior [4], and here we focus on the effect of the catalyzing treatment of the amorphous ribbon surface on nonelectric Co-Fe-B alloy deposition. We will present the anomalous deposition behavior in terms of electrocatalysis of the substrate electrode.

Nonelectrical deposition was carried out on the roll side surface of Ni-based ribbon, which was catalyst-treated several times for 0 to 60 s after Sn-sensitizing for 60 s. The deposits exhibited coexistence of bcc Fe and fcc Co (or hcp Co, which is not distinguishable by XRD alone) phases, each of which was a solid solution. XRD profiles of these deposits, shown in Fig. 3, tell us the ratio of two phases of the deposit versus the duration of the catalyzing treatment. In order to evaluate the influence of the catalyzing treatment

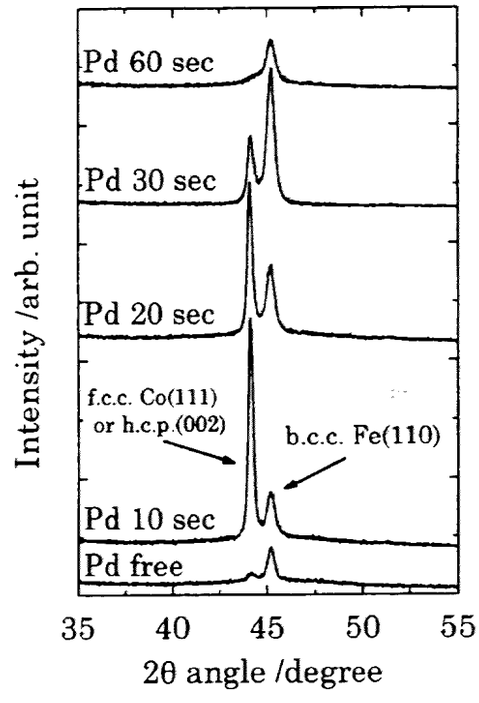

Fig. 3. XRD profiles of nonelectrically deposited Co-Fe-B films on amorphous NiSiB (15BY) ribbon electrodes. The dependence of the crystal phase of films on the time of catalyzing treatment.

on the electrocatalysis of amorphous ribbon electrode for the anodic oxidation of DMAB, the anodic *i–E* curves were measured in the anodic partial bath. Figure 4 shows the *i–E* curves for several amorphous electrodes of the roll side of ribbons, and the catalyzed Cu sheet. Even the electrocatalysis of noncatalyzed ribbon electrodes exceeded that of the catalyzed copper substrate. The effect of the catalyzing treatment on the electrocatalysis of amorphous ribbon electrode consisted of a shift of the anodic oxidation potential in a more favorable direction and a decrease in the gradient of the anodic oxidation current, behavior similar to that when using $NaH_2PO_3 \cdot H_2O$ as a reducing agent. It is speculated that the area density of Pd on the substrate surface is dependent on the duration of the catalyzing treatment, which results in an influence on the electrocatalysis of the substrate electrode. We believe that the crystallinity of the deposits shown in Fig. 3 is caused by the initial step of the electrochemical deposition behavior with the deposition potential determined by the electrocatalysis of the substrate electrode.

The electrochemical behavior of the nonelectric deposition is summarized as follows. The initial step of the nonelectric deposition is evaluated by the electrochemical polarization measurement using the substrate as an electrode, where the deposition potential is influenced by the electrocatalysis of the substrate electrode, dependent on the alloying element of the substrate, and is caused by the change in the electrocatalysis due to the catalyzing treatment. This is because the initial deposition potential may promote nucleation and crystal growth, which determine the structural and magnetic properties of deposits. More detailed investigation of the mechanism of the electrocatalysis of the substrate electrode requires solution of the problem as to why the properties of deposits with thickness of micrometer order are influenced by the substrate.

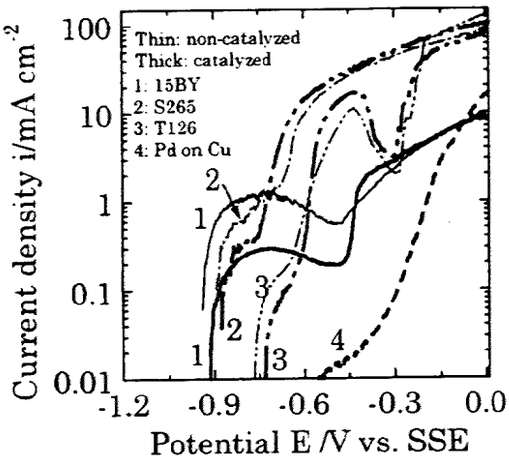

Fig. 4. Partial anodic polarization curves of respective amorphous ribbons, in the partial bath containing Na-citrate, and DMAB as a reducing agent. Regular and bold curves refer to noncatalyzed and catalyzed electrodes, respectively.

3.2 Electrical Deposition of Co

3.2.1 Properties of deposits

Magnetic properties of the electrically deposited Co (~2.5 μm thick) on Ni-based amorphous ribbon and Cu polycrystalline sheet are shown versus the current density of the deposition in Fig. 5. We believe that these magnetic properties are those of only the deposit layer because of the nonmagnetic substrate for the Ni-based ribbon, and the paramagnetic substrate for the Cu sheet, whose magnetization was easily separable from the component for the deposit layer in the measurements. The coercive force (H_c) was increased with an increase of the current density of deposition. On the other hand, for Cu substrate, a larger remanent magnetization (M_r/M_s) was obtained at lower current density (decreased by up to half). This tendency of M_r/M_s was prominent for the Ni-based amorphous substrate. These properties of deposits were dependent not only on the current density but also on the species of substrates. There is a possibility that the composition of the substrate is one of the factors controlling the magnetic properties of the deposits. The magnetic properties of deposits on Fe-based and Co-based amorphous ribbons were difficult to separate from those of the bilayer materials, because of the ferromagnetic substrates.

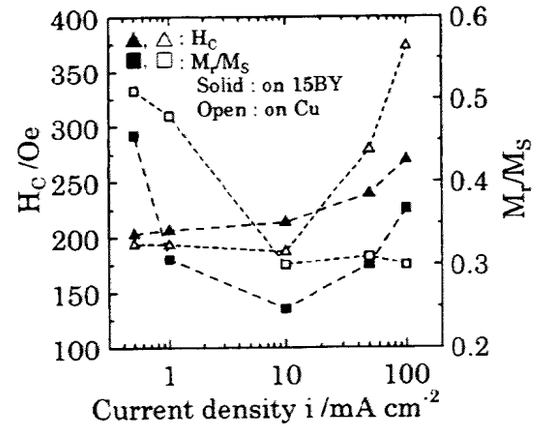

Fig. 5. Magnetic properties of electrodeposited Co films on amorphous NiSiB (15BY) ribbon and polycrystalline Cu sheet.

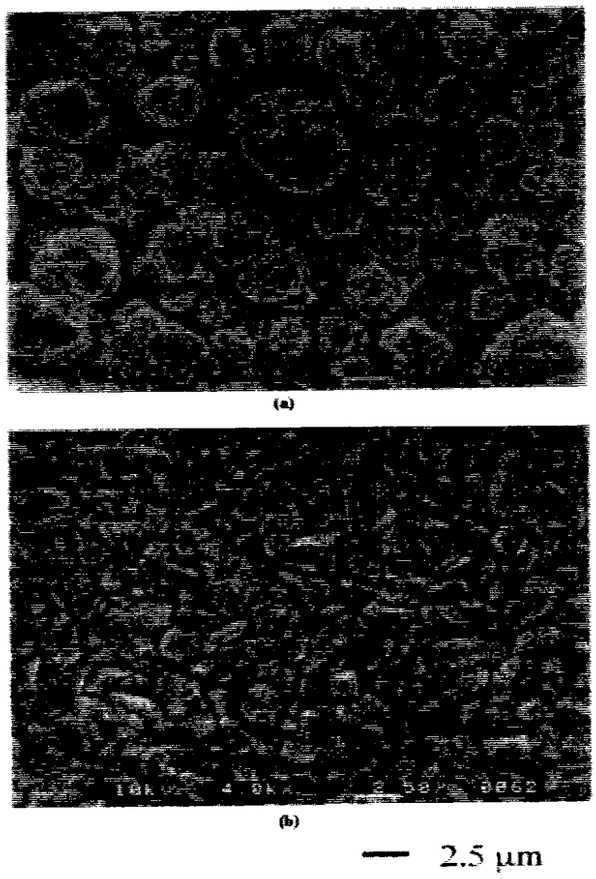

Fig. 6. (a) SEM surface images of electrically deposited Co films on amorphous NiSiB (15BY) ribbon and (b) polycrystalline Cu sheet, at a current density of 50 mA/cm^2.

Figures 6(a) and 6(b) show surface SEM images of deposits at a current density of 50 mA/cm^2. The shape and size of the needlelike formations were dependent on the species of substrate. The surface morphology of the deposits on the other amorphous substrate was different owing to the alloying elements of the amorphous substrate.

Each XRD profile of the deposits on several substrates presented 5 peaks of hcp Co. The *degree of preferred orientation* estimated by the XRD profiles is shown versus the current density in Fig. 7. For Ni-based amorphous substrate, as shown in Fig. 7(a), the crystal face of the deposit had a preferred orientation of (002). This preferred orientation of (002) and the other orientations within 20% changed with the current density. A similar tendency was obtained for the other substrates, but the degree of preferred orientation and its dependence on the current density differed with the species of substrate. On the other hand, Fig. 7(b) shows the results for polycrystalline Cu substrate. The degree of preferred orientation of faces other than (002) of this substrate was larger than for the other amorphous substrates at almost all current densities. In Fig. 7(c), the preferred orientations of (002) are shown versus the current density for four kinds of substrates. For amorphous substrates, there was a slight correlation of the composition of substrates with the preferred orientation. The result for copper substrate was significantly different from that for amorphous substrates, which was large only at 10 mA/cm^2. This behavior means that there is a possibility of an electrodeposition reaction controlled by not only the underlayer composition but also by its crystallinity.

3.2.2 Electrochemical deposition behavior

So far we have experimentally confirmed the structural and magnetic properties of Co deposits dependent not only on the current density but also on the species of underlayer. Pangarov's theory [6] on two-dimensional nucleation and crystal growth explains that the preferred orientation of deposit is determined by the overpotential of the electrodeposition. Our idea is that the overpotential may be affected by the immersion potential of the substrate in the initial step of deposition. The overpotential of the initial step is easily estimated by the cathodic i–E curve of the substrate used as a working electrode.

The cathodic i–E curves for electrodes of four kinds of substrates are shown in Fig. 8(a). For each electrode, measurement was carried out from the immersion potential to the potential at a current density of 150 mA/cm^2. Another i–E curve is for a Co electrode electrodeposited on a Cu substrate. The same curves (data not shown) were obtained for Co electrodes deposited on the other substrates. The overpotential (η) of the electrodeposition is usually defined as follows:

$$\eta \equiv E_{dep} - E_{rev} \tag{1}$$

where E_{rev} is the reversible potential, and E_{dep} the electrode potential during deposition. For instance, E_{rev} is usually the equilibrium potential of a Co electrode for $Co^{2+} + e \Leftrightarrow Co$. It is supposed that for the same equilibrium reaction, E_{rev} gives the immersion potential of the substrate used. However, in the case of the deposition of some other element on a substrate, E_{rev} of the substrate is not equal to that of the deposit surface. We imagine that the overpotential of the initial step is determined by E_{rev} of the substrate, which is dependent on the alloying element of the substrate. Figure 8(b) shows this overpotential versus the current density for respective substrates. It is natural that the reversible potential during electrodeposition is that of the deposit surface on which the influence of the immersion potential of the substrate is negligible, after the substrate is covered with one atomic layer of deposit. However, we believe that this

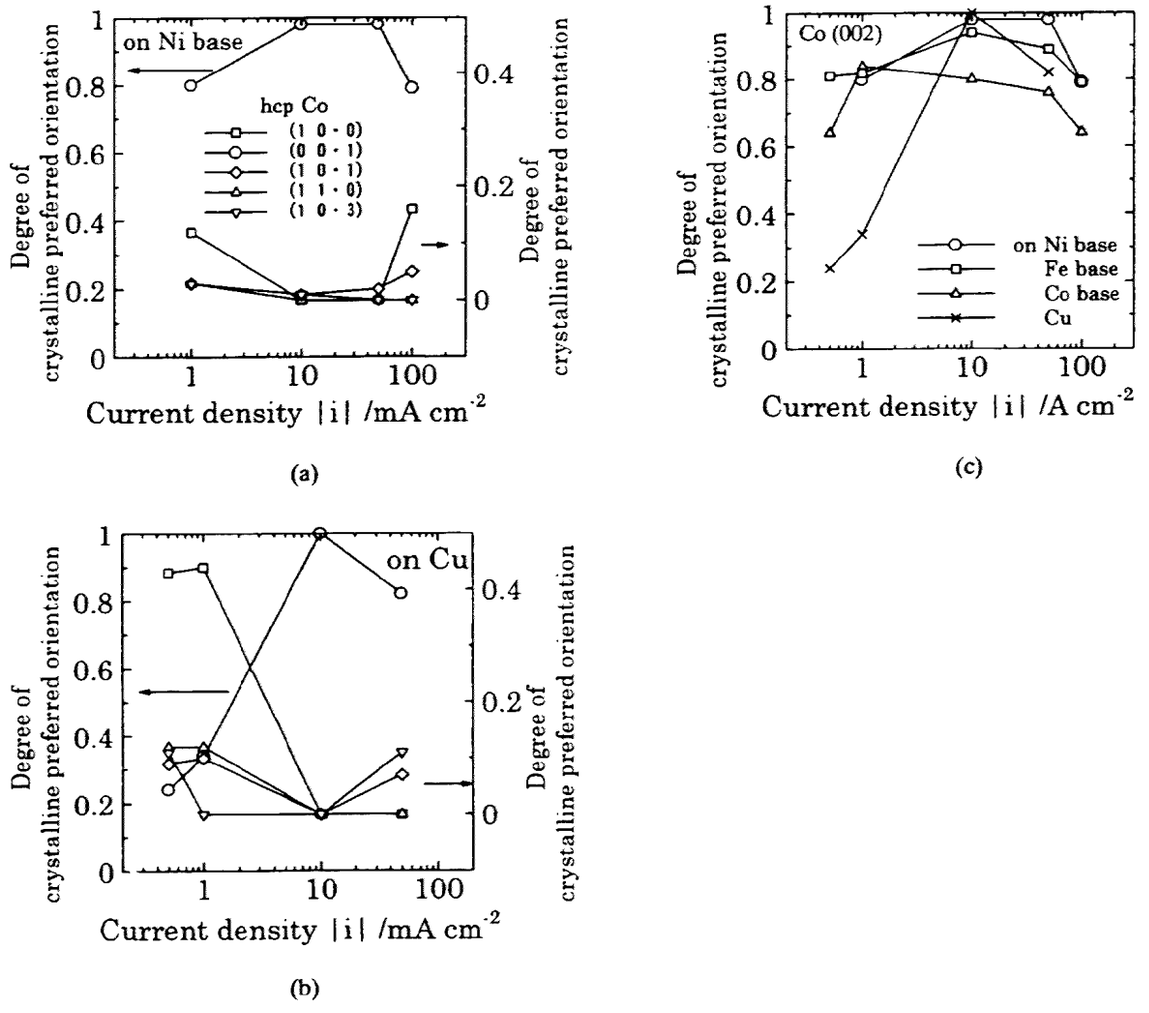

Fig. 7. *Degree of preferred orientation* (defined in the text) of XRD profiles for the electrically deposited Co films on (a) amorphous NiSiB (15BY) ribbon and (b) polycrystalline Cu sheet. (c) Only the data of hcp Co(002) for the films on respective substrates.

overpotential in the initial step of deposition is related to the structural and magnetic properties of deposit through nucleation and crystal growth. Indeed, for an amorphous substrate, the order of preferred orientation of Co(002) deposited, as shown in Fig. 7(c), may be related to the order of the overpotential of the substrate electrode. Also, the difference of surface morphology of deposits depending on the species of substrates is related to the influence of the species of substrates on the deposition behavior on the surface of thick deposit [3]. It was reported that a hydrogen reaction occurred with electrodeposition, which was affected by the overpotential of deposition [7]. The structural and magnetic properties of the deposit are influenced by hydrogen absorbed into the deposit. The current efficiency of Co electrodeposition is shown in Fig. 8(c) for several substrates. The current efficiency for Fe-based substrate was 100% over the whole range of current density, and for Ni-based and Co-based substrates, it was 40 to 50% at lower current density. The current efficiency was significantly different depending on the species of the substrates, which may be explained by the different deposition in the initial step for different species of substrates. Therefore, we believe that this initial electrochemical deposition behavior is one of the factors affecting formation of the deposit. The result for the Cu substrate exhibited the most common result of current efficiency, which gives a high level at low current density and decreases with increasing current density due to the hydrogen reaction. In the case of the electrodeposition of Co on Fe-based substrate, therefore, a significantly high current density may be obtained because of not only the overpotential of deposition but also other factors (e.g., adsorption of ions in the solution). This is an

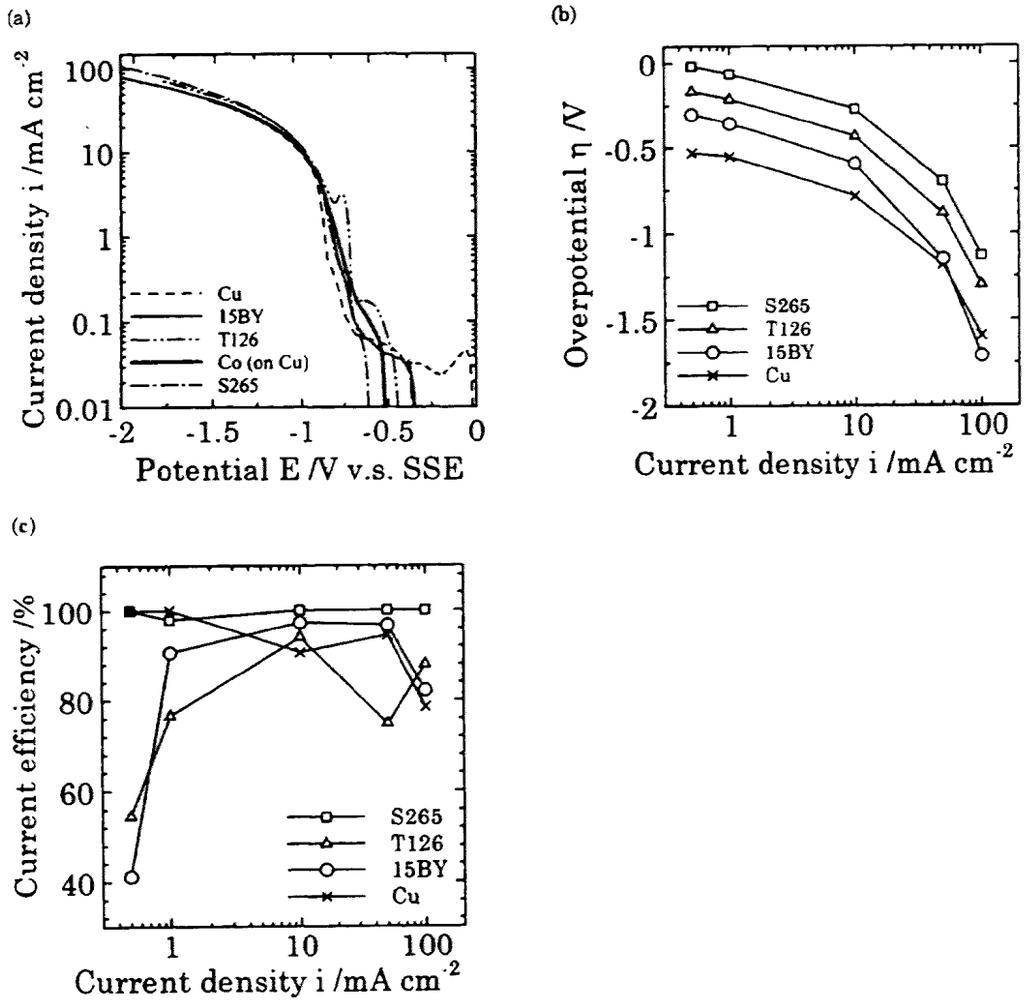

Fig. 8. (a) Cathodic polarization curves of respective amorphous ribbon electrodes, Cu sheet, and electrodeposited Co on Cu sheet. (b, c) Overpotential and current efficiency of electrodeposition of Co for these electrodes versus current density, respectively.

interesting phenomenon from the fundamental and technological viewpoints, which is applicable to the restraint of the hydrogen reaction.

This study is focused on the relationship between the structural and magnetic properties of electrically deposited Co on the amorphous alloy and Cu substrates and the electrochemical cathodic reaction dependent on the substrate. The properties of the deposit are found to be related to the different overpotentials of deposition, depending on the composition of the substrate.

4. Conclusion

It is found that the structural and magnetic properties of nonelectrically deposited films are determined by the initial step of electrochemical parameters dependent on the species of substrate. This is because the nucleation and crystal growth are related to the electrocatalysis of the substrate electrode for the anodic oxidation of the reductant in nonelectric deposition, and the overpotential of electrodeposition, whose parameters are dependent on the alloy element of substrate. The properties of both nonelectrically deposited and electrically deposited films a few micrometers thick are influenced by the initial behavior of electrolytic deposition.

Acknowledgments

We are indebted to Dr. I. Ohno (formerly a professor at Tokyo Institute of Technology) for important discussions.

We thank Professor K. Nagata, Tokyo Institute of Technology, for measurements by the atomic absorbance method. Thanks are also due Mr. A. Yamaguchi and Ms. M. Masuda (students in our laboratory) for cooperation in the experiments.

REFERENCES

1. Maruyama K, Sato T, Ohno I, Numata H. J Magn Soc Jpn 1997;21:919.
2. Maruyama K, Numata H, Ohno I, Sato T. J Surf Finish Soc Jpn 1996;47:1054.
3. Maruyama K, Sato T, Ohno I, Numata H. Proc ICMFM 96 (International Conference on Microstructure and Functions of Materials), p 185.
4. Maruyama K, Numata H, Sato T, Ohno I. J Surf Finish Soc Jpn 1996;49:618.
5. Ohno I, Wakabayashi O, Haruyama S. J Electrochem Soc 1985;132:2323.
6. Pangarov NA, Volmer SD. Electrochim Acta 1962;7:139.
7. Maruyama Y, Numata H, Ohno I, Haruyama S. J Surf Finish Soc Jpn 1997;48:68.

AUTHORS (from left to right)




Koh-ichi Maruyama (nonmember) (D.Eng. degree, Tokyo Institute of Technology, 1998) is a domestic research fellow of Japan Science and Technology Corporation at the National Research Institute of Metals. His current research activities concern magnetic materials and the surface science of liquid methods. He is a member of the Physical Society of Japan, the Japan Society of Applied Physics, the Electrochemical Society, and the Magnetic Society of Japan.

Hiroo Numata (nonmember) (D.Eng. degree, Tokyo Institute of Technology, 1979) is a research associate at Tokyo Institute of Technology. His current research activities involve the kinetic study of molten carbonate fuel cell reaction, electrodeposition from molten salts, and analysis of the metal hydrogen system. He is a member of the Electrochemical Society of Japan, the Institute of Metals of Japan, and the Surface Finishing Society of Japan.

Takashi Sato (member) received his B.S. and M.S. degrees in physics from the University of Tokyo in 1963 and 1965, and his Ph.D. degree from Tohoku University in 1991. From 1965 to 1993, he worked for Nippon Steel Corporation. He joined Tokyo Institute of Technology as a professor in 1993. His research interests include the development of amorphous magnetic alloys and their application.

Osamu Nittono (nonmember) (D.Eng. degree, Tokyo Institute of Technology, 1970) is a professor at Tokyo Institute of Technology. His current research activities involve the fundamental study of structural properties of thin films including magnetic and conductive films, and their characterization with X-ray diffraction technique and transmission electron microscopy. He is a member of the Physical Society of Japan, the Institute of Metals of Japan, the Crystallographic Society of Japan, and the Crystal Growth Society of Japan.

Proceedings of the International Conference
on Solid-Solid Phase Transformations '99 (JIMIC-3)
Edited by M. Koiwa, K. Otsuka and T. Miyazaki
The Japan Institute of Metals, 1999.

Common Features of Phase Changes in Metastable Transition Metal Carbides such as Fe-C, Ni-C and Co-C prepared by Reactive Sputtering

Osamu Nittono, Minako Azumi, Yuji Hashiba and Miku Wakamori

Department of Metallurgy, Tokyo Institute of Technology, Meguro-ku, Tokyo 152-8552, Japan

Keywords: phase change, decomposition, phase stability, metastable phase, metal carbide, transition metal, annealing, reactive sputtering, magnetic property, formation ability

Abstract

Transition metal-carbon alloy films, such as Fe-C, Co-C and Ni-C alloys, were prepared by a new type of co-sputtering deposition technique. Their phase changes caused by annealing were examined together with decomposition behavior. The formation ability and thermal stability of metastable phases, such as cobalt and nickel carbides, are explained by the difference in the formation enthalpy for cabides. After annealing, graphite particles were always seen to grow around metal particles decomposed from carbides, probably due to the so-called metal-mediated nucleation and growth. Common features of the phase changes including decomposition behavior are also explained based on the same concept, partly taking account of subsequent dissociation of carbon from the carbides during annealing.

Introduction

Transition metal-carbon(M-C; M:Fe,Ni,Co) alloy systems have attracted research interests so far because of their scientific and industrial importance. Hardness and high melting point are unique properties of transition metal carbides and some of magnetic properties of transition metal-carbon alloys including amorphous alloys and metal carbides are also important. Among these transition metals, Ni and Co are known to form a simple eutectic binary phase diagram with carbon (or graphite), and metastable metal-metal carbide phase boundaries may be drawn on the equilibrium phase diagram (so-called double diagram)[1].

Understanding the thermal stability of metastable phases including amorphous states and metal carbides of these alloy systems is indispensable for a reliable application of these metastable materials. However, a few systematic studies of crystallization behavior were performed for these alloys. In order to extend our knowledge about the thermal stability of such metastable metal-carbon alloys, it is essential to understand the decomposition behavior of such metastable phases, especially crystallization and precipitation behavior from metastable phases to stable phases in the transition metal-carbon systems. In previous studies, crystal structures of such metastable carbides are reported in the literature:Co_3C, Ni_3C (orthorhombic) Co_2C(orthorhombic), and $Co_{2\text{-}3}C$(hexagonal). The orthorhombic Co_3C(Ni_3C) is isomorphous with cementite (Fe_3C) and the Co_2C can also be viewed as a distorted close-pack hexagonal.

In order to investigate such metastable phases, the development of the fabrication technique of such films is an important key. A faster cooling rate is required to fabricate such metastable phases. In previous studies, these metastable carbides have been formed by the cementation of metal powders and thin films with mixed gas of methane(CH_4) and hydrogen(H_2)[2,3]. Recently, such materials including thin films and powders were fabricated by co-sputtering of metal and carbon targets[4,5], by mechanical alloying[6,7] and by ion implantation[8]. Among these fabrication methods, co-sputtering is the most simple, and it provides a faster cooling rate than the splat-cooling. The present authors have designed a dual source deposition system (IBS+CVD) which combines ion beam sputtering (IBS) deposition for metals and microwave (ECR) plasma chemical vapour deposition (CVD) for carbon, and applied it to fabricate the Ni-C alloy films[9]. As a result, metastable Ni_3C nanocrystallites were found to be easily formed by adjusting the supply of CH_4 gas. This codeposition method was also found to be very useful for examining the structure properties of transition metal-carbon alloy films, because various films, such as amorphous, carbides and composite (carbon + nanoparticles) films, are easily obtained by changing deposition conditions [10].

In this study, therefore, we prepared M-C (M:Fe, Co, Ni) alloy films by the codeposition method and investigated their microstructure changes and phase changes which

took place during annealng. Common features of phase changes, including crystallization from amorphous phases and decomposition of metastable phases, are summarized and also discussed from the viewpoint of the formation ability of metastable phases in the M-C alloy systems.

Experimental procedures

Formation of metal-carbon alloy films (thichness: 300 to 600nm) was performed by the same codeposition method(IBS+CVD) as used in our previous studies[9,10]. The base pressure of the chamber was less than 4.0×10^{-5}Pa and sputtering was carried out in a 3×10^{-2} Pa Ar atmosphere with an ion beam courrent of 20mA and an applied voltage of 2kV. The purity of metal targets, such as Fe, Co and Ni, was 99.99%. The gas flow of CH_4 varied from 0.005 to 0.03sccm by using a mass flow controller with a flow rate of hydrogen(H_2) of 20sccm, and thereby the carbon content was adjusted in the films. The carbon content was examined by energy dispersive spectroscopy(EDS). The deposition rate was estimated by measuring the film thickness, being 0.04nm/s for metal and 0.09nm/s for carbon. Corning 7059 glass plates were used as substrates, and substrate temperature was variable upto 873K. This apparatus is also equipped with an energy dispersive X-ray diffractometer, and thereby in-situ analysis of deposited films can be perfomed during annealing. The crystal structure of the prepapred films was identified by X-ray diffraction (XRD) using CuKα radiation, before and after annealing at elevated temperatures. The microstructure was examined by electron diffraction-transmission electon microscopy(ED-TEM), supplemented with high-resolution cross-sectional TEM. Magnetic property was evaluated by a vibrating sample magnetometer.

Results and discussion

1. Formation ability of metal carbides for three transition metal-carbon alloy systems

All the as-deposited alloy films were found to be amorphous-like and granular states depending mainly on the CH_4 flow rate. As shown in Fig,1, cobalt carbides are formed more easily under smaller flow rates. Observed peak broadening is ascribed to very fine grains of formed carbides. This tendency was almost similar to the cases of other metal carbides [10]. Lots of experiment showed that metal carbides, such as Ni_3C, Co_3C($Co_{2\text{-}3}C$), Co_2C, except Fe_3C, were easily formed in as-deposited films with smaller flow rates of CH_4. Among them, the formation of nickel carbides was slightly easier at elevated temperatures below 673K, as shown in Fig. 2. Cobalt carbides were slightly easy to form in a wide range of carbon contents, being consistent with the results by Tanaka et al.[7]. On the contrary, iron carbides were found to form only under a very small flow rate of CH_4, indicating that only a slight extension of solubility of carbon takes place in the α-Fe phase.

Here, in order to confirm the formation ability of such carbides under thermodynamical conditions, multilayered Co/C films were annealed at 673K for more than 3h, but no metal carbide was seen to form in the films, as shown in Fig. 3. On the other hand, amorphous iron-carbon films were found to easily form iron carbides (Fe_3C) by annealing

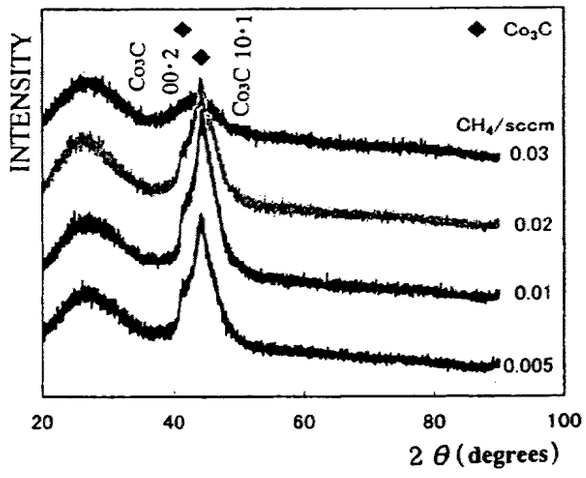

Fig. 1 Formation of Co carbides deposited with various gas flow rates(XRD).

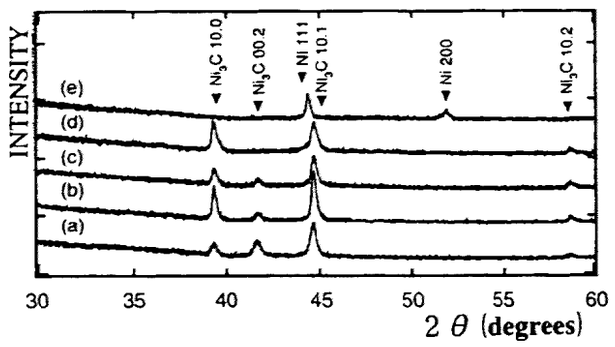

Fig. 2 Formation of Ni carbides deposited at elevated temperatures. (a)ambient temperature, (b)473K, (c)573K, (d)673K and (e) 773K (XRD).

after deposition, as shown in Fig. 4. Experimental results of the formation ability of these metal carbides suggest that transition metal carbides can be qualitatively explained by the difference in the formation enthalpy for transition metal carbides (the order of the formation enthalpy for the carbides: Ni-C>Co-C>Fe-C, as reported by Tanaka et al.[7]).

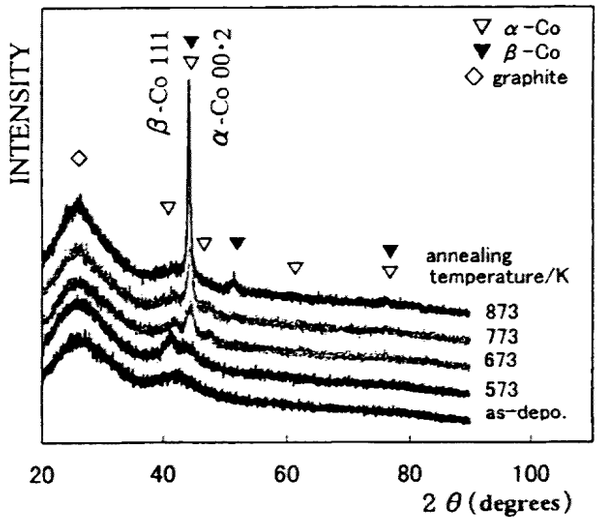

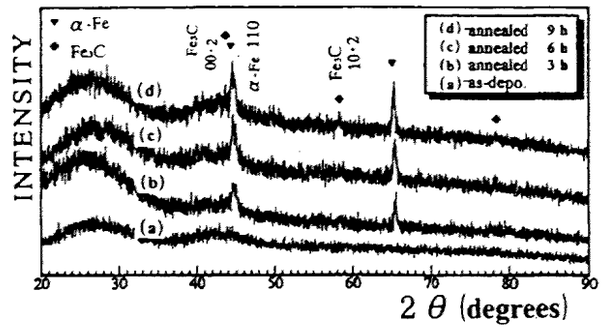

Fig. 4 Formation of iron carbide for a Fe-20at%C film, when annealed at 723K for different times(XRD).

← Fig. 3 No formation of cobalt carbide for annealed Co/C multilayers.

2. Microstructure and phase changes during annealing at elevated temperatures

Here, we discuss the thermal stability of metastable phases, especially carbides. 2.1 Ni-C alloy films: XRD and TEM observations revealed that metastable Ni_3C nanocrystallites were formed and distributed in amorpohous carbon matrix. Both amorphous-like and granular (or nanocrystalline) Ni-C films were formed depending on the carbon contents in the films. It was also shown that, when the Ni_3C carbide was formed throughout the film, no fcc Ni phase was seen, and excess carbon was formed as amorphous phase, being similar to the results shown in Fig. 2. This is almost consistent with the results by Tanaka et al.[7] that when the formation of Ni_3C carbide takes place after long milling(MA) time (partly corresponding to annealing at elevated temperatures), the metastable supersaturated fcc Ni phase almost completely disappears. This nature may also be explained in terms of the formation enthalpy for metal carbide. After annealing, carbides decomposed into fcc Ni phase and carbon:$Ni_3C \rightarrow$ fcc Ni + C (carbon, graphite). Graphite particles were always seen to nucleate and grow around decomposed Ni particles, probably due to the so-called metal-mediated nucleation-growth of crystalline graphite phase. This was also confirmed by in-situ analysis during annealing. In this connection, it was also found that the lattice spacing of (0001) planes decreases slightly but linearly with increasing deposition temperatures without any remarkable increase in crystalline size [9]. These results suggest that the decomposition of the Ni_3C cabide is perfomed by dissociation of carbon and supersaturated fcc Ni phase is decomposed from the nickel carbide. Similar results have been reported for the films prepared by mechanical alloying[7]. Microstructure changes were found to be strongly related to the changes in magnetic properties, as already reported in our previous study [10]. 2.2 Co-C alloy films: It was shown that Co_3C (or $Co_{2\text{-}3}C$) carbides, which were identified as hexagonal [8] in this study, were formed with a strong preferred (10·1) orientation even at ambient tenperature (about 300K), and that Co_2C and Co_3C ($Co_{2\text{-}3}C$) carbides were formed independently depending on methane gas flow rates. When annealed at elevated temperatures, cobalt carbides decomposed into α-Co, β-Co (both solid solutions) and carbon (or graphite) depending on carbon contents and deposition temperatures, as shown in Fig. 5. It is noted here that no remarkable β-Co phase is seen in as-deposited films, but after annealing at 573K, below the α to β transition temperature(693K), a large amount of β-Co phase coexists with α-Co phase. After decomposition by annealing, a slight peak-shift toward the higher angle was noted for the cobalt carbides, probably being attributed to a small amount of dissociation of carbon from the carbides, thus resulting in the lattice expansion. This is similar to the case of the nickel carbides, but the cobalt carbides decomposed less easily than the nickel carbides. The two decomposition reactions are summarized:(1)$Co_3C \rightarrow$α-Co(slightly supersatureted hcp

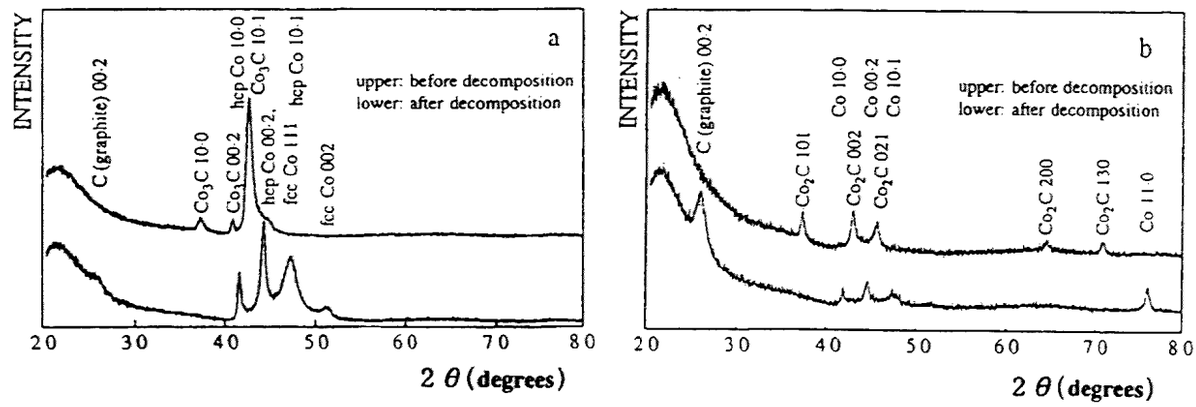

Fig. 5 Decomposition of cobalt carbides, such as Co_3C in (a) and Co_2C in (b) before and after phase decomposition subjected to annealing at 573K (XRD)

phase)+β-Co(slightly supersaturated fcc phase) + C (carbon or graphite), and (2) $Co_2C \rightarrow$ α-Co(slightly supersaturated hcp phase) + C (carbon or graphite). As for the appearance of the β-Co phase below 693K, it is reported that, when the grain size of α-Co phase is very fine, the high temperature β-Co phase become much stable [12]. This explanation appears plausible, because the sputtered films are always composed of very fine. However, it is not valid for the present case. This reason is not clear. It may be explained by the difference in crystal system between Co_3C(hexagonal) and Co_2C(orthorhombic), because the distortion due to the introduction of carbon into the cobalt lattice is different for both carbides, thus resulting in different relaxation mode by dissociation of carbon from the carbide.

2.3 Fe-C alloy films: As-deposited films were of amorphous-like, as shown in Fig. 4, and iron carbides(Fe_3C) were formed in as-deposited films only under a very small supply of carbon, indicating that the solubility of carbon in α-Fe phase is not so large in comparison with the Co-C system and the Ni-C system. It was shown that iron carbides(Fe_3C) decomposed at slightly higher temperatures than the cobalt and nickel carbides, being similar to the previous results[2,3]. This is also qualitatively explained based on the formation enthalpy for carbides.

Conclusion

Phase changes including decomposition of transition metal carbides were examined and their features were summarized. The supersaturated solid solution was formed in the wide composition range for both the Ni-C and Co-C systems, whereas only a slight extension of solid solubility of carbon was realized in the Fe-C system. The thermal stability of metastable carbides is explained based on the concept of formation enthalpy for carbides. The present results support the formation ability for the transition metal carbides(Ni-C<Co-C<Fe-C) reported by Tanaka et al.[7]. A higher formation enthalpy of carbide means that the carbide phases are less thermally stable. The decomposition behavior is also qualitatively explained based on the same concept, partly taking account of dissociation of carbon from the carbides.

References

1)T.B.Massalski:*Binary Alloy Phase Diagrams*,ASM,Metals Park,(1986),556[Co],579[Ni].
2)S.Nagakura: J. Phys. Soc. Jpn., 13(1958),1005.
3)S.Nagakura: J. Phys. Soc. Jpn., 16(1961),1213.
4)T.J.Konno and R.Sinclair: Acta Metall. Mater., 42(1994),1231.
5)T.J.Konno and R.Sinclair: Met.Sci. & Eng., A179/A180(1994),297.
6)T.Tanaka, S.Nasu, K.N.Ishihara and R.H.Shingu: J. Less. Common Met., 1(1991),872.
7)T.Tanaka, K.N.Ishihara and R.H.Shingu: Met. Trans., 23A(1992),2431.
8)B.X.Liu, J.Wang and Z.Z.Fang: J. Appl. Phys., 69(1991),7342.
9)J.Shi and O.Nittono: J. Mater. Scie. Lett., 11(1992),22.
10)M.Azumi, J.Shi, Y.Haga and O.Nittono: Proceedings of PRICM 3, (1998), 953.
11)R.C.Ruhl and D.M.Cohen: Scripta metall., 1(1967),73.
12)M.C.Cadeville, C.Lerner and J.M.Friedt: Physica B, 86-88(1977),432.

The Rigaku-Denki Journal 29(2) 1998

研究ノート

X線回折と材料科学の研究

入戸野　修*

X-ray Diffraction and Studies of Materials Science

Osamu Nittono

Faculty of Engineering, Tokyo Institute of Technology, Ookayama 2-12-1, Meguro-ku Tokyo 152-0033

1. はじめに

結晶（固体・単結晶あるいはその集合体）の構造は，通常単位胞内の平均構造（一次構造）と単位胞外の構造（二次構造）に分類して解析される．前者は構造解析であり，後者は構造評価と呼ばれる．結晶の性質は一次構造のみでは決まらないで，むしろ結晶の完全さ・不完全さ（二次構造）に関わっていることが多い．原子レベルでの構造評価の方法としては，電子やX線などの回折現象を利用したものが有効で，すでにいくつかが確立されている．このうち電子回折を利用し，電子回折図形ばかりでなく，原子レベルの分解能で原子の配列状態を直接観察できる電子顕微鏡法（電顕法）がよく知られ，現在広く活用されている．

一方，X線回折は結晶格子の乱れに対して電子回折よりも敏感である．しかし，X線では使用できるレンズ系がなく原子的構造を直接観察できない．ところが，1958～59年には電顕法による転位の直接観察の発展に刺激されて，乾板上に高い分解能が得られるようにして記録した一つの回折斑点を光学系で拡大し，その中に転位などの結晶欠陥を見る手法，つまりX線回折顕微法（X線トポグラフ法，X-ray topography）が開発された．今日では，大きな単結晶の結晶完全性が良くなっているが，平均原子配列からのわずかなずれや乱れが問題になり，それらが材料物性に敏感に作用する場合が多い．したがって，新材料の開発では材料の精密な構造評価がますます重要な意味を持って来ている．

ところで，著者らはこれまで新しい方法や装置を導入し，それまでの理論を実証あるいはその不完全性を指摘すること，直観的なひらめきに基づくアイディアを確認することなどを研究動機として研究して来ている．そこで，本稿では，そのような観点からX線回折の動力学的回折現象と運動学的回折現象を材料科学の研究に活かした著者らの研究例，すなわちX線回折トポグラフ法とX線ゴニオメーター法の応用研究を中心に紹介する．

* 東工大・工学部

2. X線回折トポグラフ法

2.1. X線回折トポグラフ法の原理と特徴

X線トポグラフ法 (X-ray topography) では，結晶の各点で回折されたX線の強度がフイルム（乾板）上に試料結晶と1:1の幾何学的対応が付いた像（トポグラフ）が記録される (Fig. 1)．この記録された像コントラストを解析することにより各場所の原子構造や歪み場を決定できる．回折としては，通常はラウエ・ブラッグの正常反射が用いられるが，規則反射，衛星反射，散漫散乱が利用されることもある．回折波の他に透過波が利用されることもある．前者はいわゆる暗視野像に，後者は明視野像に対応する．この意味でX線トポグラフ法は電顕法と類似の観察手法である．X線トポグラフ法の撮影方法の特徴は大雑把に Table 1 に示すように分類できる．

X線トポグラフ法の特徴は電顕法との対比から次のようにまとめられる：(1) X線の透過能が大きいので，厚いバルク結晶 (～5 mm) の内部構造を非破壊的に観察できる．(2) 低い空間分解能（X線テレビ系で高々6 μm）であるが，格子面間隔 ($\Delta d/d$) や格子面の曲がり ($\Delta\theta$) の場所的変化を高感度に検出できる．つまり，$\Delta d/d = 10^{-5}$～10^{-8} および $\Delta\theta = 10^{-5}$～10^{-8} rad であるから，転位像の幅は数十 μm となり低転位密度（10^8 m/m^3 以下）の結晶中の転位を低倍率で直接観察できる．具体的に言うと，X線法では観察できる転位像は，主として転位芯から数十 μm 離れた歪みの小さい領域からの運動学的像（後述）である．一方，電顕法では，電子回折が歪みに鈍感であるため原子配列の乱れの大きい転位芯の部分（～数十 nm）の像として現れる．(3) 試料結晶を各種の負荷

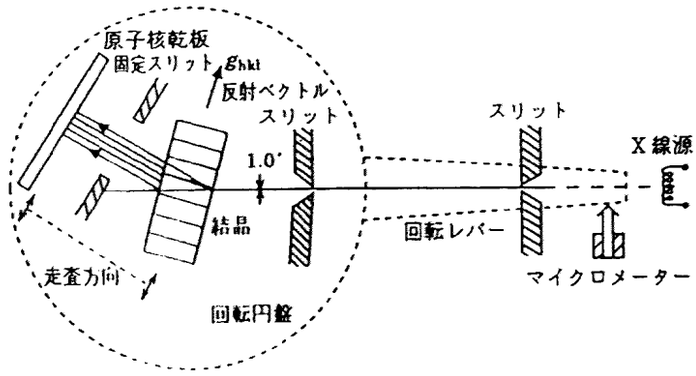

Fig. 1. X線トポグラフ法（Lang法）の幾何学的配置.

Table 1 主な撮影方法の特徴

撮影法	線質・配置	特徴および得られる情報	最高分解能
Schulz法	発散連続X線①	方位調整容易，像の拡大可能，結晶粒の傾きと方向検出	10 μm～
回転振動法(I)	発散単色X線②	試料乾板回転振動，広面積撮影，大傾角・わん曲検出，露出時間短縮	10 μm～
回転振動法(II)(OMD)	発散単色X線②③	方位調整容易，広面積撮影，傾角検出(10′)，大傾角亜結晶粒界の分布	1～2 μm
Lang法	狭幅X線②	方位調整面倒，広面積走査型撮影，欠陥変位ベクトル決定，断面静止像	1～2 μm
改良Lang法(SOT)	狭幅X線②	走査＋微小角回転振動，湾曲結晶中の欠陥検出，大面積高分解能像	1～2 μm
改良Lang法(CAC)	狭幅X線②	特殊装置，波長分散効果減少，高分解能欠陥像，高次反射有効	～1 μm
Berg-Barrett法	広幅X線③	簡単な装置，像の歪み大，面積静止撮影(透過型，反射型)	数 μm～
フィルター法	広幅X線③	簡単装置，Ruフィルター(Ag$K\alpha$線)，方位調節容易，広面積静止撮影	数 μm～
ソーラスリット法	広幅X線③	改良Berg-Barrett法，任意X線波長使用，高分解大面積静止撮影	数 μm～
二結晶法 平行(+, −), 非平行(+, −), (+, +)	広幅X線③	モノクロメーター使用，$K\alpha_1$線使用，高分解能像静止撮影 高精度角度分解・格子面傾斜検出	1～2 μm

①点状焦点，連続X線　②点状焦点，特性X線　③線状焦点，特性X線

条件下に置き広範囲にわたる動的現象を追跡観察できる.

最近，強力なX線発生装置やシンクロトロン軌道放射が開発され，また観察方式にテレビ映像技術を導入し，高感度のX線撮像管を利用して観察に要する時間の短縮化および像分解能と画質の改善が図られており，X線回折トポグラフ法の難点が大幅に解消され，電顕法と同様に，その場観察法として利用できるようになった.

この手法では，回折強度の変化，つまり回折コントラストを与える原因は，運動学的回折効果と動力学的回折効果によるものに分けられる．前者では，結晶中の欠陥部で回折されたX線がそのまま乾板上に記録される．一方，後者での回折現象は複雑で，欠陥部で回折されたX線がその周囲で幾重にも回折され，入射X線とも干渉した波動場の強度が乾板上に記録される．前者によるものには，(1) 結晶構造そのものに起因するもの（結晶構造因子，異常分散），(2) 消衰効果，(3) 回折の角度位置のずれがある．一方，後者によるものとして，(4) 異常透過（Borrmann効果），(5) 回折の角度位置のずれ，(6) 波の干渉効果（ペンデル縞，モワレ縞）などが挙げられる．実際の像のコントラストはこれらのいくつかが組合わさったものである．多くの場合，欠陥の場所的情報については運動学的回折コントラストによる像（運動学的像 kinematical image）を取扱うだけでも十分である．その場合，この像コントラストの消滅条件を解析することによって各場所の原子的構造，歪場の性質（バーガースベクトルなど）を決定できる．一方，歪み場の詳細や回折現象を調べるためには動力学力学的回折理論による解釈が必要である（付録）．以下にX線回折トポグラフ法を用いた著者らの研究例を紹介する.

2.2. 融解・凝固過程のその場観察

融解・凝固過程のその場観察は，単一元素からなる場合と合金結晶の場合についていくつか行われている[1),2)]．筆者らは厚さ 0.2 mm の低転位密度 ($<10^3/cm^3$) の錫 (Sn) 単結晶（純度：99.999%）(Fig. 2)[3),4)] と Fe–Si 合金単結晶の融解・凝固過程[5)] を放射光トポグラフ法でその場観察している．その結果，Sn の場合，融液・固

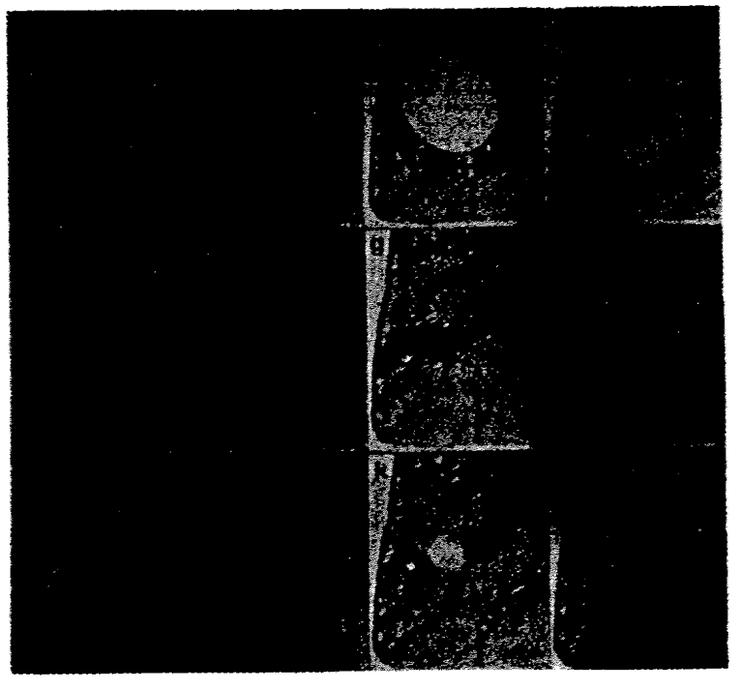

Fig. 2. 錫単結晶の融解・凝固過程の動的X線トポグラフ観察（031反射使用）.
(a) 中の矢印はX線撮像管（サチコン）の損傷部分である．スケール：1 mm.

Table 2 インジウム基合金における構造相転移とその特徴.

相転移のタイプ	結晶構造変化	In基合金	温度履歴 (K)	体積変化
I	fcc—fct($c/a>1$)	In–(18–30 at%)Tl	0–2	0.016
		In–(4–5.5 at%)Cd	2–3	0.03
		In–(6.8–7 at%)Hg	—	—
II	fcc—fct($c/a<1$)	In–(28–36 at%)Pb	10–15	~0.3
III	fct($c/a<1$)—fco—fct($c/a>1$)	In–(12–16 at%)Pb	10–15	~0.3
IV	fct($c/a<1$)—fct($c/a>1$)	In–(13–15 at%)Sn	30–40	~0.7
(参考)	fcc—bcc	Fe–30 at% Ni	~400	~2.7

体界面にはトポグラフ像上で反射強度の異常は認められず，Siの場合のような過冷却層による構造変化は存在しないこと，grown-in転位でも融液界面に接し，新しく成長した結晶部分に長距離にわたって継承するものは少なく，転位が結晶成長に必ずしも関与していないこと，結晶中に存在する転位の多くは，主として凝固完了時の不均一熱勾配や不純物偏析による応力で発生した転位群であることを指摘している．さらに，これらの結果から，融解凝固法で良質な金属単結晶を育成するための条件として，できるだけ薄い結晶が望ましいこと，試料上での温度勾配はできるだけ少なくすること，融体と容器（るつぼ）壁との間の摩擦をできるだけ少なくすること，原材料は純度が高いほど望ましいことを指摘している．実際にこの要請条件を参照して低融点金属（Cd, Zn, Snなど）の低転位密度の単結晶の育成法を開発している[6].

2.3. 相転移の観察

筆者らは変形（歪み）誘起相転移を起こし，いわゆる形状記憶挙動を示すIn基合金の相転移挙動の特徴を明らかにするために，相転移過程における格子変形をX線回折トポグラフ法で詳細に調べた[7],[8]. Inは3価の金属で周期律表中で隣接するCd, Tl, Sn, Pb, Hgと一次固溶体合金を作り，しかも溶質元素の増加で相変化を起こし，また温度変化で相転移を起こす特徴がある（Table 2）．つまり，高温相と低温相の境界が温度軸に対して傾斜しているので，温度変化により高温相→低温相の相転移が起こる．これらの合金の相転移は2次の相転移に非常に近い1次の相転移であり，いわゆるマルテンサイト的（無拡散的）相転移挙動を示す．しかも，低温相では

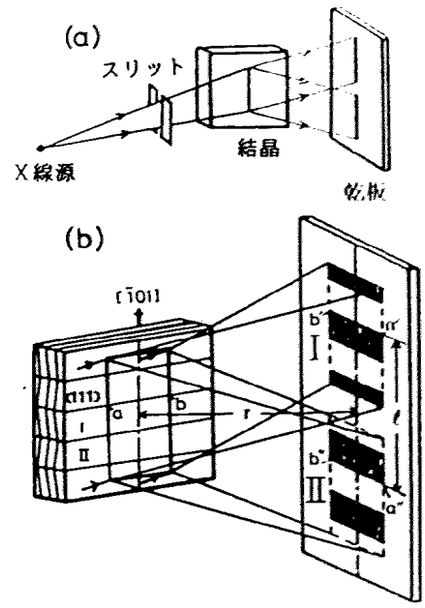

Fig. 3. X線回折トポグラフ法の配置 (a) 反射トポグラフ法，(b) 表面起伏とX線トポグラフ像との対応．隣接する双晶Iと双晶IIの像間の距離 l と軸比 (c/a) の関係は，$c/a=\{1+\sqrt{1-\cos\theta(2\cos\theta-1)}\}/(2\cos\theta-1)$ であり，$\tan\theta=l/4r$ で与えられる．

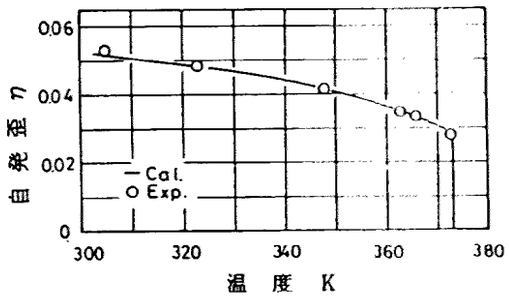

Fig. 4. In–Cd合金における軸比 (c/a) 温度依存性の実験値と計算値の比較．縦軸 η は自発歪であり，この場合は $\eta=2(c/a-1)/\sqrt{3}$ である．

{110} 面上の変態双晶 (transformation twining) のために帯状領域構造 (banded domain 構造) の表面起伏を示す．そこで相転移過程に於ける各温度での表面起伏の変化をX線回折トポグラフ法で調べ，軸比と温度の関係を求めた (Fig. 3)．この表面起伏の大きさは格子定数（正しくは軸比）に関係しており，温度により変化する (Fig. 4)．

これらの結果をまとめて，In基合金に於ける相転移の全体を現象論的に説明することができた[8),(9)]．すなわち，これらの合金相転移に起こる結晶対称性の変化 (Table 3) に着目し，In基合金で出現する合金相は位数

Table 3 インジウム基合金における構造相転移の点群の変化．

相転移タイプ	結晶点群の変化
I	$O_h^5(Fm\,3\,m)$—$D_{4h}^{17}(I\,4/m\,mm)$
II	$O_h^5(Fm\,3\,m)$—$D_{4h}^{17}(I\,4/m\,mm)$
III	$D_{4h}^{17}(I\,4/m\,mm)$—$D_{2h}^{23}=V_h^{23}(Fmmm)$—$D_{4h}^{17}(I\,4/m\,mm)$
IV	$D_{4h}^{17}(I\,4/m\,mm)$—$D_{4h}^{17}(I\,4/m\,mm)$

(grade) の最高の8面体群 O_h を原型 (prototype) 相とした一連の対称性の変化を伴う相転移，O_h^5–D_{4h}^{17}–D_{2h}^{23} のような逐次相転移によって出現したものと解釈した．これらの相転移はほとんど2次の相転移であるとして取扱えるとすると，熱力学的状態（熱力学的ポテンシャル）は転移点でほとんど連続的に変化する．2次の相転移の場合には，相転移点はそれぞれの相自身にとってある物理量がゼロになる（または発散する）特異な点で，この点を境にして相接する両相の間には空間群の既約表現の種類に関する一般的な関係がある[10]．これを適用すると，In基合金合金の場合の逐次相転移 (O_h^5–D_{4h}^{17}–D_{2h}^{23}) では，並進対称性の変化がないので，相転移に関与するのは波数ベクトル $\mathbf{q}=0$（第一ブリルアンゾーンの原点Γ点）における既約表現だけとなる．このことは点群 O_h の既約表現に着目すれば良いことを意味する．いくつかの手順を踏むと，結局点群 O_h の既約表現は10個 {Mulliken の記号で表わすと，偶表現 (gerade) $A1_g$, $A2_g$, E_g, $T1_g$, $T2_g$, 奇表現 (ungerade) $A1_u$, $A2_u$, E_u, $T1_u$, $T2_u$} あり，2次の相転移を起こし得る資格条件（ランダウ・リフシッツの条件[10]）を満たすものとして2次元既約表現 E_g のみが相転移に関与することが分かる．

2次の相転移の特徴である「相転移点で熱力学的状態の変化は連続的である」ということは，数学的には相転移点近傍では状態の変化を定量的に特徴づける秩序パラメータはいくらでも小さい値をとれることを意味する．この取り扱いでは，相の熱力学的ポテンシャル Φ を秩序パラメータ (η_1, η_2) のベキ級数で以下のように展開できるものと仮定する．

$$\Phi(T,\eta)=\Phi_0+\frac{1}{2}\alpha_1 H_1+\frac{1}{4}\alpha_2 H_1^2+\frac{1}{6}\alpha_3 H_1^3$$

$$+\frac{1}{3}\beta_1 H_2+\frac{1}{6}\beta_2 H_2^2+\gamma H_1 H_2$$

$$=\Phi(H_1(\eta_1,\eta_2), H_2(\eta_1,\eta_2))$$

ここで，$H_1=\eta_1^2+\eta_2^2$, $H_2=\eta_1^3-3\eta_1\eta_2^2$ であり，また秩序パラメータ η_1 と η_2 は立方対称 (O_h) からの外れを示す．今の場合，$\eta_1=(2\varepsilon_{zz}-\varepsilon_{xx}-\varepsilon_{yy})/\sqrt{6}$, $\eta_2=(\varepsilon_{xx}-\varepsilon_{yy})/\sqrt{2}$ であたえられる自発歪みで，2次の歪テンソル成分 ε_{ij} の1次結合で表せる．

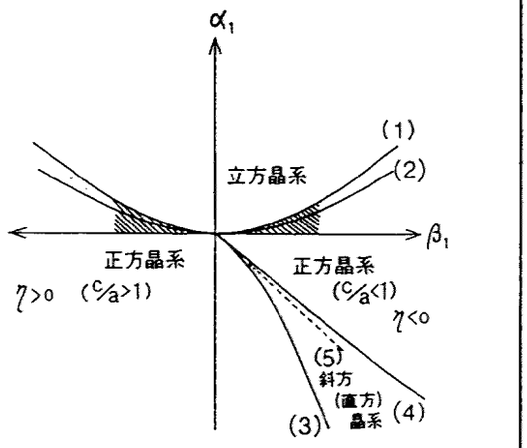

Fig. 5. 熱力学的ポテンシャルから決定される (α_1, β_1) 空間における相図．斜線部分は立方晶系と正方晶系が共存しうる領域を示す．

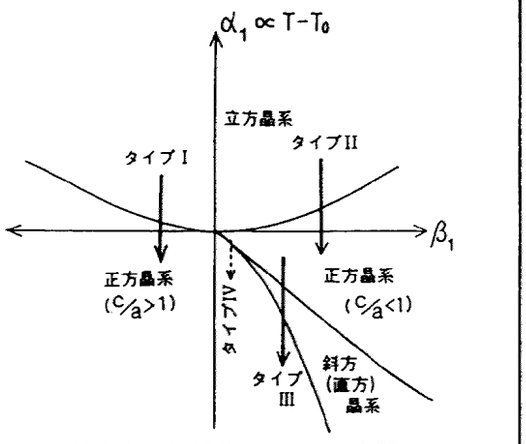

Fig. 6. In 基合金の相転移の (α_1, β_1) 空間における位置づけ．各タイプの合金については Table 2 を参照のこと．

この熱力学的ポテンシャル Φ から，$\partial\Phi/\partial\eta_1=0$ および $\partial\Phi/\partial\eta_2=0$ の平衡条件式を求め，また，相安定条件として $\Phi(H_1, H_2)$ の極小値を求める条件，

$$(\partial^2\Phi/\partial^2H_1^2)(\partial^2\Phi/\partial^2H_2^2)-(\partial^2\Phi/\partial H_1\partial H_2)>0$$

および

$$(\partial^2\Phi/\partial^2H_1^2)^2>0 \quad \text{かつ} \quad (\partial^2\Phi/\partial^2H_2^2)^2>0$$

を用いると，結果的に In 基合金における全ての相の出現を熱力学的パラメータ (α_1, β_1) 空間に表示できる (Fig. 5, Fig. 6)．

このように現象論的に説明できたと言うことは，In 基合金の相転移が変形誘起相転移で強弾性を呈すると言うことを間接的に証明したことになる．実際に，熱力学的ポテンシャルから自発歪みや弾性定数 (Fig. 7)，応力－歪み曲線を算出し，実験結果と比較して議論した[8]．

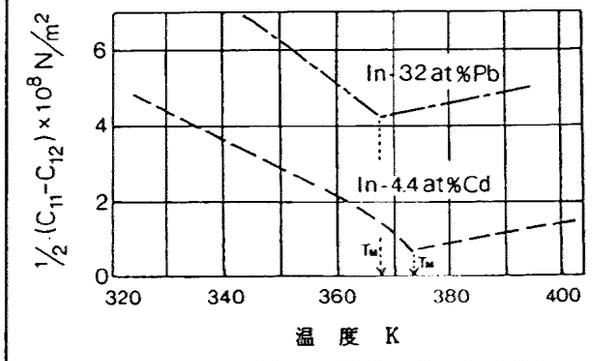

Fig. 7. インジウム基合金の弾性定数の温度依存性（計算値）．

2.4. 膜応力の測定

薄膜は真空蒸着法やスパッタ法で作られる．通常，これらの成膜法では，飛散して来る原子は基板（下地）上に熱力学的に非平衡な状態で凝縮するので，堆積した薄膜は必ずしも熱力学的に平衡相な状態ではなく，また多く場合に膜応力が存在する．

ここでは Si ウェハー上に堆積したスパッタ膜の応力を X 線回折トポグラフ法を利用して測定する方法を紹介する[11]．この測定法の原理と特徴は以下の通りである．すなわち，特性 X 線の K_α 線が $K_{\alpha1}$ 線と $K_{\alpha2}$ 線の 2 つの波長からなっていることを利用し，薄膜の膜応力のために曲がったシリコン基板に対する 2 つの X 線の波長によるトポグラフ像（実際には，線状の像である）を撮り (Fig. 8)，回折条件を満足した像間の距離から基板の曲がりを測定し，次のような弾性変形の式

$$\sigma_f=\pm\left(\frac{t_s^2}{6Rt_f}\right)\left(\frac{E_s}{1-\nu}\right)$$

を用いて膜応力 σ_f を算出する．ここで，±は＋で引張応力，－で圧縮応力を示す．t_s と t_f はそれぞれ下地（Si 基板）と膜の厚さ，R は Si 基板の曲がり半径，E_s は基板のヤング率，ν は基板のポアソン比である．半径 R は図中の走査距離 L と線像間距離 L' を用いて，

$R=L/\Delta\theta_B=L'/\cos\theta_B\Delta\theta_B$,

で与えられる．ここで，$\Delta\theta_B$ は $K_{\alpha1}$ 線と $K_{\alpha2}$ 線の 2 つの波長に対するブラッグ角（MoKα, 220 反射）の差である．結局，既知の数値を入れると膜応力 σ_f は次式で与えられる．

$$\sigma_f=\pm\left(\frac{1.115t_s^2}{6L't_f}\right)\left(\frac{E_s}{1-\nu}\right)\times10^{-6}\ (\mathrm{N/m^2})$$

この測定法では，Si 基板の既知の弾性定数（ヤング率）を用いてその曲がりから膜応力を求めるもので，膜については膜の厚さだけを測定すれば良いのが特徴である．著者らは，この測定法を具体的に鉄スパッタ膜と鉄窒素

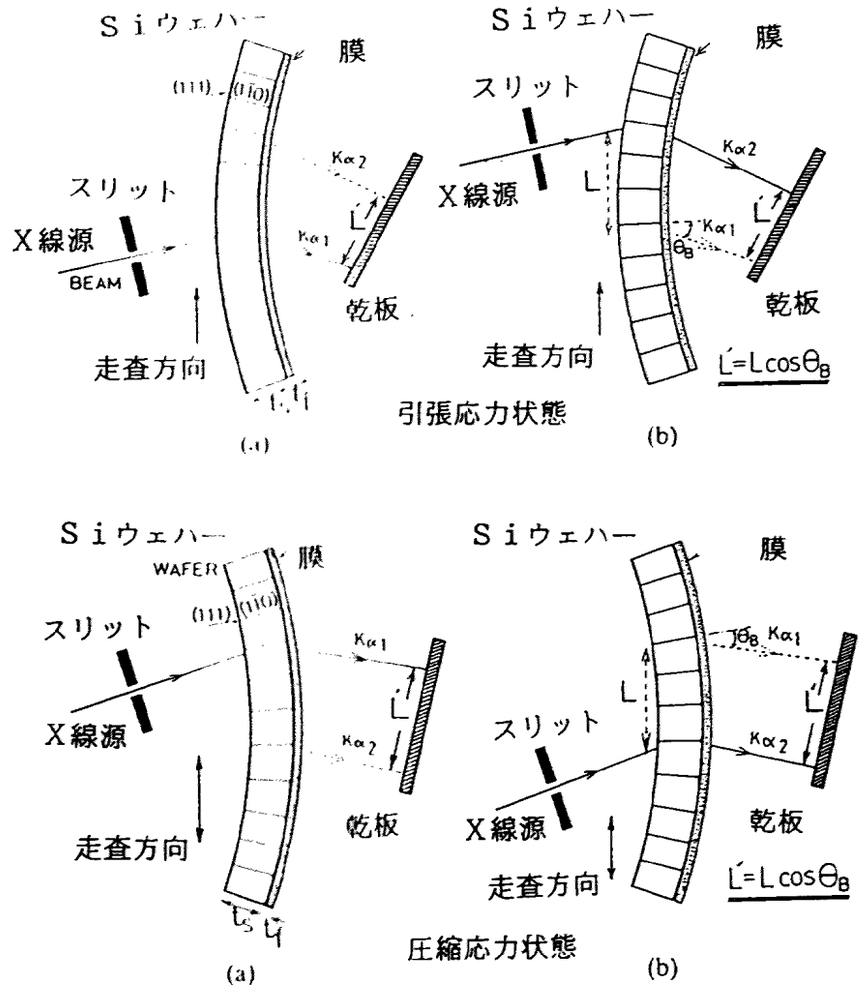

Fig. 8. X線回折トポグラフ法による曲がった単結晶からのトポグラフ線像の撮影．曲がっている．引張応力状態と圧縮応力状態では基板の曲がりが逆である．それぞれの図で，(a) は $K_{\alpha 1}$ 線が，(b) は $K_{\alpha 2}$ 線が回折条件を満たす．

膜を測定し，前者が圧縮応力であり，後者が引張応力であることを示した (Table 4).

また，著者らは類似な方法であるが，$K_{\alpha 1}$ 線の自然波長幅のみを用いて，基板上にエピタキシャル成長した薄膜の格子歪みを局所的な膜厚の変化と関連付けた測定法を開発している[12]．この測定法では，試料と乾板を断続的に走査することで基板と膜の両方からのトポグラフ線像を分離して撮影するのが特徴である (Fig. 9)．この測定法では，実際には試料結晶を試料表面の法線の周りに90°おきに回転させて同様にトポグラフ像を撮影し，膜と基板からのトポグラフ線像の分離具合を観察し，格子歪を格子面間隔の違いによるものと格子面の曲がりによるものとを分離解析できる．

3. X線ゴニオメータ法

3.1. X線ゴニオメータ法の原理と特徴

この方法では，結晶モノクロメータの回折を利用して平行かつ単色な入射X線束をつくり，これを結晶に入射し結晶を回転させて反射曲線（ロッキングカーブ）を測定し，その反射曲線の解析から結晶における微小変形，つまり，格子面の傾きと格子面間隔の変化が高い精度で評価できる．ロッキングカーブの特徴を示す諸量は研究目的により使い分けられる．通常，積分強度，ピーク強度，ロッキングカーブの形状（半値幅，1/4, 1/8 値幅），ピークあるいは重心の角度位置，回折線の角度分布（散漫散乱）が利用される．たとえば，長距離の歪み場を持つ格子欠陥があると，ピークの強度は低下し，半値幅（1/4, 1/8 幅）は大きくなり，曲線下の面積（積分強度）は増大する．点欠陥やその集合体のような短距離の歪み場を持つものが，乱雑分布をしている場合には，格子定数が変化して回折角度位置が変わったり，半値幅が減少したり，裾の部分に散漫散乱が現れたり，カーブ全体の形状が変化する．トポグラフ法のように，個々の欠陥像を直接観察することはできないが，照射部分での結晶完

Table 4 X線回折トポグラフ法で決定した膜応力の例．(a) 鉄スパッタ膜（圧縮応力），(b) 窒化鉄スパッタ膜（引張応力）．σ_f は膜応力，t_s と t_f はそれぞれ基板と膜の厚さ．

(a) 鉄スパッタ膜

$t_s(\mu m)$	$t_f(\mu m)$	L'(mm)	R(m)	$\sigma_f(10^8\ N/m^2)$
152	1.0	2.00	1.76	−4.92
162	1.4	3.55	3.13	−2.25
160	1.8	2.20	1.94	−2.75
175	2.0	1.95	1.72	−3.34
167	2.6	1.38	1.22	−3.30
167	4.0	0.68	0.60	−4.36

(b) 窒化鉄スパッタ膜

$t_s(\mu m)$	$t_f(\mu m)$	L'(mm)	R(m)	$\sigma_f(10^8\ N/m^2)$
197	0.65	1.83	1.61	13.89
135	1.04	0.70	0.62	10.66
190	1.38	1.34	1.18	8.31
210	1.61	1.65	1.46	7.07
215	1.96	1.45	1.28	6.92

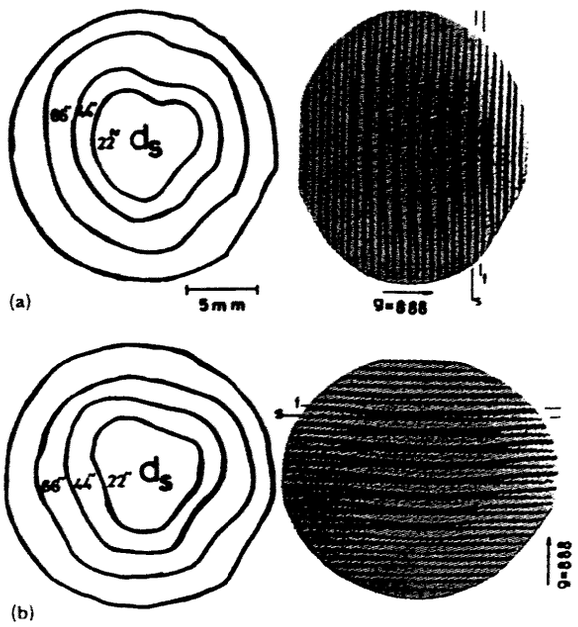

Fig. 9. 基板上にエピタキシャル成長した膜からのトポグラフ像．線像の s と f はそれぞれ基板（ガドリニウム・ガリウム・ガーネット，$Gd_3Ga_5O_{12}$）と薄膜（$(YEuEr)_3(FeGa)_3O_{12}$）からのトポグラフ線像である．左図は格子面の等傾角線図である．(a) を表面法線の回りに 90° 回転したものが (b)．

全性からの平均的なずれを検出できる．この測定法による格子定数の測定精度 $\Delta d/d$ は，X線光学系にもよるが，絶対測定で～10^{-6}，相対測定で～10^{-12} である．この他に異常透過が歪みに高感度であることを利用して厚い結晶中に乱雑分布した微小点欠陥を検出する方法もある．この手法は高精度であるがゆえに，主に微量不純物の拡散や偏析，転位ループ，格子間原子などが問題となる半導体結晶を対象とした研究に用いられている．

3.2. 3結晶法（+，+，±）配置による原子散乱因子の測定

この測定法の操作は，幾つかの単結晶からの反射を同一散乱面の上で起こさせるように設定するので難しいが，基本的には先のX線トポグラフ法の結晶セッティングと同様である．この測定法では，試料結晶から得られたロッキングカーブを理想完全結晶から期待されるものと比較することにより，試料結晶の完全性からのずれが評価される．したがって，試料結晶からできるだけなまのロッキングカーブを測定することが望ましい．

平面波に近いX線束による実験を2結晶法で行うには，コリメーター結晶と試料結晶の格子面間隔が等しい反射面を選ぶ必要がある．一方，多くの結晶では，コリメーターとして使用可能なほどに完全性の高い結晶を得ることは難しい．このため，通常はX線源からの放射X線をモノクロメータとコリメーターの使用（複結晶配置）で単色性と平行性の高い（波長分散および角度のひろがりを制限した）入射X線束を用いる．(+，+) 配置は角度発散も波長拡がりも小さくできる．こうして得られた入射X線束を試料結晶に入射させ，試料結晶を微小角回転させながら反射X線の強度を計測してロッキングカーブを得る．これが（+，+，±）配置による測定法である．複結晶法における波長と回折方向の関係の理解には Du Mond の図形[13] が役立つ．さらに精密な測定法として，第3結晶の試料結晶からの反射X線強度をアナライザー結晶（第4結晶）を用いて数秒の差で計測することで，熱振動や微小欠陥による散漫散乱（運動学的散乱）を動力学的散乱から分離解析する測定法もある．

回折の起こる角度範囲 $\Delta\theta$ はX線動力学的回折理論により $\Delta\theta=(e^2\lambda^2/nmc^2)(1/v\ \sin 2\theta)b^{-1/2}F_g e^{-M}\Delta W$ で与えられ，結晶構造因子 F_g に比例する．ここでの記号のほとんどは通常のX線回折理論で通常用いられるものであり，ΔW は回折からの外れを示すパラメーターである．b は非対称因子と呼ばれ，回折格子面と結晶表面となす角度を α とすると，$b=\sin(\theta-\alpha)/\sin(\theta+\alpha)$ で与えられる．$\alpha=0$ のとき，結晶表面と回折格子面が平行であり，この場合を対称反射 ($b=1$) と呼び，そうではない場合を非対称反射 ($b\neq1$) と呼ぶ．入射線束の幅 l_0 と反射X線束の幅 l_g との間には $l_g=l_0/b$ の関係がある．つま

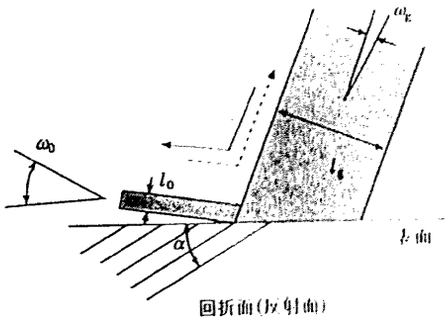

Fig. 10. X線束の回折角度範囲と空間幅の幾何学的関係.

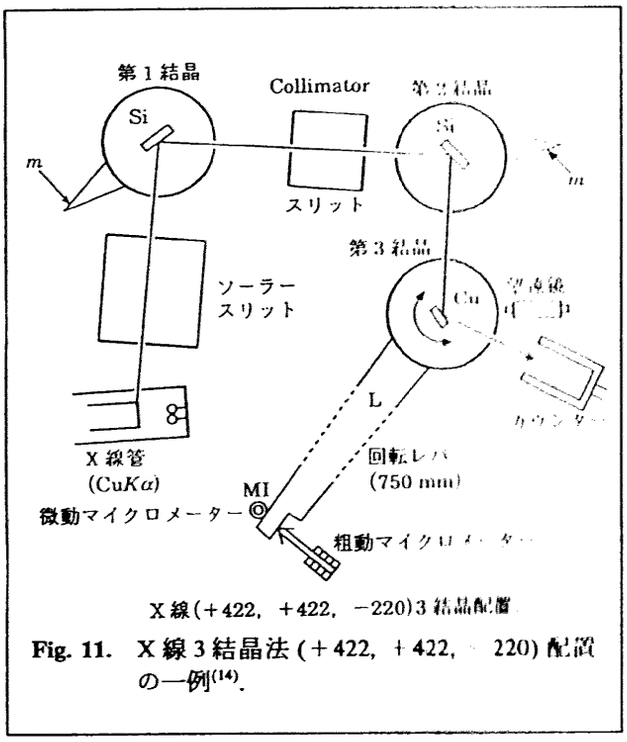

Fig. 11. X線3結晶法(+422, +422, −220)配置の一例[14].

り，$b<1$のときは，狭い入射X線束から幅広い反射X線束を得ることができる．また，入射X線の回折角度幅ω_0と出射（反射）X線の値ω_gは対称反射の回折角度幅ω_sを用い$\omega_0=\omega_s/\sqrt{b}$, $\omega_g=\sqrt{b}\,\omega_s$, $\omega_g=b\omega_0$で与えられる(Fig. 10)．通常はこれらの関係を利用して，各自でSi単結晶から実験目的に合わせてモノクロメーターを造り，平行で(ω_gが小さい)単色の入射X線束を得る．測定されるロッキングカーブはモノクロメーターと試料結晶の両者の反射曲線のコンボリューション（たたみ込み）であるから，入射X線束をできるだけ単色かつ平行性の高いものにすることが精度を挙げ，解釈を簡単にするためには重要である．たとえば，Si220反射で$MoK_{\alpha1}$線に対してブラッグ角は10°38′であり，σ-偏光成分では$\omega_s=2.3''$である．このとき，$\alpha=10°18'$となるように結晶を切り出して，非対称反射を用いると$b=0.017$となり，$\omega_g=0.3''$となるので，角度拡がり0.3″の入射X線束が用いられる．Fig. 11は著者らが手造りゴニオメータ法を用いて設定した$CuK_{\alpha1}$線に対する3結晶(+422, +422, −220)配置を示す．使用X線源の強度(40 kV, 20 mA)の関係から，第1および第2結晶で完全なシリコン(111)単結晶からの422反射を用い，第3結晶として試料結晶（鋼ひげ結晶）を置き，(110)表面からの220表面反射(Bragg case, $b=1$)のロッキングカーブが測定された．この配置では，422反射（ブラッグ角$\theta\fallingdotseq\pi/4$, $\cos2\theta\fallingdotseq0$）を用いることにより，X線の偏りは電場ベクトルが散乱面に垂直な偏光状態(σ偏光)になっている．鋼ひげ結晶への入射X線束の角度拡がりは1.3×10^{-5} rad（約2.8秒）である．測定される曲線は3つの結晶の反射曲線のコンボリューションであることを考慮し，理論曲線と実測曲線とをbest fitting法で評価した(Fig. 12)．その結果，鋼ひげ結晶の表面層は結晶完全性が良いことがわかり，実測曲線の半値幅$\Delta\theta$から鋼の原子散乱因子として$f_{220}=16.75\pm0.08$を得た．この値はその後の研究で参照値として用いられている(Table 5).

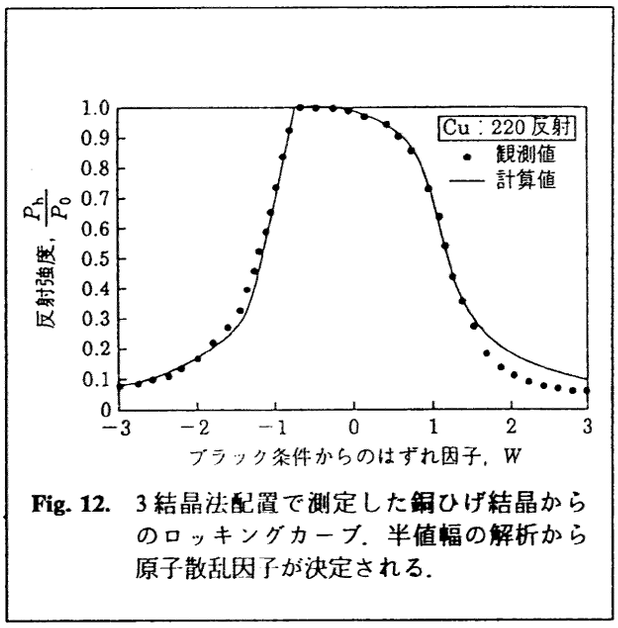

Fig. 12. 3結晶法配置で測定した鋼ひげ結晶からのロッキングカーブ．半値幅の解析から原子散乱因子が決定される．

X線3結晶法でも，結晶表面からの反射X線を乾板上に記録することで，表面の微小歪の場所的情報が得られる（X線平面波反射トポグラフ法）．この場合，①結晶表面にすれすれにX線を入射して全反射を利用する方法，②表面層の微小変形に敏感である結晶表面に斜めに傾いた格子面からの回折を用いてトポグラフの拡大を図る方法，③表面の微小ステップに対してX線の屈折率の効果を利用する方法などにより，成長表面における凹凸や成長ステップについての場所的情報も得ることができる．

3.3. 多孔質シリコンの格子変形

電子デバイス材料として広く利用されているシリコン(Si)は，バンドギャップが小さく(1.1 eVで赤外領域)，また間接遷移型半導体であるため発光効率が悪い等の理

Table 5 Cu の原子散乱因子 f^0_{hkl} の比較

	実験								理論		
研究者	T.S.	B.C.D.	J.C.D.	H.Y.	N.Y.N.	W.U.F.	A.U.T.W.	S.H.K.	F.W.	D.T.	W.Y.
試料	完全結晶	粉末結晶	ほぼ完全	粉末結晶	完全結晶	完全結晶	完全結晶	単結晶	A	B	C
	白色X線	MoK_α	MoK_α	CuK_α	$CuK_{\alpha 1}$	電子回折	電子回折	γ 線			
f′	Cromer の f′	0.35	0.35	−2.1	−2.019			0			
B(A^2)	0.5345	0.5429	0.55	0.584	0.5343	0.54	0.54	0.554 (290K)			
hkl											
111	21.80±0.06	21.29±0.34	21.52±0.1	22.07±0.09		21.78±0.13		21.51±0.05	22.14	22.08	21.72
200	20.28±0.11	19.75±0.34		20.68±0.18			20.40±0.16	20.22±0.04	20.76	20.72	20.46
220	16.75±0.08	16.37±0.30		17.10±0.13	16.75±0.08			16.45±0.05	16.76	16.78	16.63
311	14.74±0.04			14.91±0.09				14.54±0.05	14.74	14.78	14.64
222	14.36±0.06		14.01±0.1	14.34±0.09				14.07±0.05	14.19	14.23	14.10
400	12.46±0.06			12.42±0.45				12.29±0.06	12.40	12.46	12.34

T.S., Takama and Sato (1982); B.C.D., Batterman, Chipman and DeMarco (1961); J.C.D., Jennings, Chipman and DeMarco (1964); H.Y., Hosoya and Yamagishi (1966); N.Y.N., Nittono, Yamagishi and Nagakura (1979); W.U.F., Watanabe, Uyeda and Fukuhara (1969); A.U.T.W., Arii, Uyeda, Terasaki and Watanabe (1973); S.H.K., Schneider, Hansen and Kretschmer (1981); F.W., Freeman and Watson (1961); D.T., Doyle and Turner (1968); W.Y., Wakoh and Yamashita (1971).

A, 自由原子, Hartree–Fock; B, 自由原子, 相対論的 Hartree–Fock; C, 結晶中の原子.

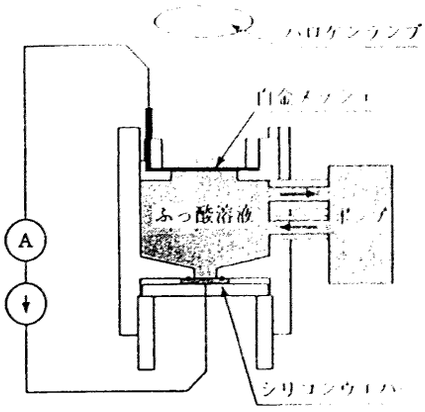

Fig. 13. PS作製のために使用した反応セル.

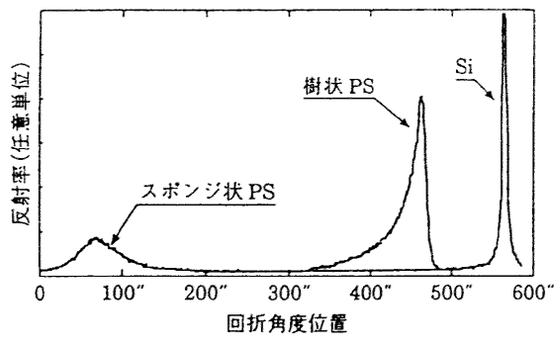

Fig. 14. 樹状PSとスポンジ状PSからの400ロッキングカーブ.

由から発光デバイス材料としての役目を果たさないでいた．しかし，単結晶Siのメゾスコピックスケール化の結果として得られたポーラスシリコン（多孔質シリコン，porous silicon, PS）が緑色のレーザー光照射により赤色に発光することが報告され[15]，Siを基にした新たな発光デバイスの期待が高まっている．Siから可視発光を発現させるには可視発光のエネルギーより高いエネルギーギャップを作り出す必要がある．これがSi/Ge超格子，Si超微粒子，ポリシランやPSなどの形で実現される．PSの基本構造は量子細線や量子箱などのSi低次元構造から成ると考えられており，構造の低次元化により新たな量子準位を造ったり，状態密度を変化させることができる．このようなメゾスコピックな構造がバルクSiでは考えられなかった可視発光を発現させるのではないかと考えられている．しかし，これ以外にもシロキセン等の発光性生成物の合成説，ポリシラン発光説等が提案されているが，未だ可視発光の特徴を十分に説明できる発光機構の解明には至っていない．これはPSからの可視発光が微細構造に敏感であるにも関わらず，作製条件と微細構造に関する系統的な研究例[16],[17]が少なく，また難しいこともあり，光物性と微細構造との関係が定性的にしか議論されて来なかった．著者らは，可視発光発現のメカニズムの解明にはPSの結晶性を含めた微細構造と発光特性の関係を調べることが不可欠であると考えPSを評価してきた．ここでは，その各種の条件（作製条件・焼鈍条件など）を与えた多孔質シリコン層のX線反射曲線の特徴と他の測定手段（光ルミネッセンスPL測定，赤外吸収IR測定など）から得た結果を併せて発光特性と微細構造の関連について考察した結果を紹介する[18]-[22].

Fig. 13はP作製のために試作した反応セルである．陽極にSiウェハーを，対極に白金(Pt)メッシュを用い，電解液はふっ酸基の溶液で定電流電源より所定の電流(～300 A/m^2)を流す．陽極化成中にSiウェハーから発生する水素の気泡をSi表面から除去するためにエチルアルコールと水の添加が有効である．Siの溶解反応にはホール(hole)が必要であるから，n型Si基板の場合には反応中の光照射が重要となる．そのため，対極には透光性のあるPtメッシュを用いた．反応後の水洗はPSの結晶性を著しく劣化させるので，反応後は直ちにPSを真空室（ロータリーポンプ排気）中に保存する．Fig. 14はP型Siウェハー上に生成したPSによるX線反射曲線を示す．低抵抗基板と高抵抗基板とで生成したPSの結晶性は著しく異なる．透過型電子顕微鏡観察の結果，高抵抗(>0.1Ω m)のものは樹枝状構造を示し，低抵抗基板のものはスポンジ状構造になっていることが分かった．作製条件にもよるが，一般に細孔径は前者の方が後者のより1桁大きく，比表面積は逆に後者の方が前者の3倍以上も大きい．PSによる反射ピークがいずれの場合もSiウェハーのピークより低角側に大きく外れていることから，PS部分（残留シリコン部分）は下地Siより表面に垂直な方向に格子面間隔が大きくなつていること（格子膨張）を意味する．著者らは，この格子膨張の主原因についてPS層中の水素濃度の増加に伴い格子膨張が起こるという実験事実から，陽極化成中にSi基板から発生する水素の吸着および内部拡散による効果と考えている．また，樹枝状PSおよびスポンジ状PSのロッキングカーブはいずれも低角度側に裾を引いた非対称な形をしている．前者の半値幅は後者のものにより著しく狭い．これは前者の方が残留シリコンの結晶性はSi基板に相当する程度に良好であるが，後者は結晶性は悪く，サイズも小さいことを示す．Fig. 15はn型低抵抗基板の反応時間と反射曲線の関係を示す．一方，He–Cdレーザー（波長325 nm, 425 nm）の照射で，スポンジ状PSは肉眼でも明瞭に橙色の発光が観察できたが，樹枝状PSからは観察されなかった．

著者らは可視発光発現のメカニズムは，p型PSもn型PSも同じものであると考え，陽極化成条件と微細構

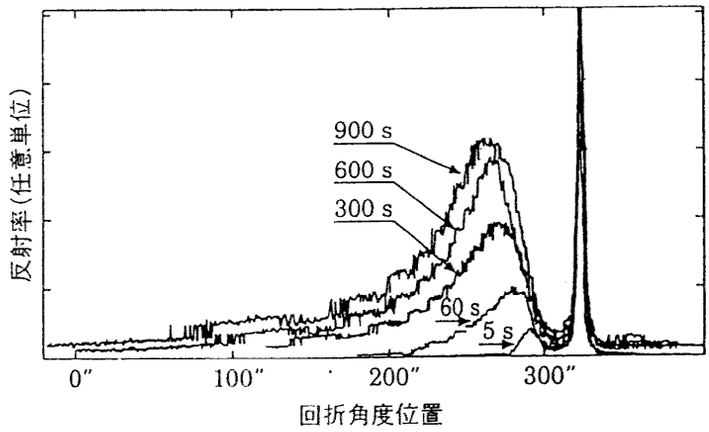

Fig. 15. 電流密度 1000 A/m², 異なる反応時間で作製した PS の 400 ロッキングカーブ.

造の関係を調べるには，p 型低抵抗基板を，微細構造と発光特性の関係を調べるには n 型低抵抗基板を用いて調べ，両実験結果を比較検討した．この結果，いずれの場合にも残留シリコンの全部あるいは表面に近い部分をスポンジ状化することで可視発光させることができることが示唆された．この推論に基づき実際に非発光の p 型低抵抗基板を高い電流密度 (>2500 A/m²) で陽極化成した PS が He–Cd レーザー励起により，赤色の発光することを確認した．微細構造を作製条件で制御しての実験結果からは，可視発光には量子サイズの Si 細線や超微粒子 Si 等の低次元構造が関与していると言える．今後，発光機構の解明には，サイズばかりでなく表面や界面の問題，特に表面の電子構造との関係などが明らかにされる必要がある．となると，最早 X 線回折法はこれ以上立ち入れず，XPS などの状態分析手法が有力であろう．

4. 運動学的 X 線回折による材料研究

X 線回折の主流は何と言っても結晶構造解析への応用である．未知物質の新しい機能性はその結晶構造と関係するので，構造解析は特に重要な意義を持つ．しかし，単に物質同定や格子定数の精密測定などで多くの情報が得られ，それだけで研究上十分な議論ができる場合も多い．ここでは，著者らが最近行っている研究例を紹介する．

4.1. 多層膜の膜応力の特徴

金属薄膜の物性はいろいろな因子，特に成膜法によって大きく影響されることが知られている．そこで，同一構成金属（Cu と Ag）からなる金属多層膜を 2 つの成膜法，真空蒸着法とスパッタ法で成膜し，その積層構造および格子ひずみの特徴を詳細に調べた[23]．真空蒸着装置中に導入したモーターの軸にシャッターを取付け，2 つの蒸着源（バスケット型フィラメント）からの蒸発金属を交互に遮断して基板ガラス上に多層膜を堆積した．膜

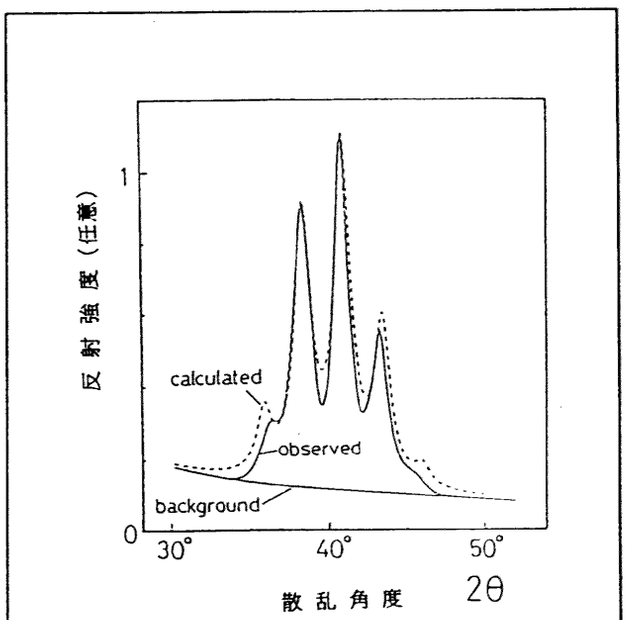

Fig. 16. Cu-Ag 多層膜からの X 線反射曲線と計算曲線との比較.

厚モニター（水晶振動子）からの信号でシャッター開閉時間を調整して堆積膜厚をパソコンで制御した．一方，スパッタ装置は対向陰極型直流スパッタ装置を用いた．この装置では，2 つの円板ターゲット（直径 10 cm）の間にプラズマが閉じ込められるので，堆積膜への高速電子やイオンによる衝撃損傷が少ないのが特徴である．

両装置で合成した Cu/Ag 多層膜からの X 線回折（θ–2θ 法）曲線を測定し，合成した多層膜の各層に対して格子定数の変化を考慮した変調積層構造モデルによる理論的回折強度と比較する構造解析法を利用して，実際の構成金属層の格子定数の違いの特徴を調べた (Fig. 16)．その結果，スパッタ法による多層膜では，真空蒸着法によるものに比べ，構成金属，特に Cu の格子ひずみが大きいことが分かった (Table 6)．このことはスパッタ法に

Table 6 真空蒸着法 (E) とスパッタ法 (S) で作製した Cu/Ag 組成変調膜における各層の格子定数の解析結果.

試料	周期長 (nm)	原子層の数 n_{Ag}	n_{Cu}	バルクからの外れ・ $\Delta d_{Ag}/d_{Ag}^{bulk}$ (%)	$\Delta d_{Cu}/d_{Cu}^{bulk}$ (%)
E-1	3.76	8	9	−0.4	+0.1
E-2	4.65	10	11	−0.3	−0.1
E-3	5.55	12	13	+0.1	±0.0
E-4	6.44	15	14	+0.1	−0.1
S-1	3.17	7	7	+1.6	+1.9
S-2	4.49	10	10	+0.6	+1.5
S-3	6.05	13	14	+0.5	+1.5
S-4	8.49	18	20	+0.6	+0.9

＊誤差範囲は± 0.2 ～± 0.5 %である.

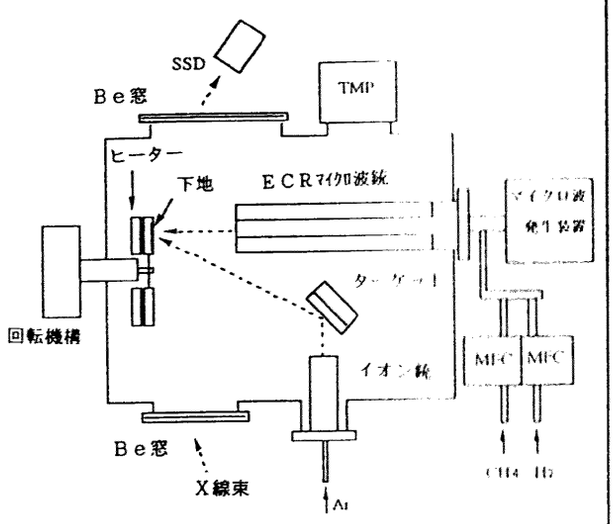

Fig. 17. 複合堆積機構 (IBS + ECR/PCVD) を備えた装置と膜成長のその場計測系.

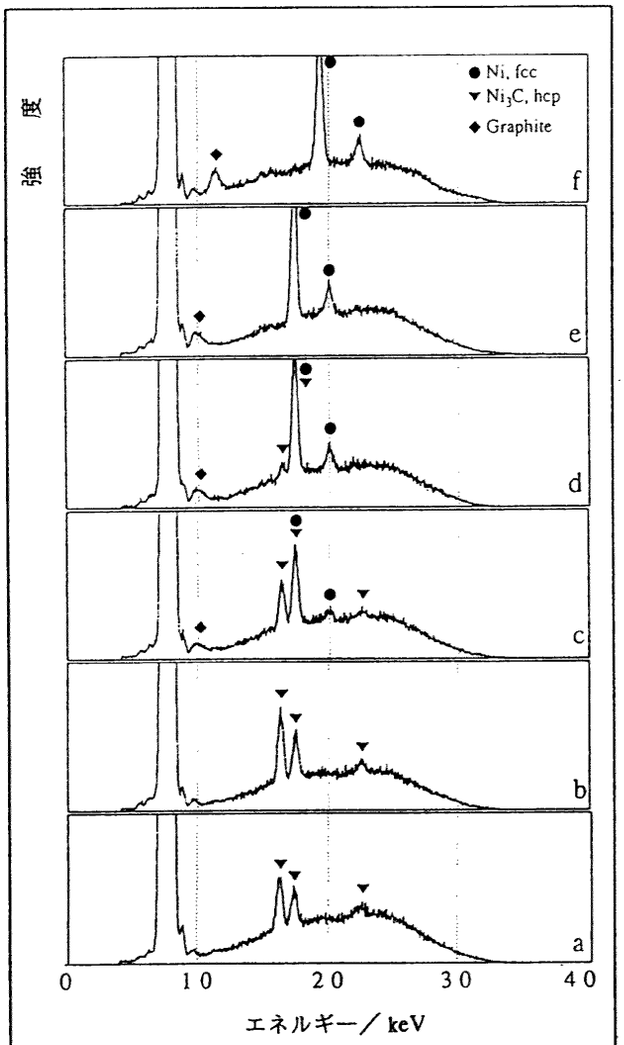

Fig. 18. 非平衡 NiC_3 膜の加熱過程における測定結果 (EDXRD). a) 堆積まま, b) 300℃, c) 400℃, 30 min. d) 400℃, 60 min. e) 500℃, f) 500℃.

よる薄膜の膜応力を受け易いという特徴は多層膜にも引継がれていることを意味する. 現在, この装置を用いて金属多層膜 (Co/Cu, Co/Ag) や島状磁性膜/非磁性膜 (一種のグラニュラー型多層膜) を合成しそれらの巨大磁気抵抗効果 (GMR) を調べているが, このような場合にも, 格子定数の変化により膜物性が影響されるので, X線回折曲線の精密測定が膜物性発現の解明の鍵を与えるのではと著者らは考えている.

4.2. 薄膜生成・分解の in situ 観測

プラズマが関与する成膜法のいくつかを併用すると熱力学的に生成が不可能な非平衡相を合成することができる. 著者らは, イオンビームスパッタ (カウフマン型イオン銃) による金属とメタンと水素の混合ガスを用いたマイクロ波イオン源 (ECR) による炭素を同時堆積する装置 (Fig. 17) を設計製作した. その際, 薄膜の形成初期段階の観察は, 良質な薄膜を形成するために重要な基礎的データを提供するとの考えから, X線回折の特徴を活かしたその場計測仕様を考慮した. 著者らは, 半導体検出器 (SSD) をX線源の向かい側に配置して, 堆積する薄膜の初期過程やその後の加熱過程 (800℃まで加熱可能) に起こる構造成長過程を観察できる装置とした. この装置で遷移金属 (Co, Ni) の炭化物が低温で合成でき, いずれも強磁性体であることを明らかにした[24]. Fig. 18 は遷移金属炭化物 (CoCx) の加熱過程における SSD の測定結果を示したものである. 堆積時に既に非平衡相の Ni_3C 相が生成されており, 400℃ から炭化物の分解が起こり, Ni (fcc) が生成し, また, 金属 Ni に接触している非晶質炭素が結晶化 (金属接触誘起非晶質－結晶相転移) の結果としてのグラファイト結晶の生成が観測されている. このグラファイト相は生成装置全体を回転して入射X線束の試料表面への入射角を 18° から 20° にすることで良好に分離されることが分かる (図中 f). X線回

折によるその場計測は計測時間の短縮する検出器の利用によりさらに改善されると考えて現在それを計画中である.

5. おわりに

ここで紹介したX線回折法を用いたこれまでの研究は，他の実験法で得られた結果および推論を再評価し，それらに明確な証拠を与えると言うことが主体であった．しかし，今日では比較的大きな単結晶が容易に得られるようになって来ているので，今後はX線動力学的回折現象を利用した手法は，他の観察法，たとえば光学顕微鏡法や電子顕微鏡法などでは観察不可能な現象や欠陥像の観察に極めて有効であり，特に二次構造と材料物性の関係を調べるのに威力を発揮することが期待される．メゾスコピックな領域の構造と物性の関係の解明にはX線回折と電子回折とが互いにその特徴を活かせる手法が要求されることになろう.

参考文献

まず，X線動力学的回折理論の基本的な事項を参照するのに適した代表的な参考書を挙げる.

1) 日本結晶学会誌：[特集・X線トポグラフィー]，**13** (6) (1971).
2) B. K. Tanner & D. K. Bowen: Characterization of Crystal Growth Defects by X-ray Methods, Plenum Press, New York, (1980).
3) A. R. Lang: Recent Applications of X-ray Topography in "Modern Diffraction and Imaging techniques in Material Science"; Ed. by S. Amelinckx, R. Gevers, G. Remaut. J. Van Landuyt, North Holland Publishing Company, Amsterdam, (1970), 407.
4) A. Authier: Contrast of Images in X-ray Topography in "Modern Diffraction and Imaging techniques in Material Science", Ed. by S. Amelinckx, R. Gevers, G. Remaut. J. Van Landuyt, North Holland Publishing Company, Amsterdam, (1970), 481.
5) 加藤範夫：回折と散乱，朝倉書店，東京，(1978).

本文中の参考文献：

(1) 千川純一，白井省三：日本結晶成長学会誌，**4** (1977), 2.
(2) J. Chikawa: J. Cryst. Grpwth, **39** (1977), 328.
(3) O. Nittono et al.: Jpn. J. Appl. Phys., **23** (1984), L581.
(4) O, Nittono et al.: Mat. Res. Soc. Symp. Proc., **41** (1985), 95.
(5) T. Matsumiya, O. Nittono et al.: Metall. Trans., **A18** (1986), 723.
(6) O. Nittono et al.: Jpn. J. Appl. Phys., **20** (1981), 1329.
(7) O. Nittono and Y. Koyama: Trans. JIM, **23** (1982), 285.
(8) O. Nittono and Y. Koyama: Jpn. J. Appl. Phys., **21** (1982), 680.
(9) O. Nittono et al.: Sci. Rep. Res/Inst. Tohoku Univ., **29** (1981), 53.
(10) ランダフ・リフシッツ：統計物理学（下），(岩波, 1967).
(11) O. Nittono: et al.: Jpn. J. Appl. Phys., **26** (1987), 157.
(12) O, Nittono and S. Shimizu: J. Cryst. Growth, **45** (1978), 476.
(13) J. W. Du Mond: Phys. Rev., **52** (1937), 872.
(14) O. Nittono et al.: J. Appl. Cryst., **12** (1979), 141.
(15) L. T. Canham: Appl. Phys. Lett., **57** (1990). 1046.
(16) Y. Kamemitsu et al.: Phys. Rev. **B48** (1993), 2827.
(17) Y. H. Xie et al.: J. Appl. Phys., **71** (1992), 2403.
(18) H. Sugiyama and O. Nittono: Jpn. J. Appl. Phys., **28** (1989), l2013.
(19) H. Sugiyama and O. Nittono: J. Cryst. Growth, **103** (1990), 156.
(20) K. Takamoto and O. Nittono: Trans, Mat. Res. Soc. Jpn, **13** (1993), 6.
(21) T. Takamoto and O. Nittono: Jpn. J. Appl. Phys., **33** (1994), 6432.
(22) 竹本邦子，入戸野修：まてりあ，**34**(8) (1995), 981.
(23) K. Hazama et al.: Materials Transactions, JIM., **32** (1991), 1102.
(24) J. Shi and O. Nittono: J. Mat. Sci. Lett., **15** (1996), 928.

[付　録]

ここでは，紹介したX線法を利用するに必要な最少限のX線回折現象の基礎的事項を定性的に説明する.

(1) **結晶構造そのものに起因するもの**：これは回折強度が局所部の結晶構造因子に依存していることと関係する．局所的に原子配列が異なる部分は，原子散乱因子，したがって結晶構造因子が周囲の部分と異なるのでコントラストが生ずる．また，入射X線が構成原子の吸収端と近いか離れているかでX線原子散乱因子が大きく異なるので，これも回折強度の違いとして現れる.

(2) **消衰効果**：これに起因するコントラストは，一般に格子が乱れた不完全な結晶から回折されるX線の積分反射強度は，完全な結晶からのそれより大きくなる，いわゆる消衰効果の減少に関係したものである．歪んだ結晶の回折に関与する角度範囲は，一般に完全結晶のそれより数十～数百倍広く，分の程度（10^{-3}～10^{-4} ラジアン）である．したがって，その程度の角度広がりのある入射X線束が結晶の欠陥部に入射する場合，欠陥部全体がX線束を回折するため，欠陥部からの積分反射強度は完全部分からのものより大きくなる（Fig. 2 参照）．つまり，欠陥は回折強度の増大した部分として観察される（直接像と呼ばれる）．この像コントラストは鮮明なので広く転位などの欠陥像の観察に用いられている.

(3) **回折の角度位置のずれ (I)**：これはX線回折が回折角度に敏感であることに関係している．単結晶の中で局所的に結晶格子面が傾いているか，または格子面間隔

が僅かに違っていると，一定方向からの入射X線に対しその部分で回折の角度位置がずれる．局所部分の格子変形が入射X線束の角度広がりよりも大きいと，結晶の大部分からはX線が回折されるのに，その部分からはX線は回折されない．したがって，乾板上に記録された結晶像にコントラストが生ずる．このことを利用して，結晶粒相互間の傾きなどの測定ができる．

(4) **異常透過**：これは比較的厚い結晶における異常透過の現象によるコントラストである．異常透過（Borrmann効果）は次のような現象である．ほぼ完全な結晶で1つの反射面で回折が起ると2つ（偏光を考慮すると4つ）の波動場（回折波と透過波）が形成されるが，一方の波動場の吸収係数は平均吸収係数より小さく，他方のそれは大きい．そのため，回折が起こっていなければX線がほとんど透過しない厚い結晶でも，結晶が完全で回折条件が満足されていると，吸収係数の小さい波動場の回折波と透過波が十分な回折強度を持って結晶を透過する．この現象は結晶が厚いほど顕著であり，$\mu t \geq 10$（μ: 平均線吸収係数，t: 厚さ）では，ほぼ厳密に回折条件が満たされているときだけ，一方の波動場だけが生残り結晶を透過する．したがって，透過し易い波動場の通り道（振幅が最小の面は原子面列に一致する）に乱れた部分（欠陥）があるとX線が透過せず，その分強度が減ずる．異常透過による欠陥像コントラストは，小さい歪みにも極めて敏感で，点欠陥の集合体などを検出できる．

(5) **回折の角度位置のずれ(II)**：こちらの角度位置のずれは入射X線束の角度広がりが極めて狭く，つまり平行X線束の場合のコントラストである．大きな完全結晶での回折現象は動力学的回折理論で説明され，回折を起こす角度範囲が定義される．入射X線束の角度広がりがこの回折の角度範囲と同程度か，あるいはそれ以下の極めて平行な線束の場合，角度位置のずれた部分とその他の部分とでは反射率（ロッキングカーブ）が異なる．したがって，そのような変化に対応したコントラストが観測される．ほぼ完全な結晶の回折の角度範囲は通常秒程度（$\sim 10^{-5}$ ラジアン）なので，$10^{-6} \sim 10^{-7}$ の微小な格子変形が検出できる．より厳密に言うと，格子歪みが結晶の厚さ方向で変化している場合，X線の侵入とともに回折角度位置が変化するので，回折波と透過波の振幅比も変わり，その振幅比の変化は実効的な歪みの勾配の向きに関係している．また，実効的な歪み勾配は結晶の弾性的変位 $\mathbf{u}$ と回折ベクトル $\mathbf{g}$ の内積 $(\mathbf{g}\cdot\mathbf{u})$ で与えられる．したがつて，こうした歪みによる回折強度は波動場の振幅比と吸収係数で決まるから，回折ベクトル $\mathbf{g}$ を反転 $\mathbf{g} \rightarrow -\mathbf{g}$ とすると黒白が白黒に反転する．この例として転位芯から数十 μm 離れた強度分布がある．

(6) **波の干渉効果**：これは結晶内の波動場に関係した回折コントラストである．動力学的回折理論によると，2つの波動場は波動ベクトルが僅かに異なるために互いに干渉する結果，回折強度のうなりが生ずる．このため，試料の厚さが変化したもの，特に厚さが急激に変化したくさび型結晶や僅かにわん曲した結晶では，強度のうなりに関係した干渉縞（等厚干渉縞，ペンデル縞，等傾角縞）が観測される．この他，結晶中に欠陥があると波動場が乱され，新たな波動場が可干渉的に励起され，上述した縞に類似の干渉縞が生ずる．また，結晶中に面間隔や結晶格子面が周りと僅かに異なっている部分が入射X線方向から見て重なっていると，モワレ縞が生ずる．前者によるものは平行モワレ，後者によるものは回転モワレと呼ばれる．電顕法での場合と同様に，結晶の乱れがモワレ模様の変化として大きく拡大されて観察される．モワレ縞とペンデル縞は，入射X線の波長を変えたり，回折条件を僅かに変化されたときの縞間隔を調べれば区別できる．モワレ縞とペンデル縞の間隔の変化しないが，ペンデル縞は変化する．これらを利用すると結晶欠陥の検出が可能である．一般にモワレ縞の間隔は入射波長によって変わらないが，ペンデル縞の間隔は波長に依存する消衰距離の変化に応じて変わる．平行性の良い入射X線束を用いた場合，入射角を厳密な回折条件の近傍でごく僅か変えると，ペンデル縞の間隔は変化するのに対して，モワレ縞の間隔は変化しない．これらの特徴を利用すると結晶欠陥と干渉効果によるもの（像）とを区別して検出することが可能である．

「材料創造工学」の研究分野　　入戸野　修

物質の性質は電子や原子の状態に関係している。物質が状態が外部からの場（光，熱，応力，電場，磁場）により変化することを利用して，新しい機能性を発現させることができます。　物質科学はそうした物質の変化の変化を調べ応用する学問領域です。地球環境と調和し人類が発展していくための持続可能な材料技術を物理・化学・生物などを基盤として進展していく学問領域でもあります。エネルギー効率，リサイクル性，環境負荷低減などを強く意識した「ものづくり」を目指す学問領域が「材料創造工学」であります。

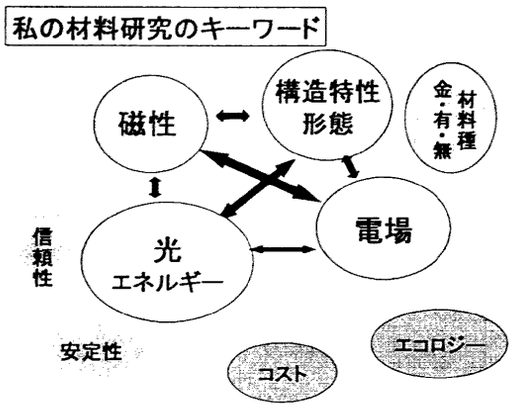

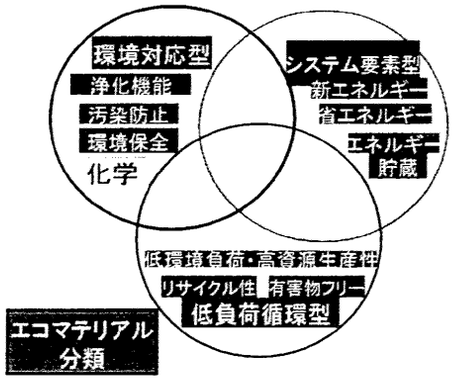

○どんな研究分野に取り組んでいるか？

1）環境調和材料の創製：生体に優しい二酸化チタン中に孤立分散した磁性粒子のトンネル電流を利用して血液流の以上を感知する磁気センサー素子を開発する。

2）低環境負荷材料の開発：磁場下凝固で鉛フリーはんだの特性を改質する。

3）プラズマ雰囲気による材利用の改質：有害材料の改質と有効利用

4）外部場による物性の変化を利用した新機能性材料の創製

5）ナノコンポジット薄膜の合成法の開発：無機・有機材料の複合化合成法

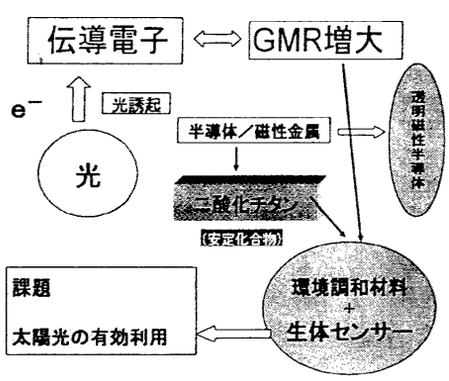

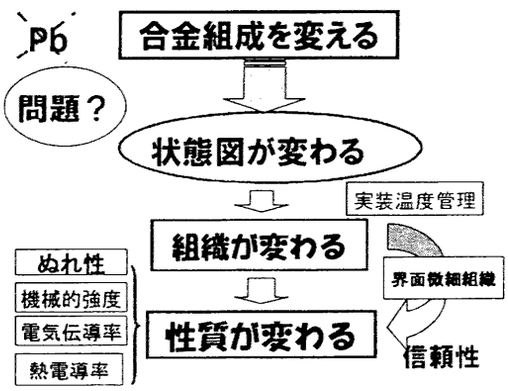

ナノ環境調和材料の研究

材料創造工学　　入戸野 修

物質の性質は電子や原子の状態に関係して変化する。状態が外部から与えられた環境（光，熱，応力，電場，磁場など）により変化することを利用して，物質の本来の性質を制御することで新しい機能性を発現させることができる。物質科学（材料科学）はそうした物質の変化の様子を調べ，材料としての利用を目指す学問領域です。また，地球環境と調和しながら人類が発展していくための材料および材料技術を発展させるために役立つ学問領域です。

現在，物質・エネルギー効率の高い材料，リサイクル性に富み低環境負荷で処分できる材料，環境浄化機能を持つ材料特に薄膜材料の開発を目指す基礎的研究を行っています。

エコマテリアルに求められる領域

有害物質フリーな材料
低環境負荷で製造できる材料
物質・エネルギー効率の高い材料
リサイクル性に富む材料
環境浄化機能を持つ材料
環境調和型エネルギーシステム用材料

■酸化チタンには3種類の結晶がある

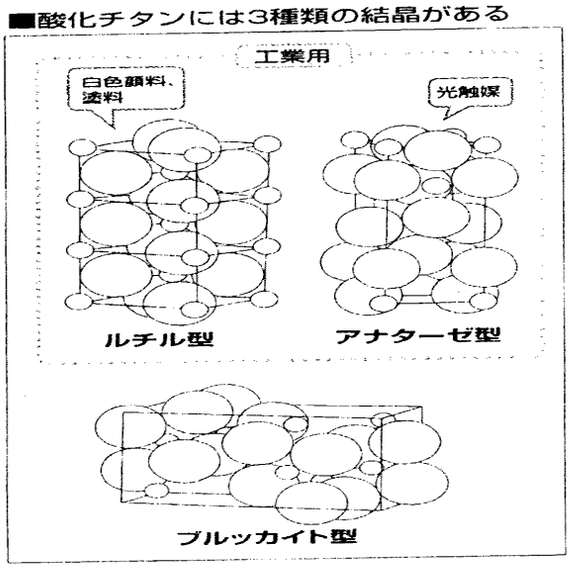

研究目的:

可視光応答型光触媒開発とセンサー特性

- **低コスト製造法の開発**
- **窒素中スパッタ膜**
- **複合型機能性膜**
- **添加／WO3，Ag，Cu**
- **鉄微粒子分散膜の磁気抵抗効果**

光エネルギーを化学エネルギーに変換し、大気浄化、脱臭、浄水、抗菌、防汚など様々な機能が利用できる新たな環境調和材料として期待されている。そんな光触媒能を示す物質の中で化学的に安定、人体に無害、地球上に豊富に存在、低コスト等の理由から、二酸化チタンという物質がもっとも代表的な光触媒材料として使用されている。本研究ではゾルゲル法を用いて二酸化チタン薄膜を作製しその吸着効果などを調べた。ゾルの作製条件，薄膜の焼結条件（焼結温度と保持時間など）について詳細に調べ，X 線評価とメチレンブルーによる色素分解評価の結果、今回の実験では焼結温度 370℃～380℃、焼結時間 3 時間の薄膜作製条件が最適であることが分かった。また，スパッタ法で鉄微粒子分散膜を作成し，巨大磁気抵抗効果の発現を確認した。現在その効率化の生成条件を調査中である。

「実験結果１」

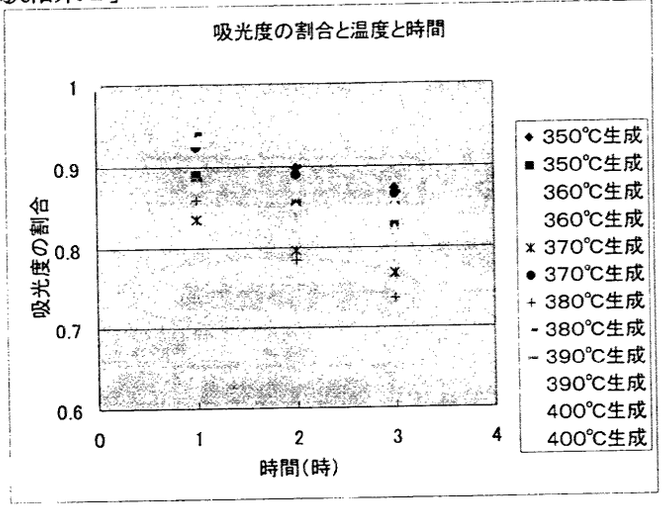

「実験結果２」**磁気抵抗効果**

Sample B

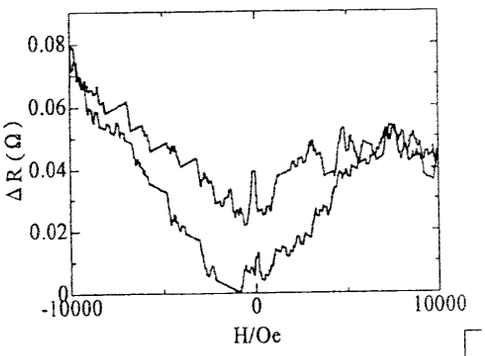

MR : 1.8×10^{-2} %

Magnetic Properties of Nickel Layers Electrodeposited on Amorphous Carbon

K. Maruyama[1], E. Arakawa[2], K. Hiraki[3], H. Yamaguchi[4], H. Numata[5], A. Matsushita[4], T. Yokoyama[1], T. Koide[6], K. Namikawa[2], and O. Nittono[7]

[1]Institute of Molecular Science, [2]Tokyo-Gakugei Univ., [3]Gakushuin Univ., [4]National Institute for Material Science, [5]Tokyo Institute of Technology, [6]Photon Factory of KEK, [7]Fukushima Univ. [1]38, Nishi-gonaka, Okazaki, Aichi, 444-8585, Japan, [2]4-1-1, Nukui-kita, Koganei, Tokyo, 186-8501, Japan, [3]1-5-1, Mejiro, Toshima, Tokyo, 171-8588, Japan, [4]1-2-1, Sengen, Tukuba, Ibaraki, 305-0047, Japan, [5]2-12-1, Ookayama, Meguro, Tokyo, 152-8552, Japan, [6]1-1, oho, Ibaraki, 305-0801, Japan, [7]1,Kanayagawa, Fukushima, Fukushima, 960-1296, Japan

The electrodeposition of the initial several layers is well known to be different from the normal behavior at thicker ranges. We previously verified that the electrode potentials of cobalt and cobalt-nickel alloy are noticeably dependent on the layer thickness by using controlled pulsed current. The immersion potential (E_{imm}) for the substrate or the deposit reflects the nature of the electrode surface. E_{imm} can be measured as the electrode potential for the pulse-off (E_{off}). In the previous studies it was found that E_{imm} of the deposit at the initial stage is different from the steady value at about 50 ML. In the case of the Co-Ni alloy, the elemental composition was also found to vary up to 50 ML. On the other hand, by measuring the *i-E* curve for the electrodes before and after the deposition, it was clarified that the overpotential of cathodic deposition at the initial 50 ML stage is also different from the steady value. The shifts of the immersion potential and the overpotential can be ascribed to the changes of the film morphology and/or texture. However, the possibility of diffusion of the substrate element into the film layer cannot be excluded. In this work, we have investigated the structure and magnetic properties of nickel films electrodeposited on amorphous carbon. Carbon substrate was employed because it is not solved in the electrolytic solution or is not diffused into the film. The structure and magnetic properties may be influenced by the electrochemical behavior at the initial stage.

Figure 1 shows the potential curve during the deposition by the pulsed current (J=25mA/cm^2, T_{on}=100ms, and T_{off}=1000ms). E_{imm} at the initial stage up to 10-20 pulses was particularly different from that above 10-20 pulse region. This indicates that the E_{imm} change is characteristic of the deposit surface itself, without any diffusion of carbon. This electrochemical behavior may be related to the chemical condition of the deposits surface. Figure 2 shows the XPS of the Ni films of 1 to 50 ML. Ni metal and NiO phases were predominant for more than 10 ML films, while the oxide phase and another unclear one for less than 5 ML. The last phase might be the hydroxide, and the peak positions seem to be dependent on the film thickness.

Electrodeposited Ni films composed of several chemical phases exhibit different nanostructure dependent on the film thickness. The MCXD experiment is useful to estimate separately the spin and orbital moments, and provides the magnetic properties of the nanostructure. Figure 3 shows the MCXD spectra of 1 to 50 ML Ni films. The MCXD intensity for the films thicker than 50 ML was similar to that of 50 ML, and for the film thickness of less than 10 ML, the MCXD intensity decreases as the film is thinner. These results are contradictory with those given by SQUID. This is because the thinner the Ni films are, the more non-ferromagnetic phase is present in the deposit, and the MCXD intensity originates only from the corresponding metallic nickel phase. Hence, we tried to modify the MCXD intensity by using a ratio of magnitude of only the metallic phase, which could be calculated from the XAS spectra. The modified MCXD intensity is consistent with the magnetization given by SQUID. Unfortunately, the modification is difficult for less than 5 ML films because of the presence of the complicated phases.

Our next step is to prepare the films without surface oxide layer by capping thin gold layer. It will be expected to determine the magnetization of those deposits more clearly.

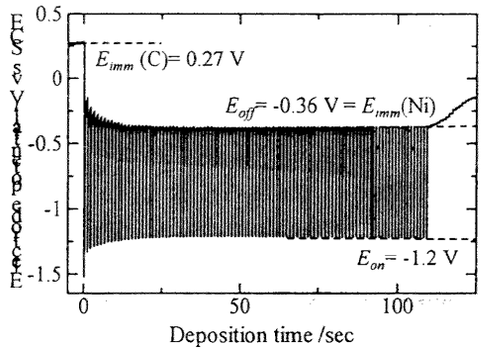

Fig. 1 Potential curve of the electrodeposition of nickel on carbon substrate, with the pulsed current. About 1 ML of nickel electrodeposits with 1 pulse of the current.

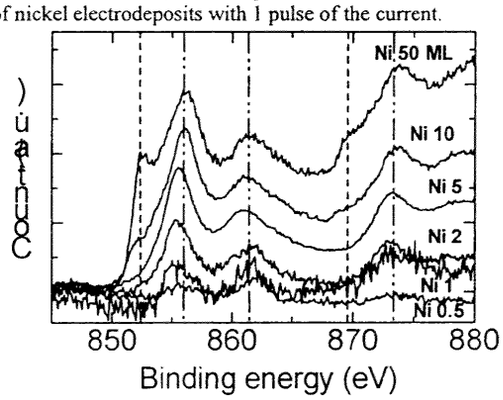

Fig. 2 XPS in the Ni2p region for 1 to 50 ML Ni films deposited on amorphous carbon. Dotted and broken lines denote the metallic Ni and NiO phases, respectively. For less than 5 ML, another phase exists, which can be ascribed to nickel hydroxide.

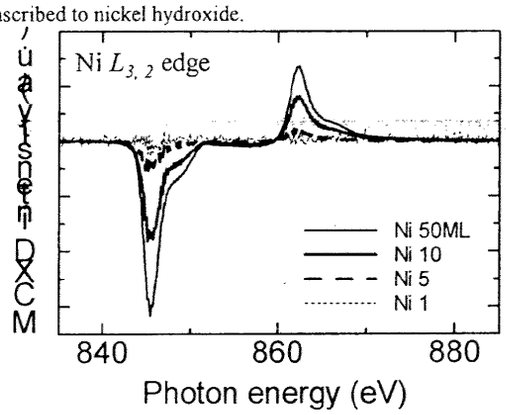

Fig. 3 MCXD spectra of nickel films, which were obtained by normalizing XAS in a conventional manner.

30aWR-1

電析ニッケル薄膜の磁気的特性

分子研，東学大教育[A]，学習院大理[B]，物材研機構[C]，東工大院理工[D]，物講研[E]，福大教育[F]
丸山耕一，荒川悦雄[A]，開康一[B]，渡邊廣憲，山口仁志[C]，沼田博雄[D]，
松下明行[C]，横山利彦，小出常晴[E]，並河一道[A]，入戸野修[F]

Magnetic Properties of Electrodeposited Nickel Thin Film

IMS, Tokyo-gakugei Univ.[A], Gakushuin Univ.[B], NIMS[C], Tokyo Institute of Technol.[D], PF-KEK[E], Fukushima Univ.[F]
K.Maruyama, E.Arakawa[A], K.Hiraki[B], H.Watanabe, H.Yagaguchi[C], H.Numata[D], A.Matsushita[C], T.Yokoyama, T.Koide[E], K.Namikawa[A], O.Nittono[F]

著者らは，アモルファスカーボン基板上に定電流パルス電析法で作製したニッケル膜の構造および磁気特性を検討している。50 原子層程度まで膜表面の電極電位が変位し，Ni L 吸収端近傍でのＸ線磁気円二色性(MCXD)信号も膜厚に依存した[1]。今回，数原子層程度の厚みのニッケル膜の 300K での磁気モーメントが増大したので報告する。

磁化測定は，量子干渉磁束計(SQUID，最大磁場 7T)で，T=2～300K での測定とし，MCXD 実験は KEK-PF, AR-NE1B のステーションで行い，磁場 1T 程度の永久磁石を用いて室温で行った。膜の質量分析を誘導共析プラズマ発光分析法で，化学種の状態分析をＸ線光電子分光法で，表面形状の観察を原子間力顕微法で，それぞれ行った。

SQUID の磁化曲線から基板の不純物磁性成分を除いて，ニッケル膜の磁化の 3～4T で飽和する強磁性(FM)成分と，7T で飽和した FM と超常磁性(SPM)成分とを求め，図１に丸印(FM:実丸，SPM:白丸)で表した。これらの値を便宜的にパルス数（１パルスで１原子層の厚みに相当）で割った値をﾀﾞｲｱﾓﾝﾄﾞ印で示した。図には示さないが，5 原子層以下の膜で磁化が増大した。

膜のニッケル相の粒子サイズが膜厚に依存すること，酸化物相，水酸化物相が混在することを考慮し，膜の磁化をその温度依存性から議論する。

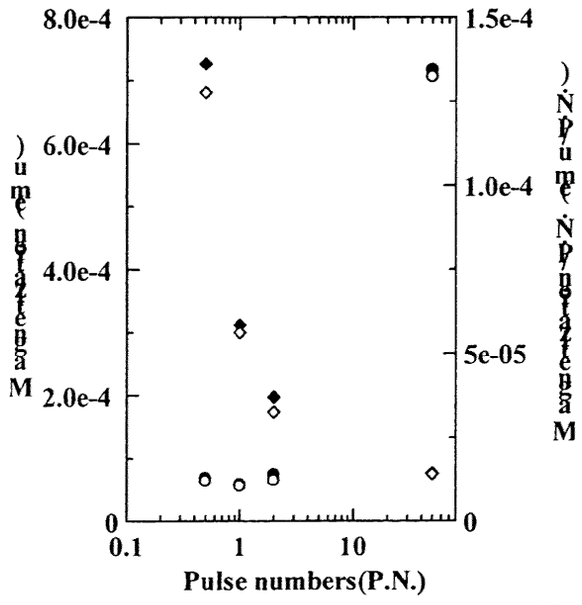

Fig.1 Magnetization of Ni films(T=300K). Solid circles mean the magnetization for ferromagnetic (FM) and super paramagnetic (SPM) phases, and open ones, for only FM. And diamond marks denote the magnetization divided by the pulse numbers (P.N.).

[1] 丸山耕一，松下明行等：日本物理学会 2001 年秋季大会講演概要集第３分冊 p. 335 (2001)

下地組成に依存する電気めっきニッケル薄膜の磁気特性

Magnetic Properties of Nickel Electrodeposits Governed by Alloying Elements of Underlayer Materials

分子研[1]，物材研[2]，茨城県立医療大[3]，城西大[4]，物講研[5]，東京学芸大[6]，福島大[7]，○丸山　耕一[1]，横山　利彦[1]，藤原　基靖[1]，山口　仁志[2]，松下　明行[2]，森　浩一[3]，加藤　立久[4]，小出　常晴[5]，荒川　悦雄[6]，並河　一道[6]，入戸野　修[7]

IMS[1], NIMS[2], Ibaraki pref. Univ.[3], Josai Univ.[4], KEK-PF[5], Tokyo-Gakugei Univ.[6], Fukushima Univ.[7] Koh-ichi Maruyama[1], Toshihiko Yokoyama[1], Motoyasu Fujiwara[1], Hitoshi Yamagaguchi[2], Akiyuki Matsushita[2], Kouichi Mori[3], Tatsuhisa Kato[4], Tsuneharu Koide[5], Etsuo Arakawa[6], Kazumichi Namikawa[6], Osamu Nittono[7]

maruko@ims.ac.jp

はじめに：これまで多結晶銅基板・アモルファスカーボン基板といった組成の異なる基板上に，定電流（パルス）めっきによって，金属イオンを含む溶液中から基板上にコバルト・亜鉛・ニッケルおよびこれらの合金の析出を検討してきた。基板組成に依存して，これらの金属イオンのカソード析出の化学ポテンシャルが異なるため，50 原子層程度の厚みの微細組織を電気化学的析出挙動によって制御することを可能とした。本講演では，ニッケル膜の数原子層程度の厚みに焦点をあてて，それらの微細構造と磁気特性の関係を検討する。

実　験：Cu および C 基板に加えチタン基板を用いた。膜表面の大気中での自然酸化を防止する目的で，めっき直後にスパッタ法で金層を被覆した。膜の磁気特性は，室温から 2K までの SQUID 磁力計測および ESR 法，また，KEK-PF, AR 施設の軟 X 線 MCD 実験で評価した。

結　果：C 基板上の Ni 膜の結果の詳細はすでに報告済みであるが，1T 以下の磁場の印加で飽和する磁気相と，3-4Tesla 程度の磁場の印加で飽和する磁気相との２相に分類される。数原子層程度以下の膜の磁化に増大が膜厚に依存して観測され，バルクの 10 倍程度の値を達成した。これは，数十 nm 程度の粒径の微粒子の微細構造および化学種に関係すると考えている。基板組成によって Ni 膜の微細組織が異なるため，磁化の温度挙動の基板による違いが現れ，この詳細を講演時に報告する。

24aPSA-66　電析ニッケル薄膜の磁気的特性 I I

分子研，東学大教育[A]，学習院大理[B]，物材機構[C]，東工大院理工[D]，
茨城医療大[E]，城西大理[F]，物講研[G]，福島大理工[H]
丸山耕一，荒川悦雄[A]，古川貢，開康一[B]，山口仁志[C]，酒井雅弘，
沼田博雄[D]，中村敏和，森浩一[E]，横山利彦，松下明行[C]，加藤立久[F]，
小出常晴[G]，並河一道[A]，入戸野修[H]

Magnetic Properties of Electrodeposited Nickel Thin Film II

IMS, Tokyo-gakugei Univ.[A], Gakushuin Univ.[B], NIMS[C],
Tokyo Institute of Technol.[D], Ibaraki Prefectural University of Health Sciences[E], Jyosai Univ.[F], PF-KEK[G], Fukushima Univ.[H]
K.Maruyama, E.Arakawa[A], K.Furukawa, K.Hiraki[B], H.Yagaguchi[C], M.Sakai, H.Numata[D], T. Nakamura, K.Mori[E], T.Yokoyama, A.Matsushita[C], T.Kato[F], T.Koide[G], K.Namikawa[A], O.Nittono[H]

アモルファスカーボン基板上に定電流パルス電析法で作製した数原子層程度の厚みのニッケル膜は，300K での磁気モーメントがバルクの数～十倍程度に増大した[1]。本研究は，磁化の温度依存性からこの磁化の増大の起源を明らかにすることを目的とする。

量子干渉磁束計(SQUID)の磁化測定より基板の微小磁化成分を除去すると，1-100 原子層の厚みの膜は，磁場 3～4T で強磁性成分が飽和し，7T では超常磁性成分も充分飽和する。磁化の増大はその大部分が強磁性成分に由来し，また，厚みに依存する酸化ニッケルなどの化学種とその特異なナノ構造に関係すると考えている。磁化の強磁性成分を 50K のそれで規格化して温度変化を図１に示す。100 原子層の厚い膜はバルクのニッケルと同様の挙動を示し，図には示さないが 10 原子層程度の厚みまでは大差ない。１原子層の磁化は，温度の増加で増大した。300K での磁化の増大はこれに起因する現象である。発表時には，強磁性共鳴(FMR)測定によって得られた強磁性相を明らかにする。

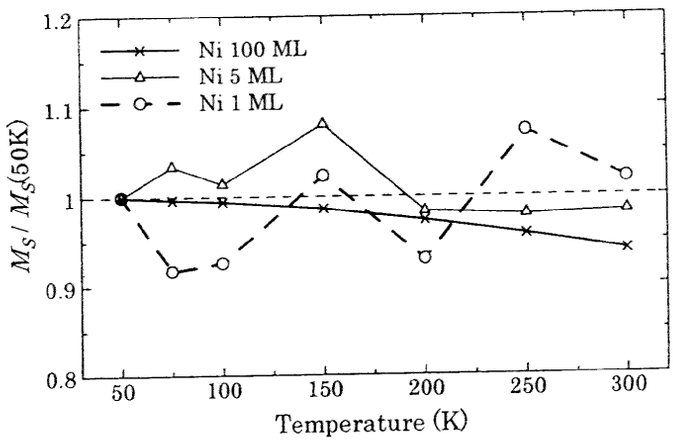

Fig.1 Ferromagnetic components of electrodeposited Ni films on amorphous carbon. An increase in magnetization of 1ML deposit exhibits as increasing temperature. This behavior is different from that for the bulk ferromagnetic nickel like the 100ML electrodeposit.

[1]丸山，荒川ら：物理学会 2004 年年会 30aWR-1

留学生に対する科学技術専門書読解のための教科書作成に向けて

—化学工学における専門日本語漢字—

入戸野　修・武　田　明　子

福島大学地域創造 第14巻 第２号（2002.12）

福島大学地域創造支援センター

調 査 報 告

留学生に対する科学技術専門書読解のための教科書作成に向けて

—化学工学における専門日本語漢字—

入戸野　修・武 田 明 子

目　次

はじめに
1．理工系大学院課程の留学生と科学技術日本語
2．科学技術専門書の特徴
3．表音文字の文化圏の留学生と表意文字「漢字」
4．化学工学の専門分野に出現する漢字
5．効果の期待できる漢字学習指導
むすび

はじめに

近年，留学生の受け入れ先は高等教育機関から実技訓練機関や企業研修に至るまで広がっている（文部科学省 2001)。このことは，留学生の目的が多様化しており，同時に，留学生がある限られた目的を達成するために日本に滞在して学習することが有効であることを示している。このような状況を日本語教育の立場から受け止めるならば，留学生のニーズを見据えた，実際に役立つ日本語の教科書の作成が望まれていることになる。実践的な教科書の作成には，まず留学生の留学目的を分類する必要がある。その上で，目的に合った語句の収集，使用頻度の高い構文の抽出，必要な基本漢字の選定を実行し，学習の効率化を図る取り組みが不可欠である。

武部（1989）も述べているように，非漢字圏の留学生からは，日本語で何がむずかしいかという質問に対して「漢字」という答えが返ってくることが最も多い。したがって，学習者のニーズを考慮した教科書を作成するには，どうしても効果的な漢字学習とは何かという問題を解決しておかなければならない。

そこで，本稿では，留学生に大きな障害になっているこの「漢字」を取り上げ，理工系の中でも特に化学工学を専攻する留学生の場合に的を絞って，専門書が読解できるようになるための漢字とはどのような性格のものであるのか，また，その習得のための指導方法の基本をどこに置いたら良いのか，の２点について収集資料を基に分析し，考察する。

1．理工系大学院課程の留学生と科学技術日本語

大学院課程から来日し，科学技術の分野で研究活動を行おうとする非漢字圏の留学生には，来日後初めて日本語を学習する者が多い。理工系の専門分野では，英語が公用語と考えられる傾向があり，日本においても英語だけでも十分に研究を続けることが可能である。しかしながら，著者らの体験から言うと，多くの留学生は滞日して研究室に所属し，他の人の発表を聞いたり，討論をしているうちに，日本語で専門書を読んだり，自分の専門について語ったりできることが，情報収集・伝達の上でも，研究を発展させる上でも，大切であると実感するようである。

一方，個々人の内的な欲求とは別に，留学生は繰り返し行われる実験，観察，輪講，ゼミなどに忙殺された日常生活を送っており，日本語を学習する時間的な余裕がないのも実状である。このような状況下にある留学生をできるだけ短時間で日本語の論文がどうにか読めるようにしようとするには，留学生の目的に合った日本語の教科書で学習効果を上げることが必要である。とは言え，理工系のそれぞれの専門分野は日進月歩であり，また日々細分化しており，すべてを満足できるような日本語の教科書を作成することは不可能に近い。しかしながら，著者らが数年にわたり理工系の

専門書，他の一般書，文化系の専門書の日本語を比較検討したところ，理工系専門書の専門用語以外の日本語ではその表現様式がかなり限られた特徴を有する傾向にあることが分かった（武田 1994，1995，武田・入戸野 1997①，②）。したがって，個々の留学生の目的を達成するために効率よく作成された教科書による学習が行われれば，自分の専門分野では他の分野よりも専門書が読解できるようになるまでの期間を短縮することが期待できる。その意味で専門科学技術書で多用される漢字とはどのような性格のものであるかを調査することは意義がある。

2．科学技術専門書の特徴

著者らの分析結果（武田・入戸野 1997①，②）によると，理工系分野における専門書の日本語（ここでは，研究論文で用いられる記述文や口頭発表するときに使用される日本語を指す）には次のような顕著な特徴がある。

(A) 構文上の特徴
- (1) 使用される動詞が限定されている。
  例：示す，用いる，使う，考える，求める　など。
- (2) 助詞に相当する句が多用され，限定されている。
  例：として，により，に対して，について　など。
- (3) 使われる接続詞が限定されている。
  例：しかしながら，したがって，すなわち　など。
- (4) 主述関係が定式化されている。
  例：～に～を示す（与える），～に～を使う（用いる），～から～を求める（得る）　など。
- (5) 受動態文が多用されている。
  例：示される，与えられる，使われる，用いられる，求められる　など。

(B) 語（用語）の特徴
- (6) 動詞以外も用言の使用が限られている。
  ＜形容詞＞狭い，軽い，良い，軽い，細い，深い，詳しい，速い　など。
  ＜形容動詞＞安定，明らか，重要，～的　など。
  ＜副詞＞初めて，～故に，単に，直ちに，必ず，最も，全く　など。
- (7) 専門用語に漢語およびカタカナ語が多く用いられる。

(C) 読解を支援する手段としての特徴
- (8) 書き手の意思表示に用いられる文末表現が簡単である。
  例：～と思われる，～であろう，～ことにするなど。
- (9) 詳細な説明のために図，式，表などを有効に活用できる。

この分析結果は慶応大学の行った調査（1989）や東京大学の行った調査（1992）の結果とも基本的な点では一致している。これらの特徴は，通常の留学生が日本語学習の初級後半で習う日常会話を主体とした日本語の特徴とはかなり異なる。このため，多くの留学生にとっては，日常生活で使う日本語と専門書で使う日本語は違うものであるものと捉えられ，科学技術専門書の読解は大変難しいものであると受け止められている。しかし，別の視点から見ると，科学技術書の日本語は繰り返される同型の文型パターンで構成されているので，一度その特徴を習得してしまえば，逆に容易に読み進めることができるようになると言うこともできる。

ここで解決しなければならないのが漢字の問題である。それは専門書の文章には多くの漢字が含まれるからである。漢字は意味を知っている者には，その概念が理解し易いと言う特徴がある。しかし，そうでない者には意味をなさない単なる記号にすぎない。したがって，どんなに専門書の文体が理解できるようになったとしても，平仮名だけで書いてあれば理解できるというのでは，日本語を読解することにならない。漢字を難しいと敬遠し学習しない者は，結局，専門書の読解そのものができないことになる。特に非漢字圏の留学生には，どうしても乗り越えなければならない障壁として，「漢字」の読解がある。それ故に専門書読解において漢字学習の効率化が強く望まれているのである。

3．表音文字の文化圏の留学生と表意文字「漢字」

日本人は小学校に入学してから，初めて漢字を学習し始める（現実には就学前にすでに学習し始めている者も多いが）。しかし，漢字が意味を表し，同じ発音（読み方）でも表記する漢字によって意味が全く異なることを認識できるようになるのはかなり高学年になっ

てからである。この同音異議の漢字が存在することを認識する意義は大きい。子供達が小学校に入って学習するのは，この仕上げとして漢字を覚えることである。それでも，覚えるのは大変な作業であり，子供達は小学校の６年間をかけて，996字の教育漢字を各学年に分けて少しずつ学習している。

これに対し，既に成人に達している留学生は，日本人が幼少の頃から習い覚えてきた漢字をはじめて学び，覚えていかなければならない。特に，非漢字圏の留学生は漢字のもつ意味を理解すること，漢字の読み方を学ぶこと，その書き方を覚えることの全てを同時に行わなければならない。漢字を習い始めた当初の留学生は必ずと言っていいほど次のような同じ反応を示す。まず，絵からできたと説明されて絵と似ている漢字を教わり，「漢字は面白い」と感じる。次に，読み方の複雑さに「変だ」「納得できない」と悩み，最後には，覚えなければならない漢字の数の多さに驚いて，「いくつ覚えればいいのだろうか」と不安になる。

それまで表音文字に慣れ親しんできた留学生にとっては，漢字は読み方よりも意味との関連の方が密接であることを肌で感じ取るのは大変にむずかしい。どうしても発音（読み方）に引きずられてしまう傾向がある。たとえば，漢字の「来」であるが，この漢字の基本的な意味を十分に理解すれば，「来院」「到来」「来週」「未来」などの語はたとえ読めなくても，その意味を想像することができる。しかし，実際には，留学生は学習を開始した当初は発音に引きずられてしまい，「来る（くる)」「来ない（こない)」「来ます（きます)」と一つの動詞に異なる読み方が当てられることを機能的でないと感じ，「変だ」「おかしい納得できない」と連発する。漢字は意味を表すが，意味は発音を表すものではないということ，つまり同じ意味の漢でも必ずしも同じ発音ではないことを納得するのにかなりの時間がかかる。

また，留学生が必要な漢字のどれだけの数を学習したかを常に気にするのも，表音文字の文化から見るならば当然と言える。留学生の使用する文字が数十であるのに比べれば，漢字の数は無限にあるとも言えるからである。短期間に目的を達成しようと試みる留学生にとっては，５万の漢字が収録されている辞書があるとか，常用漢字は2000であるとか，日本人は3,000～4,000の漢字が楽に読み書きできるとか聞かされても，強い圧迫感を受けるだけで，学習の熱意はそがれるばかりである。それよりも，300とか500とかの具体的な数が示され，それらの漢字さえ覚えれば，読みたい本が必ず読めるようになるのだと言われれば，それだけで勇気づけられる。そのためには，留学の目的に合った基本になる必須漢字を抽出して留学生に提示することが重要な意味を持つ。この考え方は，非英語圏の人に対するBasic Englishのように最低限の必須英語を提示し学習させて英語によるコミュニケーションを図るやり方と類似している。

4．化学工学の専門分野に出現する漢字

ここでは，理工系の専門書読解ための漢字学習を効果的にするために必要な学習漢字の抽出とそれらの漢字の特徴について述べる。理工系分野として化学工学を選択した理由は，工学分野でかなり広範囲の学問分野を対象にしているので，専門書に出現する漢字について一般的特徴が見出され易いと考えたからである。

(1) 資料の分析

化学工学を専門とする留学生にとって，必須漢字とはどのようなものであるのかを知るために，この分野に使用されている漢字について調査した。資料は化学工学の研究者達が論文の投稿場所の一つとして考えている『化学工学論文集』である。2000年に刊行された第１巻から第６巻までの154論文すべてを対象にして漢字の抽出を行った。ただし，所属機関と著者名は対象外とした。延べ漢字数は380,560字，異なり漢字数は1,501字である。ここで，延べ漢字数は調査に出現したすべての漢字であり，異なり漢字数は，そのうち，同じ漢字を一種類として数えた数である。たとえば，＜化学工学会会誌＞は，延べ漢字数７，異なり漢字数５の文字集合である。

表１は３つの対象資料，すなわち『化学工学論文集』

表１　『化学工学論文集』（化工）と新聞と雑誌の使用度数分布の比較

上位字数	化工 %	新聞 %	雑誌 %	全体の%	化工 字数	新聞 字数	雑誌 字数
10	11.4	10.6	8.8	80	264	512	638
50	35.1	27.7	25.5	85	322	633	777
100	52.9	40.2	37.1	90	400	800	992
200	72.5	56.1	52.0	95	536	1,081	1,358
500	94.0	79.4	74.5	96	578	1,168	1,479
1,000	99.6	93.9	90.0	97	631	1,277	1,617
1,500	99.9	98.4	96.6	98	705	1,428	1,832
2,000	99.9	99.6	98.6	99	827	1,659	2,157
2,500	99.9	99.9	99.5	100	1,501	3,213	3,328
3,000	99.9	99.9	99.9				

(表中では<化工>と表記)，<新聞>，<雑誌>における漢字の使用度数分布を比較したものである。<新聞>と<雑誌>のそれぞれの値は国立国語研究所が1963年と1976年に行った調査結果を抜粋した海保(1984)の表による。それぞれの対象資料の文字総数が異なるため相対的な比較ではあるが，右欄に示すように，漢字の文字総数に占める割合（%）には大きな違いがないことが分かる。一方，左欄の数値は，各対象資料に出現する頻度の高い上位ｎ字までの字数（上位字数）が文字総数に占める割合（%）を示す。これらを比較すると，上位字数200字では，<化工>(72.5%）が<新聞>（56.1%）を16.4%，<雑誌>（52.0%)を20.5%上回っており，<化工>が他の資料に比べて著しく異なっていることが分かる。このことは，<化工>のような限られた事象を取り扱う資料では，<新聞>や<雑誌>といった広範囲の事象を取り扱う資料に比べて，少ない漢字数が多用されていることを意味する。このことと関連して，<化工>では，400字で全体の90%を占めるのに対して，<新聞>では２倍の800字，<雑誌>では約2.5倍の992字である。つまり，化学工学の分野では一般の事象を対象にする資料よりは使用漢字数が少ないのが特徴である。

図１は『化学工学論文集』から抽出した漢字の使用度数の分布を示す。この図は表１の左欄を詳細に解析したものでもある。図では，資料に出現した漢字を使用度数の多い順に配列し，その上位から順に使用度数を累積した値を百分率で示してある。この図から分かる顕著な特徴は，僅か89字で50%に達しており，264字で80%を越え，400字で90%に達しており，使用頻度は上位字数の漢字に集中していることである。

また，この結果は，限られた事象を取り扱う資料<化工>では，出現する漢字がどれも同じ重みで使用されるわけではないことをも意味する。つまり，この分析結果は，限られた専門分野の漢字学習では，個々の漢字を同じ重みで習得する必要のないことを示唆する。小学校６年間をかけて覚える漢字が996字であることを考えれば，非漢字圏の留学生が多数の漢字を覚えるために費やされる労力と時間は計り知れない。完璧を期した全漢字の学習より，使用度数の高い漢字をできるだけ繰り返して学習する方が，学習者の意欲を持続させる上でも，効率の上でも好ましいことが推測できる。

以上の分析結果は，専門書が読解できるようになるための漢字とはどのような性格のものであるかに対する解を見出す鍵となると考える。

図１　『化学工学論文集』の使用度数分布

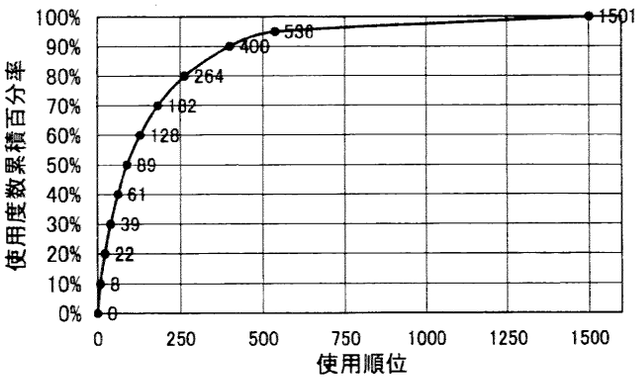

(2)　いくつの漢字を学習目標にするか

短期間に，しかも効率よく学習できる漢字数となると，その数は限られる。市販されている教材の多くは500字程度の漢字を初級段階での学習目標としている。これは500字という数が400時間前後の学習時間に習得可能な漢字数の上限として経験的に認識されているためである。しかし，実際に留学生を対象にして教える立場からすると，この数値は現場での学習の進捗状況が理想的であるとして算出された場合の上限であり，実際にはこの数よりかなり少なくなっているのが実状である。研究分野（化学工学）で研究生活と日本語学習を平行して行わなければならない留学生の場合には，たとえ500字の漢字の習得を目指す学習意欲があったとしても，その1/2～2/3の数が習得できれば十分であると考えざるを得ないのが実状である。したがって，専門書読解のための漢字学習の第１段階としては，250～300字の漢字の習得を目指すのが現状に合った目標数値であろうと考える。

ここで，この目標数値がどの程度合理的であるかを，国際交流基金と（財）日本国際教育協会が共同主催する日本語能力試験の学習目標漢字を参照して検討してみる。これは日本語を学習し，日本の大学に入学する目的を持つ留学生のほぼ全ての者が受ける試験である。４級から１級までの４段階に分かれており，３級までが日本語の初級学習と考えられている。４級では103字，３級ではそれに181字を追加した284字の漢字を覚えることが要求されている。３級修了時点では，日本語を300時間程度学習し，基本的な文法や語彙が分かり，簡単な文章が読み書きできるようになっている。２級になると600時間を越える日本語学習歴が要求され，学習漢字はさらに700字程度が追加された約1,000字の学習が要求されている。時間的な制約からみて，

化学工学の分野で研究活動を主目的とする留学生に対する日本語学習では，３級程度の漢字数（284字）の習得を第１段階に据えるのが，実際的に妥当な数である。

次いで分析結果を具体的に考察する。３級で必修の漢字数284字は，『化学工学論文集』で見ると全出現漢字の81.8%をカバーする（図１参照)。つまり，上位284位までの漢字（表２）を習得すれば良いと言うことになる。因みに，全出現漢字の284位に当たる「運」という漢字は＜化工＞では346回出現している。一見使用度数が多そうにみえるが，第１位の「度」が7,097回，第２位の「分」が5,982回，第３位の「定」が4,369回であるのに比べると，その使用頻度は1/20～1/10である。しかしながら，出現度数が100回以下の漢字が970もあることを考えると，著者らは約300の漢字数は第１段階での学習目標数として妥当であると考える。

表２　『化学工学論文集』に出現する上位284位までの漢字

1	度	51	験	101	理	151	各	201	周	251	容
2	分	52	考	102	析	152	求	202	透	252	粘
3	定	53	方	103	程	153	多	203	見	253	排
4	化	54	力	104	回	154	微	204	報	254	操
5	合	55	下	105	能	155	転	205	必	255	無
6	用	56	測	106	効	156	設	206	察	256	硫
7	子	57	素	107	造	157	光	207	炉	257	論
8	性	58	相	108	作	158	学	208	付	258	非
9	成	59	法	109	件	159	及	209	推	259	拡
10	流	60	表	110	吸	160	現	210	管	260	触
11	応	61	関	111	条	161	位	211	油	261	培
12	粒	62	内	112	研	162	常	212	金	262	境
13	数	63	物	113	料	163	近	213	固	263	範
14	反	64	計	114	有	164	態	214	図	264	極
15	示	65	燃	115	収	165	伝	215	単	265	和
16	水	66	電	116	影	166	御	216	目	266	初
17	量	67	式	117	特	167	討	217	共	267	題
18	温	68	算	118	器	168	様	218	領	268	例
19	動	69	本	119	制	169	二	219	象	269	束
20	体	70	質	120	小	170	較	220	蒸	270	言
21	結	71	発	121	積	171	原	221	炎	271	傾
22	熱	72	部	122	抽	172	装	222	差	272	価
23	大	73	焼	123	製	173	剤	223	塩	273	仮
24	出	74	次	124	究	174	媒	224	供	274	類
25	果	75	層	125	響	175	開	225	口	275	所
26	間	76	膜	126	空	176	密	226	留	276	縮
27	実	77	以	127	重	177	移	227	認	277	続
28	一	78	状	128	期	178	種	228	使	278	伴
29	的	79	径	129	検	179	明	229	孔	279	決
30	加	80	形	130	存	180	工	230	処	280	保
31	面	81	最	131	布	181	前	231	持	281	慮
32	液	82	増	132	離	182	含	232	当	282	観
33	時	83	構	133	散	183	接	233	壁	283	利
34	場	84	過	134	型	184	調	234	属	284	運
35	酸	85	基	135	混	185	長	235	換		
36	値	86	置	136	界	186	活	236	細		
37	速	87	係	137	可	187	等	237	不		
38	中	88	同	138	点	188	在	238	安		
39	気	89	平	139	機	189	囲	239	組		
40	解	90	炭	140	試	190	通	240	段		
41	濃	91	線	141	全	191	紛	241	放		
42	上	92	着	142	少	192	約	242	脱		
43	高	93	入	143	適	193	確	243	給		
44	行	94	系	144	域	194	進	244	添		
45	比	95	低	145	減	195	異	245	与		
46	対	96	得	146	外	196	断	246	石		
47	率	97	要	147	射	197	板	247	品		
48	生	98	後	148	均	198	導	248	衡		
49	変	99	圧	149	直	199	配	249	起		
50	溶	100	向	150	火	200	側	250	従		

(3) 『化学工学論文集』に多出する漢字の特徴

表３は，『化学工学論文集』中のある日本語要旨について，３級の日本語能力試験で要求されている284

表３　＜３級＞284漢字と＜化工＞284漢字の比較
（■：該当漢字）

(a)　＜３級＞必修284漢字

撹拌槽内の流れについて，境■条件を満■する独■な４個の流れ関数を仮定し，Navier-Stokes ■程式から導■した流れ関数による連■常微■■程式の数値解析を■った。槽内速度成■の相互相関関数の解析から，撹拌槽内流動の■周期ゆらぎ現象は，槽全■スケールで循環する■域的な流れパターンにより■じ，実■結果とよく■致した。またその■周期変動の周期は，■部■■周期の約34倍であり，実■で求めた■周期変動が羽根■過周期の約20～30倍であるという■実に■かった。流れ関数の数を３から４に増加した効果は，周波数解析と相互相関関数の結果から，■■系的性■に対する効果よりも，流れの局■的な現象の■徴を表現するのに寄与する効果の■が■きいことが■かった。■数の変数による決定論的記述による解析■法は，撹拌槽内に■■する■周波変■に関する現象の■■系挙■を予測するのに非常に■効であることが確認された。

(b)　＜化工＞の上位284漢字

撹拌槽■の■れについて，■■■■を満足する独立な４個の■れ■■を■■し，Navier-Stokes ■■■から■■した■れ■■による連立■■■■■■■の■■■■■を■った。槽■■■■■の■互■■■■■の■■から，撹拌槽■■■■の■■■■ゆらぎ■■は，槽■■スケールで循環する■■■■な■れパターンにより■じ，■■■■■とよく■致した。またその■■■■■の■■は，■■■■■■■の■34倍であり，■■■で■めた■■■■■■が羽根■■■■■の■20～30倍であるという事■に■かった。■れ■■の■を３から４に■■した■■は，■波■■■と■互■■■■■の■■■から，■■■■■■■■に■する■■よりも，■れの局■■■な■■■の■徴を■■するのに寄■する■■の■が■きいことが■かった。■■の■■による■■■■記述による■■手■は，撹拌槽■に■■する■■■波■■■に■する■■■の■■■■挙■を予■するのに■■■に■■■であることが■■■された。

字の漢字と化学工学の分野に多出する284字の漢字の使用状況を比較したものである。(a)と(b)は同じ文章である。(a)の■は学習目標漢字群に含まれる漢字であり，(b)の■は＜化工＞の多出漢字群に含まれる漢字である。いずれの場合も■の部分が学習すべき漢字であるから，文章中の■の数は読解の難易度を示し，(b)の文章を読むには＜3級＞の284字の学習だけでは十分でないことが分かる。しかし，別の言い方をすると，＜化工＞の284字が習得されていれば，かなりの漢字が理解可能であり，文章の読解の可能性が高いことが期待される。これが上述した専門分野に特有の漢字群の抽出が重要であるという理由の一つでもある。

表4は＜化工＞と＜3級＞の各284漢字を取り上げ，それらの漢字群が4分野の専門書，すなわち『現代経済学入門』（以下＜経済＞；表では「経」），『社会人類学』（以下＜社会＞；表では「社」），『日本の短編』（以下＜文学＞；表では「文」），＜理工＞（表では「理」）に出現する多出漢字の上位284漢字との重なり傾向を比較して示したものである。本調査では，＜経済＞は理工系の要素を含む文化系の専門書として，＜社会＞は日常生活に関する要素を含む文化系の専門書として，＜文学＞はいわゆる専門分野とは離れたさまざまな日常生活が記述される分野の代表書として選択した。また，＜理工＞の資料は著者の一人が既に行った理工系分野の専門書29冊の分析結果（武田1994）から，多出漢字の上位284位までを取り出したものである。表では，ある漢字が4分野すべての資料に出現した場合を「4分野」，いずれかの3分野と重なった場合を「3分野」，いずれかの2分野と重なった場合を「2分野」，1分野だけと重なった場合を「1分野」，いずれとの分野にも重ならなかった場合を「0分野」と表記している。

表4　＜化工＞と＜3級＞に出現する284漢字の比較

		① 化工&3級	② 化工のみ	③ 3級のみ
	合　計	81	203	203
4分野	小　計	*43*	17	7
3分野	小　計	15	46	26
	理 経 社	5	*36*	2
	理 経 文	5	6	0
	理 社 文	2	3	3
	経 社 文	3	1	*21*
2分野	小　計	12	41	37
	理 経	7	*20*	3
	理 社	0	*13*	1
	理 文	4	5	4
	経 社	0	1	6
	経 文	0	2	4
	社 文	1	0	*19*
1分野	小　計	11	62	70
	理	4	*45*	4
	経	2	7	5
	社	2	7	*12*
	文	3	3	*49*
0分野	小　計	0	*37*	63

ここで，表中の斜体（下線付）で表記した数値を中心にそれらの特徴について説明する。表中の①列は，＜化工＞と＜3級＞のそれぞれに出現する284漢字のうち，いずれかの分野に重なって出現した漢字は81字であり，そのうち半分以上の43字漢字が4分野の全てに出現しており，また，いずれの分野にも見出せなかった場合が0ということを示す。詳細に見ると，3分野，2分野，1分野と重なり分野の数による著しい違いは見られず，どの分野でも均等に使用されていることが分かる。この分析結果から，＜化工＞にも＜3級＞にも重なる漢字は，分野を問わず漢字学習上の基本漢字として採用できると結論できる。

②列は＜化工＞には出現するが＜3級＞には出現しなかった漢字が203字であることを示す。そのうち，最も多いのは1分野にしか重ならない62字（全体の31％）の漢字である。しかし，特徴的なのは，このうちの45字（該当部分の73％）が＜理工＞とのみ重なっていることである。この分析結果から，＜化工＞に多出する漢字は化学工学の分野の漢字であると同時に理工系分野の漢字でもあると解釈できる。この事実は，著者らが理工系の代表として化学工学を選定したことが正しかったことを裏付ける。さらに詳しく分析すると，＜化工＞の漢字は＜理工＞だけでなく＜経済＞，＜社会＞とも重なるものが多いのが特徴である。すなわち，3分野に重なる漢字では46字のうち36字（該当部分の78％）が該当し，＜理工＞と＜経済＞，または＜理工＞と＜社会＞と2分野に重なる漢字を合計すると20＋13＝33字（該当部分の80％）が該当する。このことは，＜化工＞と＜理工＞は理工系の分野において，また，＜経済＞と＜社会＞は文化系の分野において，それぞれの専門概念や論理を類似した記述様式で行っているという事実と矛盾しない。したがって，＜経済＞や＜社会＞と重なる漢字は，特別に理工系の分野であることを意識しなくても，「専門書」というジャンルに

共通に使用される頻度の高い漢字群であると解釈できる。

③列は＜3級＞には出現するが＜化工＞には出現しなかった漢字が203字であることを示す。＜3級＞の漢字は基本的な語彙の理解という目的で選定されているため，極めて日常性の高い漢字である。したがって，当然に予想されることではあるが，ここでは②列と対照的な傾向が見られる。すなわち，②列と同様に1分野にしか重ならない漢字が最も多く70字（全体の34%）あり，そのうちの＜文学＞と重なる漢字が49字（該当部分の70%）と最多である。＜社会＞の12字も＜理工＞や＜経済＞と較べると数が多いと言える。これは＜社会＞が日常生活との関連要素を多くもつ分野であるためと考えられる。同様な傾向は3分野に重なる漢字26字のうち21字（該当部分の81%）が＜経済＞，＜社会＞，＜文学＞と重なり，＜理工＞と重なる漢字がほとんどない（2あるいは3）という結果にも現れている。2分野に重なる漢字もまた同様な傾向にあると言える。このことは，＜経済＞と＜社会＞は日常生活の諸現象を対象にして分析・考察する学問なので，その記述において＜理工＞よりも日常生活で用いる漢字を多用する特徴があるためと解釈できる。

上述した漢字の使用頻度の特徴から，＜化工＞に多出する上位284の漢字は図2のように3層に分類することができる。A層に属する漢字群は②列の中の1分野＜理工＞とのみ重なる漢字（45字）と＜化工＞（0分野）にのみ出現する漢字（37字）を合わせた82字である。C層には＜化工＞に出現する284漢字のうち，表4の①列の全出現漢字数（81字）と②列で＜文学＞にも出現する漢字（37字＝17＋6＋3＋1＋5＋2＋3）を合わせた118字である。B層は，②列にある漢字のうち，A層とC層に属する漢字を除いた84字である。

図2　化学工学の専門書に多出する漢字の構成

A：化学工学の漢字（82） （理工系専門書の漢字）	理工系の専門書読解の漢字（284）
B：専門書読解のための漢字（84）	
C：一般的な日本語の読解のための基本的な漢字（118）	

ここで各層にはどんな漢字が属するかについて簡単に説明する。C層には，「一，二，三，上，中，下，大，小，高，低，有，前，後・・・・」などの，日常生活でのごく基本的な漢字が集まっている。ここで問題なのは，こうした漢字選択の配慮とは無関係に，多くの留学生は日常使う日本語と専門書で使われる日本語とを分けて捉えるため，漢字もそれぞれ異なるものであると考える傾向が強いと言うことである。そのため，留学生の多くは短期間で両方を別々に学習するのは不可能であると考えてしまいがちである。上の分析結果は，専門書を読解するための漢字は日常生活にも十分に応用できること，またその逆もあることを意味する。したがって，この事実を留学生に早い時期に知らせることは彼らが日本語学習に意欲を持つようになるのに大いに役立つことが期待される。

B層には，「的，類，例，象，単，配，接，常，変，比，表，形，化，必・・・・」などの漢字が属する。この層の漢字は，他の研究分野でも多用される漢字である。詳細な解析については今後の詳しい分析を待たなければならないが，これらの漢字の特徴は，1つの漢字，たとえば「比」からは「比べる，比する，比例，比較，対比・・・・」などの語が容易に連想あるいは派生できることである。ここで挙げた例示語は論文調の文体であるにしても，特別に理工系専用の語（漢字）であるとか，化学工学に特有の語であると言った印象を与えないものである。B層の漢字が化学工学の専門書にも多く使用されるのは，理工系の専門書が多くの場合論文調の文体で書かれているから当然であるとも言える。

A層の漢字になると，化学工学の専門分野に特有な語を連想するような漢字が多くなる。実際，＜化工＞にしか出現しなかった漢字には「粒，酸，濃，素，燃，圧，膜，媒，硫，触，脱，透・・・・」がある。しかしながら，この層の漢字は化学工学の分野に特有な漢字であると同時に，理工系の広域分野全般にも多用される漢字である。たとえば，我々日本人はこれらの漢字から，「粒子，酸化，濃度，元素，素子，燃焼，圧力，薄膜，媒体，硫黄，触媒，脱離，透過・・・・」などの語を直ちに思いつくが，一方，これらの漢字から日常生活でよく使う日本語を思い付くのには時間がかかる。これがA層の漢字こそが化学工学の専門書を読解するために必要な漢字であると言え理由である。したがって，この層に出現する漢字こそが，化学工学を含む理工系の分野に特有な漢字であり，言い換えるとこれらの漢字が組み合わさって，化学工学の専門書

が書かれていることになる。

以上の分析結果を参考にして漢字教育の立場から捉えてみると，化学工学の分野を専攻する留学生に日本語の学習指導をするに当たっては，次の3つの漢字群を設定するのが効果的であると結論できる。

(a) 日常型の漢字群（C層の漢字群）
　化学工学の専門書に多く出現するが，一般の日本語の教科書でも学ぶ漢字

(b) 論文型の漢字群（B層の漢字群）
　すべてのジャンルの「専門書」全般で共通して使用される漢字

(c) 理工系（化学工学）型の漢字群（A層の漢字群）
　化学工学などの理工系の専門書に多く出現する漢字

5．効果の期待できる漢字学習指導

ここでは，それぞれの漢字群を実際に学習指導する際に特に留意すべき点について簡潔に述べる。ここでの学習指導者は，必ずしも日本語専門の教師だけを指すのではなく，指導教官あるいはチューターなどの留学生に対する学習に関与する人たちを意味する。

(1) 日常型の漢字群の指導

この漢字群は，一般の日本語の読解を目的に学習している者であれば，必ず覚えなければならない基本的な漢字である。そのため，これらの漢字群は特に専門分野を意識しなくても学習する機会が多い。この群の漢字をできるだけ数多く，しかも達成度高く学習指導できれば，留学生の漢字に対する学習意欲は，飛躍的に伸びることが期待できる。したがって，まず最初にこの漢字群の日常生活で普通に使用される用例を通して学習させるのが効果的である。それと同時に化学工学の分野を専攻する留学生に対してはこれらの漢字が専門書を読解するために重要な役割を果たすということを明確に説明する形で指導することが重要である。具体的には，日常的な語を学習させた後で，専門分野でよく使われる漢字などを数多く例示し，それらが専門書を読解するのにいかに役立つかを実感させるように指導することが必要である。

ここで漢字「分」について具体的な学習指導の一例を示す。

＜例：漢字「分」の学習指導＞

・初級用の教科書の漢字：わける，わかる，ごふん，ろっぷん

・専門書読解用の追加漢字：ぶんし，ぶんすう，びぶん，せきぶん，ぶんり

まず，漢字を大きな字で板書し，ふりがなを振り，読み方を教える。このとき同時に，必ずその語句の持つ漢字の意味を繰り返し説明する。読み方（発音）が異なることばかりを強調すると，学生がどのように覚えたら良いかと悩むのでできる限り必要最低限とする。説明に当たっては，理工系の留学生が論理的な思考に慣れていることを利用した説明様式，たとえば図表やグラフなどを併用して示すなどの工夫を凝らすのが効果的である。ここで重要なのは，学問的に詳細にかつ正確に説明するのではなく，多少間違っていても良いから「なるほど，そうか」と納得してしまうような意味の説明パターンを多数用意して，留学生の反応を見ながら例示することである。このとき，未だ習っていない漢字をも敢えて提示して見せると言う試みは，常に漢字を目に馴染ませ，あらゆる機会に漢字と意味との間には密接な関係があることを認識させることから言っても効果的であると言える。

しかしながら，ここで留意しなければならないことは，日本語の教師は留学生が漢字が書けるようになることをあまり期待してはならないと言うことである（武田・入戸野 1997①，④）。日本語の学習期間ではあっても，実験に参加したり発表したりする時間的制約が多い留学生が，学習する漢字の全部が書けるようになることを要求されたら，漢字学習への意欲は急速に低下することを肝に銘じておくことは重要である。われわれ日本人も漢字を少しずつ覚えたことを忘れてはならない。コンピュータを駆使し，電子辞書を自由自在に操る留学生にとっては，書けることではなく，正しく読めることの方が重要である（武田・入戸野 1997③）。読めれば辞書が引け，さらに読み慣れれば，漢字の持つ意味の把握も正確になり，自分で電子辞書やワープロから正しい漢字が選択できるようになる。漢字に興味を抱くようになれば，書けるようになるのも早い。最初は書ける漢字だけを書けばいいという方針で留学生が楽しく学習し続けられるような指導様式が最終的には効果的であると著者らは考えている。

(2) 論文型の漢字群の指導

この群の漢字には一般の日本語教科書の初級段階では出現しないものも多く，化学工学の専門書を読解するために新しく学習しなければならない漢字である。そうは言ったが，特別なものではなく，学習指導者が

どんな漢字がどのように「専門書」に使用されているのかを明確に把握しているならば，いつでもそれらを提示できる漢字群でもある。たとえば，「～ほどではありません」という構文を学習したあとで，いくつかの例文を練習させ，十分に習熟したときを見計らって，「ほど」を取り上げて，「この字ほ本当は平仮名で書くけれども，もし漢字で書けば」と言って，「程」を提示する。そして，「程」の意味と学習した文型の意味を対比して説明し，その上で，「程度」「過程」などという専門書に多く現れる語や，やさしい文例を提示するのは大変効果的である。著者らの体験からは，たとえば，漢字「量」の場合，「質」（質問）という漢字を学習した後で，専門書では「量」は「質量」とか「分子量」などとして使われているということを気軽く提示して見せるなどの指導技術は漢字の理解を深めるのに大変効果的であることが分かった。

また，留学生の小さな質問や誤りを利用するのも，漢字学習の意欲を盛り上げるのに大切な指導方法である。たとえば，「計る」と「図る」を学んだ学生がその使い分けを間違えた場合，なぜ意味の違いが漢字の違いになるのかを説明し，併せて「量」と「測」をも一緒に説明して興味を持たせるのである。覚えてもらうことを期待するよりも，漢字に対して興味を抱いてもらうことに指導の重点を置くことが最大の学習促進に繋がる。

結論的に提案するが，非漢字圏の留学生には何よりも漢字に慣れ親しむことが最重要である。そのためには漢字を覚えることをあまり強制しない方が良い指導方法である。何よりも大切なのは，専門書に多く使用される語や文例に，できるだけ頻繁に出会う機会を持つことの方が大切である。当然のことであるが，学習指導者は常に前向きに留学生に接し，「なるほど論理的である」と納得できるような上手な説得力のある説明が行えるように常に切磋琢磨する必要がある。いかにして「あの先生の指導を受けるならば，安心して漢字学習に取り込める」と留学生が感じる授業様式や教授技術を身に着けるようにできるかが，良い教材を効果的に活用するここと併せて重要な課題である。

(3) 理工系型の漢字群の指導

この漢字群は化学工学などの理工系の専門書だけに出現する漢字であるから，日本語で書かれた専門書を読解するには，留学生がどうしても覚えなければならない漢字である。著者らの体験からは，留学生は自分の専門分野の漢字はむしろ覚え易いと言う。留学生は専門用語の漢字を知らなくても，その言葉（発音）を頻繁に耳にしており，少なくとも自国語ではその意味を理解している。したがって，他の群の漢字に比べて意味が把握し易く，すでにある程度は漢字が読めるようになる段階に達していると言える。より厳密に言えば，留学生は自分では漢字を正しくは書けない（読めない）ものの，その漢字の全体的な形から問題の漢字と同一のものであると認識できる。例を上げると，ある留学生が一番初めに覚えた漢字は，「閾値」であった。その留学生は，研究室の研究発表会や討論などでしばしば「しきいち」という言葉を耳にしており，その英語の意味をしっており，また「閾」という漢字も目にしていた。そのため，「閾値」が「しきいち」であると分かると，たちまち「閾」という漢字を覚えたのである。同様な手順で，留学生は自分の専門分野によって漢字を「細胞」「分子」「濾過」「溶液」「真空」などと習い覚えた語と共に覚えてしまうことも多い。学習指導者はこうした漢字学習の相乗効果や連鎖効果も学習効率を高めることに役立つことを認識しておく必要がある。

以上述べたように，非漢字圏の留学生にとって，必ずしも教科書の第一課の漢字が覚えやすくて優しいものであるとは限らない。留学生にとっては，頻繁に出合う漢字こそが，易しくて覚えやすい漢字なのである（武田・入戸野 1997①）。指導者は常にそのような漢字の特性を頭に入れておき，機会あるたびに繰り返し繰り返し，覚えさせたい漢字が留学生の目に触れるように工夫し，漢字の発音が耳に留まるように聞かせることが大事である。同様に，漢字学習の指導にあたっては，留学生が覚えたいと思っている漢字はどのような種類のものであるかにも常に気を配るような配慮も必要である。

む す び

非漢字圏の留学生に専門書を読解するための漢字を指導するには，教える者（学習指導者）にもそれ相当の指導能力と指導技術の改善に向けての努力が必要である。それだけに，教える者が指導上の要点を教科書の形で学習者と共有する意義は大きい。教える者と学習する者とが同一の教科書を共有することによって，教える者同士の横の連絡も取り易くなり，更に実践体験を活かしてより質を高めた教科書を目指すことも可能になる。また，学習する者にとっても，実用的で学習効果の高い教科書を使用することで学習目標の設定

が明確になり目的達成の大きな拠り所となる。ここで考察してきたように，専門書を読解するための漢字数は必ずしも多くはない。しかも，専門書を読解するための漢字は日常生活にも十分に応用できること，またその逆もあることを留学生に早い時期に知らせることは彼らが日本語学習に意欲を持つようになるのに大いに役立つ。だからと言って，漢字を単に他との関連なしに個々に取り上げて学習指導するだけでは留学生は専門書を読解できるようになることはできない。専門書の中ではこれらの漢字が組み合わさって専門用語を作り出し，論文調を醸し出す漢語を形成して，特徴ある構文を作っているからである。したがって，学習効果の高い実用的な教科書を目指すには，漢字の学習がそのまま読解の学習にもなるような，文字（漢字）と語と構文が一体化した教科書の作成とそれを使用しての学習指導システムの構築が不可欠である。

この最終目的のためには，今回抽出した漢字を中心にして，語の構成ならびに多用される語についてさらに実践的な分析が現在進行中である。また，ここで述べた考え方が他の専門分野の専門書読解のためにも同じように適応できるものであるかについても現在資料の収集・分析中である。

参考文献

海保博之（1984）:『漢字を科学する』，「漢字の特性をはかる」，有斐閣選書。

慶應義塾大学（1989）:『福沢基金共同研究－科学技術日本語教育のための調査研究報告書（代表　橋本芳一）。

武田明子（1994）:『専門書読解における効率的漢字学習方の実証的研究－大学院課程理工系留学生のために』，松下国際財団1993年度研究報告書。

武田明子（1995）:『専門書読解における効率的漢字学習方の実証的研究－大学院課程理工系留学生のために』，松下国際財団1994年度研究報告書。

武田明子・入戸野修（1997①）:「科学技術文献読解のための漢字指導法の見直し」，科学教育研究，Vol. 21，No 4，207～216。

武田明子・入戸野修（1997②）：語彙分析と実験授業から得た初級日本語学習者のための理工学漢字の選定，日本科学教育学会第21回年会論文集，275～276。

武田明子・入戸野修(1997③)：電子辞書による漢字検索時間の検討，教育工学関連学協会連合第5回全国大会論文集，155～156。

武田明子・入戸野修（1997④）：初級日本語を学ぶ理工系研究留学生のための漢字教授方法の提案，平成9年度日本語教育学会秋季大会論文集，155～160。

武部良明（1989）:『漢字の教え方－日本語を学ぶ非漢字系外国人のために』アルク。

東京大学（1992）:『東京大学大学院工学系研究科における留学生日本語実体調査』，東京大学工学部日本語教育調査研究会。

文部科学省（2001）:『我が国の留学生制度の概要』，文部科学省国際局留学生課。

An Effective Approach to Teaching International Students How to Read Technical Papers (Towards the Creation of "Technical Terms in Chemical Engineering")

Osamu Nittono and Akiko Takeda

How to learn Chinese characters (Kanji) is necessary for foreign graduate students, especially from non-Kanji countries, who want to learn research activities such as technical and scientific papers written in Japanese. The aims of this study are to find out how to do effectively Kanji teaching, and to propose an effective teaching approach to reading such papers. We analyzed quantitatively 380,560 characters including 1501 different characters, which were picked up from six volumes of "Kagaku Kogaku Ronbunshu" published in 2000. As a result, the following points were revealed:(1) 284 characters are used most frequently in the field of chemical engineering, which can cover upto 81.8% of the whole characters. (2) They are classified into three groups, I, II and III: Group I characters are useful not

only to read technical papers, but also to understand basic daily life (118/284). Group II characters are widely and frequently used in many blanches of academic knowledge fields including scientific and technical ones (82/284), and Group III characters are used only in the field of chemical engineering (84/284). Groupe III includes slightly difficult characters from elementary Japanese, but if the foreign students learn them along the guide lines of Group I to Group III by use of the synergism in their scientific and technical field, they will be able to master technical Japanese Kanji within a short term. Several effective teaching techniques are also discussed on the basis of the analyzed results. The present study suggested sevral imporatnt points on the preparation for text book of technical Japanese in chemical engineering.

研究留学生が科学技術の専門書を読解するための基本漢字の例示語選定に関する検討

入戸野　修・武田明子

福島大学教育学部論集 理科報告 第67号　抜　刷

２００３年６月

研究留学生が科学技術の専門書を読解するための基本漢字の例示語選定に関する検討

入戸野　修・武田　明子*

Selection Requirements of Basic Kanji for Teaching International Students How to Read Technical Papers

by

Osamu NITTONO and Akiko TAKEDA*

Materials Science Laboratory, Faculty of Education, Fukushima University
1 Kanayagawa, Fukushima 960-1296 Japan

Recieved April 16, 2003

Abstract

How to learn Chinese characters (Kanji) is necessary for foreign graduate students from non-Kanji countries, who want to have research activities in Japan as soon as possible. In general, foreign students must start to learn basic Kanji for everyday life in the Japanese elementary course, and, at the same time, they also must learn to read Kanji used in scientific research papers. The aim of this study is to propose an ideal process for selection of basic Kanji which are useful not only for everyday life, but also for reading technical books. We gathered many Kanji from various text books, and analyzed them with reference to common features. As a result, it is shown that four requirements are useful for selection of Kanji which will be effectively used for scientific research students to read technical Japanese papers.

はじめに

現在，科学技術の進展は著しく，しかもグローバル化している。科学技術を伝える言語としては英語が主流であるが，ある国独自に発展した科学技術を正しく理解するにはその国の文化の視点からその国の言葉で理解することが重要である。近年，留学生（研究留学生）の受け入れ先は高等教育機関から実技訓練機関や企業研修所に拡がっている。研究生活に１日のほとんどの時間を費やす理工系留学生，特に非漢字圏の研究留学生は，できるだけ少ない漢字とそれらの漢字の組み合わせを学び，その結果から多くの日本語が理解できるようになる必要がある。このためには，理工学系留学生を意識した日本語の選定とその学習法に関する研究が不可欠である。

国立国語研究所は，これまで現代日本語の書き言葉に関する基礎資料を提供することを目的に90種類の雑誌について語彙調査を行ってきている[1～3]。著者らはこのような調査を理工系分野の用語を対象にしても行う必要があると考え，1993年から語彙の調査を実施してきた[4]。また，この調査の調査と併行して実施した留学生の日本語学習に関する実態調査から，日本語学習で何が難しい

＊独協大学日本語教育（外国語学部言語文化学科）非常勤講師（元東京工業大学留学生センター非常勤講師）

かと言う質問に対して，非漢字圏の留学生だけでなく，漢字圏の留学生からも「漢字」であるとの調調査結果を得ている[5)]。そこで，研究留学生の専門書読解の学習法を開発するためには，彼らが大きな障害と感じている「漢字」の問題を解決することが必要であると考え，語彙の中から特に「漢字」を抽出し，集中的に調査・分析した[4～7,11)]。その結果，①初級者用漢字テキストで扱われる漢字の半分は理工系分野の漢字に重複していること，②残りの漢字のさらに半分は，いわゆる論述形式をとる文章に共通する特徴があることを明らかにした。また，漢字を含む語（以後，語と記述する）に関しては，科学技術専門書では，③７割が体言に分類され，そのほとんどが２字漢字語であること，④動作性名詞の使用が他の分野に比して多いこと，⑤動詞は定型的であること，⑥形容詞・形容動詞・副詞の類は出現語が極端に少なく，同じ語が繰り返して使用されることが分かった。さらに，著者らは，理工系の専門書に多出する語と日常の生活に多出する語（日常生活語）とを融合させた学習を日本語学習の初級段階から行うことを目的として，先に得られた分析結果を再分析し，相補的な漢字530を抽出し，それらの漢字を用いた簡単なモデルテキストを作成して実験授業を実施し，良好な達成度が得られることを示した[8～10)]。しかし，学習効率のよいテキストとするためには，提示する例示語の選定方法を再考し，より適切なものを選定し，それに適した学習法を実施する必要があるとの結論を得た。

本研究は，既に報告した「化学工学における専門日本語」を対象にした分析結果[11)]をより一般的に検証するために実施した。今回は専門分野を広めて理工系分野の資料（教科書・専門書）（別表）から統計処理を経て出現頻度の高い漢字を含む語を取り出し，これらを同義・類義の視点で分類して意味の分布傾向を調べ，効果的な学習の期待できる理工系分野の専門日本語の選定基準について検討する。

１．語の抽出資料の選定および分析方法

本研究では，理工系資料として29種類34冊の専門書（別表）を選定し，これらに出現する語（延べ数約200万語）を抽出し，全体の90%までを占める高出現頻度の語を統計処理の対象とした（統計処理の詳細は報告書[6)]を参照されたい）。理工系分野の語の特徴を他の分野と比較するために，理工系分野と類似点の多いと考えられる経済学分野と，類似点の少ないと考えられる社会人類学分野からの専門書を選定し，それぞれの累積百分率90%までの語を対象とした．経済学と社会人類学は，論を展開する形式で記述されている（文章的表現形式）専門書である点で理工系資料と同質である。さらに，より多く日常的表現がとられていると予測される文学作品と実際の初級者用テキスト３種類（計５冊）も同様な方法で語を選定し比較した。文中では文学作品を［文学］，初級者用漢字テキストを［初級］と略記する。また，資料そのものを指すときは略記名で表記（例えば［理工］）し，資料の分野全体を指すときは「分野」と表記（例えば「理工系分野」）する。

表１　語の意味の分類

カテゴリー	意味の範囲	具体的内容例
Ⅰ　抽象的関係	人間や自然の在り方や枠組み	事実　存在　状態　力　変化 空間　時間　形　数量など
Ⅱ　人間活動の主体	活動の主体	人　集団　機関など
Ⅲ　人間活動	活動そのものの様相	精神　行為
Ⅳ　人間活動の生産物	人間活動尾相手としての存在	作製物　利用器具
Ⅴ　自然	自由に外界に存在するもの 人間の主体的活動から比較的	自然物　自然現象
Ⅵ　固有名詞	地名・国名・人名	

表２　カテゴリーに見る各分野の語の意味の分析

	［理　工］	［文　学］	［経　済］	［社　会］
Ⅰ	1）340（68.0）	1）187（37.4）	1）269（53.8）	1）252（50.4）
Ⅱ	5）6（1.2）	3）99（19.8）	3）38（7.6）	3）95（19.0）
Ⅲ	2）95（19.0）	2）101（20.2）	2）163（32.6）	2）132（26.4）
Ⅳ	4）16（3.2）	4）41（8.2）	4）15（3.0）	6）3（0.6）
Ⅴ	3）43（8.6）	4）41（8.2）	5）13（2.6）	5）7（1.4）
Ⅵ	6）0（0.0）	6）31（6.2）	6）2（0.4）	4）11（2.2）

語の意味の分類分析には国立国語研究所の『分類語彙表』[3)]を参照した。分類語彙表では，語彙を構成する一つ一つの単語が，それぞれどのような意味で用いられるかを一覧できるように，単語が表し得る意味の世界を分類してその各項にそれぞれの単語を配置してあり，その結果，抽象的関係，人間活動の主体，人間活動，人間活動の生産物，自然の５つのカテゴリーに分類されている。本研究では，さらに固有名詞を示す個々の語を一括して「固有名詞」として扱い，６つのカテゴリーとして分類した（表１）。

［理工］では，累積百分率70％までの異なり語が500語，90％までが1,227語，90％以上が8,249語であった．語の表す意味の特徴は上位に位置するものほど顕著であると考え，今回は上位500語までを対象範囲とした。その内訳は，１字漢字語（漢字１字またはこれに送りがながついて語として働く動詞，名詞，形容詞，形容動詞，副詞）が168語，２字漢字語（漢字２字またはこれに送り仮名がついて語として働く名詞，形容詞，サ変名詞，副詞）が308語，その他24語である。比較のため，［文学］［経済］［社会］からも同条件で語を抽出して示した。

２．理工系の語の意味の分布

表２に［理工］［文学］［経済］［社会］の語の意味の分布をカテゴリーごとに出現実数で示した。１～６）は出現順位，数値は出現語の実数，（　）は実数が500語に占める割合である。対象とした全ての資料で第１位と第２位はカテゴリーⅠ（抽象的関係）とⅡ（人間活動）である。この２つのカテゴリーで［理工］は全体の87％，［文学］は57.6％，［経済］は86.4％，［社会］は76.8％を占め，どの分野でも語が集中する傾向がある。特に［理工］ではカテゴリーⅠの分布が多く68.0％である。第３位になると，［理工］と他の資料との間に分布傾向の相異が顕著である。［理工］ではカテゴリーⅤ（自然）が，［文学］［経済］［社会］ではカテゴリーⅡ（人間活動の主体）が第３位である。カテゴリーⅣ（人間活動の生産物）とカテゴリーⅥ（固有名詞）は分布が少ない。特に［理工］ではカテゴリーⅥの語の分布はゼロである。理工系の分布はカテゴリーⅠとⅢ，およびカテゴリーⅤに集中していることが分かる。

表３はこの３つのカテゴリー（Ⅰ，Ⅲ，Ⅴ）について，『分類語彙表』を参考にして，語の意味の分布傾向を，意味のより近いもの同士でまとめたものである。表中の理・文・経・社はそれぞれ［理工］［文学］［経済］［社会］を指す。順は語の出現順位を，○で囲った数字はカテゴリー内の項目を，（　）は出現実数を示す。カテゴリーⅠ（抽象的関係）では［理工］［文学］［経済］［社会］の全てで10項目の語が出現した。ここで，［理工］の第10位の語の出現数が９語であるので，これをカテゴリーの項目が集中する語の最低基準とすると，この基準を満たす項目の合計がカテゴリーⅠでは34項目，カテゴリーⅢ（人間活動）では18項目，カテゴリーⅤ（自然）では２項目で，カテゴリーⅠの項目が最も多い。

カテゴリーⅠでは第３位までに語の出現の60％程度が集中し，［理工］は62.6％，［文学］は61.5％，［経済］は59.1％，［社会］は54.0％である。この範囲の項目には⑩「量」，⑥「作用」，②「関

表３　［理工］の語の意味の分布が集中するカテゴリーの項目

Ⅰ　抽象的関係

順	理	文	経	社
1	⑩(91)	⑩(54)	⑩(74)	②(54)
2	⑥(68)	⑦(40)	②(44)	⑩(52)
3	②(54)	⑥(21)	⑥(41)	⑥(30)
4	⑧(28)	①(17)	⑦(36)	⑧(26)
5	④(24)	②(17)	①(18)	⑦(25)
6	③(19)	⑧(15)	③(16)	①(22)
7	⑦(17)	③(12)	④(16)	③(17)
8	⑨(16)	④(10)	⑧(15)	④(16)
9	①(14)	⑨(7)	⑤(5)	⑤(6)
10	⑥(9)	⑤(1)	⑨(4)	⑨(4)

Ⅲ　人間活動

順	理	文	経	社
1	①(49)	①(49)	⑧(59)	①(49)
2	②(16)	②(18)	①(43)	②(20)
3	⑨(13)	④(13)	②(18)	⑨(16)
4	⑧(7)	⑨(9)	⑨(16)	④(13)
5	⑦(4)	③(4)	⑦(12)	⑤(11)
6	③(2)	⑧(3)	⑤(7)	⑧(10)
7	⑤(2)	⑥(2)	④(5)	⑦(7)
8	④(1)	⑦(2)	⑥(3)	⑥(6)
9	⑥(1)	⑤(1)	③(－)	③(－)

Ⅴ　自　然

順	理	文	経	社
1	②(36)	⑧(19)	②(6)	①(2)
2	⑥(3)	②(7)	⑦(3)	③(2)
3	⑧(2)	①(5)	⑧(2)	⑧(2)
4	①(1)	⑨(4)	③(1)	⑦(1)
5	③(1)	③(2)	⑨(1)	②(－)
6	④(－)	⑥(2)	①(－)	④(－)
7	⑤(－)	⑦(2)	④(－)	⑤(－)
8	⑦(－)	④(－)	⑤(－)	⑥(－)
9	⑨(－)	⑤(－)	⑧(－)	⑨(－)

（項目の内訳）

Ⅰ	①事柄	②関係	③有無	④様相	⑤力
	⑥作用	⑦位置	⑧空間	⑨形	⑩量
Ⅲ	①心態	②言動	③創作	④文化	⑤義務
	⑥交流	⑦支配	⑥取得	⑧仕事	
Ⅴ	①刺激	②自然	②宇宙	④生物	⑤生
	⑥動物	⑦体	⑧生命	⑨健康	

表４　理工系の語の意味の分布が集中する項目

A）全分野に共有	Ⅰ	事柄　関係　有無　様相
		作用　位置　空間　量
	Ⅱ	心態　言動
B）［経済］［社会］と共有	Ⅲ	仕事
C）［理工］のみ	Ⅰ	形
	Ⅴ	自然　力

係」がある。⑩「量」は［理工］［文学］［経済］で第１位を占め，カテゴリーⅠの代表的な項目である。また，⑨「形」と⑤「力」の２項目は［理工］のみに基準値以上の語が分布し，理工系の語が集中する項目であると言える。

以上の分析結果から出現頻度の特徴から，理工系の語の意味の分布が集中する傾向を示す項目を選定すると14項目となり，それを分布の特徴から分類すると，表４のようにまとめられる。

３．理工系分野の語の選定基準

理工系分野の語の選定基準を検討するために，表４の結果に［文学］［社会］［経済］における基準値を満たす語の意味の分布を４つの象限上に表示したのが図１である。図では各資料の語の意味

図1　語の意味の分布の重複関係

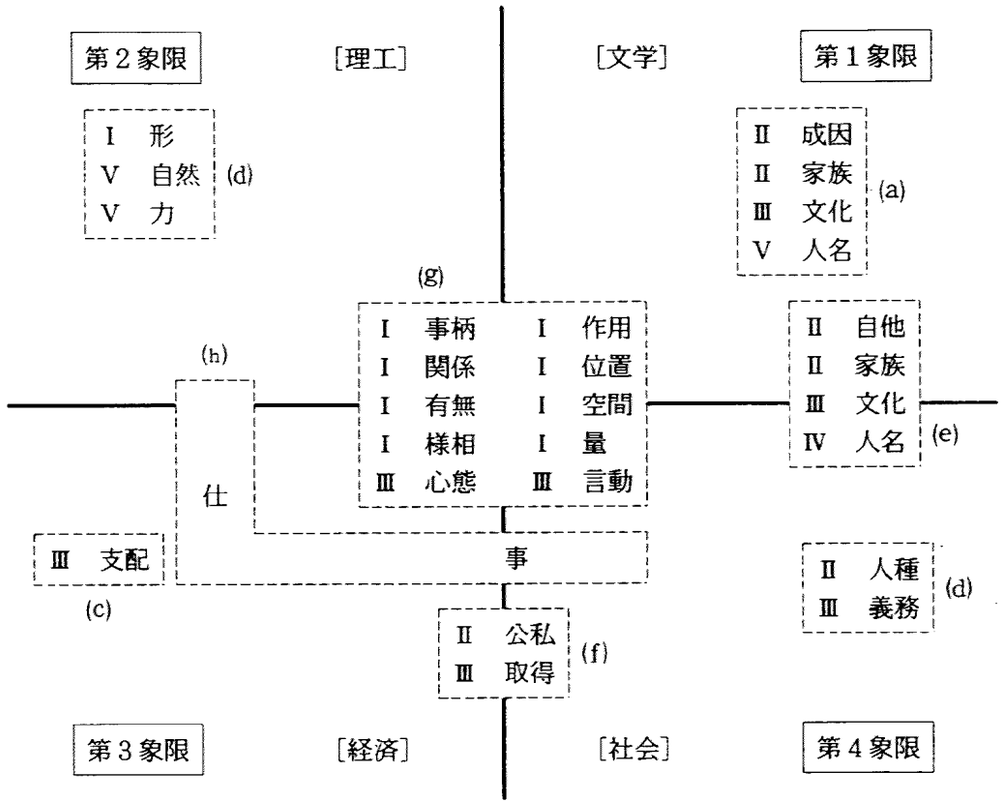

表5　項目と語例

分野	項目	語					
[経済]	支配	行政	財政	雇用	……		
[社会]	人種	部族	民族	京都	……		
	義務	役割	権利	資格	……		
[文学]	成員	学生	教師	先生	……		
	社会	学校	世界	会社	……		
	住居	階段	台所	部屋	……		
	生命	病気	自殺	成長	……		
[理工]	形	曲線	直線	軌跡	三角	粒子	……
	自然	溶解	結晶	金属	分子	固体	……
	力	出力	昨日	圧力	磁束	応力	……

の分布を，互いに共有する項目をもつ資料同士を隣接させて４象限に配置した。項目の語例は表５に示す。語の意味の分布は共有の有無を基に分類し３領域に分けられる：(1) 他の資料とは項目を共有せず，分野に独自に出現するもの［非共有領域，(a) (b) (c) (d)の領域（計10項目)]。(2) 共有する項目が２分野または３分野にわたるもの［部分的共有領域，(e) (f) (h)の領域（計７項目)]。(3) 全ての資料で項目を共有するもの［共有領域，(g)の10項目]。

３．１　「部分的共有領域」と「非共有領域」に属する理工系分野の語の選定基準

部分的共有領域（ｅ，ｆ，ｈ）では，互い共有する数は(e)，(f)，(h)の順で減少し，第２象限と第３象限の間では僅か１項目（仕事）のみである。ここで特徴的なのは，第１象限と第２象限の境界域には部分的共有領域が存在しなかったことである。すなわち，理工系分野は共有領域に見られる

項目以外は，おおむね非共有領域のみで分野独特の語の意味の分布を持つと言うことができる。この分野独特の語の意味の分布を持つと言う分析結果は先の分析結果[11]と同じである。

ここで，理工系分野が他の分野とは孤立した様子を示す理由について考えてみる。そのため，表１の分類を参照してカテゴリーの意味の範囲を人間活動との関係の視点から分類し直したのが表６である。［理工］の非共有領域にある「形」「力」はカテゴリーⅠ，「自然」はカテゴリーⅤで，共に人間活動との関係がない。他の分野はほとんどが人間活動と関係のあるカテゴリーで構成されている。分野ごとに非共有領域の特徴を人間活動との関係で捉えてみると，［経済］［社会］［文学］の語の意味の分布は人間活動との関係が特に密接なもの（行為者主体型）である。

表６　カテゴリーの意味の範囲と人間活動との関わり

	意味の範囲	人間活動との関わり
Ⅰ	枠組み（非人格的）	無
Ⅱ	人間活動の主体	有
Ⅲ	人間活動の様相	有
Ⅳ	生産物（活動の相手）	有
Ⅴ	外界存在物	無
Ⅵ	固有名詞(人名，国名，地名)	有

一方，［理工］の語の意味の分布は人間活動との関係が薄く，客観的事実がそのまま示されたもの（事実主体型）である。言い換えると，人間活動は通常，「意見（感情）」を含んだ記述になるが，事実主体型は「事実」のみを記述すると特徴づけられる。この分析結果は，人間活動との関係の深いカテゴリーⅡに［理工］の語が僅か６語しか出現しなかった（表２参照）ことからも確認できる。理工系分野の６語は「人々」「我々」「人」「者」「著者」「筆者」のみであり，語の意味の分布の幅が非常に狭いことが特徴であることが分かる。

以上の理工系漢字の例示語の分析から，選定基準の第１条件を次のように提案する。

選定条件１．　理工系分野の基本漢字の例示語には「事実主体型」の語を選定する。

３．２　共有領域に属する理工系の語の選定基準

共有領域の10項目は［理工］［文学］［経済］［社会］で共有されるので，理工系分野に集中する語も他の分野に集中する可能性がある。この点を検証するため，この10項目に属する［理工］の語

表７　理工系の語に重複する他分野の語

群	順			理工語	共通語	共通語の割合	
A	＜1＞	Ⅰ量	(91)	60	31	34.1%	
	＜4＞	Ⅲ心態	(49)	29	20	40.8%	
	＜2＞	Ⅰ作用	(68)	53	15	22.1%	
	＜6＞	Ⅰ空間	(28)	15	13	46.4%	
	＜7＞	Ⅰ様相	(24)	14	10	41.7%	（A全体の34.2%）
B	＜3＞	Ⅰ関係	(54)	20	34	63.0%	
	＜8＞	Ⅰ有無	(19)	7	12	63.2%	
	＜9＞	Ⅰ位置	(17)	6	11	64.7%	
	＜10＞	Ⅲ言動	(16)	6	10	62.5%	
	＜11＞	Ⅰ事柄	(14)	5	9	64.3%	（B全体の63.3%）
C	＜11＞*	Ⅰ形	(16)	11	5	31.3%	
	＜5＞*	Ⅴ自然	(36)	32	4	11.1%	
	＜13＞*	Ⅰ力	(9)	7	2	22.2%	（C全体の18.0%）
	合　計		(441)	265	176	39.9%	

が別の資料の語と重複する様相を調べた分析結果を表７に示す。比較のため，［理工］の非共有領域の３項目も加えた．＜１＞～＜13＞は語の出現順位，Ⅰ，Ⅲ，Ⅴはカテゴリー，（　）は語の実数，＊は参考に示した非共有領域の項目である。ここでは，重複する語を「共通語」，重複しない語を「理工語」と呼ぶ。

共有領域は共通語の数が理工語を下回るＡ群と，共通語の数が理工語を上回るＢ群とに分けられる。Ａ群では共通語の絶対数はＢ群の数に比べると多いが，実際にはＡ群全体に対する比率は34.2％である。一方，Ｂ群では共通語の絶対数はＡ群より少ないが，Ｂ群全体に対する比率は63.3％である。これに対して，Ｃ群は［理工］の非共有領域であり，いずれも共通語の絶対数はＡ群やＢ群より著しく少なく，しかもＣ群全体に対する共通語の比率は18％と低い。以上の分析から，共有領域に分布する語は非共有領域に分布する語に比べて，共通語の比重が高いことが分かる。

当然のことであるが，共通語は理工系分野のみならず，多分野でも頻繁に使用される語である。したがって，共有領域の語を積極的に活用することは，理工系分野の語を学習するために役立つばかりか，共通語の学習を通して読解する能力を増強できることを意味する。すなわち，基本漢字の学習では，共有領域の「関係」の項目の語（たとえば，「基本」「同様」「従う」など）は，次の例のように結合化した文型，文体学習として活用することがより効果的である。

（学習例１）基本

「基本」→　～を基本にして＋（文）　→　～に基づいて＋（動詞）　→
～に基づく＋（名詞）　→　基礎　→　……

（学習例２）同様

「同様」→　～と同様に　→　～と等しい　→　同等　→　……

（学習例３）従う

「従う」（動詞として）　→　～に従う＋（動詞）　→　～に従って＋（動詞）
→　（文.）＋従って　→　……

一般的に言えることであるが，できるだけ早い時期からこのような活用学習法で共有領域の語を学習することが漢字の読解力を増すには望ましいと考える。したがって，選定基準の第２条件を次のように提案する。

選定条件２．　理工系分野の基本漢字の例示語には異種分野での「共通性」の高い語を優先する。

４．理工系必須基本漢字テキスト作成のための語の選定基準

著者らの最終目的は科学技術専門書を読解できる能力を効率よく習得するための必須基本漢字テキストの作成にある。そのようなテキストでは，実際に学習する漢字（語）ができるだけ「日常生活語」と「理工系の語」で共通する範囲に位置する語であることが望ましい。そこで，日常語的表現形式をとる［文学］と［理工］の語を比較することにより，共通する特徴を見出し，それに基づいて理工系必須基本漢字の選定基準を検討する。

４．１　文章語的表現形式と日常語的表現形式

表８は表７の共通語の内訳を示す。Ａは理工系の語が［経済］［社会］と重複する共通語，Ｂは［経済］［社会］［文学］と重複する共通語，Ｃは［文学］とのみ重複する共通語である。表から，理工系の語の共通語はＡに最も多く，共通語全体の67.6％を占める．Ｂでは29％，Ｃでは３％にすぎない。［理工］の語が［文学］とのみ一致する６語は「働く」「通る」「入れる」「空気」「水」「書く」であり，ほとんどが日常生活で頻繁に使われる日常語的表現（日常生活語）である。

［文学］が理工系分野の語と重複しにくい理由については，宮島[12]が文章語的表現と日常語的表

表8　理工系の語と重複する共通語の内訳

順		共通語		A 理・経・社	B 理・経・社・文	C 文
＜1＞	Ⅰ量	31	:	23	8	−
＜2＞	Ⅰ作用	15	:	11	1	3
＜3＞	Ⅰ関係	34	:	28	6	−
＜4＞	Ⅲ心態	20	:	14	6	−
＜5＞	Ⅴ自然	4	:	1	1	2
＜6＞	Ⅰ空間	13	:	10	3	−
＜7＞	Ⅰ様相	10	:	6	4	−
＜8＞	Ⅰ有無	12	:	9	3	−
＜9＞	Ⅰ位置	11	:	3	8	−
＜10＞	Ⅲ言動	10	:	7	2	1
＜11＞	Ⅰ形	5	:	3	2	−
＜12＞	Ⅰ事柄	9	:	4	5	−
＜13＞	Ⅰ力	2	:	−	2	−
	合計	176	:	119（67.6%）	51（29%）	6（3%）

現を区別している観点，つまり「文章語的表現は，公的な場で使われるということであり，その使用場面に応じて，表す対象も大規模なもの，公的なものに偏り易くなる」ことから理解できると考えている。このことは，日常生活語では「手紙」「道」「運ぶ」を使用するが，文章語的表現では「書簡」「道路」「運搬」を使用することからも理解できる。

したがって，このような重複し難い条件の中でも敢えて重複している共通語は，理工系の必須基本漢字として採用しなければならない語と言える。そこで，選定基準として次の選定条件3を提案する。

選定条件3．　理工系の意味の分布の範囲にある語が日常生活語と共通する場合，これを優先的に理工系分野の基本漢字の例示語にとして採択する。

4．2　テキスト作成のための［文学］に属する語の役割

日常生活語と理工系の語で共通する語を効果的に選定するには，日常生活語の意味の分布が多い資料（［文学］など）の分析結果を活用することが有効である。たとえば，「作用」の項目では，「変化」「接触」「減少」「増加」の語（文章語的表現）が属する。これらの語を理工学系の共通語として取り上げるには，それらの代替語である日常生活語，「変わる」「触れる」「減る」「増える」の出現頻度を調査する必要がある。何故ならば，［文学］のような日常生活を反映する資料の中に，これらの語の分布が多く見られれば，日常生活語として使用頻度の高いものであると言えるからである。実際に，著者らが行った今回の計量的分析では，［文学］では，「変わる」「触れる」「減る」「増える」はそれぞれ64位，300位，234位，276位であり，いずれも上位500位までに出現していた。

［文学］に日常生活語が多出することは，非共有領域や部分的共有領域でも同様である。実際に，［社会］の項目には「世界」「大学」「会社」「病院」などの語が，「住居」の項目には「部屋」「台所」「階段」などの語が上位に出現する。すなわち，日常生活語の採択に関しては，［文学］での出現頻度と，それがどのような意味の分布範囲に属するかの2要素を考慮することが選定基準となる。しかしながら、日常生活語の範囲は広く，どれを日常生活語と考えるかは個々人の考えや環境で大きく異なり，定量的基準はない。現時点では，著者らは客観的かつ適切に日常生活語を選定する工程としては，上述した理工系分野で非共有領域の語に対する選定基準と同様な選定基準を［文学］な

どの日常生活語の出現が多いものにも適用することが望ましいと考える。そこで日常語の範囲から必須基本漢字を選定するための選定基準として，次の条件を加える。

選定条件４． 資料［文学］の非共有領域および部分的共有領域に意味の分布が集中している語は，日常生活語として可能な範囲（数的）で優先的に理工系分野の必須基本漢字の例示語として選定する。

５．選定条件を活かした実際例

著者らの調査した初級者用漢字テキスト（別表）中には，日常生活語としてもほとんど使用しない「牽牛」「猿楽」「羽毛」が例示語となっている。また，漢字「金」の例示語には，「金魚」「金庫」「金色」「金曜」「借金」「料金」などはある。ところが，理工系分野の上位90％（漢字数200万の計量調査で累積頻度90％）以内に出現する「金属」「白金」「合金」は採用されていない。これらの出現順位は著者らの今回の調査では，110位，670位，835位である。出現頻度だけで例示語を選定した場合，上位500位から外れる「白金」と「合金」は例示語から削除される可能性がある。しかし，著者らが提案する必須基本漢字の選定基準を適用すると，上述した語は「選定条件１」を満足しており，例示語に採択することができる。以上の説明から，例示語の選定基準には，語の出現頻度と，その語の意味の分布の２要素を考慮するのが重要であることが明確であろう。具体的に言うと，理工系必須基本漢字として漢字「金」を学ぶ場合，［初級］にある「借金」「資金」「頭金」などの語に代えて，「金属」「白金」「合金」などを例示する漢字学習法の方がより効率的かつ効果的である。

表９　漢字「子」の例示語

A［理工］
(01)電子＜0011＞Ⅴ② (02)分子＜0020＞Ⅴ② (03)原子＜0029＞Ⅴ②
(04)粒子＜0101＞Ⅰ⑨ (05)格子＜0122＞Ⅴ② (06)量子＜0322＞Ⅴ②
(07)因子＜0529＞Ⅰ② (08)素子＜0682＞Ⅴ② (09)端子＜0809＞Ⅴ②
(10)様子＜1145＞Ⅰ④ (11)陽子＜1167＞Ⅴ② (12)振子＜1229＞Ⅳ②
(13)光子＜1707＞Ⅴ②

B［経済］
(01)利子＜1707＞ (02)電子＜1110＞

C［社会］
(01)息子＜0102＞Ⅱ② (02)子供＜0241＞Ⅱ① (03)男子＜0256＞Ⅱ①
(04)養子＜0336＞Ⅱ② (05)子孫＜0347＞Ⅱ② (06)親子＜0750＞Ⅱ②
(07)子弟＜0934＞Ⅱ② (08)弟子＜1005＞Ⅱ⑤ (09)女子＜1035＞Ⅱ①
(10)末子＜1275＞Ⅱ②

D［文学］
(01)子供＜0035＞Ⅱ① (02)様子＜0214＞Ⅰ④ (03)調子＜0363＞Ⅰ④
(04)息子＜0407＞Ⅱ② (05)椅子＜0520＞Ⅳ⑤ (06)硝子＜0528＞Ⅳ②
(07)帽子＜0947＞Ⅳ③ (08)菓子＜1022＞Ⅳ④ (09)障子＜1079＞Ⅳ⑤
(10)梯子＜1359＞Ⅳ⑤

E［初級］
花子　紀子　秋子　春子　雪子　道子　洋子　礼子　真理子
子牛　子馬　玉子
王子　子息　女子　息子　男子　子孫　弟子
帽子　椅子　帽子　羽子板
利子　原子　調子

次に，提案した「選定条件１～４」を適用して，実際に例示語の選定を試みる。［初級］の全てに採用されている漢字「子」は［理工］でも多出し，今回の調査では５位の出現頻度である。漢字「子」の例示語を10語とした場合の選定する工程を表９を用いて説明する。（　）は番号，＜　＞は出現頻度，Ⅰ～Ⅴはカテゴリー，○で囲んだ数字はカテゴリー内の項目である。まず，「選定条件３」から［理工］と［文学］の共通語として「様子」④，「選定条件２」から［理工］と［経済］または［社会］の共通語として「電子」の２語が選定できる。次に，「選定条件１」から非共有領域の項目に該当する語として，「分子」「原子」「粒子」「格子」「量子」「素子」「端子」「陽子」「振子」「光子」の10語が選定できる。この提示例では例示語を10語に限定しているので，頻度による出現順位を参考にすると，［分子」「原子」「粒子」「「格子」「量子」の５語が選定できる。最後に，「選定条件４」を満足するものとして，［文学］の非共有領域および部分的共有領域から，「子供」「息子」「調子」の３語が選定できる。

以上から，理工系必須基本漢字テキストの学習漢字に例示する10語は以下のようになる。

電子　分子　原子　粒子　格子　量子　子供　息子　様子　調子。

これらを表中の㊄［初級］と比較してみる。［初級］では「子」の多くが名前を示すものとして扱われている。その他の例示語では，語の選定基準が客観性に欠けている。こうした選定基準の不明確さが，学習者の側からは，「子」の持つ意味が把握し難く，未知語への類推に困難を感じることになっている。これに対し，著者らの提案する選定基準を適用すれば，選定した例示語からは「子」が，何かある小さな加算可能なもの（生物，または無生物）を意味すると同時に，何かある状態の様相を意味する語であることが理解でき，未知語に遭遇したときにその類推から理解を助けることが期待される。

お　わ　り　に（残された今後の課題）

本稿では，例示語を選定する場合，語の出現頻度と語の意味の分布傾向から選定基準を定めることが有効であり，漢字学習の効率を高めることを述べた。しかし，図１に示したようにカテゴリーⅥ（人間活動の生産物）に語の意味の分布傾向が顕著には現れなかったことは，抽出資料の選定が完璧でなかった，つまり今回の資料は適切な抽出資料ではなかったと言う原因以外にも，提案した選定基準にはまだ検討されていない要素があることを示唆する。この点を検討してみる。

外界は人間が作り出した物やそのために利用する物，すなわち，カテゴリーⅥに該当する「人間活動の生産物」で構成されている。にもかかわらず，著者らの今回の調査では，カテゴリーⅥは［文学］の非共有領域に「住居」のみが見られるだけであった（図１参照)。しかし，実際の語を調査する限り，［理工」に出現する「材料」「容器」「機械」，［文学］に見られる「着物」「道具」「電車」，［経済］の「商品」「製品」「食料」などは，日常生活語と言って良いものばかりである。これらの語は，ある物を個々に具体的に表現する個別的な語であると分類するよりは，個々の語をまとめた総体としての呼び名として捉えられる語である。これを「総称」と名付ける。「総称」については，上位・下位概念をどのように規定するのかによって，多くの解釈がある[13~15]。ここでは「総称」を「個々の呼び名のまとまり」として認識できるという意味にのみ限定して使用する。

このような「総称」は，個々のものの個別的な名前を知らない留学生にとっては便利なものである。実際に，著者らが行った漢字に関する実態調査では，留学生の多くがこれらの総称の中に属する語を「すぐに思いつく語」として回答している[10]。現在のところ，一律に選定基準を設けて機械的に選定することが難しいカテゴリーⅥの語の例示語の選定については，すべての語に対して経験や勘だけに頼った選定をする場合が多い。それならば，多少面倒になるが，出現頻度に注目し，上位にある語で，語の「総称」と呼べるものは，できるだけ選定語として採択するような人為的な処置が最良の解決策であると考える。現時点では，このような人為的な配慮の必要がカテゴリーⅥに限られるという不完全さはあっても，著者らの提案した選定条件を適用した選定工程を行うことは

効果的に適切な必須基本漢字を選定できる言える。

理工系分野の語の意味の分布の幅は狭い。筆者らの提案するような選定方法を採用した必須基本漢字を活用すれば，日常語と理工語を比較的早い時期から同時に習得することが可能になることが期待される。良い漢字テキストの作成にあたっては，例示語の選定時に主観に頼る部分が少ない方が望ましい。適切な例示語を客観的に選定するには，語の意味の分布の特徴をできる限り定量的に，かつ機械的に選定処理できる方法を構築する必要がある。著者らの提案した選定条件はこの要求を十分に満たしており，この方法を採用すれば，かなり高い精度で適切な例示語が学習語として選定できることが期待できる。今後，この結果を実際の基本漢字テキストの作成に活用していきたい。

文　　献

1）国立国語研究所：現代雑誌90種の用語用字　第一分冊，国研報告，21（1962）.

2）国立国語研究所：現代雑誌90種の用語用字　第一分冊，国研報告，22（1963）.

3）国立国語研究所：『分類語彙表』，秀英出版（1964）.

4）武田明子：科学技術日本語テキストにおける基本漢字の分析－理工系大学院留学生の専門書読解のために，計量国語学，19 (2)，(1993) 61-69.

5）武田明子：松下国際財団報告書，(1994) 1 -252.

7）武田明子：松下国際財団報告書，(1995) 1 -152.

8）武田明子・入戸野修：日本語科学技術文献読解のための効率的漢字学習法に関する実証的研究，日本科学教育学会20周年記念論文集，(1996) 373-384.

9）武田明子・入戸野修：学習者のニーズに応える漢字習得法の考察，日本教育工学学会第12回全国大会，(1996) 99-100.

10）武田明子・入戸野修：科学技術文献読解のための漢字指導法の見直し，科学教育研究，21 (4)，(1997) 1 - 9 .

11）入戸野修・武田明子：留学生に対する科学技術専門書読解のための教科書作成に向けて（化学工学における専門日本語漢字），福島大学地域創造，14 (2)，(2002) 77-87.

12）宮島達夫：語彙の体系，『講座日本語９』，(岩波書店．1977) 1 -42.

13）荻野綱男：シソーラスのための語彙の意味分類をめぐって－「焼き魚」は魚かー，日本語学，(1993) 18-30.

14）景浦　峡：専門用語のシソーラスー情報検索用シソーラスにおける専門用語および概念の分類と組織化－，日本語学，(1992) 11-18.

15）玉村文郎：日本語における漢字－その特質と教育－，日本語教育，80 (1993) 1 -14.

［別表］ 分析に使用した資料

(a) 理工学関係の資料

01　解析概論［1］　小松勇作著　廣川書店　(1983)

02　古典熱力学　上・下　物理学叢書11　ゴールドシュタイン著（瀬川富士夫ら訳）　吉岡書店　(1990)

03　化学熱力学　原田義也著　裳華房　(1992)

04　非線形関数解析学－不動点定理とその周辺－　現代数学ゼミナール７　高橋渉著　近代科学社　(1988)

05　複素解析入門　基礎数学叢書９　阪井章著　新曜社　(1993)

06　基礎材料工学　渡邊慈ら著　共立出版　(1987)

07　工学基礎　材料科学　坂田亮著　培風館　(1978)

08　固体の力学　中沢一ら著　養賢堂　(1991)

09　機器分析の手引き　泉美治ら監修　東京化学同人　(1992)

10　バーロー物理化学　上・下　バーローら著（藤代亮一訳）　東京化学同人　(1992)

11　モリソン／ボイド有機化学　上・中・下　モリソンら著（中西ら訳）　東京化学同人　(1992)
12　化学工学演習　藤田重文編　東京化学同人　(1988)
13　工学基礎　電気工学　雨宮好文著　倍風館　(1991)
14　機械振動学通論　入り江敏博著　朝倉書店　(1987)
15　熱力学概論　森康夫ら著　陽賢堂　(1989)
16　フィードバック抑制の基礎　片山徹著　朝倉書店　(1987)
17　経営工学シリーズ4　確率・統計　田淵玄一ら著　日本規格協会　(1981)
18　コンピュータの理論設計　マノ著（奥川峻史ら訳）　共立出版　(1983)
19　大学講義　最新電気機器学　宮入庄太著　丸善　(1979)
20　森北電気工学シリーズ4　半導体工学－半導体物性の基礎－　高橋清著　森北出版　(1988)
21　情報と符号の理論　宮下洋ら著　岩波書店　(1983)
22　制御基礎理論－古典から現代まで－　中村道男ら著　昭晃堂　(1982)
23　計画のための最適化数学　熊田禎宣ら著　井上書院　(1987)
24　都市計画教科書　都市計画教育研究会編　彰国社　(1987)
25　測量学　中村英夫ら著　義報堂出版　(1981)
26　バーロー生命科学のための物理化学　バーロー著（野田晴彦訳）　東京化学同人　(1983)
27　物理化学実験法　様島実三郎著　裳華房　(1992)
28　基礎無機化学　戸田不二緒著　講談社　(1992)
29　生物工学基礎　戸田不二緒著　講談社サイエンティフック　(1988)

(b)　人文・社会学関係資料
30　現代経済学入門　本間幸作編著　新評論社　(1986)
31　社会人類学－アジア諸社会の考察－　中根千枝著　東京大学出版会　(1987)

(c)　文学作品
32　日本の短編60　上・下　井上靖ら編　文藝春秋　(1989)

(d)　初級用漢字教科書
33　基本漢字500　Vol.1・2　加納智恵子ら著　凡人社　(1992)
34　新日本語の基礎漢字練習帳　Ⅰ・Ⅱ　鶴尾能子ら著　スリーエーネットワーク　(1993)
35　日本語初歩　川瀬生郎ら著　凡人社　(1986)

研究留学生に対する科学技術専門書読解のための漢字記述語の分析

—化学工学における漢字を含む語—

入戸野　修・武田明子

福島大学地域創造 第15巻 第２号（2003. 12）

福島大学地域創造支援センター

研究ノート

研究留学生に対する科学技術専門書読解のための漢字記述語の分析

—化学工学における漢字を含む語—

入戸野　修・武田明子

目　次

はじめに
1．「化学工学論文集」に多出する漢字を含む語の特徴
2．品詞ごとに見た語の特徴
3．分析結果の総括と漢字学習法の提案
おわりに

はじめに

前報（入戸野・武田 2002）で著者らは，化学工学を専攻する留学生の場合を例にとり，専門書の読解に役立つ漢字の特徴を分析した。化学工学分野を取り上げのは次の理由による：『マグローヒル科学技術用語大辞典（第3版 1996)』では，化学工学は「化学工業プラントの設計，運転およびそれに必要な装置を取り扱う学問であり，すべての工業製品は，広範囲な条件で起こる化学反応を含む化学的なプロセスで作られ，しばしば物理的な状態または形の変化を伴う」と説明されている。また，同辞典によると，物理は「基本原理や基本法則を理解できる自然の様相の研究」であり，応用数学は「物理現象の応用から生まれた学問」であり，工学は「物質の性質や動力源を，建造物，機械，製品として役立たせるようにする学問」であると説明されている。つまり，化学工学分野には物理，数学，化学，工学といった自然科学系の学問分野がすべて含まれており，自然科学系の広範囲の分野の語を含む「理工学分野」全般の代表的分野であるからである。前報では，抽出した漢字の学習指導法の基本方針について，先に報告した著者らの研究結果（1997①～④）も考慮に入れて考察した。その結果，日本語の科学技術書を読解したいと言う目的を持った研究留学生に対して，基本を押さえた効率的なテキストによる漢字学習を行えば，比較的短期間に専門書の読解が可能になることが期待されることを示した。

では，どのような語を通して基本的な漢字を学習すればよいのだろうか。この問題を解決する一つのアプローチとして，著者らは，理工系分野の留学生が漢字を学ぶときに提示する例示語の選定基準を提案した（入戸野・武田 2003)。その結果，基本漢字を実用に供するにはいくつかの検討すべき問題が残っており，その一つに多出する漢字から構成されている語（漢字を含む語）を抽出して，その特徴を分析する必要があることを指摘した。さらに，文字の羅列でしかない漢字だけを学習しても駄目で，個々の漢字が組み合わさってどのような語として文章の中で使用されているのか，その特徴を把握し，それを実際の語として示すことができなければ読解力の増強にはならないであろうと述べた。

本稿では，留学生の専門書読解力を伸ばすには，適切な漢字が適切な学習用語として示されてはじめて可能となるという前提に立って，多出する漢字を含む語の特徴を化学工学分野を中心に分析する。分析資料は，前報（2002）と同じく「化学工学論文集」，「現代経済学入門」，「社会人類学」，「日本の短編」，「理工」（著者の一人が行った理工系分野の専門書29冊の分析結果（武田 1994①②））である。これらの資料は前報（2002）と同様に，文中ではそれぞれを＜化工＞＜経済＞＜社会＞＜文学＞＜理工＞と記述し，表中では「化」「経」「社」「文」「理」と表記する。分析で使用した使用度数分布等の定義と表示は前報（2002）と同じである。注意すべき点は，本稿で取り扱う語の分析は「漢字を含む語」に限ることであり，平仮名または

カタカナ表記だけのものは含まれていない。

１.「化学工学論文集」に多出する漢字を含む語の特徴

(1)　語の抽出基準

今回対象とした語は以下の規則により抽出し分析した。

１）漢字１字からなる語は基本形で抽出する。
　例：大きくなる　→　大きい
　　書いてみる　→　書く

２）漢字３字以上の語で漢字２字で意味のある語に分けられるときは分けて抽出する。
　例：熱交換　→　熱／交換
　　圧縮応力　→　圧縮／応力
　　一般的　→　一般／的
　　統計学的手法　→　統計／学／的／手法

３）漢字２字からなる動作性名詞と形容動詞は漢字だけ抽出する。
　例：規定する　→　規定
　　簡単な　→　簡単

４）一つ，何れ，相まってなど，漢字１字と平仮名からなる語は，今回の分析では「その他」の項として分類する。

５）漢字１字に平仮名のつく副詞句はそのまま抽出する。
　例：既に　→　既に
　　特に　→　特に
　　現に　→　現に

６）複合動詞はそのまま基本形で採用する。
　例：溶け始めて　→　溶け始める
　　取り除きつつ　→　取り除く

７）常に決まった規則で名詞や形容詞を作るものは２つに分けて抽出する。
　例：作り方　→　作る／～方
　　作り易い　→　作る／～易い

８）助動詞的役割を果たすものやテ形補助動詞に類するものは２つに分けて抽出する。
　例：考え得る　→　考える／～得る
　　分かって来る　→　分かる／～来る

９）送りがなは統一して抽出する。
　例：表す／表わす　→　表す

(2)　出現する語の一般的特徴

表１は「化学工学論文集」(2000年第１巻～６巻）に出現した漢字（延べ語数380,560字，異なり語数1,501字）を使用した語の使用度数分布を表わす。

表１　『化学工学論文集』（化工）に出現する漢字を含む語の使用度数分布

	異なり語数	異なり語累計	延べ語数	延べ語数累計
10%	12	12	23,582	23,582
20%	20	32	23,473	47,055
30%	30	62	23,259	70,314
40%	45	107	23,053	93,367
50%	69	176	23,416	116,783
60%	98	274	23,130	139,913
70%	147	421	23,405	163,318
80%	248	669	23,279	186,597
90%	515	1,184	23,191	209,788
100%	3,867	5,051	23,298	233,086
			(平均) 23,309	

＜化工＞に出現する1,501字の漢字は5,051の語を構成するものとして分析されていることが分かる。表１の異なり語の10%毎の増加数は，累積百分率が40%になるまでは50語以下だが，50%で増加し60%ではほぼ100語，それ以上では10%毎の増加語数は加速度的に増加し，累積百分率が81～90%の間で515語，91～100%では3,867語となっている。これを異なり語の累計数でみると，107語で全出現語の40%に達するが，60%に達するにはその2.6倍の数（274語）が，80%に達するには6.3倍の数（669語）が必要である。

一方，延べ語数の10%毎の語数は，いずれも平均値（23,309語）から大幅に外れていない。累積百分率が10%までの語の延べ語数が最も多い（23,582語）ことを考慮すると，出現回数の多い上位語が読解作業に及ぼす影響が大きく，上位と下位との１語では「語の重要度」に大きな違いがあることが推測される。

この推論を検証するために，累積百分率の10%毎に存在する１語が持つ「語の重要度」を分析したのが表２である。ここで，「ポイント」は表１の累積百分率の10%毎の延べ語数をそのときの異なり語数で除した数値（たとえば，10%では23,582/12＝1,965），「全体に占める割合」はポイントをその総語数（5,303）で除した数値の百分率である。累積百分率40%までのポイントが全体の83.8%（37.1＋22.1＋14.6＋10＝83.8）を占めており，累積百分率40%を越すと，全体に占める割合は極端に少なくなり，90%を超えている語はゼロに等しいことが分かる。この分析結果と表１の結果

を合わせると，累積百分率40%までの107語が習得できれば，＜化工＞の読解が容易になるが，累積百分率が91～100%の間に出現する3,867語を学習しても，労力に比して読解作業への貢献は少ないと言うことができる。つまり，漢字読解作業を考えると，上位語の重要度が高いことが分かる。

表２　累積百分率10%毎にみた１語が持つ語の重要度

累積百分率	ポイント（延べ数：5303）	ポイントが全体に占める割合(A)	(A)累計
10%	1,965	37.1%	37.1%
20%	1,173	22.1%	59.2%
30%	775	14.6%	73.8%
40%	512	10.0%	83.8%
50%	339	6.4%	90.2%
60%	236	4.5%	94.7%
70%	159	3.0%	97.7%
80%	93	1.8%	99.5%
90%	45	0.8%	100.3%
100%	6	0.1%	100.4%

表３は＜化工＞に出現した5,051語を品詞別にまとめた結果である。表中の「１字漢字語」とは具体的には漢字１字で名詞となるものであり，形容詞や動詞などの他の品詞は含まれていない。ただし，接頭辞と接尾辞は含まれている。「２字漢字語」は漢字２字からなる語（主に漢語）であり，この中には名詞，動作性名詞（表ではサ変），形容動詞（表では形動）を一括して分類している。「形容詞」は漢字１字＋「い」のいわゆる「イ形容詞」であり，「３字漢字」は漢字が３字連なって１語を形成しているものである。「その他」は以上の分類に含まれなかったものである。

表３　＜化工＞に出現した5,051語の品詞語内訳

１字漢字語	469	(9.2%)
２字漢字語	3,792	(75.1%)
名詞	2,525	
サ変	1,138	
形動	129	
動詞	615	(12.2%)
形容詞	65	(1.3%)
形容動詞	15	(0.3%)
副詞	41	(0.8%)
３字漢字	18	(0.4%)
その他	36	(0.7%)

表３では，２字漢字語として出現する語の全体に占める割合が総語数の75%を占めている。２字漢字語の多くは漢語名詞であり，モノ名やコト名を表す重要な役割がある。また，その中に含まれるサ変動詞は動詞としての働きを，形容動詞は形容詞としての働きを併せ持つ特徴があるから，これらの語も無視できない。

(3)　＜化工＞と他分野の上位語の比較

表４は＜化工＞に多出する上位107語が他の資料の上位107位までに入っているかどうかを調べた結果である。＜化工＞に出現した語が，＜理工＞＜経済＞＜社会＞＜文学＞の全てに出現した場合を「４資料に出現」，いずれか３資料に出現した語を「３資料に出現」，２資料に出現した語を「２資料に出現」，１資料に出現した語を「１資料に出現」として記述している。また，「化工のみ出現」は＜化工＞では上位107位までに出現している語であるが，他資料ではそれ以下の順位で出現しているか，あるいは語が出現しなかったものである。

分析結果は，分野を狭める，つまり重なる資料数が少ないと資料間で重なる語も多くなることを示す。「３資料に出現」と「２資料に出現」の計22語のうち，１語を除いた21語が＜理工＞と重なっている。これは，＜化工＞が理工系の学問分野に属していることから当然と言える。同じのことが，「１資料に出現」の43語のうち，37語が＜理工＞と重なっていることについても言える。分野を狭めると重なる語も多くなるということは，それぞれの分野に特徴的な語が存在することを意味しており，分野に多出する語を抽出することがその分野を理解するのに有効であることを示唆する。ところで，＜化工＞に出現した語が「４資料全てに出現」する数が３語と極めて少ない。このことは，＜化工＞に出現する語が特異であるという理由からではなく，単に，分野に関わらず使用される語は元来あまり数多くないためであろうと考えている。

しかしながら，「３資料に出現」と「２資料に出現」の計22語のうち，＜経済＞と重なる語が15語，＜社

表４　＜化工＞に多出する107語が他の資料の多出語として出現する数

４資料に出現【３語】	
３資料に出現【10語】	理経社(７語)　理経文(２語)　理社文(１語)
２資料に出現【12語】	理経　(５語)　理社　(４語)　理文　(２語)　経社(１語)
１資料に出現【43語】	理　(37語)　経　(２語)　社　(２語)　文　(２語)
化工のみ出現【39語】	

会＞と重なる語が13語であり，どちらも半数以上の数が＜化工＞と重なっている。＜文学＞が＜化工＞と重なる語が５語であることと比較すると，＜理工＞＜経済＞＜社会＞はすべて「専門書」の範疇に属するので，互いに共通する特徴があるためと推測できる。この傾向は前報の結果と極めて類似している（入戸野・武田2002）。

以上の結果をまとめると，専門書読解という目的を達成するためには，留学生の目的に適う研究分野に合った使用頻度の高い語を，「専門分野の語」と「専門書一般の語」の両側面を考慮して抽出し提示することが，学習効果が期待できる効率的な漢字学習であると言うことができる。

(4)　上位語の特徴

ここでは，累積百分率の上位の語だけで効果的で効率よい漢字読解学習ができるかどうかを検討する。表５は表４の内容を実際の語で示した。

「４資料に出現」した語は「的」，「間」，「大きい」の３語である。「的」は様々な漢語名詞や外来語に付加されて，名詞を形容動詞化したり，他の名詞と結合したりする接尾辞として使用されるので，どの分野でも出現する可能性が高くなったと考えられる。同様に，「間」も位置関係や期間を示す語として分野に偏らないものであり，「大きい」も本来の意味「物の面積や体積，あるいはものごとの規模や範囲などが他のものに比べて上回っている状況を示す」（例解国語辞典第３版）だけでなく，数値，年齢，程度などが他に比べて上（以上）であることを示す語として，分野に関係なく出現したと言える。

表５の上位107語を品詞別に分析すると，２字漢字語が58語（54.2%），１字漢字語が36語（33.6%），動詞が10語（9.3%），形容詞が３語（2.8%）である。表中の１字漢字語もまた名詞の類であることを考慮すると，107語中の87.8%までが名詞となる。この分析結果は表３の一般的傾向と矛盾しない。しかしながら，この数値が＜化工＞に特徴的に現れたものでないことは，『図説日本語』（林大編 1982）の調査（辞典の見出し語の73%が名詞である）でも同様な結果が得られていることから推測できる。名詞が多用されると言うこの特徴は，情報を伝達する手段としての文章に一般的な傾向と言えよう。しかしながら，一般的に文章は２字漢字語の名詞だけでは完成しない。

当然なことであるが，名詞も述部には成り得るが，文の完成には「ナニガ　ドウシタ」と言った動作や，「ナニガ　ドンナデアル」と言った状態を示す語（述部語）もなくてはならない。したがって，多出語であるという理由で，名詞ばかりを学習語として取り上げると，述部を欠いた不完全な漢字読解学習にな

表５　＜化工＞の上位107語と重なり合う他資料の語*

４資料に出現【３語】		：	的　間　大きい
３資料に出現【10語】	理経社（７語）	：	性　化　場合　関係　以上　行う　対する
	理経文（２語）	：	中　物
	理社文（１語）	：	考える
２資料に出現【12語】	理経　（５語）	：	量　率　系　変化　必要
	理社　（４語）	：	点　構造　形成　方法
	理文　（２語）	：	水　小さい
	経社　（１語）	：	高い
１資料に出現【43語】	理　（37語）	：	値　式　法　液　数　熱　各　器　型　内　体　度 反応　粒子　結果　濃度　温度　速度　測定 時間　計算　条件　係数　表面　分布　制御 分子　状態　平均　平衡　金属　方向 示す　用いる　得る　求める　表す
	経　（２語）	：	分　増加
	社　（２語）	：	研究　比較
	文　（２語）	：	後　時
出現なし（化工のみ）【39語】		：	本　層　比　膜　高　剤　約　径　相　部 実験　燃焼　抽出　混合　影響　生成　流動 解析　重合　検討　酸化　装置　以下　可能 吸着　空気　分解　成分　特性　効果　減少 領域　加熱　密度　火炎　活性　分離　発生 関する

＊例示は多出順ではない。

る恐れがあることは注意しておきたい。

今回の分析では，類似する性質を示す語がほぼ同じ割合で多出するという必然性は見出されなかった。たとえば，「大きい」が４分野に出現するのに，類似する性質を示す語「小さい」は，＜理工＞と＜文学＞の２分野だけに出現している。同類の語が上位語として出現しないのであれば，少数の上位語だけの例示語を学んでもそれ程役立たないと言える。この傾向が何に原因するのか解明することは漢字読解学習のためには重要な意義があるが，現時点では不明で解析できていない。この点については今後の課題である。

２．品詞ごとに見た語の特徴

前報（2002）では，＜化工＞に多出する上位284の漢字が全出現漢字の80%を超えることを示した。今回抽出した＜化工＞の5,051語については，上位の多出漢字が多様に組み合わさって化学工学分野の語を構成している結果を示していると考えている。このことは，２字漢字語のそれぞれを独立に教えなくても，造語力の高い漢字を選択し他の２字漢字語の意味の類推が容易になるような２字漢字語を意識的に選別して提示することで，学習効果が上げられることを示唆する。このように考えれば，上位の２字漢字語が多数存在するために，結果的に下位順位になった動詞や形容詞の語，いわゆる用言についても分析する必要があると言えよう。

表６は＜化工＞および他の分野に多出する上位語から品詞別に抽出し，その上位20位までを示したものである。ただし，名詞は漢字１字のものを１字漢字語，漢字２字からなるものを２字漢字語と区別してある。表中では，品詞は(1)と(2)の対で示されている。(1)は＜化工＞に出現する上位20語が他の分野にも出現したもの，また，(2)は他の分野と重ならなかった＜化工＞の語，および他の分野で＜化工＞には出現しなかった語である。表中の番号１～20は＜化工＞の20語につけた番号である。ただし，＜化工＞の語が他の分野と重なり合うかどうかに注目して並べたので，番号は多出順位を示さない。たとえば，１字漢字語では＜化工＞の１～14番までの語が他の分野と重なることのある語であり，残りの15～20番までの６語が重ならない語である。

以下に，上位20位までの品詞について理工系に関わる視点からその特徴を分析する。

表６　＜化工＞に出現する語と他資料の比較

①　１字漢字語

	化	理	経	社	文
(1)	＜化工＞と重なる語				
1	間	間	間	間	間
2	化	化	化	化	
3	性	性	性	性	
4	的	的	的	的	
5	量	量	量		
6	中	中			中
7	系	系			
8	式	式			
9	水	水			
10	数	数			
11	値	値			
12	熱	熱			
13	物	物			
14	率		率		

	化	理	経	社	文
(2)	＜化工＞と重ならない語				
15	液	上	第	第	上
16	後	図	年	年	何
17	層	表	者	者	顔
18	比	線	国	国	今
19	法	形	制	制	気
20	膜	次	一	家	家
		点	億	私	私
			万	人	人
			円	方	方
			財	点	声
			税	学	前
			費	氏	男
			総	諸	女
			力	族	彼
				村	眼
				町	手
					時
					日

② 形 容 詞

(1) <化工>と重なる語

	化	理	経	社	文
1	強い	強い	強い	強い	強い
2	近い	近い	近い	近い	近い
3	高い	高い	高い	高い	高い
4	小さい	小さい	小さい	小さい	小さい
5	新しい	新しい	新しい	新しい	新しい
6	多い	多い	多い	多い	多い
7	大きい	大きい	大きい	大きい	大きい
8	広い	広い	広い	広い	
9	少ない	少ない	少ない	少ない	
10	著しい	著しい	著しい	著しい	
11	低い	低い	低い	低い	
12	長い	長い		長い	長い
13	深い		深い	深い	深い
14	速い	速い	速い		
15	等しい	等しい	等しい		
16	短い	短い			短い
17	薄い	薄い			
18	良い		良い		

(2) <化工>と重ならない語

	化	理	経	社	文
19	厚い	弱い	安い	弱い	晴い
20	遅い	詳しい	激しい	詳しい	遠い
		正しい	厳しい	悪い	悪い
		望ましい	乏しい	遠い	黒い
			難しい	古い	赤い
				濃い	白い
				親しい	細い
					若い
					早い
					美しい

③ 副　　詞

(1) <化工>と重なる語

	化	理	経	社	文
1	既に	既に	既に	既に	既に
2	更に	更に	更に	更に	更に
3	再び	再び	再び	再び	再び
4	最も	最も	最も	最も	最も
5	少し	少し	少し	少し	少し
6	全く	全く	全く	全く	全く
7	特に	特に	特に	特に	特に
8	必ず	必ず	必ず	必ず	必ず
9	決して	決して	決して	決して	決して
10	単に	単に	単に	単に	
11	常に	常に	常に	常に	常に
12	共に	共に		共に	共に
13	何ら		何ら	何ら	何ら
14	極めて	極めて		極めて	
15	直ちに	直ちに		直ちに	
16	殆ど	殆ど			殆ど
17	予め	予め			
18	即ち	即ち			
19	全て		全て		
20	但し		但し		

(2) <化工>と重ならない語

	化	理	経	社	文
		徐々に	徐々に	徐々に	恐らく
		故に	仮に	遂に	遂に
		未だ	実に	実に	未だ
			初めて	初めて	初めて
			極く	因みに	何とか
			絶えず		絶えず
					何となく

④ 動　詞

(1) <化工>と重なる語

	化	理	経	社	文
1	考える	考える	考える	考える	考える
2	異なる	異なる	異なる	異なる	
3	関する	関する	関する	関する	
4	含む	含む	含む	含む	
5	行う	行う	行う	行う	
6	述べる	述べる	述べる	述べる	
7	対する	対する	対する	対する	
8	得る	得る	得る	得る	
9	生じる	生じる	生じる		
10	求める	求める	求める		
11	示す	示す	示す		
12	与える	与える	与える		
13	加える	加える			
14	表す	表す			
15	用いる	用いる			

(2) <化工>と重ならない語

	化	理	経	社	文
16	及ぼす	呼ぶ	呼ぶ	限る	感じる
17	調べる	知る	働く	知る	知る
18	分かる	書く	占める	占める	帰る
19	比べる	使う	買う	使う	居る
20	現れる	入れる	伴う	出る	出る
			達する	入る	入る
			決まる	属する	出す
			増える	分ける	思う
				受ける	死ぬ
				結ぶ	持つ
				住む	言う
				思う	笑う
					聞く
					行く
					歩く
					来る
					立つ
					見る
					見える

⑤ 2字漢字語

(1) <化工>と重なる語

	化	理	経	社	文
1	場合	場合		場合	
2	温度	温度			
3	条件	条件			
4	測定	測定			
5	速度	速度			
6	反応	反応			
7	変化	変化			
8	時間				時間

(2) <化工>と重ならない語

	化	理	経	社	文
9	影響	関係	支出	関係	仕事
10	計算	関数	消費	機能	生活
11	研究	結合	生産	構成	学校
12	混合	制御	投資	組織	学生
13	実験	存在	労働	血縁	気持
14	生成	原子	企業	構造	言葉
15	抽出	気体	社会	社会	子供
16	燃焼	状態	価格	集団	自分
17	係数	定理	経済	人口	叔父
18	粒子	電子	国債	人類	少年
19	濃度	分子	国民	成員	新聞
20	結果	必要	産業	全体	人間
		一般	市場	村落	相手
			資本	父系	電車
			需要	文化	彼女
			収支	民族	病院
			所得	階層	部屋
			商品	学者	母親
			政府	家族	老人
			貿易		

(1)　1字漢字語の特徴（表6①）

はじめに，5分野に出現している語「間」を取り上げる。この語はモノやコトの位置関係や時間関係を表す語である。位置関係や時間関係は分野によらず，情報を相手に伝える際に必要な要素である。この理由から，専門を扱う文章でも，日常的な内容を扱う文章でも，分野によらず使用される語として多出していると解釈される。位置関係を示す「中」が＜化工＞＜理工＞＜文学＞に，「上」が＜理工＞＜文学＞に重なりを示すのも同じ理由によると考えられる。＜文学＞には出現していないが，＜化工＞＜理工＞＜経済＞＜社会＞の4分野に出現している語に「化」，「性」，「的」がある。これらの語はいわゆる接尾辞の働きをもつ語であり，「化」が前の語の変化を表し，「性」は前の語の性質を示す。「的」は前の語を形容動詞化したり，前の語と後ろに続く語を結び付ける働きを持つ。つまり，ある状態の変化や性質を示したり，熟語と熟語をつないで長い専門用語を作ったりすることが多く，表5で示したように分野によらず専門書で多用される語と言える。

次に，2分野で重なる語について考察する。＜化工＞と＜理工＞で重なる語は「式」，「数」，「値」，「系」，「水」，「熱」，「物」の7語である。「式」，「数」，「値」は数式に関係する語として，「系」は「高圧系」，「制御系」，「混合系」などの理工系の専門書に必要な2字漢字語に付く接尾辞として，「水」は水溶液に関する語を示す語として，「熱」や「物」は物質や生成物を表現する語として，共に特に理工系の分野で多用される語であると言える。

最後に，分野間での重なりが見られない語について考察する。重なりが見られないのは，前報（2002）で明らかにしたように，これらの語の中にはそれぞれの専門分野の特徴を色濃く表している語が多いからだと考えられる。しかしながら，＜化工＞と＜理工＞は同類分野のため，それぞれの分野の漢字の特徴を確定できなかった。たとえば，＜化工＞にある「液」，「層」，「膜」は化学工学の分野の特徴を示す語であると同時に理工系の分野全般にわたってよく用いられる語である。今回の結果では，＜理工＞の「図」や「表」は＜化工＞の多出語にはなっていない。これは資料とした『化学工学論文集』では図をFig.と，表をTableと表記する決まりがある（科学技術論文では雑誌ごとに特定の記述様式を指定する場合がある）ことと関係している。これに対し，ここでは詳述しないが，＜経済＞＜社会＞＜文学＞ではそれぞれの分野の特徴を示す語が比較的明確である。

以上の分析結果から，＜化工＞や＜理工＞などの科学技術文献に多出する1字漢字語の特徴は以下のようにまとめられる。

(1)　時間・期間を表す語，変化や状態・性質を表す語，位置関係を表す語は専門書一般に使用される語として科学技術文献にも多出する。

(2)　人を個別的に指し示す語や人の具体的な生活を示す語は，科学技術文献にはあまり使われない。

(3)　科学技術文献には人間の社会生活を分析する語は表れにくく，これに代わり，物質や自然現象を分析する語が多く出現する。これは科学用語は主として事実を述べる用語であり，日常用語は主に感情や意見を述べる用語であることと深く関係している。

(2)　形容詞および副詞の特徴（表6②③）

はじめに，形容詞について考察する。ここでの形容詞はいわゆる「イ形容詞」である。＜化工＞に出現する20語のうち「厚い」「遅い」の2語を除いて残る18語はほぼすべての分野に出現し，分野間の特徴を特定できない。すなわち，＜化工＞に出現する語は＜理工＞＜経済＞＜社会＞の間にも出現するだけでなく，＜文学＞にも出現する。すべての分野に同じ語が同じように使用される理由としては，形容詞がモノ・コトの属性を表す語であることが主因と考えられる。モノ・コト・ヒトがどのような特徴（あるいは性質）を示し，どんな状態にあるのかを描写（記述）するのは客観的な作業であり，たとえ＜文学＞であっても描写は客観的記述になる。したがって，多くの形容詞は分野を超えて共通に使用される語になりえるのだと考えても間違いではなかろう。

同じ結果は＜化工＞と重なりがなかった語からも類推できる。たとえば，＜化工＞にしか出現しなかった「遅い」と対になる「速い」は＜理工＞および異なる分野の＜経済＞に出現している。また，＜理工＞と＜社会＞には出現しなかった「弱い」の対立語「強い」はすべての分野に出現している。さらに，＜社会＞と＜文学＞に出現しなかった「遠い」の対立語「近い」はすべての分野に出現している。この結果からは，対立語が多分野に出現するのは，むしろ分野毎に別の語が多用されたに過ぎず，特別な理由によるものではないと考えられる。理工学分野で使用される1字漢字語の特徴は，自然現象を客観性を重視して表現していることである。こう考えると，理工系分野には，主観的

な要素を強くもつ形容詞の「親しい」,「若い」,「美しい」は，使用されない類の語であることが理解されよう。

しかしながら，専門書で排除される傾向が強い主観性の強い記述が＜文学＞では許されるかと言えば，必ずしもそうではない。それは今回取り上げた資料＜文学＞では「感情形容詞」が全く出現しなかったことからも推測できる。感情形容詞とは，「嬉しい」「痛い」「楽しい」などの語で，人の内的な状態を表すものである。これらの語はその感情をもつ本人にしか使用が許されないのが普通である。この点に関しては，＜文学＞のように日常生活における人間の悲喜こもごもが記述される文章でも，「私」が主人公の「私小説」でない限り，著者は「彼は嬉しがった」のように動詞化した語として表現すると報告されている（下川 1993)。

次に副詞について考察する。副詞の場合も，＜化工＞に出現する多出語は他の分野のどれかと重なって出現している。形容詞と同様に分野に特定する語は見出せず，出現した語が全ての分野で同じ重みをもって使用されていると考えた方が適切である。しかしながら，副詞には出現する語の特殊性から形容詞とは大きく異なる特徴がある。出現した形容詞，「強い」,「高い」,「大きい」などの語の多くは初級学習者になじみ深いものであり，彼らはそれらを日常会話に直結した語として学んでいる。これに対し，出現した副詞の多くは初級段階の学習者には耳慣れないものである。たとえば，通常は，「最も」,「常に」,「共に」,「全く」などの語は初級段階では，「いちばん」,「いつも」,「いっしょに」,「ぜんぜん」などと，より平易な話し言葉として学習するからである。

以上の考察結果をまとめると，上述した形容詞と副詞は科学技術文献に関わらず，文章読解を助ける必須用語であると言える。したがって，文章読解を効率的に学習するには，副詞に関しては日常生活語とは別に新たに覚えなければならない。このような傾向は，農学系の学術雑誌の語彙調査結果にも認められると報告されている（村岡・柳 1995)。専門書に限らず，文章によって読み手に情報を伝達するかぎりは，どの分野の文章でも「書き言葉」の範疇に属するので，形容詞と副詞は書き言葉の理解を助ける重要な伝達用語であると言える。

以上の分析から，科学技術文献で使用される形容詞と副詞の特徴は，以下のようにまとめられる。

(1) 形容詞も副詞も，分野を問わず同じ言葉が使用され，専門分野による違いはない。

(2) 使用される形容詞は客観性形容詞の類に限られ，日常生活語としても使われる。

(3) 使用される副詞はどの分野でも同じ語として使用されるが，文章用語であり，日常生活語としてはあまり使われない。

(3) 動詞の特徴（表６④）

動詞に現れる顕著な特徴は，＜化工＞と＜文学＞に重なって出現する語が少ないことである。多出する上位20語の動詞の中では「考える」だけが＜文学＞にも出現している。しかし，その表現形態は異なっており，＜化工＞＜理工＞＜経済＞＜社会＞ではほとんどが「考えられる」という受動態文で記述されているのに対し，＜文学＞では「考える」という語で使用されている。これについては，大久保（1970）が指摘している視点の位置問題が関係している。すなわち，＜文学＞では「ダレがドウシタ」が記述の中心であるため，動作主（行為者）に視点がある行為者主体の文章として記述されるからだと言える。同様に，＜経済＞には「働く」が，＜社会＞には「住む」が動作主を主体とする語として出現しているが，これは＜経済＞や＜社会＞の，人間活動との密な関わりの一側面を示したものだと推測できる。一方，専門書，特に科学技術の専門書では動作主にではなく出来事の事柄に視点を置き，モノ・コトがどうなったのかという，事柄主体の文章が中心となる。したがって，「考える」,「示す」,「用いる」,「得る」,「求める」のような自動詞を持たない他動詞の多くは受動態に変形されて使用される傾向にあると考えられる。この点については，英語の文章では主に「物主語」として記述されるのと対照的である。

専門書と記述形態の異なる＜文学＞を除くと，＜化工＞に出現する動詞が他の分野に出現する頻度は高く，＜理工＞では20語のうちの15語が，＜経済＞では12語が，＜社会＞では８語が出現している。これは専門書では分野を問わず，書かれる内容が「問題を提起」し，「立場を表明」し，実験や調査や引用などによって「比較」「分析」「考察」「判断」「説明」を繰り返して「結論」に至るという工程をとる特徴に関係している。

このような観点から，＜化工＞＜理工＞＜経済＞＜社会＞に出現する動詞は，その用法から次のように分類できる（働く，買う，結ぶ，住むは除外する)。

(a) 引用：述べる　書く　書く　関する　調べる　知る

(b) 説明：行う　呼ぶ　決まる　受ける

(c) 分類：分ける　属する

(d) 定義：表す　限る
(e) 比較・対照：比べる　対する　異なる　伴う
(f) 因果関係：考える　生じる　求める　得る　現れる
(g) 図表説明：達する　及ぼす　占める　含む　与える　加える　用いる　使う　入れる　出る　入る　増える
(h) 判断・評価：分かる　考える　示す　思う

これらの動詞の多くがいずれも分野を越えて専門書一般に出現する，論文読解のためのごく一般的な語群であると予測できる。

以上の分析結果から，科学技術文献に出現する動詞の特徴は次のようにまとめられる。

(1) 専門書には日常生活の基本的な動詞は現れにくいが，特に科学技術論文に現れることはほとんどない。
(2) 科学技術論文に出現する動詞の多くは論理的な文章表現の語として広く専門書一般に出現する動詞と一致する。
(3) 動詞の多くは引用，説明，分類，定義，比較・対照，因果関係，図表の説明などに用いられる動詞である。

(4) 2字漢字語の特徴（表6⑤）

一般的に言うと，2字漢字語には分野間での語の重なりが非常に少ない特徴が見られる。全分野に重なって出現する語はなく，＜化工＞＜理工＞＜社会＞の3分野に重なる語は「場合」だけである。また，2分野間に重なる語は，＜理工＞と＜社会＞で「関係」，＜経済＞と＜社会＞では「社会」だけである。＜化工＞と＜理工＞は理工系分野の資料であるが，重なる語は「場合」，「温度」，「条件」，「測定」，「速度」，「反応」，「変化」の7語である。この理由は，前述した（1(3)）と同様と考える。この特徴は，多数の2字漢字語（名詞）が他の品詞の語に比べると，それぞれの専門分野で固有に使用されていることを意味し，学習基本漢字の選定に当たって重要な要素である。

＜化学＞と＜理工＞の分析結果は，本質的には1字漢字の場合と同様である。このことをさらに検証するために，＜化工＞＜理工＞に出現する2字漢字語から『広辞苑第5版（1998)』の第2義までの説明を基準として，理工系分野の語と分類できる語を抽出した。結果は以下の18語となった：

「温度」「測定」「速度」「反応」；（＜化工＞と＜理工＞に出現）
「燃焼」「係数」「粒子」「濃度」「混合」「生成」；（＜化工＞だけに出現）
「関数」「結合」「制御」「原子」「気体」「電子」「分子」「定理」；（＜理工＞だけに出現）

＜化工＞だけに出現する語が化学工学の分野の特徴を適確に表していると断言するのは難しく，18語全体が他分野の語に比べて，物理的な現象，自然現象，化学的な変化，数式などに関わっており，理工系分野の語の特徴を示していると言う方がより適切である。

最後に，＜化工＞と＜理工＞に出現したにもかかわらず，理工系分野に特有の語としなかった15語について考察する。「存在」，「一般」，「必要」は専門書が通常要求する文体の特徴を表した2字漢字語であると言える。分野にかかわらず，一般的に客観性が求められる専門書では常体（である体）記述が使われる。常体記述ではどちらかと言うと漢語が好まれ，「ある」は「存在する」，「ふつうは」は「一般には」，「一般的には」と表記される。「必要」は，なくてはならないことを意味する語で，代替語がないため日常用語としても定着している。したがって，これら2字漢字語は必ずしも理工系分野に特有の語とは言えない。残りの12語（関係，状態，変化，影響，時間，抽出，計算，実験，場合，条件，結果，研究）は，専門書の記述形態の特徴と合致する2字漢字語であると言える。なぜならば，専門分野の記述では，対象とする事柄（問題）を設定して，ある問題と他の問題との関わりについて考察し，それらの現状を過去の研究と比較し，これらを基に様々な条件を設定して，実験，計算，調査などを実施し，そのプロセスや結果をまとめて論理的に述べ結論を導出するのが一般的であるからである。

結局，＜文学＞が日常生活そのものを扱い，＜社会＞が人間生活の成り立ちを扱い，＜経済＞が人間社会を流通の面から扱ったものであるのに対し，理工系分野では，人間生活の利便性に寄与する物を装置や器械を利用し，自然現象を応用する面を客観的に扱っていると言うことができる。

以上の分析結果から，科学技術文献に出現する2字漢字語の特徴をまとめると以下のようになる。

(1) 科学技術文献，特に理工系分野では日常生活で使用される具象的な2字漢語はあまり使われない。
(2) 科学技術文献には，抽象的（概念的）な語が多く使われ，それらの語は他の分野の語とはあまり重ならない。ただし，文献の記述が問題提起，実験・調査，検証，考察，結論の一連の記述様式でなければならないと規定されている場合には，他

の分野で使われる語も同じように多用される。

(3) 2字漢字語（名詞）は他の品詞に比べて，それぞれの専門分野の特徴を強く示す。

3．分析結果の総括と漢字学習法の提案

研究留学生ができるだけ早期に専門書の読解を始めるには，関係する分野の漢字を最初に覚えることが絶対条件である。しかも，ある一定期間継続した学習の積み重ねが不可欠である。そのためには，学習者のニーズを絞り，現実的な漢字学習とその効率化を図った適切な学習漢字の選定およびその学習法の開発が必要である。以下では，今回の分析結果を基に効果的な漢字学習法を開発するための具体的な留意事項について考察する。

前章の分析結果は，初級学習者が専門書を読む場合，状態形容詞の優先的な学習が重要であることを示唆する。状態形容詞は日常生活用語としても，専門書読解用語としても同じ語が用いられる特徴があり，「悲しい」「嬉しい」のような感情形容詞よりは，「大きい」「高い」，「少ない」，「黒い」などの語を学ぶことの方が日常生活にも研究生活にも役に立つからである。

引き続く学習段階で学習する語は純粋に名詞として働く1字漢字語である。この学習段階では最初に位置関係を示す「上」，「下」，「中」，「間」などを学習するのが適切である。これらの語は専門分野による制限がなく，しかも日常生活語としても利用できるからである。専門用語へと転用できる1字漢字語は，これらの語の学習後に導入するのが効果的である。＜化工＞などの理工系であれば，「図」，「式」，「表」，「線」など専門分野の基礎的な用語，さらには分野の影響を考慮した「層」，「膜」，「液」などが考えられる。

1字漢字語がある程度学習できたら，第3段階では動詞を導入する。動詞の場合，日常生活の語と専門的な語ではかなり異質な使われ方をしているので，最低限の生活に必須な動詞を学びながら，専門書を読むための必須な動詞をも適宜補完的に学習するのが望ましい。たとえば，説明文，定義文，分類文，比較文，対比文，引用文，判断・断定文など，専門分野で多用される定型構文があることを指導し，それぞれの定型構文を適切に記述できる基本的な1字漢字動詞を導入する。

かなりの漢字が学習できた段階で，はじめて2字漢字語を導入する。既に学習した1字漢字を組み合わせることで，漢字数が増えることにより漢字の広義な使用が可能になることを認識させ，さらに役に立つ一般語，読解のための文型語，専門語を導入する。副詞については，多くの副詞は，既に知っている日常会話の語に置き換えられるので，それらを確実に覚えるまでは代替語を利用することで理解は図れる。少しずつ専門書の文章が読めるようになった学習段階で，書き言葉，つまり記述文として必須の副詞を導入するのが望ましい。具体的な例示語については，本分析結果を踏まえた実践的学習指導の後に改めて提示したい。

おわりに

本稿では，理工系留学生のための効率的な漢字学習のためのテキスト化を目指して，「化学工学論文集」に多出する漢字を含む語を抽出し，他の資料の多出語と比較し，その特徴を考察した。その過程で，それぞれの分野に多出した1字漢字語を効果的に組み合わせることで，日常生活にも専門書読解にも役立つ語が選定できるという予測ができた。特に形容詞では，一般的に基礎漢字と分類されている語が専門書読解に必要な語と重なる確率が高いことが分かった。しかし，2字漢字語については，出現語が多いため，分野間で重なる語の特徴を限定することは難しかった。これらの語のより効果的な選定の仕方については，前報（入戸野・武田 2003）で提案した選定条件を活用することが適切であると考えられるので，今後はそれらを考慮した選定方法を検討したい。

一方，初級学習者の教科書に出現する動詞や副詞だけでは，書き手がどこに視点を置くかで使用される動詞が異なってくる場合や副詞のように書き言葉と日常生活言葉で全く異なった語を使用する場合を理解させるのは難しいことが分かった。これらが専門書読解を補助する重要な役割を果たすことを理解させること，およびそれらをどう漢字学習にリンクするかといった具体的な学習法の改善・開発は今後の課題である。

漢字は文字であるから，単に漢字だけを学習しても効果か低いのは言うまでもない。学習漢字が旨く学習者の実用漢字として定着してはじめて，漢字の習得が完成する。漢字が理解できなければ，文献を読み進めることはできないため，提示した漢字にどのような例示語を付けるかは大きな問題である。次回は，前報で取り出した284漢字に今回抽出した漢字を含む語を配置し，提示漢字とそれに付加する例示語や文章を具体的に選定することで，理工系分野の読解に役立つ初級者用のテキスト試案を供したいと考えている。

文　献

大久保忠利（1975）:『日本文法と言語の理論』春秋社。
下川浩（1993）:『現代日本語構文法』三省堂。
武田明子（1994①）:『松下国債財団報告書』1～252。
武田明子（1994②）:『松下国債財団報告書』1～152。
武田明子・入戸野修（1997①）: 化学技術文献読解のための漢字指導法の見直し」, 科学教育研究, Vol. 21, No. 4, 207～216。
武田明子・入戸野修（1997②）: 語彙分析と実験授業から得た初級日本語学習者のための理工学漢字の選定, 日本科学教育学会, 第21回年会論文集, 275～276。
武田明子・入戸野修（1997③）: 電子辞書による漢字検索時間の検討, 教育工学関連学協会連合第5回全国大会論文集, 155～156。
武田明子・入戸野修（1997④）: 初級日本語を学ぶ理工系研究留学生のための漢字教授方法の提案, 平成9年度日本語教育学会秋季大会論文集, 155～160。
入戸野修・武田明子（2002）: 留学生に対する科学技術専門書読解のための教科書作成に向けて－化学工学における専門日本語漢字－, 福島大学地域創造, 第14巻第2号, 77～87。
入戸野修・武田明子（2003）: 研究留学生が科学技術専門書を読解するための基本漢字の例示語選定に関する検討, 福島大学教育学部論集, 理科報告第67号, 1～12。
林大（1982）:『図説日本語』, 角川小辞典9, 角川書店。
林四郎（2000）:『例解新国語辞典』（第5版）, 三省堂。
村岡貴子・柳智博（1995）: 農学系学術雑誌の語彙調査, 日本語教育85号, 80～89。

Analysis of Technical Terms Including Kanji in Chemical Engineering for Teaching International Students How to Read Scientific Papers

Osamu Nittono and Akiko Takeda

We have analyzed the characteristics of technical terms usually used in chemical engineering and tried to search an effective and valuable teaching technique for international research students, who are eager to understand scientific and technical Japanese papers. We analyzed 380,560 characters (Kanji) including 1,501 different characters, which were extracted from six volumes of "Kagaku Kogaku Ronbunshu" published in 2000. In this study we examined four parts of speech such as noun, adjective, adverb and verb which contain Kanji and are common words in written-style papers. Their characteristics were evaluated and compared with those of different fields such as science, sociology, literature and economics. Terms extracted were also evaluated qualitatively in terms of frequency in use. It is shown that adjectives are widely used in various fields, while adverbs usually used in scientific papers are not familiar in everyday life. And our previously proposed requirements proved to be useful for selection of ideal Kanji-vocabularies when we pay attention to other parts of speech including adjective and adverb. This study suggested several important points on the preparation for the text book of technical Japanese terms for research students from non-Kanji countries. We also proposed several how-to techniques for premitive Kanji learning which will be effectively used for scientific research students to read technical Japanese papers.

科学技術専門書読解のための漢字の例示語の提示に関する一考察

入戸野　修・武　田　明　子

福島大学地域創造 第17巻 第１号（2005.9）

国立大学法人　福島大学地域創造支援センター

調査報告

科学技術専門書読解のための漢字の例示語の提示に関する一考察

入戸野　修・武田明子

目　次

はじめに
1．例示語選定の基準
2．284漢字が持つ語の特徴
3．異なり語数が9以下の漢字と50以上の漢字の比較
4．漢字に対して例示する語の選択の試み
5．「論を立てる」用語の漢字学習から読解へと結びつける学習法
おわりに

はじめに

筆者らは「化学工学」の専門分野を取り上げ，科学技術文献読解のために最適な必須漢字とはどんなものか，どのような語（漢字を含む語）が多出するのか，これらにはどのような特徴があるのか　などを分析し，考察を行ってきた（入戸野・武田（2002および2003ｂ））。「化学工学分野」を分析対象にしたのは，物理，数学，科学，工学といった自然科学系の学問分野がすべて含まれており，自然科学系の広範囲の分野の語を含む理工学分野であると考えたからである。その結果，資料『化学工学論文集，2000年第1巻～第6巻』には1051の異なり漢字が出現し，5051の異なり語を作っていることを明らかにした。

このうち上位284位までの漢字が全体の80％を補っているが，これらの漢字を知っていても，文章も80％理解できるというわけにはいかない。学習漢字がうまく学習者の実用漢字として定着するには何千と出現する語の意味ができるだけ多く類推できるような漢字学習が必要となる。そのためには，意味の類推が可能になるような例示語を提示する必要があることを指摘した（2003ｂ）。

本稿では，この漢字学習における例示語に焦点をあて，上位284位までの多出漢字に対して例示語をどのように提示したら学習効果が期待できる実用性の高い漢字学習に結びつくかの分析とその結果について考察する。

1．例示語選定の基準

筆者ら（2003ａ）は，異分野間に出現する語を比較して，理工学分野の語について以下の選定条件を仮説とした。

(1)　理工系分野の基本漢字の例示語には「事実主体型」の語を選定する。

(2)　理工系分野の基本漢字の例示語には異種分野での「共通性」の高い語を優先する。

(3)　理工系に多出する語が日常生活語と共通する場合，これを優先的に理工系分野の基本漢字の例示語として採択するのが望ましい。

(4)　資料［文学］の非共有領域および部分的共有領域に意味の分布が集中している語は日常生活語として可能な範囲（数的）で優先的に理工系分野の必須基本漢字の例示語として選定する。

（注：資料［文学］の非共有領域および部分的共有領域に意味の分布が集中するとは，いわゆる日常生活では使用するが理工系分野および科学的な手法を使って記述する論理的な文章には出現しないごく一般的な生活語である）。

今回の例示語の選択は具体的に『化学工学論文集』に出現した語を対象にしているため，これらの選定条件をそのまま使うことはできない。しかし，(1)および(2)は『化学工学論文集』の語の分析から逆に，出現する語が事実主体型であること，その中には他の分野でも多用される記述文としての共通語が出現していることをすでに明らかにしている。(3)については，多出語

だけでなく『化学工学論文集』に出現するすべての語を観察対象とすることで部分的に対処できると考えられる。出現頻度が低くなると，その語は記述文の特徴を持ちながらも，化学工学としての特徴を離れていく傾向が見られたからである。しかし，(4)については，化学工学分野の多出漢字とを比較し検討することを目的としているため，今回の漢字および例示語選択では特には考慮しなかった。

以上の考察から，本稿では上記(1)〜(3)の条件を踏まえて，以下のような選択方法で例示語を採択した。

(1) 漢字の提出順位

漢字を学習する際の提出順位は，大雑把に分類すると，(a)「一」「山」「川」「木」のように画数の少ないものから学習する，(b)「多」「少」「大」「小」のように意味の似た漢字をまとめて学習する，(c)「家の中」「駅」などのように場面を設定して同じカテゴリーの語から学習する，(d)文章を読み進めながら出現した順に学習する方法がある。

今回の漢字は『化学工学論文集』という一つの大きなジャンルの中で多出する漢字に例示語を提示するという方法を採るため，上述の(a)〜(d)のいずれの方法も適してはいない。すなわち，(a)の方法でやさしい漢字から学ぶのではなかなか適切な例示語を選択することができない。(b)の方法でもほぼ同様である。『化学工学論文集』を一つの場と考えれば，(c)に該当するとも言えるが，(c)ではもともと場（場面）に即した語から漢字を学習していくことが前提であり，選択基準となり難い。さらに，漢字学習のための漢字の選択という目的からは(d)は想定外である。

ところで，最多出漢字と最多出語は必ずしも一致しない。筆者らの調査でも同様な結果であり，漢字の最多出漢字は「度」であるが，最多出語は「示す」となっている。ここで，出現語の上位から漢字を例示語として提示すると，ある語だけが多出するという場合も考えられる。ある漢字が上位に来るということは，その漢字を使った語が延べ語数にせよ，異なり語数にせよ確実に多出現することを意味する。つまり，多出漢字は例示語が探し出せる要素をより多く含むと言える。したがって，本稿では試行段階ではあるが，学習のための提出漢字は多出漢字の順に行うことにした。

(2) 取り出す例示語の範囲

漢字に提示する例示語は全出現語を対象とする。前報（2003ｂ）で全体の40%を補う多出上位語107語を分析した結果，名詞が87.8%を占め，特に2字漢字語は58語と，半数を超えた。これに対し，用言（名詞以外のもの）は，動詞が10語，形容詞が3語と少なく，用言は上位には現れにくいという傾向が示された。これは，一つひとつの漢字が組み合わさるという「漢字の造語力」に視点を置いた学習指導が必要なことを示唆する。しかし，同時に，上位の多出語のみを例示語として提示するだけでは，実際には多くの名詞を学習することをも意味する。すなわち，名詞のみの学習では，複数品詞として活躍する性質を持っているはずの漢字の本来の働きを示せなくなるという危険に陥る可能性が高い。語の第一義の意味が理解できなければ意味の類推もむずかしい（2003ａ）。

科学技術文献を読む作業とは，記述文が主述関係の完結を持って構成されるという視点に立った学習や教育の上に成り立つ行為である。述語になることができる品詞には名詞・形容詞・形容動詞・動詞がある。もし多出語であるという理由で名詞のみを学習することになれば，主語が形容詞・形容動詞・動詞と関わって示す文の特徴を学習することが困難になる。したがって，一つひとつの漢字の持つ意味を確認し，複数品詞としての働きを持つ漢字には，多出するか否かだけではなく，漢字の語としての働きにも注意した例示語を提示する配慮しなければならない。このためには全出現語を対象として漢字が持つ中心的な意味が下位語にあれば，その語も同時に例示語として採択する必要がある。同様な理由から，今回はその語が多出語にない場合には，これを例示語として補充することとした。

(3) 覚えなければならない例示語の提示方法

漢字は多くの語を作っているが，学習する該当漢字の例示語には未学習の漢字が含まれる語は使用しないこととする。たとえば「理解」という語を例示語として提示する場合，最初に出現する学習漢字が「理」であり，「解」がそれより後置されている場合，「理解」という例示語は「解」を学習するときに提示する。「理」を学習するときに「理解」が例示されていることは日本人にとっては不都合を感じない処置であるが，「解」が284位内にある場合には，この漢字の学習の際にすでに学習した「理」と結びついた「理解」が示されれば，それは既習漢字の意味の理解の確認にもなるし，復習にもなると考えられる。この処置により，一つの漢字の核となる意味をきちんと理解する上で，組合わさるもう一方の漢字の意味についても同時に理解しなければならないという事態が避けられる。

(4) 覚えなくてもよい例示語の提示方法

前項と矛盾するようであるが，学習漢字にない漢字，つまり上位284位に入らない漢字との組み合わせの語はできるだけ多く例示語として提示する。これは，ある漢字を学習し，その意味を理解しても実際に意味の類推の仕方がむずかしいことが多いという学習者の戸惑いを少しでも減らすためである。ここでは学習者の母国語で既得されている知識を利用するのが得策と考えた。彼らは日本語には未熟でも，若い研究者として多くの専門用語，またはそれに類する語彙を豊富に持つ。加えて科学技術の分野には英語が公用語として使われることが多く，彼らが読む専門書には専門的な用語には英語が併記されることが多い。したがって，ある語にかかわる例示語を振り仮名を使い，英語の意味を添付して示すことは，学習者にとっては学習漢字の意味の類推の仕方に習熟できるとともに，目に触れた漢字を理解漢字として増やしていくこともできる。この選択方法により極く少数の学習漢字を補い，化学工学の分野には多出とまではいかなかったが，論理的な，いわゆる事実主体型の科学技術論文に共通することの多い語を理解することができる。

「覚えなければならない」漢字や語，「覚えなくてもよい」漢字や語といっても，筆者らは漢字が書けるようになることを期待してはいない（武田・入戸野1997)。今回の例示語の選定は，できるだけ多くの漢字や語に必然的に日常的に出会うということが，記述文の全体背景の理解に大切であると考えた上での実験的な試みである。

(5) 具体的な選択の仕方

多出順位21位の「結」という漢字を例に具体的に説明する。先の結果（2002）によると，異なり語は16語【①結ぶ，②結合，③結果，④結言，⑤結論，⑥焼結，⑦直結，⑧結（晶)，⑨（完）結，⑩結（局)，⑪結（語)，⑫結（集)，⑬結（節)，⑭（締）結，⑮（凍）結，⑯（連）結】である。まず，「結」の基本的な意味として①の「結ぶ」が採択される。②の「結合」は「合」が多出順位５位で既習のため，覚えなければならない語の例示語として選択する。次に，③～⑦の語は結びつくそれぞれの漢字が「結」より後で284位内に出現しているので，例示語はその漢字につけることで，ここでは省く。最後に漢字の意味の理解を助ける，覚えなくてもよい例示語として⑧～⑯の語を採択する。結局「結」の漢字に例示語として提示される語は「覚えなければならない漢字」が２語，「覚えなくてよい」意味の類推方法の理解に役立てる語が10語となる。「結」と結びつく⑦～⑯の漢字は284位内には入らないため，今回の学習漢字としては取り上げられない。しかし，「締結」の「締」がこの１語しか見られないのを除けば，あとは一般によく見られる漢字である。特に「集」「連」などは多くの異なり語を持つ。そこでこれらの漢字と結びつくもう一方の漢字が284位以内にあれば，その都度これを理解を助ける例示語としてその漢字の「覚えなくてもよい語」に採択することにした。こうした選定処理で，これらの漢字の意味も把握できるようになる可能性が高ったと言う留学生の意見があったからである。このような選択の仕方が効果的なのか，あるいは「締結」のように極稀にしか使用されない語だけを省略するのか，この点については今後の更なる検討が必要である。今回は次回の検討へ正しく継続するように，できるだけ削除しないでこれらの語を多く残した。

(6) 語の選定条件

以上の検討から，本稿での語の選定条件は以下のようにまとめられる：

条件①　『化学工学論文集』に出現したすべての語を多出漢字の例示語の対象として選択する。

条件②　出現語の中に漢字の意味の核となる語を求め，これを例示語として提示する。

条件③　必須学習語である２字漢字語については，両方の漢字が学び終わった時に例示語として採用する。

条件④　学習漢字以外の漢字と結びつく２字漢字語はできるだけ削除しないで理解のための例示語として残す。

2．284漢字が持つ語の特徴

表１は『化学工学論文集』に出現する上位284漢字が，それぞれいくつの語数を持っているかを分析した結果を示す。表の「異なり語数」は，この284漢字の中で，それぞれの漢字が持つ，『化学工学論文集』に出現した異なり語数である（2002)。また，「284漢字」はその異なり語数の範囲内に出現する漢字の数である。右覧の「40%」～「100%」はこれらの漢字を含む語が累積百分率のどの範囲に出現しているかを数で示す。たとえば，グループⅠ①では，86の漢字が９語を上限とする語をもち，その中には出現語全体の40%を補う語が42語，41～50%を補う語が28語あるということを

表1　上位284漢字がそれぞれにもつ語数の概略

	異なり語数	284漢字	40%	50%	60%	小計	70%	80/70	80%	90/80	90%	100/90	100%	小計
Ⅰ	①01～09	86	42	28	25	95	23 (1.5)		35 (1.4)		48 (5.9)		284	390
	②10～19	116	46	44	49	139	71 (1.3)		89 (2.1)		189 (6.0)		1134	1483
	計	202	88	72	74	234	94 (1.3)		124 (1.9)		237 (6.0)		1418	1873
Ⅱ	③20～29	40	22	14	25	61	32 (1.5)		47 (2.3)		107 (6.7)		722	908
	④30～39	21	22	6	17	45	23 (1.6)		36 (2.3)		83 (6.4)		528	470
	⑤40～49	11	16	7	9	32	16 (2.0)		32 (1.5)		47 (7.2)		340	435
	計	72	60	27	51	138	71 (1.6)		115 (2.1)		237 (6.7)		1590	2013
Ⅲ	⑥50～59	6	9	7	12	28	11 (1.5)		16 (1.6)		26 (7.2)		209	262
	⑦60～69	2	2	3	4	9	3 (1.7)		5 (1.2)		6(17.8)		107	121
	⑧70～79	2	7	3	1	11	8 (0.9)		7 (2.7)		19 (5.2)		99	133
	計	10	18	13	17	48	22 (1.3)		28 (1.8)		51 (8.1)		415	516
		284	166	112	142	420	187		267		525		3423	1102
		*	(107)	(69)	(98)		(147)		(248)		(515)		(3862)	

＊：本来の語数（この表には2字漢字語のそれぞれに語が該当語として数えられるため、実数との相違がある）

示している。この表ではそれぞれの総数が実数とは合わないが，これは語が2字漢字語である場合には，それぞれの漢字に同語が出現語として数えられるためである。また，91～100%の間で出現する語については実数より少ない数になっており，284漢字に含まれない語が多いことを示す。

はじめに，異なり語数と284漢字との関係を説明する。両者の関係は3つのグループⅠ～Ⅲに分けられる。グループⅠには異なり語数が19語までの100前後の漢字が，グループⅡには異なり語数が50以下の2桁の漢字が，グループⅢには異なり語数が50以上の1桁の漢字がある。そして，全体としては最も出現漢字の多いグループⅠ②の116字に見られるように，20前後の異なり語を持つ漢字が最も多くなっている。

次に，累積百分率における語の出現数について説明する。異なり語数の多少にかかわらず全ての範囲に語の出現が見られる。これを全出現語の40%を補う語を基準にして各グループの計で見ると，いずれのグループでも60%を越してから（表の70%以降）40%までに出現する語数を上回る数が示される。そこで，40～60%の範囲の各計を見てみると，どのグループでも40%＞60%＞50%の順に異なり語を持っていることがわかる。しかし，比較的僅差であるから，必ずしも累積百分率の値が高い順に必須度が下がるとは言えない。すなわち，例示語を提示する際には40%を補う語だけでなく，範囲を広げて学習を視野に入れた適切な語を選択する必要性のあることを示唆している。

一方，この範囲を超えた累積百分率では各範囲での語の出現数に有意な差が見られる。表の80／70，90／80，100／90は隣接する累積百分率の数の比較である。たとえば，Ⅰ①の列の70%の後にある（1.5)は，70%にある語の数の1.5倍の語が80%には出現していることを示す。この数値を各グループの計で比較すると，どのグループでも80%では70%の1.5倍程度の語が，90%では80%の2倍程度の語が，100%では90%の6倍以上の語が出現しており，91～100%の間を補う語が他範囲より多くなっている。この数を詳細に見ると，グループⅠでは6倍を超えることはないが，グループⅡでは7倍を超え，グループⅢになると⑦のように17倍を超える数値を示す。この結果は，91～100%の間の語数の数の差が全体の異なり語数の差に強い相関関係があると言える。

しかし，結果がそうであったとしても，異なり語数の差の原因をすべて累積百分率の低い部分にある数に帰することはできない。グループⅠにある202の漢字は19を上限とする語数しかもたず，このうちの86漢字にいたってはわずか1～9の語しかもたない。多出漢字であって，しかも異なり語数が少ない漢字となると，出現する語に累積百分率40%を補う語が多出することは容易に推測できる。しかし，グループⅢでは10の漢

字が50以上の語を持つ漢字として存在し，しかも該当漢字数10字を上回る18語が累積百分率40%を補う語として出現している。上位に多出し，全漢字の80%を補う284の漢字の異なり語数が，1～79語の範囲にこれほど広く拡散して分布する原因は化学工学分野の漢字に特徴と言うよりは漢字そのものにあると考えざるをえない。

3．異なり語数が9以下の漢字と50以上の漢字の比較

(1) 数値による比較

表2は表1のグループⅠ①の86漢字が持つ語が最初に出現する累積百分率の個所を示す。異なり語が1つしかない漢字は5つあり，その全ては40%までの累積百分率の範囲に出現しているが，これ以外の漢字が持つ語には40%を超えて初めて出現する語もある。たとえば，異なり語数が2つの漢字では3漢字のうちの2漢字が，異なり語数が3つの漢字では11漢字のうち7漢字がこれに該当する。異なり語数が7つの漢字のように累積百分率が80%の範囲になってからようやく最多の語が出現する漢字もある。これらの事実は上位284漢字であっても，常に累積百分率40%までの範囲に語の出現が見られるわけではないことを示す。

異なり語数の多少の原因を探るには，異なり語数が少ない漢字と多い漢字をサンプリングして比較することが有効である。異なり語数が多い漢字には表1のグループⅢ⑥⑦⑧が該当し，少ない漢字にはグループⅠ①が該当する。しかし，①には86の漢字があるのに対して，⑥⑦⑧には合計でも10語しかない。そこで，表2からそれぞれの累積百分率の範囲に最初に出現した語を機械的に取り上げてグループⅠ①の代表とし，グループⅢと比較してみることにする。ただし，70%の部分に関しては異なり語数3は既に採取してあるので，異なり語数5にある漢字を選択する。したがって，グループⅠから取り上げる漢字は，40%の個所では異なり語数1の5漢字，50%では異なり語数2の2漢字，60%では異なり語数3の3漢字，70%では異なり語数5の1漢字，80%では異なり語数7の1漢字の計12漢字である。

表3は取り上げた漢字が持つ，累積百分率における語の分布を表示したものである。(A)には異なり語数が9以下の「条」「響」「御」「討」「領」「操」「慮」「察」「非」「運」「硫」「容」の12漢字が該当し，(B)には異なり語数が50以上の「定」「熱」「合」「流」「上」「出」「一」「数」「分」「水」の10漢字が該当する。表の表示「順位」は該当漢字の出現順位である。たとえば，異なり漢字数1の「条」の漢字は全出現漢字の111番目に多く出現する漢字，異なり語数50の「定」の漢字は3番目に多く出現する漢字である。

この順位で漢字全体を眺めると，(A)では最も出現順位の高い「条」でも111位であり，「運」は上位80%を

表2　異なり語数が9以下の漢字86字の出現様相

異なり語数	1	2	3	4	5	6	7	8	9	計
40 %	5	1	4	5	2	7	5	6	4	39
50 %	−	2	3	2	7	4	2	0	2	22
60 %	−	−	3	2	4	0	1	4	2	16
70 %	−	−	1	0	1	1	0	2	3	8
80 %	−	−	−	−	−	−	1	0	0	1
計	5	3	11	9	14	12	19	12	11	86

表3　語の累積百分率の分布

	(A) 異なり語が9以下の語												(B) 異なり語が50以上の語									
異なり数	1	1	1	1	1	2	2	3	3	3	5	7	50	50	52	52	58	58	63	67	70	74
順　位	111	125	166	167	218	254	281	206	258	284	256	251	3	22	5	10	42	24	28	13	2	16
漢　字	条	響	御	討	領	操	慮	察	非	運	硫	容	定	熱	合	流	上	出	一	数	分	水
40 %	1	1	1	1	1	0	0	0	0	0	0	0	1	2	3	1	1	1	0	2	6	1
50 %	0	0	0	0	0	1	1	0	0	0	0	0	3	1	0	2	1	0	2	1	1	2
60 %	0	0	0	0	0	0	0	2	1	1	0	0	6	0	0	3	2	1	2	2	1	0
70 %	0	0	0	0	0	0	0	0	1	1	1	0	2	1	3	3	0	2	2	1	6	2
80 %	0	0	0	0	0	0	0	0	0	0	1	3	2	0	3	4	2	5	4	1	4	3
90 %	0	0	0	0	0	0	0	1	0	0	2	1	4	6	2	6	3	5	4	2	11	8
100 %	0	0	0	0	0	1	1	0	1	1	1	3	32	40	41	33	49	44	49	58	41	58

補う284漢字の284番目の漢字に相当する。これは，少ない語が頻繁に出てきて漢字の出現順位を押し上げていることを示すが，漢字自体は他の漢字と結びつくことが少ないことを意味する。このことは(A)に「0」の値が目立つことからも明らかであり，化学工学の分野では必須の語を作る漢字として重要ではあるが，一般的には漢字の持つ造語力はそれ程高くはないことを示す。これに対し，(B)では10漢字のうち「定」「合」「流」「分」の4つが上位10位以内，「数」「水」の2つが20位以内，「熱」「出」「一」の3つが30位以内であり，残る1つ「上」も42位と，漢字の出現順位は非常に高い。これは表にほとんど「0」の値が見られず，各累積百分率の範囲で1つの漢字がさまざまな語に使用されていることからも明らかである。それを最も特徴的に裏付けるのが累積百分率が100%の個所である。この個所は(A)では1～3と，あっても極少であるが，(B)では32～58と多く，他の漢字と結びつく力が非常に強いことを示している。

(2)　異なり語数が9以下の漢字と語の分析結果

表4は表3の結果を実際の語で具体的に示したものである。ここでは語そのものを対象とすることから，上位に多出する漢字が持つ語の出現頻度の多少に関わる原因を探る。表中の語で「容（易）」「操（業）」の語は，括弧内の漢字が284位までに入っていない漢字であることを示す。また，漢字の上欄に示した「番号」は便宜的に各漢字につけたものである。なお，(B)の異なり語が50以上の語では，100%の欄に語の記述がないが，これは誌面の関係で省略したからである。

漢字(1)～(5)の特徴：(1)～(5)はそれぞれただ一つの語が多出して累積百分率が40%までの上位に入っている漢字である。これらの漢字が持つ基本的な意味からその品詞を分けてみると，名詞が基本となる漢字は(1)の「条」と(5)の「領」の2漢字である。

「条」の基本的な意味は「あることを一つずつ示すこと」(『例解新国語辞典　第6版2000，以下意味の説明はこれに準ずる）を表す。しかし「条」だけでは独立した語とはなれず，他の漢字と結びついてその中に本来の意味を内包させる。したがって，「条件」「条理」「条項」「条約」「条例」「第1条」のような語が挙げられるが多用ではなく，漢字の造語力はそれほど強くはない。このうち「条理」は抽象的な語であり，「条項」「条約」「条例」「第1条」は政治的な語と言える。あることが実現する前提として成り立たなければならない「条件」のみが多出するのは化学工学や理工系分野ならずとも，内容を論理的に事実主体型で論じようとする文章に多出するであろうことは容易に推測できる。「領」もまた同様である。基本的な意味は「ある事柄の最も大本となるもの」であるが，「イギリス領」のように接尾辞として使われる用法を含め，他の漢字と結びつかなければ独立した語としては使われない。多くは「領土」「領海」「領空」など土地や国などを治める語として使われるため，その意味の幅は狭く，より一般的に使用される語としては「領域」「要領」などが挙げられる。

(2)～(4)の「響」「御」「討」ではいずれも意味の基本となる品詞は動詞である。「響」の基本的な意味は「響く」であり，特に「音や振動が広がったりぶつかって跳ね返ったりする行為」を表す。これらの意味では「交響」「反響」が挙げられるが，響くことが抽象的に使用される一般的な語としては「影響」があるが数は少ない。「御」の基本的な意味は「御する」という動詞に持つ。しかしこの語は人を操る時には「御する」，組織を操る時には「統御する」，機械などを操る時には「制御する」と使い分けがなされるのが普通のため，化学工学のような科学的な文章においては「制御」のみが出現することになる。この「御」は尊敬を表す接頭辞の働きをも併せ持ち，「御社」「御手洗」「御婚礼」「御主人」「御中」などと多彩である。しかし，事実主体型の文章（科学技術論文）では尊敬語を使用しないので，論理的な世界では「御」の造語力は弱いと言うことができる。

「討」の第一義である基本的な意味は「討つ」であり，「討伐」「掃討」などの語として使用される。第二義には「研究する」の意味があるが，この意味では「討議」「討論」のように他の漢字と一緒にならなければ語を形成することはできない。論文を読むのに必要な語の意味は「研究」に関わることが普通であるから，他の漢字と一緒にならなければこの意味が表せない「討」は形の上では「条」や「領」に準ずる漢字であると言える。

以上から，漢字はそれぞれに意味を持つが，その意味をその漢字一つで語として表すことがむずかしいもの，あるいは第一義から派生した第二義以降の特定の意味に使われることが多い漢字にはあまり造語力が強いものがなく，2字漢字語という漢字2字の組み合わせでまとまって一つの漢字に内包される意味を共有して表すと考えられる。

漢字(6)～(12)の特徴：(6)～(12)の7つの漢字は異なり語数

表4　各累積百分率に出現する語の実際

(A) 異なり語が9以下													(B) 異なり語が50以上									
異なり語数	1	1	1	1	1	2	2	3	3	3	5	7	異なり語数	50	50	52	52	58	58	63	67	70	74
順位	111	125	166	167	218	254	281	206	258	284	256	251	順位	3	22	5	10	42	24	28	13	2	16
番号	(1)	(2)	(3)	(4)	(5)	(6)	(7)	(8)	(9)	(10)	(11)	(12)	番号	(13)	(14)	(15)	(16)	(17)	(18)	(19)	(20)	(21)	(22)
漢字	条	響	御	討	領	操	慮	察	非	運	硫	容	漢字	定	熱	合	流	上	出	一	数	分	水
40 %	条件	影響	制御	検討	領域								40 %	測定	加熱 熱	混合 重合 場合	流動	以上	抽出		係数 数	成分 分 分解 分子 分布 分離	水
50 %						操作	考慮						50 %	安定 一定 仮定	伝熱		流体 流量	上		一定 一方	関数	分散	水素 水溶
60 %								観察 考察	非	運動			60 %	確定 決定 固定 設定 定常 定数			電流 流れる 流速	向上 上(昇)	出口	一(致) 均一	数値 定数	部分	
70 %									非常	運転	脱硫		70 %	推定 定(義)	(蓄)熱	化合 結合 合成	対流 (乱)流 流束		算出 出力	一次 一(般)	変数	十分 分かる 分(級) 分析 分配 分率	加水 (練)水
80 %											硫(黄)	容(易)	80 %	所定 定量		(割)合 組み合わせる (複)合	(噴)流 流 流入 流(路)	上(記) 上部	検出 析出 導出 排出 溶出	一つ 一部 (第)一 同一	(指)数	水分 積分 分(割) 分(裂)	水酸 水相 水分
90 %								推察			硫化 硫酸	容積	90 %	(想)定 定める 定性 (判)定	熱的 熱量 排熱 発熱 比熱 (予)熱	合わせる (集)合	下流 (還)流 気流 整流 層流 流通	上げる 上下 上(述)	見い出す (取)り出す 出(来)る 人出 放出	一 一様 一例 単一	(個)数 (複)数	回分 灰分 微分 分かれる 分ける 分圧 分極 分光 分野 分量 油分	水(田) (海)水 外水 (純)水 (親)水 水中 水平 内水
100 %						操(業)	配慮		非水	運用	硫物	(許)容 形容 内容	100 % (省略)	32	40	41	33	49	44	49	58	41	58

が2～9の漢字である。このうち，名詞を基本的な意味として持つ漢字は(9)の「非」と(11)の「硫」の2字である。(9)の「非」は「正しくないこと」を意味し，「彼には非がない」のように漢字1字でも名詞として使われる。「非」の主たる働きは，累積百分率が60%の個所に出現している「非」のように接頭辞としての働き，あるいは「非常に」というすでに固定化した言い回しのみである。接頭辞「非」は後に続く言葉を打ち消す役割を持つ。累積百分率100%の個所に出現する「非水」はその一例である。接頭辞としてのこの働きに注目すれば，「非社会性」「非人間性」「非公式」など「非」と一緒に使うことができる語の数は増す。しかし，「非」には「非難」「非行」のように，語に相手やできごとを非難する意思を示すことが多いことから，ただ単に「ない」と否定するだけにとどまる「不」(16の異なり語が出現する）および「無」(13の異なり語が出現する）と比べ，その使用範囲は限られている。

(11)の「硫」は鉱物のイオウを意味する語で，使用範囲は更に限られていて専門性がある。この漢字も「硫」1字では使われず他の漢字と一緒になってその意味を表す。「硫黄」や「硫酸」は専門知識の必要な語であり，他に出現する「脱硫」「硫化」などは一般生活では殆ど使用されない。したがって，「硫」は，意味の幅は非常に狭いが化学工学の専門分野において特に多く使用される漢字であると言える。

残る5つの漢字は基本的な意味が動詞にある。(6)の「操」は「操る」の意味である。既出の「御する」とは異なり，人・物・事にも組織にも機械にも使うことができる。しかし科学的な文章では1字漢字より2字漢字の語の方が好まれるという傾向があるため，「操る」に代わって累積百分率50%に出現している「操作」が多用される。(7)の「慮」の基本的な意味は動詞「慮る」であり，「そのことについてよく考える」という意味である。しかし，現在では硬い表現である。一方，「熟慮」「考慮」「配慮」などのように他の漢字と一緒になってその語に意味を内包させることの多い定型的な語である。したがって，「慮る」が出現せず，「考慮」「配慮」が多出するのはごく一般的な傾向であると言える。(8)の「察」は「察する」が基本的な意味であり，「よく考えて見通しをつけること」を示す。しかし，この語は「周りの状況から相手の事情や気持ちのおおよそを知る」という対人関係で使われるのが普通である。モノやコト，あるいは理論について「察する」と表現することはなく，多出した「観察」「考察」「推察」などのもう一つの漢字との結び合った語が多様される。したがって，これらの語は論理的な文章を書き進める必要のある科学的な記述文章全般に利用される語と言える。(10)の「運」は「運ぶ」という動詞が基本的な意味である。モノやコトや概念などを移動させていくことから，「運動」「運転」「運用」などが使用される。「運」には「運がよい」「幸運」「運勢」「運命」などのように科学を超えた意味を表す語としても存在する。しかし，論理的な分析をする科学的記述文では使用されにくく，その意味で化学工学の分野には出現が少ない。(12)の「容」は「容れる」が基本の意味である。異なり語が9以下の漢字の中では最も多い7語が出現している。これは「容」の持つ基本的な意味が明確であることによると言える。その意味は「ゆったりとした受け入れ」であり，いずれの語もこの意味の範囲の中で語がつくられている。すなわち，「容器」「容積」「内容」では中にいれることを，「許容」ではおおらかに受け入れることを，「形容」「容易」ではある状態をゆったりと受け入れることを表している。

以上の(6)～(12)を総括すると，たとえ漢字にそれ1字で語をつくるだけの力があっても，意味内容に感情・情緒が含まれるもの，すでに使い方が古く，定式化した語のみが用いられるものなどは化学工学の分野では使われる語が限定されている。したがって，これらの漢字が作る2字漢字語を学習する際には，1つの漢字の意味に固執するよりは結び合った語をひとつの塊と考えて全体としての意味を理解させる学習法が望ましいと言える。

(3)　異なり語数が50以上の漢字と語の分析

ここでは，表4の(B)に出現する(13)～(22)の漢字について分析する。(19)の「一」と(22)の「水」の2字が名詞の意味を持つ漢字，その他の漢字「定」「熱」「合」「流」「上」「出」「数」「分」が動詞の意味を持つ漢字である。これらの漢字は名詞も動詞もすべて漢字1字の中に明確な意味を持ち，いずれもがそれ1字で語を作ることができる。つまり，(A)に比べると，漢字そのものに語としての役割が強く，それゆえに他の漢字との結びつきも強くなっている。また，それぞれの漢字が語として働く様子を見てみると，第一義での働きが強い。たとえば，(13)の「定」の基本的な意味（第一義）は動詞「定める／定まる」であり，その意味は「ものごとをきちんと決めて動かなくする（あるいはその状態）」である。「測定」が「はかって動かなくする」，「安定」が「落ち着いた状態で動かなくする」「一定」が「一つ状態で動かなくする」など，どれをとっても「定め

る／定まる」と第一義の働きが明確に反映されている。

他の漢字もすべて同様である。たとえば，(B)の第1行目を見てみると，「加熱」は熱を加えて「熱くする」，「混合」は混ぜて「合わせる」，「流動」は「流れて」動く，「抽出」は抜いてそこから「出す」，「成分」はある成り立ちのものを他から「分ける」など漢字の持つ意味と合成された語の意味が明確に類推できる。すなわち，漢字が持つ意味が明確で，かつそれ1字が語として働けるような漢字が作る語が重なる場合には，たとえそれが初めて目にした語であっても非常に意味の取りやすい，類推が容易な語であること，また，学習者にとっては理解度がはるかに大きいことが期待される。

以上から，(B)の異なり語数が50以上のものについては，(A)とは反対の結論が得られる。すなわち，異なり語の多い漢字については，ある漢字が持つ基本的な意味が名詞であっても用言であっても，その漢字だけで語としての働きを強く持つ。そのため，漢字の造語力も強く，さまざまな漢字と結びついて多様な2字漢字語を作る。このような漢字が作る2字漢字語を学習する際には，1字1字の漢字の意味をきちんと理解し，その意味を掛け合わせれば，たとえ新語であっても，その語の意味の類推が可能となることを示唆する。

4．漢字に対して例示する語の選択の試み

表5は表4に出現した漢字と語を分析し，提案した条件①～④を考慮して，各漢字に実際に例示する語を取り出した結果を示す。284全漢字の例示語を表示することは誌面の関係で割愛する（要求があれば提供）。この表で例示語の選択の試みについて説明する。

上段の(A)が異なり語が9以下の漢字，下段の(B)が異なり語が50以上の漢字である。表の左端から順に「順位」は該当漢字の多出順位，「異なり」はその漢字がもともと持っていた異なり語の数で，表4の異なり語数と一致する。「実数」は条件①～④を考慮して取捨した結果，該当漢字の例示語として提示した語の数，「番号」は便宜的につけた各語の記号，例示語の上欄の番号①～⑩は語数が数え易いようにつけた便宜的な番号である。

表中の例示語につけたマークについて説明する。何のマークもない語は該当漢字における「覚えなければならない例示語」，（ ）で囲んだ漢字は284位までに出現しておらず，学習対象から外れた漢字で，「覚えなくてもよい例示語」である。＜ ＞で囲んだ語は，『化学工学論文集』からは採取できなかった語であるが，漢字の意味を理解するために必要だと判断して，筆者らの体験的判断から追加した語で，漢字の基本的な意味を表す語であるため，「覚えなければならない語」に準ずる。更に［ ］で囲んだ語は，＜ ＞と同様に採取できなかった語であるが，漢字の意味の理解を助けるために選定した方がよいと判断して付け加えた語であり，「覚えなくてもよい例示語」に準ずる。たとえば，番号(1)の「条」にある［(第)（九）条］は採取できなかった語であるが，「～条」という表現を知っておく方が語の理解を助けると考えられるので追加した語であり，「第」も「九」も284位外の漢字である。番号(2)の「響」にある＜響く＞は採取されなかったが，語の意味を理解する上で基本となる語として追加した「覚えなければならない例示語」である。

各語の「異なり数」と「実数」を比べると(A)では番号(8)の「察」以外では語数が増えている。これは(A)では出現した異なり語の数が少ないので，相対的に＜ ＞や［ ］が多くなっているためである。「察」は表4では「観察」「考察」「推察」の3語が出現語として記載されていたが，表5では＜察する＞と「考察」の2語が例示語として提示されている。これは「察」の基本的な意味を示す「察する」が出現しないので，＜察する＞を追加した。「考察」は「考」が第52位で206位の「察」より先に学習されているので，例示語として採択されたが，「観察」「推察」の2語は「観」が282位で未習，「推」が209位で未習のため，選定条件に従い例示語として採択しなかった。(B)では実数が異なり漢字数より大幅に減っているが，これも同様な選定条件に従った取捨の結果である。

このような選択をすれば，必ず学習しなければならない漢字の意味だけをきちんと理解することで，覚えなければならない語については比較的に混乱することなく理解できる。同時に参考としての例示語により，学んだばかりの漢字の意味とその使い方を深めることができる。筆者らの少ない体験ではあるが，（ ）にある漢字はもし余裕があれば学習者の興味を引くであろうし，それが煩雑だと思う学習者はこれを飛ばすこともできることが分かった。（ ）の中にある漢字は284位内に出現する漢字に比べれば出現頻度は低いが，基本的な日常生活でも使われる漢字がこれらに該当することが多い。たとえば，ごく基本的である数字は，番号(19)の「一」以外には「二」が169位に多出漢字として出現するだけで「三」～「十」「百」「千」「万」

表5　実際に例示語として取り出した語の一覧

(A) 異なり語が9以下の漢字												
順位	異なり	実数	番号		①	②	③	④	⑤	⑥	⑦	⑧	⑨	⑩
111	1	2	(1)	条	条件	[((第)(九)条]								
125	1	3	(2)	響	〈響く〉	影響	[反響]							
166	1	6	(3)	御	〈御する〉	制御	[御～]	[御中]	[御主人]	[御手洗]				
167	1	2	(4)	討	〈討つ〉	検討								
218	1	5	(5)	領	領域	[(日)(本)領]	[領(土)]	[領収(書)]	[要領]					
254	2	4	(6)	操	〈操る〉	操作	操(業)	[操(縦)]						
281	2	3	(7)	慮	考慮	配慮	「(遠)慮]							
206	3	2	(8)	察	〈察する〉	考察								
258	3	10	(9)	非	〈非ず〉	非水	非常に	[非常口]	非～	[非論理的]	[非現実的]	〈非公式〉	〈非常識〉	
284	3	9	(10)	運	〈運ぶ〉	運転	運動	運用	[運]	[不運]	[(幸)運]	〈運転(手)〉		
256	5	5	(11)	硫	脱硫	硫化	硫酸	硫化物	硫(黄)					
251	7	10	(12)	容	〈容れる〉	容器	容量	容積	内容	定容	(許)容	容(易)	[容認]	

(B) 異なり語が50以上の漢字														
順位	異なり	実数	番号		①	②	③	④	⑤	⑥	⑦	⑧	⑨	⑩
3	50	7	(13)	定	定まる	定める	(規)定	(限)定	(想)定	(判)定	定(義)			
22	50	10	(14)	熱	熱	〈熱い〉	〈熱する〉	温熱	水熱	熱流	(蓄)熱	(除)熱	(予)熱	熱(風)
5	52	7	(15)	合	合わせる	合う	(足)し合わせる	化合	(集)合	(複)合	(会)合			
10	52	10	(16)	流	流れる	流す	流用	(交)流	流(跡)	(乱)流	(主) 流	流し(込)む	上流	下流
42	58	20	(17)	上	上	上げる	上がる	(立)ち上がる	(立)ち上げる	(引)き上げる	(汲)み上げる	(巻)き上げる	(押)し上げる	(取)り上げる
					(仕)上げる	上流	面上	(右)上	(軸)上	上(昇)	上(記)	上(述)	上(限)	
24	58	14	(18)	出	出す	出る	出し合う	流出	動き出す	(引)き出す	(押)し出す	(打)ち出す	(抜)き(出)す	(飛)び出す
					(取)り出す	出(典)	(提)出	出(来)る						
28	63	29	(19)	一	一	一つ	一定	一応	一度	一分	一(人)	一(日)	一(台)	一(段)
					一(個)	一(晩)	一(番)	一(括)	一(級)	一(乗)	一(枚)	一(桁)	一(歩)	一(因)
					一(貫)	一(辺)	一(覧)	一(致)	一(般)	(第)一	(唯)一	(統)一		
13	67	20	(20)	数	数	数度	定数	数分	(複)数	(総)数	数(日)	数(年)	数(十)	数(万)
					数(倍)	数(個)	数(字)	数(々)	数える	(個)数	(指)数	(代)数	数(百)	
2	70	17	(21)	分	(五)分	(何)分	(毎)分	アルコール分	〈X分のY〉	分(母)	(半)分	(余)分	(幾)分	分かる
					分ける	分かれる	(区)分	(色)分け	(振)り分ける	分(裂)	分(別)			
16	74	10	(22)	水	水	水分	水性	水(洗)	水(道)	水(滴)	水(田)	水(源)	水(深)	(海)水

はすべて284位内には入っていない。数字はアラビア数字を使うことが多いためであるが，それでもこれらの漢字は一般には漢字学習において最も早く学習する基本漢字である。これらの語を学習漢字として取り上げていなくても，例示語として繰り返し見れば，自然に理解し，覚えることが期待される。「年」「日」「月」「何」などの，日本語能力試験では4級から3級での必須漢字となっている漢字の多くはこれらがあまりにも基本的であるため上位漢字としては現れない。筆者らは，これらの語については，例示語の中で頻繁に目にすることで自然に理解できる漢字として学習すれば，いたずらに学習漢字を増やすよりは効率的かつ効果的でもあると考えている。

いくつかの漢字には複合動詞を作る特徴が見られる。(17)の「上」，(18)の「出」ではこれが顕著である。位置が移動することを意味する語にこの傾向の強さが見られ，284位外に出現する「引」では17語のうちの16語が，「押」では8語のうちの6語が，「込」では20語のうち19語が複合動詞となっている。これらの漢字も機会あるごとに組み合わさる一方の漢字と共に参考語彙として例示語として取り上げれば，学習者の助けになることが予想できる。

また，表5の例示語から漢字の持つ(a)具体性，(b)抽象性，(c)専門性がある程度見て取れる。具体性の強い漢字は名詞であれ用言であれ，漢字が示す意味もまた具体性に富んでいる。「水」「分」「数」「一」「上」「熱」などの漢字は具体的であり，これを使う語もまた具体的と言える。(22)の「水」では「水」のほかに「水分」「水性」などがあるが，これらは語が指し示す意味が明確である。これに対して(6)の「操」，(13)の「定」などはより抽象性が強い漢字と言える。「操作」や「想定」であっても「水分」や「一日」などの語に比べると意味は理解できても，その内容は抽象性が高い。また，(11)の「硫」は専門性に富んだ漢字である。多出順位229位に「孔」という漢字が出現するが，これも非常に専門性に富んだ漢字である。「孔」は「あな」であり，誰にでも理解できるが，日常的では「穴」の方が使われる。実際に例示語として提示した語も「多孔」「気孔」「開孔」「空孔」「孔部」「孔径」「孔数」「単孔」と一般の辞書ではまず見られない専門生の高い語である。

選定試行した例示語の特徴から，具体性の強い漢字がいわゆる「生活」にかかわる用語となる場合が多いこと，一方，抽象性の強い漢字が「論を立てる」用語に多いこと，さらに，専門性の強い漢字が「専門用語」を作り出す確率が高いことが明らかになった。

5.「論を立てる」用語の漢字学習から読解へと結びつける学習法について

前章では『化学工学論文集』に多出する漢字に例示語を提示して，漢字の基本的な意味の理解が語の意味の理解へとつながることを明らかにした。その結果，化学工学などの専門分野では，抽象性の高い語が「論を立てる」用語と多用されることを示した。具体的な語は実際の「モノ」や「コト」を観察したりすれば理解できる。このことは専門性の高い語も同じであると考えられる。ある語が専門用語であれば，それはその分野では常用の研究分野における日常語とも言えるからである。しかし，抽象性の高い語については，専門分野の記述文を正しく理解することと関係するため，文章読解の方法論にかかわる問題を内包していると言える。そこで，本章では「論を立てる」用語の漢字学習から読解へと結びつける学習法について考察する。

(1) 漢字学習と文章読解

文章読解の研究においては，その構造を把握する言語的手がかりとして，signaling（指標）や cue words, discourse marker などの語群がよく研究されており，読解指導上の具体的な示唆になることが明らかにされている（たとえば，Groz et al. 1989や Meyer 1985など）。これを科学技術文献の読解作業における漢字教育という視点から見ると，手がかりとなる語（ここでは漢字を含む語）はどのように規定でき，どのような取り扱いで教育に組み込まれることが望ましいのであろうか。

筆者らは多出漢字の分析において，いわゆる専門書に多出する漢字が，①一般的な読解のための漢字，②専門書一般の読解のための漢字，③特定の専門分野の書を理解するための漢字の3層から成っていることを示した（入戸野・武田 2002）。このことは，語にもまた①～③の，「漢字」を「語」に置き換えた同様な層があることを示唆する。すなわち，(1)日本語の文章を読むに当たっての一般的な語，(2)専門書というジャンルの文章を読むに当たっての専門書全体に共通する語，(3)ある特定の専門分野の文章の内容を理解するための，その分野に特有な語の3層である。

しかし，既に前章の例示語で示したように，これら(1)層～(3)層に属する語はその傾向を示すが，自動的にそれぞれの層に分類されるとを意味しない。たとえば，

「養生」という語である。この語は「病後は養生が必要だ」のような言い方ができ，(1)層であると言えるが，一方で，設備関係の仕事では「エレベーターの配線を養生する」と言い，一般の国語辞典などには見られない専門性のある語として(3)層に属する。また，「競売」という語は，ごく一般的なオークションの場合には「きょうばい」と読まれ(1)層として認識されるが，法的措置によるオークションの場合には「けいばい」と読まれ(3)層となる。更に，「干渉」という語は，(1)層では「よけいな口出し」を意味する語として認知されているが，物理学の分野では全く異なる意味内容を持って(3)層に属し，「二つ以上の音や光の波が重なり合って，その力を大きくしたり小さくしたりする現象」を意味する。

このように考えると，専門分野で多用される語を日常的な語，専門書一般の語，専門用語と厳密に区分けすることは難しい。むしろ読み手がその語をどの層の意味として認識するかによって，ある語がある層に属するというよりは，ある語のあるべき場所が定まると言うべきである。言い換えれば，読み手がある語について，「読んでいる文章の内容に依存している」と認識するときには専門用語（(3)層）であり，「読んでいる文章の記述様式を担っている」と認識するときには専門書としての構造様式に関わる語（(2)層）であり，「これらのどちらとも認識しない」ときには日常一般の用語（(1)層）になると考えられる。　この点について，辻井（1985）は機械翻訳の立場から専門文献翻訳について，ある専門分野の体系が明らかになっても，そこから直接意味が与えられる単語だけが現れるわけではないことを指摘し，実際に頻繁に現れる，いわゆる日常語（たとえば「紹介する」「発展する」「優位」などといった語が示す概念）に明示的な定義を与えることは，非常に困難で，機械の苦手とするところであると述べている。

機械が苦手とするこのような推察作業は，漢字の学習に苦慮する留学生にもまた同様に苦手となる。だからこそ，教授者には苦手が克服できるように配慮した語学教育が望まれるのであり，そのためには，漢字の学習に対してより効果の期待できるテキストの作成とその提供が重要となると筆者らは考える。

(2)　留学生を対象とした基本語彙の概念について

留学生のための基本語彙を取り扱った成書は既にいくつか出版されている。その代表的なものを見ても，基本語彙の線引きは「いかなる目標を持つて日本語を学習するにしても，一応は通るべき基礎的な学習語を第一次，第二次に分けての選定（『日本語教育における基礎学習語』（加藤，1963，1964）であったり，「留学生等外国人の日本語学習者が専門領域の研究または職業訓練に入る基礎としてはじめに学習しておくべき，日本語の一般的・基本的語彙について，妥当な標準を得るための基礎資料として作成」（『日本語教育基本語彙第一次集計資料2000語』（国立国語研究所，1978）であったりする。

これらは日本語教育の観点から，「専門語彙」と「一般語彙」の線引きをし，基本語彙として一般語彙の中から第一に必須なものを集めようとしたものである。つまり，いずれもが専門語彙を学ぶ前に知っておくべき一般語彙として基本語彙を選定していると言える。しかし，ここには専門語彙と一般語彙の間にあって，専門書としての特徴を示す語彙が分離されておらず，専門書が専門書としてあることが認知できるための語彙，つまり，専門書としての特徴を担う語の規定がない。その理由としては，日本語教育が一般とか専門とかいった，個々に孤立した範囲を超えた，「相互に関連性のある整合的な言語的コミュニケーションの基本単位」（天満 1989）として研究されてきているためと思われる。つまり，読解教育は未だに抽象的ないわゆる談話型教育という立場から捉えられている現状であると言うことができる。

これらとは異なる観点から基本語彙を選定しようとしたものに林（1985）の基本語彙545というものがある。これは新聞を資料とし，ここに出現した語を，(1)辞に連続する詞，(2)思考運用のための用語，(3)事象認知のための用語，(4)話題の題目用語の4つのカテゴリーに分け，語の使われ方の意味から教育上必要な基本語彙を系統化して捉えようとしたものである。しかし，日本語教育か，あるいは専門教育かといった二分法での分析でないところが非常にユニークである。

留学生が専門書を読もうとするとき，それが専門書であることが認識できる語がきちんと理解できるような漢字・語彙教育は，結局は正しい内容把握へ留学生を導くことになると言える。したがって，漢字を学習するということは「語」として文章（科学技術論文）との関わりを学ぶことでもある。ここに，漢字教育を読解のための signaling（指標）として捉え直し，語という具体的なリストでその守備範囲を明確に示すことの意義があると考える。では，漢字教育を読解のための signaling（指標）として捉える方法はあるだろうか。

(3) 日常の語，専門の語，文章を読み進めるための構造把握の語と言う分類

教授する側ばかりでなく，文章を読む（学ぶ）側にも，一般の語，専門用語，文の構造を把握するための語に何か線引きのようなものがあるはずである。統計処理ができるほどのきちんとした調査ではないが（調査のための事前調査），研究留学生40人を対象に，日本語について「一般の語」，「専門の用語」，「文章を読み進めるための構造にかかわる語」のイメージを自由回答形式で挙げてもらった（1997a，1997b）。

その結果，ほとんどの理工学系研究留学生が「一般の語」とは電子辞書で調べられる語であり，「専門用語」は専門用語辞典で調べられる語であると回答した。しかし，「文章を正しく理解して読み進めるための語とはどのようなものか」という質問に関しては，①「序論」「本論」「結論」「一章」「一節」のような表現，②「しかるに」「本論文」「すなわち」「以上から」「端的に」といった書き言葉，③2字漢字語，④受け身の表現，⑤辞書にない言葉，といった回答であった。

これらは筆者らの予測した回答と大きくずれてはいない。しかし，「文章」にはさまざまな種類があるにもかかわらず，研究留学生にとっては①に示されたように日本語を論文として捉えられているということは興味深い。それほどに彼らの日常では「論文を読む」ということが日常的であるということであり，正に，彼らの研究留学生活での切実さの現れと言える。しかしながら，全ての回答が，理工系分野の文章や論文という枠を超えて，事実を示すための文章，論理的な思考を必要とする文章という事実主体型の論理的な文章表現の語として広く一般に出現する語そのものであることは重要な意義を持つ。

⑤の「辞書にない言葉」とは，文の意味を分かろうとして辞書を調べても，該当する語が専門用語辞典にも電子辞書にもないということであり，このような語を知らないと正しく読解できないという意味である。たとえば，「～に際する（名詞）」「～に際して，（文）」という表現では，「際し」も「際する」も「際」も文の理解に役立つ形では電子辞書に出現はしていない。たとえそれらが見つかって例示文があったとしても，それらは彼らの文章読解にはあまり役立つものではない。専門用語とも言えないため，専門用語辞典にも現れず，ちょうど一般の語と専門の語の狭間にある言い回しと言うことができる。これらの多くは「～に関して，（文）」「～及ぶ（名詞）」などといった，いわゆる助詞相当句に属するものが多く，その漢字に「動詞」の意味が含まれているが，かなり抽象的な表現となっているものである。

(4) 多くの例示語を提供する必要性

論理的な文章としての科学技術論文を読み進めるためには，上に挙げたような留学生の「文章を正しく理解して読み進めるための語」に対する理解の特徴に配慮し上でその解決をはかる必要がある。しかし，彼らにはまた別の課題もある。専門用語も一般的な用語も辞書で調べられが，問題はその読み方である。今は電子辞書が進化しているので，読めない漢字は直接手書きすれば機械が読みとる。しかし，専門用語に類するものは電子辞書には収録がない。このようなことを勘案すると，やはり多くの語を例示することは学習者の漢字に対する理解を高める上では有効なことであると考えられる。

また，彼らの回答からは記述文章としての表現語を漢字学習の中に十分取り入れる必要のあることを示している。「大変」や「非常に」や「即ち」は，科学雑誌の編集要領で副詞として平仮名書きすることが勧められているが，未だ一般的には漢字が多く使われる。このような語であっても，多用されるならば多出する語として取り扱うのが学習者を助けることになる。さらに，受け身文型については，漢字の学習時に語の形の派生として取り入れたり，文例を付加することで解決できる。論文に多用される名詞についても例示語で解決できる。彼らは文章を読む（学ぶ）ということを，論理的な文章を読むと理解しているということ，抽象的な漢字や語をうまくまとめあげて表現したいことを意味する。そのためには，留学生の母国語での思考様式を日本語学習に運用することが重要な意義を持つ。研究分野を問わず，科学技術文献を読解する上ではこの点の解決を図ることができるような語を例示語として選択し，実作業効率の高い漢字教育へ結びつける必要がある。

おわりに

『化学工学論文集』に出現した多出漢字と語を検討・考察し，1つの試みとして，上位284字に付す例示語を提示する方法について考察した。筆者らの少ない実践体験ではあるが，学習効果はおおむね満足のいくものであり，学習者はこれにより意味の類推がしやすくなったと捉えているようである。しかしなから，特に抽象性の強い「論を立てる」用語をつくる，いわゆる

思考運用型の漢字については，一括してまとめ上げてみる検討も必要であることが課題として出てきた。このためには，教師が専門文献に現れた語彙を単なる名詞とか動詞などとしてではなく，論理遂行のための「思考運用型」のパターンを理解させるという意識を持って授業や教材づくりをする必要がある。ある語が使われる意図，その展開の規則性を規定できなければ，文章読解の作業の上では，辞典などの項目に「論文などで使われる語彙」と記述する程度の貢献しかできない。「思考運用型」と分類しても，これらの語の組み合わせが読解作業の上でどのような運用上の特性を持って使われるかを明らかにするためのより細かい分類作業が必要になろう。筆者らが提案した284漢字の選定条件とその提示順序は適切なものであると考えているが，今回提示した理解するための例示語とその例示方法については実践体験を踏まえてさらに改善したいと考えている。今後はそれらの検討を踏まえて，「思考運用型」用語の選定条件と例示方法について考察を進めて行きたい。

引用文献

Meyer, B. J. F., (1975a) : Theories of Text Analysis: Prose Analysis: Purposes, Procedures, and Problems, pp. 11-64, Hillsdale, New Jersey.

林四郎（1985）:『応用言語学講座1　日本語の教育』明治書院。

辻井潤一（1987）: 機械翻訳と理解，心理学評論，心理学評論刊行会，Vol. No. 3，213～230。

天満美智子（1989）:『英文読解のストラテジー』，「読解とは」，8～9　大修館書店。

Groz, J. B. et al., (1989) : Foundation of Cognirive Science, (ed. Michel I. Posner)（邦訳『言語への認知的接近』認知科学の基礎②，佐伯　胖，土屋俊監訳，第3章「談話」，113～152，産業図書。

武田明子・入戸野修（1997a）: 科学技術文献読解のための漢字指導法の見直し，科学教育研究，Vol. 21，No. 4，207～216。

武田明子・入戸野修（1997b）: 電子辞書による漢字検索時間の検討，教育工学関連学協会連合第5回全国大会論文集，155～156。

入戸野修・武田明子（2002）: 留学生に対する科学技術専門書読解のための教科書作成に向けて－化学工学における専門日本語漢字－，福島大学地域創造，第14巻第2号，77～87。

入戸野修・武田明子（2003a）: 研究留学生が科学技術専門書を読解するための基本漢字の例示語選定に関する検討，福島大学教育学部論集，理科報告第67号，1～12。

化学工学会（2000）:『化学工学論文集』，Vol. 26，No. 1～6。

入戸野修・武田明子（2003b）: 研究留学生に対する科学技術専門書読解のための漢字記述語の分析－化学工学における漢字を含む語－，福島大学地域創造，第15巻第2号，51～62。

Comments on Selected Examples for Practice of Basic Kanji for Teaching Foreign Graduate Students How to Read Japanese Technical Papers

Osamu NITTONO and Akiko TAKEDA

How to learn Japanese Kanji is necessary for foreign graduate students from non-Kanji countries, who are eager to understand scientific and technical Japanese papers, and then to have research activities in Japan as soon as possible. We have analyzed the characteristics of technical terms usually used in papers of chemical engineering, especially in Kagaku Kogaku Ronbunshu, and showed that only 284 different Kanji can cover 80% of the total number of Kanji included in the papers. In this study we tried to find how to select examples for practice of basic Kanji for each Kanji, which are useful not only for everyday life, but also for knowing a meaning of unknown Kanji by analogy. Our several trails for foreign students proved such examples for practice were effective for knowing a meaning of unknown Kanji by analogy. This study showed a number of logical expressions usually contain highly abstract or nonrepresentational words including Kanji, and also suggested that such Kanji used in logical expressions need to be selected for reading scientific and technical Japanese papers.

Symbiotic Systems Science Vol. 3
Report for Grant-in -Aid for Scientific Research (B) (2003 ～ 2005)
Fabrication of semi-conductor titanium oxide films containing isolated fine iron-based metal particles and measurement of the GMR effect under illumination of UV light

共生のシステム Vol.3
科学研究費補助金研究成果報告書 (2003 ～2005)
鉄基磁性微粒子を孤立分散した半導体酸化チタン膜の合成と磁気抵抗の光誘起効果の測定

2006 年 3 月 31 日 発行
発行者 福島大学 理工学群 共生システム理工学類
〒960-1296 福島県福島市金谷川 1 番地
電話 024-548-5213
印刷・製本 阿喜印刷所

Printed in Japan 非売品